



UNIVERSITAT DE BARCELONA

Forefront cold spray additive manufacturing development by leveraging new spraying strategies

Rodolpho Fernando Vaz

ADVERTIMENT. La consulta d'aquesta tesi queda condicionada a l'acceptació de les següents condicions d'ús: La difusió d'aquesta tesi per mitjà del servei TDX (www.tdx.cat) i a través del Dipòsit Digital de la UB (diposit.ub.edu) ha estat autoritzada pels titulars dels drets de propietat intel·lectual únicament per a usos privats emmarcats en activitats d'investigació i docència. No s'autoritza la seva reproducció amb finalitats de lucre ni la seva difusió i posada a disposició des d'un lloc aliè al servei TDX ni al Dipòsit Digital de la UB. No s'autoritza la presentació del seu contingut en una finestra o marc aliè a TDX o al Dipòsit Digital de la UB (framing). Aquesta reserva de drets afecta tant al resum de presentació de la tesi com als seus continguts. En la utilització o cita de parts de la tesi és obligat indicar el nom de la persona autora.

ADVERTENCIA. La consulta de esta tesis queda condicionada a la aceptación de las siguientes condiciones de uso: La difusión de esta tesis por medio del servicio TDR (www.tdx.cat) y a través del Repositorio Digital de la UB (diposit.ub.edu) ha sido autorizada por los titulares de los derechos de propiedad intelectual únicamente para usos privados enmarcados en actividades de investigación y docencia. No se autoriza su reproducción con finalidades de lucro ni su difusión y puesta a disposición desde un sitio ajeno al servicio TDR o al Repositorio Digital de la UB. No se autoriza la presentación de su contenido en una ventana o marco ajeno a TDR o al Repositorio Digital de la UB (framing). Esta reserva de derechos afecta tanto al resumen de presentación de la tesis como a sus contenidos. En la utilización o cita de partes de la tesis es obligado indicar el nombre de la persona autora.

WARNING. On having consulted this thesis you're accepting the following use conditions: Spreading this thesis by the TDX (www.tdx.cat) service and by the UB Digital Repository (diposit.ub.edu) has been authorized by the titular of the intellectual property rights only for private uses placed in investigation and teaching activities. Reproduction with lucrative aims is not authorized nor its spreading and availability from a site foreign to the TDX service or to the UB Digital Repository. Introducing its content in a window or frame foreign to the TDX service or to the UB Digital Repository is not authorized (framing). Those rights affect to the presentation summary of the thesis as well as to its contents. In the using or citation of parts of the thesis it's obliged to indicate the name of the author.



UNIVERSITAT DE
BARCELONA

**FOREFRONT COLD SPRAY ADDITIVE MANUFACTURING
DEVELOPMENT BY LEVERAGING NEW SPRAYING
STRATEGIES**

Rodolpho Fernando Vaz



UNIVERSITAT DE BARCELONA

Faculty of Chemistry

Doctoral Program in Engineering and Applied Sciences

FOREFRONT COLD SPRAY ADDITIVE MANUFACTURING DEVELOPMENT BY LEVERAGING NEW SPRAYING STRATEGIES

Ph.D. Thesis

Rodolpho Fernando Vaz

SUPERVISORS

Irene Garcia Cano, Ph.D.
Profesor at Universitat de Barcelona
CEO at Thermal Spray Center, CPT

Javier Sanchez, Ph.D.
Director at Thermal Spray Center, CPT

TUTOR

Irene Garcia Cano, Ph.D.
Profesor at Universitat de Barcelona
CEO at Thermal Spray Center, CPT

ACKNOWLEDGMENTS

Many thanks to those who supported my activities through this doctorate journey. My most sincere thanks:

First, the almighty God for the life that He had blessed me with, for guiding me through difficult times, and for giving me the courage to face each challenge in my path. To my family, especially my lovely wife, Michelli Crepaldi, and sons, Gabriel Crepaldi Vaz and Mariana Crepaldi Vaz, who had abstained from my company for many moments so that I dedicated much time to the investigation. To my parents, Donizeti Tavares Vaz and Jedir de Melo Vaz, who invested time and financial resources in my formal education.

My thesis tutor, Dr. Irene Garcia Cano, and thesis director, Dr. Javier Sanchez, who always believed in my capacity to face the challenges during the doctorate period, trusting me, and supporting my suggestions of collaboration or experiments. Before all of my colleagues from Thermal Spray Center (CPT), I thank Dr. Karen Juliana Vanat,, from Serviço Nacional de Aprendizagem Industrial (SENAI), who introduced me to CPT directors in 2018, and Dr. Ramón Sigifredo Cortés Paredes, from Universidade Federal do Paraná (UFPR), who motivated me to move from Brazil do Spain. From the CPT group, I thank Victor Gomez for the hundreds of sample depositions, Unai Ocaña and Ziortzia Garcia Corral for accepting the challenge of writing and developing the robot programs, Dr. Ana Maria Martos, Dr. Alessio Silvello, Dr. Vicente Albaladejo, Dr. Beatriz Garrido, Andrea Garfias, and Edwin Torres, besides Dr. Sergi Dosta, from Universitat de Barcelona (UB), for the innumerable discussions about experiment designs and results. I also thank Josep Martorell for his contribution and Engineering grade final degree project, studying the effects of CSAM Metal Knitting parameters on the properties of CSAM-ed Al parts. From the Scientific and Technological Centers (CCiT) facilities of UB, I thank Dafne de Sande, Dr. Xavier Alcobe, and Dr. Josep Maria Bassas, for the dozens of laser scattering and X-ray diffractometry samples characterization.

The kind scholars who collaborated in experiments that were not supported in the CPT and UB or CCiT, Dr. Vladimir Luzin, and Dr. Filomena Salvemini, from the Australian Nuclear Science and Technology Organisation (ANSTO), Dr. Anderson Geraldo Marendra Pukasiewicz, from Universidade Tecnológica Federal do Paraná

(UTFPR) campus Ponta Grossa, M.Sc. Claiton Mattos, from Lactec Institute, Dr. Julián Ávila, from Universitat Politècnica de Catalunya (UPC), Dr. Pasquale Cavalière, from Università del Salento, and Dr. Laura Capodiecì, Dr. Antonella Rizzo, and Dr. Daniele Valerini, from Agenzia Nazionale per le Nuove Tecnologie, l'Energia e lo Sviluppo Economico Sostenibile (ENEA), Dr. Giovani Gonçalves, from Universidade de São Paulo (USP), and Dr. Guilherme Abreu Faria, from Deutsches Elektronen-Synchrotron (DESY).

The financial support received once the presented work had been possible by a predoctoral working contract at CPT during the first doctorate year and by the Catalanian Government for the program's remaining years. Grant: 2020 FISDU 00305. The grant PID2020-115508RB-C21 and EIN2020-112379 was funded by MCIN/AEI/10.13039/501100011033 and, as appropriate, by “ERDF A way of making Europe”, by “European Union NextGenerationEU/PRTR”.



Thermal Spray Center
Centro de Proyección Térmica
Centre de Projecció Tèrmica



Agència
de Gestió
d'Ajuts
Universitaris
i de Recerca
AGAUR



**Generalitat
de Catalunya**



**Funded by the
European Union**
NextGenerationEU

TABLE OF CONTENTS

Abstract	3
Thesis Structure	7
1. Introduction	13
Article 1 “A Review of Advances in Cold Spray Additive Manufacturing”	15
2. Scope of the Work	65
3. Experimental Procedures.....	69
3.1. Feedstock Materials and their Characterization	69
3.2. Samples and Parts Production.....	71
3.2.1. Cold Spray Deposition	72
3.2.2. High-Velocity Oxy-Fuel Deposition	73
3.2.3. Post-Treatments	74
3.2.3.1. Heat Treatment.....	74
3.2.3.2. Spark Plasma Sintering	75
3.2.3.3. Hot Isostatic Pressing.....	76
3.3. Materials Characterization.....	76
3.3.1. Microstructural Evaluation	76
3.3.2. Mechanical Properties	78
3.3.2.1. Microhardness	78
3.3.2.2. Adhesion Testing	78
3.3.2.3. Nanomechanical Properties.....	79
3.3.2.4. Tensile Testing	79
3.3.2.5. Residual Stress Measurement.....	80
3.3.2.5.1. X-Ray Diffraction.....	81
3.3.2.5.2. Neutron Diffraction	82
3.3.3. Wear Performance.....	83
3.3.3.1. Abrasion Wear Testing	83
3.3.3.2. Friction Wear Testing.....	84
3.3.3.3. Water Impingement Wear Testing	85
3.3.3.4. Scratch Testing.....	85
3.3.3.5. Fretting Wear Testing	86
3.3.4. Corrosion Behavior	87
4. Results and Discussions.....	91
4.1. CSAM Feedstock Powders	92
4.1.1. Characterization and Selection.....	92

4.1.2.	Influence of Powder Characteristics on CSAM-ed Parts Manufacturing and Properties	99
	Article 2 “The Influence of the Powder Characteristics on 316L Coatings Sprayed by Cold Gas Spray”	103
4.2.	Geometric Limitations of CSAM Deposition Strategies	123
4.2.1.	Conventional Approach to Produce CSAM-ed Parts	123
	4.2.1.1. Effects and Optimization of CSAM Traditional Strategy Parameters on Part’s Shape	125
4.2.2.	New Approach to Produce CSAM-ed Parts	128
	Article 3 “Metal Knitting: A New Strategy for Cold Gas Spray Additive Manufacturing”	129
	4.2.2.1. CSAM Traditional and Metal Knitting Strategies for Al Parts	148
4.3.	CSAM-ed Parts	150
4.3.1.	Characterization of CS-ed Samples.....	150
	Article 4 “Fretting Wear and Scratch Resistance of Cold-Sprayed pure Cu and Ti”	151
4.3.2.	Residual Stress Evaluation.....	171
	4.3.2.1. Residual Stress on CS-ed Samples.....	171
	4.3.2.2. Residual Stresses on CSAM-ed Samples	174
	Article 5 “The Effect of Annealing and Deposition Strategy on 316L Properties Produced by Cold Spray Additive Manufacturing”	175
4.3.3.	CSAM-ed Parts Obtained	211
4.3.4.	Post-treatments	212
	4.3.4.1. Heat Treatments	213
	4.3.4.1.1. Heat Treatment of CSAM-ed 316L.....	213
	4.3.4.1.2. Heat Treatment of CSAM-ed Ti Alloys	216
	4.3.4.1.3. Heat Treatment of CSAM-ed Al	219
	4.3.4.2. Hot Isostatic Pressing	223
	4.3.4.3. Spark Plasma Sintering	226
4.4.	Hybrid Thermal Spray System for AM	230
	4.4.1. HVOF Feedstock Powders Characterization	230
	Article 6 “Improving the Wear and Corrosion Resistance of Maraging Part Obtained by Cold Gas Spray Additive Manufacturing”	235
5.	Overall Discussions	253
5.1.	Influence of Feedstock Powders on CSAM-ed part Properties	253
5.2.	Improvement of Geometric Accuracy	254
5.3.	CSAM-ed Parts Mechanical Properties	255
5.4.	Thermal Spraying Hybrid System.....	257

5.5. Final Considerations.....	257
6. Conclusions	261
7. References	267
8. Appendix.....	279
8.1. Works Published	279
8.2. Works Presented in Congresses.....	284
8.3. Awards and Funding Projects	289
8.4. CSAM-ed Parts, Strategy, Parameters, Geometric Aspects, and Images..	291

ABSTRACT

ABSTRACT

Additive manufacturing (AM) builds a physical object by adding material layer by layer rather than removing material through machining. It is also known as 3D printing, as it typically involves using a digital model to create a physical object by adding material in a series of layers. AM has been studied for many materials, such as polymers, ceramics, composites, biomaterials, and metallic alloys. It has also been employed for many applications and purposes, such as customization, complex geometries, lightweight structures, and sustainable manufacturing.

Different processes have been presented and studied for AM of metals, highlighting the laser- and welding-based ones presented in the literature, which are more industrially mature. Cold Spray Additive Manufacturing (CSAM) is an alternative to produce freeform parts by accelerating powder particles at supersonic speed, which impacting against a substrate material trigger a process to consolidate the CSAM-ed part by bonding mechanisms. As with any other AM processing, CSAM has pros and cons. Its advantages include its high deposition rate and efficiency, low thermal input, wide range of spraying materials, and low part distortion. However, low geometric accuracy, high equipment costs, and low mechanical properties are some CSAM disadvantages.

Scholars have contributed to improving the CSAM industrial maturity by solving some technique limitations. This thesis presents alternatives developed and evaluated to push this frontier of knowledge even further and make CSAM an even more attractive AM process. First, understanding the state-of-art through a critical review in the introduction section; second, presenting the solutions already published by scholars, which were the base for developing new and innovative solutions, and then evaluating the effectiveness of these new strategies.

For the CSAM geometric accuracy limitation, this thesis presents different robot manipulation strategies, changing the CS gun linear velocity and deposition angles. It makes a constant part sidewall inclination that demands an angle rectifying layer. An innovative CSAM strategy named Metal Knitting has been designed, developed, and tested. In this strategy, the CS gun does not follow a linear path but a virtual cone-like one, which results in a high control of the part shape, e.g., vertical bulk sidewalls or thin and high walls.

To improve the CSAM-ed material mechanical properties, the CS process parameters are optimized to reach the most appropriate particle velocity, resulting in lower porosity and higher bonding and cohesion of particles. Besides that, deposition post-treatments are evaluated. For 316L, heat treatments improve the cohesion of particles and material isotropy but reduce its hardness. For CSAM-ed Maraging, the deposition of carbides by HVOF improved the material wear performance, presenting a hybrid thermal spraying system with a CSAM-ed bulk strengthened by a hard coating layer.

Considering the economic feasibility of CSAM, the use of less sophisticated, and therefore less costly, feedstock powders has been deposited. They can be deposited, obtaining parts with similar properties to those obtained using more sophisticated and pricey powders. Water atomized 316L performs similarly to the gas atomized powders, which are at a higher-level price. Irregular particles are also good choices for CSAM Al and Ti deposits. Regarding this reduction of CSAM deposition costs, the Metal Knitting strategy has an advantage over the traditional ones because of its shorter spraying time and higher layer thickness.

THESIS STRUCTURE

THESIS STRUCTURE

This thesis is structured in several chapters that are assembled in a way that allow for an organized and logical flow of information, from the reasons and objectives until the conclusions deriving from the results obtained. This document includes as well some published articles written as a result of the research done in this thesis. This thesis also contains the information about additional research that supplement the published papers and extend the scope of the thesis beyond the articles' results. It is schematically presented in Figure 1, followed by a summary of their contents.

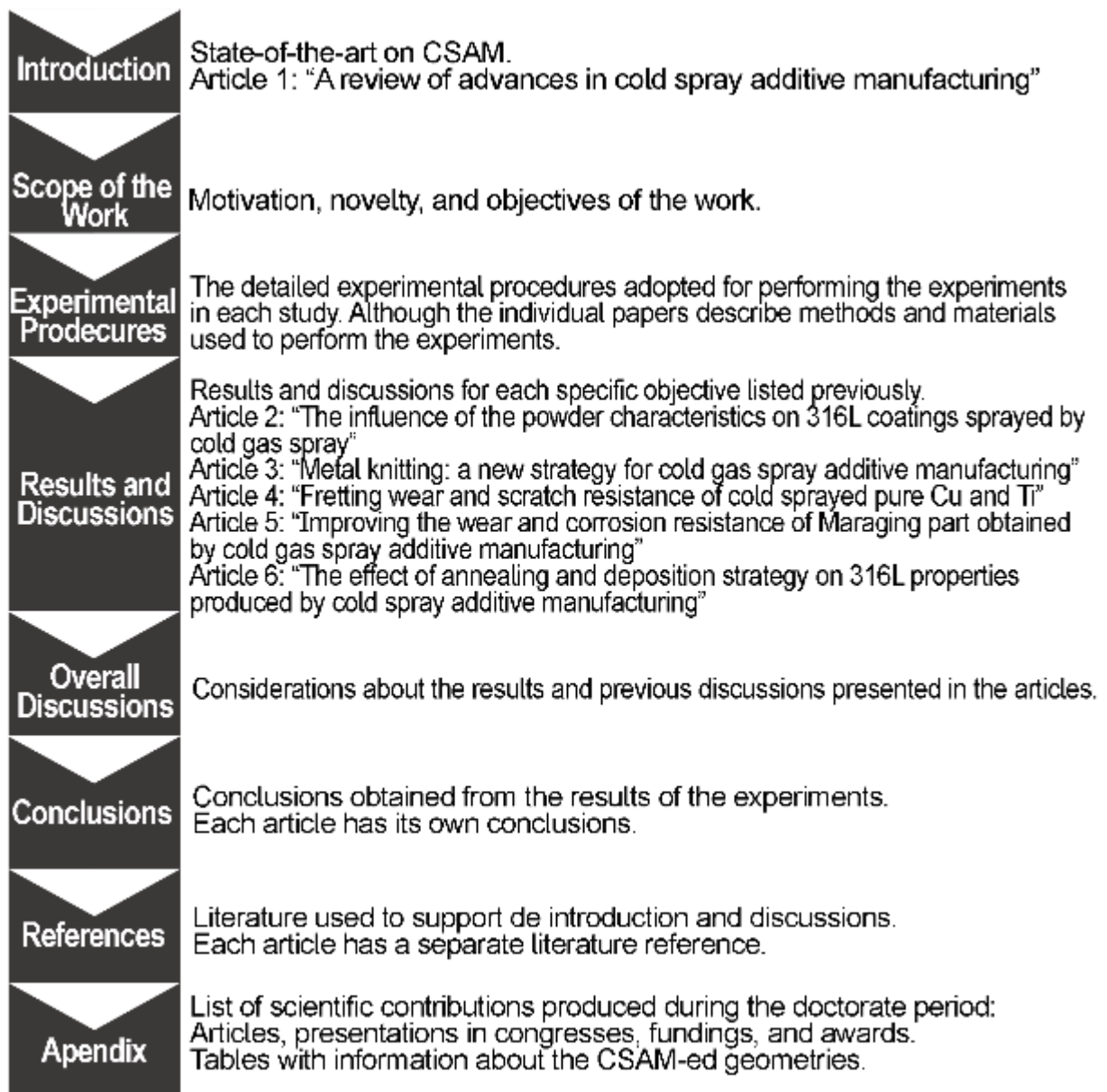


Figure 1: Thesis structure.

Chapter 1, "Introduction", presents the state-of-the-art in CSAM, starting by placing CS in the role of AM techniques, then explaining CSAM principles, listing the feedstock materials commonly applied and their adequate properties. The sequence lists the limitations, pros and cons, and challenges of the technique. Finally, the section indicates the academic interest in the theme CSAM through a bibliometric review and the technical solutions or alternatives to improve the CSAM-ed materials' properties, i.e., post-treatments and assisted CSAM or hybrid systems. Chapter 1 is composed primarily of Article 1, "A Review of Advances in Cold Spray Additive Manufacturing". This state of the art description serves as a framework to identify the areas still to be developed in CSAM which points at the reasons why this thesis is done that are explained in Chapter 2.

Chapter 2, "Scope of the Work", shows the motivation to develop this thesis and its main and specific objectives, which are linked with the Chapter 4 sections.

Chapter 3, "Experimental Procedures", presents the CSAM-ed materials and explains all the characterizations, testing, and performance evaluations. The Chapter details the tests, lists the applicable standards, and shows the equipment used for the activities.

Chapter 4, "Results and Discussions", is divided into sections to present the achievements for each specific objective listed in Chapter 2. The first part of Chapter 4 was focused on materials selection and its influence on the properties of CSAM-ed samples. Some of these results were published in Article 2, "The Influence of the Powder Characteristics on 316L Coatings Sprayed by Cold Gas Spray"; other feedstock powders for CSAM are characterized and analyzed in Chapter 4.

Making CSAM parts with the selected powders, their basic properties were considered, and then new strategies for CSAM were developed and evaluated. In this section, Article 3, "Metal Knitting: A New Strategy for Cold Gas Spray Additive Manufacturing", presents CSAM spraying strategy development to improve the geometric accuracy of CSAM-ed parts. Also, the properties of CSAM-ed parts and their improvement are discussed for 316L, Cu, Ti, and Maraging in Article 4, "Fretting Wear and Scratch Resistance of Cold-Sprayed pure Cu and Ti", Article 5, "The Effect of Annealing and Deposition Strategy on 316L Properties Produced by Cold Spray

Additive Manufacturing”, and Article 6, “Improving the Wear and Corrosion Resistance of Maraging Part Obtained by Cold Gas Spray Additive Manufacturing”.

The final part of Chapter 4 deals with the proposed post-treatments to improve the properties and performance of the CSAM-ed parts, evaluating this improvement by different tests and techniques, such as microstructural characterization, hardness evolution, fretting, tensile strength and/or residual stresses. Also, a hybrid thermal spray process is considered to combine different techniques.

Chapter 5, “Overall Discussions”, makes an outline correlating and crossing the results and discussions shown in the Chapter 4 sections and each article published. This overall discussion helps to obtain a typical CSAM behavior or a trend, as the effectiveness of the technical solutions presented along the thesis for the CSAM limitations and to link the results obtained with the initial objectives of this thesis.

Chapter 6, “Conclusions”, summarizes the more relevant outcomes of the thesis.

Chapter 7, “References”, indicates the literature cited in the thesis, considering that some of these documents are duplicated in the articles’ reference sections, which are unique for each article.

Finally, Chapter 8, “Appendix”, lists the scientific contributions of the Ph.D. candidate during the doctorate program period (Sep. 2019 to Aug. 2023), considering articles published, works presented in congresses and conferences, and funding, projects, and awards received.

Chapter 1

INTRODUCTION

1. INTRODUCTION

This section presents the evolution of Additive Manufacturing (AM) as a family of processes capable of processing diverse materials for making parts. The materials most studied and industrially applied are polymers, but ceramics, composites, and metals have increased their applications. Each material has one or more adequate fabrication methods and wariness that must be considered to obtain the best part quality, highlighting the highest dimensional accuracy, mechanical properties, the lowest costs, or minimum time elapsing for making it, among others. ISO/ASTM 52900-15 [1] presents AM definitions, terminology, and a general classification of AM process in different categories, as schematically shown in Figure 2 for metallic materials. Although this standard also contemplates polymers, ceramics, and composites as AM-ed materials.

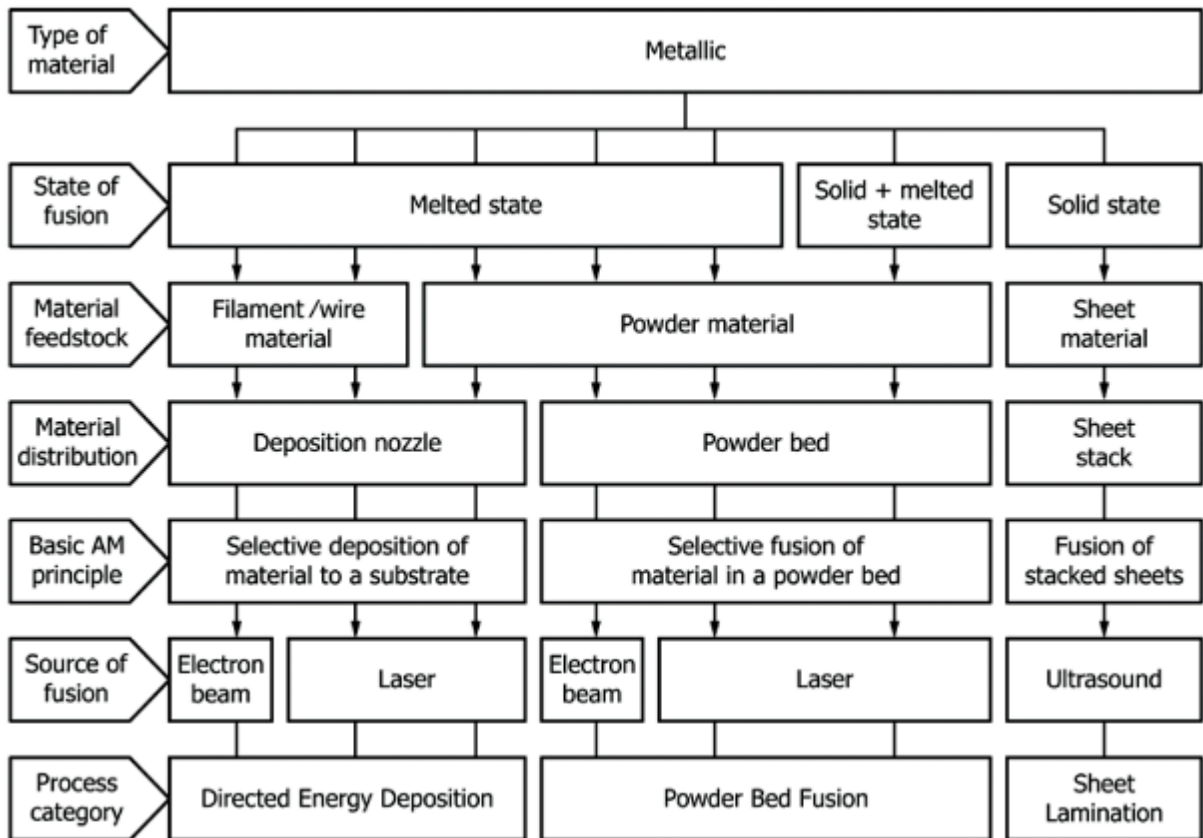


Figure 2: AM classification, as ISO/ASTM 52900:15 [1].

ISO/ASTM 52900:15 [1], as seen in Figure 2, does not contemplate Cold Spray (CS) as an AM process; however, in that scheme, CSAM should be classified as Metallic > Solid State > Powder Material > Deposition Nozzle, though from the fifth row, CSAM does not fit into any category, mainly because CS does not melt or sinter the

sprayed material for the CSAM-ed part consolidation. CS has been classified as a thermal spraying process, developed to make coatings for the most different purposes. CS' principles are based on high kinetic and low thermal energy sprayed particles, resulting in coatings with very low porosity and oxidation, competing with other thermal spraying processes, as presented in Figure 3. With the evolution of the thickness of CS-ed layers, scholars have developed the CSAM as a feasible method to grow not only coatings but also large parts or repair damaged components, introducing CSAM.

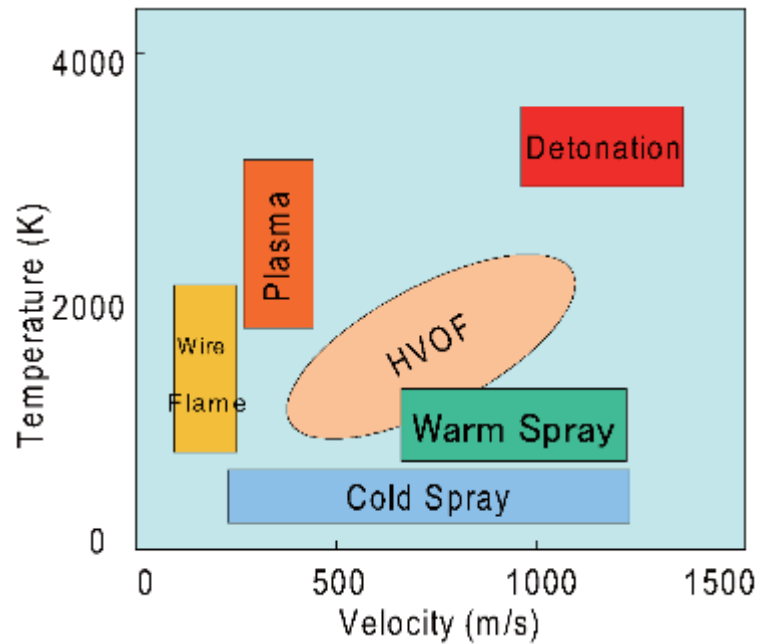


Figure 3: Classification of thermal spraying processes.

Article 1 presents an overview of the CSAM evolution, its place among the metal AM processes, CS principles or fundamentals, characteristics, facing challenges, and some solutions presented in the literature to overtake the CSAM cons, e.g., robot new strategies, heat treatments, or hybrid systems of deposition, among others. This article also presents a bibliometric review that indicates how scholars have increased their interest in publishing solutions for the CSAM limitations and advancing the CSAM from the academic field to solve real problems in the industry. Based on the challenges presented in the Introduction section, a set of experiments were performed considering the selection of CSAM feedstock powders, CSAM-ed mechanical properties, and microstructural characteristics, CSAM-ed residual stresses, wear and corrosion performance or behavior, and the effect of post-treatments on these characteristics.



ARTICLE 1 “A REVIEW OF ADVANCES IN COLD SPRAY ADDITIVE MANUFACTURING”

R.F. Vaz, A. Garfias, V. Albaladejo, J. Sanchez, I.G. Cano



[10.3390/coatings13020267](https://doi.org/10.3390/coatings13020267)

This work presents CSAM as a process capable to make freeform parts, its principles, bonding mechanisms, examples of use compared to other AM processes, and technical solutions to improve CSAM-ed materials' quality and properties. Furthermore, the post-treatments already applied for CSAM-ed materials and hybrid processing are presented. In addition, this work contributes to compiling important information from the literature and shows how CSAM has advanced quickly in diverse sectors and applications.

Another approach presented is the academic contributions by a bibliometric review, showing the most relevant contributors, authors, institutions, and countries during the last decade for CSAM research. Finally, this work presents a trend for the future of CSAM, challenges, and barriers to overcome. This work helps the readers to have an overall view of the CSAM and makes it easier to understand the selected focus of the following results and articles.

A Review of Advances in Cold Spray Additive Manufacturing

Rodolpho Fernando Vaz *, Andrea Garfias, Vicente Albaladejo, Javier Sanchez and Irene Garcia Cano

Thermal Spray Centre CPT, Universitat de Barcelona, 08028 Barcelona, Spain

* Correspondence: rvaz@cptub.eu

Abstract: Cold Spray Additive Manufacturing (CSAM) produces freeform parts by accelerating powder particles at supersonic speed which, impacting against a substrate material, trigger a process to consolidate the CSAM part by bonding mechanisms. The literature has presented scholars' efforts to improve CSAM materials' quality, properties, and possibilities of use. This work is a review of the CSAM advances in the last decade, considering new materials, process parameters optimization, post-treatments, and hybrid processing. The literature considered includes articles, books, standards, and patents, which were selected by their relevance to the CSAM theme. In addition, this work contributes to compiling important information from the literature and presents how CSAM has advanced quickly in diverse sectors and applications. Another approach presented is the academic contributions by a bibliometric review, showing the most relevant contributors, authors, institutions, and countries during the last decade for CSAM research. Finally, this work presents a trend for the future of CSAM, its challenges, and barriers to be overcome.

Keywords: cold spray; additive manufacturing; 3D-printing; geometries; properties; innovation

Citation: Vaz, R.F.; Garfias, A.; Albaladejo, V.; Sanchez, J.; Cano, I.G. A Review of Advances in Cold Spray Additive Manufacturing. *Coatings* **2023**, *13*, 267. <https://doi.org/10.3390/coatings13020267>

Academic Editor: Mohamudreza Daroonparvar

Received: 31 December 2022

Revised: 19 January 2023

Accepted: 20 January 2023

Published: 23 January 2023



Copyright: © 2023 by the authors. Licensee MDPI, Basel, Switzerland. This article is an open access article distributed under the terms and conditions of the Creative Commons Attribution (CC BY) license (<https://creativecommons.org/licenses/by/4.0/>).

1. Introduction

Additive Manufacturing (AM) has been an industrial revolution in recent decades, starting with producing polymeric parts and advancing to metallic components. Many alloys and methods have been studied, some more industrially mature and others in a developing stage. The definition of Additive Manufacturing (AM) given by ISO/ASTM 52,900:2015 standard [1] is the “process of joining materials to make parts from 3D model data, usually layer upon layer, as opposed to subtractive manufacturing and formative manufacturing methodologies”. Other nomenclatures have been used worldwide as synonyms for AM, such as 3D printing, additive fabrication, rapid prototyping, and others. AM has been used to build prototypes, manufacture the final products, or even repair damaged components, innovating the global manufacturing industry [2–6]. Many companies have invested in developing new AM techniques and materials, optimizing the process parameters, reducing costs, and making the AM a competitive piece of technology [7,8]. Different sectors have benefited from using AM [9,10], such as medical [11–16], aerospace [17–20], automotive [21–23], supply chain [6,24–26], and others. Compared to the traditional subtractive manufacturing techniques, AM is characterized by being less wasteful, enhancing resource efficiencies, and changes in the design and production phases. Kozoir [27] presents the effectiveness of optimizing AM processing parameters to reduce the mass of models, keeping the desired mechanical properties. AM also extends the product life cycle by repairing high-cost parts, and reconfigures the value chains to be shorter, collaborative, and offer remarkable sustainability benefits [6,28]. In this way, AM offers clear benefits from the viewpoint of sustainability [29–31].

The commercial use of AM emerged for polymers in the 1980s, introducing Stereolithography (SL), which involves curing a photosensitive liquid polymer by a laser beam [32,33]. An evolution in equipment changed the raw material to the powder form, using Selective Laser Sintering (SLS) to fuse this powder [34]. Other classes of AM for polymers are Material Jetting (MJ) [35,36], Binder Jetting (BJ) [37,38], Material Extrusion (ME) [39,40], and Sheet Lamination or Laminated Object Manufacturing (LOM) [41]. The techniques consolidated for polymers have been successfully applied for other materials also, such as BJ for ceramics and metals [37,42,43], LOM for metals [44,45], and ME for composites [40,46]. Various processes are available for metal AM processing for the most different alloys and applications. The selection or choice of the adequate process depends on the part's geometry, complexity, mechanical properties, and other factors [47,48].

The metal AM processes differ from the heat source and metal feeding method or type. Some options are the laser process, Selective Laser Melting (SLM) or Sintering (SLS), Direct Metal Laser Melting (DMLM) or Sintering (DMLS), or Laser Metal Fusion (LMF), besides the Electron Beam Melting (EBM) process [49–51]. These are methods which are applied to the parts that need low or no machining post-processing or are used directly as end-use products. Other processes are presented in the literature but are not capable of producing complex geometries, such as Gas Tungsten Arc Welding (GTAW) [52–54], Gas Metal Arc Welding (GMAW) or Wire Arc Additive Manufacturing (WAAM) [55–58], Plasma Arc Welding (PAW) [57,59–61], Friction Stir Energy Manufacturing (FSAM) [62,63], and Ultrasonic Additive Manufacturing (UAM) [64,65]. Examples of AM by welding processes that demand post-machining are repairing long fatigue cracks in hydro powerplant runners [66] or repairing eroded gas turbine blades [67].

Cold Spray (CS) is a thermal spray process designed for coatings that has extended its use to produce freeform parts [28,68–70]. CS produces harder microstructures than other AM processes, as studied by Gamon et al. [71], who present CSAM-ed Inconel 625 with 600 HV. On the other hand, WAAM, SLM, EBM, DMLM, and BJ resulted in less than 300 HV. Figure 1 presents the AM technology maturity, evidencing the actual industrial use of the laser processes, SLM and DMLM, as WAAM. The prediction is to use CSAM industrially in a short time, less than two years, but a long development journey for FSAM and UAM [72]. This work aims to present the trodden path by CS as an AM technique and the foreseen way to consolidate and diffuse CSAM in the industry. Figure 2 shows examples of AM-made products employing different strategies.

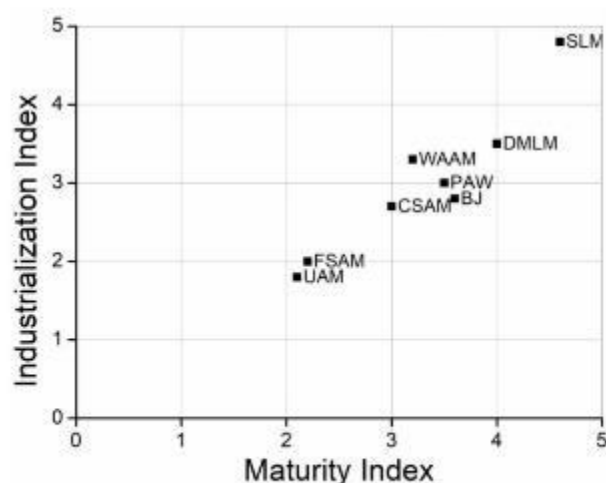


Figure 1. AM maturity index for producing metallic parts.

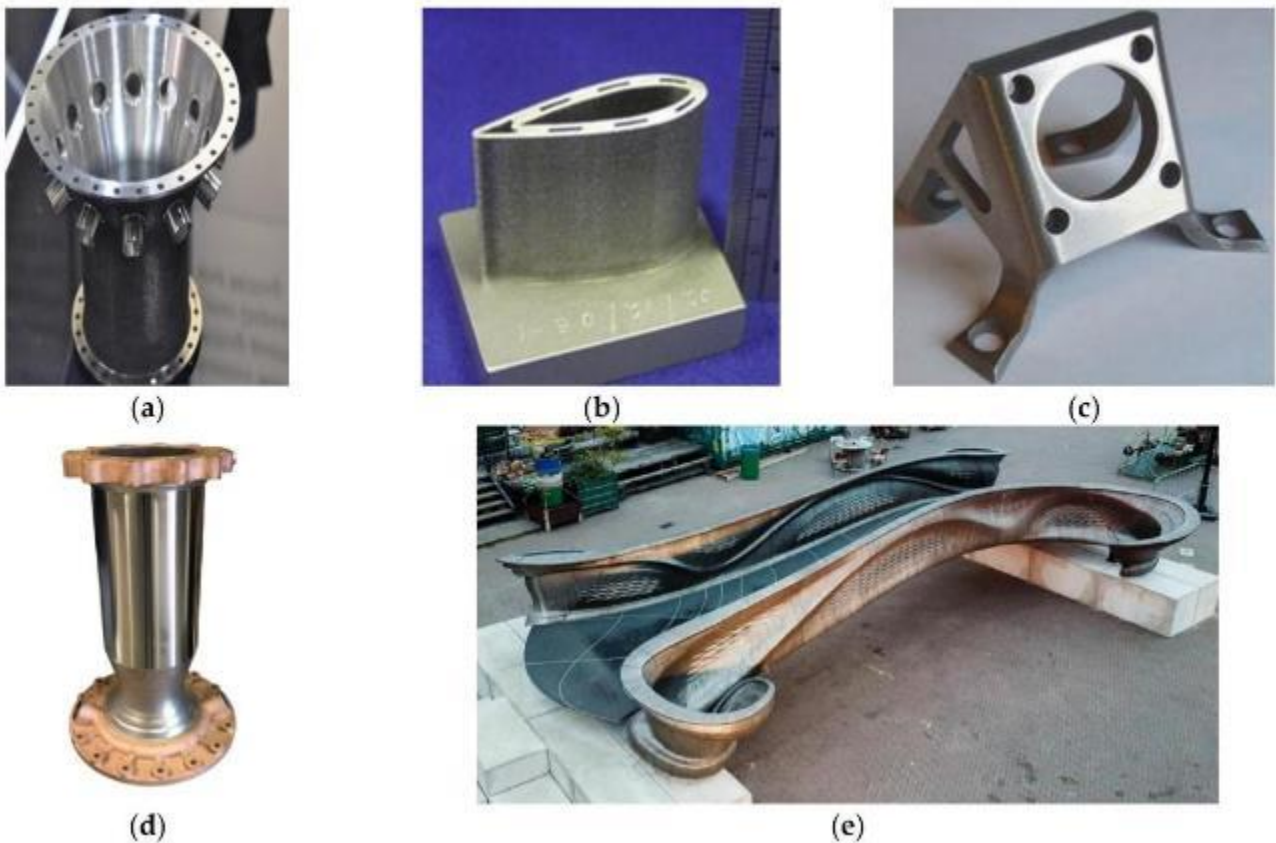


Figure 2. Metal AM parts. (a) DMLM-ed stainless steel gas turbine housing. Reprinted with permission from Ref [18], Elsevier, 2017. (b) DMLM-ed Ti6Al4V airfoil [18]. (c) CSAM-ed Ti bracket. Reprinted with permission from Ref [2], Elsevier, 2018. (d) CSAM-ed and DMLM-ed bimetallic thrust chamber. Reprinted with permission from Ref [73], NASA, 2021. (e) WAAM-ed stainless steel bridge in Amsterdam. Reprinted with permission from Ref [74], Elsevier, 2019. Unit: mm.

This paper presents and discusses the evolution and advances of CSAM critically, following the scheme shown in Figure 3.

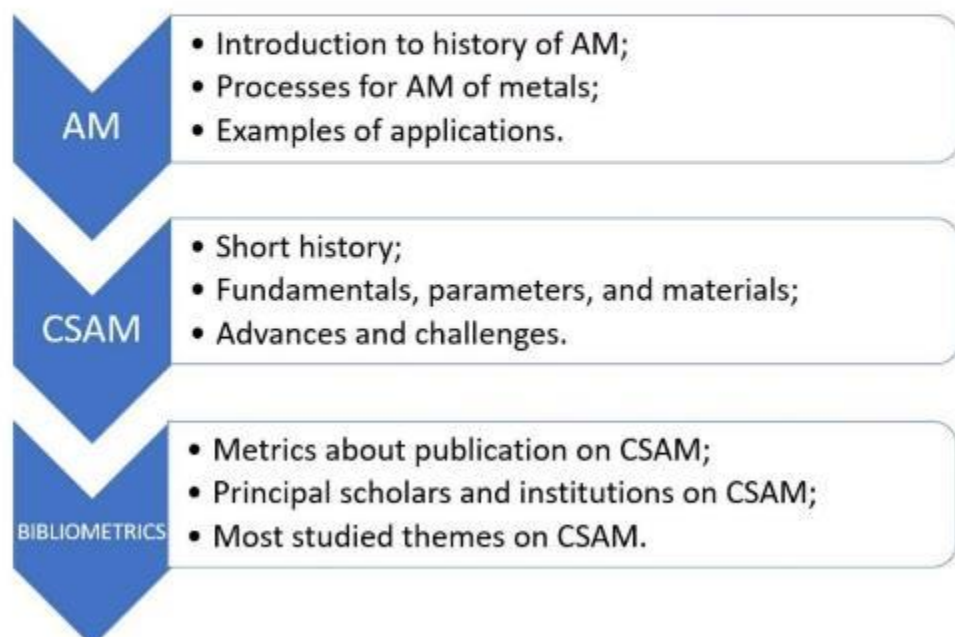


Figure 3. Flowchart of the topics presented in the work.

2. Cold Spray Process

This section describes the CS process, its fundamentals, principles, parameters, and their selection, which is essential to understanding and placing CS as an AM process. CS is a thermal spray process investigated and presented by many authors as an alternative to producing AM freeform parts. It has severe differences from the laser, welding, and other thermal spray processes since CS does not change the properties of the feedstock powder by heating or melting during the AM part fabrication because the powder is kept below its recrystallization temperature during the spraying time [75–77]. However, CSAM produces parts with a very high density, >99%, due to the very high velocity imposed on the particles, reaching supersonic velocity values [78–80]. Therefore, the correct selection of feedstock powder, deposition parameters, and strategy are fundamental for achieving high Deposition Efficiency (DE) and good CSAM performance [81–84]. CS also prevents materials oxidizing during the deposition due to the relatively low temperature that the material absorbs at the spraying time [85]. In addition, CS avoids other harmful effects seen in other AM or thermal spray processes, such as evaporation, melting, recrystallization, tensile residual stresses, debonding, and gas releasing, besides the ability to deposit high-reflective metals such as Cu and Al [28,83,86,87]. A great CSAM advantage is the possibility of the deposition of dissimilar materials, e.g., a sandwich-like structure of Cu and Al [88], which is not feasible by welding.

Historically, CS has been presented in the literature by different names: “kinetic energy metallization”, “kinetic spraying”, “solid-state deposition”, or “high-velocity powder deposition”, and others [78,89]. Its principle and physics of operation were studied during the XX century, with the operational evolution starting in the 1980s. Still, its commercial development started just in the early 2000s [86,89,90], increasing its expansion from the R & D sector to the industry since then, and with a prediction of widespread industrial use in less than two years [91]. CS is the thermal spraying process to which a large number of studies and publications have been devoted over recent years, presenting its principles and physics, but, nowadays, emphasizing industrial or real applications of the technique and mainly its use in the AM field [2,28,81,92–97]. The monetary benefits are imperative to select CSAM as an industrial production technology. A comparison among the metal AM technologies was presented by Munsh et al. [91], and CSAM was highlighted as the lowest cost per volume fabricated and the highest deposition rate, reaching $\text{kg}\cdot\text{h}^{-1}$ [79,81]. Besides the component at hand, the advantages of AM over traditional or subtractive fabrication processes include the redesign potential of the whole system, which is not easily measurable [91].

CSAM produces a coating or bulk component generated by a solid-state cohesion during the powders’ impact on a substrate. The working gas is previously heated in a chamber, reaching high pressure, flowing through a de Laval or similar convergent–divergent nozzle, accelerating it to supersonic velocities, and dragging the feedstock powders. [68,78,98]. The working gas pressure classifies CS, as presented schematically in Figure 4. Low-Pressure Cold Spray (LPCS) operates under 1 MPa, and High-Pressure Cold Spray (HPCS) uses higher pressure levels. A Medium-Pressure Cold Spray (MPCS) is a commercially available system, Titomic D623. LPCS is limited to a few materials and can be portable or manually operated, accrediting it for in-field operation and repair services. At the same time, HPCS is the CSAM used for many materials, but has heavier and more equipment than LPCS, employing a bigger gun, heat exchanger, energy source, robot, and acoustic enclosure (soundproof booth) for the operation, because the noise usually exceeds 100 dB [2,10,99,100]. This change in gas pressure and equipment configuration influences the sprayed particle velocity since the high velocity of particles is a consequence of high gas pressure and the nozzle design [101–105]. Another difference between the LPCS and HPCS is the powder feeding; for the first one, the particles are dragged by the working gas in the nozzle directly, using a downstream mode. On the other hand, HPCS uses an upstream injection mode, and the powder feeder is connected to a feeding gas

line, which improves the powder flowability, and increases the range of powders which are CS sprayable [90,106].

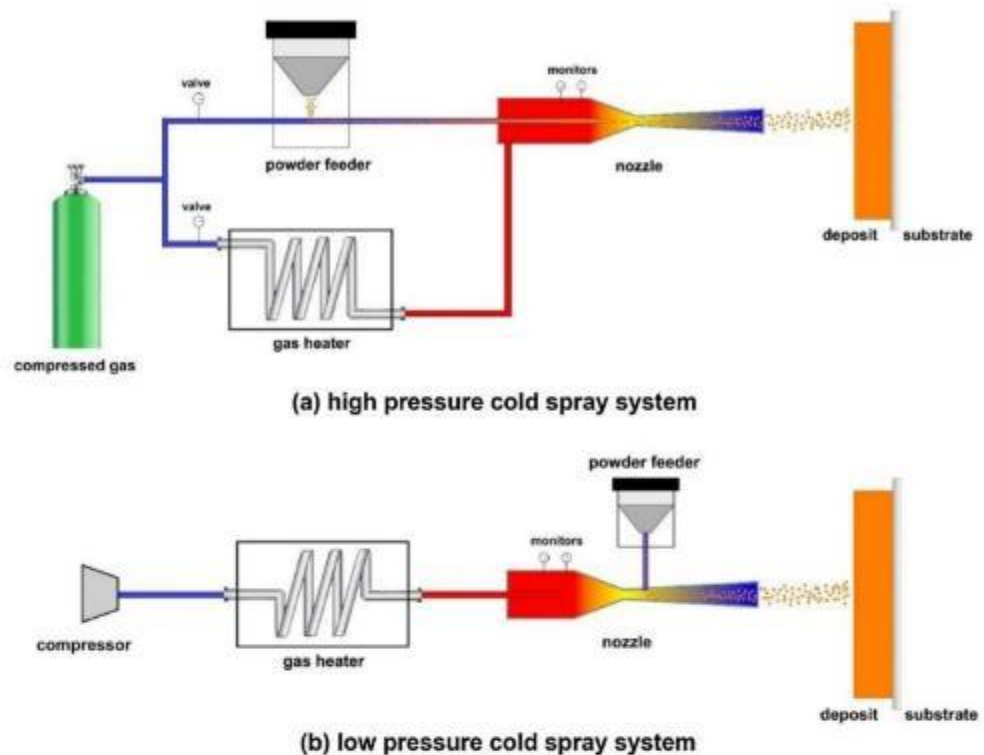


Figure 4. LPCS and HPCS schemes. Reprinted with permission from Ref [2], Elsevier, 2018.

The bonding mechanism of the solid-state particles to a substrate still has to be understood entirely. However, it is believed that their high energy at the impact disrupts the oxide films on the particle and substrate surfaces, pressing their atomic structures into intimate contact with each other under short high interfacial pressures and temperatures. This mechanism is called Adiabatic Shear Instability (ASI) [107,108]. It supports the success in coating ductile materials, such as Cu and Al, and flops in spraying brittle materials, such as ceramics or carbides [78]. At the impact, most of the kinetic energy from the in-flight particles is converted into heat or the plastic deformation of the substrate and the particle, which can produce strain, ultimately shear instability, and jetting. With an increase in local temperature, thermal softening alters the capacity of the material to transmit shear forces, and eventually, the softening process dominates over strain hardening [109–111]. Hassani-Gangaraj et al. [112] show the jetting happening with or without the material having a thermal softening capacity, proposing that CS jetting is formed as a result of strong pressure waves in the particles, expanding the particle edges. This mechanism is related to hydrodynamic processes that promote jetting, such as liquid droplet impacting, shaped-charge jetting, and explosion welding. The critical velocity (V_c) of particle for the bonding was mathematically related to the bulk speed of sound, which was minutely commented by Assadi et al. [113], who refuted those conclusions and sustained the ASI as the strongest and the primary bonding mechanism for CS-ed particle. Chen et al. [114] also proposed a low-velocity impact-induced metal bonding, in which the conventionally accepted metal jetting and melting may not be prerequisites for solid-state impact-induced bonding.

2.1. Cold Spray Parameters

The properties of CSAM-ed parts, such as density, porosity, adhesion, or hardness, depend on the CS spraying parameters, which have to be set to spray the particles in a specific velocity range or deposition window [79,80,85,103]. A velocity of a particle below a $V_{critical}$ or V_{cr} value does not promote the particle bonding, and an excessive velocity, $V_{erosion}$ or V_{er} , results in the erosion of the substrate instead of a deposition consolidation. This ideal velocity depends on the particles' properties and substrate materials [80,115,116]. Table 1 lists the V_{cr} and V_{er} for the most CSAM-ed materials.

Table 1. Window of deposition for CS.

Material	$V_{critical}$ [$m \cdot s^{-1}$]	$V_{erosion}$ [$m \cdot s^{-1}$]	Ref.
Al	625	1250	[79,117]
316L	550	1500	[79,117–119]
Cu	570	1000	[79,120]
Ti	700	1750	[79,117,121]
Ti6Al4V	750	2500	[122]
Ni	570		[117,120]
Inconel 718	600	1700	[123,124]

Process parameters optimization is based on particular applications and equipment, working gases, substrate and feedstock materials' characteristics, and others. Typically, these parameters include the gas type, temperature, pressure, nozzle geometry, throat size, and deposition robot strategy. In addition, a critical point is the feedstock powder material itself, particle size distribution, shape, and particle attributes, such as oxide skins and mechanical properties, which influence the ability to form a compacted layer [78,80,83–85,99].

For the CSAM, the working or main gas commonly used is N_2 or He, or N_2/He mixtures, but for LPCS and MPCS, compressed air is a low-cost option also [2,90,125,126]. N_2 has a lower cost than He and, due to the high consumption of the working gas, it is the choice for the main gas. For CS using He instead of N_2 , the particles are propelled with a higher velocity due to He's higher atomic mass [126–130], e.g., CS-ed 316L (particle size 28 μm) with He reaches 750 $m \cdot s^{-1}$, but less than 500 $m \cdot s^{-1}$ with N_2 as the working gas [131]. The CS working gas temperature is set up to high values in the CS gun heating chamber, e.g., 1100 $^\circ C$ for spraying 316L [132]; however, after passing through the nozzle, the gas expands, reducing the density and temperature [131,133]. Lee et al. [134] presented a CFD gas flow simulation in which a CS gas heating chamber at 1200 K and 20 bar resulted in less than 800 K in the CS gas jet, but a velocity higher than 1300 $m \cdot s^{-1}$. Considering the heat transfer inertia from the gas to the particle and the short time of exposition, the temperature of the particles is much lower than 800 K, maintaining the sprayed particles below their recrystallization temperature. It influences the properties of the sprayed material, such as the particles' cohesion, adhesion, strength, and others. For example, for Ti coatings, the cohesion measured by TCT (Tubular Coating Tensile) [135] had a linear relation with the gas temperature [121], and higher cohesion corroborates a material with a lower porosity, higher strength, and DE. However, by selecting a high gas temperature, the cold work and hardness in the material are dwindled by partial recovery and recrystallization phenomena [136,137].

The Standoff Distance (SD) is how far the substrate surface is from the gun nozzle exit. This distance has an optimum value, where the velocity of particles reaches the peak, impacting the substrate with the highest energy possible. A relation presented in the literature as a reference for an excellent SD is seven times the gas jet diameter. Further, the pressure reduces drastically [86], e.g., for a 3 mm gas jet diameter, the SD should be 21 mm. Turbulences, the oscillation of the gas jet, and the irregular distribution of the particles impacting the substrate are also seen to increase the SD, which reduces the DE [138].

as confirmed experimentally for CS-ed Al, Cu, and Ti [139]. The adherence of CSAM-ed Ti6Al4V on the steel substrate increased by optimizing the SD parameter, reaching the best value of 50 mm without delamination [140], showing that the relation of an SD seven times the gas jet diameter proposed by Kosarev et al. [86] is just a starting point for parameter optimization and not a rule.

The robot path and velocity influence the characteristics and properties of the CS-ed material; the step between the sprayed single tracks has to be optimized to guarantee good adherence and produce a flat and smooth deposit surface because an insufficient overlapping distance results in a wave surface [138]. Therefore, rotating is one of the most applied strategies for CSAM, building up the part by coating a rotating pipe-like substrate, resulting in parts with symmetry, such as the one presented in Figure 2d, after the post-machining process. This strategy promotes the good adhesion and cohesion of particles but limits the geometries feasible to the symmetrical ones. The use of alternate directions, Figure 5b with the CS laden-jet particles in the Z-direction, increased the material's isotropy when compared to the traditional strategy, Figure 5a with the CS laden-jet particles in the Z-direction, for CS-ed Cu thick parts [141]. Compression tests in the X- and Y-direction indicated different crack propagation paths for the bidirectional strategy, revealing that the robot path influences the preferential direction for crack propagation [142]. The robot path also may change the angle of the impact of particles, drastically affecting the DE and material microstructure. For CSAM, the robot path has a crucial function since the part sidewalls grow up and follow an angle, which has to be rectified to the designed and desired inclination. An adequate robot programme can spray on the inclined sidewall with a jet angle that corrects it, improving DE [92,143–145].

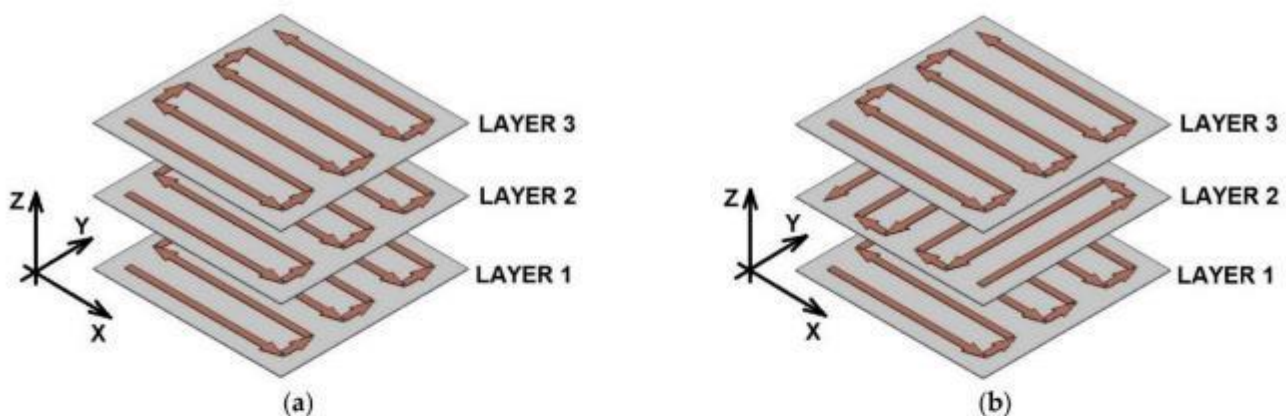


Figure 5. Different robot path strategies for CS-ed deposition. (a) Traditional or bidirectional, and (b) cross-hatching.

CS almost always uses conventional powders as feedstock materials developed for Air Plasma Spray (APS), High-Velocity Oxy-Fuel (HVOF), or laser processes in a spherical and finer particle size range at best. Various techniques are available to produce metallic powders, which are chosen by the chemical composition, characteristics, and/or properties required for the powder [146]. For the CS, the particles' metallurgical, morphological, and physico-chemical characteristics influence the spraying success and material performance [83]. Since CS does not promote recrystallization during the deposition, a deposit with a refined microstructure is obtained by selecting a small grain-size feedstock powder. It improves the mechanical properties; however, a larger grain size promotes more ductility to the particle. Using HT to reach the ideal powder microstructure was an alternative presented by Poirier et al. [147] for CS-ed H13 tool steel and by Story and Brewer [148] for aluminum alloys, resulting in a DE increase from 35 to 60% and from 70 to 90% to Al7075 and Al6061, respectively. Silvello et al. [84] summarized the relationship between powder characteristics, CS process parameters, and the CS-ed material properties by modeling

and the experimental results. Table 2 presents coefficients for the model proposed using modeFRONTIER software, in which negative values represent inverse input/output relationships. It is noticed that the particle diameter and hardness influence the CS-ed material characteristics, highlighting the porosity, which is responsible for some CS drawbacks, such as a short fatigue life.

Table 2. Correlation behavior among the different input/output for CS [84].

Input / Output	Particle Diameter	Particle Hardness	Gas Pressure	Gas Temperature	Particle Velocity	Deposit Hardness	Porosity	DE	FR
Particle diameter	1	0	0	0	-0.431	-0.187	-0.213	0.104	0.097
Particle hardness	0	1	0	0	0	0.935	0.109	0	-0.324
Gas pressure	0	0	1	0	0.594	0.417	-0.682	0.768	0.804
Gas temperature	0	0	0	1	0.498	0.297	-0.471	0.592	0.897
Particle velocity	-0.431	0	0.594	0.498	1	0.682	-0.734	0.803	0.817
Deposit hardness	-0.187	0.935	0.417	0.297	0.682	1	0	0	-0.352
Porosity	-0.213	0.109	-0.682	-0.471	-0.734	0	1	0	-0.819
DE	0.104	0	0.768	0.592	0.803	0	0	1	0
FR	0.097	-0.324	0.804	0.897	0.817	-0.352	-0.819	0	1

CS powders must be characterized before spraying, measuring their particle size distribution by the ASTM B214 standard [149], a sieving separation of the larger and smaller particles, or the laser scattering, classifying the particle size distribution by measuring the laser-illuminated flowing particles. The powder flowability is measured by the time elapsed to flow a certain powder mass through a certified Hall flowmeter, following the ASTM B213-20 standard [150], which is used to measure the powder's apparent density, as indicated by the ASTM B212-21 standard [151]. A previous characterization of the powder is imperative since powders with a flowrate higher than $1 \text{ g}\cdot\text{s}^{-1}$ tend to build up and block the gas flow in the nozzles for LPCS [146]. For HPCS, Vaz et al. [132] presented the flowability for different 316L, resulting in 9 and $17 \text{ g}\cdot\text{s}^{-1}$ for the irregular and spherical shapes, respectively. This powder characteristic impacted the CS powder feeding, which was 0.43 and $0.55 \text{ g}\cdot\text{s}^{-1}$ for the irregular and spherical shapes, respectively. By machine learning, Valente et al. [152] show how to predict a novel powder flowability on a per-particle basis, which can help scholars develop their alloys and powders for CSAM.

An irregular shape of the particles does not necessarily result in a coating or CSAM-ed part with worse properties [153–155]. The high deformation of the CS-ed particles at the impact can act as compensation for their shape irregularity and even for the particle size distribution, which enables using coarse particles, as presented by Singh et al. [153], who obtained similar material strength by coarse and fine Cu particles. CS-ed 316L coatings using water-atomized powders, which had an irregular shape, presented corrosion behavior and a wear-resistance performance very similar to, or even better than, the coatings obtained with spherical gas-atomized powders [132], indicating the viability of using a lower-cost raw material for CS, since the 316L gas-atomized powders are more expensive than the water-atomized ones. Wong et al. [155] obtained very similar porosity values ($3.0 \pm 0.5\%$), DE (100%), and hardness ($200 \pm 10 \text{ HV}$) for CS-ed Ti coatings employing irregular and spherical shape powders, but considering coating quality, the authors suggested the medium-sized spherical powder the best CS option. For Ti6Al4V, spherical

particles presented a higher hardness and cohesive strength than a very irregular powder obtained by the Armstrong process, as shown by Munagala et al. [156]. In addition, the powder size distribution influences the CS-ed particles' velocity; smaller particles reach higher velocities than bigger and weightier ones, as presented in a simulation performed for 5, 25, and 50 μm Al particles. The first one resulted in a velocity higher than $600\text{ m}\cdot\text{s}^{-1}$, but the last one was lower than $500\text{ m}\cdot\text{s}^{-1}$ [157]. For CS-ed Cu particles, small particles, 5 μm , reached a velocity of $700\text{ m}\cdot\text{s}^{-1}$, while big particles, 90 μm , accelerated up to $300\text{ m}\cdot\text{s}^{-1}$. Bagherifard et al. [119] presented a 316L fine powder, $-29 + 12\ \mu\text{m}$, with a higher spraying velocity than coarse particles, $-45 + 19\ \mu\text{m}$, which resulted in a material with higher particle deformation, mechanical properties, and electrical conductivity. Meanwhile, the V_{cr} is dependent on the particle size, and smaller particles have a much higher V_{cr} than the bigger ones, resulting in an even higher velocity, meaning small particles may not bond, and an optimum size range is achieved for each material, which is generally between 10 and 60 μm . When improving the temperature of particles, V_{cr} is reduced, revealing the need to improve the CS working gas temperature to increase the temperature of smaller particles and the velocity of bigger particles [133,158,159]; however, higher gas temperatures put the equipment in an undesired condition, overloading it and promoting nozzle clogging.

The literature explains how the CS nozzle wall at a high temperature induces clogging because low-melting-point hot particles flow through the nozzle and collide against the nozzle's inner hot wall, inducing the bonding between the particles and nozzle wall, resulting in nozzle clogging [157,160]. Different solutions have been evaluated by researchers aiming to reduce the clogging and improve the nozzles' service life: the assembly of cooling systems surrounding the nozzle to reduce its temperature [157]; redesigning the nozzle for a bi-material component, using glass and WC [161]; aligning the sprayed particles by an electric field and avoiding them to touch the nozzle's hot wall [162]; and others. Clogging can be solved by cleaning methods, such as spraying hard particles at high temperatures or a chemical cleaning with acids. However, besides the monetary loss of clogging, it reduces the DE, can overload the gun chamber dangerously, and imposes maintenance stops during the deposition, generating undesired temperature transitions for large CSAM-ed parts. Sun et al. [10] comment that clogging has been one of the limitations of a more industrial CSAM application.

2.2. Challenges for CSAM

CSAM is a technique with great benefits compared to other AM methods. Therefore, it has excellent potential to be implemented in the solid-state AM industry to produce free-standing parts or repair worn components [2,163]. Yet, CSAM is still an emerging technology facing several challenges that need to be studied, such as low as-sprayed geometric tolerances, inferior mechanical properties compared to wrought materials, residual stresses, and low DE-depositing hard materials. In this section, these challenges are discussed, along with the strategies studied to overcome them. Figure 6 presents a scheme of the pros and cons of CSAM over other metal AM processes. It also indicates the advances studied and investigated to overcome the drawbacks.

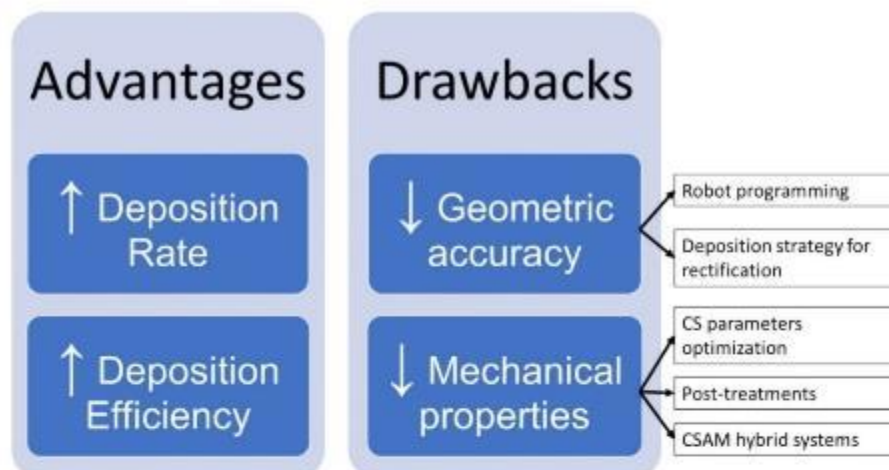


Figure 6. CSAM advantages and drawbacks, and the alternatives presented in the literature to overcome them.

2.2.1. Possible CSAM Geometries

The AM technologies rely on building an object layer by layer. Thus, controlling geometric tolerances is imperative to produce complex shapes or near-net-shape parts. Still, CSAM has to be more precise, and the literature presents some reasons for this CSAM limitation. First, because the velocity profile of the particles in the jet spot that exits the nozzle is uneven, the center of the laden-jet particles has a higher density of particles and greater velocities, promoting a superior deposition on this region than on the jet periphery. Cai et al. [138] simulated the single-track deposit profile, concluding that a 2D distribution profile approximately fits a Gaussian curve. Ikeuchi et al. [164] evaluated different machine learning approaches to accurately preview the CSAM track profile, saving much experimental time and CSAM spraying costs. Furthermore, Kotoban et al. [165] investigated the relationship between the shape of a single-track coating and the DE, concluding that in the first layer deposition, the particles on the jet periphery have a slight decrease in DE compared to the jet core, producing a triangle shape deposit that sharpens layer by layer. Finally, Wu et al. [166] developed a model to compensate the layer thickness by optimizing the robot velocity at the different regions on the substrate surface, resulting in a smoother CS-ed material surface.

Knowing that CSAM-ed deposits tend to produce pyramid-shaped coatings, some robot path trajectories and strategies have been developed to obtain near-net-shape parts [144,167–173]. For instance, Wu et al. [167] established a new stable layer-by-layer building strategy that sprays at a deflected angle towards the inclined walls of the pyramid-shaped coating, which allows building components with straight walls. Another example is the work of Vaz et al. [144], where a new method was implemented that consists of spraying with a circular movement at an angle different than the normal and allows free-standing building with controlled shapes, as presented schematically in Figure 7, but well described in the literature by Vaz et al. [144]. Yet, further studies on deposition strategies and the production of free-standing components are encouraged since they can expand the application areas of CSAM.

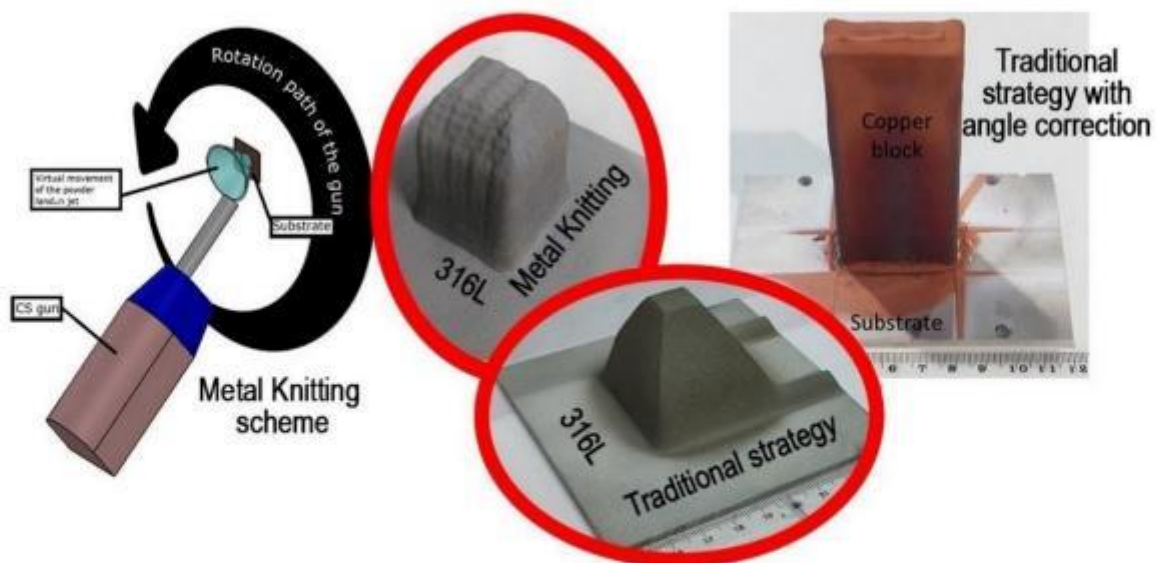


Figure 7. Metal Knitting, a CSAM alternative strategy to the traditional deposition. Reprinted with permission from Ref. [171], Springer Nature, 2020. Unit: mm.

CSAM can produce arrayed structural components, as presented in Figure 8 for CSAM-ed Ti on stainless steel. It was made by masking the substrate to shadow the areas where the sprayed material was not supposed to cover. Masking has been presented in the literature for other thermal spray processes, using tapes, pastes, shields, or other high-temperature resistant material removed after the coating deposition [174–177]. CFD has been developed to understand the influence of the masks on the CS gas flow, disturbances on the particle's trajectory, and the formation of bow shockwaves, which reduces the gas velocity [178]. It suggests using a higher particle velocity and setting the CS parameters to suppress this harmful effect of the masking strategy. Klinkov et al. [179] presented a model showing the impact of the mask on the particle behavior, velocity, and trajectory. The distance of the mask to the substrate cannot be excessive because it affects the deposition geometry, decreasing the width of the masked zone and diminishing the accuracy of the CSAM-ed geometry. An industrial application of the CSAM masking strategy is the fabrication of compact heat exchangers for electronic devices [180–183]. As well as array structures, diverse geometries are feasible, such as Braille impression for blind people or raised areas in molds for plastic injection, among others.



Figure 8. CSAM-ed Ti on stainless steel using masking strategy. Unit: mm.

Applying CSAM with other processes is a hot topic for industrial applications, e.g., for a unique component, some regions can be CSAM-produced, which is faster, and others can be DMLM-made, resulting in more details or complex geometries. Another CSAM use is joining dissimilar materials because CS has no metallurgic union with the substrate. It

is helpful for composites, e.g., a carbon-fiber-reinforced polymer or a sintered SiC. This Al interlayer strategy was tested by Xie et al. [184] for joining TiN/Ti6Al4V, but using a hot dip to make a 25 μm -thick Al coating; however, it can promote an undesired atomic diffusion depending on the materials and process temperatures and time, which is prevented by using CSAM. These hard- or impossible-to-weld materials can have a surface coated by a thick CSAM weldable material, e.g., Al or 316L, which can be joined on other structures quickly. Champagne Jr and Champagne III [185] presented this method for using CS directly as the joining element and growing a CSAM-ed volume on the part to be arc-welded on another element. This joining was tested for a light-alloy magnesium ZE41A-T5, employing Al as the filler metal [186], joining Al 6061 to a ZE41A Mg alloy using CS sprayed Al as the transition material on the Mg alloy surface and welded to Al 6061 by FSW [187,188], and joining Al to Cu by FSW with a Ni interlayer [189]. Daroonpavar et al. [190] presented CS with the capability to make a corrosion-resistant coating on an AZ31B Mg alloy, employing the metallurgically incompatible Ta–Ti–Al layers, also reducing the wear rate from 10^{10} to $10^8 \mu\text{m}^3\cdot\text{N}^{-1}\cdot\text{m}^{-1}$.

2.2.2. Improving the Mechanical Properties

To date, CS processes have been used mainly in the aerospace, automotive, marine, and defense industries, where the performance requirements of the deposits are very demanding [99,163]. Therefore, one of the main issues with CSAM is the mechanical properties of the deposits. Apart from the hardness, which tends to be greater than the bulk due to the cold work hardening of particles during impact [132,144,191], the as-sprayed deposits present less favorable mechanical properties, such as lower strength, ductility, electrical and thermal conductivity, and wear resistance. It is attributed to the inherent microstructural defects of the CS process, such as micro-pores and interparticular boundaries [2,191]. Moreover, as the particles are arranged layer by layer, anisotropic responses have been reported in the literature for CSAM-ed deposits [141]. The literature presents anisotropy for other processes that deform the material in a preferential direction, e.g., cold rolling [192–194], extrusion [195], friction stir welding [196], or even laser AM processes [197,198]. For CSAM, high isotropy was observed in a plane parallel to the substrate surface [141,199–201], but in a vertical or Z-direction, the material had lower strength. This behavior is presented in the literature for CSAM-ed Cu [171], Al [202], and 316L [203].

Moreover, the use of CS is also limited by the intrinsic characteristics of the materials. For example, only soft and ductile materials, such as Cu and Al, are easily deposited, which is deduced from the number of papers linking “cold spraying” and “aluminum” or “copper” keywords. In contrast, hard materials (e.g., Maraging steels, Ti6Al4V, Inconel 718, etc.) with the poor capability to deform at a solid state can hinder the formation of a dense component [28]. Therefore, recent studies focus on optimizing the CS process parameters to obtain the ideal V_{cr} for each material so that quality coatings are produced [77,99,123,204–206]. For instance, Li et al. [205] did a literature review on the solid-state CS-ed Ti alloys, focusing on the process parameters, deposition characteristics, and limitations of these materials. Another example is the work of Pérez-Andrade et al. [123], which presents the optimization of parameters and post-treatment processes for obtaining high-quality thick deposits of Inconel 718 for AM applications.

CS-ed coatings also tend to be influenced by compressive residual stresses generated by the severe impact deformation of the particles. Such compressive stresses can be beneficial up to a certain point. However, if they are too high, the adhesion of the deposit is usually hindered, and a crack can nuclei and grow in the interface substrate/coating, or it can completely detach, de-coating from the substrate [207,208]. For CSAM, these residual stresses are accumulated layer by layer, and if the particles have poorly adhered to the substrate, the deposit separates from the substrate. Making freeform parts is not a problem because the substrate has to be eliminated and only acts as a base or support. Still, with the employment of CSAM as a repairing method, this detachment and low adhesion is highly prejudicial of the excellent performance of the repairing service.

These challenges represent a drawback for CSAM compared to other AM methods. Nevertheless, several process strategies have been successfully explored in the literature, such as post-processing methods (e.g., HT) or hybrid deposition technologies, such as Laser-Assisted Cold Spray (LACS) and Cold Spray Shot Peening (CS-SP).

Heat Treatments (HT) are one of the most effective ways to enhance the microstructure of CSAM-ed deposits [2]. The tailoring of the final properties of a broad range of materials with HT, such as Cu [136,208–210], Al alloys [208,211–213], Ti alloys [208,214–216], Ni alloys [81,123,124,204,217–219], 316L [119,208,220], among others, is reported in the literature. Furthermore, HT relieves residual stresses, reduces the microstructural defects (e.g., porosity and particle boundaries), and improves the cohesion between particles which significantly influences the material performance, since the failure mechanism during the stress loading changes from an interparticular mode to a cleavage-like and ductile mode. In the first one, the crack grows surrounding the particles and detaches one to the other. HT promoted a metallurgical bonding of particles, increasing cohesion, material strength, and plasticity or ductility. Dimples evidenced it in SEM images of the fracture surface [202,210,221–223]. For Inconel 718, Sun et al. [124] applied induction for heating the material, which represents a possibility to select the CSAM-ed part region to be HT-ed, instead of the whole material, e.g., treat only the component areas that are exposed to wear or friction. The induction HT promoted the cohesion of the particles by the eddy current, as well as the atomic diffusion, which resulted in higher mechanical properties due to higher dislocations and twin densities in the neck formed between the particles than in the particles' center [224]. Due to the hardness reduction, Zhang et al. [225] presented the HT-positive effects on the post-machining process of Al7075. Another heating process is Electric Pulse Processing (EPP), in which applying high-density electron charges through the material promotes changes in the microstructure and mechanical behavior of alloys, such as precipitates distribution, yield strength, elongation, and hardness [226]. For example, for CSAM-ed Cu, Li et al. [210] show an expressive improvement in its mechanical properties, reaching a UTS of 200 MPa over 100 MPa in the as-sprayed condition and elongation of 20% over 2%.

Particularly, annealing is considered a simple post-processing method that positively impacts the as-sprayed CSAM microstructure. It promotes diffusion and recrystallization processes that mitigate the undesired microstructural defects and change the mechanical properties; the work-hardened deposits are softened, increasing their ductility, but reducing their hardness compared to their as-sprayed counterparts.

Spark Plasma Sintering (SPS) is a technique developed for ceramics and powder metallurgy that has improved CSAM-ed density and mechanical properties. SPS is pressing compacted powder and applying a pulsed current discharge that can reach thousands of Amperes but low voltage under pressure. It generates plasma between the intimate close particles, which results in micro welding, forming necks at contact points, atomic diffusion, and plastic flow [224,227–229]. In addition, Joule heating and plastic deformation enhance the sinter's densification, improving the particles' cohesion and material strength [230]. For the CS-ed TiC–Cu composite, SPS eliminated the interparticular region [231]. The SPS temperature was directly related to improving the mechanical properties, ductility, and decreasing the hardness of the CSAM-ed Cu, as presented by Ito and Ogawa [230], who selected 50% of the Cu melting point as the maximum SPS temperature for 5 min. This short time is an advantage of SPS over annealing, which typically keeps the material in the furnace for hours. Figure 9 shows the microstructures of CSAM-ed Ti6Al4V as-sprayed and after SPS post-treatment.

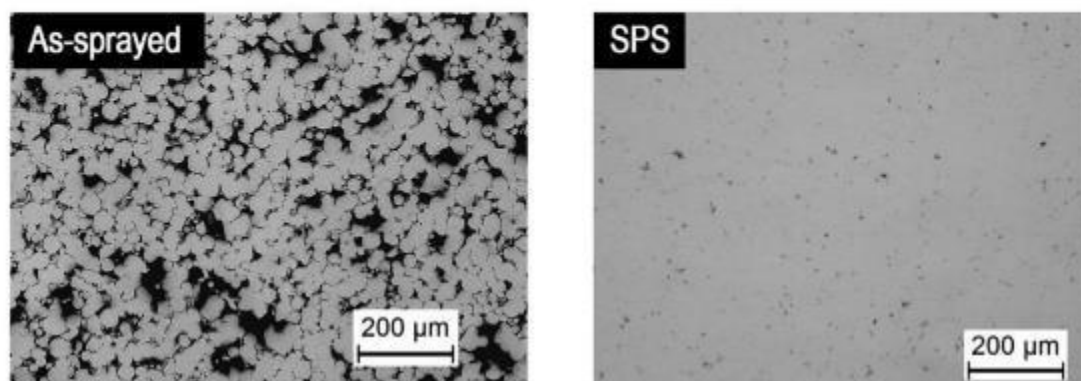


Figure 9. SPS effect on CSAM-ed Ti6Al4V microstructure.

Another HT that has recently drawn attention in the field of CSAM is Hot Isostatic Pressing (HIP), which is presented in detail by Bocanegra-Bernal [232] and by Atkinson and Davies [233]. The HIP technique can be used directly to consolidate a powder or supplementary to densify a cold-pressed, sintered, or cast part. This method can eliminate the pores and micro-cracks of the material by compressing the samples with high temperatures, e.g., 1000 °C for Ti alloys, to an isostatic pressure in the order of hundreds of MPa at the same time, resulting in fully isotropic material properties [234,235]. It has been successfully applied to metals, composites, and ceramics obtained by different processes. However, few studies are available in the literature for CSAM, and they are focused on hard materials that are difficult to deposit by CS, such as Ti [236,237], Ti6Al4V [237–239], and Inconel 718 [123].

Figure 10 presents the densification and phase changes, precipitating β in an α matrix, in CSAM-ed Ti6Al4V employing N_2 and He as the CS working gas. However, this post-treatment cannot close exposed porosity because the HIP gas fills these pores. A solution is a pre-HIP process of encapsulating the sample and converting those into internal pores to be removed by the HIP. The HIP also cannot remove large internal pores since diffusion bonding does not occur when metal/metal contact is not intimate. It happens when the CS-ed material has low plasticity even in high temperatures, if the surfaces of the internal defect are oxidized, or if there is a gas inside the pore that does not diffuse, e.g., air, He, or N_2 [232]. It represents a limitation for CSAM HIP use if the CS-ed deposition process cannot produce parts with very low porosity and a very thin interparticular region, which occurs when spraying low-ductility powders.

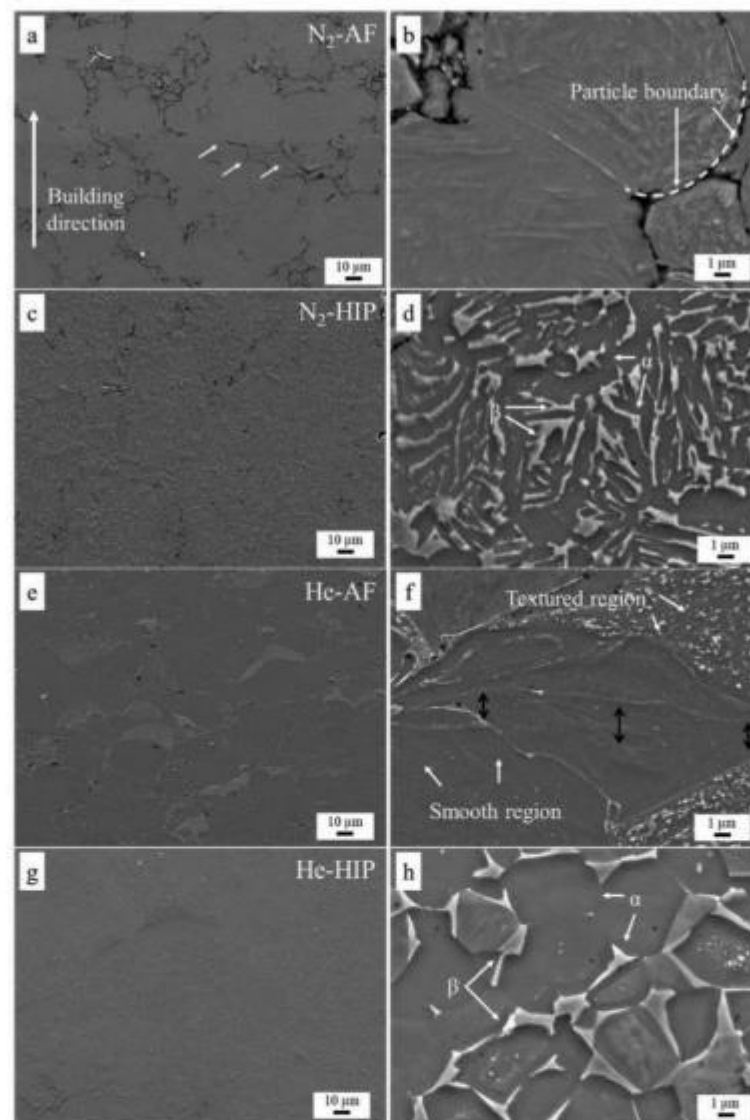


Figure 10. Effect of HIP on the microstructure of CSAM-ed Ti6Al4V, densification, and phase change. SEM images with (a,c,e,g) low magnification and (b,d,f,h) high magnification. Reprinted with permission from Ref. [238], Elsevier, 2019.

The melting or sintering AM processes drastically change the microstructure of the feedstock material during the processing, and CS represents an advantage over SLM or DMLM in this point. However, a hybrid process of coating a CSAM-ed part can significantly improve its wear and corrosion performance, as presented by Vaz et al. [240] coating CSAM-ed Maraging with HVOF-sprayed WC. In addition, Feng et al. [241] used induction heating to remelt AlCoCrCuFeNi HEA, improving the wear resistance by phase transformations. Laser remelting or glazing has been investigated as a post-treatment on CSAM, eliminating micropores within the deposit and enhancing the cohesion of particles. Remelting changes the ASI and other CS bonding mechanisms for metallurgical bonding. Laser remelting of CS-ed Al onto steel substrate presented an FeAl intermetallic formation, improving its wear resistance [242]. For Ti, Astarita et al. [243] and Marrocco et al. [244] obtained a thin and dense remelted layer, which improved the corrosion behavior in a 3.5% NaCl solution, reaching the same performance as a wrought Ti bulk. Kumar et al. [245] showed an improvement in the wear resistance for the Ti-based MMC.

The laser glazing applied on CS-ed Inconel 625 eliminated the cold-worked microstructure, generating a columnar dendritic one. It reduced the hardness but eliminated the interconnections between the pores, increasing the material corrosion performance

[246]. Zybala et al. [247] improved the surface hydrophobicity of CSAM-ed irregular powders Ti6Al4V and Ti after laser surface post-treatment. This condition is attractive for CSAM-ed parts developed for the Oil and Gas sector, where Ni-based alloys have been employed as CO₂ and H₂S corrosion-resistant materials. Other cheaper heat sources can be studied, and it is a lack in the literature, e.g., PAW, used by Pukaszewicz et al. [248,249] for HVOF-sprayed FeMnCrSi coatings, or GTAW, applied by Zabihi and Soltani [250] for FS Al-based MMC coatings.

Plasma Electrolytic Oxidation (PEO) or micro-arc oxidation has been used to produce hard ceramic coatings on Al and other alloys [251]. It improves their wear and corrosion resistance due to the formation of the protective ceramic coating on the material enabled by the plasma discharges, supported by an aqueous electrolyte [252]. For CS-ed Al, Rao et al. [253] presented a stable, well-adhered, and harder PEO layer formed on the CS-ed Al7075 coating, 1353 and 144 HV, respectively, which resulted in a higher dry sliding wear resistance. It also improved the corrosion resistance, with a three-order lowered corrosion current density. Using PEO on CS-ed Al + Al₂O₃ on a Mg alloy substrate, Rao et al. [254] reduced the sliding and abrasion wear rates ten times, mainly due to the increase in hardness from 700 to 1300 HV.

The infrared irradiation as a heating source for the HT of CSAM-ed Cu alloys was tested by Chavan et al. [255]. This heat source is cheaper than laser equipment and has a wavelength range similar to lasers. Still, a significant advantage of infrared irradiation is the absence of a furnace, a chamber, or a controlled atmosphere, as occurs for annealing. It enables this system for CSAM in situ repairs or repairing large components that do not fit in conventional furnaces, e.g., oversized axles or injection molds. Infrared irradiation has been previously used for arc-sprayed Zn alloys coatings, improving wear and corrosion resistance [256].

Shot Peening (SP) is a post-treatment technique of cold working by propelling glass, ceramic, or steel balls against the material, reducing the material's surface roughness, inducing the surface compressive residual stress, and, consequently, increasing the part's fatigue resistance by retarding crack initiation [257]. Moridi et al. [258] showed the SP applied for CSAM-ed Al6082, reduced roughness from R_a 12.4 to 4.7 μm and improved the depth of the compressive stress layer from 350 to 400 μm, but without a significant compressive stress value improvement. Furthermore, due to porosity and plastic deformation reduction, the hardness and corrosion resistance were improved in CS-ed Zn by SP post-process [259]. Similar mechanisms and results were obtained by Ball-Burnishing (BB), a process in a ceramic or hard ball, with a diameter of <10 mm, which compresses and deforms the CS-ed material, as occurs with SP, but without impact, more similar to a rolling process. BB was applied to CS-ed 17-4PH stainless steel, improving the depth from 130 to 190 μm of 200 MPa compressive residual stress [260,261]. In general, any technique that improves the part's fatigue life is attractive for CSAM; however, SP has presented low effectiveness and does not indicate more research interest or industrial promisor use.

Waterjet Cavitation Impact (WCI) is another technique presented in the literature that should be tested for CSAM, since there is a lack of this in the literature, aiming to improve the material surface properties, especially the compressive residual stress. Cavitation is a phenomenon in which the static pressure of a liquid reduces to below the liquid's vapour pressure, forming microbubbles that collapse when subjected to a higher pressure. It generates shock waves that impact the material surface [262]. For WCI, the material is exposed to a water jet under controlled conditions, promoting its plastic deformation and densification, as occurs for SP. WCI has been applied in the industry since the 1990s for parts produced by different techniques and exposed to fatigue degradation, such as gears, shafts, and other [263]. Good results have been exposed in the literature, Zhang et al. [264] reached 175 MPa compressive residual stress in a 2A12 Al alloy by a WCI with a water jet under 75 MPa and 20 degrees off-normal inclined; Soyama and Okura [265] presented how WCI resulted in a significant improvement in the fatigue life of Ti6Al4V.

Cold Rolling (CR) was experimented with for CS-ed Cu on steel by Bobzin et al. [266], resulting, after a 14% thickness reduction, in cracks and delamination on the coating/substrate interface, which was resolved by annealing at 500 °C before CR, a Thermo-Mechanical Treatment (TMT) or Hot Rolling (HR). It resulted in good adhesion to the substrate without cracks in the Cu coating but lower hardness due to the annealing process that dwindled the cold working in the particles from the CS-ed deposition. Tariq et al. [267] employed TMT for CSAM-ed Al-B₄C MMC, reducing by 60% in thickness, improving the mechanical properties, increasing UTS from 35 to 131 MPa, and elongation from 0.5% to 5% due to the interfaces of the particles dramatically enhanced by the diffusion activity. TMT has been applied for materials that have poor formability at room temperatures, such as Mg alloys [268] or TiAl-based alloys [269,270], as well as the CSAM-ed Ni-Al [271], A380 alloy [272], and Al-B₄C [267]. Depending on the CSAM part's geometry designed, such as plate-like, TMT is adequate. However, TMT promotes a considerable anisotropy for a bulk-like shape due to the unidirectional plastic deformation induced by the post-treatment.

Friction Stir Processing (FSP) imposes a friction force on the CSAM-ed material that softens the surface, increasing the amount of shear straining in the processed region and promoting dynamic recrystallization. Microstructural changes and grain refinement showed this, altering the CSAM-ed material's mechanical properties, porosity, and cohesion of particles [273]. The literature presents the FSP applied for Al alloys [274], Mg alloys [275], MMC [276], and 316L [220], focusing on the improvement of their tribological and corrosion performance. Ralls et al. [220] studied CS-ed 316L + HT + FSP, showing that the post-treatments eliminated the δ -ferrite contained in the powder by atomic diffusion. In addition to that, the authors observed a reduction in porosity to values close to zero and hardness from 330 to 190 HV, as HT-ed; however, FSP increased it from 190 to 280 HV. On the other hand, FSP harmed the CSAM-ed 316L wear resistance, from 2.27×10^{-9} to 1.02×10^{-9} mm³·N⁻¹·mm⁻¹. Table 3 summarizes the CSAM post-treatments presented in the literature, considering their main effects and results studied by scholars.

Table 3. Post-treatments applied for CSAM.

Material	Post-Treatment	Post-Treatment Effects Obtained	Ref.
Cu	HT	Improved conductivity, mechanical properties, isotropy, and ductility; reduced hardness.	[208,210,230,277,278]
Cu	SPS	Improved mechanical properties and ductility, reduced hardness.	[230]
Cu	FSP	Microstructure changed, refining grain size, improved mechanical properties and ductility, reduced hardness	[210]
Cu	EPP	Microstructure changed, refining grain size, improved mechanical properties and ductility, reduced hardness	[210]
Cu-Al	Infrared irradiation HT	Improved electrical conductivity, maintained the elastic moduli, improved cohesion of particles, reduced hardness.	[255]
TiC-Cu	SPS	Promoted phase change and sintering Ti-C-Cu, eliminated interparticular region, increased hardness.	[231]
Al6082	SP	Improved compressive stress layer depth, changed the fatigue fracture mechanism from intercrystalline to transcrystalline.	[258]
Al-Mg-Sc-Zr	HIP	Maintained a very low porosity, improved mechanical properties, improved the compression resistance.	[237]
Al-Al ₂ O ₃	HT	Promoted phase change, reduced porosity and hardness, improved mechanical properties and ductility.	[213]
Al-B ₄ C	HT	Improved mechanical properties and ductility, reduced hardness.	[267]

Al-B ₄ C-	TMT	Improved adhesion, mechanical properties, and ductility, reduced hardness.	[267]
316L	HT	Reduced porosity and hardness, maintained phase composition, improved ductility and fatigue performance.	[119,208,220,279]
316L	HIP	Reduced porosity and hardness, maintained phase composition, improved ductility and fatigue performance.	[119,237]
316L	HT + FSP	Improved mechanical properties, reduced porosity, reduced hardness negligibly, reduced the wear resistance.	[220]
Ti	HT	Maintained the same porosity, increased the mechanical properties and ductility.	[208,216,280]
Ti	HIP	Reduced porosity from 4.3 to 2.2%, improved mechanical properties, changed pores morphology.	[236,237]
Ti	Remelting	Reduced hardness, transformed microstructure, eliminated interparticular region, improved corrosion behavior.	[243,244,281]
Ti6Al4V	HT	Reduced porosity, promoted phase changes, improved mechanical properties and ductility, reduced hardness,	[154,214,282]
Ti6Al4V	HIP	Reduced porosity, promoted phase changes, grain refine, improve mechanical, improve the ductility.	[237–239,282]
Ti6Al4V	Remelting	Improved hardness, increased surface roughness, coefficient of friction in wear testing, and tensile residual stress.	[247,283]
Invar 36	HT	Improved mechanical properties, ductility, reduced the compressive residual stress.	[284]
Inconel 625	HT	Increased hardness and the fatigue performance.	[217]
Inconel 625	Remelting	Reduced hardness, transformed cold worked microstructure in the particles to columnar dendritic, improved corrosion behavior.	[246]
Inconel 718	HT	Reduced porosity, improved mechanical properties and ductility, reduced the compressive residual stress.	[81,124,204,218,219,285]
Inconel 718	HIP + solution HT + aging HT	Reduced porosity and compressive residual stress, improved conductivity.	[123]

2.2.3. Avoiding Post-Treatments

The first post-treatment needed for CSAM-ed parts is the machine processes because CSAM cannot produce parts with the final geometry or roughness, which is a challenge for CSAM, as stated by Kumar and Pandey [126]. However, with the development of more complex robot manipulations, the machining has been planned for specific and essential areas of the component, such as bearing houses, screws, or axles journals, among others.

Regarding the materials' properties and characteristics, Laser-assisted Cold Spray (LACS), also called Supersonic Laser Deposition (SLD), is a relatively recent manufacturing process that combines the CS process with a complementary laser that heats the deposition zone while spraying. This method combines the benefits of both technologies, the CS solid-state deposition of metals at short times with little material waste and the bonding strength by heating the deposition zone with a laser without increasing the oxygen levels within the deposit [108,286,287], even applied for the LPCS process [288]. Lupoi et al. [289] and Bray et al. [290] presented LACS as an option to suppress the disadvantage of N₂ as a working gas (with a low particle velocity) by the implementation of a laser source to illuminate the spraying location. It softens the substrate during the CS deposition, promoting particle plasticity, even by phase transformation. Barton et al. [291] showed an Fe-based alloy transforming the ferritic into an austenitic phase, which is more ductile; and Birt et al. [287] concluded that LCAS is capable of depositing Ti6Al4V using N₂ as the working gas with densities as high as or higher than those deposited using He

without the laser assistance. Furthermore, the adhesion of CoNiCrAlY onto Inconel 625 and Cu onto Al were improved by particles/substrate local melting at a micro level and intermetallic formation [292], heating the particles to 80% of the powder melting point [293].

Another LACS option presented in the literature is using the laser to heat, clean, and ablate the substrate milliseconds before the CS deposition. It intends to soften the substrate, allowing the particles to deform and consolidate CS-ed material at an impact velocity lower than its V_{cr} [294]. The use of CSAM for hard materials has been one of the biggest challenges for the industry and researchers.

Regarding the selection of laser parameters, the laser (CO_2 , Nd-YAG, or Yb-fiber), wavelength, pulse duration, and energy affect the penetration depth of the thermal energy transferred by phonons to the metal [295]. Therefore, their optimization and selection depend on the materials' characteristics and properties. For example, some authors presented experiments for a LACS employing power between 1 and 5 kW, with expressive benefits to the CSAM microstructure and DE using high-power laser assisting [293,296–298]. Still, an excessive heat input can result in grain growth and hardness reduction, i.e., the LACS process results in annealing effects on the cold-worked particles during deposition [299].

Overall, LACS increases the temperature of the particles at the impact, improving the DE and reducing porosity in the deposit microstructure, as presented by Olakanmi et al. [296], reaching pore- and crack-free Al-12Si CS-ed on stainless steel. LACS also broadens the range of CS-ed materials [290]. As a result, LACS has successfully deposited dense parts of hard materials with high DE, such as oxide-free Ti [290], Ti6Al4V [287], MMC [300], Stellite-6 [289], CrMnCoFeNi high entropy alloy (HEA) [301], $\text{Fe}_{91}\text{Ni}_8\text{Zr}_1$ [291,299], 15-5 PH stainless steel [302], and AISI 4340 [297]. Another methodology employed for substrate pre-heating and adhesion improvement was induction, presented by Ortiz-Fernandez and Jodoin [303], spraying Al onto Ti6Al4V, resulting in higher DE and lower porosity.

During CS, particles are accelerated and sprayed at high velocities. At the moment of impact of the first layer, these particles are deformed and remain attached to the substrate. In the subsequent layers, the particles now impact the deposited material, causing the so-called tampering or tamping effect: new particles crush the previous layers of deposited material, causing compaction of the coating, thereby reducing porosity, a peening effect [89,304]. This effect can also be activated by mixing larger particles with the CS feedstock particles to deform the deposited material [305], as presented by Ghelichi et al. [306], mixing $-30 + 5$ with $-90 + 45$ μm Al particles, and Lett et al. [140], mixing $-45 + 15$ with $-250 + 90$ μm Ti6Al4V particles. Luo et al. [219,307] studied the effects of in situ CS-SP on the microstructure of Ti, Ti6Al4V, and Inconel 718. They presented it as an effective way to increase the DE while reducing porosity and improving inter-particle bonding and cohesion.

However, the $-24 + 7$ μm Inconel 718 were mixed with $-187 + 127$ μm stainless steel particles in different concentrations, and this last did not participate in the final sprayed material. Still, it acted for the peening effect, resulting in a drastic porosity reduction from 5.5 to 0.2%, improving the DE from 22 to 33%, and improving the hardness from 420 to 510 $\text{HV}_{0.05}$ [219]. For CS-SP-ed Ti6Al4V, increasing the mass of larger particles from 50 to 90% vol. in the feedstock powder, the porosity reduced from 6 to 0.2% [140] and induced compressive residual stress of $444 \text{ MPa}\cdot\text{m}^{-1}$, instead of the tensile residual stress of $126 \text{ MPa}\cdot\text{m}^{-1}$ obtained without SP. Hybrid use of CS was shown by Li et al. [308], spraying on the AA2219 alloy GTAW welded joint, altering the residual stress drastically and even promoting the compressive residual stress in some areas near the welding bead. Daroonparvar et al. [305] listed the use of CS-SP for different coatings on Mg alloy substrates, using other materials for the coating and SP; e.g., Ni with 410 stainless steel 150–200 μm and Al6061 with 1Cr18Ni stainless steel 200–300 μm , among others.

2.2.4. Measuring of Properties

Regarding the characterization, CSAM-ed samples have been evaluated as other thermal sprayed coatings. Conventional characterization techniques, such as optical or light microscopy, SEM, and microhardness have been seen in the literature [309]. These are potent tools for experts in the CSAM theme because the researchers can infer important materials' properties from the material microstructure. By image analysis, the Flattening Ratio (FR) is obtained, a measure of the compression of a sphere along a diameter to form an ellipsoid-like splat; the higher the FR, the higher the material plasticity. Electron Back Scattering Diffraction (EBSD) is a technique capable of identifying material phases at each analysis point and presenting the 3D orientation of the crystal lattice at each point. It has been used in CSAM to interpret the orientation in crystallographic planes in the different particles, which is even more important for the characterization of CSAM post-treatments [200]. Figure 11 shows CSAM-ed Ni/FeSiAl in as-sprayed and HT-ed conditions, Figure 11a,b, respectively. HT promoted a recrystallization, grain coarsening, and phase transformation in the material, as interpreted from the size of each colored area, which is more significant in Figure 11b. This image has fewer areas without a defined atomic lattice plane of the crystalline structure, as seen in the as-sprayed condition as dark green. These dark green areas represent patterns uninterpreted by the detector, which is related to the severe particle deformation during the CS deposition. The improvement in this indexing rate from 78 to 90% represents the recrystallization phenomena from HT post-treatment [310].

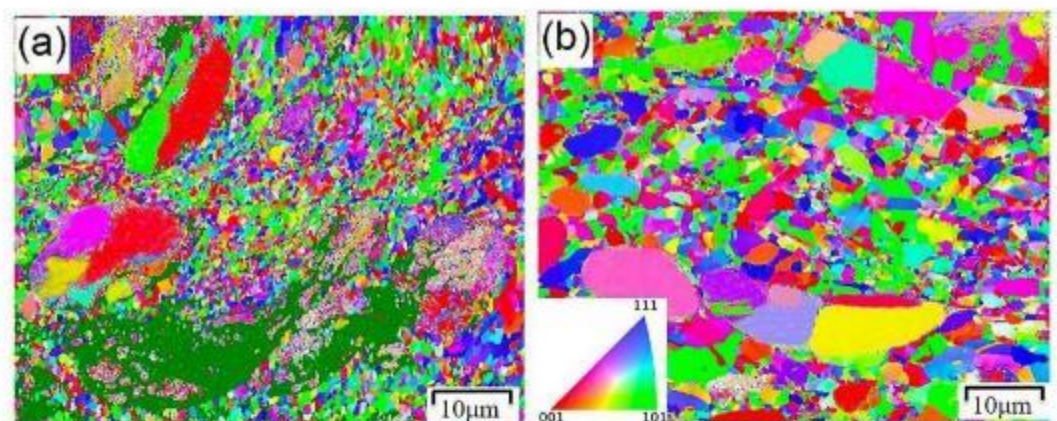


Figure 11. EBSD image of CSAM-ed Ni/FeSiAl before and after HT. (a) As-sprayed condition and (b) annealed condition. Reprinted with permission from Ref. [310], Elsevier, 2019.

Porosity has been calculated by CSAM cross-section image analysis [130,132,311], but other techniques have been presented in the literature as alternatives for higher accuracy in porosity measurements or a non-destructive approach, e.g., gas or He pycnometry [312,313], X-ray microtomography [314,315], laser-ultrasonic inspection [316], water absorption or the Archimedes method [317], and electrochemical impedance spectroscopy [318]. In addition, microhardness (Vickers and Knoop) employing low loading and nano-hardness techniques have been used to determine the hardness gradient in single particles. At the same time, microhardness utilizing higher loadings results in a macro evaluation of the material and fracture toughness by interpreting cracks grown due to the indenter loading [309,319]. Furthermore, the same Berkovich indenter used for the nano-hardness test provides the material elastic moduli, as described in the ISO 14577-1:2015 standard [320–322], an important property to preview the deformation of the material under the service loading.

Using CSAM for repairing processes or as a hybrid stage above a substrate made by other processes infers the need for good adhesion, which is the bonding strength between the CS-ed material and substrate. For thermally sprayed coatings, the ASTM C633-13

standard [323] is the most used technique to measure its adhesion, known as Tensile Adhesion Testing (TAT), which is basically comprised of a thermal-spray-coated disk, dia. 1 in., that is attached with epoxy to a complimentary uncoated plug and detached by a uniaxial tensile loading, the relation loading-area results in the bonding strength, in MPa or ksi [309,324]. However, for bulks, ASTM C633-13 [323] is inadequate. A technique within the sample machined from the CSAM-ed freeform part has been presented in the literature as a more effective method, modified tensile testing, based on the ASTM E8-22 standard [325]. Ichikawa et al. [326] machined adhesion samples of CSAM-ed Cu onto an Al substrate, eliminating the interference of a bonding agent, epoxy adhesive, and guaranteeing the rupture in the Cu/Al interface. Boruah et al. [327] used a similar technique, but with CS Ti6Al4V on a washer surrounding an exposed pin-like substrate, which are tensile together, rupturing in the coating/substrate interface. Figure 12 shows the schemes for TAT and ASTM E8-22 modified adhesive testing.

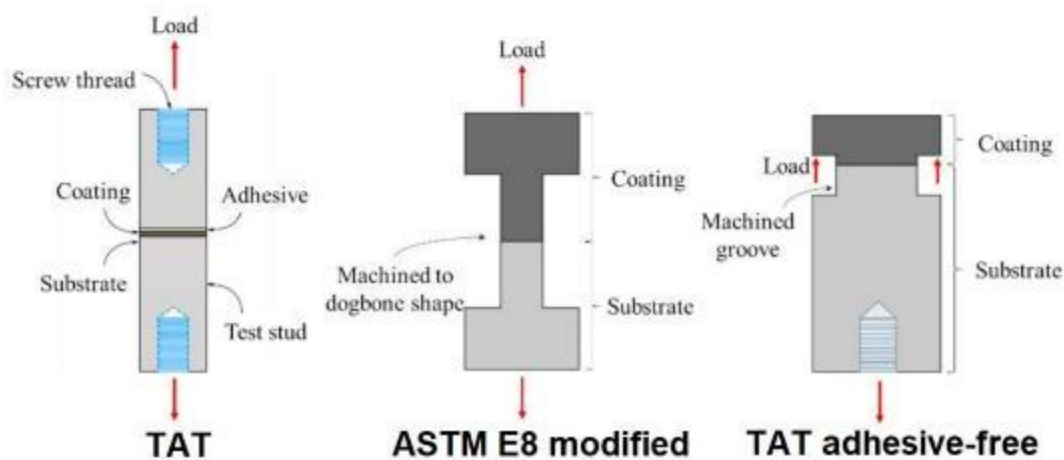


Figure 12. Schemes for CSAM adhesive testing. Reprinted with permission from Ref. [327], Elsevier, 2020.

The surface properties and the whole component quality are important for AM parts. Tensile testing has been done for different materials and fabrication strategies to measure the materials' strength and ductility [186,211,282]. Machining samples in different CSAM-ed part directions make the interpretation of mechanical isotropy possible, as performed by Yang et al. [200], Ren et al. [222], and Wu et al. [328]. The literature has presented the CSAM-ed mechanical resistance and ductility as a consequence of a good cohesion of particles, which TCT can easily measure. The TCT principle coats the circumference of two cylinders together head-to-head that are pulled in a universal testing machine. The stress or cohesion of particles is calculated as a relation between the loading collected and the coating thickness value, following the instructions of the EN 17,393:2020 standard [135].

Residual stress is crucial information for developing the CSAM as an industrial process, and the realization of the CSAM limitations is perhaps the main motivation behind the scholars' efforts to provide a reliable framework to study residual stresses in CS-ed deposits, initially by means of experimental and theoretical analyses, and later by finite element modeling. The residual stresses are divided into three types: the first order is macro-stresses homogeneous over multiple grains; the second order is micro-stresses over single grains; and the third order is micro-stresses in single grains, but with being inhomogeneous over the smallest areas such as unit cells [329]. Non-destructive diffraction measurement techniques for micro-stress have been used for CS-ed material, X-ray, and neutron diffraction. The first has a shallow penetration in the material, in order of micrometers, accrediting it just for superficial evaluation [258]. However, FEA was applied by Wang et al. [330] to simulate the residual stress along the CSAM-ed Cu part from X-ray diffractometry superficial residual stress results.

On the other hand, neutron diffraction penetrates the material in order of centimeters, but needs a long time exposition to achieve good results, in order of tens of minutes per measurement point [309]. Both methods are restricted to crystalline materials, and neutron diffraction has been studied for CSAM, as presented by Luzin et al. [331] and Vargas-Uscategui et al. [332] for Ti, Sinclair-Adamson et al. [333] for Cu, Loke et al. [334] for Al6061, and Boruah et al. [335] for Ti6Al4V. Despite being restricted to a few facilities worldwide and being an expensive technique, neutron diffraction has presented valid results in understanding the evolution of residual stress in CSAM deposition. In addition, it helps researchers to find new deposition strategies to reduce the regions with deleterious tensile fields.

Incremental Hole Drilling (IHD) is semi-destructive testing presented in the literature for the first-order residual stress measurement, which has been used for different materials and processes of fabrication for decades, including thermally sprayed coatings [336–338]. The IHD principle is based on drilling a small hole, <1 mm, into the material and collecting data about the deformations around the drilled hole using optical instruments or strain gauges. The material deformation or relaxation is related to the residual stress in the volume of the removed material through drilling [339], and the testing procedure is ruled by the ASTM E837-20 standard [340]. IHD is a technique routinely used for cast or rolled materials, and its use for CSAM promises high accuracy, easy sample preparation, and fast results. However, the literature still needs documents discussing the results and limitations and comparing IHD to other residual stress techniques, focusing on CSAM-ed bulks, which is a need to be filled by scholars.

In situ Coating Properties (ICP) measure the substrate curvature during and after deposition. The evolution of the sample curvature can be linked to the evolution of stresses in the thermally sprayed material using a variety of models [341]. Figure 13 shows an example of typical curves obtained by the ICP sensor, where there is evidence of the spraying time or deposition stress and the cooling time until room temperature, culminating in the residual stress. For HVOF sprayed coatings, normally, tensile residual stress is obtained, as indicated in Figure 13, with positive curvature values; however, for CS-ed coatings, the residual stress has negative curvature values, which is compressive. ICP has the advantages of being fast and not demanding the machining of samples, but it is limited to coatings, as shown by Singh et al. [342], comparing ICP to X-ray for Inconel 718 coatings thinner than 1 mm, resulting in similar compressive residual stress values for both techniques. Furthermore, ICP does not apply to larger CSAM-ed parts, even though ICP results help the researchers optimize the CS parameters used for CSAM, mainly regarding improving adhesion.

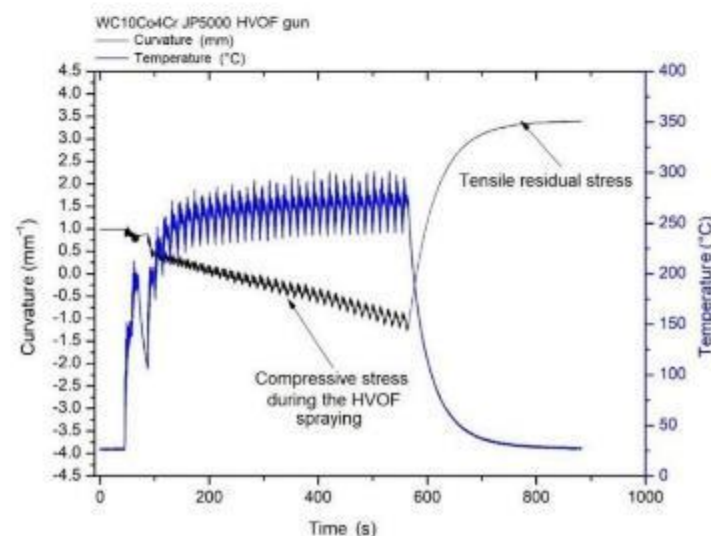


Figure 13. Typical curves obtained with ICP sensor.

Mechanical elements under cyclic loadings are subject to fatigue, reducing their life cycle. For CSAM-ed parts, Sample et al. [343] presented the influence of different CS properties, e.g., hardness, tensile properties, residual stress, etc., on the material fatigue performance. For CSAM-ed parts and CS-coated materials, different fatigue tests have been presented in the literature, which are designed and classified by the force or loading type: direct (axial) stress, plane bending, rotating beam, alternating torsion, or combined stress. Rotating beam and bending fatigue testing evaluate the parts exposed to revolutions under loading, such as axles, shafts, or wheels. Rotation bending exploits a rotating bending moment obtained through a rotating unbalanced mass, while the rotation beam places the load in the center of a supported sample at the ends. Applying CS as a coating improved the sample fatigue life by inserting compressive residual stress in the surface [258,344–348].

Using axial cyclic loading, three- and four-point bending fatigue testing have been presented in the literature. Xiong and Zhang [349] showed the improvement of mechanical resistance and fatigue life for an AZ91D Mg alloy after an LPCS-ed Al coating; Yamazaki, Fukuma, and Ohno [350] presented a low level of improvement in the fatigue life of CSAM repaired 316L samples, accrediting the repairing services for this material. Ševčec et al. [351] studied the benefits of CS-ed coatings on the Zircaloy-4 high-temperature fatigue life and displacement under cyclic loading. Considering the CSAM-ed bulk, Julien et al. [202] used compact tension specimens, following the ASTM E399-22 standard [352], to evaluate the fracture toughness (K_{Ic}) of CSAM-ed Al6061. Wrought reference samples had much higher values than the CSAM-ed ones, 26.5 over 13.0 $\text{MPa}\cdot\text{m}^{0.5}$, resulting from the CS-ed typical microstructure and the interparticular crack growth. A higher K_{Ic} reduction was presented by Kovarik et al. [221] for CSAM repairing Al, Ti, Ni, and Cu compared to rolled materials. Making the CSAM-ed parts have similar properties to bulks produced by traditional processes represents a challenge for CSAM's industrial application. Scholars have employed efforts to find solutions and possibilities to achieve solutions for this, such as post-treatments. Regarding the material fatigue life, Li et al. [353] proposed a probabilistic fatigue modeling for a GH4169 Ni alloy, using the weakest link theory applied to calculate the number of cycles to crack initiation. Similar modeling should be performed for CSAM-ed materials to compare how their microstructure defects and characteristics influence the material performance, deviating the experimental results from the mathematical and statistical model formulated.

3. Bibliometric Analysis

This section presents CSAM from an academic viewpoint, considering how the literature, scholars, and institutions cover the theme of CSAM. Bibliometric analysis has gained immense popularity in many research areas in the last decade due to being a powerful tool for interpreting the massive amount of data available nowadays, which, depending on the theme studied, may reach hundreds or even thousands of relevant documents [354]. Scholars use bibliometric analysis for different reasons, such as uncovering emerging publishing and journal performance trends, looking for investigation collaborators, or exploring the intellectual structure of a specific domain in the study [355]. The exciting use of bibliometric research is to identify knowledge gaps in the literature, helping the researchers to generate a novelty character in their future works filling these gaps.

It is not a new technique, the term bibliometrics was presented in the 1960s [356], and the evaluation of metrics regarding an area of interest in scientific publishing has been developed for more than a century [357]. Nowadays, in the big data era, this tool has been even more helpful in filtering and interpreting a large amount of information and data available for scholars. For AM, it is not different, and the bibliometric analysis has been related to the AM impact on business [358], on the supply chain [26], on industry 4.0 [359], AM-specific applications in orthopedics [360], or the general AM overview and trends [361], among others. Regarding CS, the literature presents the use of bibliometric analysis

for a general overview comparing CS to other thermal spray processes [362–364]; however, there is a gap in the literature presenting the evolution of publishing focused on CSAM, or who the researchers and the institutions involved in this important theme are.

This work aims to understand the research status and development trends in the CSAM field, and identify the most relevant themes of study in the CSAM field, as there are some remarkable challenges. Therefore, it is important to carry out a bibliometric analysis that maps the current guidelines in this domain, which can inspire scholars in their future research lines and works. Furthermore, it gives them insights into the most active authors and journals that publish this theme and the countries that invest more in AM-related research. It provides a scientific cartography that reveals the dynamics and structure of scientific fields. For this purpose, a bibliometric analysis is conducted to map CSAM R&D trends.

3.1. Data Mining Strategy

The bibliometric data was extracted from the Scopus database using a query string containing keywords to search in the title, abstract, and keyword fields. Since this work has aimed to see the trend in publishing on CSAM over the last decade, the query string was refined to exclude articles published before 2012 and those in other languages. The following string retrieved more than 450 items as of 27 December 2022: TITLE-ABS-KEY (cold AND spray* AND additive AND manufactur*) OR TITLE-ABS-KEY (cold AND spray* AND 3d AND print*) AND PUBYEAR > 2011. These documents were subjected to further text cleaning and bibliometric analyses.

Due to their irrelevance to the studied theme, some articles were eliminated after a manual screen or database cleaning. The articles were limited to the subject area “materials science” OR “engineering” OR “physics and astronomy” OR “chemistry” OR “chemical engineering” OR “energy” OR “mathematics”. The articles listed were carefully reviewed by reading their abstracts or full paper. The documents with an unclear relationship with the theme studied were eliminated, refining the results, resulting in the number of works for the statistical analysis being 439. Finally, the bibliometric analysis software VOSviewer was used to analyze the publications. VOSviewer is a software that graphically presents the bibliometric network mapping, which facilitates the interpretation of maps and data. The main networks are co-citation, bibliographic coupling, co-author, and/or co-word analysis. The authors and index keywords were selected for the co-occurrence analysis. VOSviewer identified many similar keywords, and to make the data more coherent, they were classified manually, such as “cold spray”, “cold spraying”, “cold gas dynamic spray”, and “cold gas spray”, which were merged to “cold spray”.

3.2. Results and Discussions

Figure 14 presents the scientific productivity regarding the CSAM theme, limited to the last decade (2012–2022). The number of published documents each year indicates this technology’s academic impact or interest by researchers, funding institutions, and journals. The number of documents per year significantly rose from 4 documents in 2012 to a maximum of 84 papers in 2022. This trend remained steady from 2020 and 2021, keeping around 81 publications per year. It is reasonable because the number of research groups researching CSAM and their productivity has not maintained the growth rate, despite the increasing number of researchers, groups, and equipment observed in the last decade [68].

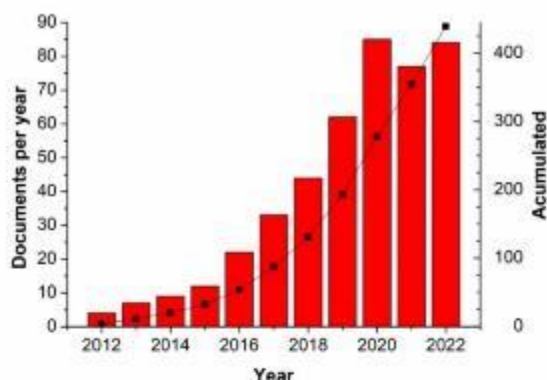


Figure 14. Year-wise publication of documents in CSAM field.

Furthermore, implementing the LPCS process demands less investment because the equipment is less expensive, and the noise level during the operation is low [2,99]. Additionally, an LPCS gun is light and typically uses compressed air as the working gas and can be manipulated manually or using a small robot. However, to operate with HPCS equipment, a reasonable noise-insulated booth is demanded, as a facility for dozens of N₂ or He bottles [10], as well as the fact that the equipment costs of hundreds of thousands of dollars and a large size robot to support the gun, following the robot classification proposed by Dobra [365].

As seen in Figure 15, Halin Liao, who has an h-index of 61 in the Scopus database, is the researcher with more publications on the CSAM topic, with 35 documents. Liao has been a researcher at the Laboratoire Interdisciplinaire Carnot de Bourgogne/Université Bourgogne Franche-Comté (France) since 1994, and is co-author of 500 articles in diverse themes, such as materials characterization and performance, surface engineering, coatings, tribology, and corrosion, among others. Due to the relation of Liao with many other authors, his affiliation figures in the first position among the most important research groups, as seen in Figure 16, followed by Trinity College Dublin, due to the strong and numerous collaborations between Lupoi, Yin, and Chinese co-authors.

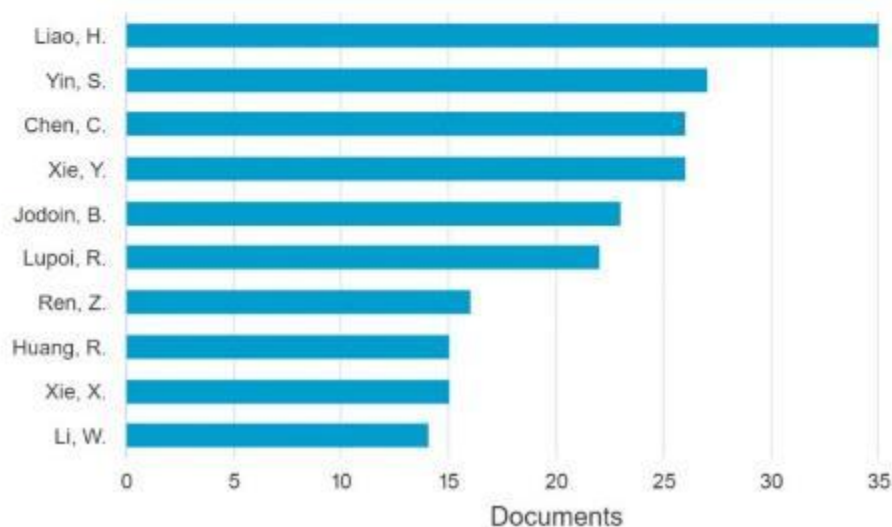


Figure 15. Number of documents per author.

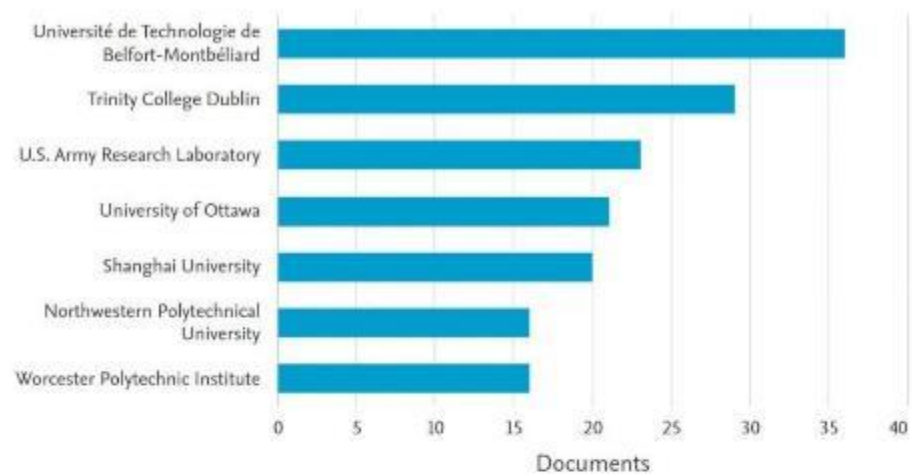


Figure 16. Number of documents by affiliation.

Most of the works published are in collaboration with researchers from Chinese institutions. For example, Shuo Yin, who has an h-index 36 in the Scopus database, is the second author in the number of published articles and worked with Halin Liao and Chaoyu Chen in France. Since 2015, he has been a researcher at Trinity College Dublin, where Rocco Lupoi, who has an h-index 31 in the Scopus database and is sixth on the publishers' list, develops his research too. Bertrand Jodoin, who has an h-index 33 in the Scopus database, is the fifth influential author in Figure 15 and works at the University of Ottawa (Canada).

China has the highest volume of documents published, mainly for collaborative works, as presented in Figure 17. China also leads this ranking, as it occurs in many other areas, due to the vast number of PhD students and active researchers at the Universities and research centers, as well as due to the massive amount of investments and R & D by governmental programs [366–369]. Even with an expressive high number of articles published by Chinese authors, the most cited articles in CSAM have only 6 Chinese figuring among the 25 co-authors enrolled in Table 4. However, the situation in the United States is worse because none of the important works presented in Table 4 has American co-authorship, for which the majority are Europeans. It reflects the importance given by the scientific community for the Chinese and American works, which could be by a lack of novelty seen in most of the hundreds of published works. Another consideration is that most works did not present new concepts but did an application and some important discussion on the concepts previously proposed by other original documents. Original documents or review articles have been cited more, as seen in Table 4. That article type is essential to consolidate the concepts but does not typically promote many citations, such as original or review articles [370,371]. It has caused a preoccupation by the Chinese institutions, which have looked at methodologies to make their work more recognized by the scientific community [372,373].

Table 4. The articles most cited in CSAM theme.

Title	Citations	Contributions and Goals	Ref.
Cold spraying—A material’s perspective	592	An overview regarding the CS principles, ASI bonding mechanism, materials characteristics, and applications.	[77]
Cold spray additive manufacturing and repair: Fundamentals and applications	372	Summarizing and reviewing the CSAM-related work, comparing CSAM to fusion-based AM techniques, presenting the effects of HT on a CSAM-ed material’s properties, and CSAM real applications.	[2]
Solid-state additive manufacturing and repairing by cold spraying: A review	235	Summarizing and reviewing the CSAM-related work, different possibilities of CSAM application, alloys, process parameters, post-treatments, and their effects on CSAM-ed material mechanical properties.	[374]
Cold gas dynamic manufacturing: A non-thermal approach to freeform fabrication	217	Introducing the application of CS as an AM technique to produce freeform parts, comparing CSAM to other AM processes and CSAM strategies.	[169]
Cold gas dynamic spray additive manufacturing today: Deposit possibilities, technological solutions and viable applications	212	Presenting the evolution in investments in CSAM, adhesion and cohesion mechanisms for CSAM-ed material, listing materials and applications, characteristics, and industrial applications.	[68]
Potential of cold gas dynamic spray as additive manufacturing technology	212	Presenting the CSAM principles, geometric characteristics, and materials’ properties, as well as the potential in using CSAM and its compatibility with other metal AM techniques.	[97]

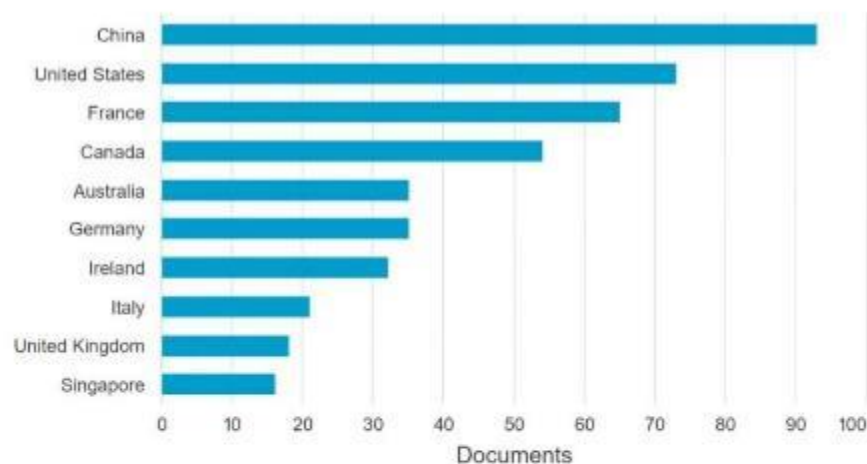


Figure 17. Number of documents by country.

Collaborative works have characterized the articles and publishing in CSAM because of the mutual interests and the synergy in sharing equipment to develop the experiments and applying a kind of knowledge synergism to interpret the experimental results obtained. Regarding the authors’ collaboration, the co-authorship relations were obtained by VOSviewer software, limiting the results to authors with more than ten articles published, reducing the total of 972 authors to the 16 presented in Figure 18. The circle size around the authors’ names represents the number of articles in co-authorship, the color indicates a cluster of authors where the authors have more connections, and the line or link between the circles means the strength of their association; a thicker line means more collaborations. Chen and Xie are the leading authors in a cluster of Chinese cooperation, Yin and Lupoi are the most important authors in a cluster formed at Trinity College Dub-

lin, and Liao is ahead of the French group. An interpretation of the map presented in Figure 18 is that its central persons are Liao, Xie, Chen, and Yin, indicating they act as bridges between the Chinese, Irish, and French institutions.

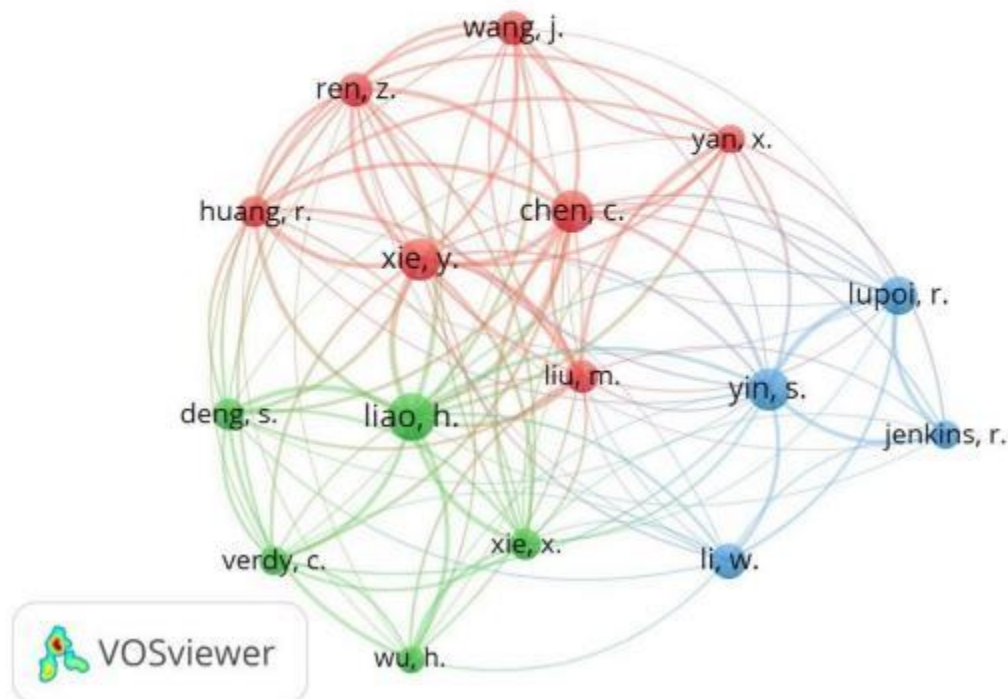


Figure 18. Authors' collaboration. Minimum of 10 articles per author.

The journal with more documents published, 48 articles, was the Journal of Thermal Spray Technology (JTST), a journal focused on surfaces, coatings, and films, justifying why the CS authors chose it to submit and publish their works. However, JTST places in the 70th percentile, or Q2, and has a cite score of 4.6 in the Scopus database. The second influential journal, with 29 papers, was Surface and Coatings Technology (SCT), older than JTST, in the 88th percentile, Q1, and with a cite score of 7.6 in the Scopus database. Open access journals have increased their contribution to CSAM publishing, attracting authors due to the faster publishing process and free access to the readers. Between the ten more relevant publishers, MDPI's journals Coatings, Materials, and Metals have 7, 10, and 10 documents published in the CSAM theme, respectively, from 2019 to 2022. MDPI's Metals has increased its relevance in the scientific community, publishing 6 documents only in 2021, reaching the 76th percentile, Q1, and 3.8 in the Scopus database.

Keywords represent the synthesis of the essential content of the documents, and their analysis aims to study the structure of the research related to the discipline. The analysis principle is based on the co-occurrence of keywords in the selected documents, revealing how closely they are connected in terms of the concepts they deal with, making it possible to understand the main themes of interest for the scholars. VOSviewer software identified more than 3000 keywords, and after a manual and critical evaluation, many of them were merged due to the similarity of their meaning. In addition, only keywords with at least 15 occurrences were considered, resulting in 70 keywords for the study, which are graphically presented in Figure 19b by their density, i.e., a darker and bigger circle represents more times the Keywords are listed: it results that "3d printing", "additive manufacturing", and "cold spraying" are the main terms, followed by "manufacturing processes", "additives", "coatings", and "microstructure" keywords.

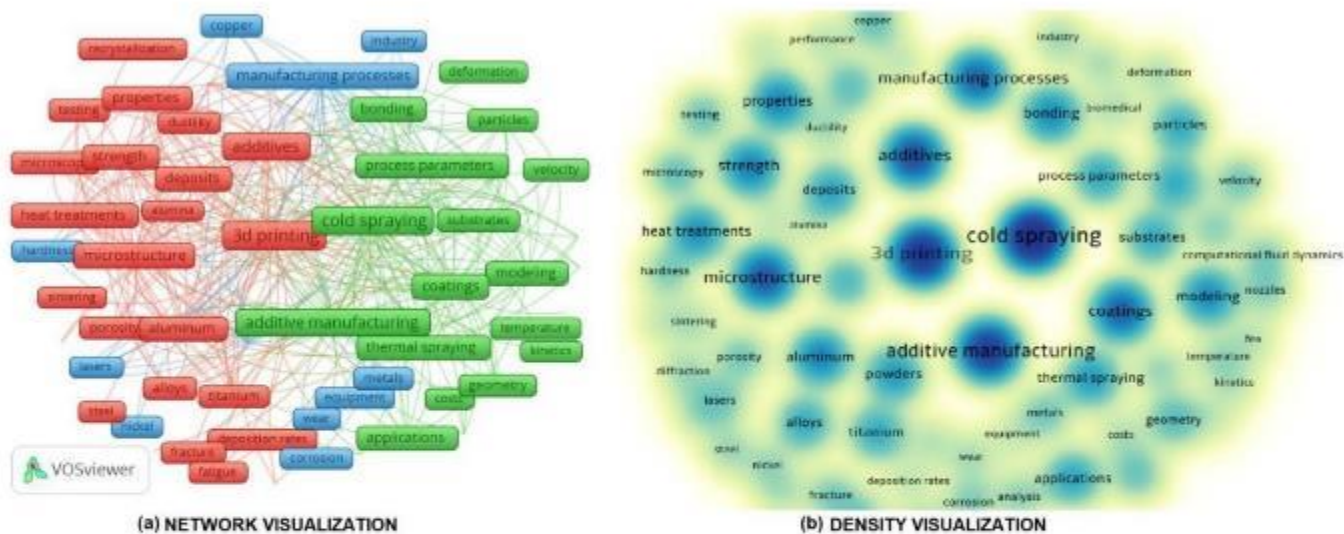


Figure 19. Co-occurrences keywords. Minimum 15 occurrences.

By analyzing the mapping network of co-occurrence, three clusters were formed, identified by the colors, Figure 19a. The clusters result from the link strength between the keywords, i.e., a stronger link means the same keywords group is used in more documents. VOSviewer resolution was set to 1.00 to avoid too small clusters. The smallest cluster, the blue one, has 18 items. The primary term is “manufacturing processes”, which is a more generalist approach to making parts by CS, laser, and hybrid processes and is also linked to AM-processed materials, such as Cu, Ni, and composites. The other two clusters have the same number of items, 27; the green one has the main terms “cold spraying” and “additive manufacturing” that are strongly linked to “coatings”, which makes perfect sense since CS has been developed prior for coating. The authors usually present these keywords together. From the query string used for searching in the Scopus database, it was predictable that CS and AM would figure as the primary keywords for the papers.

A relation is understood from the materials linked to CSAM, which are Cu, Ti, and Al, as observed reading the articles, but these are presented in Figure 19a with stronger links in the blue cluster. Additionally, material properties and process parameters are highlighted because most works are experimental and present the materials’ evaluation and testing. The red cluster presents the keyword “3d printing” linked to material properties, such as the microstructure, porosity, and strength. The keyword “3d printing” could be merged with “additive manufacturing”, mixing the red and green clusters, following the AM nomenclatures in the literature. It makes perfect sense, considering the content of the papers that present these keywords. However, the “3d printing” term is a legacy from the AM of polymers and has been presented as a friendlier expression to AM non-experts. On the other hand, “rapid prototyping” had been a keyword widely used for AM [78,89], but in the last decade, it has been substituted for “3d printing” and “additive manufacturing”, as indicated by Jemghili, Ait Taleb, and Khalifa [361]. It was confirmed by the VOSviewer keywords list and Figure 19, where “rapid prototyping” was not mentioned, indicating that this keyword has not been linked to CSAM.

4. Summary and CSAM Future Trends

This article briefly introduces CSAM, its characteristics, advantages over other AM processes, limitations, and some answers or alternatives to overtake them based on the literature. In addition, the paper presents challenges that still have to be overcome. Nevertheless, the innovation potential of this research field is outcoming, and new applications have emerged in different industrial fields, supporting the crescent number of publications dedicated to CSAM industrialization. Based on the state-of-art and interpretation of the most recent literature contents, some trends are listed:

- CSAM for repairing services, with its application on expensive components or damages that do not need extensive restoration [2]. Improving the CSAM-ed geometries control generates a hot topic for research, including geometry construction simulation, robot programming, and robot self-learning for an adaptive path, spraying angle, or gun displacement velocity. Research on this theme has been done by the Italian group of Politecnico di Milano [375], the Spanish group of Thermal Spray Center [144], and the Australian company Speed3D, among others;
- CSAM for hard materials, improving the CSAM-ed deposit adherence on materials such as Inconel, Ti6Al4V, HEA, or martensitic steels. For this, studies on the optimization of pre- and process-heating or CS parameters must be exploited. Some examples are using the expensive He as a working gas only for the first layers and N₂ for the others, the CS-SP process, or introducing HT between the layers to reduce the tensile residual stress on the CSAM/substrate interface and improve the adhesion and repairing quality;
- Improve CSAM-ed properties, reaching close or better than the wrought reference materials. As well as the well-established HT and HIP, new post-treatments have to be investigated in this theme. SPS presented good properties, but strict limitations in the geometries are feasible, requiring more flexibility for more complex geometries;
- CS hybrid systems consolidation, such as CS-SP or LACS, to avoid post-treatments and eliminate steps in the AM production chain [286]. Most studies are related to CS-ed coatings, promoting a better adhesion to the substrate and cohesion of particles, besides a low porosity. Therefore, CSAM hybrid systems' use is a hot topic to provide a good performance CSAM-ed parts;
- CSAM applied with other AM processes, optimizing the manufacturing chain to make the low complexity part areas by the fast CSAM process and dedicate the slower but more accurate laser process to the areas that demand more geometrical control. It is feasible because other AM techniques have increased their maturity as industrial processes; however, this mixing of methods is a lack in R & D, which is a hot topic for scholars.

Regarding the bibliometric analysis, the literature characteristics and metrics were studied, collecting data from more than 420 documents published in the last decade for CSAM and related themes. The analysis covered several dimensions, including subject areas through keyword analysis, productive journals, the most influential authors, most cited documents, and referent affiliations and countries. The main results of the bibliometric analysis can be summarized as follows:

- A total of 56% of the total publications in the CSAM theme were registered during the last three years, indicating the increase of academic interest in this research field, considering that in 2010 the number of documents published was zero. The main topics actively explored in the papers were related to the processing parameters' optimization and other experiments focused on improving the CSAM-ed material's performance to make this process more industrially mature;
- China is the country with more documents published, followed by the United States and France, where the most relevant research group in CSAM is from, the Université de Technologie de Belfort-Montbéliard, which is the affiliation of Liao, the author with the most documents published. The publishing mapping presents a collaboration between Chinese and European institutions, signing for a fast CSAM industry maturity since the Chinese founding objectives are scientific development and even more advances in mass production;
- The current scenario of publication in CSAM points to a future consolidation of CSAM as an industrial technique, first for specific applications in high-cost components, such as multi-alloy nozzles for rockets in the aerospace industry or repairing expensive components, such as turbine blades or vanes. However, in the medium-term and long-term, CSAM applications tend to expand their use;

- “Costs” is the keyword that indicates a crucial point for CSAM advances. For the feedstocks, scholars have studied less expensive materials and improved DE, reaching more than 95% for some materials. A considerable challenge and trend for reducing processing costs and improving CSAM reliability is making the processing more independent of experts but easier for industrialization.

Author Contributions: Conceptualization, R.F.V.; funding acquisition, J.S. and I.G.C.; investigation, R.F.V. and A.G.; methodology, R.F.V. and A.G.; project administration, J.S. and I.G.C.; writing—original draft preparation, R.F.V., A.G., J.S., and V.A.; writing—review and editing, R.F.V., A.G., J.S., and V.A.; supervision, I.G.C. All authors have read and agreed to the published version of the manuscript.

Funding: The grant PID2020-115508RB-C21 and EIN2020-112379 was funded by MCIN/AEI/10.13039/501100011033 and, as appropriate, by “ERDF A way of making Europe”, by “European Union NextGenerationEU/PRTR”. A.G. and R.F.V. have AGAUR Ph.D. grants 2021 FISDU 00300, and 2020 FISDU 00305, respectively.

Institutional Review Board Statement: Not applicable.

Informed Consent Statement: Not applicable.

Data Availability Statement: The data presented in this study are available on request from the corresponding author.

Conflicts of Interest: The authors declare no conflict of interest. The funders had no role in the design of the study; in the collection, analyses, or interpretation of data; in the writing of the manuscript, or in the decision to publish the results.

Abbreviation

The following abbreviations are used in this manuscript:

AM	Additive Manufacturing
APS	Air Plasma Spray
ASI	Adiabatic Shear Instability
BB	Ball-Burnishing
BJ	Binder Jetting
CFD	Computational Fluid Dynamics
CR	Cold Rolling
CS	Cold Spray
CSAM	Cold Spray Additive Manufacturing
CS-SP	Cold Spray Shot Peening
DE	Deposition Efficiency
DMLM	Direct Metal Laser Melting
DMLS	Direct Metal Laser Sintering
EBM	Electron Beam Melting
EBSD	Electron Back Scattering Diffraction
EPP	Electric Pulsing Processing
FR	Flattening Ratio
FS	Flame Spraying
FSP	Friction Stir Processing
FSAM	Friction Stir Additive Manufacturing
FSW	Friction Stir Welding
GMAW	Gas Metal Arc Welding
GTAW	Gas Tungsten Arc Welding
HEA	High Entropy Alloy
HIP	Hot Isostatic Pressing
HPCS	High-Pressure Cold Spray
HR	Hot Rolling
HT	Heat Treatment
HVOF	High-Velocity Oxy-Fuel
ICP	In situ Coating Properties

IHD	Incremental Hole Drilling
JTST	Journal of Thermal Spray Technology
K _{IC}	Fracture Toughness
LACS	Laser-Assisted Cold Spray
LMF	Laser Metal Fusion
LOM	Laminated Object Manufacturing
LPCS	Low-Pressure Cold Spray
MMC	Metal Matrix Composite
ME	Material Extrusion
MJ	Material Jetting
MMC	Metal Matrix Composite
MPCS	Medium-Pressure Cold Spray
PAW	Plasma Arc Welding
PEO	Plasma Electrolytic Oxidation
R&D	Research and Development
SCT	Surface and Coatings Technology
SD	Standoff Distance
SEM	Scanning Electron Microscopy
SL	Stereolithography
SLD	Supersonic Laser Deposition
SLM	Selective Laser Melting
SLS	Selective Laser Sintering
SP	Shot Peening
SPS	Spark Plasma Sintering
TAT	Tensile Adhesion Testing
TCT	Tubular Coating Tensile
TMT	Thermo-Mechanical Treatment
UAM	Ultrasonic Additive Manufacturing
UTS	Ultimate Tensile Strength
V _{cr}	Critical Velocity
V _{er}	Erosion Velocity
WAAM	Wire Arc Additive Manufacturing
WCI	Waterjet Cavitation Impact

Reference

1. ISO/ASTM 52900-21; Standard Terminology for Additive Manufacturing—General Principles—Terminology. ASTM International: West Conshohocken, PA, USA, 2022.
2. Yin, S.; Cavaliere, P.; Aldwell, B.; Jenkins, R.; Liao, H.; Li, W.; Lupoi, R. Cold Spray Additive Manufacturing and Repair: Fundamentals and Applications. *Addit. Manuf.* **2018**, *21*, 628–650. <https://doi.org/10.1016/j.addma.2018.04.017>.
3. Saboori, A.; Aversa, A.; Marchese, G.; Biamino, S.; Lombardi, M.; Fino, P. Application of Directed Energy Deposition-Based Additive Manufacturing in Repair. *Appl. Sci.* **2019**, *9*, 3316. <https://doi.org/10.3390/app9163316>.
4. Campbell, I.; Bourell, D.; Gibson, I. Additive Manufacturing: Rapid Prototyping Comes of Age. *Rapid Prototyp. J.* **2012**, *18*, 255–258. <https://doi.org/10.1108/13552541211231563>.
5. Dilberoglu, U.M.; Gharehpapagh, B.; Yaman, U.; Dolen, M. The Role of Additive Manufacturing in the Era of Industry 4.0. *Procedia Manuf.* **2017**, *11*, 545–554. <https://doi.org/10.1016/j.promfg.2017.07.148>.
6. Horst, D.J.; Duvoisin, C.A.; Vieira, R.D.A.; Horst, D.J.; Vieira, R.D.A. Additive Manufacturing at Industry 4.0: A Review. *Int. J. Eng. Tech. Res.* **2018**, *8*, 3–8.
7. Parupelli, S.K.; Desai, S. A Comprehensive Review of Additive Manufacturing (3D Printing): Processes, Applications and Future Potential. *Am. J. Appl. Sci.* **2019**, *16*, 244–272. <https://doi.org/10.3844/ajassp.2019.244.272>.
8. Wong, K.V.; Hernandez, A. A Review of Additive Manufacturing. *ISRN Mech. Eng.* **2012**, *2012*, 1–10. <https://doi.org/10.5402/2012/208760>.
9. Huang, S.H.; Liu, P.; Mokasdar, A.; Hou, L. Additive Manufacturing and Its Societal Impact: A Literature Review. *Int. J. Adv. Manuf. Technol.* **2013**, *67*, 1191–1203. <https://doi.org/10.1007/s00170-012-4558-5>.
10. Sun, W.; Chu, X.; Lan, H.; Huang, R.; Huang, J.; Xie, Y.; Huang, J.; Huang, G. Current Implementation Status of Cold Spray Technology: A Short Review. *J. Therm. Spray Technol.* **2022**, *31*, 848–865. <https://doi.org/10.1007/s11666-022-01382-4>.
11. Kruth, J.; Vandenbroucke, B.; Van Vaerenbergh, J.; Naert, I. Rapid Manufacturing of Dental Prostheses by Means of Selective Laser Sintering/Melting. In Proceedings of the Les 11emes Assises Europeennes du Prototypage Rapide, Paris, France, 4–5 October 2005.

12. Jamieson, R.; Holmer, B.; Ashby, A. How Rapid Prototyping Can Assist in the Development of New Orthopaedic Products—A Case Study. *Rapid Prototyp. J.* **1995**, *1*, 38–41. <https://doi.org/10.1108/13552549510104456>.
13. Hieu, L.C.; Bohez, E.; Vander Sloten, J.; Phien, H.N.; Vatcharaporn, E.; Binh, P.H.; An, P.V.; Oris, P. Design for Medical Rapid Prototyping of Cranioplasty Implants. *Rapid Prototyp. J.* **2003**, *9*, 175–186. <https://doi.org/10.1108/13552540310477481>.
14. Esses, S.J.; Berman, P.; Bloom, A.I.; Sosna, J. Clinical Applications of Physical 3D Models Derived from MDCT Data and Created by Rapid Prototyping. *Am. J. Roentgenol.* **2011**, *196*, 683–688. <https://doi.org/10.2214/AJR.10.5681>.
15. Sun, J.; Zhang, F.Q. The Application of Rapid Prototyping in Prosthodontics. *J. Prosthodont.* **2012**, *21*, 641–644. <https://doi.org/10.1111/j.1532-849X.2012.00888.x>.
16. Popov, V.V.; Muller-Kamskii, G.; Kovalevsky, A.; Dzhenzhera, G.; Strokin, E.; Kolomiets, A.; Ramon, J. Design and 3D-Printing of Titanium Bone Implants: Brief Review of Approach and Clinical Cases. *Biomed. Eng. Lett.* **2018**, *8*, 337–344. <https://doi.org/10.1007/s13534-018-0080-5>.
17. Nickels, L. AM and Aerospace: An Ideal Combination. *Met. Powder Rep.* **2015**, *70*, 300–303. <https://doi.org/10.1016/j.mprp.2015.06.005>.
18. Liou, F.; Liu, R.; Wang, Z.; Sparks, T.; Newkirk, J. Aerospace Applications of Laser Additive Manufacturing. In *Laser Additive Manufacturing: Materials, Design, Technologies, and Applications*; Brandt, M., Ed.; Woodhead Publishing: Duxford, UK, 2017; pp. 351–371.
19. Uriondo, A.; Esperon-Miguez, M.; Perinpanayagam, S. The Present and Future of Additive Manufacturing in the Aerospace Sector: A Review of Important Aspects. *J. Aerosp. Eng.* **2015**, *229*, 1–16. <https://doi.org/10.1177/0954410014568797>.
20. Singamneni, S.; Yifan, L.V.; Hewitt, A.; Chalk, R.; Thomas, W.; Jordison, D. Additive Manufacturing for the Aircraft Industry: A Review. *J. Aeronaut. Aerosp. Eng.* **2019**, *8*, 1–13. <https://doi.org/10.35248/2168-9792.19.8.215>.
21. Mantovani, S.; Barbieri, S.G.; Giacomini, M.; Croce, A.; Sola, A.; Bassoli, E. Synergy between Topology Optimization and Additive Manufacturing in the Automotive Field. *J. Eng. Manuf.* **2021**, *235*, 1–13. <https://doi.org/10.1177/0954405420949209>.
22. Juechter, V.; Franke, M.M.; Merenda, T.; Stich, A.; Körner, C.; Singer, R.F. Additive Manufacturing of Ti-45Al-4Nb-C by Selective Electron Beam Melting for Automotive Applications. *Addit. Manuf.* **2018**, *22*, 118–126. <https://doi.org/10.1016/j.addma.2018.05.008>.
23. Böckin, D.; Tillman, A. Environmental Assessment of Additive Manufacturing in the Automotive Industry. *J. Clean. Prod.* **2019**, *226*, 977–987. <https://doi.org/10.1016/j.jclepro.2019.04.086>.
24. Thomas, D. Costs, Benefits, and Adoption of Additive Manufacturing: A Supply Chain Perspective. *Int. J. Adv. Manuf. Technol.* **2016**, *85*, 1857–1876. <https://doi.org/10.1007/s00170-015-7973-6>.
25. Delic, M.; Evers, D.R. The Effect of Additive Manufacturing Adoption on Supply Chain Flexibility and Performance: An Empirical Analysis from the Automotive Industry. *Int. J. Prod. Econ.* **2020**, *228*, 107689. <https://doi.org/10.1016/j.ijpe.2020.107689>.
26. Nuñez, J.; Ortiz, Á.; Ramírez, M.A.J.; González Bueno, J.A.; Briceño, M.L. Additive Manufacturing and Supply Chain: A Review and Bibliometric Analysis. In *Engineering Digital Transformation. Lecture Notes in Management and Industrial Engineering*; Ortiz, Á., Romano, C.A., Poler, R., García-Sabater, J.-P., Eds.; Springer: Berlin/Heidelberg, Germany, 2019; pp. 323–331.
27. Kozior, T. The Influence of Selected Selective Laser Sintering Technology Process Parameters on Stress Relaxation, Mass of Models, and Their Surface Texture Quality. *3D Print. Addit. Manuf.* **2020**, *7*, 126–138. <https://doi.org/10.1089/3dp.2019.0036>.
28. Prashar, G.; Vasudev, H. A Comprehensive Review on Sustainable Cold Spray Additive Manufacturing: State of the Art, Challenges and Future Challenges. *J. Clean. Prod.* **2021**, *310*, 127606. <https://doi.org/10.1016/j.jclepro.2021.127606>.
29. Gutowski, T.G.; Branham, M.S.; Dahmus, J.B.; Jones, A.J.; Thiriez, A.; Sekulic, D.P. Thermodynamic Analysis of Resources Used in Manufacturing Processes. *Environ. Sci. Technol.* **2009**, *43*, 1584–1590. <https://doi.org/10.1021/es8016655>.
30. Peng, T.; Kellens, K.; Tang, R.; Chen, C.; Chen, G. Sustainability of Additive Manufacturing: An Overview on Its Energy Demand and Environmental Impact. *Addit. Manuf.* **2018**, *21*, 694–704. <https://doi.org/10.1016/j.addma.2018.04.022>.
31. Agnusdei, L.; Del Prete, A. Additive Manufacturing for Sustainability: A Systematic Literature Review. *Sustain. Future* **2022**, *4*, 100098. <https://doi.org/10.1016/j.sfr.2022.100098>.
32. Bártalo, P.J.; Gibson, I. History of Stereolithographic Processes. In *Stereolithography: Materials, Processes and Applications*; Bártalo, P.J., Ed.; Springer: Boston, MA, USA, 2011; pp. 37–56.
33. Mohd Yusuf, S.; Cutler, S.; Gao, N. Review: The Impact of Metal Additive Manufacturing on the Aerospace Industry. *Metals* **2019**, *9*, 1286. <https://doi.org/10.3390/met9121286>.
34. Gokuldoss, P.K.; Kolla, S.; Eckert, J. Additive Manufacturing Processes: Selective Laser Melting, Electron Beam Melting and Binder Jetting—Selection Guidelines. *Materials* **2017**, *10*, 672. <https://doi.org/10.3390/ma10060672>.
35. Gülcan, O.; Günaydin, K.; Tamer, A. The State of the Art of Material Jetting—A Critical Review. *Polymers* **2021**, *13*, 2829. <https://doi.org/10.3390/polym13162829>.
36. Dickens, P.M. Research Developments in Rapid Prototyping. *Proc. Inst. Mech. Eng. Part B J. Eng. Manuf.* **1995**, *209*, 261–266. https://doi.org/10.1243/pime_proc_1995_209_082_02.
37. Ziaee, M.; Crane, N.B. Binder Jetting: A Review of Process, Materials, and Methods. *Addit. Manuf.* **2019**, *28*, 781–801. <https://doi.org/10.1016/j.addma.2019.05.031>.
38. Sachs, E.; Cima, M.; Williams, P.; Brancrazio, D.; Cornic, J. Three Dimensional Printing: Rapid Tooling and Prototypes Directly from a CAD Model. *J. Eng. Ind.* **1992**, *114*, 481–488. <https://doi.org/10.1115/1.2900701>.
39. Turner, B.N.; Strong, R.; Gold, S.A. A Review of Melt Extrusion Additive Manufacturing Processes: I. Process Design and Modeling. *Rapid Prototyp. J.* **2014**, *20*, 192–204. <https://doi.org/10.1108/RPJ-01-2013-0012>.

40. Bochnia, J.; Blasiak, M.; Kozior, T. A Comparative Study of the Mechanical Properties of FDM 3D Prints Made of PLA and Carbon Fiber-Reinforced PLA for Thin-Walled Applications. *Materials* **2021**, *14*, 7062. <https://doi.org/10.3390/ma14227062>.
41. Molitch-Hou, M. Overview of Additive Manufacturing Process. In *Additive Manufacturing*; Elsevier: Amsterdam, The Netherlands, 2018; pp. 1–38.
42. Gonzalez, J.A.; Mireles, J.; Lin, Y.; Wicker, R.B. Characterization of Ceramic Components Fabricated Using Binder Jetting Additive Manufacturing Technology. *Ceram. Int.* **2016**, *42*, 10559–10564. <https://doi.org/10.1016/j.ceramint.2016.03.079>.
43. Allahverdi, M.; Danforth, S.; Jafari, M.; Safari, A. Processing of Advanced Electroceramic Components by Fused Deposition Technique. *J. Eur. Ceram. Soc.* **2001**, *21*, 1485–1490. [https://doi.org/10.1016/S0955-2219\(01\)00047-4](https://doi.org/10.1016/S0955-2219(01)00047-4).
44. Yi, S.; Liu, F.; Zhang, J.; Xiong, S. Study of the Key Technologies of LOM for Functional Metal Parts. *J. Mater. Process. Technol.* **2004**, *150*, 175–181. <https://doi.org/10.1016/j.jmatprotec.2004.01.035>.
45. Prechtel, M.; Otto, A.; Geiger, M. Rapid Tooling by Laminated Object Manufacturing of Metal Foil. *Adv. Mater. Res.* **2005**, *6–8*, 303–312. <https://doi.org/10.4028/www.scientific.net/AMR.6-8.303>.
46. Ferrández-Montero, A.; Lieblich, M.; Benavente, R.; González-Carrasco, J.L.; Ferrari, B. Study of the Matrix-Filler Interface in PLA/Mg Composites Manufactured by Material Extrusion Using a Colloidal Feedstock. *Addit. Manuf.* **2020**, *33*, 101142. <https://doi.org/10.1016/j.addma.2020.101142>.
47. Ngo, T.D.; Kashani, A.; Imbalzano, G.; Nguyen, K.T.Q.; Hui, D. Additive Manufacturing (3D Printing): A Review of Materials, Methods, Applications and Challenges. *Compos. Part B* **2018**, *143*, 172–196. <https://doi.org/10.1016/j.compositesb.2018.02.012>.
48. Lewandowski, J.J.; Seifi, M. Metal Additive Manufacturing: A Review of Mechanical Properties. *Annu. Rev. Mater. Res.* **2016**, *46*, 151–186. <https://doi.org/10.1146/annurev-matsci-070115-032024>.
49. Murr, L.E.; Gaytan, S.M.; Ramirez, D.A.; Martinez, E.; Hernandez, J.; Amato, K.N.; Shindo, P.W.; Medina, F.R.; Wicker, R.B. Metal Fabrication by Additive Manufacturing Using Laser and Electron Beam Melting Technologies. *J. Mater. Sci. Technol.* **2012**, *28*, 1–14. [https://doi.org/10.1016/S1005-0302\(12\)60016-4](https://doi.org/10.1016/S1005-0302(12)60016-4).
50. Negi, S.; Nambolan, A.A.; Kapil, S.; Joshi, P.S.; Manivannan, R.; Karunakaran, K.P.; Bhargava, P. Review on Electron Beam Based Additive Manufacturing. *Rapid Prototyp. J.* **2020**, *26*, 485–498. <https://doi.org/10.1108/RPJ-07-2019-0182>.
51. Parthasarathy, J.; Starly, B.; Raman, S.; Christensen, A. Mechanical Evaluation of Porous Titanium (Ti6Al4V) Structures with Electron Beam Melting (EBM). *J. Mech. Behav. Biomed. Mater.* **2010**, *3*, 249–259. <https://doi.org/10.1016/j.jmbbm.2009.10.006>.
52. Ma, Y.; Cuiuri, D.; Shen, C.; Li, H.; Pan, Z. Effect of Interpass Temperature on In-Situ Alloying and Additive Manufacturing of Titanium Aluminides Using Gas Tungsten Arc Welding. *Addit. Manuf.* **2015**, *8*, 71–77. <https://doi.org/10.1016/j.addma.2015.08.001>.
53. Spaniol, E.; Ungethüm, T.; Trautmann, M.; Andrusch, K.; Hertel, M.; Füssel, U. Development of a Novel TIG Hot-Wire Process for Wire and Arc Additive Manufacturing. *Weld. World* **2020**, *64*, 1329–1340. <https://doi.org/10.1007/s40194-020-00871-w>.
54. Moreira, A.F.; Ribeiro, K.S.B.; Mariani, F.E.; Coelho, R.T. An Initial Investigation of Tungsten Inert Gas (TIG) Torch as Heat Source for Additive Manufacturing (AM) Process. *Procedia Manuf.* **2020**, *48*, 671–677. <https://doi.org/10.1016/j.promfg.2020.05.159>.
55. Tabernero, I.; Paskual, A.; Álvarez, P.; Suárez, A. Study on Arc Welding Processes for High Deposition Rate Additive Manufacturing. *Procedia CIRP* **2018**, *68*, 358–362. <https://doi.org/10.1016/j.procir.2017.12.095>.
56. Jin, W.; Zhang, C.; Jin, S.; Tian, Y.; Wellmann, D.; Liu, W. Wire Arc Additive Manufacturing of Stainless Steels: A Review. *Appl. Sci.* **2020**, *10*, 1563. <https://doi.org/10.3390/app10051563>.
57. Artaza, T.; Suárez, A.; Murua, M.; García, J.C.; Tabernero, I.; Lamikiz, A. Wire Arc Additive Manufacturing of Mn4Ni2CrMo Steel: Comparison of Mechanical and Metallographic Properties of PAW and GMAW. *Procedia Manuf.* **2019**, *41*, 1071–1078. <https://doi.org/10.1016/j.promfg.2019.10.035>.
58. Pattanayak, S.; Sahoo, S.K. Gas Metal Arc Welding Based Additive Manufacturing—A Review. *CIRP J. Manuf. Sci. Technol.* **2021**, *33*, 398–442. <https://doi.org/10.1016/j.cirpj.2021.04.010>.
59. Veiga, F.; Del Val, A.G.; Suárez, A.; Alonso, U. Analysis of the Machining Process of Titanium Ti6Al-4V Parts Manufactured by Wire Arc Additive Manufacturing (WAAM). *Materials* **2020**, *13*, 766. <https://doi.org/10.3390/ma13030766>.
60. Poolperm, P.; Nakkiew, W.; Naksuk, N. Experimental Investigation of Additive Manufacturing Using a Hot-Wire Plasma Welding Process on Titanium Parts. *Materials* **2021**, *14*, 1270. <https://doi.org/10.3390/ma14051270>.
61. Mercado Rojas, J.G.; Wolfe, T.; Fleck, B.A.; Qureshi, A.J. Plasma Transferred Arc Additive Manufacturing of Nickel Metal Matrix Composites. *Manuf. Lett.* **2018**, *18*, 31–34. <https://doi.org/10.1016/j.mfglet.2018.10.001>.
62. Kumar Srivastava, A.; Kumar, N.; Rai Dixit, A. Friction Stir Additive Manufacturing—An Innovative Tool to Enhance Mechanical and Microstructural Properties. *Mater. Sci. Eng. B* **2021**, *263*, 114832. <https://doi.org/10.1016/j.mseb.2020.114832>.
63. Mishra, R.S.; Palanivel, S. Building without Melting: A Short Review of Friction-Based Additive Manufacturing Techniques. *Int. J. Addit. Subtractive Mater. Manuf.* **2017**, *1*, 82. <https://doi.org/10.1504/IJASMM.2017.10003956>.
64. Hehr, A.; Norfolk, M. A Comprehensive Review of Ultrasonic Additive Manufacturing. *Rapid Prototyp. J.* **2019**, *26*, 445–458. <https://doi.org/10.1108/RPJ-03-2019-0056>.
65. Friel, R.J.; Harris, R.A. Ultrasonic Additive Manufacturing—A Hybrid Production Process for Novel Functional Products. *Procedia CIRP* **2013**, *6*, 35–40. <https://doi.org/10.1016/j.procir.2013.03.004>.
66. Váz, R.F.; Tristante, R.; Pukaszewicz, A.G.M.; Capra, A.R.; Chicoski, A.; Filippin, C.G.; Paredes, R.S.C.; Henke, S.L. Welding and Thermal Spray Processes for Maintenance of Hydraulic Turbine Runners: Case Studies. *Soldag. Insp.* **2021**, *26*, 1–13. <https://doi.org/10.1590/0104-9224/si25.40>.

67. Keshavarz, M.K.; Gontcharov, A.; Lowden, P.; Chan, A.; Kulkarni, D.; Brochu, M. Turbine Blade Tip Repair by Laser Directed Energy Deposition Additive Manufacturing Using a Rene 142–MERL 72 Powder Blend. *J. Manuf. Mater. Process.* **2021**, *5*, 21. <https://doi.org/10.3390/jmmp5010021>.
68. Raelison, R.N.; Verdy, C.; Liao, H. Cold Gas Dynamic Spray Additive Manufacturing Today: Deposit Possibilities, Technological Solutions and Viable Applications. *Mater. Des.* **2017**, *133*, 266–287. <https://doi.org/10.1016/j.matdes.2017.07.067>.
69. Srikanth, A.; Mohammed Thalib Basha, G.; Venkateshwarlu, B. A Brief Review on Cold Spray Coating Process. *Mater. Today Proc.* **2019**, *22*, 1390–1397. <https://doi.org/10.1016/j.matpr.2020.01.482>.
70. Bagherifard, S.; Roscioli, G.; Zucoli, M.V.; Hadi, M.; D’Elia, G.; Demir, A.G.; Previtali, B.; Kondás, J.; Guagliano, M. Cold Spray Deposition of Freestanding Inconel Samples and Comparative Analysis with Selective Laser Melting. *J. Therm. Spray Technol.* **2017**, *26*, 1517–1526. <https://doi.org/10.1007/s11666-017-0572-3>.
71. Gamon, A.; Arrieta, E.; Gradl, P.R.; Katsarelis, C.; Murr, L.E.; Wicker, R.B.; Medina, F. Microstructure and Hardness Comparison of As-Built Inconel 625 Alloy Following Various Additive Manufacturing Processes. *Results Mater.* **2021**, *12*, 100239. <https://doi.org/10.1016/j.rinma.2021.100239>.
72. Additive Manufacturing Metal Technology. Available online: <https://additive-manufacturing-report.com/additive-manufacturing-metal-technology> (accessed on 18 November 2022).
73. Guerges, M. NASA 3D-Printed Manufactured Rocket Engine Hardware Passes Cold Spray, Hot Fire Tests. Available online: <https://www.nasa.gov/centers/marshall/news/releases/2021/nasa-additively-manufactured-rocket-engine-hardware-passes-cold-spray-hot-fire-tests.html> (accessed on 29 November 2022).
74. Buchanan, C.; Gardner, L. Metal 3D Printing in Construction: A Review of Methods, Research, Applications, Opportunities and Challenges. *Eng. Struct.* **2019**, *180*, 332–348. <https://doi.org/10.1016/j.engstruct.2018.11.045>.
75. Pathak, S.; Saha, G.C. Development of Sustainable Cold Spray Coatings and 3D Additive Manufacturing Components for Repair/Manufacturing Applications: A Critical Review. *Coatings* **2017**, *7*, 122. <https://doi.org/10.3390/coatings7080122>.
76. Ashokkumar, M.; Thirumalaikumarasamy, D.; Sonar, T.; Deepak, S.; Vignesh, P.; Anbarasu, M. An Overview of Cold Spray Coating in Additive Manufacturing, Component Repairing and Other Engineering Applications. *J. Mech. Behav. Mater.* **2022**, *31*, 514–534. <https://doi.org/10.1515/jmbm-2022-0056>.
77. Assadi, H.; Kreye, H.; Gärtner, F.; Klassen, T. Cold Spraying—A Materials Perspective. *Acta Mater.* **2016**, *116*, 382–407. <https://doi.org/10.1016/j.actamat.2016.06.034>.
78. Crawmer, D.E. Cold Spray Process. In *Thermal Spray Technology*; Davis, J.R., Ed.; ASM International: Materials Park, OH, USA, 2013; pp. 77–84.
79. Schmidt, T.; Gärtner, F.; Assadi, H.; Kreye, H. Development of a Generalized Parameter Window for Cold Spray Deposition. *Acta Mater.* **2006**, *54*, 729–742. <https://doi.org/10.1016/j.actamat.2005.10.005>.
80. Canales, H.; Cano, I.G.; Dosta, S. Window of Deposition Description and Prediction of Deposition Efficiency via Machine Learning Techniques in Cold Spraying. *Surf. Coat. Technol.* **2020**, *401*, 126143. <https://doi.org/10.1016/j.surfcoat.2020.126143>.
81. Bagherifard, S.; Monti, S.; Zucoli, M.V.; Riccio, M.; Kondás, J.; Guagliano, M. Cold Spray Deposition for Additive Manufacturing of Freeform Structural Components Compared to Selective Laser Melting. *Mater. Sci. Eng. A* **2018**, *721*, 339–350. <https://doi.org/10.1016/j.msea.2018.02.094>.
82. Li, W.; Liu, P.; Liaw, P.K. Microstructures and Properties of High-Entropy Alloy Films and Coatings: A Review. *Mater. Res. Lett.* **2018**, *6*, 199–229. <https://doi.org/10.1080/21663831.2018.1434248>.
83. Jeandin, M.; Rolland, G.; Descurninges, L.L.; Berger, M.H. Which Powders for Cold Spray? *Surf. Eng.* **2014**, *30*, 291–298. <https://doi.org/10.1179/1743294414Y.0000000253>.
84. Silvello, A.; Cavaliere, P.D.; Albaladejo, V.; Martos, A.; Dosta, S.; Cano, I.G. Powder Properties and Processing Conditions Affecting Cold Spray Deposition. *Coatings* **2020**, *10*, 91. <https://doi.org/10.3390/coatings10020091>.
85. Assadi, H.; Schmidt, T.; Richter, H.; Kliemann, J.O.; Binder, K.; Gärtner, F.; Klassen, T.; Kreye, H. On Parameter Selection in Cold Spraying. *J. Therm. Spray Technol.* **2011**, *20*, 1161–1176. <https://doi.org/10.1007/s11666-011-9662-9>.
86. Kosarev, V.F.; Klinkov, S.V.; Alkhimov, A.P.; Papyrin, A.N. On Some Aspects of Gas Dynamics of the Cold Spray Process. *J. Therm. Spray Technol.* **2003**, *12*, 265–281.
87. Karthikeyan, J. The Advantages and Disadvantages of the Cold Spray Coating Process. In *The Cold Spray Materials Deposition Process*; Champagne, V.K., Ed.; Elsevier: Cambridge, UK, 2007; pp. 62–71.
88. Wu, H.; Xie, X.; Liu, S.; Xie, S.; Huang, R.; Verdy, C.; Liu, M.; Liao, H.; Deng, S.; Xie, Y. Bonding Behavior of Bi-Metal-Deposits Produced by Hybrid Cold Spray Additive Manufacturing. *J. Mater. Process. Technol.* **2022**, *299*, 117375. <https://doi.org/10.1016/j.jmatprotec.2021.117375>.
89. Guo, D.; Kazasidis, M.; Hawkins, A.; Fan, N.; Leclerc, Z.; MacDonald, D.; Nastic, A.; Nikbakht, R.; Ortiz-Fernandez, R.; Rahmati, S.; et al. Cold Spray: Over 30 Years of Development Toward a Hot Future. *J. Therm. Spray Technol.* **2022**, *31*, 866–907. <https://doi.org/10.1007/s11666-022-01366-4>.
90. Singh, H.; Sidhu, T.S.; Kalsi, S.B.S.; Karthikeyan, J. Development of Cold Spray from Innovation to Emerging Future Coating Technology. *J. Braz. Soc. Mech. Sci. Eng.* **2013**, *35*, 231–245. <https://doi.org/10.1007/s40430-013-0030-1>.
91. Munsch, M.; Schmidt-Lehr, M.; Wycisk, E. *Additive Manufacturing New Metal Technologies*; AMPower GmbH & Co. KG: Hamburg, Germany, 2020; Volume 6.
92. Lynch, M.E.; Gu, W.; El-Wardany, T.; Hsu, A.; Viens, D.; Nardi, A.; Klecka, M. Design and Topology/Shape Structural Optimization for Additively Manufactured Cold Sprayed Components. *Virtual Phys. Prototyp.* **2013**, *8*, 213–231.

- <https://doi.org/10.1080/17452759.2013.837629>.
93. Wang, X.; Feng, F.; Klecka, M.A.; Mordasky, M.D.; Garofano, J.K.; El-Wardany, T.; Nardi, A.; Champagne, V.K. Characterization and Modeling of the Bonding Process in Cold Spray Additive Manufacturing. *Addit. Manuf.* **2015**, *8*, 149–162. <https://doi.org/10.1016/j.addma.2015.03.006>.
 94. Benenati, G.; Lupoi, R. Development of a Deposition Strategy in Cold Spray for Additive Manufacturing to Minimize Residual Stresses. *Procedia CIRP* **2016**, *55*, 101–108. <https://doi.org/10.1016/j.procir.2016.08.042>.
 95. Villafuerte, J. Considering Cold Spray for Additive Manufacturing. *Adv. Mater. Process.* **2014**, *172*, 50–52.
 96. Řehořek, L.; Dlouhý, I.; Jan, V. Cold Gas Dynamic Spray Deposition as Additive Manufacturing of Architected Materials. *Mater. Eng. Mater. Inž.* **2017**, *24*, 115–123.
 97. Sova, A.; Grigoriev, S.; Okunkova, A.; Smurov, I. Potential of Cold Gas Dynamic Spray as Additive Manufacturing Technology. *Int. J. Adv. Manuf. Technol.* **2013**, *69*, 2269–2278. <https://doi.org/10.1007/s00170-013-5166-8>.
 98. Al-Mangour, B. Fundamentals of Cold Spray Processing: Evolution and Future Perspectives. In *Cold-Spray Coatings: Recent Trends and Future Perspectives*; Cavaliere, P., Ed.; Elsevier: Cham, Switzerland, 2018; pp. 3–24.
 99. Rokni, M.R.; Nutt, S.R.; Widener, C.A.; Champagne, V.K.; Hrabe, R.H. Review of Relationship Between Particle Deformation, Coating Microstructure, and Properties in High-Pressure Cold Spray. *J. Therm. Spray Technol.* **2017**, *26*, 1308–1355. <https://doi.org/10.1007/s11666-017-0575-0>.
 100. Moridi, A.; Hassani-Gangaraj, S.M.; Guagliano, M.; Dao, M. Cold Spray Coating: Review of Material Systems and Future Perspectives. *Surf. Eng.* **2014**, *30*, 369–395. <https://doi.org/10.1179/1743294414Y.0000000270>.
 101. Suo, X.; Yin, S.; Planche, M.P.; Liu, T.; Liao, H. Strong Effect of Carrier Gas Species on Particle Velocity during Cold Spray Processes. *Surf. Coat. Technol.* **2015**, *268*, 90–93. <https://doi.org/10.1016/j.surfcoat.2014.04.039>.
 102. Gilmore, D.L.; Dykhuizen, R.C.; Neiser, R.A.; Roemer, T.J.; Smith, M.F. Particle Velocity and Deposition Efficiency in the Cold Spray Process. *J. Therm. Spray Technol.* **1999**, *8*, 576–582. <https://doi.org/10.1361/105996399770350278>.
 103. Schmidt, T.; Assadi, H.; Gärtner, F.; Richter, H.; Stoltenhoff, T.; Kreye, H.; Klassen, T. From Particle Acceleration to Impact and Bonding in Cold Spraying. *J. Therm. Spray Technol.* **2009**, *18*, 794–808. <https://doi.org/10.1007/s11666-009-9357-7>.
 104. Maev, R.G.; Leshchynsky, V. Air Gas Dynamic Spraying of Powder Mixtures: Theory and Application. *J. Therm. Spray Technol.* **2006**, *15*, 198–205. <https://doi.org/10.1361/105996306X108048>.
 105. Alonso, L.; Garrido, M.A.; Poza, P. An Optimisation Method for the Cold-Spray Process: On the Nozzle Geometry. *Mater. Des.* **2022**, *214*, 110387. <https://doi.org/10.1016/j.matdes.2022.110387>.
 106. Da Silva, F.S.; Cinca, N.; Dosta, S.; Cano, I.G.; Benedetti, A.V.; Guilemany, J.M. Cold Gas Spray Coatings: Basic Principles Corrosion Protection and Applications. *Eclét. Quím. J.* **2017**, *42*, 9–32. <https://doi.org/10.26850/1678-4618eqj.v42.1.2017.p09-32>.
 107. Grujicic, M.; Zhao, C.L.; DeRosset, W.S.; Helfritsch, D. Adiabatic Shear Instability Based Mechanism for Particles/Substrate Bonding in the Cold-Gas Dynamic-Spray Process. *Mater. Des.* **2004**, *25*, 681–688. <https://doi.org/10.1016/j.matdes.2004.03.008>.
 108. Assadi, H.; Gärtner, F.; Stoltenhoff, T.; Kreye, H. Bonding Mechanism in Cold Gas Spraying. *Acta Mater.* **2003**, *51*, 4379–4394. [https://doi.org/10.1016/S1359-6454\(03\)00274-X](https://doi.org/10.1016/S1359-6454(03)00274-X).
 109. Hassani-Gangaraj, S.M.; Moridi, A.; Guagliano, M. Critical Review of Corrosion Protection by Cold Spray Coatings. *Surf. Eng.* **2015**, *31*, 803–815. <https://doi.org/10.1179/1743294415Y.0000000018>.
 110. Champagne, V.K.; Helfritsch, D.; Leyman, P.; Grendahl, S.; Klotz, B. Interface Material Mixing Formed by the Deposition of Copper on Aluminum by Means of the Cold Spray Process. *J. Therm. Spray Technol.* **2005**, *14*, 330–334. <https://doi.org/10.1361/105996305X59332>.
 111. Hussain, T.; McCartney, D.G.; Shipway, P.H.; Zhang, D. Bonding Mechanisms in Cold Spraying: The Contributions of Metallurgical and Mechanical Components. *J. Therm. Spray Technol.* **2009**, *18*, 364–379. <https://doi.org/10.1007/s11666-009-9298-1>.
 112. Hassani-Gangaraj, M.; Veysset, D.; Champagne Jr, V.K.; Nelson, K.A. Adiabatic Shear Instability Is Not Necessary for Adhesion in Cold Spray. *Acta Mater.* **2018**, *158*, 430–439. <https://doi.org/10.1016/j.actamat.2018.07.065>.
 113. Assadi, H.; Gärtner, F.; Klassen, T.; Kreye, H. Comment on ‘Adiabatic Shear Instability Is Not Necessary for Adhesion in Cold Spray.’ *Scr. Mater.* **2019**, *162*, 512–514. <https://doi.org/10.1016/j.scriptamat.2018.10.036>.
 114. Chen, C.; Su, H.; Wang, X.; Liu, Y.; Zhao, L.; Wei, X.; Zhao, Y.; Pan, J.; Qiu, X. Impact-Induced Bonding Process of Copper at Low Velocity and Room Temperature. *Mater. Des.* **2023**, *226*, 111603. <https://doi.org/10.1016/j.matdes.2023.111603>.
 115. Macdonald, D.; Nastic, A.; Jodoin, B. Understanding Adhesion. In *Cold-Spray Coatings: Recent Trends and Future Perspectives*; Cavaliere, P.D., Ed.; Springer: Cham, Switzerland, 2016; pp. 421–450.
 116. Li, C.J.; Wang, H.T.; Zhang, Q.; Yang, G.J.; Li, W.Y.; Liao, H.L. Influence of Spray Materials and Their Surface Oxidation on the Critical Velocity in Cold Spraying. *J. Therm. Spray Technol.* **2010**, *19*, 95–101. <https://doi.org/10.1007/s11666-009-9427-x>.
 117. Wang, Z.; Cai, S.; Chen, W.; Ali, R.A.; Jin, K. Analysis of Critical Velocity of Cold Spray Based on Machine Learning Method with Feature Selection. *J. Therm. Spray Technol.* **2021**, *30*, 1213–1225. <https://doi.org/10.1007/s11666-021-01198-8>.
 118. Gärtner, F.; Stoltenhoff, T.; Schmidt, T.; Kreye, H. The Cold Spray Process and Its Potential for Industrial Applications. *J. Therm. Spray Technol.* **2006**, *15*, 223–232. <https://doi.org/10.1361/105996306X108110>.
 119. Bagherifard, S.; Kondas, J.; Monti, S.; Cizek, J.; Perego, F.; Kovarik, O.; Lukac, F.; Gaertner, F.; Guagliano, M. Tailoring Cold Spray Additive Manufacturing of Steel 316 L for Static and Cyclic Load-Bearing Applications. *Mater. Des.* **2021**, *203*, 109575. <https://doi.org/10.1016/j.matdes.2021.109575>.
 120. Raletz, F.; Vardelle, M.; Ezo'o, G. Critical Particle Velocity under Cold Spray Conditions. *Surf. Coat. Technol.* **2006**, *201*, 1942–1947. <https://doi.org/10.1016/j.surfcoat.2006.04.061>.

121. Binder, K.; Gottschalk, J.; Kollenda, M.; Gärtner, F.; Klassen, T. Influence of Impact Angle and Gas Temperature on Mechanical Properties of Titanium Cold Spray Deposits. *J. Therm. Spray Technol.* **2011**, *20*, 234–242. <https://doi.org/10.1007/s11666-010-9557-1>.
122. Vidaller, M.V.; List, A.; Gaertner, F.; Klassen, T.; Dosta, S.; Guilemany, J.M. Single Impact Bonding of Cold Sprayed Ti-6Al-4V Powders on Different Substrates. *J. Therm. Spray Technol.* **2015**, *24*, 644–658. <https://doi.org/10.1007/s11666-014-0200-4>.
123. Pérez-Andrade, L.L.; Gärtner, F.; Villa-Vidaller, M.; Klassen, T.; Muñoz-Saldaña, J.; Alvarado-Orozco, J.M. Optimization of Inconel 718 Thick Deposits by Cold Spray Processing and Annealing. *Surf. Coat. Technol.* **2019**, *378*, 124997. <https://doi.org/10.1016/j.surfcoat.2019.124997>.
124. Sun, W.; Bhowmik, A.; Tan, A.W.; Li, R.; Xue, F.; Marinescu, I.; Liu, E. Improving Microstructural and Mechanical Characteristics of Cold-Sprayed Inconel 718 Deposits via Local Induction Heat Treatment. *J. Alloy. Compd.* **2019**, *797*, 1268–1279. <https://doi.org/10.1016/j.jallcom.2019.05.099>.
125. Oyinbo, S.T.; Jen, T.-C. A Comparative Review on Cold Gas Dynamic Spraying Processes and Technologies. *Manuf. Rev.* **2019**, *6*, 25. <https://doi.org/10.1051/mfreview/2019023>.
126. Kumar, S.; Pandey, S.M. The Study of Assessment Parameters and Performance Measurement of Cold Spray Technique: A Futuristic Approach Towards Additive Manufacturing. *MAPAN* **2022**, *37*, 859–879. <https://doi.org/10.1007/s12647-022-00597-8>.
127. Wong, W.; Irissou, E.; Ryabinin, A.N.; Legoux, J.G.; Yue, S. Influence of Helium and Nitrogen Gases on the Properties of Cold Gas Dynamic Sprayed Pure Titanium Coatings. *J. Therm. Spray Technol.* **2011**, *20*, 213–226. <https://doi.org/10.1007/s11666-010-9568-y>.
128. Al-Mangour, B.; Vo, P.; Mongrain, R.; Irissou, E.; Yue, S. Effect of Heat Treatment on the Microstructure and Mechanical Properties of Stainless Steel 316L Coatings Produced by Cold Spray for Biomedical Applications. *J. Therm. Spray Technol.* **2014**, *23*, 641–652. <https://doi.org/10.1007/s11666-013-0053-2>.
129. Borchers, C.; Schmidt, T.; Gärtner, F.; Kreye, H. High Strain Rate Deformation Microstructures of Stainless Steel 316L by Cold Spraying and Explosive Powder Compaction. *Appl. Phys. A* **2008**, *90*, 517–526. <https://doi.org/10.1007/s00339-007-4314-0>.
130. Pukasiewicz, A.G.M.; de Oliveira, W.R.; Váz, R.F.; de Souza, G.B.; Serbena, F.C.; Dosta, S.; Cano, I.G. Influence of the Deposition Parameters on the Tribological Behavior of Cold Gas Sprayed FeMnCrSi Alloy Coatings. *Surf. Coat. Technol.* **2021**, *428*, 127888. <https://doi.org/10.1016/j.surfcoat.2021.127888>.
131. Belgroune, A.; Alhoussein, A.; Aissani, L.; Zaabat, M.; Obrosov, A.; Verdy, C.; Langlade, C. Effect of He and N₂ Gas on the Mechanical and Tribological Assessment of SS316L Coating Deposited by Cold Spraying Process. *J. Mater. Sci.* **2022**, *57*, 5258–5274. <https://doi.org/10.1007/s10853-022-06950-1>.
132. Vaz, R.F.; Silvello, A.; Sanchez, J.; Albaladejo, V.; Cano, I.G.G. The Influence of the Powder Characteristics on 316L Stainless Steel Coatings Sprayed by Cold Gas Spray. *Coatings* **2021**, *11*, 168. <https://doi.org/10.3390/coatings11020168>.
133. Yin, S.; Meyer, M.; Li, W.; Liao, H.; Lupoi, R. Gas Flow, Particle Acceleration, and Heat Transfer in Cold Spray: A Review. *J. Therm. Spray Technol.* **2016**, *25*, 874–896. <https://doi.org/10.1007/s11666-016-0406-8>.
134. Lee, M.-W.; Park, J.-J.; Kim, D.-Y.; Yoon, S.S.; Kim, H.-Y.; James, S.C.; Chandra, S.; Coyle, T. Numerical Studies on the Effects of Stagnation Pressure and Temperature on Supersonic Flow Characteristics in Cold Spray Applications. *J. Therm. Spray Technol.* **2011**, *20*, 1085–1097. <https://doi.org/10.1007/s11666-011-9641-1>.
135. UNE EN 17393; Thermal Spraying. Tubular Coating Testing. Asociación Española de Normalización: Madrid, Spain, 2020.
136. Gärtner, F.; Stoltenhoff, T.; Voyer, J.; Kreye, H.; Riekehr, S.; Koçak, M. Mechanical Properties of Cold-Sprayed and Thermally Sprayed Copper Coatings. *Surf. Coat. Technol.* **2006**, *200*, 6770–6782. <https://doi.org/10.1016/j.surfcoat.2005.10.007>.
137. Meng, X.; Zhang, J.; Zhao, J.; Liang, Y.; Zhang, Y. Influence of Gas Temperature on Microstructure and Properties of Cold Spray 304SS Coating. *J. Mater. Sci. Technol.* **2011**, *27*, 809–815. [https://doi.org/10.1016/S1005-0302\(11\)60147-3](https://doi.org/10.1016/S1005-0302(11)60147-3).
138. Cai, Z.; Deng, S.; Liao, H.; Zeng, C.; Montavon, G. The Effect of Spray Distance and Scanning Step on the Coating Thickness Uniformity in Cold Spray Process. *J. Therm. Spray Technol.* **2014**, *23*, 354–362. <https://doi.org/10.1007/s11666-013-0002-0>.
139. Li, W.-Y.; Zhang, C.; Guo, X.P.; Zhang, G.; Liao, H.L.; Li, C.-J.; Coddet, C. Effect of Standoff Distance on Coating Deposition Characteristics in Cold Spraying. *Mater. Des.* **2008**, *29*, 297–304. <https://doi.org/10.1016/j.matdes.2007.02.005>.
140. Lett, S.; Quet, A.; Hémerly, S.; Cormier, J.; Meillot, E.; Villechaise, P. Residual Stresses Development during Cold Spraying of Ti-6Al-4V Combined with In Situ Shot Peening. *J. Therm. Spray Technol.* **2022**, *1–15*. <https://doi.org/10.1007/s11666-022-01514-w>.
141. Yin, S.; Jenkins, R.; Yan, X.; Lupoi, R. Microstructure and Mechanical Anisotropy of Additively Manufactured Cold Spray Copper Deposits. *Mater. Sci. Eng. A* **2018**, *734*, 67–76. <https://doi.org/10.1016/j.msea.2018.07.096>.
142. Baek, M.-S.; Kim, H.-J.; Lee, K.-A. Anisotropy of Compressive Deformation Behavior in Cold Sprayed Cu Bulk Material. *J. Nanosci. Nanotechnol.* **2019**, *19*, 3935–3942. <https://doi.org/10.1166/jnn.2019.16147>.
143. Vargas-Uscategui, A.; King, P.C.; Yang, S.; Chu, C.; Li, J. Toolpath Planning for Cold Spray Additively Manufactured Titanium Walls and Corners: Effect on Geometry and Porosity. *J. Mater. Process. Technol.* **2021**, *298*, 117272. <https://doi.org/10.1016/j.jmatprotec.2021.117272>.
144. Vaz, R.F.; Albaladejo-Fuentes, V.; Sanchez, J.; Ocaña, U.; Corral, Z.G.Z.G.; Canales, H.; Cano, I.G. Metal Knitting: A New Strategy for Cold Gas Spray. *Materials* **2022**, *15*, 6785. <https://doi.org/10.3390/ma15196785>.
145. Nardi, A.T.; El-Wardany, T.I.; Viens, D.V.; Lynch, M.E.; Hsu, A.; Klecka, M.A.; Gu, W. Additive Topology Optimized Manufacturing for Multi-Functional Components. U.S. Patent 2014/0277669 A1, 2014; pp. 1–33.
146. Brodmann, F.J. Cold Spray Process Parameters: Powders. In *The Cold Spray Materials Deposition Process*; Champagne, V.K., Ed.; Elsevier: Cambridge, UK, 2007; pp. 105–116.

147. Poirier, D.; Thomas, Y.; Guerreiro, B.; Martin, M.; Aghasibeig, M.; Irissou, E. Novel Powder Modification Method for the Cold Spray of Hard Steels. In Proceedings of the International Thermal Spray Conference, Quebec City, QC, Canada, 24–28 May 2021; ASM Thermal Spray Society: Materials Park, OH, USA, 2021; pp. 603–610.
148. Story, W.A.; Brewer, L.N. Heat Treatment of Gas-Atomized Powders for Cold Spray Deposition. *Metall. Mater. Trans. A* **2018**, *49*, 446–449. <https://doi.org/10.1007/s11661-017-4428-8>.
149. ASTM B214-22; Standard Test Method for Sieve Analysis of Metal Powders. ASTM International: West Conshohocken, PA, USA, 2022.
150. ASTM B213-20; Standard Test Method for Flow Rate of Metal Powders. ASTM International: West Conshohocken, PA, USA, 2020.
151. ASTM B212-21; Standard Test Method for Apparent Density of Powders Using the Hall Flowmeter Funnel. ASTM International: West Conshohocken, PA, USA, 2021.
152. Valente, R.; Ostapenko, A.; Sousa, B.C.; Grubbs, J.; Massar, C.J.; Cote, D.L.; Neamtu, R. Classifying Powder Flowability for Cold Spray Additive Manufacturing Using Machine Learning. In Proceedings of the 2020 IEEE International Conference on Big Data (Big Data), Atlanta, GA, USA, 10–13 December 2020; IEEE: Atlanta, GA, USA, 2020; pp. 2919–2928.
153. Singh, R.; Kondás, J.; Bauer, C.; Cizek, J.; Medricky, J.; Csaki, S.; Čupera, J.; Procházka, R.; Melzer, D.; Konopík, P. Bulk-like Ductility of Cold Spray Additively Manufactured Copper in the as-Sprayed State. *Addit. Manuf. Lett.* **2022**, *3*, 100052. <https://doi.org/10.1016/j.addlet.2022.100052>.
154. Wong, W.; Irissou, E.; Legoux, J.G.; Vo, P.; Yue, S. Powder Processing and Coating Heat Treatment on Cold Sprayed Ti-6Al-4V Alloy. *Mater. Sci. Forum* **2012**, *706–709*, 258–263. <https://doi.org/10.4028/www.scientific.net/MSF.706-709.258>.
155. Wong, W.; Vo, P.; Irissou, E.; Ryabinin, A.N.; Legoux, J.-G.; Yue, S. Effect of Particle Morphology and Size Distribution on Cold-Sprayed Pure Titanium Coatings. *J. Therm. Spray Technol.* **2013**, *22*, 1140–1153. <https://doi.org/10.1007/s11666-013-9951-6>.
156. Munagala, V.N.V.; Akinyi, V.; Vo, P.; Chromik, R.R. Influence of Powder Morphology and Microstructure on the Cold Spray and Mechanical Properties of Ti6Al4V Coatings. *J. Therm. Spray Technol.* **2018**, *27*, 827–842. <https://doi.org/10.1007/s11666-018-0729-8>.
157. Wang, X.; Zhang, B.; Lv, J.; Yin, S. Investigation on the Clogging Behavior and Additional Wall Cooling for the Axial-Injection Cold Spray Nozzle. *J. Therm. Spray Technol.* **2015**, *24*, 696–701. <https://doi.org/10.1007/s11666-015-0227-1>.
158. Li, C.J.; Li, W.Y.; Wang, Y.Y.; Yang, G.J.; Fukunuma, H. A Theoretical Model for Prediction of Deposition Efficiency in Cold Spraying. *Thin Solid Films* **2005**, *489*, 79–85. <https://doi.org/10.1016/j.tsf.2005.05.002>.
159. Schmidt, T.; Gaertner, F.; Kreye, H. New Developments in Cold Spray Based on Higher Gas and Particle Temperatures. *J. Therm. Spray Technol.* **2006**, *15*, 488–494. <https://doi.org/10.1361/105996306X147144>.
160. Foelsche, A.F. Nozzle Clogging Prevention and Analysis in Cold Spray. Master's Thesis, University of Massachusetts, Amherst, MA, USA, September 2020.
161. Fukunuma, H. Cold-Spray Nozzle and Cold-Spray Device Using Cold-Spray Nozzle. U.S. Patent 9,095,858B2, 4 August 2015; pp. 1–11.
162. Tronsson, H.C. Feasibility of Electric Field Assisted Clogging Reduction in Cold Gas Spraying Nozzle. Bachelor's thesis, Dartmouth College, Hanover, NH, USA, June 2020.
163. Saboori, A.; Biamino, S.; Valente, A.; Gitardi, D.; Basile, G.; Lombardi, M.; Fino, P. The Capacity of Cold Spray Additive Manufacturing Technology for Metallic Part Repairing. In Proceedings of the Euro PM 2018 Congress and Exhibition, Bilbao, Spain, 14–18 October 2018.
164. Ikeuchi, D.; Vargas-Uscategui, A.; Wu, X.; King, P. Data-Efficient Neural Network for Track Profile Modelling in Cold Spray Additive Manufacturing. *Appl. Sci.* **2021**, *11*, 1654. <https://doi.org/10.3390/app11041654>.
165. Kotoban, D.; Grigoriev, S.; Okunkova, A.; Sova, A. Influence of a Shape of Single Track on Deposition Efficiency of 316L Stainless Steel Powder in Cold Spray. *Surf. Coat. Technol.* **2017**, *309*, 951–958. <https://doi.org/10.1016/j.surfcoat.2016.10.052>.
166. Wu, H.; Liu, S.; Lewke, M.; Li, W.; Raelison, R.-N.; List, A.; Gärtner, F.; Liao, H.; Klassen, T.; Deng, S. Strategies and Analyses for Robot Trajectory Optimization in Thermal and Kinetic Spraying. In Proceedings of the International Thermal Spray Conference, Vienna, Austria, 4–6 May, 2022; ASM Thermal Spray Society: Vienna, Austria, 2022; pp. 299–305.
167. Wu, H.; Xie, X.; Liu, M.; Verdy, C.; Zhang, Y.; Liao, H.; Deng, S. Stable Layer-Building Strategy to Enhance Cold-Spray-Based Additive Manufacturing. *Addit. Manuf.* **2020**, *35*, 101356. <https://doi.org/10.1016/j.addma.2020.101356>.
168. Chen, C.; Gojon, S.; Xie, Y.; Yin, S.; Verdy, C.; Ren, Z.; Liao, H.; Deng, S. A Novel Spiral Trajectory for Damage Component Recovery with Cold Spray. *Surf. Coat. Technol.* **2017**, *309*, 719–728. <https://doi.org/10.1016/j.surfcoat.2016.10.096>.
169. Pattison, J.; Celotto, S.; Morgan, R.; Bray, M.; O'Neill, W. Cold Gas Dynamic Manufacturing: A Non-Thermal Approach to Freeform Fabrication. *Int. J. Mach. Tools Manuf.* **2007**, *47*, 627–634. <https://doi.org/10.1016/j.ijmactools.2006.05.001>.
170. Sokore, M.; Wu, H.; Li, W.; Raelison, R.-N.; Deng, S.; Liao, H. Perspective of 3D Near-Net-Shape Additive Manufacturing by Cold Spraying: An Empirical Study Using Pure Al Powders. In Proceedings of the International Thermal Spray Conference, Vienna, Austria, 4–6 May 2022; ASM Thermal Spray Society: Vienna, Austria, 2022; pp. 306–313.
171. Hutasoit, N.; Rashid, R.A.R.; Palanisamy, S.; Duguid, A. Effect of Build Orientation and Post-Build Heat Treatment on the Mechanical Properties of Cold Spray Additively Manufactured Copper Parts. *Int. J. Adv. Manuf. Technol.* **2020**, *110*, 2359. <https://doi.org/10.1007/s00170-020-06051-w>.
172. Wu, H.; Raelison, R.N.; Zhang, Y.; Deng, S.; Liao, H. Cold Spraying of 3D Parts—Challenges. In *Thermal Spray Coatings*; Thakur, L., Vasudev, H., Eds.; CRC Press: Boca Raton, FL, USA, 2021; pp. 37–58.

173. Nguyen, X.A.; Vargas-Uscategui, A.; Iohr, H.; Chu, C. A Continuous Toolpath Strategy from Offset Contours for Robotic Additive Manufacturing. *Research Square* **2022**, 1–17. <https://doi.org/10.21203/rs.3.rs-2211954/v1>.
174. Prudhomme, C.A.; Holtzinger, J.; Goldstein, G.H.; Tzivani, M.J.; Noonan, W.E.; Austin, R.J. Thermal Spray Masking Tape. U.S. Patent 9.434,137B2, 6 September 2016; pp. 1–15.
175. Pergande, P.E.; Kinane, J.A.; Pank, D.R.; Collins, D.R. Making and Using Thermal Spray Masks Carrying Thermoset Epoxy Coating 2000. U.S. Patent 6,060,117, 9 May 2000.
176. Beck, J.E.; Prinz, F.B.; Siewiorek, D.P.; Weiss, L. Manufacturing Mechatronics Using Thermal Spray Shape Deposition. In Proceedings of the Solid Freeform Fabrication Symposium, Austin, TX, USA, 3–5 August 1992; pp. 272–279.
177. Tejero-Martin, D.; Rezvani Rad, M.; McDonald, A.; Hussain, T. Beyond Traditional Coatings: A Review on Thermal-Sprayed Functional and Smart Coatings. *J. Therm. Spray Technol.* **2019**, *28*, 598–644. <https://doi.org/10.1007/s11666-019-00857-1>.
178. Kosarev, V.F.; Klinkov, S.V.; Melamed, B.M.; Trubacheev, G.V.; Usynin, S.Y.; Shikalov, V.S. Investigation of Gas Flow through a Mask at Cold Spraying. *AIP Conf. Proc.* **2020**, *2288*, 030013. <https://doi.org/10.1063/5.0028710>.
179. Klinkov, S.V.; Kosarev, V.F.; Ryashin, N.S. Comparison of Experiments and Computations for Cold Gas Spraying Through a Mask. Part 2. *Thermophys. Aeromech.* **2017**, *24*, 213–224. <https://doi.org/10.1134/S0869864317020068>.
180. Cormier, Y.; Dupuis, P.; Farjam, A.; Corbeil, A.; Jodoin, B. Additive Manufacturing of Pyramidal Pin Fins: Height and Fin Density Effects Under Forced Convection. *Int. J. Heat Mass Transf.* **2014**, *75*, 235–244. <https://doi.org/10.1016/j.ijheatmasstransfer.2014.03.053>.
181. Cormier, Y.; Dupuis, P.; Jodoin, B.; Corbeil, A. Mechanical Properties of Cold Gas Dynamic Sprayed Near-Net Shaped Pin Arrays. *J. Therm. Spray Technol.* **2015**, *24*, 476–488. <https://doi.org/10.1007/s11666-014-0203-1>.
182. Cormier, Y.; Dupuis, P.; Jodoin, B.; Corbeil, A. Pyramidal Fin Arrays Performance Using Streamwise Anisotropic Materials by Cold Spray Additive Manufacturing. *J. Therm. Spray Technol.* **2016**, *25*, 170–182. <https://doi.org/10.1007/s11666-015-0267-6>.
183. Dupuis, P.; Cormier, Y.; Fenech, M.; Jodoin, B. Heat Transfer and Flow Structure Characterization for Pin Fins Produced by Cold Spray Additive Manufacturing. *Int. J. Heat Mass Transf.* **2016**, *98*, 650–661. <https://doi.org/10.1016/j.ijheatmasstransfer.2016.03.069>.
184. Xie, J.; Chen, Y.; Yin, L.; Zhang, T.; Wang, S.; Wang, L. Microstructure and Mechanical Properties of Ultrasonic Spot Welding TiNi/Ti6Al4V Dissimilar Materials Using Pure Al Coating. *J. Manuf. Process.* **2021**, *64*, 473–480. <https://doi.org/10.1016/j.jmapro.2021.02.009>.
185. Champagne, V.K., Jr.; Champagne, V.K., III. Method to Join Dissimilar Materials by the Cold Spray Process. U.S. Patent 2016/0089750A1, 31 March 2016; pp. 1–12.
186. Champagne, V.; Kaplowitz, D.; Champagne, V.K.; Howe, C.; West, M.K.; McNally, B.; Rokni, M. Dissimilar Metal Joining and Structural Repair of ZE41A-T5 Cast Magnesium by the Cold Spray (CS) Process. *Mater. Manuf. Process.* **2018**, *33*, 130–139. <https://doi.org/10.1080/10426914.2016.1257137>.
187. Curtis, T.R.; Champagne, V.K.; West, M.K.; Rokni, R.; Widener, C.A. Joining Al 6061 to ZE41A Mg Alloy by Friction Stir Welding Using a Cold Spray Transition Joint. In *Friction Stir Welding and Processing IX*; Hovanski, Y., Mishra, R., Sato, Y., Upadhyay, P., Yan, D., Eds.; Springer: Cham, Switzerland, 2017; pp. 221–236.
188. Champagne, V.K.; West, M.K.; Reza Rokni, M.; Curtis, T.; Champagne, V.; McNally, B. Joining of Cast ZE41A Mg to Wrought 6061 Al by the Cold Spray Process and Friction Stir Welding. *J. Therm. Spray Technol.* **2016**, *25*, 143–159. <https://doi.org/10.1007/s11666-015-0301-8>.
189. Hou, W.; Shen, Z.; Huda, N.; Oheil, M.; Shen, Y.; Jahed, H.; Gerlich, A.P. Enhancing Metallurgical and Mechanical Properties of Friction Stir Butt Welded Joints of Al–Cu Via Cold Sprayed Ni Interlayer. *Mater. Sci. Eng. A* **2021**, *809*, 140992. <https://doi.org/10.1016/j.msea.2021.140992>.
190. Daroonparvar, M.; Khan, M.U.F.; Saadeh, Y.; Kay, C.M.; Kasar, A.K.; Kumar, P.; Esteves, I.; Misra, M.; Menezes, P.; Kalvala, P.R.; et al. Modification of Surface Hardness, Wear Resistance and Corrosion Resistance of Cold Spray Al Coated AZ31B Mg Alloy Using Cold Spray Double Layered Ta/Ti Coating in 3.5 Wt% NaCl Solution. *Corros. Sci.* **2020**, *176*, 109029. <https://doi.org/10.1016/j.corsci.2020.109029>.
191. Poza, P.; Garrido-Maneiro, M.Á. Cold-Sprayed Coatings: Microstructure, Mechanical Properties, and Wear Behaviour. *Prog. Mater. Sci.* **2022**, *123*, 100839. <https://doi.org/10.1016/j.pmatsci.2021.100839>.
192. Montheillet, F.; Jonas, J.J.; Benferrah, M. Development of Anisotropy During the Cold Rolling of Aluminium Sheet. *Int. J. Mech. Sci.* **1991**, *33*, 197–209. [https://doi.org/10.1016/0020-7403\(91\)90046-6](https://doi.org/10.1016/0020-7403(91)90046-6).
193. Park, M.; Kang, M.S.; Park, G.-W.; Kim, H.C.; Moon, H.-S.; Kim, B.; Jeon, J.B.; Kim, H.; Park, H.-S.; Kwon, S.-H.; et al. Effects of Annealing Treatment on the Anisotropy Behavior of Cold-Rolled High-Manganese Austenite Stainless Steels. *Met. Mater. Int.* **2021**, *27*, 3839–3855. <https://doi.org/10.1007/s12540-020-00785-8>.
194. You, Z.; Fu, H.; Qu, S.; Bao, W.; Lu, L. Revisiting Anisotropy in the Tensile and Fracture Behavior of Cold-Rolled 316L Stainless Steel with Heterogeneous Nano-Lamellar Structures. *Nano Mater. Sci.* **2020**, *2*, 72–79. <https://doi.org/10.1016/j.nanomats.2020.03.001>.
195. Park, C.M.; Jung, J.; Yu, B.C.; Park, Y.H. Anisotropy of the Wear and Mechanical Properties of Extruded Aluminum Alloy Rods (AA2024-T4). *Met. Mater. Int.* **2019**, *25*, 71–82. <https://doi.org/10.1007/s12540-018-0164-x>.
196. Zhang, Z.H.; Li, W.Y.; Feng, Y.; Li, J.L.; Chao, Y.J. Global Anisotropic Response of Friction Stir Welded 2024 Aluminum Sheets. *Acta Mater.* **2015**, *92*, 117–125. <https://doi.org/10.1016/j.actamat.2015.03.054>.
197. Kok, Y.; Tan, X.P.; Wang, P.; Nai, M.L.S.; Ioh, N.H.; Liu, E.; Tor, S.B. Anisotropy and Heterogeneity of Microstructure and

- Mechanical Properties in Metal Additive Manufacturing: A Critical Review. *Mater. Des.* **2018**, *139*, 565–586. <https://doi.org/10.1016/j.matdes.2017.11.021>.
198. Deev, A.A.; Kuznetsov, P.A.; Petrov, S.N. Anisotropy of Mechanical Properties and Its Correlation with the Structure of the Stainless Steel 316L Produced by the SLM Method. *Phys. Procedia* **2016**, *83*, 789–796. <https://doi.org/10.1016/j.phpro.2016.08.081>.
 199. Seiner, H.; Cizek, J.; Sedláč, P.; Huang, R.; Cupera, J.; Dlouhy, I.; Landa, M. Elastic Moduli and Elastic Anisotropy of Cold Sprayed Metallic Coatings. *Surf. Coat. Technol.* **2016**, *291*, 342–347. <https://doi.org/10.1016/j.surfcoat.2016.02.057>.
 200. Yang, K.; Li, W.; Yang, X.; Xu, Y. Anisotropic Response of Cold Sprayed Copper Deposits. *Surf. Coat. Technol.* **2018**, *335*, 219–227. <https://doi.org/10.1016/j.surfcoat.2017.12.043>.
 201. Yang, K.; Li, W.; Guo, X.; Yang, X.; Xu, Y. Characterizations and Anisotropy of Cold-Spraying Additive-Manufactured Copper Bulk. *J. Mater. Sci. Technol.* **2018**, *34*, 1570–1579. <https://doi.org/10.1016/j.jmst.2018.01.002>.
 202. Julien, S.E.; Nourian-Avval, A.; Liang, W.; Schwartz, T.; Ozdemir, O.C.; Müftü, S. Bulk Fracture Anisotropy in Cold-Sprayed Al 6061 Deposits. *Eng. Fract. Mech.* **2022**, *263*, 108301. <https://doi.org/10.1016/j.engfracmech.2022.108301>.
 203. Groarke, R.; Danilenkoff, C.; Karam, S.; McCarthy, E.; Michel, B.; Mussatto, A.; Sloane, J.; O'Neill, A.; Raghavendra, R.; Brabazon, D. 316L Stainless Steel Powders for Additive Manufacturing: Relationships of Powder Rheology, Size, Size Distribution to Part Properties. *Materials* **2020**, *13*, 5537. <https://doi.org/10.3390/ma13235537>.
 204. Wong, W.; Irissou, E.; Vo, P.; Sone, M.; Bernier, F.; Legoux, J.-G.; Fukunuma, H.; Yue, S. Cold Spray Forming of Inconel 718. *J. Therm. Spray Technol.* **2013**, *22*, 413–421. <https://doi.org/10.1007/s11666-012-9827-1>.
 205. Li, W.; Cao, C.; Yin, S. Solid-State Cold Spraying of Ti and Its Alloys: A Literature Review. *Prog. Mater. Sci.* **2020**, *110*, 100633. <https://doi.org/10.1016/j.pmatsci.2019.100633>.
 206. Chen, C.; Yan, X.; Xie, Y.; Huang, R.; Kuang, M.; Ma, W.; Zhao, R.; Wang, J.; Liu, M.; Ren, Z.; et al. Microstructure Evolution and Mechanical Properties of Maraging Steel 300 Fabricated by Cold Spraying. *Mater. Sci. Eng. A* **2019**, *743*, 482–493. <https://doi.org/10.1016/j.msea.2018.11.116>.
 207. Luzin, V.; Spencer, K.; Zhang, M.X. Residual Stress and Thermo-Mechanical Properties of Cold Spray Metal Coatings. *Acta Mater.* **2011**, *59*, 1259–1270. <https://doi.org/10.1016/j.actamat.2010.10.058>.
 208. Huang, R.; Sone, M.; Ma, W.; Fukunuma, H. The Effects of Heat Treatment on the Mechanical Properties of Cold-Sprayed Coatings. *Surf. Coat. Technol.* **2015**, *261*, 278–288. <https://doi.org/10.1016/j.surfcoat.2014.11.017>.
 209. Li, W.Y.; Li, C.J.; Liao, H. Effect of Annealing Treatment on the Microstructure and Properties of Cold-Sprayed Cu Coating. *J. Therm. Spray Technol.* **2006**, *15*, 206–211. <https://doi.org/10.1361/105996306X108066>.
 210. Li, W.; Wu, D.; Hu, K.; Xu, Y.; Yang, X.; Zhang, Y. A Comparative Study on the Employment of Heat Treatment, Electric Pulse Processing and Friction Stir Processing to Enhance Mechanical Properties of Cold-Spray-Additive-Manufactured Copper. *Surf. Coat. Technol.* **2021**, *409*, 126887. <https://doi.org/10.1016/j.surfcoat.2021.126887>.
 211. Hall, A.C.; Cook, D.J.; Neiser, R.A.; Roemer, T.J.; Hirschfeld, D.A. The Effect of a Simple Annealing Heat Treatment on the Mechanical Properties of Cold-Sprayed Aluminum. *J. Therm. Spray Technol.* **2006**, *15*, 233–238. <https://doi.org/10.1361/105996306X108138>.
 212. Al-Hamdani, K.S.; Murray, J.W.; Hussain, T.; Clare, A.T. Heat-Treatment and Mechanical Properties of Cold-Sprayed High Strength Al Alloys from Satellited Feedstocks. *Surf. Coat. Technol.* **2019**, *374*, 21–31. <https://doi.org/10.1016/j.surfcoat.2019.05.043>.
 213. Wu, D.; Li, W.; Liu, K.; Yang, Y.; Hao, S. Optimization of Cold Spray Additive Manufactured AA2024/Al₂O₃ Metal Matrix Composite with Heat Treatment. *J. Mater. Sci. Technol.* **2022**, *106*, 211–224. <https://doi.org/10.1016/j.jmst.2021.07.036>.
 214. Vo, P.; Irissou, E.; Legoux, J.G.; Yue, S. Mechanical and Microstructural Characterization of Cold-Sprayed Ti-6Al-4V after Heat Treatment. *J. Therm. Spray Technol.* **2013**, *22*, 954–964. <https://doi.org/10.1007/s11666-013-9945-4>.
 215. Li, W.Y.; Zhang, C.; Guo, X.; Xu, J.; Li, C.J.; Liao, H.; Coddet, C.; Khor, K.A. Ti and Ti-6Al-4V Coatings by Cold Spraying and Microstructure Modification by Heat Treatment. *Adv. Eng. Mater.* **2007**, *9*, 418–423. <https://doi.org/10.1002/adem.200700022>.
 216. Yu, J.S.; Kim, H.J.; Oh, I.H.; Lee, K.A. Densification and Purification of Cold Sprayed Ti Coating Layer by Using Annealing in Different Heat Treatment Environments. *Adv. Mater. Res.* **2013**, *602–604*, 1604–1608. <https://doi.org/10.4028/www.scientific.net/AMR.602-604.1604>.
 217. Cavaliere, P.; Perrone, A.; Silvello, A. Fatigue Behaviour of Inconel 625 Cold Spray Coatings. *Surf. Eng.* **2018**, *34*, 380–391. <https://doi.org/10.1080/02670844.2017.1371872>.
 218. Shrestha, D.; Azarmi, F.; Tangpong, X.W. Effect of Heat Treatment on Residual Stress of Cold Sprayed Nickel-Based Superalloys. *J. Therm. Spray Technol.* **2022**, *31*, 197–205. <https://doi.org/10.1007/s11666-021-01284-x>.
 219. Luo, X.T.; Yao, M.L.; Ma, N.; Takahashi, M.; Li, C.J. Deposition Behavior, Microstructure and Mechanical Properties of an in-Situ Micro-Forging Assisted Cold Spray Enabled Additively Manufactured Inconel 718 Alloy. *Mater. Des.* **2018**, *155*, 384–395. <https://doi.org/10.1016/j.matdes.2018.06.024>.
 220. Ralls, A.M.; Daroonparvar, M.; Kasar, A.K.; Misra, M.; Menezes, P.L. Influence of Friction Stir Processing on the Friction, Wear and Corrosion Mechanisms of Solid-State Additively Manufactured 316L Duplex Stainless Steel. *Tribol. Int.* **2023**, *178*, 108033. <https://doi.org/10.1016/j.triboint.2022.108033>.
 221. Kovarik, O.; Siegl, J.; Cizek, J.; Chraska, T.; Kondas, J. Fracture Toughness of Cold Sprayed Pure Metals. *J. Therm. Spray Technol.* **2020**, *29*, 147–157. <https://doi.org/10.1007/s11666-019-00956-z>.
 222. Ren, Y.; Tariq, N.U.H.; Liu, H.; Zhao, L.; Cui, X.; Shen, Y.; Wang, J.; Xiong, T. Study of Microstructural and Mechanical Anisotropy of 7075 Al Deposits Fabricated by Cold Spray Additive Manufacturing. *Mater. Des.* **2021**, *212*, 110271. <https://doi.org/10.1016/j.matdes.2021.110271>.

223. Cavaliere, P.; Perrone, A.; Silvello, A.; I aska, A.; Blasi, G.; Cano, I.G. Fatigue Bending of V-Notched Cold-Sprayed FeCoCrNiMn Coatings. *Metals* **2022**, *12*, 780. <https://doi.org/10.3390/met12050780>.
224. Trzaska, Z.; Couret, A.; Monchoux, J. Spark Plasma Sintering Mechanisms at the Necks between TiAl Powder Particles. *Acta Mater.* **2016**, *118*, 100–108. <https://doi.org/10.1016/j.actamat.2016.07.043>.
225. Zhang, P.; Liu, J.; Gao, Y.; Liu, Z.; Mai, Q. Effect of Heat Treatment Process on the Micro Machinability of 7075 Aluminum Alloy. *Vacuum* **2023**, *207*, 111574. <https://doi.org/10.1016/j.vacuum.2022.111574>.
226. Fard, R.A.; Kazeminezhad, M. Effect of Electropulsing on Microstructure and Hardness of Cold-Rolled Low Carbon Steel. *J. Mater. Res. Technol.* **2019**, *8*, 3114–3125. <https://doi.org/10.1016/j.jmrt.2019.02.023>.
227. Shen, Z.; Johnsson, M.; Zhao, Z.; Nygren, M. Spark Plasma Sintering of Alumina. *J. Am. Ceram. Soc.* **2002**, *85*, 1921–1927. <https://doi.org/10.1111/j.1151-2916.2002.tb00381.x>.
228. Miriyev, A.; Stern, A.; Tuval, E.; Kalabukhov, S.; Hooper, Z.; Frage, N. Titanium to Steel Joining by Spark Plasma Sintering (SPS) Technology. *J. Mater. Process. Technol.* **2013**, *213*, 161–166. <https://doi.org/10.1016/j.jmatprotec.2012.09.017>.
229. Matizanhuka, W.R. Spark Plasma Sintering (SPS)—An Advanced Sintering Technique for Structural Nanocomposite Materials. *J. S. Afr. Inst. Min. Metall.* **2016**, *116*, 1171–1180. <https://doi.org/10.17159/2411-9717/2016/v116n12a12>.
230. Ito, K.; Ogawa, K. Effects of Spark-Plasma Sintering Treatment on Cold-Sprayed Copper Coatings. *J. Therm. Spray Technol.* **2014**, *23*, 104–113. <https://doi.org/10.1007/s11666-013-0047-0>.
231. Vidyuk, T.M.; Dudina, D.V.; Korchagin, M.A.; Gavrilov, A.I.; Bokhonov, B.B.; Ukhina, A.V.; Esikov, M.A.; Shikalov, V.S.; Kosarev, V.F. Spark Plasma Sintering Treatment of Cold Sprayed Materials for Synthesis and Structural Modification: A Case Study Using TiC-Cu Composites. *Mater. Lett. X* **2022**, *14*, 100140. <https://doi.org/10.1016/j.mlblux.2022.100140>.
232. Bocanegra-Bernal, M.H. Hot Isostatic Pressing (HIP) Technology and Its Applications to Metals and Ceramics. *J. Mater. Sci.* **2004**, *39*, 6399–6420. <https://doi.org/10.1023/B:JMSE.0000044878.11441.90>.
233. Atkinson, H.V.; Davies, S. Fundamental Aspects of Hot Isostatic Pressing: An Overview. *Metall. Mater. Trans. A* **2000**, *31*, 2981–3000. <https://doi.org/10.1007/s11661-000-0078-2>.
234. Brian James, W. New Shaping Methods for Powder Metallurgy Components. *Mater. Des.* **1987**, *8*, 187–197. [https://doi.org/10.1016/0261-3069\(87\)90133-6](https://doi.org/10.1016/0261-3069(87)90133-6).
235. Benzing, J.; Hrabe, N.; Quinn, T.; White, R.; Rentz, R.; Ahlfors, M. Hot Isostatic Pressing (HIP) to Achieve Isotropic Microstructure and Retain as-Built Strength in an Additive Manufacturing Titanium Alloy (Ti-6Al-4V). *Mater. Lett.* **2019**, *257*, 126690. <https://doi.org/10.1016/j.matlet.2019.126690>.
236. Petrovskiy, P.; Sova, A.; Doubenskaia, M.; Smurov, I. Influence of Hot Isostatic Pressing on Structure and Properties of Titanium Cold-Spray Deposits. *Int. J. Adv. Manuf. Technol.* **2019**, *102*, 819–827. <https://doi.org/10.1007/s00170-018-03233-5>.
237. Petrovskiy, P.; Khomutov, M.; Cheverikin, V.; Travyanov, A.; Sova, A.; Smurov, I. Influence of Hot Isostatic Pressing on the Properties of 316L Stainless Steel, Al-Mg-Sc-Zr Alloy, Titanium and Ti6Al4V Cold Spray Deposits. *Surf. Coat. Technol.* **2021**, *405*, 126736. <https://doi.org/10.1016/j.surfcoat.2020.126736>.
238. Chen, C.; Xie, Y.; Yan, X.; Yin, S.; Fukunuma, H.; Huang, R.; Zhao, R.; Wang, J.; Ren, Z.; Liu, M.; et al. Effect of Hot Isostatic Pressing (HIP) on Microstructure and Mechanical Properties of Ti6Al4V Alloy Fabricated by Cold Spray Additive Manufacturing. *Addit. Manuf.* **2019**, *27*, 595–605. <https://doi.org/10.1016/j.addma.2019.03.028>.
239. Petrovskiy, P.; Travyanov, A.; Cheverikin, V.V.; Cheresheva, A.A.; Sova, A.; Smurov, I. Effect of Encapsulated Hot Isostatic Pressing on Properties of Ti6Al4V Deposits Produced by Cold Spray. *Int. J. Adv. Manuf. Technol.* **2020**, *107*, 437–449. <https://doi.org/10.1007/s00170-020-05080-9>.
240. Vaz, R.F.; Silvello, A.; Albaladejo, V.; Sanchez, J.; Cano, I.G. Improving the Wear and Corrosion Resistance of Maraging Part Obtained by Cold Gas Spray Additive Manufacturing. *Metals* **2021**, *11*, 1092. <https://doi.org/10.3390/met11071092>.
241. Feng, L.; Yang, W.-J.; Ma, K.; Yuan, Y.-D.; An, G.-S.; Li, W.-S. Microstructure and Properties of Cold Spraying AlCoCrCuFeNi_x HEA Coatings Synthesized by Induction Remelting. *Mater. Technol.* **2022**, *37*, 2567–2579. <https://doi.org/10.1080/10667857.2022.2046929>.
242. Jing, Z.; Dejun, K. Effect of Laser Remelting on Friction-Wear Behaviors of Cold Sprayed Al Coatings in 3.5% NaCl Solution. *Materials* **2018**, *11*, 283. <https://doi.org/10.3390/ma11020283>.
243. Astarita, A.; Genna, S.; Leone, C.; Minutolo, F.M.C.; Rubino, F.; Squillace, A. Study of the Laser Remelting of a Cold Sprayed Titanium Layer. *Procedia CIRP* **2015**, *33*, 452–457. <https://doi.org/10.1016/j.procir.2015.06.101>.
244. Marrocco, T.; Hussain, T.; McCartney, D.G.; Shipway, P.H. Corrosion Performance of Laser Posttreated Cold Sprayed Titanium Coatings. *J. Therm. Spray Technol.* **2011**, *20*, 909–917. <https://doi.org/10.1007/s11666-011-9637-x>.
245. Kumar, A.; Kant, R.; Singh, H. Microstructural and Tribological Properties of Laser-Treated Cold-Sprayed Titanium/Baghdadite Deposits. *J. Mater. Res.* **2022**, *37*, 2698–2709. <https://doi.org/10.1557/s43578-022-00675-2>.
246. Poza, P.; Múñez, C.J.; Garrido-Maneiro, M.A.; Vezzù, S.; Rech, S.; Trentin, A. Mechanical Properties of Inconel 625 Cold-Sprayed Coatings after Laser Remelting. Depth Sensing Indentation Analysis. *Surf. Coat. Technol.* **2014**, *243*, 51–57. <https://doi.org/10.1016/j.surfcoat.2012.03.018>.
247. Zybala, R.; Bucholc, B.; Kaszyca, K.; Kowiorski, K.; Soborń, D.; Żórawski, W.; Moszczyńska, D.; Molak, R.; Pakiel, Z. Properties of Cold Sprayed Titanium and Titanium Alloy Coatings after Laser Surface Treatment. *Materials* **2022**, *15*, 9014. <https://doi.org/10.3390/ma15249014>.
248. Vaz, R.F.; Pukasiewicz, A.G.M.; Siqueira, I.B.A.F.; Sucharski, G.B.; Chicoski, A.; Tristante, R. Thermal Spraying of FeMnCrSi Alloys: An Overview. In Proceedings of the International Thermal Spray Conference, Quebec City, QC, Canada, 24–28 May

- 2021; pp. 431–439.
249. Pukasiewicz, A.G.M.; Alcover, P.R.C.; Capra, A.R.; Paredes, R.S.C. Influence of Plasma Remelting on the Microstructure and Cavitation Resistance of Arc-Sprayed Fe-Mn-Cr-Si Alloy. *J. Therm. Spray Technol.* **2014**, *23*, 51–59. <https://doi.org/10.1007/s11666-013-0001-1>.
 250. Zabih, A.; Soltani, R. Tribological Properties of B4C Reinforced Aluminum Composite Coating Produced by TIG Re-Melting of Flame Sprayed Al-Mg-B4C Powder. *Surf. Coat. Technol.* **2018**, *349*, 707–718. <https://doi.org/10.1016/j.surfcoat.2018.06.040>.
 251. Simchen, F.; Sieber, M.; Kopp, A.; Lampke, T. Introduction to Plasma Electrolytic Oxidation—An Overview of the Process and Applications. *Coatings* **2020**, *10*, 628. <https://doi.org/10.3390/coatings10070628>.
 252. Egorkin, V.S.; Gnedenkov, S.V.; Sinebryukhov, S.I.; Vyalyi, I.E.; Gnedenkov, A.S.; Chizhikov, R.G. Increasing Thickness and Protective Properties of PEO-Coatings on Aluminum Alloy. *Surf. Coat. Technol.* **2018**, *334*, 29–42. <https://doi.org/10.1016/j.surfcoat.2017.11.025>.
 253. Rao, Y.; Wang, Q.; Oka, D.; Ramachandran, C.S. On the PEO Treatment of Cold Sprayed 7075 Aluminum Alloy and Its Effects on Mechanical, Corrosion and Dry Sliding Wear Performances Thereof. *Surf. Coat. Technol.* **2020**, *383*, 125271. <https://doi.org/10.1016/j.surfcoat.2019.125271>.
 254. Rao, Y.; Wang, Q.; Chen, J.; Ramachandran, C.S. Abrasion, Sliding Wear, Corrosion, and Cavitation Erosion Characteristics of a Duplex Coating Formed on AZ31 Mg Alloy by Sequential Application of Cold Spray and Plasma Electrolytic Oxidation Techniques. *Mater. Today Commun.* **2021**, *26*, 101978. <https://doi.org/10.1016/j.mtcomm.2020.101978>.
 255. Chavan, N.M.; Pant, P.; Sundararajan, G.; Suresh Babu, P. Post Treatment of Cold Sprayed Coatings Using High-Energy Infrared Radiation: First Comprehensive Study on Structure-Property Correlation. *Surf. Coat. Technol.* **2022**, *448*, 128902. <https://doi.org/10.1016/j.surfcoat.2022.128902>.
 256. Pokhmurska, H.; Wielage, B.; Lampke, T.; Grund, T.; Student, M.; Chervinska, N. Post-Treatment of Thermal Spray Coatings on Magnesium. *Surf. Coat. Technol.* **2008**, *202*, 4515–4524. <https://doi.org/10.1016/j.surfcoat.2008.04.036>.
 257. Kostilnik, T. Shot Peening. In *Surface Engineering*; Cotell, C.M., Sprague, J.A., Smidt F.A., Jr., Eds.; ASM International: Materials Park, OH, USA, 1994; Volume 1, pp. 126–135.
 258. Moridi, A.; Hassani-Gangaraj, S.M.; Vezzú, S.; Trško, I.; Guagliano, M. Fatigue Behavior of Cold Spray Coatings: The Effect of Conventional and Severe Shot Peening as Pre-/Post-Treatment. *Surf. Coat. Technol.* **2015**, *283*, 247–254. <https://doi.org/10.1016/j.surfcoat.2015.10.063>.
 259. Yao, H.-L.; Hu, X.-Z.; Yi, Z.-H.; Xia, J.; Tu, X.-Y.; Li, S.-B.; Yu, B.; Zhang, M.-X.; Bai, X.-B.; Chen, Q.-Y.; et al. Microstructure and Improved Anti-Corrosion Properties of Cold-Sprayed Zn Coatings Fabricated by Post Shot-Peening Process. *Surf. Coat. Technol.* **2021**, *422*, 127557. <https://doi.org/10.1016/j.surfcoat.2021.127557>.
 260. Sova, A.; Courbon, C.; Valiorgue, F.; Rech, J.; Bertrand, P. Effect of Turning and Ball Burnishing on the Microstructure and Residual Stress Distribution in Stainless Steel Cold Spray Deposits. *J. Therm. Spray Technol.* **2017**, *26*, 1922–1934. <https://doi.org/10.1007/s11666-017-0655-1>.
 261. Courbon, C.; Sova, A.; Valiorgue, F.; Pascal, H.; Sijobert, J.; Kermouche, G.; Bertrand, P.; Rech, J. Near Surface Transformations of Stainless Steel Cold Spray and Laser Cladding Deposits after Turning and Ball-Burnishing. *Surf. Coat. Technol.* **2019**, *371*, 235–244. <https://doi.org/10.1016/j.surfcoat.2019.01.092>.
 262. Mayer, A.R.; Bertuol, K.; Siqueira, L.B.A.F.A.F.; Chicowski, A.; Váz, R.F.; de Sousa, M.J.; Pukasiewicz, A.G.M.M. Evaluation of Cavitation/Corrosion Synergy of the Cr3C2-25NiCr Coating Deposited by HVOF Process. *Ultrason. Sonochem.* **2020**, *69*, 105271. <https://doi.org/10.1016/j.ultsonch.2020.105271>.
 263. Soyama, H. Cavitation Peening: A Review. *Metals* **2020**, *10*, 270. <https://doi.org/10.3390/met10020270>.
 264. Zhang, P.; Liu, Z.; Yue, X.; Wang, P.; Zhai, Y. Water Jet Impact Damage Mechanism and Dynamic Penetration Energy Absorption of 2A12 Aluminum Alloy. *Vacuum* **2022**, *206*, 111532. <https://doi.org/10.1016/j.vacuum.2022.111532>.
 265. Soyama, H.; Okura, Y. The Use of Various Peening Methods to Improve the Fatigue Strength of Titanium Alloy Ti6Al4V Manufactured by Electron Beam Melting. *AIMS Mater. Sci.* **2018**, *5*, 1000–1015. <https://doi.org/10.3934/matersci.2018.5.1000>.
 266. Bobzin, K.; Öte, M.; Wiesner, S.; Gerdt, L.; Senge, S.; Hirt, G. Investigation on the Cold Rolling and Structuring of Cold Sprayed Copper-Coated Steel Sheets. *IOP Conf. Ser. Mater. Sci. Eng.* **2017**, *181*, 012028. <https://doi.org/10.1088/1757-899X/181/1/012028>.
 267. Tariq, N.H.; Gyansah, L.; Qiu, X.; Du, H.; Wang, J.Q.; Feng, B.; Yan, D.S.; Xiong, T.Y. Thermo-Mechanical Post-Treatment: A Strategic Approach to Improve Microstructure and Mechanical Properties of Cold Spray Additively Manufactured Composites. *Mater. Des.* **2018**, *156*, 287–299. <https://doi.org/10.1016/j.matdes.2018.06.062>.
 268. Wu, T.; Jin, L.; Wu, W.X.; Gao, L.; Wang, J.; Zhang, Z.Y.; Dong, J. Improved Ductility of Mg–Zn–Ce Alloy by Hot Pack-Rolling. *Mater. Sci. Eng. A* **2013**, *584*, 97–102. <https://doi.org/10.1016/j.msea.2013.07.011>.
 269. Huang, H.; Liao, M.; Yu, Q.; Liu, G.; Wang, Z. The Effects of Hot-Pack Coating Materials on the Pack Rolling Process and Microstructural Characteristics during Ti-46Al-8Nb Sheet Fabrication. *Materials* **2020**, *13*, 762. <https://doi.org/10.3390/ma13030762>.
 270. Shen, Z.Z.; Lin, J.P.; Liang, Y.F.; Zhang, L.Q.; Shang, S.L.; Liu, Z.K. A Novel Hot Pack Rolling of High Nb–TiAl Sheet from Cast Ingot. *Intermetallics* **2015**, *67*, 19–25. <https://doi.org/10.1016/j.intermet.2015.07.009>.
 271. Zhao, H.; Tan, C.; Yu, X.; Ning, X.; Nie, Z.; Cai, H.; Wang, F.; Cui, Y. Enhanced Reactivity of Ni-Al Reactive Material Formed by Cold Spraying Combined with Cold-Pack Rolling. *J. Alloys Compd.* **2018**, *741*, 883–894. <https://doi.org/10.1016/j.jallcom.2018.01.170>.
 272. Qiu, X.; Tariq, N.U.H.; Qi, L.; Zan, Y.; Wang, Y.; Wang, J.; Du, H.; Xiong, T. In-Situ Sip/A380 Alloy Nano/Micro Composite

- Formation through Cold Spray Additive Manufacturing and Subsequent Hot Rolling Treatment: Microstructure and Mechanical Properties. *J. Alloys Compd.* **2019**, *780*, 597–606. <https://doi.org/10.1016/j.jallcom.2018.11.399>.
273. Li, K.; Liu, X.; Zhao, Y. Research Status and Prospect of Friction Stir Processing Technology. *Coatings* **2019**, *9*, 129. <https://doi.org/10.3390/coatings9020129>.
 274. Mondal, M.; Das, H.; Hong, S.-T.; Jeong, B.-S.; Han, H.N. Local Enhancement of the Material Properties of Aluminium Sheets by a Combination of Additive Manufacturing and Friction Stir Processing. *CIRP Ann.* **2019**, *68*, 289–292. <https://doi.org/10.1016/j.cirp.2019.04.109>.
 275. Hasani, B.M.; Hedayatmofidi, H.; Zarebidaki, A. Effect of Friction Stir Process on the Microstructure and Corrosion Behavior of AZ91 Mg Alloy. *Mater. Chem. Phys.* **2021**, *267*, 124672. <https://doi.org/10.1016/j.matchemphys.2021.124672>.
 276. Han, P.; Wang, W.; Liu, Z.; Zhang, T.; Liu, Q.; Guan, X.; Qiao, K.; Ye, D.; Cai, J.; Xie, Y.; et al. Modification of Cold-Sprayed High-Entropy Alloy Particles Reinforced Aluminum Matrix Composites Via Friction Stir Processing. *J. Alloys Compd.* **2022**, *907*, 164426. <https://doi.org/10.1016/j.jallcom.2022.164426>.
 277. Sudharshan Phani, P.; Srinivasa Rao, D.; Joshi, S.V.; Sundararajan, G. Effect of Process Parameters and Heat Treatments on Properties of Cold Sprayed Copper Coatings. *J. Therm. Spray Technol.* **2007**, *16*, 425–434. <https://doi.org/10.1007/s11666-007-9048-1>.
 278. Yang, K.; Li, W.; Yang, X.; Xu, Y.; Vairis, A. Effect of Heat Treatment on the Inherent Anisotropy of Cold Sprayed Copper Deposits. *Surf. Coat. Technol.* **2018**, *350*, 519–530. <https://doi.org/10.1016/j.surfcoat.2018.07.046>.
 279. Yin, S.; Cizek, J.; Yan, X.; Lupoi, R. Annealing Strategies for Enhancing Mechanical Properties of Additively Manufactured 316L Stainless Steel Deposited by Cold Spray. *Surf. Coat. Technol.* **2019**, *370*, 353–361. <https://doi.org/10.1016/j.surfcoat.2019.04.012>.
 280. Ren, Y.Q.; King, P.C.; Yang, Y.S.; Xiao, T.Q.; Chu, C.; Gulizia, S.; Murphy, A.B. Characterization of Heat Treatment-Induced Pore Structure Changes in Cold-Sprayed Titanium. *Mater. Charact.* **2017**, *132*, 69–75. <https://doi.org/10.1016/j.matchar.2017.08.006>.
 281. Rubino, F.; Astarita, A.; Carlone, P.; Genna, S.; Leone, C.; Memola Capece Minutolo, F.; Squillace, A. Selective Laser Post-Treatment on Titanium Cold Spray Coatings. *Mater. Manuf. Process.* **2016**, *31*, 1500–1506. <https://doi.org/10.1080/10426914.2015.1037912>.
 282. Boruah, D.; Zhang, X.; McNutt, P.; Khan, R.; Begg, H. Effect of Post-Deposition Thermal Treatments on Tensile Properties of Cold Sprayed Ti6Al4V. *Metals* **2022**, *12*, 1908. <https://doi.org/10.3390/met12111908>.
 283. Khun, N.W.; Tan, A.W.Y.; Sun, W.; Liu, E. Effects of Nd:YAG Laser Surface Treatment on Tribological Properties of Cold-Sprayed Ti-6Al-4V Coatings Tested against 100Cr6 Steel under Dry Condition. *Tribol. Trans.* **2019**, *62*, 391–402. <https://doi.org/10.1080/10402004.2018.1563258>.
 284. Chen, C.; Xie, Y.; Liu, L.; Zhao, R.; Jin, X.; Li, S.; Huang, R.; Wang, J.; Liao, H.; Ren, Z. Cold Spray Additive Manufacturing of Invar 36 Alloy: Microstructure, Thermal Expansion and Mechanical Properties. *J. Mater. Sci. Technol.* **2021**, *72*, 39–51. <https://doi.org/10.1016/j.jmst.2020.07.038>.
 285. Ma, W.; Xie, Y.; Chen, C.; Fukunuma, H.; Wang, J.; Ren, Z.; Huang, R. Microstructural and Mechanical Properties of High-Performance Inconel 718 Alloy by Cold Spraying. *J. Alloys Compd.* **2019**, *792*, 456–467. <https://doi.org/10.1016/j.jallcom.2019.04.045>.
 286. Li, W.; Cao, C.; Wang, G.; Wang, F.; Xu, Y.; Yang, X. 'Cold Spray+' as a New Hybrid Additive Manufacturing Technology: A Literature Review. *Sci. Technol. Weld. Join.* **2019**, *24*, 420–445. <https://doi.org/10.1080/13621718.2019.1603851>.
 287. Birt, A.M.; Champagne, V.K.; Sisson, R.D.; Apelian, D. Statistically Guided Development of Laser-Assisted Cold Spray for Microstructural Control of Ti-6Al-4V. *Metall. Mater. Trans. A* **2017**, *48*, 1931–1943. <https://doi.org/10.1007/s11661-017-3970-8>.
 288. Kulmala, M.; Vuoristo, P. Influence of Process Conditions in Laser-Assisted Low-Pressure Cold Spraying. *Surf. Coat. Technol.* **2008**, *202*, 4503–4508. <https://doi.org/10.1016/j.surfcoat.2008.04.034>.
 289. Lupoi, R.; Cockburn, A.; Bryan, C.; Sparkes, M.; Luo, F.; O'Neill, W. Hardfacing Steel with Nanostructured Coatings of Stellite-6 by Supersonic Laser Deposition. *Light Sci. Appl.* **2012**, *1*, e10. <https://doi.org/10.1038/lssa.2012.10>.
 290. Bray, M.; Cockburn, A.; O'Neill, W. The Laser-Assisted Cold Spray Process and Deposit Characterisation. *Surf. Coat. Technol.* **2009**, *203*, 2851–2857. <https://doi.org/10.1016/j.surfcoat.2009.02.135>.
 291. Barton, D.J.; Hornbuckle, B.C.; Darling, K.A.; Brewer, L.N.; Thompson, G.B. Influence of Surface Temperature in the Laser-Assisted Cold Spray Deposition of Sequential Oxide Dispersion Strengthened Layers: Microstructure and Hardness. *Mater. Sci. Eng. A* **2021**, *811*, 141027. <https://doi.org/10.1016/j.msea.2021.141027>.
 292. Christoulis, D.K.; Jeandin, M.; Irissou, É.; Legoux, J.-G.; Knapp, W. Laser-Assisted Cold Spray (LACS). In *Nd-YAG Laser*; Dumitras, D.C., Ed.; IntechOpen: Rijeka, Croatia, 2012; pp. 59–96.
 293. Olakanmi, E.O.; Doyoyo, M. Laser-Assisted Cold-Sprayed Corrosion- and Wear-Resistant Coatings: A Review. *J. Therm. Spray Technol.* **2014**, *23*, 765–785. <https://doi.org/10.1007/s11666-014-0098-x>.
 294. Christoulis, D.K.; Guetta, S.; Irissou, E.; Guipont, V.; Berger, M.H.; Jeandin, M.; Legoux, J.-G.; Moreau, C.; Costil, S.; Boustic, M.; et al. Cold-Spraying Coupled to Nano-Pulsed Nd-YaG Laser Surface Pre-Treatment. *J. Therm. Spray Technol.* **2010**, *19*, 1062–1073. <https://doi.org/10.1007/s11666-010-9500-5>.
 295. Lee, H.; Lim, C.H.J.; Low, M.J.; Tham, N.; Murukeshan, V.M.; Kim, Y.J. Lasers in Additive Manufacturing: A Review. *Int. J. Precis. Eng. Manuf. Green Technol.* **2017**, *4*, 307–322. <https://doi.org/10.1007/s40684-017-0037-7>.
 296. Olakanmi, E.O.; Itoileng, M.; Meacock, C.; Pityana, S.; Doyoyo, M. Deposition Mechanism and Microstructure of Laser-Assisted Cold-Sprayed (LACS) Al-12 Wt.%Si Coatings: Effects of Laser Power. *Jom* **2013**, *65*, 776–783. <https://doi.org/10.1007/s11837-013->

- 0611–6.
297. Barton, D.J.; Bhattiprolu, V.S.; Thompson, G.B.; Brewer, L.N. Laser Assisted Cold Spray of AISI 4340 Steel. *Surf. Coat. Technol.* **2020**, *400*, 126218. <https://doi.org/10.1016/j.surfcoat.2020.126218>.
 298. Olakanmi, E.O. Optimization of the Quality Characteristics of Laser-Assisted Cold-Sprayed (LACS) Aluminum Coatings with Taguchi Design of Experiments (DOE). *Mater. Manuf. Process.* **2016**, *31*, 1490–1499. <https://doi.org/10.1080/10426914.2014.984306>.
 299. Story, W.A.; Barton, D.J.; Hornbuckle, B.C.; Darling, K.A.; Thompson, G.B.; Brewer, L.N. Laser Assisted Cold Spray of Fe–Ni–Zr Oxide Dispersion Strengthened Steel. *Materialia* **2018**, *3*, 239–242. <https://doi.org/10.1016/j.mtla.2018.08.028>.
 300. Shi, J.; Wang, Y. Development of Metal Matrix Composites by Laser-Assisted Additive Manufacturing Technologies: A Review. *J. Mater. Sci.* **2020**, *55*, 9883–9917. <https://doi.org/10.1007/s10853-020-04730-3>.
 301. Nikbakht, R.; Cojocar, C.V.; Aghasibeig, M.; Irissou, É.; Kim, T.S.; Kim, H.S.; Jodoin, B. Cold Spray and Laser-Assisted Cold Spray of CrMnCoFeNi High Entropy Alloy Using Nitrogen as the Propelling Gas. *J. Therm. Spray Technol.* **2022**, *31*, 1129–1142. <https://doi.org/10.1007/s11666-022-01361-9>.
 302. Dey, D.; Sarkar, S.; Mahata, A.; Roy Choudhury, A.; Nath, A.K. Laser Assisted Cold Spray of 15–5 PH Stainless Steel in a Designed and Developed Setup. *Opt. Laser Technol.* **2023**, *158*, 108902. <https://doi.org/10.1016/j.optlastec.2022.108902>.
 303. Ortiz-Fernandez, R.; Jodoin, B. Hybrid Additive Manufacturing Technology: Induction Heating Cold Spray—Part I: Fundamentals of Deposition Process. *J. Therm. Spray Technol.* **2020**, *29*, 684–699. <https://doi.org/10.1007/s11666-020-01005-w>.
 304. Li, C.J.; Li, W.Y. Deposition Characteristics of Titanium Coating in Cold Spraying. *Surf. Coat. Technol.* **2003**, *167*, 278–283. [https://doi.org/10.1016/S0257-8972\(02\)00919-2](https://doi.org/10.1016/S0257-8972(02)00919-2).
 305. Daroonparvar, M.; Bakhsheshi Rad, H.R.; Saberi, A.; Razzaghi, M.; Kasar, A.K.; Ramakrishna, S.; Menezes, P.L.; Misra, M.; Ismail, A.F.; Sharif, S.; et al. Surface Modification of Magnesium Alloys Using Thermal and Solid-State Cold Spray Processes: Challenges and Latest Progresses. *J. Magnes. Alloy.* **2022**, *10*, 2025–2061. <https://doi.org/10.1016/j.jma.2022.07.012>.
 306. Ghelichi, R.; Bagherifard, S.; Pariente, I.F.; Guagliano, M.; Vezzù, S. Experimental Study of Shot Peening Followed by Cold Spray Coating on Residual Stresses of the Treated Parts. *SDHM Struct. Durab. Health Monit.* **2010**, *6*, 17–29.
 307. Luo, X.T.; Wei, Y.K.; Wang, Y.; Li, C.J. Microstructure and Mechanical Property of Ti and Ti6Al4V Prepared by an In-Situ Shot Peening Assisted Cold Spraying. *Mater. Des.* **2015**, *85*, 527–533. <https://doi.org/10.1016/j.matdes.2015.07.015>.
 308. Li, W.Y.; Zou, Y.F.; Wang, F.F.; Yang, X.W.; Xu, Y.X.; Hu, K.W.; Yan, D.Y. Employing Cold Spray to Alter the Residual Stress Distribution of Workpieces: A Case Study on Fusion-Welded AA2219 Joints. *J. Therm. Spray Technol.* **2020**, *29*, 1538–1549. <https://doi.org/10.1007/s11666-020-01025-6>.
 309. Ang, A.S.M.; Berndt, C.C. A Review of Testing Methods for Thermal Spray Coatings. *Int. Mater. Rev.* **2014**, *59*, 179–223. <https://doi.org/10.1179/1743280414Y.0000000029>.
 310. Xie, X.; Chen, C.; Ma, Y.; Xie, Y.; Wu, H.; Ji, G.; Aubry, E.; Ren, Z.; Liao, H. Influence of Annealing Treatment on Microstructure and Magnetic Properties of Cold Sprayed Ni-Coated FeSiAl Soft Magnetic Composite Coating. *Surf. Coat. Technol.* **2019**, *374*, 476–484. <https://doi.org/10.1016/j.surfcoat.2019.05.008>.
 311. Deshpande, S.; Kulkarni, A.; Sampath, S.; Herman, H. Application of Image Analysis for Characterization of Porosity in Thermal Spray Coatings and Correlation with Small Angle Neutron Scattering. *Surf. Coat. Technol.* **2004**, *187*, 6–16. <https://doi.org/10.1016/j.surfcoat.2004.01.032>.
 312. Baker, A.A.; Thuss, R.; Woollett, N.; Maich, A.; Stavrou, E.; McCall, S.K.; Radousky, H.B. Cold Spray Deposition of Thermoelectric Materials. *JOM* **2020**, *72*, 2853–2859. <https://doi.org/10.1007/s11837-020-04151-2>.
 313. Van Steenkiste, T.; Smith, J.R. Evaluation of Coatings Produced via Kinetic and Cold Spray Processes. *J. Therm. Spray Technol.* **2004**, *13*, 274–282. <https://doi.org/10.1361/10599630419427>.
 314. Wang, Y.; Adrien, J.; Normand, B. Porosity Characterization of Cold Sprayed Stainless Steel Coating Using Three-Dimensional X-Ray Microtomography. *Coatings* **2018**, *8*, 326. <https://doi.org/10.3390/coatings8090326>.
 315. Zahiri, S.H.; Mayo, S.C.; Jahedi, M. Characterization of Cold Spray Titanium Deposits by X-Ray Microscopy and Microtomography. *Microsc. Microanal.* **2008**, *14*, 260–266. <https://doi.org/10.1017/S1431927608080355>.
 316. Lévesque, D.; Bescond, C.; Cojocar, C. Laser-Ultrasonic Inspection of Cold Spray Additive Manufacturing Components. *AIP Conf. Proc.* **2019**, *2102*, 020026. <https://doi.org/10.1063/1.5099730>.
 317. Li, Y.-J.; Luo, X.-T.; Li, C.-J. Dependency of Deposition Behavior, Microstructure and Properties of Cold Sprayed Cu on Morphology and Porosity of the Powder. *Surf. Coat. Technol.* **2017**, *328*, 304–312. <https://doi.org/10.1016/j.surfcoat.2017.08.070>.
 318. Zhu, Q.J.; Wang, K.; Wang, X.H.; Hou, B.R. Electrochemical Impedance Spectroscopy Analysis of Cold Sprayed and Arc Sprayed Aluminium Coatings Serviced in Marine Environment. *Surf. Eng.* **2012**, *28*, 300–305. <https://doi.org/10.1179/1743294411Y.00000000036>.
 319. Dosta, S.; Bolelli, G.; Candel, A.; Lusvardi, L.; Cano, I.G.; Guilemany, J.M. Plastic Deformation Phenomena During Cold Spray Impact of WC-Co Particles onto Metal Substrates. *Acta Mater.* **2017**, *124*, 173–181. <https://doi.org/10.1016/j.actamat.2016.11.010>.
 320. ISO 14577-1:2015; Metallic Materials—Instrumented Indentation Test for Hardness and Materials Parameters—Part 1: Test Method; ISO: Geneva, Switzerland, 2015.
 321. Váz, R.F.; Silvello, A.; Cavalière, P.D.; Dosta, S.; Cano, I.G.; Capodieci, L.; Rizzo, A.; Valerini, D. Fretting Wear and Scratch Resistance of Cold-Sprayed Pure Cu and Ti. *Metallogr. Microstruct. Anal.* **2021**, *10*, 496–513. <https://doi.org/10.1007/s13632-021-00758-2>.
 322. Ctibor, P.; Boháč, P.; Stranyánek, M.; Čtvrtlík, R. Structure and Mechanical Properties of Plasma Sprayed Coatings of Titania and Alumina. *J. Eur. Ceram. Soc.* **2006**, *26*, 3509–3514. <https://doi.org/10.1016/j.jeurceramsoc.2005.12.018>.

323. ASTM C633-13; Standard Test Method for Adhesion or Cohesion Strength of Thermal Spray Coatings. ASTM International: West Conshohocken, PA, USA, 2021.
324. Shinde, S.; Sampath, S. A Critical Analysis of the Tensile Adhesion Test for Thermally Sprayed Coatings. *J. Therm. Spray Technol.* **2022**, *31*, 2247–2279. <https://doi.org/10.1007/s11666-022-01468-z>.
325. ASTM E8-22; Standard Test Methods for Tension Testing of Metallic Materials. ASTM International: West Conshohocken, PA, USA, 2022.
326. Ichikawa, Y.; Tokoro, R.; Tanno, M.; Ogawa, K. Elucidation of Cold-Spray Deposition Mechanism by Auger Electron Spectroscopic Evaluation of Bonding Interface Oxide Film. *Acta Mater.* **2019**, *164*, 39–49. <https://doi.org/10.1016/j.actamat.2018.09.041>.
327. Boruah, D.; Robinson, B.; London, T.; Wu, H.; de Villiers-Lovelock, H.; McNutt, P.; Doré, M.; Zhang, X. Experimental Evaluation of Interfacial Adhesion Strength of Cold Sprayed Ti-6Al-4V Thick Coatings Using an Adhesive-Free Test Method. *Surf. Coat. Technol.* **2020**, *381*, 125130. <https://doi.org/10.1016/j.surfcoat.2019.125130>.
328. Wu, H.; Huang, C.; Xie, X.; Liu, S.; Wu, T.; Niendorf, T.; Xie, Y.; Deng, C.; Liu, M.; Liao, H.; et al. Influence of Spray Trajectories on Characteristics of Cold-Sprayed Copper Deposits. *Surf. Coat. Technol.* **2021**, *405*, 126703. <https://doi.org/10.1016/j.surfcoat.2020.126703>.
329. Hauer, M.; Krebs, S.; Kroemmer, W.; Henkel, K.M. Correlation of Residual Stresses and Coating Properties in Arc-Sprayed Coatings on Different Substrates for Maritime Applications. *J. Therm. Spray Technol.* **2020**, *29*, 1289–1299. <https://doi.org/10.1007/s11666-020-01020-x>.
330. Wang, Q.; Luo, X.; Tsutsumi, S.; Sasaki, T.; Li, C.; Ma, N. Measurement and Analysis of Cold Spray Residual Stress Using Arbitrary Lagrangian–Eulerian Method. *Addit. Manuf.* **2020**, *35*, 101296. <https://doi.org/10.1016/j.addma.2020.101296>.
331. Luzin, V.; Kirstein, O.; Zahiri, S.H.; Fraser, D. Residual Stress Buildup in Ti Components Produced by Cold Spray Additive Manufacturing (CSAM). *J. Therm. Spray Technol.* **2020**, *29*, 1498–1507. <https://doi.org/10.1007/s11666-020-01048-z>.
332. Vargas-Uscategui, A.; King, P.C.; Styles, M.J.; Saleh, M.; Luzin, V.; Thorogood, K. Residual Stresses in Cold Spray Additively Manufactured Hollow Titanium Cylinders. *J. Therm. Spray Technol.* **2020**, *29*, 1508–1524. <https://doi.org/10.1007/s11666-020-01028-3>.
333. Sinclair-Adamson, R.; Luzin, V.; Duguid, A.; Kannoopatti, K.; Murray, R. Residual Stress Distributions in Cold-Sprayed Copper 3D-Printed Parts. *J. Therm. Spray Technol.* **2020**, *29*, 1525–1537. <https://doi.org/10.1007/s11666-020-01040-7>.
334. Loke, K.; Zhang, Z.-Q.; Narayanaswamy, S.; Koh, P.K.; Luzin, V.; Gnaupel-Herold, T.; Ang, A.S.M. Residual Stress Analysis of Cold Spray Coatings Sprayed at Angles Using Through-Thickness Neutron Diffraction Measurement. *J. Therm. Spray Technol.* **2021**, *30*, 1810–1826. <https://doi.org/10.1007/s11666-021-01252-5>.
335. Boruah, D.; Ahmad, B.; Lee, T.L.; Kabra, S.; Syed, A.K.; McNutt, P.; Doré, M.; Zhang, X. Evaluation of Residual Stresses Induced by Cold Spraying of Ti-6Al-4V on Ti-6Al-4V Substrates. *Surf. Coat. Technol.* **2019**, *374*, 591–602. <https://doi.org/10.1016/j.surfcoat.2019.06.028>.
336. Ajovalasit, A. Review of Some Development of the Hole Drilling Method. In *Applied Stress Analysis*; Hyde, T.H., Ollerton, E., Eds.; Springer: Dordrecht, The Netherlands, 1990; pp. 60–71.
337. Niku-Lari, A.; Lu, J.; Flavenot, J.F. Measurement of Residual-Stress Distribution by the Incremental Hole-Drilling Method. *Exp. Mech.* **1985**, *25*, 175–185. <https://doi.org/10.1007/BF02328809>.
338. Santana, Y.Y.; La Barbera-Sosa, J.G.; Staia, M.H.; Lesage, J.; Puchi-Cabrera, E.S.; Chicot, D.; Bemporad, E. Measurement of Residual Stress in Thermal Spray Coatings by the Incremental Hole Drilling Method. *Surf. Coat. Technol.* **2006**, *201*, 2092–2098. <https://doi.org/10.1016/j.surfcoat.2006.04.056>.
339. Schajer, G.S.; Whitehead, P.S. Hole-Drilling Method Concept and Development. In *Hole-Drilling Method for Measuring Residual Stresses*; Springer: Cham, Switzerland, 2018; pp. 47–68.
340. ASTM E837-20; Standard Test Method for Determining Residual Stresses by the Hole-Drilling Strain-Gages; ASTM International: West Conshohocken, PA, USA, 2020.
341. Clyne, T.W.; Gill, S.C. Residual Stresses in Thermal Spray Coatings and Their Effect on Interfacial Adhesion: A Review of Recent Work. *J. Therm. Spray Technol.* **1996**, *5*, 401–418. <https://doi.org/10.1007/BF02645271>.
342. Singh, R.; Schrufer, S.; Wilson, S.; Gibmeier, J.; Vassen, R. Influence of Coating Thickness on Residual Stress and Adhesion-Strength of Cold-Sprayed Inconel 718 Coatings. *Surf. Coat. Technol.* **2018**, *350*, 64–73. <https://doi.org/10.1016/j.surfcoat.2018.06.080>.
343. Sample, C.M.; Champagne, V.K.; Nardi, A.T.; Lados, D.A. Factors Governing Static Properties and Fatigue, Fatigue Crack Growth, and Fracture Mechanisms in Cold Spray Alloys and Coatings/Repairs: A Review. *Addit. Manuf.* **2020**, *36*, 101371. <https://doi.org/10.1016/j.addma.2020.101371>.
344. Price, T.S.; Shipway, P.H.; McCartney, D.G. Effect of Cold Spray Deposition of a Titanium Coating on Fatigue Behavior of a Titanium Alloy. *J. Therm. Spray Technol.* **2006**, *15*, 507–512. <https://doi.org/10.1361/105996306X147108>.
345. Dayani, S.B.; Shaha, S.K.; Ghelichi, R.; Wang, J.F.; Jahed, H. The Impact of AA7075 Cold Spray Coating on the Fatigue Life of AZ31B Cast Alloy. *Surf. Coat. Technol.* **2018**, *337*, 150–158. <https://doi.org/10.1016/j.surfcoat.2018.01.008>.
346. Cizek, J.; Matejkova, M.; Dlouhy, I.; Siska, F.; Kay, C.M.; Karthikeyan, J.; Kuroda, S.; Kovarik, O.; Siegl, J.; Loke, K.; et al. Influence of Cold-Sprayed, Warm-Sprayed, and Plasma-Sprayed Layers Deposition on Fatigue Properties of Steel Specimens. *J. Therm. Spray Technol.* **2015**, *24*, 758–768. <https://doi.org/10.1007/s11666-015-0240-4>.
347. ISO 1143:2021; Metallic Materials—Rotating Bar Bending Fatigue Testing; ISO: Geneva, Switzerland, 2021.
348. Ziemian, C.W.; Sharma, M.M.; Bouffard, B.D.; Nissley, T.; Eden, T.J. Effect of Substrate Surface Roughening and Cold Spray

- Coating on the Fatigue Life of AA2024 Specimens. *Mater. Des.* **2014**, *54*, 212–221. <https://doi.org/10.1016/j.matdes.2013.08.061>.
349. Xiong, Y.; Zhang, M.-X. The Effect of Cold Sprayed Coatings on the Mechanical Properties of AZ91D Magnesium Alloys. *Surf. Coat. Technol.* **2014**, *253*, 89–95. <https://doi.org/10.1016/j.surfcoat.2014.05.018>.
 350. Yamazaki, Y.; Fukanuma, H.; Ohno, N. Anisotropic Mechanical Properties of the Free-Standing Cold Sprayed SUS316 Coating and Effect of the Post-Spray Heat Treatment on It. *J. Japan Therm. Spray Soc.* **2016**, *53*, 91–95. <https://doi.org/10.11330/jtss.53.91>.
 351. Ševeček, M.; Krejčí, J.; Shahin, M.H.; Petrik, J.; Ballinger, R.G.; Shirvan, K. Fatigue Behavior of Cold Spray-Coated Accident Tolerant Cladding. In Proceedings of the TopFuel 2018, Prague, Czech Republic, 30 September–4 October 2018; pp. 1–15.
 352. ASTM E399-22; Standard Test Method for Linear-Elastic Plane-Strain Fracture Toughness of Metallic Materials. ASTM International: West Conshohocken, PA, USA, 2022.
 353. Li, X.-K.; Zhu, S.-P.; Liao, D.; Correia, J.A.F.O.; Berto, F.; Wang, Q. Probabilistic Fatigue Modelling of Metallic Materials Under Notch and Size Effect Using the Weakest Link Theory. *Int. J. Fatigue* **2022**, *159*, 106788. <https://doi.org/10.1016/j.ijfatigue.2022.106788>.
 354. Batistič, S.; der Laken, P. History, Evolution and Future of Big Data and Analytics: A Bibliometric Analysis of Its Relationship to Performance in Organizations. *Br. J. Manag.* **2019**, *30*, 229–251. <https://doi.org/10.1111/1467-8551.12340>.
 355. Donthu, N.; Kumar, S.; Mukherjee, D.; Pandey, N.; Lim, W.M. How to Conduct a Bibliometric Analysis: An Overview and Guidelines. *J. Bus. Res.* **2021**, *133*, 285–296. <https://doi.org/10.1016/j.jbusres.2021.04.070>.
 356. Broadus, R.N. Toward a Definition of “Bibliometrics.” *Scientometrics* **1987**, *12*, 373–379. <https://doi.org/10.1007/BF02016680>.
 357. Hulme, E.W. Statistical Bibliography in Relation to the Growth of Modern Civilization: Two Lectures Delivered in the University of Cambridge in May 1922. *Nature* **1923**, *112*, 585–586. <https://doi.org/10.1038/112585a0>.
 358. Caviggioli, F.; Ughetto, E. A Bibliometric Analysis of the Research Dealing with the Impact of Additive Manufacturing on Industry, Business and Society. *Int. J. Prod. Econ.* **2019**, *208*, 254–268. <https://doi.org/10.1016/j.ijpe.2018.11.022>.
 359. Hernandez Korner, M.E.; Lambán, M.P.; Albajez, J.A.; Santolaria, J.; Ng Corrales, L.D.C.; Royo, J. Systematic Literature Review: Integration of Additive Manufacturing and Industry 4.0. *Metals* **2020**, *10*, 1061. <https://doi.org/10.3390/met10081061>.
 360. Javaid, M.; Haleem, A. Current Status and Challenges of Additive Manufacturing in Orthopaedics: An Overview. *J. Clin. Orthop. Trauma* **2019**, *10*, 380–386. <https://doi.org/10.1016/j.jcot.2018.05.008>.
 361. Jemghili, R.; Ait Taleb, A.; Khalifa, M. A Bibliometric Indicators Analysis of Additive Manufacturing Research Trends From 2010 to 2020. *Rapid Prototyp. J.* **2021**, *27*, 1432–1454. <https://doi.org/10.1108/RPJ-11-2020-0274>.
 362. Khor, K.A.; Yu, L.G. Global Research Trends in Thermal Sprayed Coatings Analyzed with Bibliometrics Tools. *J. Therm. Spray Technol.* **2015**, *24*, 1346–1354. <https://doi.org/10.1007/s11666-015-0337-9>.
 363. Li, R.-T.; Khor, K.A.; Yu, L.-G. Identifying Indicators of Progress in Thermal Spray Research Using Bibliometrics Analysis. *J. Therm. Spray Technol.* **2016**, *25*, 1526–1533. <https://doi.org/10.1007/s11666-016-0445-1>.
 364. Milanez, D.H.; de Oliveira, B.S.; Noyons, E.C.M.; Faria, L.L.L.; Botta, W.J. Assessing Collaboration and Knowledge Flow on Coatings of Metallic Glasses Obtained from Thermal Spraying Processes Using Bibliometrics and Science Mapping. *Mater. Res.* **2017**, *20*, 71–80. <https://doi.org/10.1590/1980-5373-mr-2017-0297>.
 365. Dobra, A. General Classification of Robots. Size Criteria. In Proceedings of the 23rd International Conference on Robotics in Alpe-Adria-Danube Region, Smolenice, Slovakia, 3–5 September 2014; IEEE: Smolenice Castle, Slovakia, 2014; pp. 1–6.
 366. Xie, Y.; Zhang, C.; Lai, Q. China’s Rise as a Major Contributor to Science and Technology. *Proc. Natl. Acad. Sci. USA* **2014**, *111*, 9437–9442. <https://doi.org/10.1073/pnas.1407709111>.
 367. Tollefson, J. China Declared World’s Largest Producer of Scientific Articles. *Nature* **2018**, *553*, 390–390. <https://doi.org/10.1038/d41586-018-00927-4>.
 368. Zhou, P.; Leydesdorff, L. The Emergence of China as a Leading Nation in Science. *Res. Policy* **2006**, *35*, 83–104. <https://doi.org/10.1016/j.respol.2005.08.006>.
 369. Wang, J.; Halfman, W.; Zwart, H. The Chinese Scientific Publication System: Specific Features, Specific Challenges. *Learn. Publ.* **2021**, *34*, 105–115. <https://doi.org/10.1002/leap.1326>.
 370. Stevens, M.R.; Park, K.; Tian, G.; Kim, K.; Ewing, R. Why Do Some Articles in Planning Journals Get Cited More than Others? *J. Plan. Educ. Res.* **2022**, *42*, 442–463. <https://doi.org/10.1177/0739456X19827083>.
 371. Meho, L.I. The Rise and Rise of Citation Analysis. *Phys. World* **2007**, *20*, 32–36. <https://doi.org/10.1088/2058-7058/20/1/33>.
 372. Larivière, V.; Gong, K.; Sugimoto, C.R. Citations Strength Begins at Home. *Nature* **2018**, *564*, S70–S71. <https://doi.org/10.1038/d41586-018-07695-1>.
 373. Zhou, P.; Leydesdorff, L. A Comparative Study of the Citation Impact of Chinese Journals with Government Priority Support. *Front. Res. Metrics Anal.* **2016**, *1*, 1–8. <https://doi.org/10.3389/frma.2016.00003>.
 374. Li, W.; Yang, K.; Yin, S.; Yang, X.; Xu, Y.; Lupoi, R. Solid-State Additive Manufacturing and Repairing by Cold Spraying: A Review. *J. Mater. Sci. Technol.* **2018**, *34*, 440–457. <https://doi.org/10.1016/j.jmst.2017.09.015>.
 375. Vanerio, D.; Kondas, J.; Guagliano, M.; Bagherifard, S. 3D Modelling of the Deposit Profile in Cold Spray Additive Manufacturing. *J. Manuf. Process.* **2021**, *67*, 521–534. <https://doi.org/10.1016/j.jmapro.2021.05.013>.

Disclaimer/Publisher’s Note: The statements, opinions and data contained in all publications are solely those of the individual author(s) and contributor(s) and not of MDPI and/or the editor(s). MDPI and/or the editor(s) disclaim responsibility for any injury to people or property resulting from any ideas, methods, instructions or products referred to in the content.

Chapter 2

SCOPE OF THE WORK

2. SCOPE OF THE WORK

This thesis focuses on the research of CSAM of metals from the standpoint of those more relevant issues and future perspectives. It considers its pros and cons, current challenges, and developments to make this technique more industrially mature. The main objective of this work is to develop spraying strategies or methodologies to obtain better CSAM-ed parts quality, considering the geometries feasible and properties obtained.

To achieve the main objective, it is first necessary to accomplish some specific objectives, as detailed below:

- Evaluate the powders more suitable for CSAM depositions, considering the characterization of each powder studied and an approach to the economic impact of the feedstock powder on the global CSAM cost;
- Make CSAM parts with the selected powders, characterizing their microstructure and properties achieved;
- Develop a CSAM strategy to improve the deposit geometric accuracy, controlling the part's sidewall inclination, making thin and high walls or dense large bulks;
- Evaluate the characteristics and properties obtained by employing the developed CSAM strategy, considering the geometric accuracy, microstructure, and mechanical properties achieved;
- Evaluate the effect of post-treatments on the properties of the CSAM-ed materials, focused on different heat treatments impacts on their mechanical properties and isotropy, besides homogenising the residual stress in the material;
- Evaluate the use of a hybrid thermal spraying process, making a part by CSAM and improving its wear and corrosion resistance by a coating deposited by another manufacturing process, resulting in a synergy between the CSAM's ability to make large parts and the material superficial properties improvement by a thin coating.

Chapter 3

EXPERIMENTAL PROCEDURES

3. EXPERIMENTAL PROCEDURES

This Chapter presents the materials' processing, parameters, materials selected, and characterization techniques for the feedstock powders and the CS-ed samples. Besides that, the testing performed to evaluate the quality of the CS-ed materials are described and detailed for a good comprehension and repeatability of the experiments by other scholars. Some information presented in this section is repeated in the Materials and Methods sections of the following articles.

3.1. Feedstock Materials and their Characterization

CS process demands the feedstock material in powder form, and different powders were studied in this work. All the powders selected are commercial and were previously characterized to check if they were adequate for CSAM processing. Table 1 shows the materials used for CSAM with the data informed by their respective manufacturers. It is noticed that different companies supplied similar powders, e.g., Ti AP&C and Ti CNPC, or 316L Daye and 316L Oerlikon. The selection of powders supplier was based on the powders' characteristics and properties adequate for CS; however, for similar powders, the selection was made based on the powders' price, buying the less expensive one.

The characterizations were done to measure the powder size distribution, flowability, apparent density, chemical composition, and particle shape. The images were obtained by Scanning Electron Microscopy (SEM) after hot mounting the samples in conductor Bakelite to observe the particle shape, cross-section, and free surface. The preparation followed the ASTM E1920-03 [2] and ASTM E3-01 [3] standards, mounting, grinding, and polishing. The equipment used for SEM was a Thermo Fisher Phenom Pro (Eindhoven, the Netherlands), Figure 4. The particle size distribution of feedstock powders was determined in triplicate by dry mode Laser Scattering (LS) technique using a Beckman Coulter LS13320 equipment (Brea, CA, USA), Figure 4, according to ASTM B822-02 [4] standard. The nominal composition of powders was obtained by Inductively Couple Plasma (ICP) using a Perkin Elmer Optima ICP-OES 3200 RL equipment (Waltham, MA, USA), Figure 4. For phase analysis, the XRD PANalytical X'Pert PRO MPD equipment (Malvern, United Kingdom), Figure 4, was used with radiation of Cu K α ($\lambda = 1.5418 \text{ \AA}$) from 5° to 120° 2 θ with a 0.017° step, measuring 80 s per step.



Figure 4: Powder characterization equipment.

In addition, the apparent density and flowability of the powders were measured by the Carney funnel, Figure 5, five times for each material, for statistical reasons, following the ASTM B212-21 [5] and ASTM B213-20 [6] or ASTM B417-22 [7] standards, respectively.

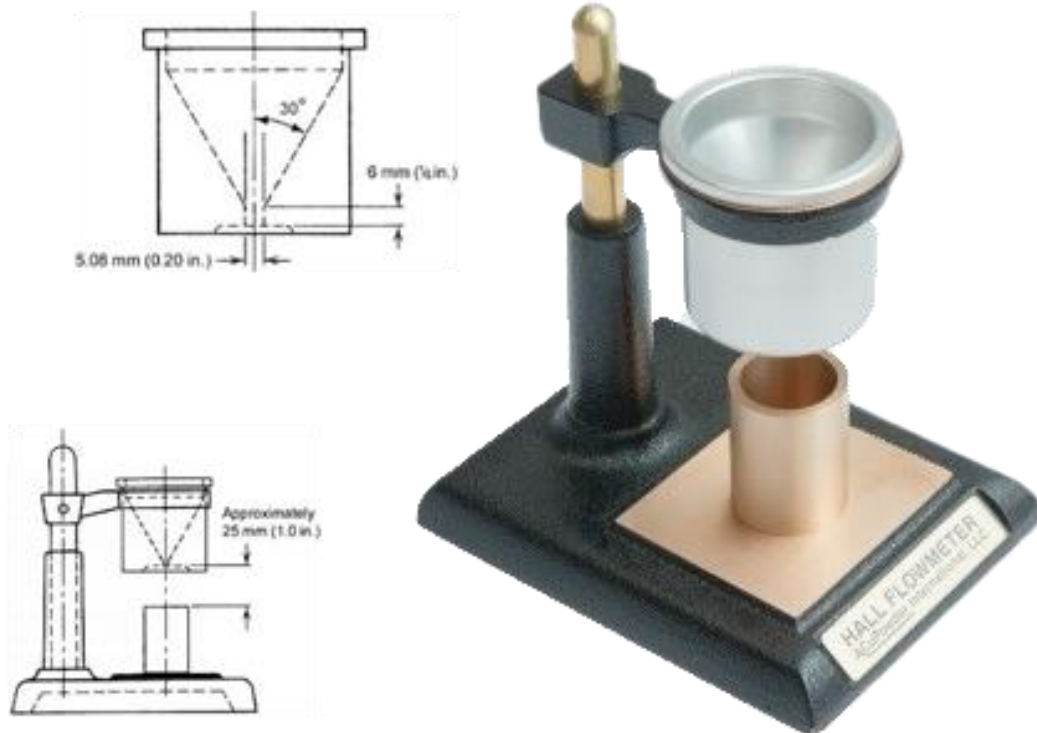


Figure 5: Flowmeter device.

Table 1: Feedstock powders.

Material	Commercial name	Manufacturer	Chemical composition ¹ [wt.%]	Particle size distribution ^{1,2} [μm]
316L	316L	Daye (Shijiazhuang, China)	Cr _{17.5} Mo _{2.7} Mn _{0.3} Si _{0.8} Fe _{bal.}	-40 +15
316L	SS316L	Plasma Giken (Saytama, Japan)	Cr _{18.0} Ni _{14.0} Mo _{3.0} Si _{1.0} Fe _{bal.}	-45 +10
316L	Diamalloy 1003	Oerlikon (Westbury, NY, USA)	Cr _{17.0} Ni _{12.0} Mo _{2.5} Si _{2.3} Fe _{bal.}	-45 +11
316L	316L	Sandvik (Neath, UK)	Cr _{17.0} Ni _{12.0} Mo _{2.5} Si _{1.0} Fe _{bal.}	-45 +20
Ti	Cp-Ti grade 2	AP&C (Boisbriand, QC, Canada)	Ti _{99.7 min.}	-44 +17
Ti	CNPC-TI300	CNPC (Shangai, China)	Ti _{99 min.}	-53 +15
Ti6Al4V	Spherical APA Ti-6Al4V	AP&C (Boisbriand, QC, Canada)	Al ₆ V ₄ Ti _{bal.}	-45 +15
Ti6Al4V	HP.X-20	Dycomet (Akkrum, the Netherlands)	Al ₆ V ₄ Ti _{bal.}	-45 +15
Cu	Cu	Safina (Vestec, Czech Republic)	CU _{99.95 min.}	-53 +15
Al	Al	Ecka (Velden, Germany)	Al _{99.5 min.}	-45 +20
Maraging	Maraging	Rovalma (Rubí, Spain)	3	-75
Maraging	MetcoAdd C300-A	Oerlikon (Westbury, NY, USA)	Ni ₁₈ Co ₉ Mo ₅ Ti ₁ Fe _{bal.}	-45 +15
Steel	1008	Dycomet (Akkrum, the Netherlands)	3	-55 +15
Inconel 625	Diamalloy 1005	Oerlikon (Westbury, NY, USA)	Cr _{21.5} Mo ₉ Nb/Ta ₄ Fe _{2.5} Ni _{bal.}	-45 +11
WC-10Co4Cr	DTS W928	Fujimi (Kiyosu, Japan)	Co ₁₀ Cr ₄ (WC) _{bal.}	-32 +10
WC-12Co	WOKA 3110	Oerlikon (Westbury, NY, USA)	Co ₁₂ (WC) _{bal.}	-25 +5

¹ Informed by the manufacturer.

² Values not considering the 10% smallest, d₁₀, and biggest, d₉₀, particles.

³ Chemical composition not informed.

3.2. Samples and Parts Production

In the different studies, several samples were made, CS-ed coatings for a first approach, as presented in Article 2 and Article 4; and CSAM-ed multiples geometries, as shown in Figure 12 of Article 3, and Figure 5 of Article 5. Some parts were thin walls produced on narrow substrates, and other were cube-like bulks. Different substrates were also used, e.g., 5 mm thick carbon steel, Ti, Ti6Al4V, Al, and Cu plates, or 3 mm thick larger Al plates, depending on the objective of each study, i.e., simulating a

repairing service of a damaged part, or producing a freeform part to be machined from the substrate.

For every deposition, the substrate was previously manually grit-blasted with alumina for a roughness greater than Ra 7 µm and Ry 40 µm. Article 6 presents the hybrid thermal spraying deposition is presented, building Maraging parts by CSAM, and coating them with cermets by HVOF process. Both techniques are presented as manufacturing processes in the following sections. Article 5 presents the use of heat treatment and its impact on the material performance and properties; however, other post-treatments were studied, listed, and explicated as manufacturing processes also.

3.2.1. Cold Spray Deposition

Two high-pressure CS equipment were used: a CGT Kinetiks 4000 (Haun, Germany), which is nowadays made by Oerlikon Metco (Westbury, NY, USA), and a Plasma Giken PCS100 (Saitama, Japan) using N₂ or He as working gas, Figure 6. The parameters change for each material sprayed and equipment, as presented in Table 2. These values were selected based on the literature and the expertise of the CPT's research group, which has previously studied them, focusing on the maximum Deposition Efficiency (DE) for each material.

Although, for this work, DE was measured, comparing the mass of fed powder and the mass of the CS-ed consolidated coating, following the ISO 17836:2004(E) [8] standard, using its recommendations for plate samples, but in a smaller sample than that indicated in this standard. Equation (1) was used to calculate the DE, where P₁ is the mass of powder fed to the powder feeder in g, P₂ is the remaining mass of powder after the deposition in g, S₁ is the substrate mass before coating in g, and S₂ is the coated substrate mass in g.

$$DE = \left(1 - \frac{(P_1 - P_2) - (S_2 - S_1)}{(P_1 - P_2)} \right) \cdot 100\% \quad (1)$$

Additionally, and in collaboration with the University of Tampere (Tampere, Finland), the CS-ed particle velocity distributions were measured employing the CS parameters from Table 2 for selected powders. The equipment used was a HiWatch equipment (Oseir, Tampere, Finland), collecting 300 values to plot results as histogram distributions.



Figure 6: CS equipment.

Table 2: CS parameters.

Material	Equipment	Pressure [MPa]	Temperature [°C]	Standoff distance [mm]	Powder feeding [g·s ⁻¹]
316L	Kinetiks	4.0	800	30	0.41
316L	PCS100	6.0	1000	25	0.44
Ti	Kinetiks	4.0	700	40	0.70
Ti	PCS100	6.5	900	25	0.74
Ti6Al4V	PCS100	6.5	1000	25	0.46
Cu	Kinetiks	3.0	400	40	0.75
Cu	PCS100	3.0	700	25	0.82
Al	PCS100	3.0	450	25	0.28
Maraging	PCS100	7.0	975	25	0.43
Steel	PCS100	7.0	975	25	0.42
Inconel 625	PCS100	6.0	1000	25	0.38

3.2.2. High-Velocity Oxy-Fuel Deposition

For the deposition of WC-12Co coatings by the High-Velocity Oxy-Fuel (HVOF) process, the equipment was composed of a gun Sulzer Metco DJ2600, control unit Sulzer Metco DJCE, and powder feeder Sulzer Metco 9MPE-DJ (Westbury, NY, USA), Figure 7. This equipment is nowadays made by Oerlikon Metco (Westbury, NY, USA). The process parameters are presented in Table 3. The HVOF fuel was H₂, and the powder transporting gas was N₂.

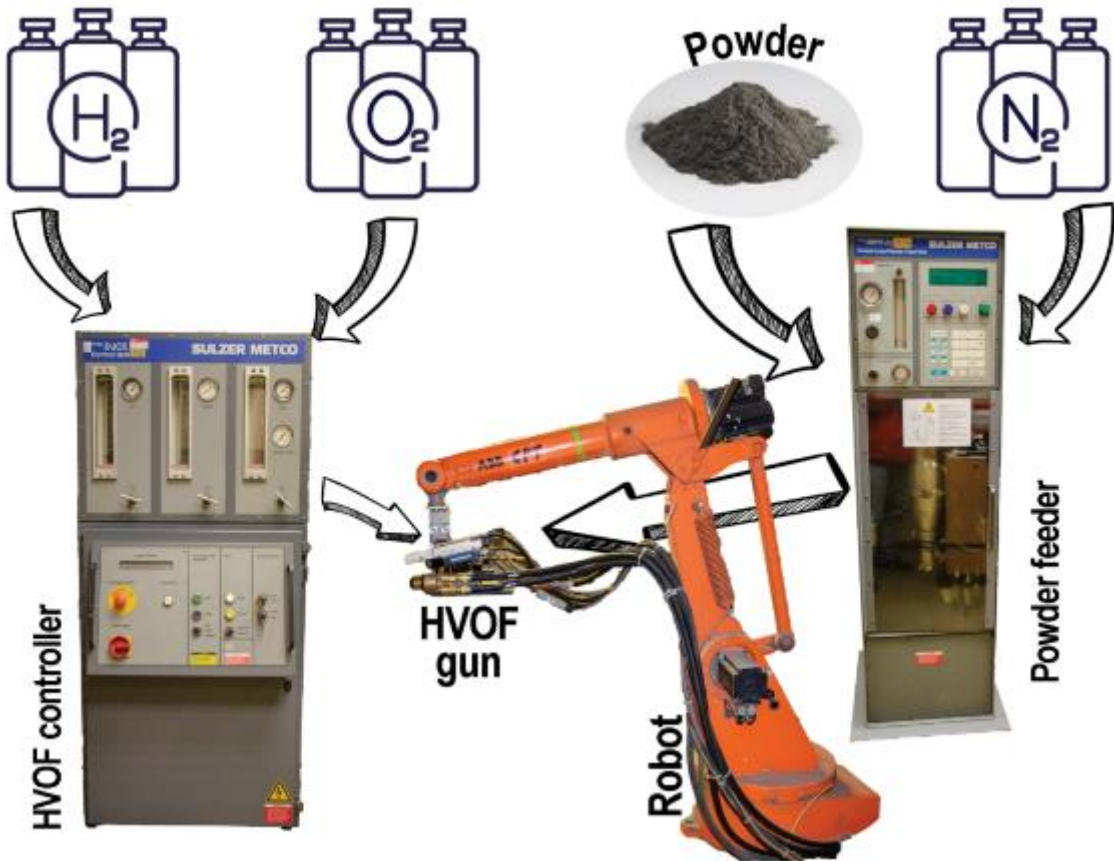


Figure 7: HVOF equipment.

Table 3: HVOF parameters.

Material	Hydrogen		Oxygen		Compressed air		Standoff distance [mm]	Powder feeding [g·s ⁻¹]
	Pressure [bar]	Flow [FMR]	Pressure [bar]	Flow [FMR]	Pressure [bar]	Flow [FMR]		
WC-12Co	9.7	44	11.7	62	6.9	44	225	0.50
WC-10Co4Cr	9.7	44	11.7	62	6.9	44	225	0.50

3.2.3. Post-Treatments

One of the specific objectives of this thesis is to evaluate the effect of post-treatments on the properties of the CSAM-ed materials, as presented in Chapter 3 “Scope of the Work”. It is required since sometimes CSAM-ed parts have characteristics and properties that need to be improved. For this reason, some post-treatments were proposed, and their effects on the material were evaluated.

3.2.3.1. Heat Treatment

The HT parameters were selected based on their effect on promoting interparticular bonding and ductility for 316L stainless steel [9–13], selecting HT of annealing, 1 h at 1000 °C in air in a furnace Hobersal CRN 4-18 (Caldes de Montbui,

Spain), Figure 8 (a) However, because of its O reactivity, CSAM-ed Ti alloys were HT-ed in a Carbolite GHA 12/450 (Hope, England) tubular furnace in Ar atmosphere, Figure 8 (b). For CS-ed Ti, the temperatures were 500, 700, 800, 900, and 1000 °C for 4 h.

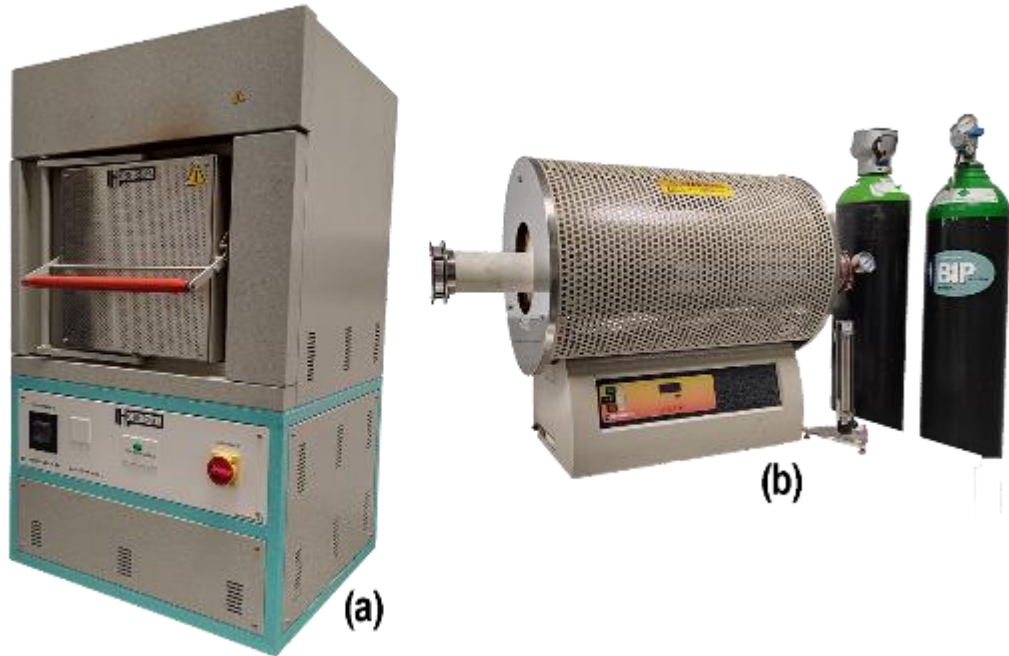


Figure 8: Furnaces for HT in (a) air and (b) argon atmosphere.

3.2.3.2. Spark Plasma Sintering

Spark Plasma Sintering (SPS) was performed in collaboration with Instituto de Cerámica y Vidrio (ICV) (Madrid, Spain) for CSAM-ed Ti6Al4V obtained by traditional and Metal Knitting strategies. SPS consists of a uniaxial pressing device in the form of graphite punches, which also serve as electrodes, a graphite die, a vacuum/air/argon gas atmosphere chamber, a pulsed DC generator, and a controlling system, as presented schematically in Figure 9 (a).

The machine uses low voltages, <math><10\text{ V}</math>, high currents, >5 kA, and heating rates up to

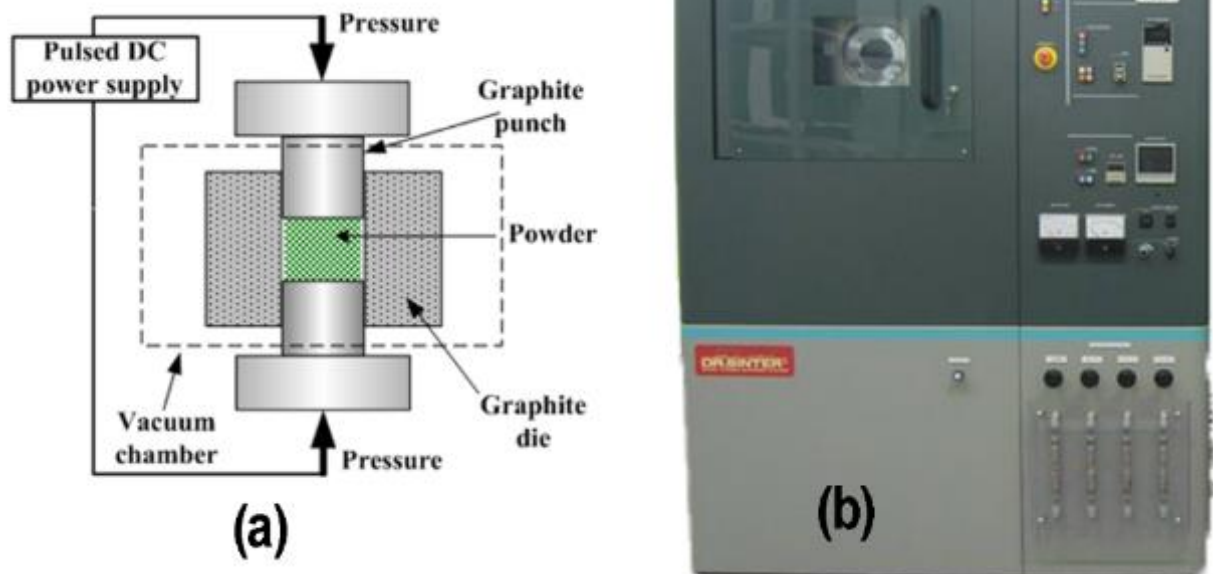


Figure 9: (a) scheme and (b) equipment for SPS.

3.2.3.3. Hot Isostatic Pressing

Hot Isostatic Pressing (HIP) was another post-treatment evaluated, consisting of an HT under controlled high pressures. HIP was performed at Centro Tecnológico CEIT, University of Navarra (Pamplona, Spain), for CSAM-ed Ti alloys. The HIP parameters were a temperature of 950 °C for 2 h under 150 MPa of Ar atmosphere. The heating rate was 10 °C·min⁻¹.

3.3. **Materials Characterization**

The CS-ed coatings and CSAM-ed parts were characterized by diverse techniques to observe their microstructural characteristics, mechanical properties, corrosion behavior, and wear resistance. Each article has a Materials and Methods section; however, the following sections present the methods in more detail.

3.3.1. ***Microstructural Evaluation***

For the observation of the CSAM-ed material characteristics and properties, a first and basic characterization was done for all the deposits, the cross-section microstructural evaluation. They were observed in SEM after hot mounting in conductor Bakelite. The preparation followed the ASTM E1920-03 [2] and ASTM E3-

11 [3] standards, cutting, mounting, grinding and polishing were done in Struers Minitom (Copenhagen, Denmark), Struers CitoPress-1 (Copenhagen, Denmark), and Struers TegraPol-11 (Copenhagen, Denmark), respectively. After that, the characterization results were obtained by SEM in a Thermo Fisher Phenom Pro (Eindhoven, the Netherlands), Optical Microscopy (OM) in a Leica DMI5000M (Wetzlar, Germany), and Electron Backscatter Diffraction (EBSD) in a Jeol JSM-7001F (Tokyo, Japan).

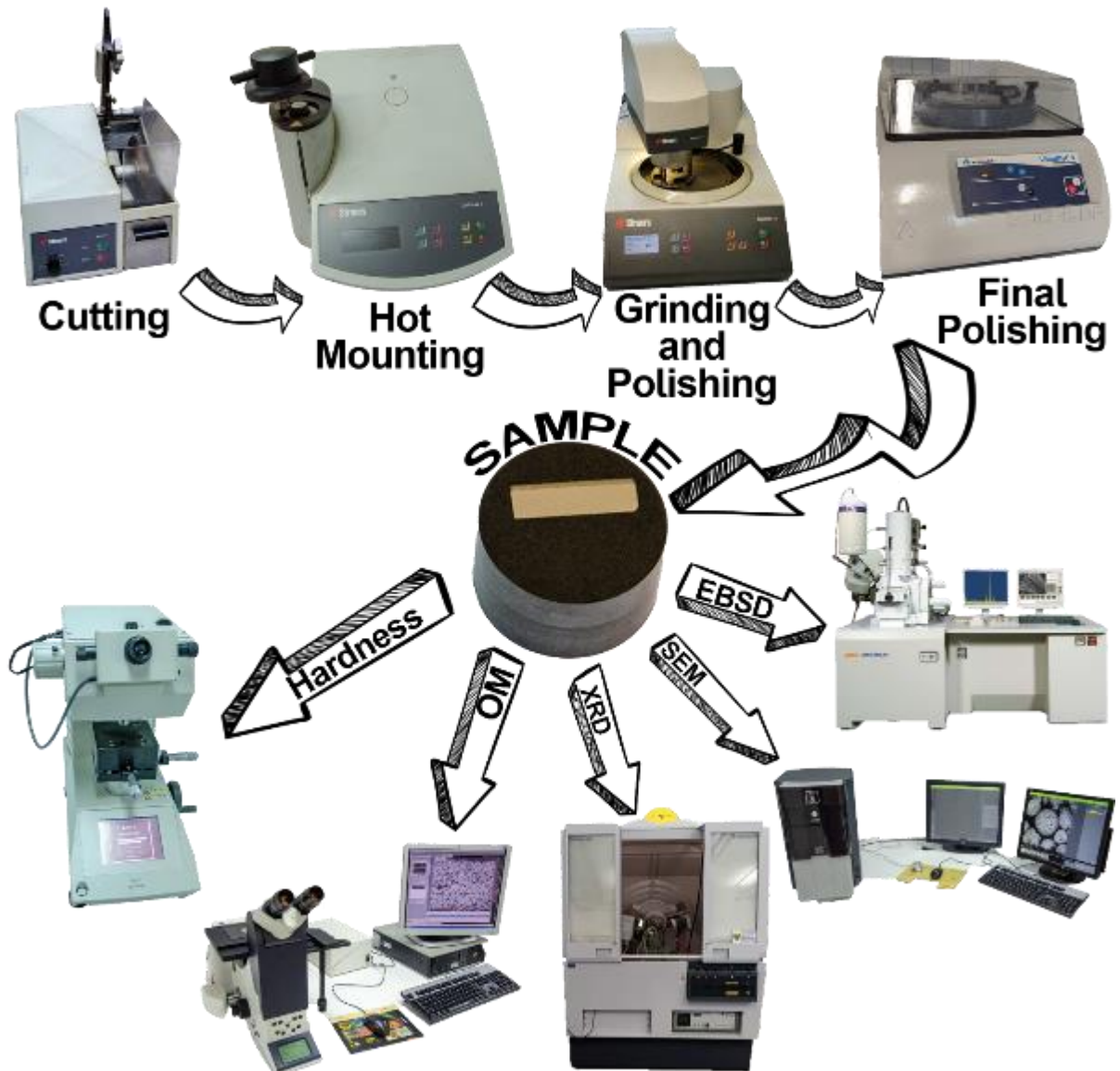


Figure 10: Equipment for samples characterization.

The material porosity was analysed using ImageJ software on OM images at 200x magnification, according to ASTM E2109-01 standard [16]. In order to compare the phases and crystal structure of the feedstock powders and CS-ed material, the

XRD equipment PANalytical X'Pert PRO MPD (Malvern, United Kingdom) was used with radiation of Cu K α ($\lambda = 1.5418 \text{ \AA}$) from 5° to 120° 2 θ with a 0.017° step, measuring 80 s per step.

CSAM-ed 316L and Al bulks were studied in collaboration with the Australian Nuclear Science and Technology Organisation (ANSTO), and CSAM bulk porosity was evaluated by Neutron Tomography (NT) performed on the imaging beamline Dingo at ANSTO [17]. The instrument was configured in high-resolution acquisition mode, corresponding to an L/D ratio of 1000 (where L is the distance between the beam collimator to the image plane, and D is the diameter of the collimator). The ZWO CMOS ASI2600MM Pro (Suzhou, China) (6248*4176) was coupled with a 50 mm lens to yield images with a pixel size of 36 μm over a 224 \times 150 mm² field of view. The detector had a 50 μm thick ⁶LiF/ZnS scintillation screen. Projections were acquired with an equiangular step of 0.19° over 360° and an exposure time of 70 s each. Flat field normalization with dose correction, dark current subtraction, ring artifacts suppression in frequency, and real space domains were applied to each dataset. The NT stacks were computed using the NeuTomPy toolbox [18]. The ThermoFisher Scientific Avizo 2020.3.1 software was employed for data visualization and evaluation.

3.3.2. Mechanical Properties

3.3.2.1. Microhardness

The microhardness of CSAM-ed material was measured by means of a Shimadzu HMV (Tokyo, Japan) equipment, following the ASTM E384-22 standard [19], applying a load of 0.3 kgf (3 N) (HV_{0.3}). Microhardness values were averages from 10 indentations in Vickers scale for each sample. The characterization equipment as the characterization activities flow is presented in Figure 10.

3.3.2.2. Adhesion Testing

The adhesion strength of the CS-ed materials was measured using a tensile test machine, following the ASTM C633-13 [20] standard, mounting the coated sample to the uncoated counterpart using the epoxy resin adhesive HTK Ultrabond 100 or FM1000 (Hamburg, Germany) at 180 °C for 1 h, with traction-adhesive strength of 70 MPa. Three tests for each material were performed in a Servosis MCH-102 ME (Madrid, Spain) equipment, Figure 11, at a 0.01 mm·s⁻¹ rate until both counterparts

detached. Then, the results were classified according to the maximum tensile strength and the failure observed (cohesive – between the coating layers –, adhesive – in the coating/substrate interface –, or glue failure – in the coating/counterpart interface).



Figure 11: Tensile testing machine for adhesion testing.

3.3.2.3. Nanomechanical Properties

CS-ed Ti and Cu were studied in collaboration with the Università del Salento and the Agenzia Nazionale per le Nuove Tecnologie, l'Energia e lo Sviluppo Economico Sostenibile (ENEA), the nanomechanical properties were studied through an Anton Paar nanoindenter model TTX-NHT2 (Ostfildern, Germany), equipped with a Berkovich diamond indenter. The tests were performed under load control, a loading and unloading rate of $20 \text{ mN}\cdot\text{min}^{-1}$, and a dwell time of 5 s. Eleven indentations per sample were performed, and the average values were recorded. Hardness in GPa and elastic modulus (E) in GPa were calculated by the Oliver-Pharr method [21] on the indentation load versus depth curves.

3.3.2.4. Tensile Testing

From CSAM-ed 316L and Ti parts, three samples in each direction were fabricated by wire EDM process for tensile testing, following the drawing in Figure 12,

which guarantees a plane-strain tension condition, following the ASTM E8-22 [22] standard. The surfaces were polished to a maximum roughness of $R_a 0.8 \mu\text{m}$. A ZwickRoell Zmart.Pro equipment with an Xforce P 10 kN load cell (Ulm, Germany) was used for the tensile testing, with a load application velocity of $1.0 \text{ mm}\cdot\text{min}^{-1}$. The fractography was performed using SEM images of the fracture surfaces.

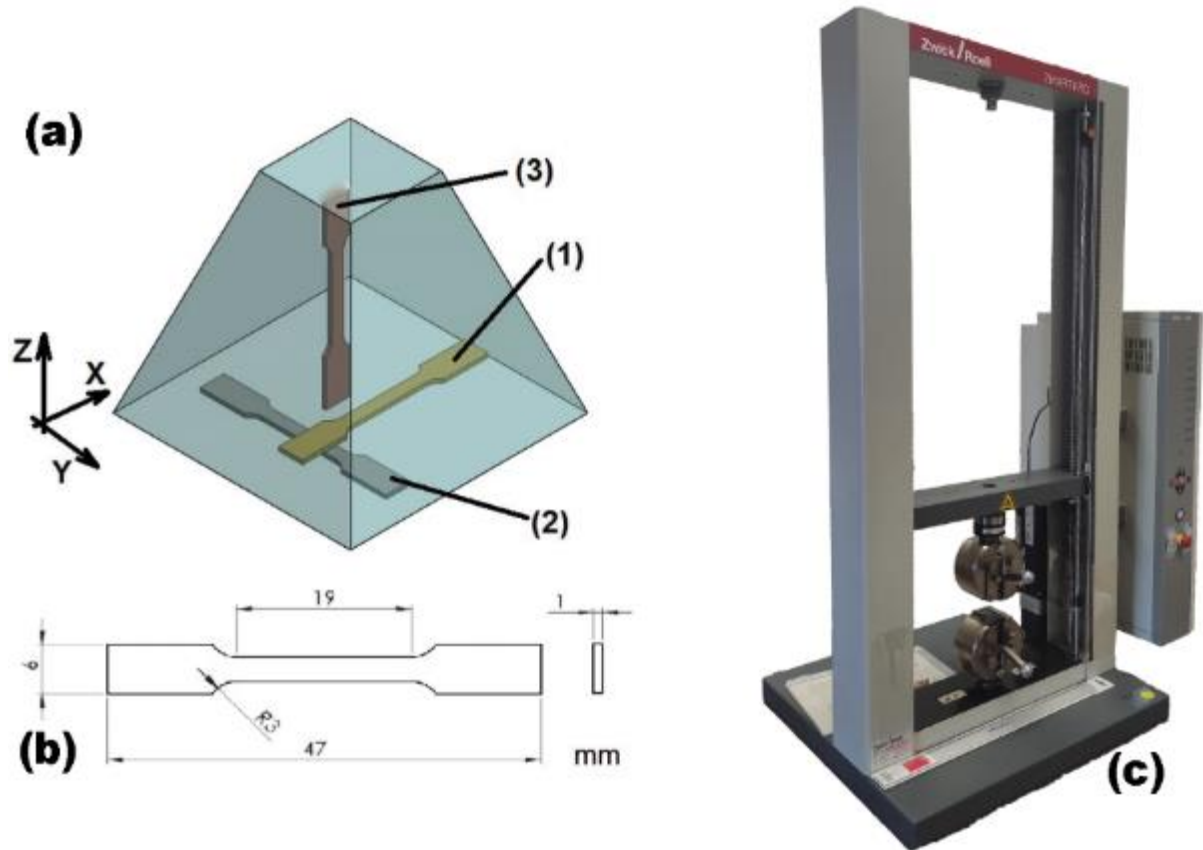


Figure 12: (a) Scheme for tensile samples machining from a CSAM-ed bulk, (1) X-direction on the XY-plane, (2) Y-direction on the XY-plane, and (3) Z-direction on the XZ-plane. (b) Tensile testing sample. (c) Equipment for tensile testing.

3.3.2.5. Residual Stress Measurement

The residual stress studies were divided into two approaches; firstly, it focused on CS coatings to understand the evolution of residual stress with the coating thickness and preview its effect on large bulks. These results would be compared in the sequence with CSAM-ed large parts residual stress distribution, particularly their surface condition. XRD was applied for CS-ed Cu, Ti, and 316L coatings, and for CSAM-ed 316L, Neutron Diffraction was selected due to its deep penetration in the material.

3.3.2.5.1. X-Ray Diffraction

X-ray diffraction (XRD) was a residual stress technique studied for CS-ed coatings, not for CSAM-ed bulks. Steel plates, 200×20×3 mm³, were used as substrates for CS Cu, Ti, and 316L with single- and multi-layer thickness coatings. Following Bragg's law, the residual stress values were determined by XRD according to the $\sin^2\psi$ - Ω -tilt method, Figure 13 (a), with $0 < \psi < 0.8$ in intervals of 0.1 degree. Stress investigations were performed in (hkl) lattice reflections conditions optimized using V-filtered $\text{CrK}\alpha$ -radiation for Cu (420), Ti (213), and γ -Fe (331) reflections, which have strain-free d-spacing (d_0) of 0.80836, 0.82160, and 1.0845 Å, respectively.

The XRD measures the deformation of the crystallographic planes, d-spacing, and a model compares it with the materials' strain-free condition, correlating this deformation with an internal stress in the material, a residual stress. Equation (2) presents this model, where σ_ϕ is the normal stress in the ϕ direction in MPa, ϕ and ψ angles are defined as the in-plane direction, and the angle between specimen normal to the surface plane and diffraction angles, Figure 13 (a), in degrees, E is Young's Modulus in GPa, ν is Poisson's ratio, $d_{\phi\psi}$ and d_0 are Inter-planar spacing of planes at an angle ψ to the surface and strain-free d-spacing in Å, respectively. Figure 13 (b) indicates the normal and shear stresses in an infinitesimal volume of material, considering the same the reference axis of the Figure 13 (a), σ is normal stress and τ is shear stress.

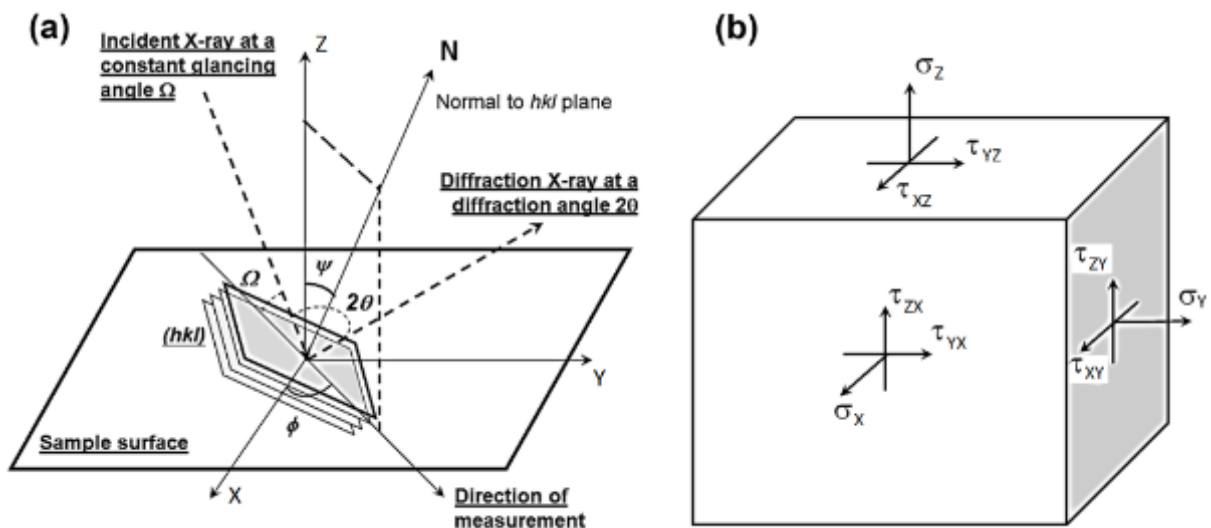


Figure 13: (a) Schematic charts of a definition of the three reference axes and the direction of XRD stress measurement; and (b) the normal and shear stresses in the 3-dimensional system [23].

$$\sigma_{\varphi} = \frac{E^{(hkl)}}{1 + \nu^{(hkl)}} \cdot \frac{\partial \varepsilon_{\varphi\psi}^{(hkl)}}{\partial \sin^2 \psi}; \quad \varepsilon_{\varphi\psi}^{(hkl)} = \frac{d_{\varphi\psi}^{(hkl)} - d_0^{(hkl)}}{d_0^{(hkl)}} \quad (2)$$

3.3.2.5.2. Neutron Diffraction

In collaboration with the Australian Nuclear Science and Technology Organisation (ANSTO), CSAM-ed 316L bulk residual stress was evaluated by Neutron Diffractometry (ND) performed on the KOWARI at the ANSTO OPAL research reactor [24]. Stress investigations were performed in conditions optimized for γ -Fe (311) reflection at the wavelength of 1.55 Å when the scattering angle was close to the optimal 90°-geometry with the take-off angle of 69° using Si (400) monochromator. The samples evaluated were CSAM-ed 316L obtained by different deposition strategies in two conditions: as-sprayed and annealed.

A cube-like gauge volume with dimensions 5×5×5 mm³ was provided by means of the focusing collimator. With this gauge volume, 2D scans across a central vertical cross-section of the deposits. The 2D mesh was chosen congruent to the size of the gauge volume with 4 mm steps in the two dimensions. The mesh was adapted for the real shape of the deposit; thus, the number of measurement points varied from 55 to 67 points. All measurement points were taken in such a way that the gauge volume was always fully submerged in the material. As a result, strain accuracy of 70 μ strain was achieved while the measurement time varied greatly depending on the exact neutron beam flightpath in the sample with a particular orientation.

The three principal sample directions were measured to reconstruct three orthogonal stress components, provided that the proper d_0 is known. Upon completion of the d-spacing measurements, it turned out that the constant- d_0 -value assumption was invalid and not applicable. Instead, the assumption of the near-to-zero stress component in the smallest sample dimension was made, which coincides with the build-up direction. The practical assumption was confirmed in the case of CS in several cases of 3D deposits [25–27], ensuring the approach's applicability. Although an alternative solution to the d_0 problem exists through the experimental approach with measurements of small stress-free coupons extracted from the samples, this approach would be destructive and require more neutron beamtime, which was unavailable.

The achieved experimental uncertainties were ~ 10 MPa, which resulted from the strain accuracy of $50 \mu\epsilon$ (microstrains, 5×10^{-5}). For stress calculations from the measured strain, the (hkl) dependent isotropic elastic diffraction constants were used and evaluated in accordance with corresponding single crystal elastic constants using ISODEC software [28].

3.3.3. Wear Performance

Wear performance is substantially dependent on the material surface condition and properties. The wear testings were performed for the CS-ed materials as coatings and not as large bulks, as studied in Article 2, comparing abrasion and friction wear resistance of coatings obtained by different 316L feedstock powders; in Article 4, evaluating the evolution of cohesion of particles with the CS-ed coating thickness, which helps to understand and preview the properties of a CSAM-ed large bulk made with these powders; and in Article 6, interpreting the effectiveness of hybrid CSAM manufacturing on the part surface properties, employing HVOF WC coatings on CSAM-ed Maraging.

3.3.3.1. Abrasion Wear Testing

For abrasion testing, the rubber wheel testing was performed following ASTM G65-16 [29] standard, using a CM4 OL-2000 (Cervello, Spain) equipment, Figure 14, at a velocity of 139 rpm, a load of 125 N, a 226 mm diameter rubber wheel, and Ottawa silica sand as the abrasive agent.

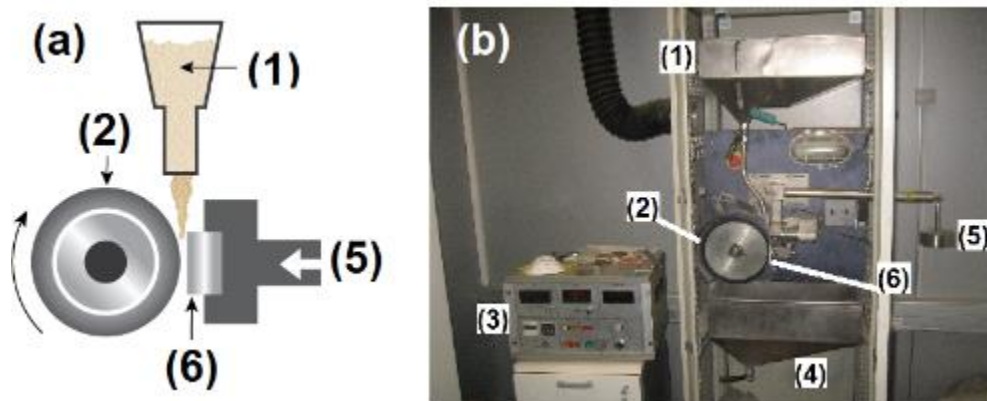


Figure 14: (a) scheme and (b) equipment for rubber wheel testing. (1) sand feeder, (2) rubber wheel, (3) controller, (4) sand collector, (5) loading, (6) sample.

The mass of the sample was measured on a Mettler AE100 scale (Columbus, OH, USA) at specific testing elapsed times. The mass loss results were converted into

volume loss, considering the density of each material, which was obtained after their type evaluation, considering the known bulk material density less the measured porosity of the CSAM-ed.

3.3.3.2. Friction Wear Testing

Ball-on-disk tests were carried out in an equipment made by CM4 (Cervello, Spain), Figure 15, following the ASTM G99-17 [30] standard. For this test, the sample testing surfaces were previously prepared by grinding and polishing to the maximum roughness R_a 0.8 μm . The tests were performed at room temperature (27 ± 2 °C) and a maximum 20% moisture in dry conditions, using a WC-Co ball (diameter 11 mm) with a sliding rate of 0.13 $\text{m}\cdot\text{s}^{-1}$ for a total sliding distance of 995 m. During the test, the Coefficient of Friction (CoF) between the surfaces was recorded and plotted with the acquisition rate of 1 value per lap, a total of 22737 CoF values. The wear volume loss of the ball-on-disk samples was calculated by Equation (3), as recommended by the ASTM G99-17 [30] standard, where R is the wear track radius, d is the wear track width, and r is the ball radius. The friction wear rate is calculated by dividing the disk volume loss by the load times the sliding distance.

$$\text{Disk Volume Loss} = 2 \cdot \pi \cdot R \cdot \left[r^2 \cdot \sin^{-1} \left(\frac{d}{2r} \right) - \left(\frac{d}{4} \right) \cdot \sqrt{(4 \cdot r^2 - d^2)} \right] \quad (3)$$

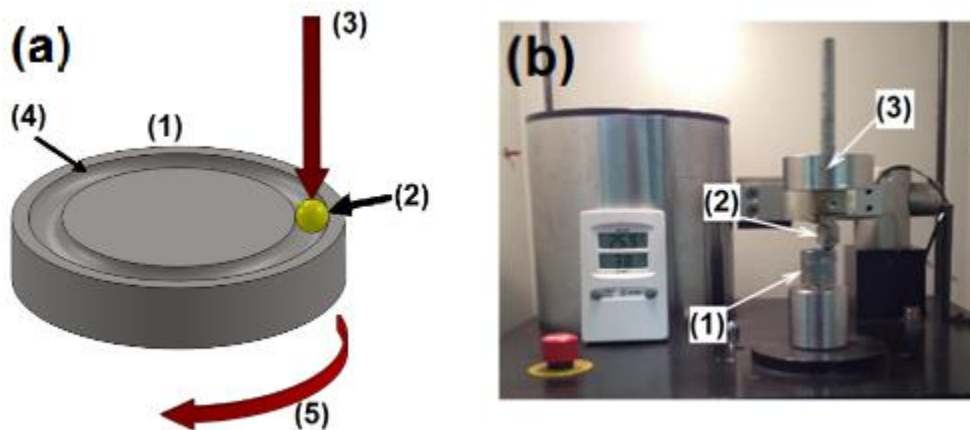


Figure 15: (a) scheme and (b) equipment for ball-on-disk testing, (1) sample, (2) ball, (3) load, (4) wear path on the sample, and (5) rotation direction of the sample.

3.3.3.3. Water Impingement Wear Testing

In addition, the jet erosion tests, ASTM G73-10 [31], were carried out. In jet erosion, a sample is abraded by repeated impacts of water jets until the degradation/destruction of the material. The jet erosion apparatus made by CM4 (Cervello, Spain), Figure 16 (a), consists of two water jets and a central rotating arm, Figure 16 (b), which can reach high rotation speed. At the end of the arm, a sample holder keeps the sample parallel to the water jets. The water jet diameter is 4 mm, and the process parameters are the water pressure (from 0.01 to 0.2 MPa), rotation speed (from 14 to 100 m·s⁻¹), and test elapsing time.

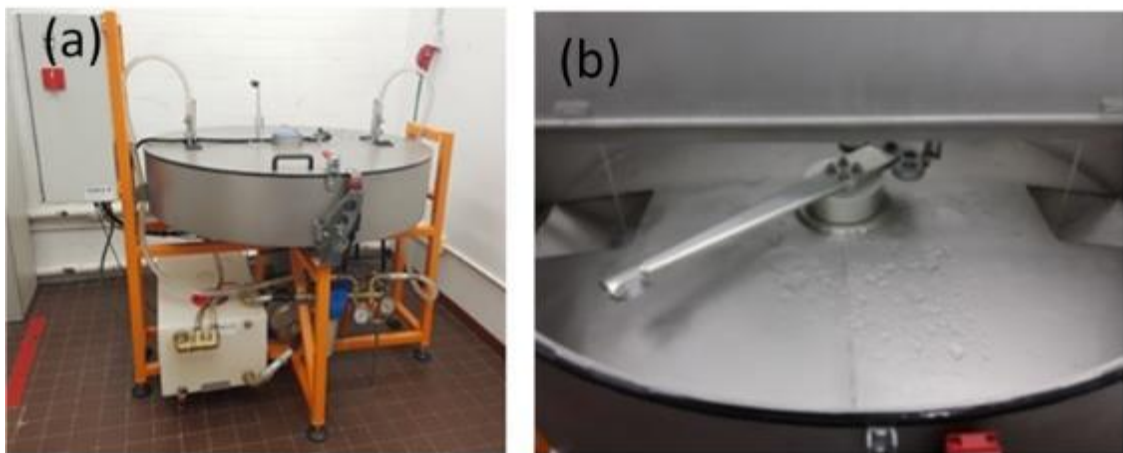


Figure 16: Jet erosion testing apparatus. (a) equipment and (b) sample holder arm.

The tests were interrupted each 30 min to measure the weight loss on a Mettler AE100 scale (Columbus, OH, USA) and the aspects of the damaged area. The test was repeated three times for each sample, and the erosion rate was measured, following the ASTM G73-10 [31] standard, plotting the mass loss slopes.

3.3.3.4. Scratch Testing

Scratch tests were performed to measure the CS-ed material strength, adhesion properties, and intrinsic cohesion behavior. The scratch test was done in an Anton Paar Revetest RST³ instrument (Ostfildern, Germany), Figure 17, with a Rockwell-C diamond indenter, following the ASTM G171-03 [32] standard. The normal load was linearly applied in the range 1–200 N over a scratch length of 10 mm at a speed of 10 mm·min⁻¹ in air at room temperature. The results were plotted as scratch vertical load versus scratch depth, as the interpretation of the scratch path surface to identify the wear mechanisms.



Figure 17: Scratch test equipment.

3.3.3.5. Fretting Wear Testing

The fretting wear resistance of the CS-ed samples was evaluated by Nanovea Tribometer T50 (Irvine, CA, USA), Figure 18, using a Linear Reciprocating Wear Module. The fretting tests were performed by WC indenter at loads of 50, 100, and 150 N, frequency of 10 Hz, and imposed amplitude of 100 μm for 10000 cycles. The wear marks were observed in a confocal profiler Zeiss LSM 5 Pascal (Jena, Germany), and by the marks' dimensions, it was possible to measure the volume loss.

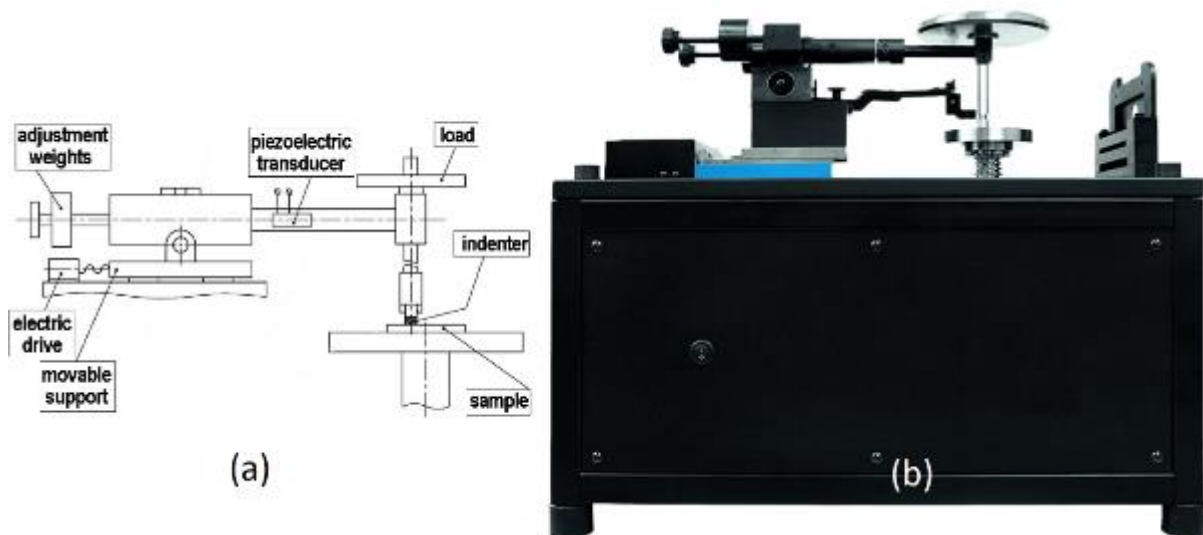


Figure 18: Fretting wear testing (a) scheme and (b) equipment.

3.3.4. Corrosion Behavior

Potentiodynamic polarization measurements were carried out, following the ASTM G59-97 [33] and ASTM G102-23 [34] standards, to determine the corrosion resistance of the coatings in 3.5 wt.% NaCl water solution. Two different areas of each sample were used for corrosion tests as working electrodes, with an exposed area of 1.0 cm², previously polished up to the maximum roughness R_a 0.3 μm. A saturated calomel (3.0 M KCl) was the reference electrode, and platinum was the counter electrode in the tests. Figure 19 shows the corrosion cell scheme and the apparatus during corrosion testing.

A scan rate of 0.05 mV·s⁻¹ and a potential range of ±25 mV with respect to E_{ocp} were used to acquire the polarization resistance (R_p), and a potential range from -250 to 1050 mV with respect to E_{ocp} was used to acquire the polarization curves with a Biologic Science Instruments VSP (Seyssinet-Pariset, France). The corrosion potential (E_{corr}) and corrosion current (I_{corr}) were calculated with the software EC-Lab V10.44. E_{corr} was obtained from a Tafel fit extrapolation. At the same time, I_{corr} was calculated according to the Stern–Geary equation, (4), where β_a and β_c are the anodic and cathodic currents, respectively, and R_p is the polarization resistance.

$$I_{\text{corr}} = \frac{(\beta_a \cdot \beta_c)}{2.303 \cdot (\beta_a + \beta_c) \cdot R_p} \quad (4)$$

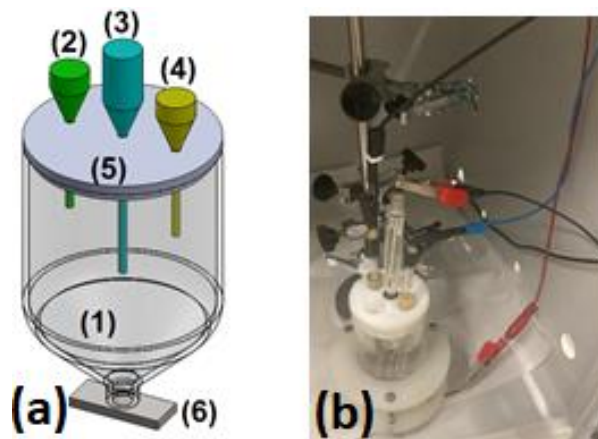


Figure 19: (a) Scheme for corrosion testing. (1) 3.5 wt.% NaCl water solution, (2) ground, (3) reference electrode, (4) counter electrode, (5) electrodes holder, (6) sample or working electrode. (b) real setup during the testing.

Chapter 4

RESULTS AND DISCUSSIONS

4. RESULTS AND DISCUSSIONS

This section presents the results achieved to reach the objectives listed for this work in the Chapter 2 “Scope of the Work”, followed by the pertinent discussions. It presents the CSAM feedstock powders characterization and selection, CSAM sample making and their microstructural characterization, final shape evaluation and inconveniences to achieve higher geometric accuracy, and mechanical properties measurements. Besides that, the use of post-treatments and hybrid processing are also presented.

Thermal spraying processes have an ideal range of particle size distribution and properties to produce coating or parts with the desired properties or characteristics. To guarantee these characteristics and confirm the information provided by the materials manufacturers, the feedstock powders were characterized regarding the powders' chemical composition and shape, particle size distribution, phase distribution, flowability, and apparent density, among other tests. A deep study of different commercial 316L feedstock powders resulted in an academic contribution by publishing Article 2. Characterization and comparison of irregular and spherical Ti powders are also conducted.

Besides, advances in CSAM technology to make more complex geometries are presented by moving the robot/substrate along different paths, aiming to control the CSAM building up geometry, and reducing or eliminating the machining post-services, which is detailed in Article 3.

From the understanding of CS-ed coatings characteristics, as presented in Article 2 and Article 4, as the XRD residual stress measurements, this section advances to the CSAM-ed samples' manufacturing and their microstructural characterization, mechanical properties, wear and corrosion testing, following evaluation of post-treatments effects on the CSAM-ed parts' properties and performance. Some tests and evaluations consisted of superficial dependent properties, such as corrosion behavior or wear performance, and structural conditions, such as residual stress distribution by XRD testing, mechanical properties, and isotropy for different materials, Ti alloys, stainless steel, Cu, Al, Maraging, and others. The materials' microstructures and morphology have affected the mechanical properties of CSAM-ed parts. The CS-ed materials are composed of splats or

deformed particles, porosity or vacancies, and interparticular interfaces, which is the weakest region of the material. The severe cold working during the deposition results in harder CS-ed material than reference bulks. However, unlike a bulk reference, CS bonding mechanisms result in a tensile strength debilitated. CS-ed parts presented wear mechanisms related to the weak bonding mechanism between the particles, as presented by Pukasiewicz et al. [35], and discussed in wear testing of CS-ed pure Cu and Ti in Article 4.

The study of CS-ed coatings residual stress by XRD was essential to support the advances from CS as a coating technique to AM processing technology. The use of substrates that can deform during the deposition, Al plates for CSAM deposition in this thesis, is a consequence of previous coating evaluations and discussions. Another technique was applied to measure residual stress, ND, which is presented in Article 5, for CSAM-ed 316L.

Once CSAM-ed parts were produced, different post-treatments were applied for different materials and their influence on the materials' characteristics and properties. Generally, the cohesion of particles improves, but the hardness tends to be reduced by the recrystallization and grain growth phenomena. SPS, HIP had been studied for Ti and Ti6Al4V, while HT is presented for 316L in the Article 5.

Finally, the Article 6 evaluated the effectiveness of using HVOF WC deposition on CSAM-ed Maraging to improve its wear- and corrosion-resistance.

4.1. CSAM Feedstock Powders

4.1.1. *Characterization and Selection*

The CSAM-ed feedstock powers were characterized regarding their shape or morphology, chemical composition, phase distribution, particle size distribution, flowability, and apparent density, as presented in Chapter 3, "Feedstock Materials and their Characterization". Selecting 316L stainless steel powder for the sequent CSAM depositions received particular attention, resulting in Article 2, evaluating different powders' shapes and manufacturing processes. This study contributed to the following CSAM 316L depositions because 316L water atomized powder is a less costly option than the gas atomized ones, which is an attractive point for manufacturing large parts.

It presented that even with an irregular shape, CSAM-ed 316L water atomized resulted in a similar performance to the gas atomized and spherical ones.

The other sprayed materials characterized have characteristics adequate for CSAM deposition, considering the particle size distribution, as shown in Figure 20 and Table 4, and chemical composition, Table 5.

Table 4: CSAM feedstock powders' characteristics.

Material	Particle Size Distribution [μm]			Shape	Apparent Density [g·cm ⁻³]	Flow Rate [g·s ⁻¹]
	d ₁₀	d ₅₀	d ₉₀			
316L Daye	16	33	60	Irregular	3.03 ± 0.01	9.03 ± 0.36
316L Oerlikon	19	30	47	Quasi-spherical ¹	2.86 ± 0.01	8.21 ± 0.49
316L Plasma Giken	17	36	60	Irregular	4.47 ± 0.01	17.61 ± 0.40
316L Sandvik	29	38	47	Quasi-spherical ¹	3.73 ± 0.01	13.44 ± 0.65
Ti AP&C	16	28	44	Spherical	1.89 ± 0.01	4.40 ± 0.20
Ti CNPC	9	36	81	Irregular	1.21 ± 0.03	²
Ti6Al4V AP&C	5	30	45	Spherical	2.43 ± 0.01	9.45 ± 0.55
Ti6Al4V Dycomet	20	31	43	Spherical	2.43 ± 0.00	5.90 ± 0.28
Cu Safina	18	28	42	Spherical	4.78 ± 0.02	20.57 ± 0.32
Al Ecka	14	30	52	Irregular	1.01 ± 0.01	²
Maraging Oerlikon	20	33	47	Spherical	4.00 ± 0.02	17.38 ± 0.24
Maraging Rovalma	11	39	73	Spherical	4.26 ± 0.04	²
Steel Dycomet	17	32	58	Irregular	4.05 ± 0.01	14.80 ± 0.28
Inconel 625	21	31	41	Spherical	4.38 ± 0.01	²

¹ presence of satellite particles.

² did not flow

Table 5: CSAM feedstock powders' chemical composition. wt. %.

Material	Cr	Ni	Mo	Mn	Fe	Al	Cu	Ti	V	Co	Nb
316 Daye	16.0	12.3	2.6	0.5	Bal.						
316L Oerlikon	16.4	10.1	2.1	1.4	Bal.						
316L Plasma Giken	16.3	11.2	2.2	0.1	Bal.						
316L Sandvik	17.1	9.6	1.8	0.6	Bal.						
Ti AP&C								Bal. ²			
Ti CNPC								Bal. ²			
Ti6Al4V AP&C						5.7		Bal.	3.8		
Ti6Al4V Dycomet						5.8		Bal.	4.0		
Cu Safina							Bal. ²				
Al Ecka						Bal. ²					
Maraging Oerlikon		17.0	6.8		Bal.	1.4		1.0		10.3	
Maraging Rovalma	6.5	9.2	1.3	0.1	Bal.	1.4			0.8	1.3	
Steel Dycomet	17.8	4.9	14.7	2.7	Bal.						
Inconel 625	19.7	Bal.	10.5		2.2						4.5

¹ used for HVOF deposition.

² other elements under 0.1 wt. %.

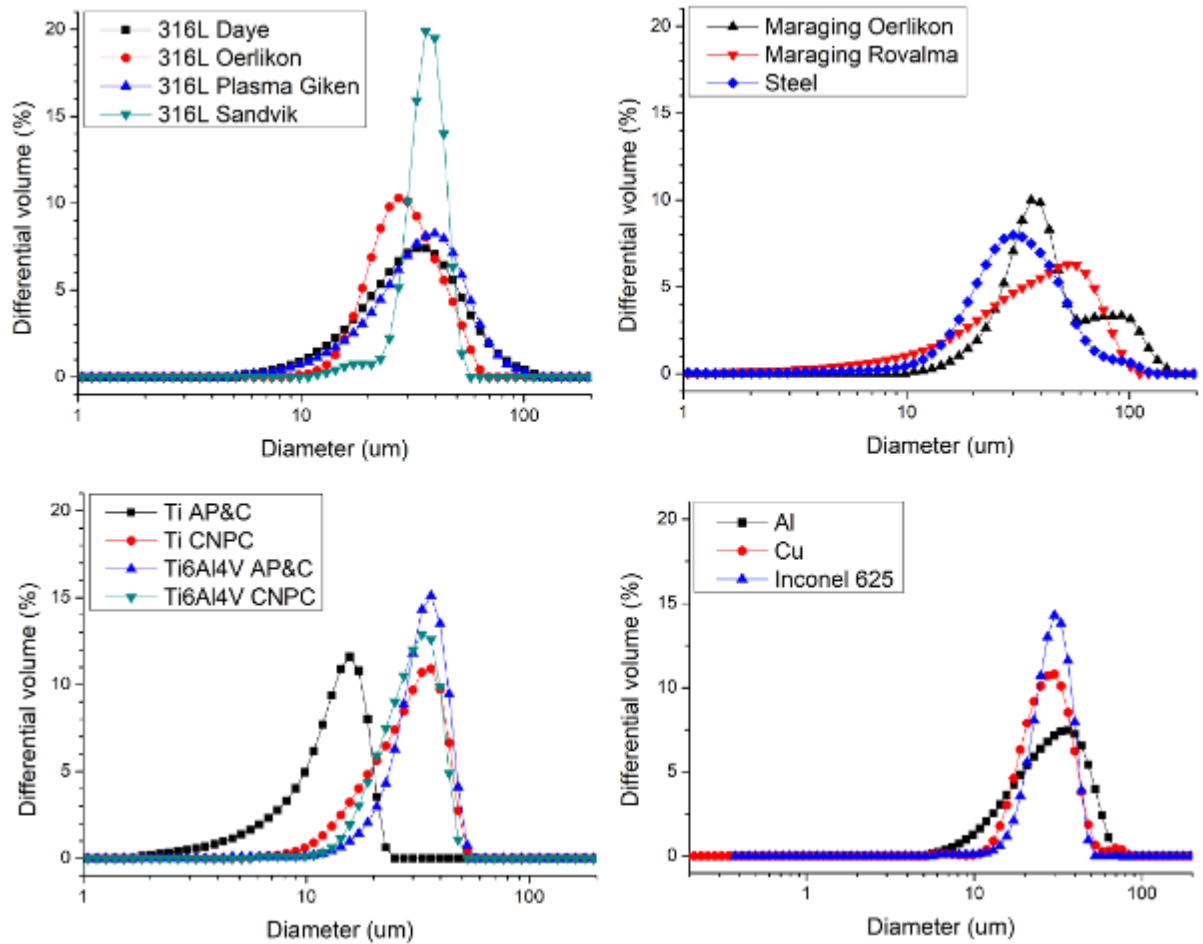


Figure 20: CSAM feedstock powders' particle size distribution.

Table 4 presents the powders' flowability, or flow rate, as their apparent density. Ben Ohoud et al. [36] presented that a powder's apparent density can be expressed by Equation (5), where ρ_a is the apparent density in $\text{g}\cdot\text{cm}^{-3}$, $W(R)$ is a mass in g of macroscopic sample of particles with an average radius R in cm, Vol_a is the total apparent volume in cm^3 , B is related to the mass of particles, C is related to the packing density, D_m is a characteristic of each particle, and D_c is a function of the type of arrangement of the particles concerning each other. From this, it is noticed that the powders' apparent density depends on the morphology or shape of particles, their size distribution or arrangement, and the materials' density property.

$$\rho_a = \frac{W(R)}{\text{Vol}_a} = \left(\frac{B}{C}\right) \cdot R^{(D_m - D_c)} \quad (5)$$

The flowability of metal powders is not an inherent property, depending not only on the physical properties, like shape, particle size distribution, and humidity, but also on the stress state, the testing performed, the equipment used, and the handling

method [37]. Jenike [38] published, among other valuable information about powder flow and storage, a model to classify a powder flowability based on the particle size distribution, Equation (6), and Zegzulka et al. [37] showed this S limit value to be considered, $S = 1.5$. Powders with $S < 1.5$ show good flow properties, while powders with $S > 1.5$ result rather worse flow properties. Applying Equation (6) to the particle size distribution shown in Table 4, only Maraging Rovalma resulted in an inadequate S value, $S_{\text{Maraging Rovalma}} = 1.59$. Explaining that even with a spherical shape, as observed in Figure 21 (l), this material should be sieved to eliminate the coarser particles, reducing the S value and improving its flowability consequently.

$$S = \frac{d_{90} - d_{10}}{d_{50}} \quad (6)$$

Ti CNPC and Al Ecka powders had adequate S values for good flowability, $S_{\text{Ti CNPC}} = 1.00$ and $S_{\text{Al Ecka}} = 1.27$, respectively; however, their flowability was harmed by their irregular shape, as presented in Figure 21 (f) and (j), for Ti CNPC and Al Ecka, respectively. Spheroidicity is a significant advantage for good flowability of metal powders [39], and a spherical shape of particles is welcome in most AM technologies. The Ti powders presented this influence of particle shape, and the spherical Ti AP&C had a flow rate of $4.40 \pm 0.20 \text{ g}\cdot\text{s}^{-1}$, while the irregular Ti CNPC did not flow during the ASTM B213-20 [6] testing in static mode; however, it did not have any difficulty to flow during the CS spraying. Among the powder shapes described in the literature, the CS starting metal powders have one of the following geometry: agglomerated, angular or irregular, out-of-round, or spherical [40]. These shapes result from the material chemical composition and fabrication method, among others. Water atomizing is commonly used to produce irregular shape powders, while inert gas atomizing produces a spherical shape.

Fedina et al. [41] compared water and gas atomized AISI 4130 steel for laser AM processing, resulting in very similar results, considering the laser welding bead profile, chemical composition, and deposition efficiency, but with a higher price for the gas atomized powder than for the water atomized one. This discrepancy regarding the feedstock powder costs was presented by Boisvert et al. [42], showing that water atomized powders are 3 to 9 times cheaper than gas atomized ones. Vargas-Uscategui et al. employed irregular shape hydride-dehydride (HDH) [43] and spherical [27] pure

Ti for CSAM, obtaining similar microstructures, especially a low porosity for expensive and less costly feedstock powders.

Figure 21 summarizes the SEM images of CS feedstock powders free surface, showing gas atomized spherical particles, like 316L Oerlikon, Ti AP&C, and Maraging Oerlikon; and water atomized irregular particles, like 316L Daye, Ti CNPC, and Al Ecka.

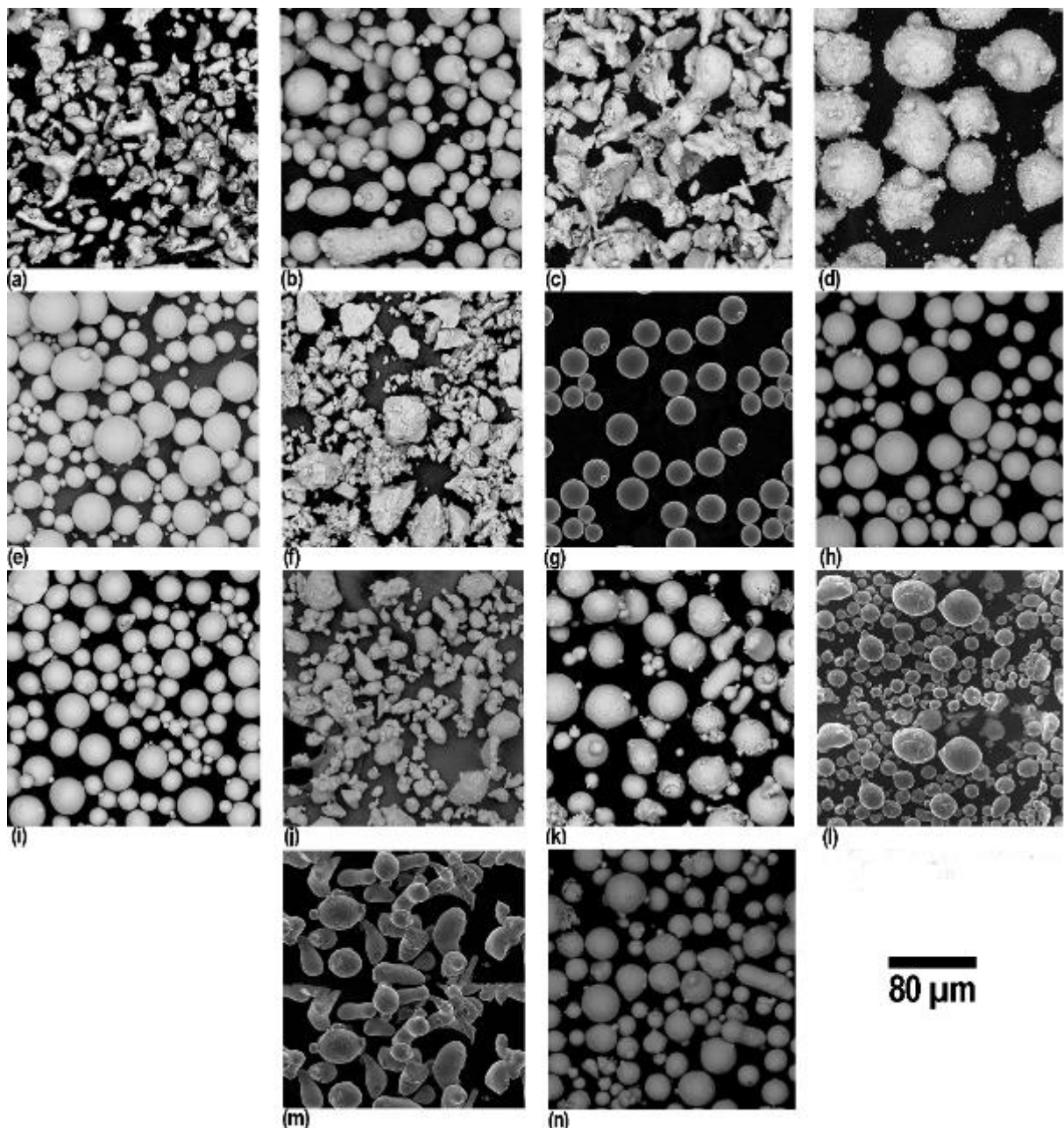


Figure 21: SEM images of CSAM feedstock powders of free surface. (a) 316L Daye, (b) 316L Oerlikon, (c) 316L Plasma Giken, (d) 316L Sandvik, (e) Ti AP&C, (f) Ti CNPC, (g) Ti6Al4V AP&C, (h) Ti6Al4V Dycomet, (i) Cu Safina, (j) Al Ecka, (k) Maraging Oerlikon, (l) Maraging Rovalma, (m) Steel Dycomet, and (n) Inconel 625.

For CS, the particle shape is a crucial factor for their bonding mechanisms since they depend on the velocity of particle. The interaction of CS atomizing gas with the particles has been studied by finite flow simulation and finite elements analysis or modeling. The particle shape significantly alters the drag coefficient, which is well known for the spherical particles but has been developed by scholars, applying Gidaspow or Papyring drag models successfully. Lohse and Palzer [44] presented a model for irregular particles, considering that these were composed of some small spherical volumes, forming a final rounded spherical geometry. It is consonant with the water atomized powders used in CSAM.

The velocities of irregular and spherical Ti and 316L particles during the CS spraying were measured using a laser HiWatch equipment. The results of 300 particles velocities for each powder are presented in Figure 22 histograms. The highest amount of values above $600 \text{ m}\cdot\text{s}^{-1}$ is noticed, and very similar negatively skewed histogram shapes. It signs that both spherical and irregular particles have similar energy dissipated as plastic deformation, resulting from the CS spraying particles' kinetic energy.

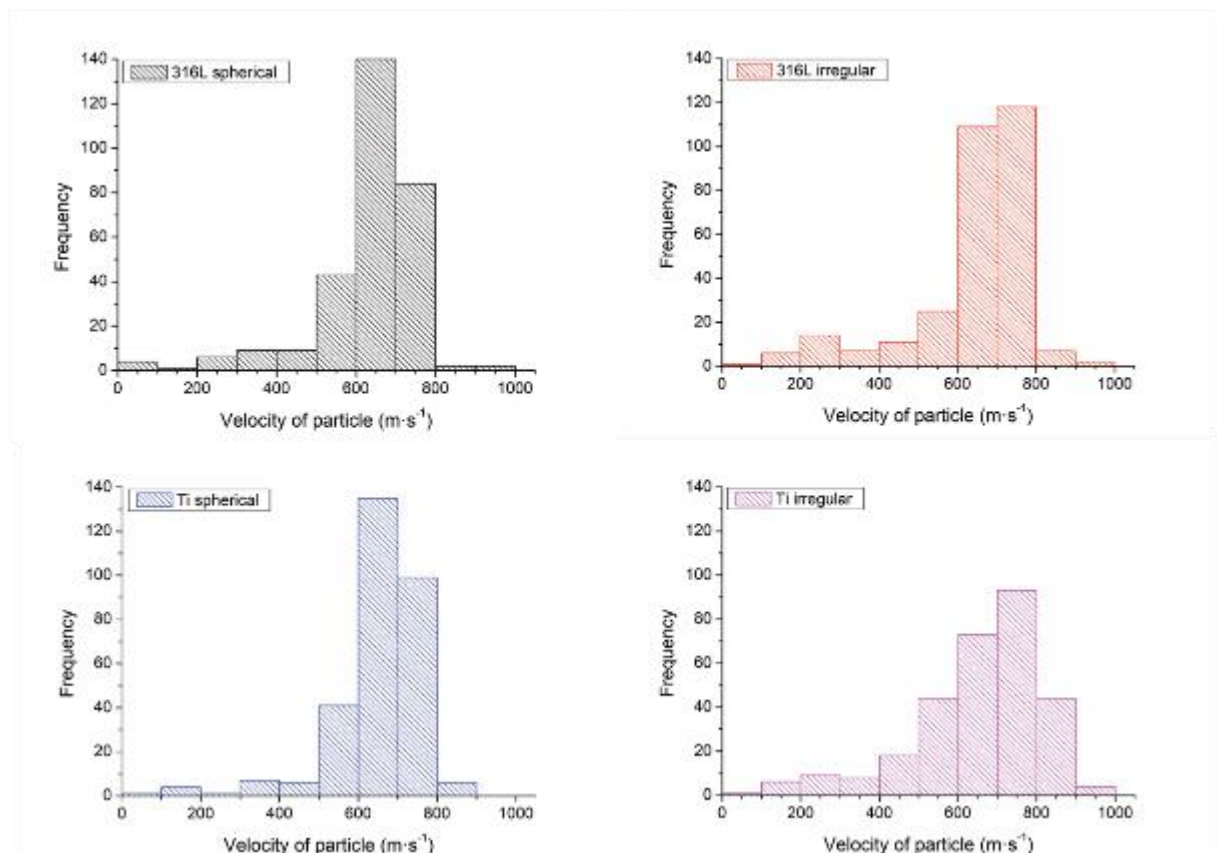


Figure 22: Comparison of velocity of spherical and irregular 316L and Ti particles.

Table 5 shows the powders' chemical compositions measured by ICP, resulting in close to the values informed by the manufacturers, except the experimental alloy Maraging Rovalma is classified as a medium alloy steel and cannot be classified as a Maraging steel because of its chemical composition did not fit to any of the grades presented by the Society of Automotive Engineers (SAE), which are grade 200 (Ni₁₇₋₁₉Co₈₋₉Mo_{3-3.5}Ti_{0.15-0.25}Al_{0.05-0.15}) 250 (Ni₁₇₋₁₉Co_{7-8.5}Mo_{4.6-5.2}Ti_{0.3-0.5}Al_{0.05-0.15}), 300 (Ni₁₈₋₁₉Co_{8.5-9.5}Mo_{4.6-5.2}Ti_{0.15-0.25}Al_{0.05-0.15}), and 350 (Ni₁₈₋₁₉Co_{11.5-12.5}Mo_{4.6-5.2}Ti_{1.3-1.6}Al_{0.05-0.15}). Other alloys had small deviations from the reference materials of from their manufacturers' datasheet, e.g., Maraging Oerlikon that was a Maraging grade 350, but with Mo_{6.8}, or 316L Sandvik that has Ni_{9.6}, but the reference ASTM A240 [45] shows Ni₁₀₋₁₄.

Figure 23 shows the XRD patterns for the CS feedstock powders. The pure metals presented the previewed unique phase, as seen for Al, Cu, and Ti diffractograms, which added to the chemical composition, Table 5, corroborate a good CS-ed material performance. It also reinforces purity level since oxides should be seen in the XRD patterns, such as TiO₂, rutile or anatase, α -Al₂O₃, alumina, and CuO or Cu₂O, for Ti, Al, and Cu powders, respectively. For CS, the powder oxidizing during the production or storage period influences the DE and deteriorates the quality of the interparticular bonding in the CS-ed deposits. The metallic powders are usually covered with an oxide layer [46]; however, an excessive oxide layer thickness makes the particle more rigid to deform at the impact, requiring more energy and velocity to enable the ASI phenomena, resulting in a lower DE [47]. The reduction of thermal and electrical conductivity are other prejudicial effects of the imprisonment of oxide particles in the interparticular region of the CS-ed materials [48].

The 316L stainless steel powders were composed only of the ductile γ -austenite phase, except the 316L Plasma Giken that presented subtle α peaks, which did not affect its plasticity or the coating properties, as interpreted from the coating microstructure, hardness, and DE presented in the Article 2. The Steel Dycomet and Maraging Rovalma also presented γ -austenite as the predominant phase composition, with a single peak of α' -martensite. Nonetheless, Maraging Oerlikon resulted in evident high α' -martensite peaks with γ -austenite retained, resulting from the fast solidification and cooling during the gas atomizing. The formation α' -martensite is not highlighted in Maraging Rovalma because of its chemical composition with a low content of Mo, Table 5. Some alloying elements of Maraging improve the material hardness and

mechanical properties by intermetallic precipitates in the martensitic matrix, especially Ni_3Mo , Fe_2Mo , $\sigma\text{-FeMo}$, and $\mu\text{-Fe}_7\text{Mo}_6$ [49]. However, after long-time heat treatments, these precipitates appear, explaining why they were not seen in the powder that cooled rapidly during the atomization process.

Ti6Al4V stabilized only α phase, an HCP lattice structure, evidenced in the diffractograms of Ti6Al4V Dycomet and Ti6Al4V AP&C in Figure 23. However, by applying a selected cooling rate, it is possible to obtain the metastable α' - or α'' -martensite phase, HCP and orthorhombic lattice structures, respectively. Martensite improves the material mechanical properties, and is normally obtained by quenching heat treatment from beta phase [50].

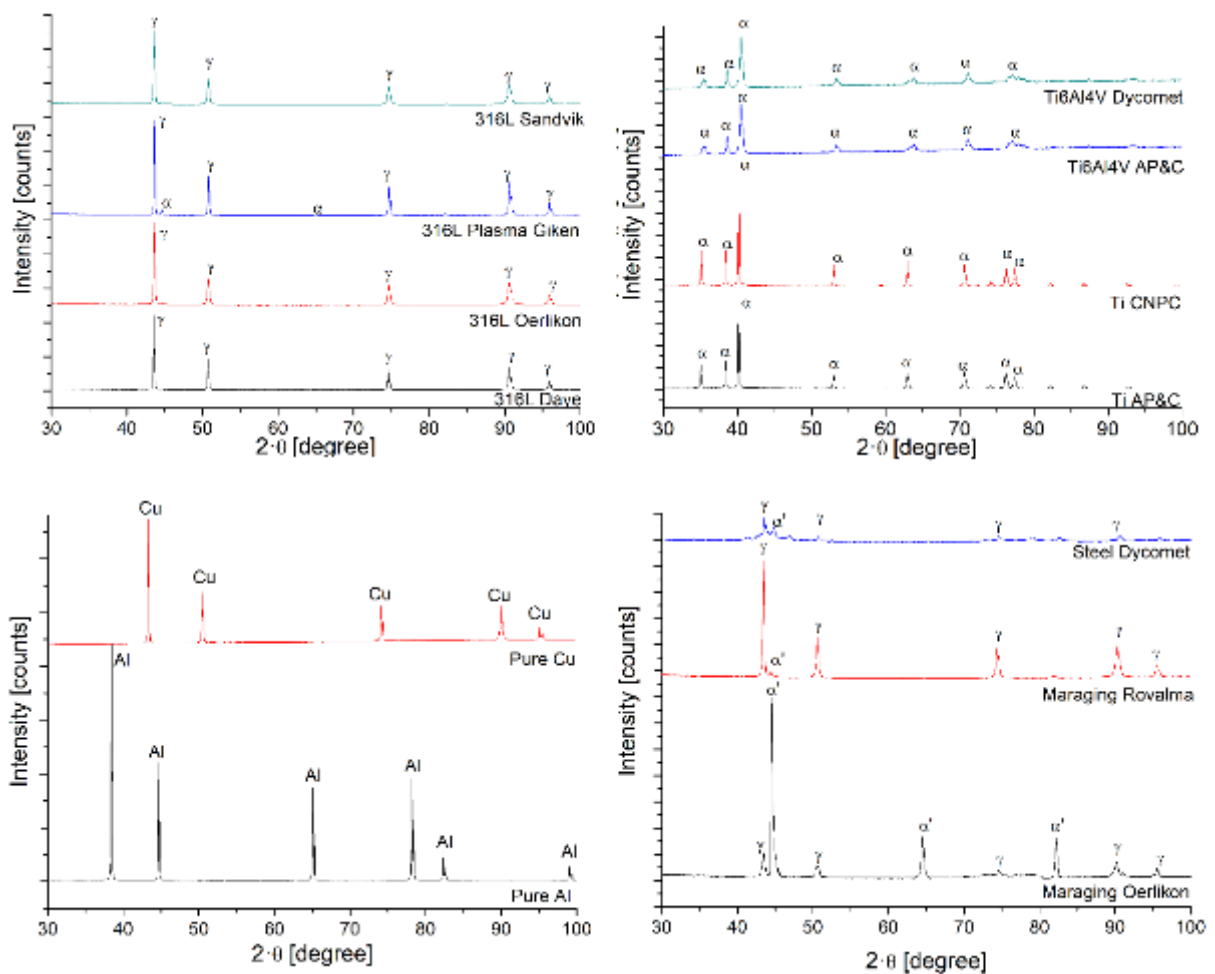


Figure 23: XRD patterns of the CS feedstock powders.

4.1.2. Influence of Powder Characteristics on CSAM-ed Parts Manufacturing and Properties

The in-flight behavior of the CS-ed particles supports the selection of adequate particle size distribution for CSAM. The literature presents the V_{cr} of the particles

dependent on their size, and smaller particles have much higher V_{cr} than the bigger ones [39,51], resulting in the fact that even with high velocity, small particles may not bond or deform at the impact. The V_{cr} of the particles decreases sharply with its size increasing up to 50 μm ; however, the effect of particle size is negligible beyond this particle size [39,52]. An optimum size range is achieved for each material, which is generally between $-60+10 \mu\text{m}$, values in which the CS materials presented in Table 4 are included, except Maraging Rovalma. which has a d_{90} of 73 μm , resulting in lower DE than Maraging Oerlikon.

In order to achieve bonding the CS-ed particles, Schmidt et al. [52] presented a model for the particles critical diameter, d_{cr} , Equation (7), where λ_p is the thermal conductivity in $\text{W}\cdot\text{m}^{-1}\cdot\text{K}^{-1}$, C_p is the specific heat in $\text{J}\cdot\text{kg}^{-1}\cdot\text{K}^{-1}$, ρ_p is the particle density in $\text{kg}\cdot\text{m}^{-3}$, and V_p is the particle velocity in $\text{m}\cdot\text{s}^{-1}$. Considering the reference V_{cr} values listed in Article 1, all the feedstock powders selected for CSAM met the d_{cr} requirement expressed in (7).

$$d_{cr} = 36 \cdot \frac{\lambda_p}{C_p \cdot \rho_p \cdot V_p} \quad (7)$$

Besides the particle size distribution, the spheroidicity is a significant advantage for good flowability of metal powders [39], which was confirmed by the poor flowability of irregular Ti CNPC compared with the high flow rate of the spherical Ti AP&C. However, both Ti powders had similar behavior during the CS deposition, considering the DE and the $V_{particle}$, as interpreted from Figure 22. In general, for CS, the similar in-flight conditions justify the similar CSAM-ed microstructure, as studied, presented, and discussed for 316L in Article 2.

For large CSAM parts, the water atomized powders were selected due to the economic impact of their employment on the bulk fabrication. In general, the spherical particles have a more homogeneous deformation at the impact, and irregular particles may present a severe deformation in their sharp edges, which have a small volume, without a substrate deformation. It decreases the particles' bonding strength; however, if the irregular particles have a smooth irregular shape, their deformation is similar to the spherical ones [39].

The irregular geometry reduces the CS V_{cr} , as presented by Palodhi, Das, and Singh [39], who studied Cu spherical and irregular particles CS-ed on a stainless steel

substrate. However, Ardeshiri Lodejani et al. [53] showed that this V_{cr} reduction is valid only for particles impacting the substrate with their longest symmetry axis perpendicular to the substrate surface, i.e., impacting the most minor particle face. Conversely, impacting the particle's largest area of contact results in a V_{cr} increase. For fortune, the gas flow tends to align the irregular particles favorably.

For CS, the material's chemical composition does not influence the CS-ed material consolidation or particle bonding because they are based on mechanisms that dependent on the particles' kinetic energy, and chemical reactions do not contribute to this [54,55]. However, the chemical composition and the powder-producing process influence the materials' phase composition. With the same composition, the same alloy can stabilize different phases, which can make more feasible or not the CS bonding, because of the particles' hardness and, more important, their ductility or plasticity [56].

However, the feedstock powder chemical composition has affected the CS gun nozzle integrity by clogging it, and this nozzle has to be selected to avoid the clogging phenomenon. For example, the WC nozzle for the PCS100 CS gun resists abrasion wear of the particles, but it is sensible to metallic alloys with Ni content higher than 4 wt.%, e.g. 316L or Inconel. To avoid clogging, the manufacturer Plasma Giken supplies glass nozzles, which are not wear-resistant, i.e., glass nozzle erodes during the depositions but is not susceptible to damage by clogging. For long-time CSAM depositions, short-lived glass nozzles become a problem because the spraying forced interruptions to change this item due to its performance reduction by the wear and profile alteration. This eroded profile reduces the $V_{particle}$, diminishing the CSAM-ed material quality. Besides the inherent cost of the nozzle, thousands of euros each, this deposition time stopped cools down the consolidated material, promoting a thermal contraction, which can result in tensile residual stress, as discussed in Article 5.



ARTICLE 2 “THE INFLUENCE OF THE POWDER CHARACTERISTICS ON 316L COATINGS SPRAYED BY COLD GAS SPRAY”

R.F. Vaz, A. Silvello, J. Sanchez, V. Albaladejo, I.G. Cano



[10.3390/coatings11020168](https://doi.org/10.3390/coatings11020168)

This work presents the powders' characteristics influences on the microstructure of CS-ed 316L coatings, such as porosity and oxide contents, which alter its corrosion behaviour and wear performances. It evaluates four 316L feedstock powders made by different manufacturers sprayed with the same CS equipment and parameters. A relation between the powders' characteristics and CS-ed coating properties was proposed based on the CS-ed coatings' characteristics and properties. Coatings microstructure, adherence, hardness, corrosion behavior, and wear resistance results are presented and discussed. The water atomized 316L powder had a similar performance to the gas atomized powders.

It supported the selection of 316L feedstock powder for the following CSAM depositions, reducing the AM-ed parts costs by using the cheapest option among the materials studied.

The Influence of the Powder Characteristics on 316L Stainless Steel Coatings Sprayed by Cold Gas Spray

Rodolpho E. Vaz ^{*}, Alessio Silvello, Javier Sanchez, Vicente Albaladejo and Irene García Cano

Thermal Spray Center CPT, University of Barcelona, Martí i Franqués 1, 7a Planta, 08028 Barcelona, Spain; asilvello@cptub.eu (A.S.); jsanchez@cptub.eu (J.S.); valbaladejo@cptub.eu (V.A.); igcano@cptub.eu (I.G.C.)

* Correspondence: rvaz@cptub.eu

Abstract: Thermally sprayed 316L stainless steel coatings are commonly used on metallic structures due to their corrosion and wear resistance when compared to carbon steel. Cold Gas Spray (CGS) is a convenient thermal spray process to deposit 316L coatings, producing thick and very dense coatings, with almost no deleterious changes on the feedstock properties to the coating condition. The powder characteristics have influence on the microstructure of the coating, such as porosity and oxide contents, which alter its corrosion and wear behavior. CGS is an efficient technique to reduce the problems associated with material melting commonly found in other conventional thermal spray methods. In this work, different 316L powders, produced by different manufacturers, were deposited by CGS, applying the same equipment and parameters, with the objective to evaluate the relation between the powders' characteristics and coating properties. Their microstructure, adherence, hardness, as well as the performance on corrosion and wear testing were evaluated. The water atomized powders presented in general better results than gas atomized powders.

Keywords: 316L; cold gas spray; powder shape; corrosion; wear



Citation: Vaz, R.E.; Silvello, A.; Sanchez, J.; Albaladejo, V.; Cano, I.G. The Influence of the Powder Characteristics on 316L Stainless Steel Coatings Sprayed by Cold Gas Spray. *Coatings* **2021**, *11*, 168. <https://doi.org/10.3390/coatings11020168>

Academic Editor: Cecilia Bartuli
Received: 11 December 2020
Accepted: 27 January 2021
Published: 31 January 2021

Publisher's Note: MDPI stays neutral with regard to jurisdictional claims in published maps and institutional affiliations.



Copyright: © 2021 by the authors. Licensee MDPI, Basel, Switzerland. This article is an open access article distributed under the terms and conditions of the Creative Commons Attribution (CC BY) license (<https://creativecommons.org/licenses/by/4.0/>).

1. Introduction

Metallic components and/or metallic structures are exposed to different conditions during their lifetime. The operational and environmental conditions must be considered during their design, fabrication, maintenance and inspection steps, since wear or corrosion could occur in working conditions. For this reasons, the application of coatings on the new components have been widely used, employing different techniques, such painting, galvanizing, Physical Vapor Deposition (PVD), Chemical Vapor Deposition (CVD), welding, thermal spraying, and other processes [1–4]. The selection of the protection methodology and coating materials depends on its purpose, such corrosion, wear, or cavitation resistance, or aesthetic purpose. Among thermal spray processes, CGS is a deposition technique used to fabricate coatings or to repair worn areas of free standing parts [5–7]. Nowadays, CGS is accepted as a spray technique capable of depositing thick metal layers on different substrates at relatively low processing temperatures, maintaining the initial phase composition of different feedstock powders. Since the starting powders used in CGS remain in the solid state during the deposition, the most common defects of the high-temperature thermal spray processes, such phase transformation or oxidation, can be avoided [8–11].

The 316L stainless steel offers high creep resistance, desirable machinability, and significant tensile strength at high temperatures, as well as wear and corrosion resistance, which accredit it to applications in aerospace, automotive, medical implants, pharmaceuticals and biomedical industries, food preparation equipment, oil and gas sectors, marine, and architectural applications [12]. It is also used to coat carbon steel or to repair 316L damaged parts.

The feedstock powder for CGS can be manufactured by different techniques, resulting in different powders characteristics and properties [13,14]. For example, the gas atomization process produces spherical powders, while the water atomization confers to the powders

an irregular shape, and it is typically a cheaper process than gas atomization [15,16]. About the selection of an specific shape powders to be used in CGS, for Jeandin et al. [17], it depends on the answering of two main questions: first, how the particles impinge during the process and second, the nature of the bonding between two adjacent splats. It is clear that both answers depend on the powder shape, which influences the particle deformation at the impact and adhesion mechanisms. The resistance on tensile testing and the hardness of Ag irregular powder CGS sprayed coatings were higher than the Ag spherical shape, even after heat treatment [17]. Some mechanisms collaborate to the adhesion of the particles to the substrate as listed by Sun et al. [18]: the adiabatic shear instability (ASI), caused by the high velocity of the powder particle, breaks the natural oxide film on the surface of both the particle and the substrate and the progressive plastic flow of the materials enables metallic bonding at atomic scale through direct contact between the adjacent fresh metal surfaces; mechanical interlocking, interfacial mixing, local melting and diffusion [19–23].

Particles velocity is among the most important parameters of CGS, which works well in a window of operation, meaning that the particles must impact to the substrate above a critical velocity and under a maximum velocity. It occurs due to the fact that slow particles does not attach or anchor to the substrate and particles with an excessive velocity erode the substrate [9]. It is well known that the higher the velocity of the particles, the lower the porosity, the higher the adhesion strength and the higher the corrosion resistance and hardness of the cold sprayed coating [10,12,24]. Fukunuma et al. [25] investigated experimentally how particle morphology affects particle acceleration in a CGS supersonic gas flow. They sprayed 316L powders with spherical and irregular morphologies, resulting the irregular 316L particles is faster than the spherical ones at the same process conditions. According to these authors, this is due to the higher drag coefficient of the angular particle. Jodoin et al. [26], using the CGS process, measured the higher velocity for particles of Al alloys cryomilled (irregular) than the atomized ones. Schmidt, Gaertner, and Kreye [24] also presented the influence of the particle size on the velocity of particles, since the bigger the particles the lower the velocity and the temperature reached, mainly due their mass and inertia to the movement. Evaluating the size of 316L particles, Adachi and Ueda [27] presents the smallest particles ($-20 + 5 \mu\text{m}$) producing denser CGS coatings than bigger particles ($-45 + 10 \mu\text{m}$ and $-53 + 20 \mu\text{m}$).

This work aims to evaluate the effect of the 316L feedstock powders characteristics on the CGS coatings properties, microstructures, corrosion, and wear performance. To accomplish this objective, fully dense 316L coatings were prepared via CGS, using four different 316L commercial starting powders. The powders characteristics and properties were measured, as the microstructure and mechanical properties of each coating, and their wear and corrosion resistance.

2. Materials and Methods

2.1. Feedstock Powders

For the tests carried out in this work, four different 316L commercial powders were used, two powders are specially designed for CGS technology and prepared by water atomization: 316L-CGS_1 (Ref: 316L from Daye, Shijiazhuang, China) and 316L-CGS_2 (Ref: SS316L from Plasma Giken, Saitama, Japan). While the other two are specific powders for conventional thermal spraying techniques and obtained by gas atomization: 316L-HVOF (Ref: Diamalloy™ 1003 from Oerlikon, Westbury, NY, USA) and 316L-APS (Ref: 316L from Sandvik, Neath, UK). In Table 1 the powders properties and characteristics informed by the manufacturers are summarized.

Table 1. Feedstock materials.

Powder Identification	Nominal Composition (wt.%)						Particle Size Distribution (μm)	Fabrication Process
	Cr	Ni	Mo	Mn	Si	Fe		
316L-CGS_1	17.6	-	2.7	0.3	0.8	Bal.	-40 + 15	Water atomized
316L-CGS_2	<18	<14	<3	-	<1	Bal.	-45 + 10	Water atomized
316L-HVOF	17	12	2.5	-	2.3	Bal.	-45 + 11	Gas atomized
316L-APS	17	12	2.5	2	1	Bal.	-45 + 20	Gas atomized

2.2. Cold Gas Spray Conditions

All the 316L powders were deposited onto flat low carbon steel substrates (S235JR type, $20 \times 50 \times 5 \text{ mm}^3$) previously grit-blasted with alumina for roughness greater than $R_a 7 \mu\text{m}$ and $R_y 40 \mu\text{m}$. Coatings were prepared by CGS using a CGT Kinetiks 4000 equipment (Impact Innovations GmbH, Haun, Germany) fitted with a water-cooled SiC nozzle. For all the coatings, four layers were sprayed at a 500 mms^{-1} axial velocity using N_2 as a propellant gas at 4 MPa and 800°C of gas pressure and temperature, respectively.

The deposition efficiency shown by each powder was calculated as the ratio of mass gained by the substrate after spraying and the mass of powder consumed during the spraying time. Identical spraying conditions to those above indicated were used for carrying out these analysis and a scale AE100 (Mettler, Columbus, OH, USA) was used for mass measuring.

2.3. Powder and Coating Characterization

The actual particle size distribution of feedstock powders was determined in triplicate by dry mode Laser Scattering (LS) techniques using a LS13320 equipment (Beckman Coulter, Brea, CA, USA), according to ASTM B822-02 standard [28]. The nominal composition of 316L powders was analyzed by inductively couple plasma (ICP) using an ICP-OES 3200 RL equipment (Perkin Elmer Optima, Waltham, MA, USA) available in the CCI TUB facilities ascribed to the University of Barcelona (Barcelona, Spain). In addition, the apparent density and flowability of the powders were measured, in accordance with the ASTM B212-99 [29] and ASTM B213-03 standards [30], respectively.

The metallographic preparation of coatings and powders cross-section was carried out in accordance with the ASTM E1920-03 [31] and ASTM E3-01 [32] standards and the etching was done in aqua regia reagent (30 mL HCl, 10 mL HNO_3 , and 20 mL H_2O). A DMI5000M (Leica, Wetzlar, Germany) microscope was used for the Optical Microscopy (OM) and coating thickness measurement, following the standard ASTM B487-85 standard [33], as an average of 10 thickness values. For Scanning Electron Microscopy (SEM) was used a Pro Desktop SEM equipment (Thermo Fisher Phenom, Eindhoven, Netherlands). The coatings porosity was analyzed with the software ImageJ on OM images at 200x magnification, according to ASTM E2109-01 standard [34].

In order to compare the phases and crystal structure of the feedstock powders and CGS coatings, the XRD equipment X'Pert PRO MPD (PANalytical, Malvern, United Kingdom) was used with a radiation of Cu $K\alpha$ ($\lambda = 1.5418 \text{ \AA}$) from 5° to $120^\circ 2\theta$ with a 0.017° step, measuring 80 s per step.

Microhardness of coatings was measured by means of a HMV (Shimadzu, Tokyo, Japan) equipment, following the ASTM E384-99 standard [35], applying a load of 0.3 kgf (3 N) ($\text{HV}_{0.3}$). Microhardness values were averages from 10 indentations in Vickers scale for each coating.

The adhesion strength of the coatings was measured using a tensile test, in accordance with the ASTM C633-13 standard [36], mounting the coated sample to the uncoated counterpart using the epoxy resin adhesive Ultrabond 100 (HTK, Hamburg, Germany) cured at 180°C for 1 h, with traction-adhesive strength of 70 MPa. Three tests for each material were performed in a MCH-102 ME (Servosis, Madrid, Spain) equipment at a rate of

0.01 mm^s⁻¹ until both counterparts are separated. The results were classified according to the maximum tensile strength and the failure observed (cohesive, adhesive, or glue failure).

The performance of the coatings in abrasive conditions was evaluated by means of the Rubber Wheel method, ASTM G65-00 standard [37]. This test was performed with the OL-2000 (CM4, Cervello, Spain) equipment at a velocity of 139 rpm, with a force of 50 N, a 22.6 cm diameter wheel and Ottawa silica sand as the abrasive agent (Sibelco, Barcelona, Spain) with less than 0.5% moisture). For the analysis of the sliding wear resistance of the 316L coatings, ball-on-disk tests were carried out following the scheme presented in Figure 1, in accordance with ASTM G99-04 standard [38]. For this test, the samples were previously prepared, by grinding and polishing up to the maximum roughness R_a 0.8 μ m. The tests were performed at room temperature (27 ± 2 °C) and maximum 20% moisture in dry conditions using a WC-Co ball ($\varnothing = 11$ mm), with a sliding rate of 0.13 m \cdot s⁻¹ for a total sliding distance of 1000 m. During the test, the coefficient of friction (CoF) between the surfaces was recorded and plotted for the load of 10 N with the acquisition rate of 1 value per lap, with a total of 22737 CoF values. The wear volume loss of the ball on disk samples was calculated by the Equation (1), as recommended by the ASTM G99-04 standard [38], where R is the wear track radius, d is the wear track width, and r is the ball radius. The friction wear rate is the disk volume loss divided by load and sliding distance.

$$\text{Disk Volume Loss} = 2\pi R \left[r^2 \sin^{-1} \left(\frac{d}{2r} \right) - \left(\frac{d}{4} \right) \left(4r^2 - d^2 \right)^{1/2} \right] \quad (1)$$

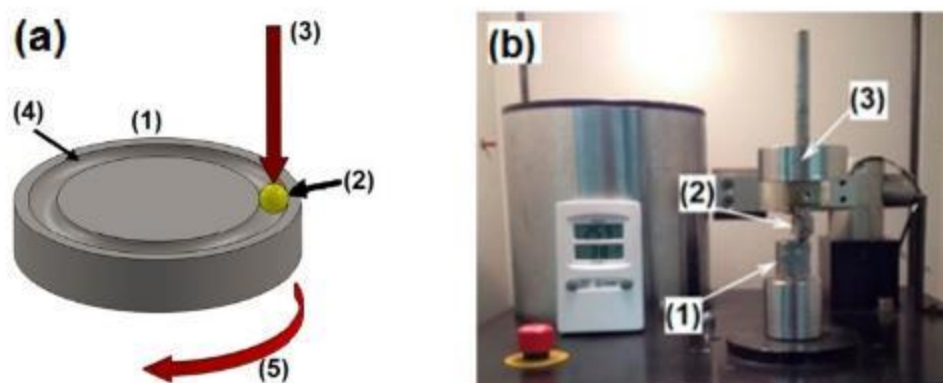


Figure 1. (a) scheme and (b) equipment for ball-on-disk testing, (1) sample, (2) ball, (3) load, (4) wear path on sample, and (5) rotation direction of sample.

Potentiodynamic polarization measurements were carried out, in accordance with the ASTM G59-97 [39] and ASTM G102-89 [40] standards, to determine corrosion resistance of the coatings in 3.5 wt.% NaCl water solution. Two different samples of each coatings and reference bulks were used for corrosion tests as working electrode, with exposed area of 1.0 cm². The exposed surfaces were grinding up to the maximum roughness R_a 0.3 μ m. A saturated calomel (3.0 M KCl) was the reference electrode and a platinum was the counter electrode in the tests. A scan rate of 0.05 mV \cdot s⁻¹ and a potential range of ± 25 mV with respect E_{ocp} were used to acquire the polarization resistance (R_p), and from -250 to 1050 mV with respect E_{ocp} to acquire the polarization curves with a VSP (Biologic Science Instruments, Seyssinet-Pariset, France) equipment. The corrosion potential (E_{corr}) and corrosion current (I_{corr}) were calculated with the software EC-Lab V10.44. E_{corr} was obtained from a Tafel Fit extrapolation, while I_{corr} was calculated according to the Stern-Geary Equation (2).

$$I_{corr} = \frac{(\beta_a + \beta_c)}{2.3 \times (\beta_a + \beta_c) \times R_p} \quad (2)$$

where, β_a and β_c are the anodic and cathodic currents, respectively, and R_p is the polarization resistance.

To benchmark the wear and corrosion behavior of CGS 316L, the wear and corrosion behavior of 316L bulk were also evaluated.

3. Results and Discussions

3.1. Characterization of Powders

Shown in Figure 2a–h are SEM images of the feedstock powders used in this study are shown. These images clearly show the differences in morphology found for these powders regarding their manufacturing process. As expected, the water atomized powders (316L-CGS_1 and 316L-CGS_2) show an irregular morphology, while the gas atomized powders (316L-HVOF and 316L-APS) are composed of quasi-spherical particles, with satellite particles attached to the bigger particles of the 316-APS. These differences are mentioned by Lagutkin et al. [15], who explained that the high sphericity of the gas atomized powders as a result of using an inert gas in the atomization process. The amount of satellite particles in gas atomized powders is attributed to the fabrication process' parameters by Beckers et al. [14], since the satellite are particles previously solidified that collide and adhere to the bigger particles, and their formation is influenced by the particle concentration in a atomization flow, the direction of atomizing gas jets, the design of the atomizing chamber, and other parameters [14]. On the other hand, the irregular shape of water atomized powders may be attributed to the relative higher cooling rates during solidification compared to the gas atomizing process [41]. A microstructure of austenite grains was revealed by observing the powders' cross-section in a SEM. These grains are identical to the presented by Sklyar et al. [42], with presence of smaller grain size in the smaller particles due to their faster solidification process.

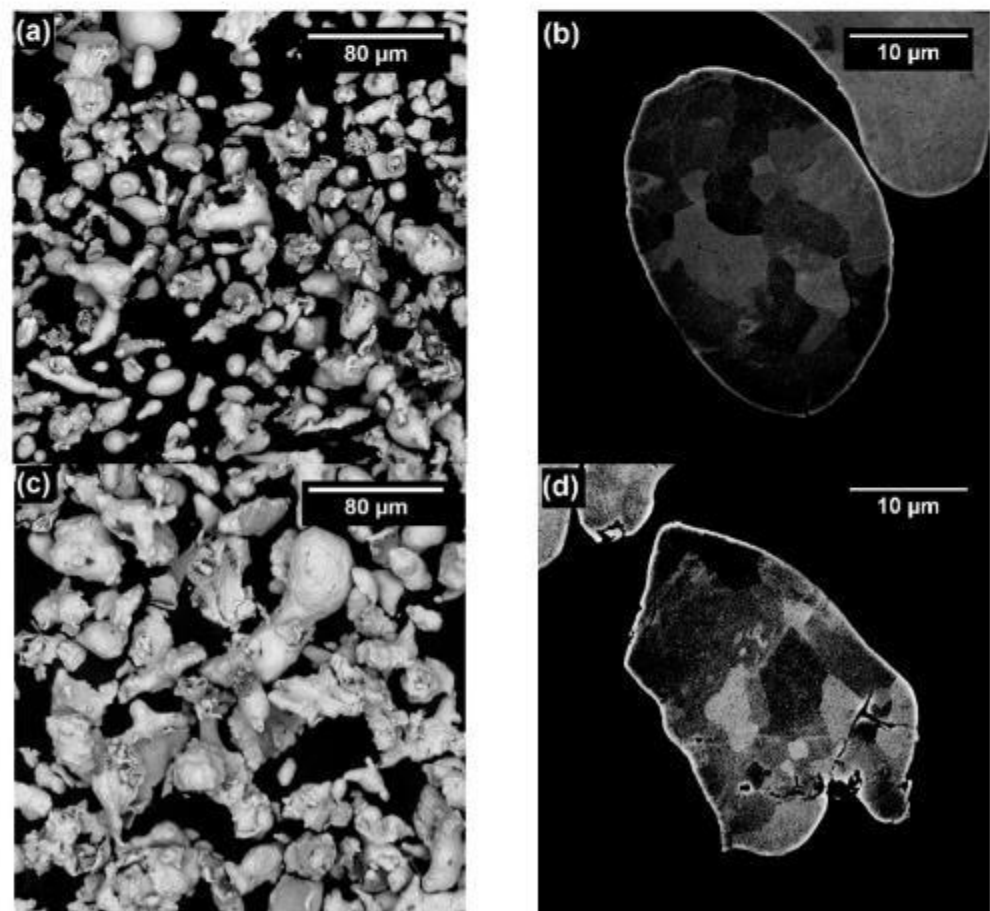


Figure 2. *Cont.*

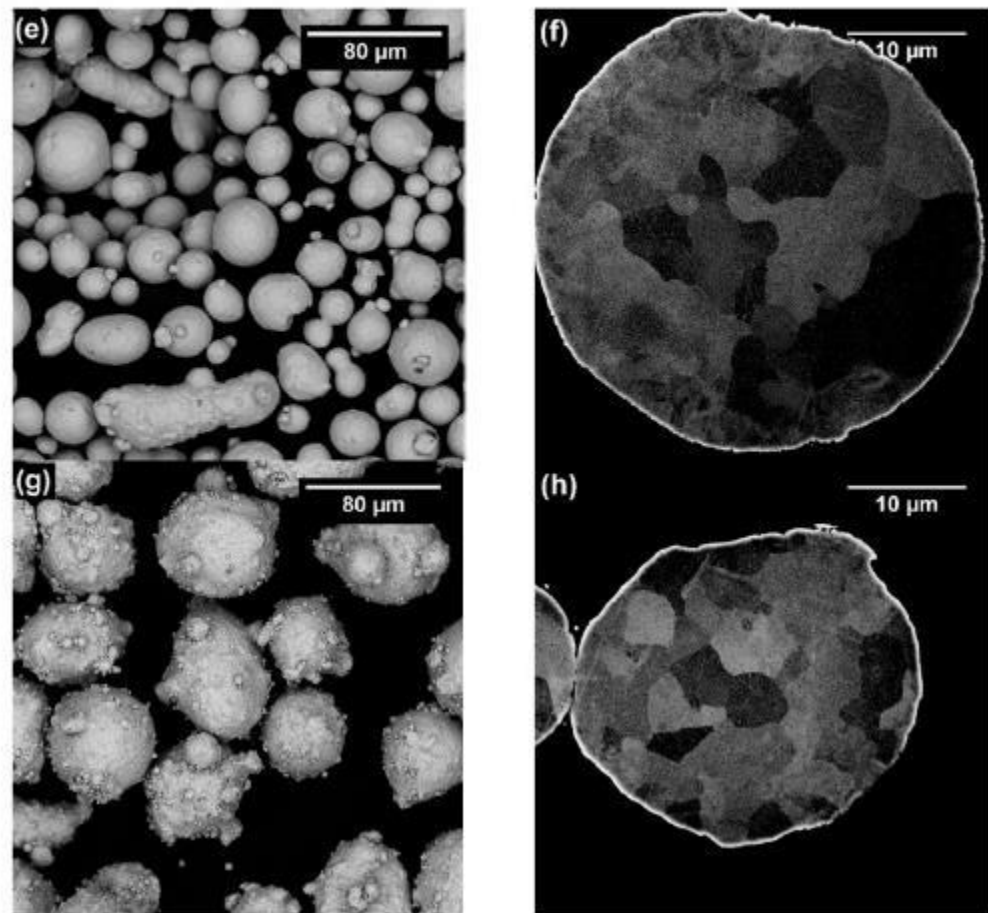


Figure 2. SEM of three dimensional and etched cross section images of powders at 1000 \times and 7000 \times , respectively. (a,b) 316L-CGS_1, (c,d) 316L-CGS_2, (e,f) 316L-HVOF, and (g,h) 316L-APS.

In order to corroborate the chemical composition and crystallographic structure of the powders used in this study, the content of alloying elements and the identification of phases in the 316L powders was carried out by ICP and XRD, respectively. The composition of the powders is shown in Table 2, which were in agreement with the 316L reference, as expected. Only a exception was observed for 316L-APS powder, the Ni and Mo amounts closely out of range. The XRD diffractograms corresponding to all the 316L powders are shown in Figure 3 and their phase analysis indicates the presence of one only phase, austenite γ (reference code: 00-023-0298), in all of the feedstock powders.

Table 2. Chemical composition of the 316L feedstock powders. wt.%.

Material	Cr	Ni	Mo	Mn	Mg	S	P	Si	Fe
316L-CGS_1	16.03	12.27	2.57	0.52	<0.1	<0.5	<0.5	<2.0	Bal.
316L-CGS_2	16.32	11.19	2.16	0.09	<0.1	<0.5	<0.5	<2.0	Bal.
316L-HVOF	16.42	10.12	2.07	1.37	<0.1	<0.5	<0.5	<2.0	Bal.
316L-APS	17.07	9.55	1.83	0.55	<0.1	<0.5	<0.5	<2.0	Bal.
316L reference [43]	16.0	10.0	2.00	2.00	-	0.030	0.045	0.75	Bal.
	18.0	14.0	3.00	max		max	max	max	

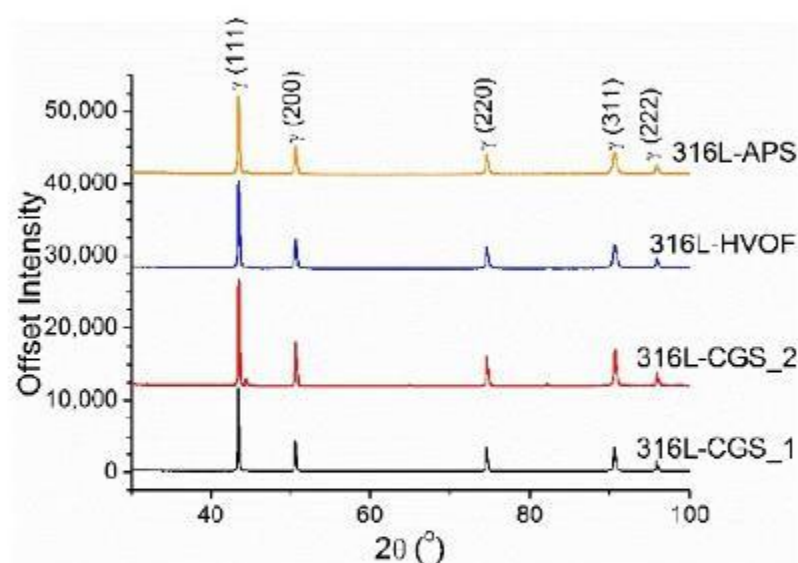


Figure 3. XRD patterns of the 316L feedstock powders.

The mentioned differences observed in the particle size between powders were confirmed by the LS technique. Figure 4 shows the particle size distribution histograms obtained by this method for all the powders. In the graphs it can be clearly observed that only the 316L-APS powder presents a narrower particle size distribution and its volume of small particles, observed in Figure 2d, was too low and did not contribute significantly for its histogram in Figure 2d, while for the other three powders, the curves were quite wide. In case of the water-atomized powders, 316L-CGS_1 and 316L-CGS_2, this result is common result, since the particle size distribution curve obtained by LS might under- and over-estimate the volume of the particles due to the irregular shape of the particles. Distribution size parameters (d_{10} and d_{90}) and apparent density of the powders are included in Table 3.

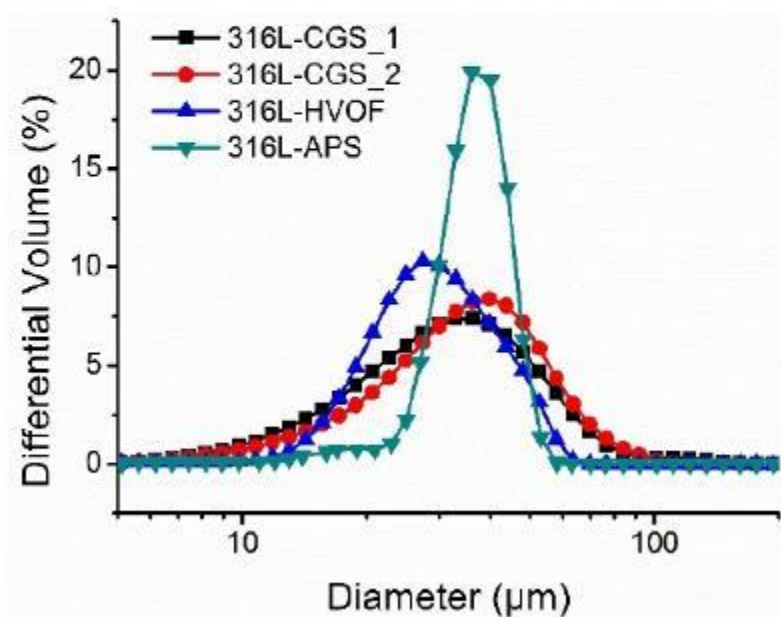


Figure 4. Particle distribution of the 316L feedstock powders.

Table 3. Particle distribution, apparent density, and flow rate of the 316L feedstock powders.

Material	Particle Size Distribution (μm)		Morphology	Apparent Density ($\text{g}\cdot\text{cm}^{-3}$)	Flow Rate ($\text{g}\cdot\text{s}^{-1}$)	Powder Feed Rate ($\text{g}\cdot\text{s}^{-1}$)
	d10 *	d90 **				
316L-CGS_1	16	60	Irregular	3.03 ± 0.01	9.03 ± 0.36	0.43
316L-CGS_2	17	60	Irregular	2.86 ± 0.01	8.21 ± 0.49	0.41
316L-HVOF	19	47	Quasi-spherical	4.47 ± 0.01	17.61 ± 0.40	0.55
316L-APS	29	47	Quasi-spherical ***	3.73 ± 0.01	13.44 ± 0.65	0.50

* d10: 10% of the powder have size under this value; ** d90: 90% of the powder have size under this value; *** Presence of satellite particles.

The flow rate and the flowability of the powders was also measured by means of a Hall funnel, ASTM B213-03 [30], are indicated in Table 3. Powder flowability is an important characteristic of powders for CGS as it influences the powder feed rate that may be achieved in the CGS equipment. In this respect, an increase of the powder flow rate of the would lead to an increase of the powder feed rate on the same spraying conditions, as confirmed in Table 3, with the highest value of apparent density, flow rate, and powder feed rate seen for the same powder, 316L-HVOF. Bearing in mind that all the powders had been sprayed under identical spraying conditions, feed rate may show a significant effect on the deposition efficiency and coating characteristics, as it will determine the amount of particles introduced into the powder laden jet, and, hence, it will affect the final particle temperature and/or velocity. The lower values presented in Table 3 for the water atomized powders, 316L-CGS_1 and 316L-CGS_2, are related to the shape of the particles, since the spherical shape tends to have higher flowability, and to the d90 value of particle size distribution, which is 60 μm for the water atomized powders and 47 μm for the gas atomized powders.

From the comparison of the SEM and LS data with the flow rate results for each powder, it can be interpreted that the morphology and size of the powder particles clearly affect to the flowability of the powders. Thus, the quasi-spherical powders showed a higher flow rate than the water-atomized materials as it is widely accepted that an irregular shape of particles has a detrimental effect on its flow rate. Unexpectedly, the flow rate measured for the 316L-APS powder (with the narrowest particle size distribution) points out that this material did not show higher flowability than the 316L-HVOF powder. This result can be justified by the presence of the satellite particles on the surface of the biggest particles among the samples, Figure 2, which significantly decreased its flowability. The powder feeding rate achieved by each powder under identical spraying conditions is included in Table 3.

3.2. Characterization of Coatings

The OM cross section images recorded for the CGS coatings deposited in this study are shown in Figure 5a–h. In these images, it can be observed that all the coatings showed the densified and typical structure of CGS coatings, with the deformed powder particles forming the lamellae/splats structure, clearly seen in the etched samples. The etching also revealed the severe grain deformation in the periphery of the particles. In addition, the Figure 6 presents an example of interface substrate/coating revealing the severe deformation of the carbon steel substrate and the intermixing between the coating and substrate materials, which are anchoring mechanisms of the CGS coatings [21–23]. The coating/substrate interfaces also did not present inclusions of alumina from sandblasting preparation process nor delamination.

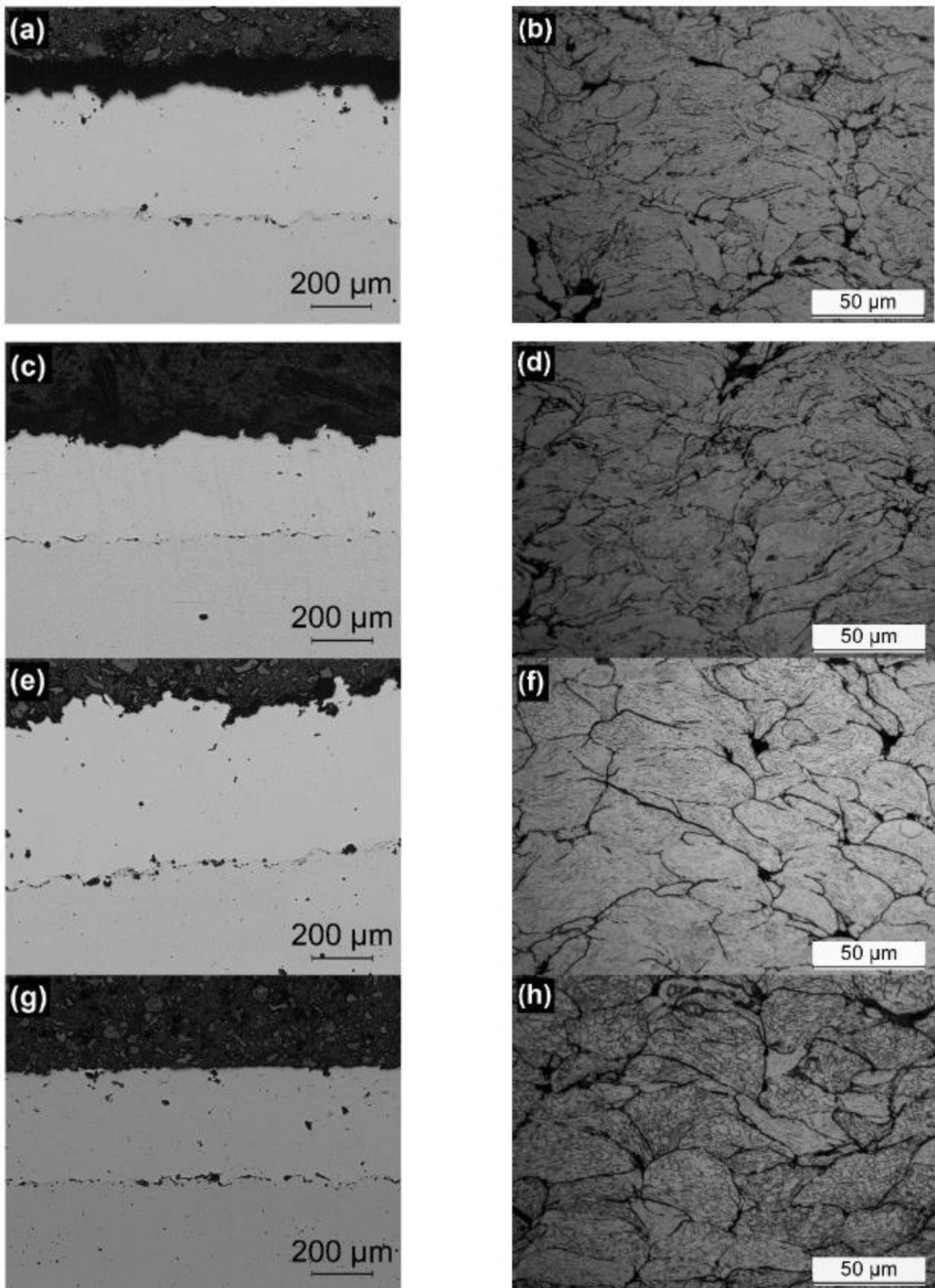


Figure 5. OM of cross-sectional image of the CGS coatings obtained at 50× as polished and 500× as etched. Powders: (a,b) 316L-CGS_1, (c,d) 316L-CGS_2, (e,f) 316L-HVOF, and (g,h) 316L-APS.

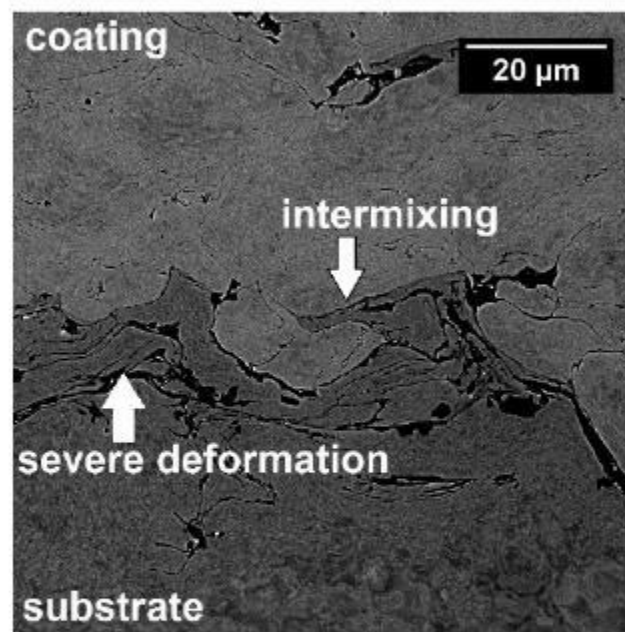


Figure 6. SEM of the interface substrate/coating of 316L-CGS_1 obtained at 3000 \times .

For comparative reasons, the porosity of all the coatings was calculated by means of image analysis and the values obtained are included in Table 4. It is worth indicating that these porosity percentages are calculated as a mean value of ten images for each material, and for this reason, the OM images shown in Figure 5 do not necessarily represent this mean value. It is accepted that the density of the coating and deposition efficiency are directly related to the particle size distribution, shape of the feedstock particles, and CGS parameters [44], as the amount of small particle composing the size distribution had severe influence on the porosity of CGS coatings, as related by Spencer and Zhang [45], presenting increasing of porosity with the powder d10 value. In this respect, coatings showing high density and deposition efficiency would be expected when the material used has a smaller d10 value in the particle size distribution and spherical morphology, favoring their flattening and homogeneity of splats phase in the coating, when compared to coatings obtained by irregular shape feedstock powders [44].

Table 4. Properties of the 316L coatings.

Material	Hardness (HV _{0.3})	Thickness (μm)	Porosity (%)	Adherence (MPa)	Deposition Efficiency (%)
316L-CGS_1	356 \pm 23	420 \pm 26	0.1 \pm 0.0	29.4 \pm 4.9	97
316L-CGS_2	348 \pm 48	331 \pm 28	0.2 \pm 0.0	19.7 \pm 2.4	85
316L-HVOF	353 \pm 44	517 \pm 21	0.2 \pm 0.1	11.0 \pm 1.9	92
316L-APS	344 \pm 25	381 \pm 12	0.4 \pm 0.2	4.5 \pm 2.1	80

All the coatings prepared in this study showed porosity percentages lower than 0.5%, regardless of the raw material features. These values of porosity are even lower than the values presented by other authors: 1.9% [27], 2.2% [46], 3.3% [8], and 1.86% [5], for identical coating materials and process. Even as the differences between coatings are not significant, the porosity results suggests that for those 316L powders, higher coating density may be achieved when water atomized powders (irregular morphology), with lower d10 value than the spheroidal, are used for CGS deposition. The powder 316L-APS, even with higher powder feed rate and apparent density, 0.50 g·s⁻¹ and 3.73 \pm 0.01 g·cm⁻³, respectively, presented the lowest deposition efficiency, 80%, which resulted in the thinnest coating, 381 \pm 12 μm . This is justified by the particle distribution and highest d10 value,

29 μm , which influenced reducing the particle energy at the impact on the substrate, and consequently the particle flattening and anchoring.

To complete the characterization of the coatings, the microhardness and adhesion strength of these 316L CGS coatings were also analyzed. The average values of microhardness measured for the coatings are shown in Table 4. They did not reveal significant differences among the different coatings, and are close to the mean values obtained by other authors: 358 HV [12], 370 HV [6], and 325 HV [47]. The CGS hardness values should be compared to other thermally sprayed 316L coatings: 190 HV [48] for flame spraying, 270 HV [48] and 312 HV [49] for HVOF, 325 HV for arc spraying [50], and 262 HV for APS [49]. The CGS process characteristics of lower temperature and higher velocity of particles than other processes justify its higher coating hardness, since its higher particles' velocity promotes the increasing in hardness due to their plastic strain hardening [51], and the relative low temperature prevents the material recrystallization, thus enabling the ASI mechanism, as explained by Sun et al. [18]. In addition, all the coatings show a hardness in the range to that reported for 316L bulk materials, 350 HV_{0.3}, approximately. It is worth underlining that the tests carried out onto the cross-section of all coatings did not present significant variation or gradient in the microhardness values from the interface substrate/coating to the top surface of the coating. These data are in agreement with the information previously interpreted from the microstructure characterization, which suggested no difference in porosity and particle-to-particle cohesion for all the 316L CGS coatings. Additionally, the indentation marks on the coatings are presented in Figure 7, showing that no cracks growing is generated from these marks, legitimating the measures.

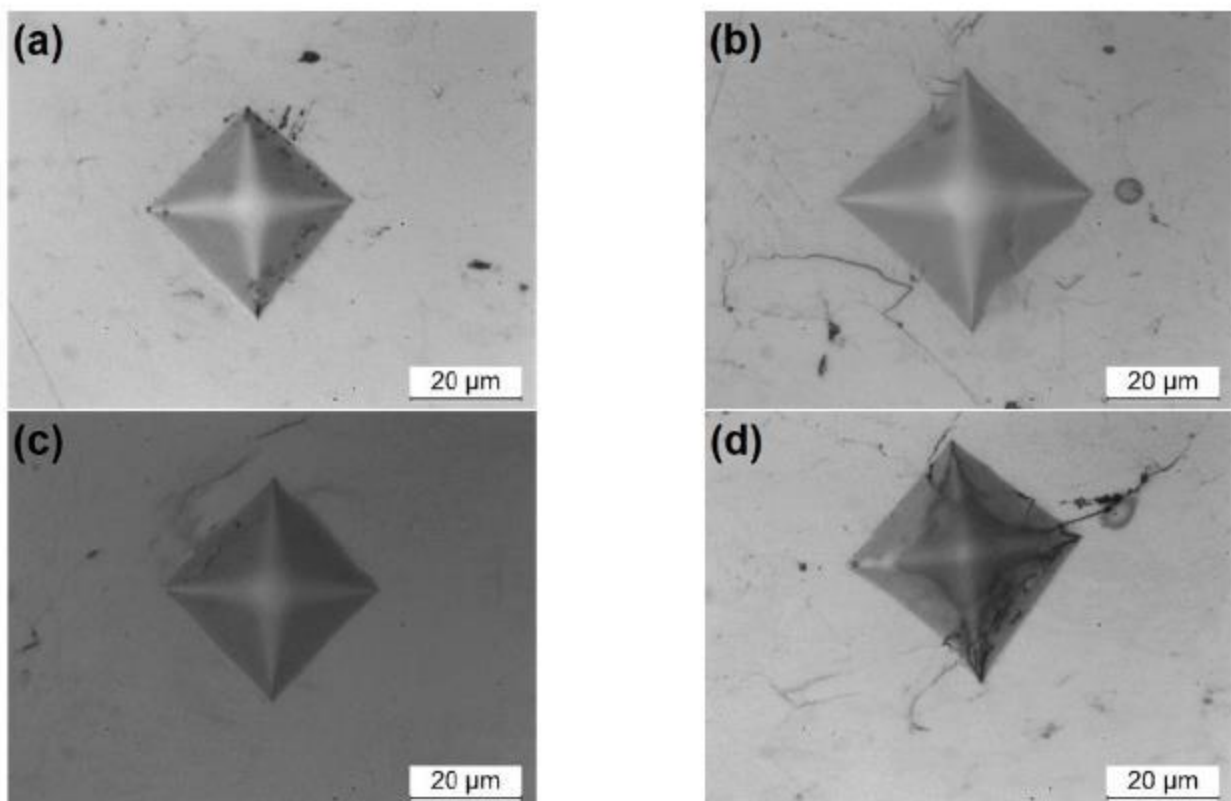


Figure 7. Marks for hardness measurements of the coatings. (a) 316L-CGS_1, (b) 316L-CGS_2, (c) 316L-HVOF, and (d) 316L-APS.

As mentioned, the adhesion strength of the coatings was also measured and the data collected are included in Table 4. In addition, all the coating show adhesive failure between coating and substrate, since all of the coatings were completely detached from the substrate. The adherence of 316L CGS coatings is presented with a wide range of values in

the literature: >53 MPa [46], >60 MPa [52], 80 MPa [53], and 13 MPa [54]. Comparing these references with Table 4, all of the studied 316L CGS coatings presented relative low values, even lower to 5 MPa for the 316L-APS coating. In spite of this, significant differences are shown between coatings, which can be ordered in terms of adherence as follows 316L-CGS_1 > 316L-CGS_2 > 316L-HVOF > 316L-APS. These differences between all the coatings might indicate that better adhesion of particles to the substrate is achieved for the water atomized 316L-CGS_1 powder. This material also showed the higher deposition efficiency, which had been related with a higher particle velocity. Thus, the adhesion results will suggest that this powder would reach the higher particle temperature, favoring the particle plastic deformation during the impact and, as a result, the anchoring of the coating to the substrate.

3.3. Corrosion Performance Testing

For the evaluation of the performance of these coatings in a corrosive media, potentiodynamic experiments were conducted with all the CGS coatings. The polarization curves obtained in these experiments are shown in Figure 8. In this figure, the polarization curve measured for a 316L bulk component is also included for comparative reasons. From these curves, E_{corr} and I_{corr} values characteristic for each coating were inferred. A significant difference in these parameters can be observed between coatings, as the 316L coatings obtained by means of the water atomized powders had corrosion potentials and current values closer to the 316L bulk reference than the gas atomized powders. This might suggest that the water atomized powders lead to the deposition of more compact coatings, which allows eliminating the effect of the substrate on the polarization response.

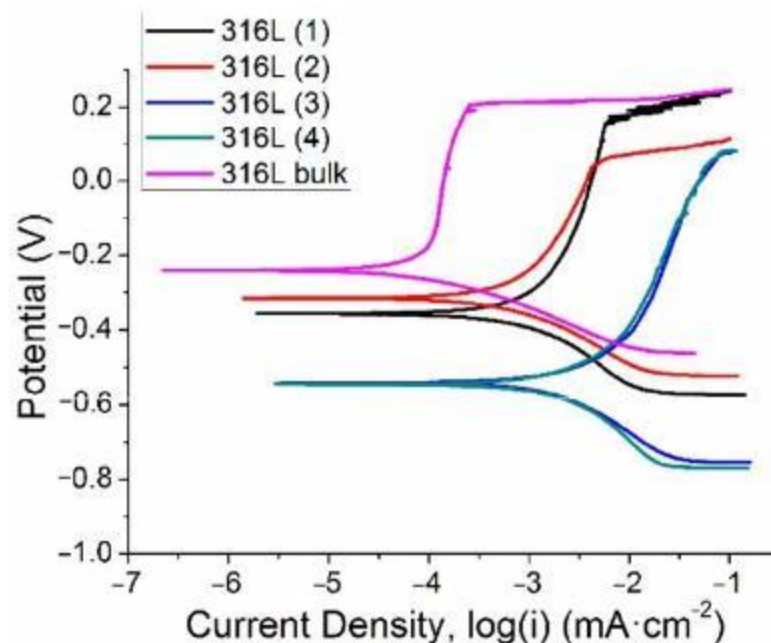


Figure 8. Tafel slopes of 316L coatings and bulk.

All the curves obtained for the 316L CGS coatings show the typical evolution expected for 316L materials. Looking at the anodic side of the polarization curve, it is observed that all the coatings showed a passivation region starting at low anodic potential. In agreement with E_{corr} and I_{corr} values, the CGS show a higher current intensity in this passivation region than that shown by the 316L bulk. This clearly indicates that, although in all the cases the coating is passivated, the 316L will be corroded or consumed at a higher rate than for the benchmark material. As previously observed, the water atomized powders allow depositing coating with a lower passive current intensity than the gas atomized precursors.

Despite the differences observed between coatings and 316L bulk material, it is worth indicating that the 316L-CGS_1 coatings showed an $E_{pitting}$ value very close to that observed for the reference material, indicating that the passive layer of this coating remains stable up to the identical anodic polarization for these two materials.

From these results (Table 5), it cannot be suggested the repair of any 316L part CGS as a promising solution considering the great performance differences between bulk material and CGS coatings. In this respect, the differences in E_{corr} indicate that the incorporation of this 316L layer to a 316L surface may generate galvanic couples which will worsen the resistance of this part to the corrosive media, accelerating its degradation and mass loss [55,56]. Anyway, comparing the results between water atomized (316L-CGS_1 and 316L-CGS_2) and gas atomized (316L-HVOF and 316L-APS) powders, it is clear that the first ones are more resistant to corrosion than those obtained with an ideal spherical powder.

Table 5. Results of corrosion testing and abrasion rate for 316L CGS coatings and bulk.

Material	Current Density i_{corr} ($\mu\text{A}\cdot\text{cm}^{-2}$)	Potential of Corrosion E_{corr} (mV)	Polarization Resistance R_p (k Ω)
316L-CGS_1	2.120	−356.332	36.119
316L-CGS_2	0.897	−315.189	45.640
316L-HVOF	3.244	−541.909	15.518
316L-APS	2.373	−546.627	14.322
316L bulk	0.100	−239.738	50.080

3.4. Tribological Behavior Testing

The coefficient of friction (CoF) between a WC-Co counterpart and the 316L CGS coatings was measured by means of ball-on-disk experiments. Figure 9 presents the evolution of the CoF obtained during the experiment for all the coatings and a 316L bulk material. The CoF values calculated at the end of the experiment, when the system reached a stationary behavior are included in Table 6. Similar CoF were measured for all the coatings prepared by CGS, independently of the powder used for their deposition. The 316L bulk CoF, 0.746, is close to results seen in literature with the same testing load, 0.7 [57] and 0.8 [58]; however, the CoF of all the coatings were higher than the bulk, with the highest CoF for the 316L-APS, 0.934.

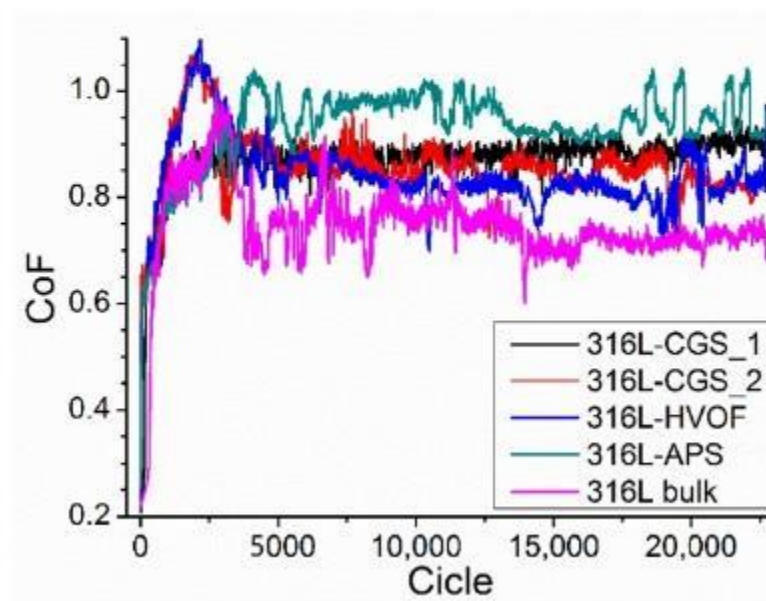


Figure 9. Results of ball-on-disk testing for 316L coatings and bulk.

Table 6. Results of ball-on-disk testing for 316L coatings and bulk.

Material	Abrasion Rate ($\text{mm}^3 \cdot \text{N}^{-1} \cdot \text{m}^{-1}$)	CoF	Friction Wear Rate ($\text{mm}^3 \cdot \text{N}^{-1} \cdot \text{m}^{-1}$)
316L-CGS_1	1.70×10^{-4}	0.869 ± 0.070	1.651×10^{-4}
316L-CGS_2	1.32×10^{-4}	0.857 ± 0.073	1.251×10^{-4}
316L-HVOF	1.60×10^{-4}	0.841 ± 0.077	1.619×10^{-4}
316L-APS	2.25×10^{-4}	0.934 ± 0.078	2.228×10^{-4}
316L bulk	1.91×10^{-4}	0.746 ± 0.100	1.692×10^{-4}

The wear mechanism of the coating and bulk samples was partially abrasive type, with typical furrows in the direction of the ball relative movement, indicated as area (1) in Figure 10b. Some debris act as a third body during the sliding wear and these materials are extensively deformed and adhered to the worn surface of wear track, presented as area (2) in Figure 10b, which refers to adhesive type wear mechanism. The wear tracks on the coatings samples are presented in Figure 11. The ratio of abrasive/adhesive type wear was higher for the bulk than for the coatings, prevailing the abrasive mode. The EDS mapping of the coating and bulk samples revealed the oxidation of the debris adhered to the wear track, as exemplified by the 316L bulk analysis in Figure 10c–f. The sample 316L-APS had the highest friction wear rate, $2.23 \times 10^{-4} \text{ mm}^3 \cdot \text{N}^{-1} \cdot \text{m}^{-1}$, while the 316L-CGS_2 had the lowest one, $1.25 \times 10^{-4} \cdot \text{mm}^3 \cdot \text{N}^{-1} \cdot \text{m}^{-1}$; however, this discrepancy of values is too small and the materials presented very similar friction performance.

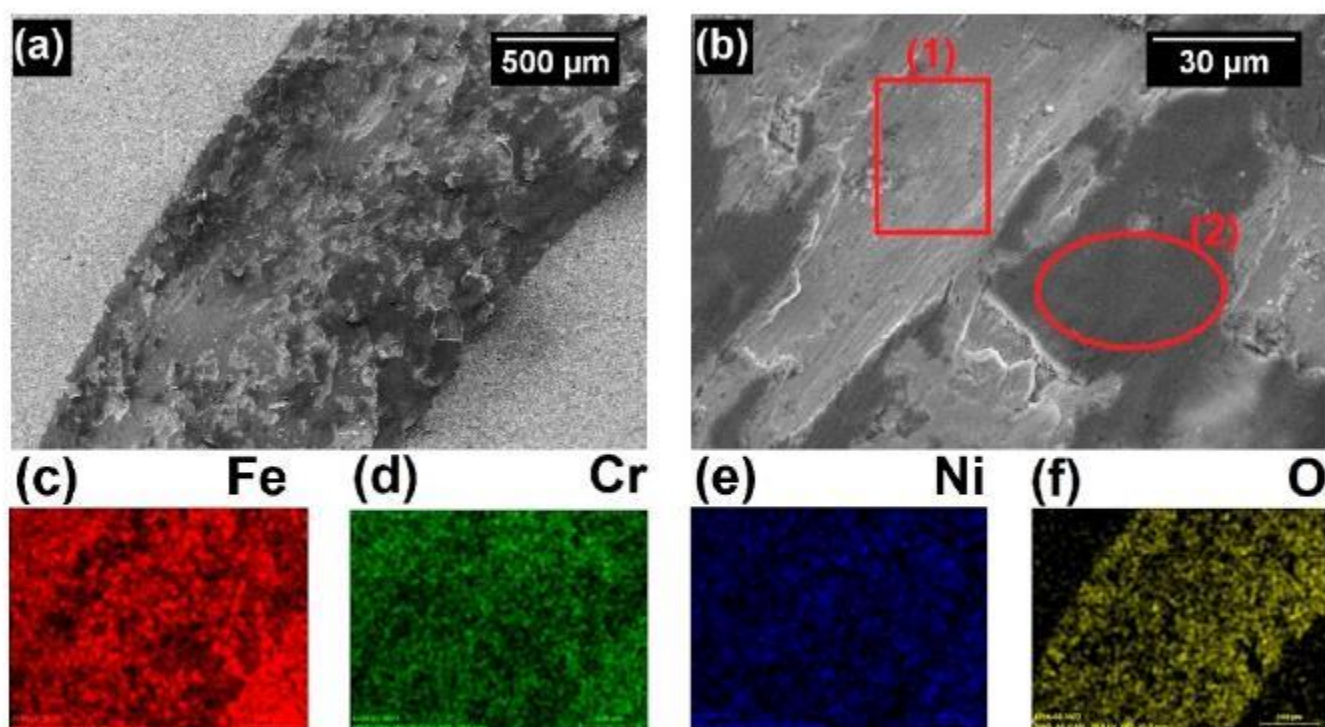


Figure 10. SEM and EDS of the 316L bulk ball-on-disk testing track. (a) 50 \times . (b) 1000 \times , where (1) is a region with abrasion-type wear marks and (2) is a region with adhesive-type wear. (c–f) EDS mappings.

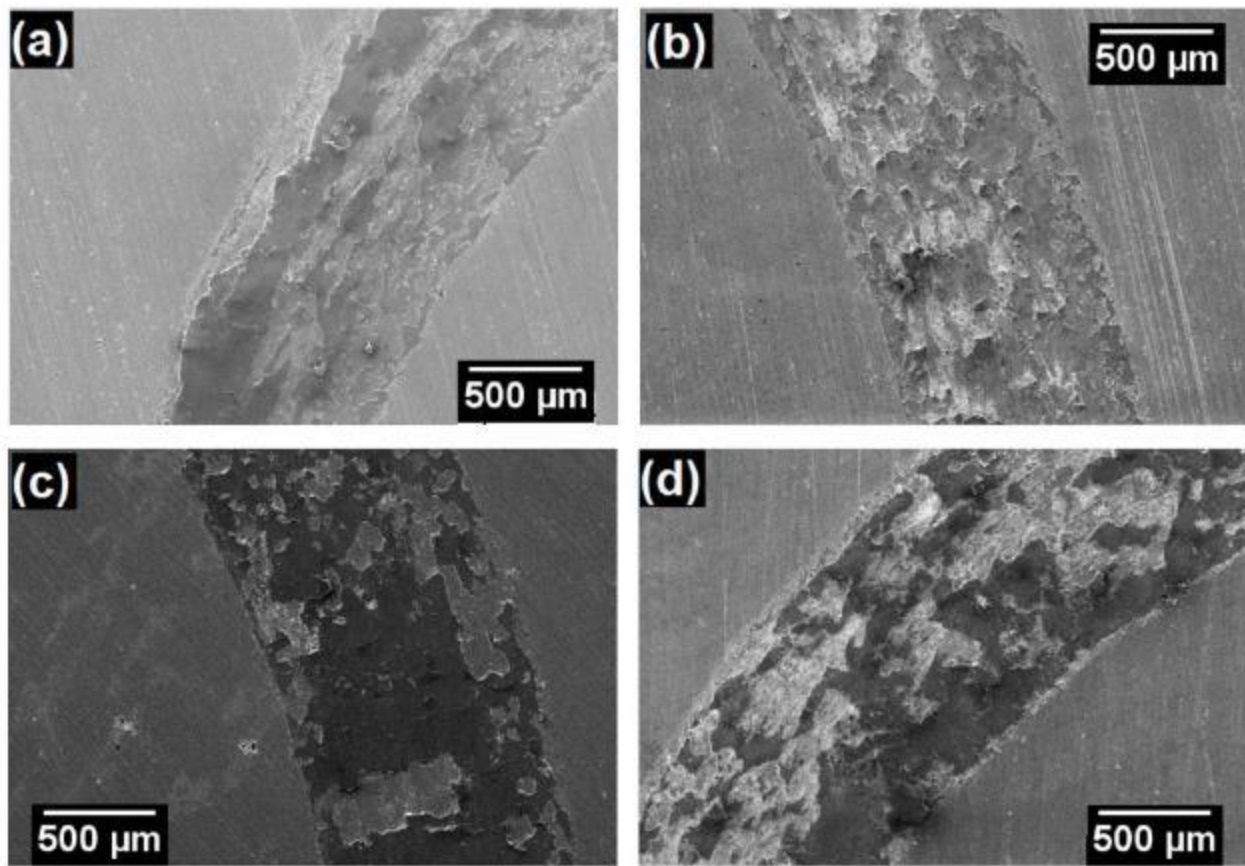


Figure 11. SEM of the coatings ball on disk testing track. 50 \times . (a) 316L-CGS_1, (b) 316L-CGS_2, (c) 316L-HVOF, and (d) 316L-APS.

Shown in Figure 12 the mass loss measured for the 316L CGS coatings under abrasive conditions, by means of dry rubber wheel tests are shown. In addition, in Table 6 the wear rate calculated for each coating from the mass loss values obtained in these experiments is included. From the comparison of these results, it can be interpreted that the coatings obtained with the water atomized (316L-CGS_1 and 316L-CGS_2) and gas atomized (316L-HVOF) powders allow obtaining 316L coatings with an abrasion resistance even higher than a 316L bulk material.

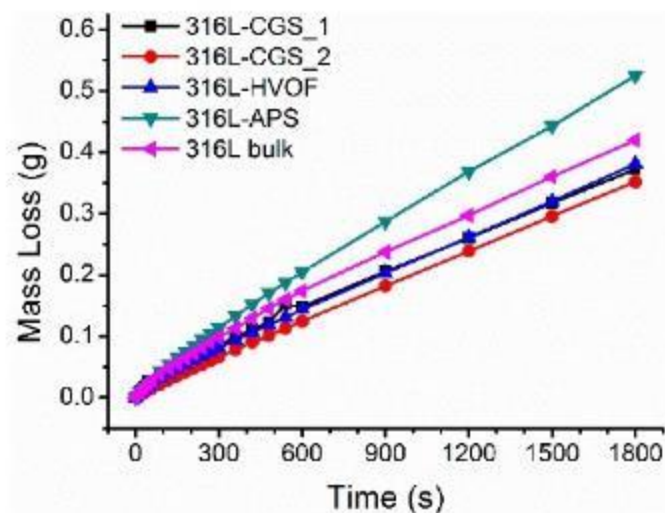


Figure 12. Results of rubber wheel testing for 316L coatings and bulk.

The abrasion resistance of a material is directly related to its Young's modulus (E), hardness, toughness, and compactness as presented by Fu, Li, and Li [59]. According to this, the close values for the abrasion results on the rubber wheel testing, for these three coatings, 316L-CGS_1, 316L-CGS_2, and 316L.HVOF, can be explained, since these CGS layers, showed very low porosity and similar hardness to the bulk material. Finally, the 316L-APS coating showed the lower abrasion resistance, which can be directly related to its physical properties, as this was the coating with the highest porosity and the lowest adhesion strength among the coatings prepared.

4. Conclusions

Four different 316L powders were evaluated to be used as feedstock for CGS process. The water atomized powders (316L-CGS_1 and 316L-CGS_2) presented irregular morphology, lower apparent density, flow rate, and powder feed rate than the gas atomized powders (316L-HVOF and 316L-APS), which had quasi-spherical morphology.

The coatings obtained by CGS with these powders were thick and dense, with porosity lower than 0.6%. The coatings hardness had values close to the 316L bulk, 350 HV, and their morphologies presented severe grain deformation on the starting powders microstructure. The coatings produced from water atomized powders had significant higher adhesion than the gas atomized ones; however this distinction was not clear for the deposition efficiency, which was above 80% for all the materials.

The coatings produced from water atomized powders had potential of corrosion and polarization resistance closer to the 316L bulk than the gas atomized ones. But this tendency was not evident for the wear performance, CoF, abrasion rate, and friction wear rate. The 316L-APS presented the worst performance for all of the performance testing.

Considering the results obtained in this comparative study, it can be concluded that there is no particular advantage to using gas atomized 316L powders over water atomized 316L powders. Thus, the four 316L feedstock powders tested, can be ranked as adequate for CGS technology as follows: 316L-CGS_1 > 316L-CGS_2 > 316L-HVOF > 316L-APS.

Author Contributions: Conceptualization, J.S.; funding acquisition, J.S. and I.G.C.; investigation, R.F.V. and A.S.; methodology, R.F.V., A.S., and J.S.; project administration, I.G.C.; writing—original draft preparation, R.F.V., A.S., J.S., and V.A.; writing—review and editing, R.F.V., J.S., and V.A.; supervision, I.G.C. All authors have read and agreed to the published version of the manuscript.

Funding: The authors thank the Spanish MINECO (MAT2016 46755-R), Generalitat de Catalunya (SGR-1777) and the support of European Regional Development Fund of the European Union in the framework of the Operational Program (FEDER-Catalonia 2014-2020).

Data Availability Statement: The data presented in this study are available on request from the corresponding author.

Conflicts of Interest: The authors declare no conflict of interest. The funders had no role in the design of the study; in the collection, analyses, or interpretation of data; in the writing of the manuscript, or in the decision to publish the results.

References

- Schweitzer, P.A. *Paint and Coatings: Application and Corrosion Resistance*; CRC Press: Boca Raton, FL, USA, 2006; ISBN 9781574447026.
- Dogan, H.; Findik, F.; Oztarhan, A. Comparative study of wear mechanism of surface treated AISI 316L stainless steel. *Ind. Lubr. Tribol.* **2003**, *55*, 76–83. [[CrossRef](#)]
- Chavan, N.M.; Kiran, B.; Jyothirmayi, A.; Phani, P.S.; Sundararajan, G. The corrosion behavior of cold sprayed zinc coatings on mild steel substrate. *J. Therm. Spray Technol.* **2013**, *22*, 463–470. [[CrossRef](#)]
- Łatka, L.; Pawłowski, L.; Winnicki, M.; Sokołowski, P.; Malachowska, A.; Kozerski, S. Review of functionally graded thermal sprayed coatings. *Appl. Sci.* **2020**, *10*, 5153. [[CrossRef](#)]
- Cortés, R.; Garrido, M.Á.; Poza, P.; Martos, A.; Dosta, S.; García, I. Cold sprayed coatings for repairing damaged metallic structures. *Key Eng. Mater.* **2019**, *813*, 74–79. [[CrossRef](#)]
- Adachi, S.; Ueda, N. Wear and corrosion properties of cold-sprayed AISI 316L coatings treated by combined plasma carburizing and nitriding at low temperature. *Coatings* **2018**, *8*, 456. [[CrossRef](#)]

7. Dikici, B.; Yilmazer, H.; Ozdemir, I.; Isik, M. The effect of post-heat treatment on microstructure of 316L cold-sprayed coatings and their corrosion performance. *J. Therm. Spray Technol.* **2016**, *25*, 704–714. [[CrossRef](#)]
8. Yin, S.; Cizek, J.; Yan, X.; Lupoi, R. Annealing strategies for enhancing mechanical properties of additively manufactured 316L stainless steel deposited by cold spray. *Surf. Coatings Technol.* **2019**, *370*, 353–361. [[CrossRef](#)]
9. Assadi, H.; Kreye, H.; Gärtner, F.; Klassen, T. Cold spraying – A materials perspective. *Acta Mater.* **2016**, *116*, 382–407. [[CrossRef](#)]
10. Rokni, M.R.; Nutt, S.R.; Widener, C.A.; Champagne, V.K.; Hrabec, R.H. Review of relationship between particle deformation, coating microstructure, and properties in high-pressure cold spray. *J. Therm. Spray Technol.* **2017**, *26*, 1308–1355. [[CrossRef](#)]
11. Tului, M.; Bartuli, C.; Bezzon, A.; Marino, A.L.; Marra, F.; Matera, S.; Pulci, G. Amorphous steel coatings deposited by cold-gas spraying. *Metals* **2019**, *9*, 678. [[CrossRef](#)]
12. Villa, M.; Dosta, S.; Guilemany, J.M. Optimization of 316L stainless steel coatings on light alloys using Cold Gas Spray. *Surf. Coatings Technol.* **2013**, *235*, 220–225. [[CrossRef](#)]
13. Sousa, B.C.; Gleason, M.A.; Haddad, B.; Champagne, V.K.; Nardi, A.T.; Cote, D.L. Nanomechanical characterization for cold spray: From feedstock to consolidated material properties. *Metals* **2020**, *10*, 1195. [[CrossRef](#)]
14. Beckers, D.; Ellendt, N.; Fritsching, U.; Uhlenwinkel, V. Impact of process flow conditions on particle morphology in metal powder production via gas atomization. *Adv. Powder Technol.* **2020**, *31*, 300–311. [[CrossRef](#)]
15. Lagutkin, S.; Achelis, L.; Sheikhaliev, S.; Uhlenwinkel, V.; Srivastava, V. Atomization process for metal powder. *Mater. Sci. Eng. A* **2004**, *383*, 1–6. [[CrossRef](#)]
16. Suri, P.; Koseski, R.P.; German, R.M. Microstructural evolution of injection molded gas- and water-atomized 316L stainless steel powder during sintering. *Mater. Sci. Eng. A* **2005**, *402*, 341–348. [[CrossRef](#)]
17. Jeandin, M.; Rolland, G.; Descurninges, L.L.; Berger, M.H. Which powders for cold spray? *Surf. Eng.* **2014**, *30*, 291–298. [[CrossRef](#)]
18. Sun, W.; Tan, A.W.; Wu, K.; Yin, S.; Yang, X.; Marinescu, I.; Liu, E. Post-process treatments on supersonic cold sprayed coatings: A review. *Coatings* **2020**, *10*, 123. [[CrossRef](#)]
19. Ichikawa, Y.; Tokoro, R.; Tanno, M.; Ogawa, K. Acta Materialia Elucidation of cold-spray deposition mechanism by auger electron spectroscopic evaluation of bonding interface oxide film. *Acta Mater.* **2019**, *164*, 39–49. [[CrossRef](#)]
20. Sun, W.; Wei, A.; Tan, Y.; Marinescu, I.; Quan, W.; Liu, E. Adhesion, tribological and corrosion properties of cold-sprayed CoCrMo and Ti6Al4V coatings on 6061-T651 Al alloy. *Surf. Coat. Technol.* **2017**, *326*, 291–298. [[CrossRef](#)]
21. Ko, K.H.; Choi, J.O.; Lee, H. Intermixing and interfacial morphology of cold-sprayed Al coatings on steel. *Mater. Lett.* **2014**, *136*, 45–47. [[CrossRef](#)]
22. Bae, G.; Kumar, S.; Yoon, S.; Kang, K.; Na, H.; Kim, H.; Lee, C. Bonding features and associated mechanisms in kinetic sprayed titanium coatings. *Acta Mater.* **2009**, *57*, 5654–5666. [[CrossRef](#)]
23. Yin, S.; Cizek, J.; Cupera, J.; Hassani, M.; Luo, X.; Jenkins, R.; Xie, Y.; Li, W.; Lupoi, R. Formation conditions of vortex-like intermixing interfaces in cold spray. *Mater. Des.* **2021**, *200*, 1–10. [[CrossRef](#)]
24. Schmidt, T.; Gaertner, F.; Kreye, H. New developments in cold spray based on higher gas and particle temperatures. *J. Therm. Spray Technol.* **2006**, *15*, 488–494. [[CrossRef](#)]
25. Fukanuma, H.; Ohno, N.; Sun, B.; Huang, R. In-flight particle velocity measurements with DPV-2000 in cold spray. *Surf. Coatings Technol.* **2006**, *201*, 1935–1941. [[CrossRef](#)]
26. Jodoin, B.; Ajdelsztajn, L.; Sansoucy, E.; Zúñiga, A.; Richer, P.; Lavernia, E.J. Effect of particle size, morphology, and hardness on cold gas dynamic sprayed aluminum alloy coatings. *Surf. Coatings Technol.* **2006**, *201*, 3422–3429. [[CrossRef](#)]
27. Adachi, S.; Ueda, N. Effect of cold-spray conditions using a nitrogen propellant gas on AISI 316L stainless steel-coating microstructures. *Coatings* **2017**, *7*, 87. [[CrossRef](#)]
28. *Standard Test Method for Particle Size Distribution of Metal Powders and Related Compounds by Laser Scattering*; ASTM B822-02; ASTM International: West Conshohocken, PA, USA, 2002;
29. *Standard Test Method for Apparent Density of Powders using the Hall Flowmeter Funnel*; ASTM B212-99; ASTM International: West Conshohocken, PA, USA, 1999.
30. *Standard Test Method for Flow Rate of Metal Powders*; ASTM B213-03; ASTM International: West Conshohocken, PA, USA, 2003.
31. *Standard Guide for Metallographic Preparation of Thermal Sprayed Coatings*; ASTM E1920-03; ASTM International: West Conshohocken, PA, USA, 2003.
32. *Standard Guide for Preparation of Metallographic Specimens*; ASTM E3-01; ASTM International: West Conshohocken, PA, USA, 2001.
33. *Standard Test Method for Measurement of Metal and Oxide Coating Thickness by Microscopical Examination of a Cross Section*; ASTM B487-85; ASTM International: West Conshohocken, PA, USA, 2002.
34. *Standard Test Methods for Determining Area Percentage Porosity in Thermal Sprayed Coatings*; ASTM E2109-01; ASTM International: West Conshohocken, PA, USA, 2002.
35. *Standard Test Method for Microindentation Hardness of Materials*; ASTM E384-99; ASTM International: West Conshohocken, PA, USA, 2000.
36. *Standard Test Method for Adhesion or Cohesion Strength of Thermal Spray Coatings*; ASTM C633-17; ASTM International: West Conshohocken, PA, USA, 2017.
37. *Standard Test Method for Measuring Abrasion using the Dry Sand Rubber wheel Apparatus*; ASTM G65-00; ASTM International: West Conshohocken, PA, USA, 2000.

38. *Standard Test Method for Wear Testing with a Pin-on-Disk Apparatus*; ASTM G99-04; ASTM International: West Conshohocken, PA, USA, 2004.
39. *Standard Test Method for Conducting Potentiodynamic Polarization Resistance Measurements*; ASTM G59-97; ASTM International: West Conshohocken, PA, USA, 2003.
40. *Standard Practice for Calculation of Corrosion Rates and Related Information from Electrochemical Measurements*; ASTM G102-89; ASTM International: West Conshohocken, PA, USA, 1999.
41. Hoeges, S.; Zwiren, A.; Schade, C. Additive manufacturing using water atomized steel powders. *Met. Powder Rep.* **2017**, *72*, 111–117. [[CrossRef](#)]
42. Sklyar, M.O.; Turichin, G.A.; Klimova, O.G.; Zotov, O.G.; Topalov, I.K. Microstructure of 316L stainless steel components produced by direct laser deposition. *Steel Transl.* **2016**, *46*, 883–887. [[CrossRef](#)]
43. *Standard Specification for Chromium and Chromium-Nickel Stainless Steel Plate, Sheet, and Strip for Pressure Vessels and for General Applications*; ASTM A240/A240M-04a; ASTM International: West Conshohocken, PA, USA, 2004.
44. Wong, W.; Vo, P.; Irissou, E.; Ryabinin, A.N.; Legoux, J.; Yue, S. Effect of particle morphology and size distribution on cold-sprayed pure titanium coatings. *J. Therm. Spray Technol.* **2013**, *22*, 1140–1153. [[CrossRef](#)]
45. Spencer, K.; Zhang, M.X. Optimisation of stainless steel cold spray coatings using mixed particle size distributions. *Surf. Coatings Technol.* **2011**, *205*, 5135–5140. [[CrossRef](#)]
46. Chu, X.; Che, H.; Teng, C.; Vo, P.; Yue, S. A multiple particle arrangement model to understand cold spray characteristics of bimodal size 316L/Fe powder mixtures. *Surf. Coatings Technol.* **2020**, *381*, 1–8. [[CrossRef](#)]
47. Wang, Y.; Adrien, J.; Normand, B. Porosity characterization of cold sprayed stainless steel coating using three-dimensional X-ray microtomography. *Coatings* **2018**, *8*, 326. [[CrossRef](#)]
48. Mindivan, H.; Kale, A.; Berse, U.; Samur, R. A comparative study of thermal sprayed AISI 316L stainless steel coatings. *El-Cezeri J. Sci. Eng.* **2017**, *4*, 127–134.
49. Zhao, L.; Lugscheider, E. Influence of the spraying processes on the properties of 316L stainless steel coatings. *Surf. Coatings Technol.* **2002**, *162*, 6–10. [[CrossRef](#)]
50. Li, Q.; Song, P.; Ji, Q.; Huang, Y.; Li, D.; Zhai, R.; Zheng, B.; Lu, J. Microstructure and wear performance of arc-sprayed Al/316L stainless-steel composite coating. *Surf. Coatings Technol.* **2019**, *374*, 189–200. [[CrossRef](#)]
51. Luzin, V.; Spencer, K.; Zhang, M.X. Residual stress and thermo-mechanical properties of cold spray metal coatings. *Acta Mater.* **2011**, *59*, 1259–1270. [[CrossRef](#)]
52. Maestracchi, R.; Sova, A.; Jeandin, M.; Malhaire, J.M.; Movchan, I.; Bertrand, P.; Smurov, I. Deposition of composite coatings by cold spray using stainless steel 316L, copper and Tribaloy T-700 powder mixtures. *Surf. Coatings Technol.* **2016**, *287*, 1–8. [[CrossRef](#)]
53. Sova, A.; Grigoriev, S.; Okunkova, A.; Smurov, I. Cold spray deposition of 316L stainless steel coatings on aluminium surface with following laser post-treatment. *Surf. Coatings Technol.* **2013**, *235*, 283–289. [[CrossRef](#)]
54. Xie, Y.; Planche, M.P.; Raelison, R.; Liao, H.; Suo, X.; Herve, P. Effect of substrate preheating on adhesive strength of SS 316L cold spray coatings. *J. Therm. Spray Technol.* **2016**, *25*, 123–130. [[CrossRef](#)]
55. Pukasiewicz, A.G.M.; Sucharski, G.B.; Siqueira, I.B.A.F.; de Andrade, J.; Váz, R.F.; Procopiak, L.A.J. Corrosion resistance of iron-based alloy coatings deposited by HVOF process. In Proceedings of the ITSC 2019 - Proceedings of the International Thermal Spray Conference, Yokohama, Japan, 26–29 May 2019; Azarmi, F., Lau, Y., Veilleux, J., Widener, C., Toma, F., Koivuluoto, H., Balani, K., Li, H., Shinoda, K., Eds.; ASM International: Yokohama, Japan, 2019; pp. 359–368.
56. Zhang, X.G. Galvanic corrosion. In *Uhlig's Corrosion Handbook*; Revie, R.W., Ed.; Wiley: Hoboken, NJ, USA, 2011; pp. 123–143. ISBN 9780470080320.
57. Fellah, M.; Labaiz, M.; Assala, O.; Iost, A.; Dekhil, L. Tribological behaviour of AISI 316L stainless steel for biomedical applications. *Tribology* **2013**, *7*, 135–149. [[CrossRef](#)]
58. Qin, W.; Kang, J.; Li, J.; Yue, W.; Liu, Y.; She, D.; Mao, Q.; Li, Y. Tribological behavior of the 316L stainless steel with heterogeneous lamella structure. *Materials* **2018**, *11*, 839. [[CrossRef](#)] [[PubMed](#)]
59. Fu, L.; Li, L.; Li, D.Y. Further look at correlation between ASTM G65 rubber wheel abrasion and pin-on-disc wear tests for data conversion. *Tribol.-Mater. Surfaces Interfaces* **2013**, *7*, 109–113. [[CrossRef](#)]

4.2. Geometric Limitations of CSAM Deposition Strategies

Compared to other AM techniques, especially laser-based ones, CSAM has the advantages of a high deposition rate, in the magnitude of $\text{kg}\cdot\text{h}^{-1}$ and deposition efficiency, $>99\%$ for some materials, like pure Ti and pure Cu; however, some limitations have to be listed too, as poor interparticular bonding strength that results in poor mechanical properties and fatigue life, and limited geometric accuracy, which restricts CSAM to make just a few simple geometries. This last one has been studied, and different deposition and robot strategies are reported in the literature for controlling the CSAM-ed geometric aspects and accuracy.

4.2.1. Conventional Approach to Produce CSAM-ed Parts

Simple robot strategies have been the most used deposition strategies for thermal spraying, including CS coating depositions. The simple strategies are called traditional for the following analysis, and the traditional has been applied for a flat substrate surface and tubular or cylindrical. Traditional strategies have a common characteristic: the CS powder-laden jet reaches the substrate at a normal angle, improving the material quality since the maximum V_{impact} is achieved. One of the CSAM traditional strategies is the rotation of a tubular or cylindrical substrate, which is coated by CS-ed layers while rotating around its axis of symmetry, as presented schematically in Figure 24.

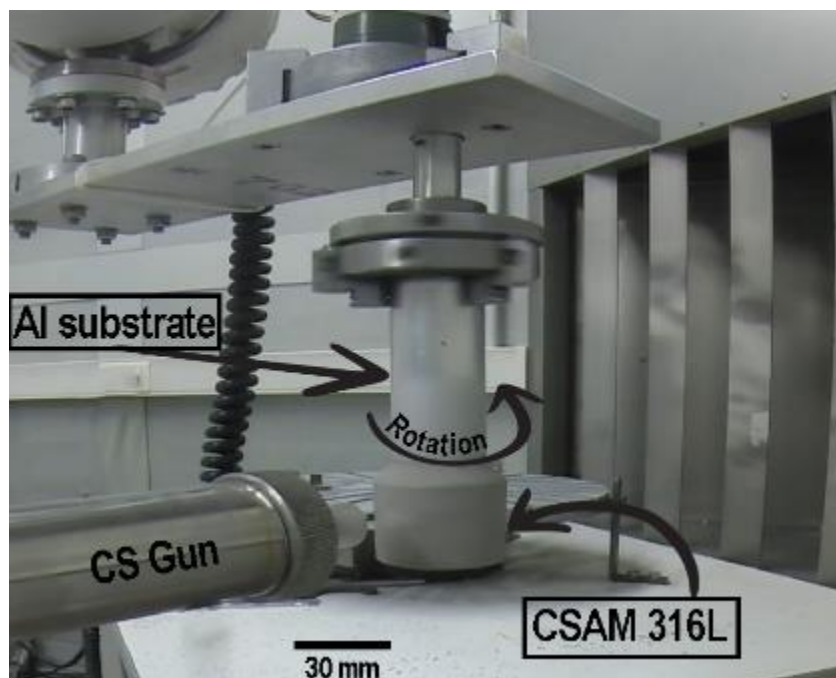


Figure 24: CSAM rotation strategy scheme. Material: 316L powder and 3 mm wall thick Al pipe substrate.

It results in high bonding strength and homogeneous residual stress distribution. However, this strategy is geometric limited to symmetrical parts, although it covers a good range of CSAM-ed parts, such as piping elements, e.g., valve bodies and flanges. CSAM rotation strategy can easily be combined with other CSAM strategies for more complex geometries. Figure 24 presents the CSAM rotation strategy depositing 316L on Al tubular substrate, with the CS Kinetiks gun kept static and the substrate rotating and moving linearly following the designed path length.

The CSAM traditional strategy, which keeps the CS powder-laden jet perpendicular to the substrate surface, is the most common strategy for CS coating deposition on flat surfaces because it guarantees the maximum V_{particle} at the impact with the substrate. Figure 25 presents a CSAM traditional strategy scheme in which the CS particle-laden jet is in the Z-direction and the substrate surface in the XY-plane. Figure 25 also shows the final pyramid-like shape obtained for the CSAM-ed 316L part. The same strategy is the standard for other thermal spray techniques, e.g., HVOF and APS. However, employing this CSAM traditional strategy results in low geometric accuracy, building the CSAM-ed deposit with a pyramid-like shape, i.e., inclined sidewalls.

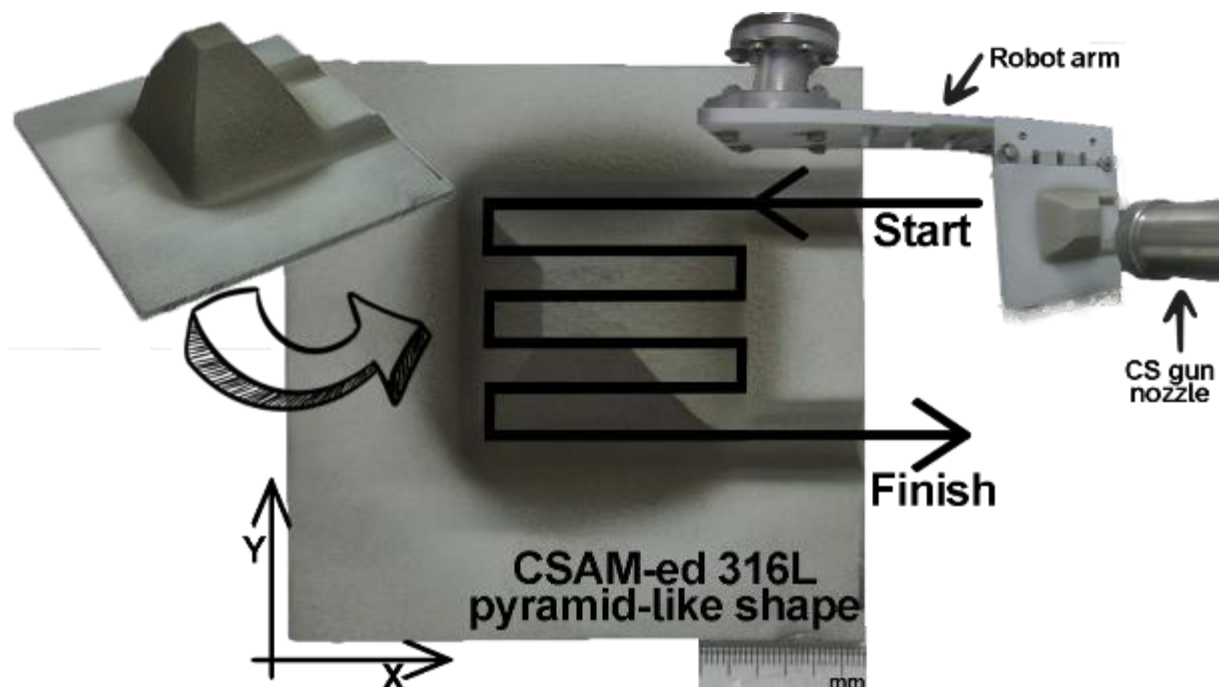


Figure 25: CSAM traditional strategy scheme for a flat substrate. Material: 316L powder and 3 mm thick Al substrate.

4.2.1.1. Effects and Optimization of CSAM Traditional Strategy Parameters on Part's Shape

Controlling the deposit sidewall inclination is a challenge for CSAM. This inclination results from the materials' sprayed properties, CS powder-laden jet characteristics, and substrate geometry. The CS particle-laden jet has a density of particle inhomogeneous, and its center concentrates more particles than its periphery by a Gaussian distribution, which is a different and particular distribution for each feedstock material. Besides that, the velocity of particles in the jet's center is higher, improving the bonding, DE, and cohesion of particles in this region. As a result, more particles usually bond where the jet's center reaches the substrate than on its periphery, producing a pyramid-like deposit, also named the tapering effect [57,58]. This effect is neglected by spraying over the substrate edges, i.e., a complete substrate surface covering, and not only in a specific area of the substrate surface, i.e., spraying only on the center of the plate, Figure 26. It is deeply discussed in Article 3.

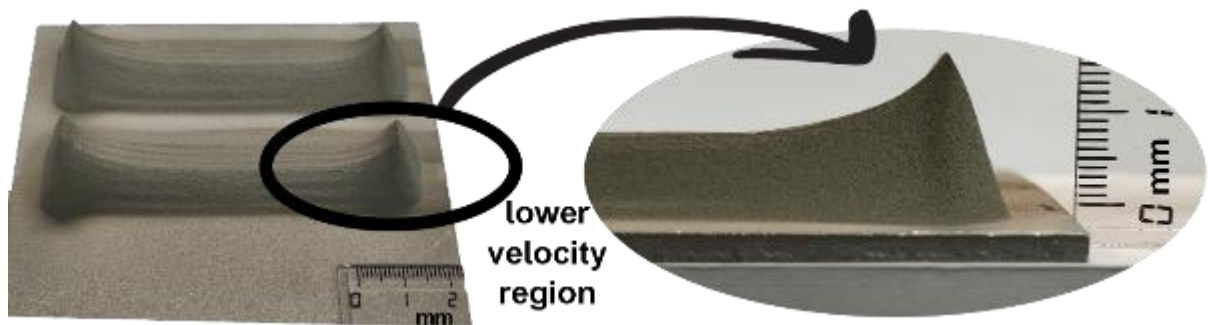


Figure 26: Results of reducing the robot velocity at its path corners. Material: 316L powder and 3 mm thick Al plate substrate.

An intent to reduce the CSAM-ed part sidewall inclination was varying the robot velocity, reducing it at the path corners. It was assumed that a lower velocity at the robot path corners should result in higher DE during the first layers, avoiding the pyramid formation, or at least more particles bonded due to a longer spraying time. However, the result was the formation of “mountains” on these path corners and the undesired sidewall angle, as seen in Figure 26 for CSAM-ed 316L. An extrapolation of this strategy was keeping the gun at the robot path corners, $v = 0$, for a second to prevent the sidewall angle initiation. This result is presented in Figure 27, with a progressive mountain formation in this endpoint with the number of layers.

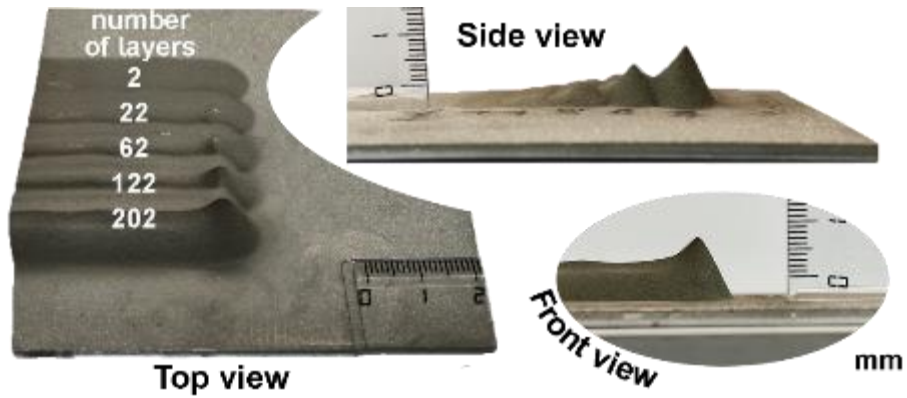


Figure 27: Results for CSAM stopping in the robot path corners. Material: 316L powder and 3 mm thick Al plate substrate.

The effect of the low velocity of particles at the CS powder-laden jet periphery supplants the effect of longer spraying time at the robot path corners. This velocity remains below the V_{cr} , derailing the bonding of particles. Besides that, after the inclined sidewall formation, the particles reach the surface with an unfavorable angle by a vector velocity decomposition, making the V_{impact} even lower. This vector decomposition is better presented in Article 5.

Another parameter optimization proved for CSAM traditional strategy was varying the robot path length of each layer, making the gun surpass the previous layer. This strategy aimed to eliminate the initiation of the sidewall inclination by spraying this area with more particles each pass, making the dense powder-laden jet center invades the region where was just its periphery in the previous layer. The results are presented in Figure 28 for CSAM-ed 316L, where the positive values indicate increasing the path length, e.g., +0.3 mm each pass, and the negative values go in the opposite direction. For the “-0+0” sample, it is noticed a shape symmetry with equal small mountains on both sidewalls.

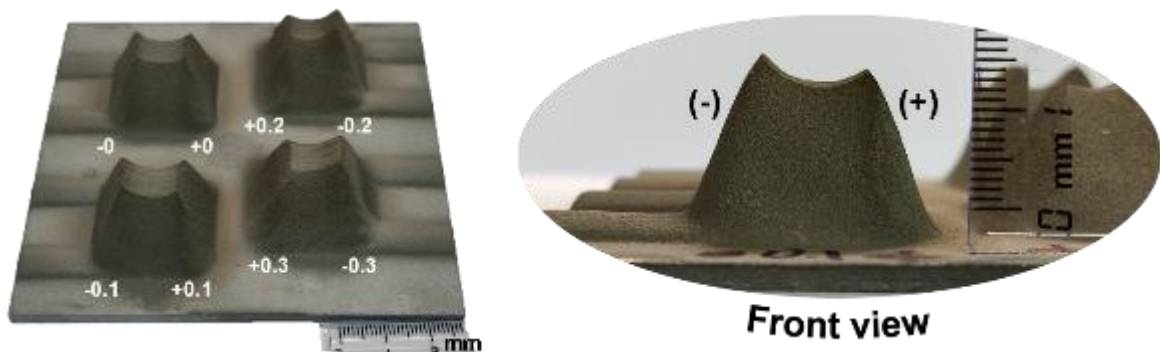


Figure 28: Results for CSAM advancing the path length each layer. Material: 316L powder and 3 mm thick Al plate substrate.

However, for the samples with the variation of path length, the positive values produced smaller mountains than the negative ones, indicating a more homogeneous or planar CSAM part top topography, while the negative values, shorting the robot travel each layer, resulted in higher mountains, as observed in Figure 27 front view. However, this strategy did not affect the sidewall angle, resulting in the same angle for all of the CSAM strategy parameters selected.

The robot manipulation has been used to rectify the CSAM-ed geometry. The layers grow with the typically inclined sidewall, but after a certain part height, a correction layer on the inclined sidewalls is applied. This strategy is reported in the literature by Nardi et al. [59] and Wu et al. [60], among others, explaining how a sequence of spraying layers with different angles with the substrate can result in a controlled part sidewall inclination. It also makes it feasible to obtain a more complex geometry, like CSAM-ed Ti square thin-wall section as presented by Vargas-Uscategui et al. [43]; however, employing two robot arms and a complex programming. These solutions limit the CSAM industrial application mainly because of the time consumption for the robot programming for a specific geometry.

This robot strategy for the sidewall angle correction layer was proved for CSAM 316L. After optimizing parameters, a set of layers was sprayed in the vertical direction (perpendicular to the substrate face), another set inclining the CS gun, again a set in vertical, and another set inclined, alternatively. The previous depositions helped to determine the gun inclination and the number of layers for each set or step of deposition because the objective was making a vertical sidewall angle. In the end, these parameters can be optimized for any desired off-normal angle, but in this experiment, 90 degrees with the substrate plane was the target.

The result of the CSAM correction layers strategy is presented in Figure 29, showing the scheme or sequence of deposition and the number of layers for each step. The final result is also noticed with an explicit correction of the sidewall angle, from 40 to 5 degrees, without visual cracks or decohesion between the layers or steps. A microscopical analysis showed a high density in all the steps, porosity <1%; however, an evident interface between the steps, exemplified by arrows between steps 1 and 3. This is the CSAM-ed material's weakest region, and a premature failure can occur in this interface due to the aligned defects.

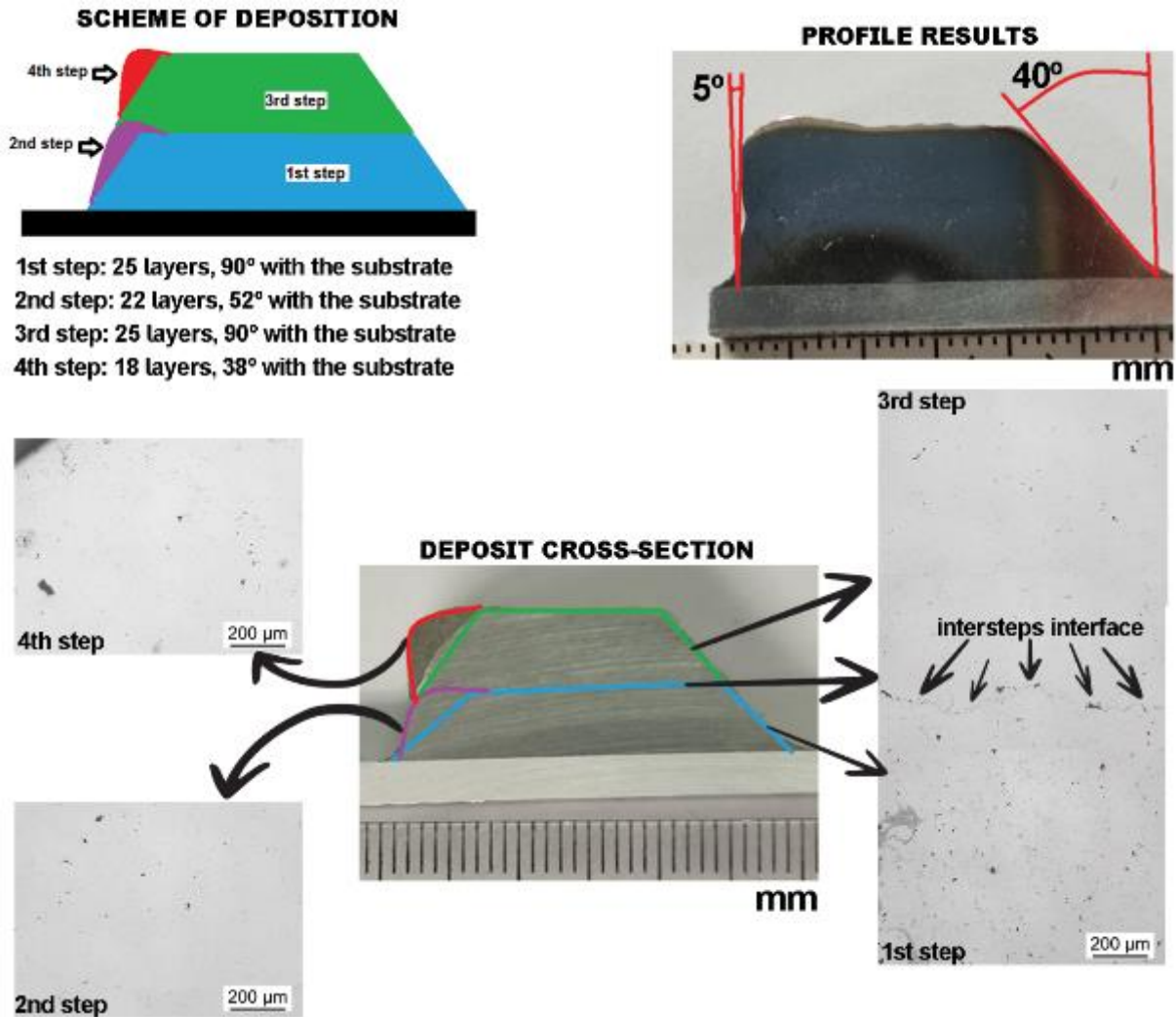


Figure 29: Results of using the sidewall inclination layer correction strategy. Material: 316L powder and 3 mm thick Al plate substrate.

4.2.2. *New Approach to Produce CSAM-ed Parts*

An alternative solution presented in this work is controlling each layer's sidewall inclination and thickness, making robot movements that rectify the inevitable pyramid-like shape of each isolated CS layer. A method named Metal Knitting has been developed, based on deposition with a non-linear path described by the robot but a constantly changing deposition angle. The final movement is a virtual cone-like, as presented in detail in Article 3. This CSAM strategy was proved for thin and high walls, made by a single robot line employing the Metal knitting movements. In addition, it was used to produce bulks, employing many parallel robot path lines. This last strategy is compared with the CSAM traditional strategy in Article 5, regarding their microstructures and mechanical properties.



ARTICLE 3 “METAL KNITTING: A NEW STRATEGY FOR COLD GAS SPRAY ADDITIVE MANUFACTURING”





R.F. Vaz, V. Albaladejo, J. Sanchez, U. Coaña, Z.G. Corral, H. Canales, I.G. Cano

 [10.3390/ma15196785](https://doi.org/10.3390/ma15196785)

This work presents a new conceptual strategy for CSAM spraying. The controlled manipulation of the robot arm combined with the proper spraying parameters aim to optimize the deposition efficiency and the adhesion of particles on the part sidewalls, resulting in geometries from thin straight walls, less than 5 mm thick, up to large bulks. This new strategy, Metal Knitting, is presented regarding its fundamentals and by comparing the parts' geometries produced by Metal Knitting with the CSAM traditional strategies. The Metal Knitting made parts with vertical sidewalls, contrasting the 40 degrees of inclination obtained by the CSAM traditional strategy. Their mechanical properties, microstructures, hardness, and porosity are also compared for Cu, Ti, Ti6Al4V, 316L stainless steel, and Al parts.

Article

Metal Knitting: A New Strategy for Cold Gas Spray Additive Manufacturing

Rodolpho F. Vaz ¹, Vicente Albaladejo-Fuentes ^{1,*}, Javier Sanchez ¹, Unai Ocaña ¹, Ziortzia G. Corral ¹, Horacio Canales ² and Irene G. Cano ¹

¹ Thermal Spray Centre CPT, Universitat de Barcelona, Carrer Martí i Franques 1, 7a planta, 08028 Barcelona, Spain

² Cátedras CONACyT—Centro de Ingeniería y Desarrollo Industrial (CIDESI), Av. Playa Pie de la Cuesta No. 702, Desarrollo San Pablo, Santiago de Querétaro C.P. 76125, Mexico

* Correspondence: valbaladejo@cptub.eu

Abstract: Cold Spray Additive Manufacturing (CSAM) is an emergent technique to produce parts by the additive method, and, like other technologies, it has pros and cons. Some advantages are using oxygen-sensitive materials to make parts, such as Ti alloys, with fast production due to the high deposition rate, and lower harmful residual stress levels. However, the limitation in the range of the parts' geometries is a huge CSAM con. This work presents a new conceptual strategy for CSAM spraying. The controlled manipulation of the robot arm combined with the proper spraying parameters aims to optimize the deposition efficiency and the adhesion of particles on the part sidewalls, resulting in geometries from thin straight walls, less than 5 mm thick, up to large bulks. This new strategy, Metal Knitting, is presented regarding its fundamentals and by comparing the parts' geometries produced by Metal Knitting with the traditional strategy. The Metal Knitting described here made parts with vertical sidewalls, in contrast to the 40 degrees of inclination obtained by the traditional strategy. Their mechanical properties, microstructures, hardness, and porosity are also compared for Cu, Ti, Ti6Al4V, 316L stainless steel, and Al.

Keywords: cold gas spray; strategy; Metal Knitting; additive manufacturing; geometries



Citation: Vaz, R.F.;

Albaladejo-Fuentes, V.; Sanchez, J.; Ocaña, U.; Corral, Z.G.; Canales, H.; Cano, I.G. Metal Knitting: A New Strategy for Cold Gas Spray Additive Manufacturing. *Materials* **2022**, *15*, 6785. <https://doi.org/10.3390/ma15196785>

Academic Editor: Damon Kent

Received: 25 August 2022

Accepted: 26 September 2022

Published: 30 September 2022

Publisher's Note: MDPI stays neutral with regard to jurisdictional claims in published maps and institutional affiliations.



Copyright: © 2022 by the authors. Licensee MDPI, Basel, Switzerland. This article is an open access article distributed under the terms and conditions of the Creative Commons Attribution (CC BY) license (<https://creativecommons.org/licenses/by/4.0/>).

1. Introduction

Manufacturing industry is always looking for new cost-effective processes showing minimal raw material consumption, zero waste generation, and minimum energy consumption. Therefore, it promotes the rise of sustainable and more efficient technologies capable of responding to these needs [1]. During recent decades, many alternatives to traditional production methods have arisen in the market with the capabilities to fabricate unique components made in special alloys, which are not feasible by the conventional fabrication processes due to production complexity, properties, or even the high costs [2]. Beginning with polymer 3D printing in the 1980s and advancing its concept to producing metallic parts, the Additive Manufacturing (AM) techniques have expanded greatly in this period. They have been presented as an alternative to satisfy some of the above-mentioned industry and societal needs. A simple research in Scopus' database can demonstrate the relevance of these technologies, where the number of documents published per year using the query "additive AND manufactur*" has grown from 278 works in 2000 to 781 in 2010 and then 10,751 in 2021, an extraordinary increase of 1300% in only one decade.

In the case of metallic AM components, some processes have become widespread, such as arc welding, laser melting or sintering, and cold gas spray (CS), among other methods [3–5]. Each process has different characteristics, limitations, or pros and cons, e.g., laser processes can produce very complex geometries but slowly and generate tensile residual stress in the material [6]. The welding or assembling of small AM individual parts is proposed in the literature as the best option to produce a large component [7].

However, this welding may result in distortion, shrinkage, or high tensile residual stress in the final AM part. Nevertheless, most of these AM techniques are based on the melting of raw material, which is an issue for some materials, such as the oxygen-sensitive Ti alloys, limiting the application of the technology.

1.1. Cold Gas Spray as an Additive Manufacturing Process

CS is a method of depositing powdered materials in the solid state, in which the cohesion of powder particles in the deposit is generated because of their impact under supersonic velocity onto a substrate/surface. For this, the CS equipment heats a gas in a chamber, discharging it under high pressure through a De Laval nozzle and accelerating it to supersonic velocity, dragging the feedstock powder under its recrystallization temperature [8,9].

The literature presents the application of CS for AM for a large number of materials, highlighting the components made from 316L stainless steel [10–14], Cu alloys [15–17], and Ti alloys [18–21], but not limited to them since Al alloys [21–24], Ni superalloys [25,26], maraging steel [27–29], and many others have also been studied. Moreover, these CSAM components have interested different sectors, such as aerospace, automotive, energy, medical, and marine sectors, among others [8,30]. In this sense, Prashar and Vasudev [31] list the CSAM benefits for sustainable manufacturing: optimizing product structures and designs, no environmental effect, component restoration rather than replacement, and improving the valuable life service of the component. The scientific interest in CSAM can be confirmed by a simple search in Scopus' database searching by the query "additive AND manufactur* AND cold AND spray*" OR "3d AND print* AND cold AND spray*", resulting in zero documents until 2011, 12 in 2015, 86 in 2020, and 81 in 2021, increasing by 675% the number of documents in the last five years.

In recent years, most of these studies have focused on CS mechanical properties and high deposition efficiency (DE). DE is the ratio between the CS sprayed powder mass and the consolidated part mass, which is directly influenced by the velocity reached by the particles when impinging the surface. Regarding CS parameters, adjustments and variations in CS working gas temperature and pressure, the nozzle design and geometry, and the spraying stand-off distance have been effective for improving the DE particle cohesion. It is widely accepted that the sprayed particles have to impact the substrate with a velocity between a critical or minimum and a maximum limit value.

1.2. CSAM Deposition Strategies

The traditional strategy used in CS for powder deposition is based on a linear and normal movement of the CS gun with respect to the substrate surface, which might repeat for depositing consecutive layers, or alternating this direction, as presented by arrows in Figure 1. This extended deposition strategy promotes the growth of CSAM part sidewalls off-normal angle with the substrate surface, which limits the use of CSAM to near-net-shape components production that should finally be post-machined until the desired geometry and dimensions are obtained. The inclination shown by CSAM part sidewalls usually leads to more or less slope depending on the material sprayed, CS spraying parameters, or the substrate geometry, such as spraying on its flat surface or edges. The literature presents some approaches to developing a suitable deposition strategy for CSAM. For instance, some authors have proposed that it is possible to compensate this inclination in consecutive spraying tests, making the particles laden jet perpendicular to this inclined surface [32–34], Figure 2. Here, it is mandatory to know the inclination angle of the growth sidewall and redress the geometry at the end. However, this strategy is not feasible when thin walls are intended. In addition, the modification of the spraying directions generates new interfaces in which the cohesion of the particles is weaker, promoting an inhomogeneity of final component properties.

The use of CSAM has grown in recent years. Some researchers have developed strategies to control the CSAM parts geometries, mainly regarding sidewall inclinations

because this is a considerable limitation for CSAM in producing freeform parts. The presence of undesired sidewall inclination represents a loss of spraying time and raw material, besides needing more post-machining time. An efficient alternative seen in the literature is the correction of the sidewall inclination by a sequence of layers with different CS jetting angles, Figure 2. However, it demands a specific robot strategy or parameters for each material and CS spraying condition. Thus, in this work, the authors aim to present the effectiveness of using a new CSAM deposition strategy in substitution for the CSAM traditional strategy commonly used. The strategies are compared not only by the CSAM geometries produced, mainly the sidewall angles inclination, but they are also evaluated regarding the microstructures obtained, and their physical and mechanical properties. The novelty in the Metal Knitting strategy is developing a robot strategy capable of producing thin vertical walls or large bulks, thereby eliminating geometry correction steps, which are demanded when using the traditional strategy.

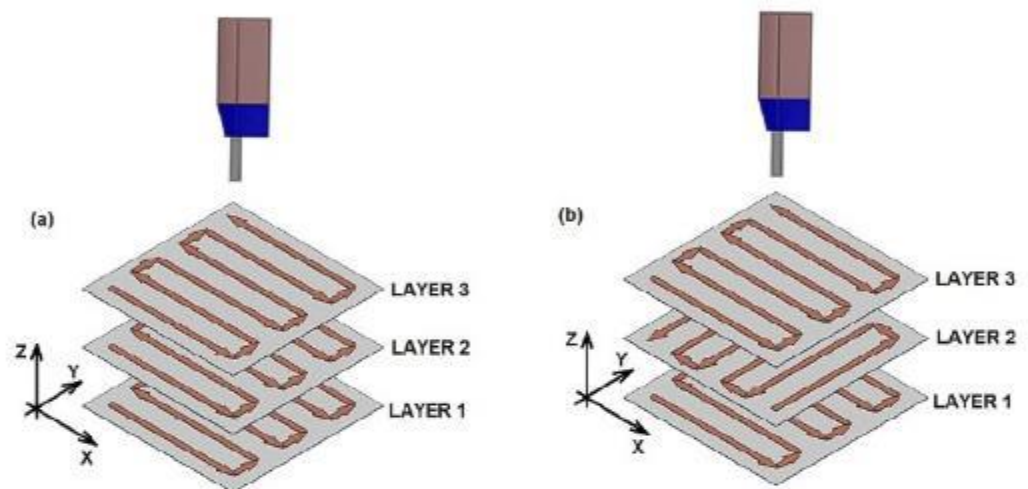


Figure 1. Strategies of robot path for CSAM, (a) traditional or bidirectional and (b) cross-hatching.

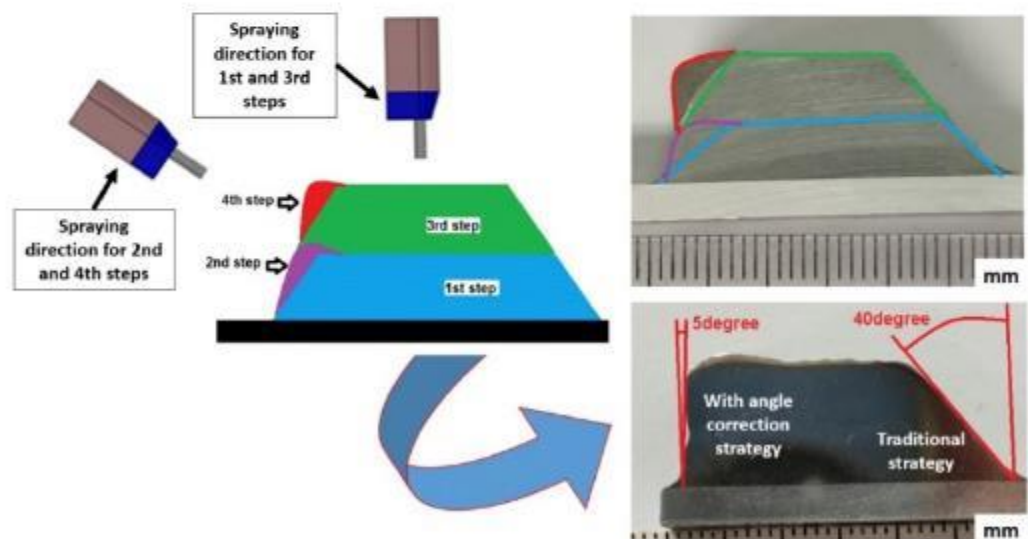


Figure 2. Scheme of strategy to compensate the sidewall inclination. The CSAM part cross-section is 316L on Al substrate.

2. Materials and Methods

316L stainless steel, pure Cu, pure Al, Ti grade 2 (pure Ti), and Ti grade 5 (Ti6Al4V) powders were sprayed using the newly developed and traditional CS strategies. Irregular and spherical water atomized powder were used in these tests in order to show the capabil-

ities for generating controlled geometries by Metal Knitting using powder with different morphologies. The feedstock powders' particle size distribution was measured by laser scattering in LS13320 (Beckman Coulter, Brea, CA, USA), and the particles' shapes were interpreted from SEM images obtained in equipment Pro Desktop (Phenon, Eindhoven, The Netherlands). The feedstock powders' chemical composition was measured by Inductively Couple Plasma (ICP) in equipment Optima ICP-OES 3200 RL (Perkin Elmer, Waltham, MA, USA) and is presented in Table 1.

Table 1. Feedstock powders chemical composition (wt.%).

Powder	Cr	Ni	Mo	Mn	Si	Fe	Cu	Ti	Al	V
316L	16	12	2.5	0.5	<0.1	Bal.				
Cu							100			
Ti								100		
Ti6Al4V								Bal.	5.9	3.9
Al									100	

The five feedstock powders for CSAM have the shapes obtained by SEM presented in Figure 3, where it is possible to see the typical irregular shape for the water-atomized ones, 316L and Al, as well as the spherical gas-atomized Ti alloys and pure Cu. The powder size distribution is also presented in Figure 4, which is quite similar for all the powders and is in the range optimal for CS processes because particles out of this range may not reach the optimal velocity at the impact on the substrate [35,36].

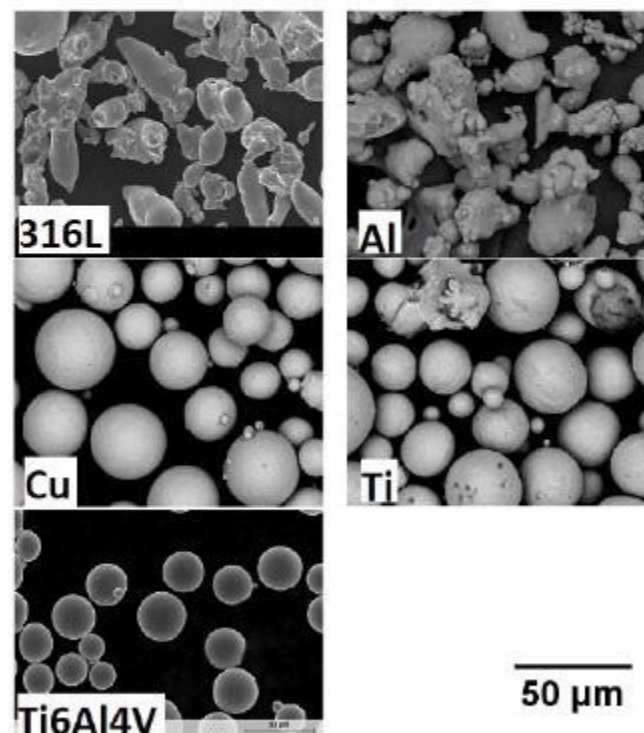


Figure 3. SEM images of feedstock powders for CSAM.

Regarding the particle shape, the water-atomized 316L and Al are cheaper options than gas-atomization powders since the production costs are lower for this manufacturing process. The raw material price is an important factor when applying the CSAM technique due to its heavy impact on the part's final costs. Previously, Vaz et al. [10] presented for CS 316L coatings the quite similar performance of gas-atomized and water-atomized powders, regarding mechanical properties, wear resistance, and corrosion behavior. It supports the selection of the irregular powder used in this article.

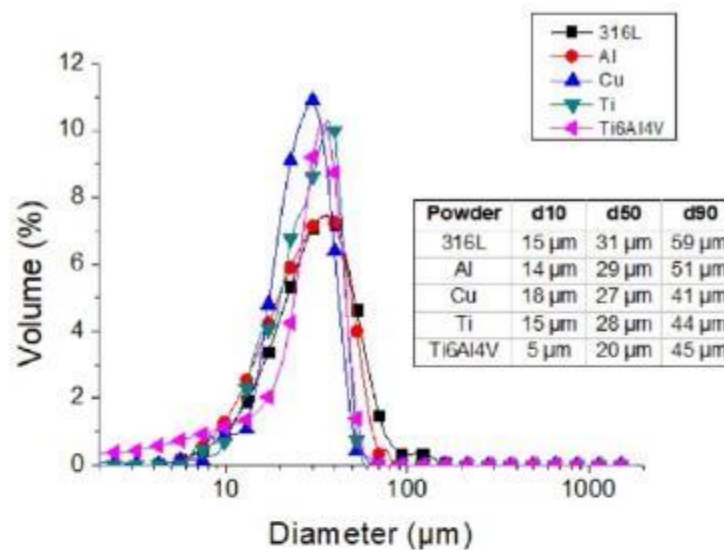


Figure 4. Feedstock particle size distribution for CSAM.

The CSAM depositions were performed using PCS100 equipment (Plasma Giken, Saitama, Japan) and N_2 as working gas. The main spraying parameters are indicated in Table 2. The robot was an IRB 2400 M2004 (ABB, Västerås, Sweden) and the programming was performed in ABB RobotStudio v6.08.01 software. The PCS100 gun was kept static while the sample holder performed all the robot arm movements. For the CSAM samples deposited by the traditional strategy, the robot path followed the Figure 1a scheme, with velocity of $500 \text{ mm}\cdot\text{s}^{-1}$.

Table 2. CS spraying parameters.

Powder	N_2 Temperature [°C]	N_2 Pressure [MPa]	Standoff Distance [mm]
316L	1000	6.0	25
Cu	700	3.0	25
Ti	900	6.4	25
Ti6Al4V	1000	6.5	25
Al	450	3.0	25

The CSAM parts produced were evaluated regarding the geometries obtained, sidewall angles, and visual characteristics. In addition, a visual inspection was performed to find CSAM part imperfections, such as cracks, delamination between the layers, and adhesion to the substrate, among others. The microhardness of samples was measured by means of HMV equipment, applying a load of 0.3 kgf (HV0.3) and presenting a mean value of 10 values for each sample. The metallographic preparation was carried out in accordance with the ASTM E1920-03 and ASTM E3-01 standards, and the porosity was analyzed from light microscopy images obtained in Leica DMI3000 M microscope at $200\times$ magnification, according to ASTM E2109-01 standard. For tensile testing, three samples of each CSAM part were manufactured by the wire Electrical Discharge Machining (EDM) process. A Zmart.Pro equipment (ZwickRoell, Eisengen, Germany) with an Xforce P 10 kN load cell was used for the tensile testing, with a load application velocity of $1.0 \text{ mm}\cdot\text{min}^{-1}$ (see Supplementary Materials).

3. Results and Discussions

3.1. Influence of Substrate Shape on CSAM Part Geometry

Before evaluating the effect of the new strategy for geometric control of CSAM deposits, 316L deposits using an irregular powder were produced by the traditional strategy that will be considered a CSAM benchmark for the Metal Knitting samples evaluations. Figure 5

shows a CSAM 316L deposit sprayed onto a carbon steel plate's thinnest face (5 mm) to highlight the effect of the traditional spraying strategy on the inclination of the sidewalls generated. Here, it can be observed that the CSAM sidewall inclinations are different for each substrate area or region scanned, considering the substrate's edge or flat surface. For example, from the substrate's edge, the CSAM 316L part grew up at 71 degrees relative to the substrate's flat face, while it grew at an angle of 28 degrees from a flat surface. Table 3 shows the sidewall angles obtained for 316L, Al, Cu, Ti, and Ti6Al4V as well. These results indicate that this inclination effect is dependent on the powder material sprayed, and not limited to stainless steel or irregular feedstock materials.

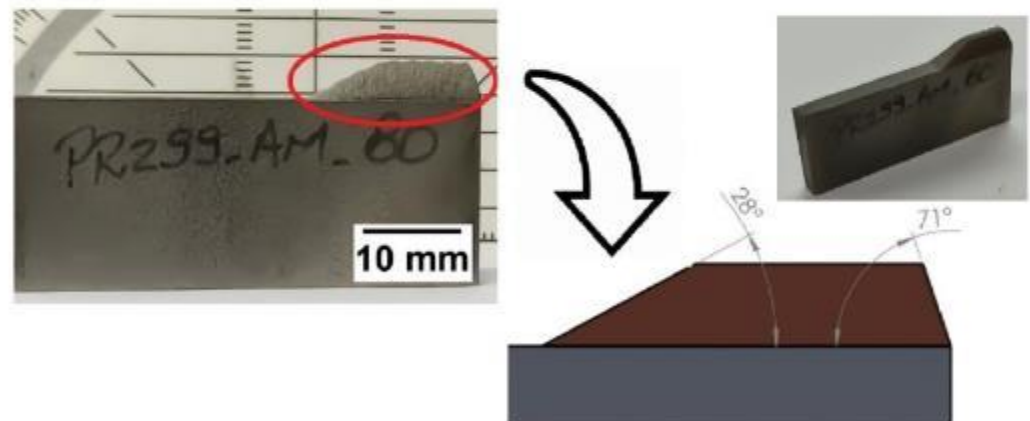


Figure 5. CSAM 316L growing from a substrate's flat surface or from its edge.

Table 3. Sidewall angles produced by traditional and Metal Knitting strategies.

Material	Sidewall Angle Relative to a Line Normal to the Substrate [Degree]			
	on Substrate's Flat Surface		on Substrate's Edge	
	Metal Knitting Strategy	Traditional Strategy	Metal Knitting Strategy	Traditional Strategy
316L	8	60	0	20
Al	0	45	0	5
Cu	0	75	0	25
Ti	10	45	0	0
Ti6Al4V	10	40	0	5

It is widely accepted that the velocity and the density of particles in the center of CS particles laden jet flow are higher than in its periphery [9,24,37–39]. A lower velocity and number of particles in the periphery of the CS particles laden jet produce a progressive thinner layer at the border of the sprayed layer (Figure 6), promoting a thickness distribution or single-track profile defined by a Gaussian distribution [40]. This effect explains the inclined sidewalls commonly obtained by the traditional spraying strategy in CSAM. The behaviour observed in different regions of the substrate is explained by considering the geometric features of the sample [38,41] since, for a deposition in a substrate edge, the CS particle plume passes completely through this edge, finishing its travel out of the sample, where the robot changes the direction and turns back to another pass. However, this does not occur for the deposition on a flat surface, where particle distribution in the CS particle plume always affects the formation and consolidation of CSAM part geometry because all the changes in robot movement directions are done on the substrate surface.

Besides considering the density of particles in different positions of the CS plume, it is worth considering that the farther the particles are radially from the jet center, the lower their velocities are, Figure 6. It is well known that the CS deposition and the part consolidation depend strongly on the velocity of the particles [42–44], but radially just a few millimetres from the CS jet center, the particles present a severe reduction in velocity, even to out of the CS deposition window of velocity. Previous CFD simulations by several

authors have predicted this behavior under specific CS parameters. For example, Al and Ti particles have a velocity of $700 \text{ m}\cdot\text{s}^{-1}$ close to the particles laden jet center, but radially 4 mm far from this center, the velocity falls to $500 \text{ m}\cdot\text{s}^{-1}$, a reduction of almost 30% [45–47]. For 316L, this trend is the same [48], which influences the CSAM part consolidated geometry.

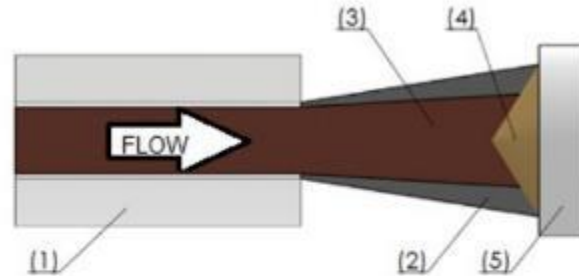


Figure 6. Scheme of CS particles laden jet. (1) Nozzle, (2) sparse particles and lower velocity particles laden jet, (3) concentrated particles and high-velocity particles laden jet, (4) sprayed material, (5) flat substrate.

Consequently, a not constant particles-laden jet is deposited onto the sprayed surface from the very beginning of the CS process, at the very first layer, which leads to the generation or growth of inclined sidewalls or geometries. This result can be directly correlated with a lower DE of particles in the periphery of the CS particles laden jet because of their above described lower impact velocity, producing a progressive thinner layer at the border of the sprayed layer [32]. Then, when subsequent particles reach the substrate, the previous sprayed material, with different angles at the edges, modifies the normal impact angle of the particles with the surface, which leads to a reduction of the DE and promotes the sidewall inclination layer by layer [32,38,39]. Higher impact angles reduce the velocity component perpendicular to the substrate by the sine of this angle, which is responsible for the particles' adherence reduction [38]. Rokni et al. [49] presented an insignificant change in particle properties by CS jet axis up to 20 degrees off-normal angle with the substrate. Li et al. [38] showed that a 30 degrees angle was enough to reduce DE from close to 100% to 40% for Al, and 50% for Cu, as an angle of 70 degrees promoted a DE of zero. The other velocity vector component, related to the cosine of the impacting angle, is a tangential velocity, which collaborates with the inclination of the CSAM part sidewall by an erosion mechanism [34,50].

Thus, in traditional CS spraying strategies based on a normal impact of particles onto the substrate or surface, an inclined CSAM part surface is established, due to the difference in velocity and density of particles in the CS particles laden jet periphery compared to its center. After a few layers of material deposition, this effect promotes the CS sprayed particles reaching the new target at off-normal impact angles, progressively reducing the DE in the periphery of the particles laden jet. Table 3 summarizes the sidewall angles produced by CSAM using traditional and Metal Knitting strategies. The higher control in this geometric CSAM part characteristic evidently results from the use of Metal Knitting, highlighting the depositions on a flat surface; e.g., Cu had 75 degrees with the vertical line by using traditional strategy versus zero degrees by employing Metal Knitting. However, this discrepancy of values was not seen on edges due to the reasons above-mentioned.

3.2. The Metal Knitting Strategy

The brand-new strategy presented in this work is named Metal Knitting, relating to the movements of needles dealing with yarn to make a woven fabric, which drastically modifies the relative gun/substrate movement from the traditional movements presented in the literature for the CSAM process to date. This new strategy aims to make the CS sprayed particles reach the substrate or the growing CSAM part with an angle that maximizes the DE at the sidewalls, simultaneously controlling the geometry growth of the CSAM part, Figure 7.

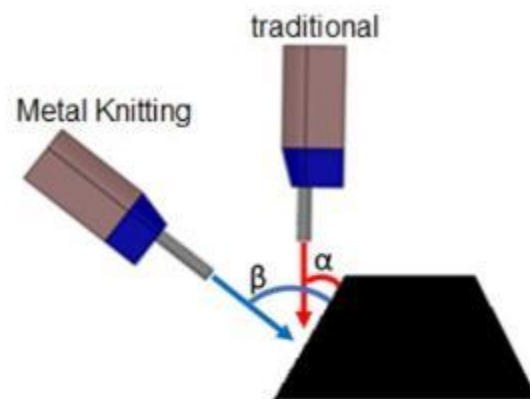


Figure 7. Scheme of the angle of impact of particles on an inclined surface by traditional (α) and Metal Knitting (β) strategies.

For this purpose, the Metal Knitting strategy impresses a circular-like movement on the substrate plane. Still, the CS particles laden jet is not perpendicular to this plane. The final path is a virtual frustum of a cone, with the axis of rotation perpendicular to the substrate plane, as presented schematically in Figure 8.

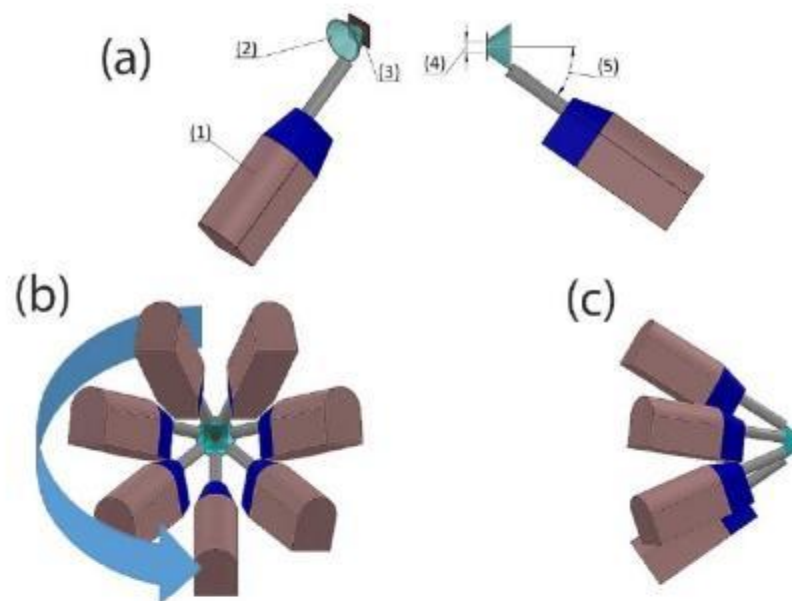


Figure 8. Metal Knitting strategy scheme. (a) (1) CS gun, (2) virtual frustum of cone path, (3) substrate, (4) radius, (5) angle. (b,c) simulation of different directions of view of CS gun describing the Metal Knitting movements.

3.2.1. Metal Knitting Parameters

The variables or parameters for Metal Knitting strategy and their influences on the CSAM part characteristics include:

- Velocity of the robot: the linear or tangential velocity described by the gun in the circular-like trajectory. The higher the velocity, the thinner the CSAM layer;
- Radius: the distance from the center of the circle to the circumference described by the particles laden jet center on the substrate surface plane, or the small radius of the virtual frustum of the cone path. Excessive radius value generates unevenness in the layer shape;
- Step: the distance from a circle to an adjacent circle. Excessive step value results in waves-like topography of the layer;

- Angle: the angle between the axis of rotation and the frustum of the cone generator described by the gun movement. Excessive angle reduces the DE by the powder's velocity component reaching the substrate.

3.2.2. The Metal Knitting Deposit Properties

A comparison between the CSAM 316L bulks produced by traditional and Metal Knitting strategies is presented in Figure 9, which also shows the real bulk part obtained. Identical deposits were CSAM fabricated with Ti and Ti6Al4V alloy powders with successful results. Visual inspection showed that none of the bulk parts produced (316L, Ti, and Ti6Al4V) presented any cracks or detachments from the substrate. In addition, the parts made by Metal Knitting showed smoother surfaces and more rounded edges compared to the rough finishing and sharp edges seen in the CSAM part produced by the traditional spraying strategy. In this sense, using the Metal Knitting strategy on the substrate's flat surface, CSAM 316L, Ti, and Ti6Al4V components showed a sidewall angle of around 80 degrees to the substrate surface. It is a significantly smaller inclination value than the inclination produced by the traditional strategy on a flat surface, as shown in Figure 9.

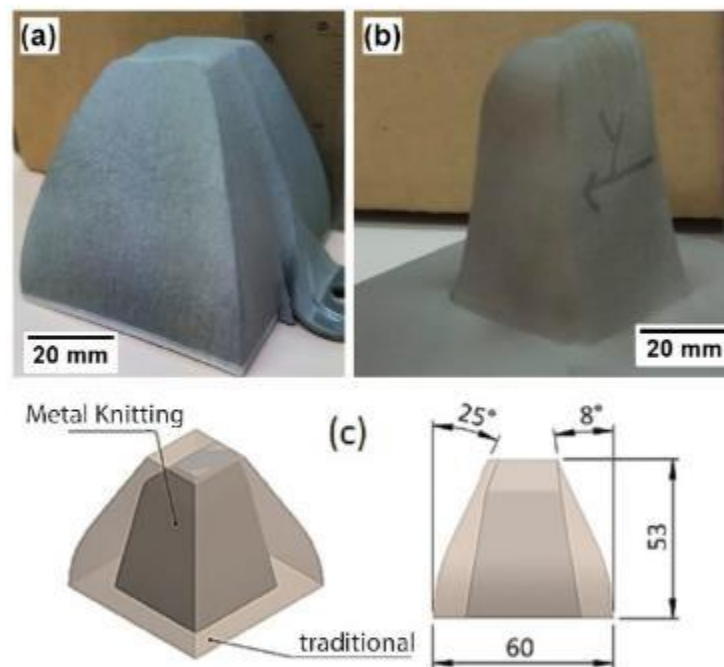


Figure 9. CSAM 316L bulks. (a) traditional strategy on the substrate edges and (b) Metal Knitting strategy on flat substrate. (c) scheme comparing the geometries obtained.

As indicated above, in CS deposition by the traditional strategy, the angle of impact of subsequent particles is always off-normal from the beginning of the process. In contrast, the Metal Knitting strategy can keep this particle impact angle constant throughout the process. As a result, during the cone-like Metal Knitting movement, the CS particles laden jet reaches the substrate with angles that promote higher DE in the side walls. It occurs by improving the velocity vector component normal to the impacting surface, as seen in the scheme presented in Figure 7, which improves the capabilities of the CSAM process to control the final geometry generated.

CSAM parts or any material obtained by CS have properties influenced by the cold-working, resulting from the severe plastic deformation under the material's recrystallization temperature. This increases the density of dislocations in the metal's crystalline structure and consequently improves the properties of the sprayed feedstock material. Figure 10 presents the as-sprayed CSAM microstructures obtained by Metal Knitting and traditional strategies, which is in consonance with observations in the literature. There is a trend of

higher density for the most ductile sprayed materials, Al and Cu, while harder materials resulted in a higher porosity, as seen for Ti6Al4V. This has influences on the material's properties, as summarized in Table 4. For the CSAM samples made by the traditional strategy, the microstructures, hardness, and porosity obtained were close to those presented in the literature for 316L [10,13,14,51], Al [21,23,24], Cu [16,17,21,52,53], and Ti alloys [19–21]; however, for Metal Knitting the literature did not present any result, because it is a brand-new strategy.

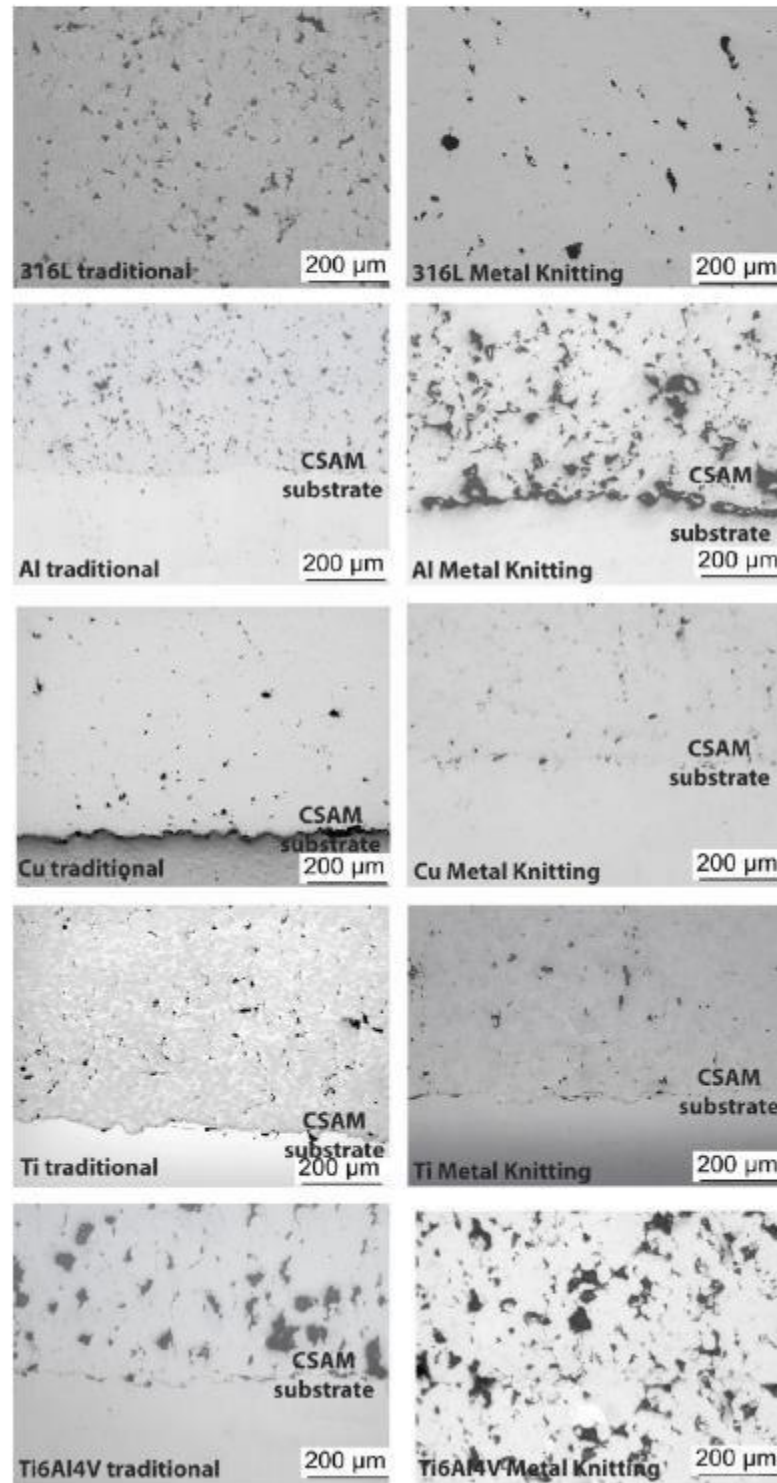


Figure 10. CSAM microstructures.

Table 4. CSAM material properties produced by traditional and Metal Knitting strategies.

Material	Strategy	Hardness [HV0.3]	Porosity [%]
316L	Metal Knitting	246 ± 33	8
	Traditional	374 ± 26	4
Al	Metal Knitting	50 ± 3	21
	Traditional	49 ± 8	3
Cu	Metal Knitting	88 ± 10	7
	Traditional	109 ± 12	3
Ti	Metal Knitting	199 ± 22	10
	Traditional	262 ± 43	7
Ti6Al4V	Metal Knitting	229 ± 31	28
	Traditional	236 ± 32	14

The Metal Knitting materials' properties must be evaluated by their comparison with the CSAM samples obtained by the traditional strategy. The CSAM Metal Knitting samples showed a higher porosity, but close hardness values. The higher discrepancy in hardness values was seen for the materials more susceptible to cold-working strain hardening, highlighting Ti and 316L, suggesting a higher deformation of particles for CSAM traditional strategy sprayed samples than for the Metal Knitting ones. On the other hand, Ti6Al4V had very close hardness values for both evaluated strategies, as expected by their similarity in microstructures.

Table 5 summarizes the tensile testing results of Ti6Al4V and 316L CSAM parts produced by Metal Knitting and traditional strategies. The latter had higher strength values because the cohesion of particles was higher, which is correlated with the lower porosity presented in Table 4. After all, the lower porosity infers a higher contact area among the particles of the CSAM consolidated material. Furthermore, the higher hardness also indicates a higher cold working by more severe particle deformation, which affects the material strength.

Table 5. CSAM produced by traditional and Metal Knitting UTS results.

Material	Strategy	UTS [MPa]
316L	Metal Knitting	61 ± 2
	Traditional	184 ± 9
Ti6Al4V	Metal Knitting	32 ± 12
	Traditional	121 ± 25

3.2.3. CSAM Geometries Produced by Metal Knitting

In order to show some capacities of this new spraying strategy, complex geometries were produced by CSAM Metal Knitting, which are not feasible by employing the CSAM traditional strategy. Thus, thin straight walls were obtained using the Metal Knitting strategy following one single-line on the substrate's flat surface, as seen in Figure 11. The geometries presented are not practicable using the traditional strategy because the sidewalls grow with a certain relative inclination, resulting in a pyramid-like shape, while the CSAM sidewalls produced by a single-line Metal Knitting were perpendicular to the substrate surface, as indicated in Table 3.

Adjustments in the Metal Knitting parameters, radius, angle, and standoff distance, promote a variation in CSAM wall thicknesses. This change in the part wall thickness may be made during the part growing, producing an even more complex geometry with steps, like the two right-side 316L samples indicated in Figure 11 (316L thin walls).

Another approach for CSAM Metal Knitting was the variation in the number of steps by layer. The progressive reduction in this quantity of steps made possible the fabrication of a controlled inclined top wall, which is indicated for CSAM Cu and 316L in Figure 11 (Cu with controlled inclination) and Figure 11 (316L with controlled inclination), respectively, resulting in shark dorsal thin like geometries.

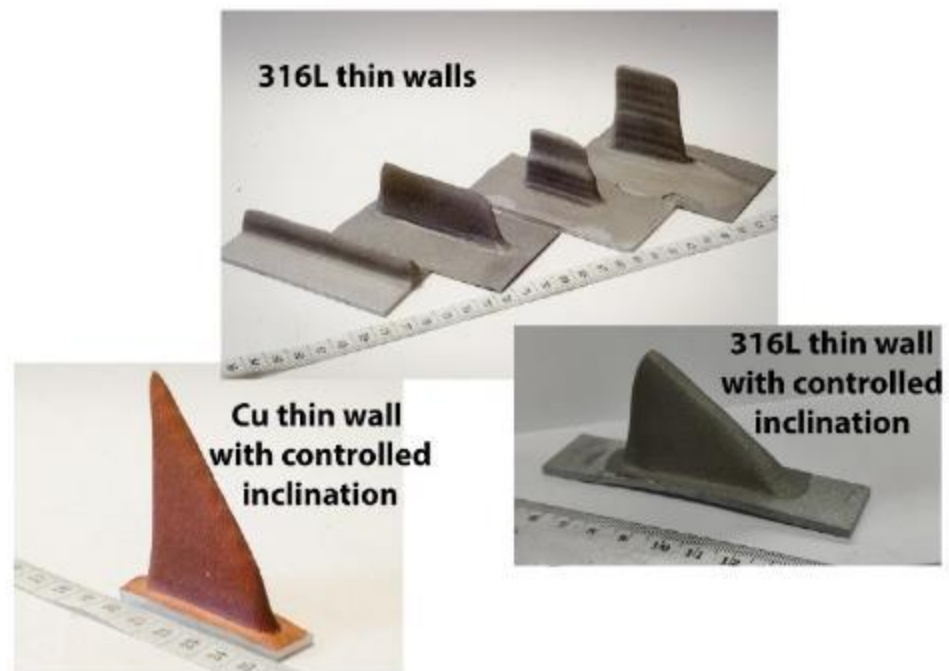


Figure 11. CSAM straight thin wall parts made by Metal Knitting strategy on flat substrate.

Additionally, the Metal Knitting strategy was used on a 50×5 mm substrate, a small area for CSAM, and the objective was to grow up the CSAM part with the same 5 mm wall thickness. For this deposition, the substrate and feedstock powder had the same composition, Cu, Ti, Al, and 316L, and a single-line Metal Knitting strategy was selected. The results showed how feasible it was to grow up a part with this 5 mm thick wall by the Metal Knitting strategy, as presented in Figure 12. Varying the Metal Knitting parameters, the 5 mm thick walls produced should be increased to 6 or 7 mm thick to produce sufficient material for a post-machining service.

The Metal Knitting was changed from a straight line based path to a curved lines based path, keeping the cone-like movements; following these non-straight lines, the production of curved walls was feasible, as presented in Figure 13. Different materials were tested, 316L, Ti, and Cu. A change in the robot program made it possible to grow multi-material close walls, Ti and Cu, on the same Al plate substrate.

The same approach presented in Figure 11 for promoting a controlled inclination for straight-line Metal Knitting 316L and Cu is indicated in Figure 13 for a curved path, growing the CSAM part with a controlled inclination. For CSAM 316L, it produced a height of 0 at the beginning of the wall and 16 mm at its end. However, reducing the number of steps per layer, a stairways-like wall was made, as seen in the highest Cu CSAM part in Figure 13. A control in the length of each pass promoted a smooth inclination of the wall, as seen for the 316L curved wall, with height 0 in the beginning of the wall, and 16 mm at its end. However, by decreasing more the length of each pass, a stairways-like top of the wall was made, as seen in the highest Cu CSAM part in Figure 13.

The CSAM Metal Knitting strategy was also evaluated for more complex geometries, which were feasible by controlling the growth direction. Figure 14 presents CSAM 316L parts. For the left and right images of Figure 14, the spraying started in a direction non-perpendicular to the substrate, indicating a good adhesion because no cracks or delamination were observed after visual inspection. The changes in growing angle and direction were performed by the inclination of the substrate holder, making this activity easier because a change in the robot program for each of these geometries would demand much time and effort to make a unique part. However, a robot program can guarantee the dimensional quality requirements for mass production, or at least dozens of components.

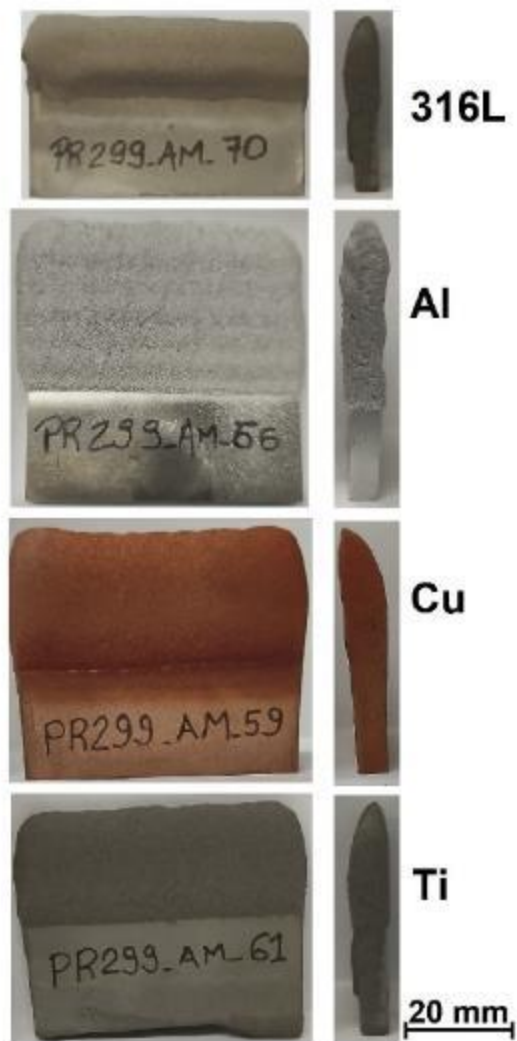


Figure 12. CSAM part on narrow substrate surface made by Metal Knitting strategy.

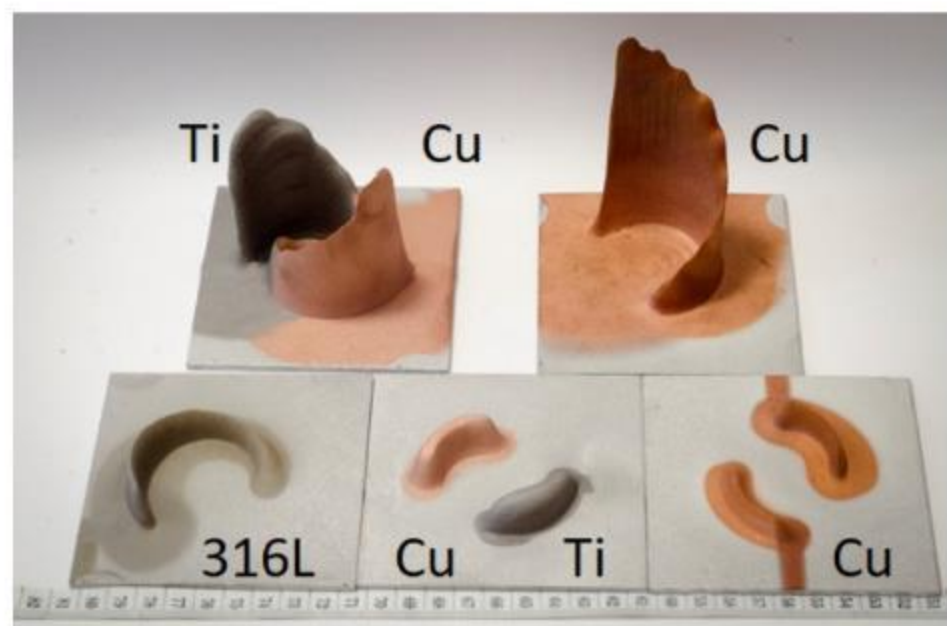


Figure 13. CSAM curved parts made by the Metal Knitting strategy.

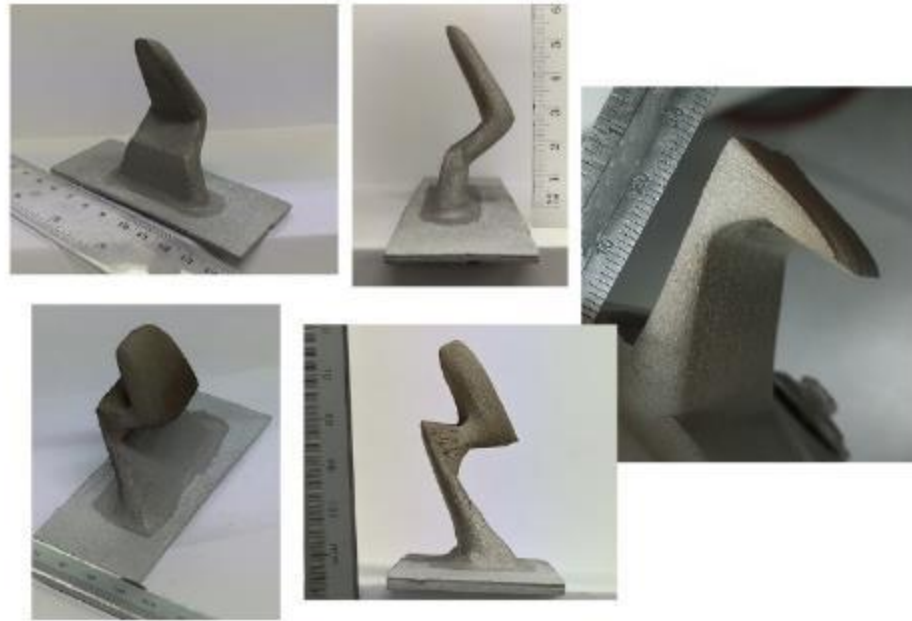


Figure 14. CSAM 316L complex geometries made by the Metal Knitting strategy.

4. Conclusions of Using the Metal Knitting CSAM Strategy and Future Perspectives

Comparing the Metal Knitting CSAM strategy to the traditional one, some points may be listed, mainly regarding future advances and possibilities of its use:

- Metal Knitting demonstrates the suitability for making geometries and dimensional capacities previously unfeasible by the traditional strategy, obtaining vertical sidewalls, despite 40 degrees of inclination in the 316L CSAM part produced by the traditional strategy;
- Metal Knitting produces materials with good mechanical properties and similar microstructures to the traditional CSAM strategy. In general, due to the constant cone-like CS gun movement, Metal Knitting results in a lower density than the traditional strategy;
- Post-processing for densification of Metal Knitting made parts have to be studied, e.g., heat treatments, Hot Isostatic Pressure (HIP), Spark Sintering Plasma (SPS), due to their effectiveness used for parts produced by the traditional CSAM strategy. This qualifies the parts made by Metal Knitting for quality improvement.
- Metal Knitting strategy is not necessarily a substitute for the traditional one. Still, it can be a complementary stage to this one, redressing the sidewalls to lower angles. Therefore, a combination of robot strategies could be a solution for specific applications, e.g., to build a large bulk, the traditional strategy can be applied for its central area, while knitting is used on the edges. This would prevent the sidewalls inclination and promote the best spraying angle deposition on the central location, which is 90 degrees, typical of the traditional strategy.
- As a CSAM technique, the Metal Knitting strategy has some challenges, e.g., needing reasonable control of its parameters, distances, and relative positions between the substrate and the CS gun, because a misunderstanding in the measurements and positioning may result in an undesired path and consequently unexpected geometry. Moreover, depending on the knitting path and part design, the robot arm does long movements, which might eventually result in a collision between the CS gun and the robot arm. Therefore, to avoid what can be catastrophic for the CS equipment, the robot user must check carefully and slowly the robot trajectory before the CS spraying.
- Looking for the potential applications of the CSAM metal knitting strategy, one possibility is using it to complement other AM techniques already in use, such as arc-welding or laser processes.

- In addition, Metal Knitting can be used for repairing elements, such as thin, worn, or damaged walls. Among a wide range of applications and industry sectors, some examples are: repairing Ti alloys turbine compressor blades' tips, fabrication of superalloys manifolds, production of special prototypes for racing cars, fabrication and repairing of special alloys piping components for the oil and gas industry, repairing of eroded martensitic stainless-steel Kaplan hydraulic runners' tips, and others.

Supplementary Materials: The following supporting information can be downloaded at: <https://www.mdpi.com/article/10.3390/ma15196785/s1>, Video S1: CSAM Metal Knitting strategy on flat substrate surface.

Author Contributions: Conceptualization, R.F.V. and J.S.; investigation, R.F.V., V.A.-F. and H.C.; methodology, R.F.V., V.A.-F., J.S., U.O. and Z.G.C.; writing—original draft preparation, R.F.V. and V.A.-F.; writing—review and editing, R.F.V., V.A.-F. and J.S.; funding acquisition, J.S. and I.G.C.; project administration, J.S. and I.G.C.; software, U.O., Z.G.C. and H.C.; supervision, I.G.C. All authors have read and agreed to the published version of the manuscript.

Funding: The research leading to these results has received funding from the grant PID2020-115508RB-C21 funded by MCIN/AEI/10.13039/501100011033 and, as appropriate, by “ERDF A way of making Europe”, by “European Union NextGenerationEU/PRTR”. In addition, R.F. Vaz thanks Generalitat de Catalunya for the Ph.D. grant 2020 FISDU 00305. The author V. Albaladejo-Fuentes is a Serra-Hunter Fellow.

Institutional Review Board Statement: Not applicable.

Informed Consent Statement: Not applicable.

Data Availability Statement: The data presented in this study are available on request from the corresponding author.

Acknowledgments: A special thanks to Victor Gómez for his essential work operating the robot and CS equipment. This work would be more difficult without his help.

Conflicts of Interest: The authors declare no conflict of interest.

References

1. De Souza Corrêa, R.; de Oliveira, U.R.; Abdalla, M.M.; Fernandes, V.A. Systematic Literature Review on Sustainable Products: Impact on Organizations, Research Opportunities and Future Perspectives. *Clean. Waste Syst.* **2022**, *1*, 100003. [CrossRef]
2. Jin, Y.; Ji, S.; Li, X.; Yu, J. A Scientometric Review of Hotspots and Emerging Trends in Additive Manufacturing. *J. Manuf. Technol. Manag.* **2017**, *28*, 18–38. [CrossRef]
3. Parupelli, S.K.; Desai, S. A Comprehensive Review of Additive Manufacturing (3D Printing): Processes, Applications and Future Potential. *Am. J. Appl. Sci.* **2019**, *16*, 244–272. [CrossRef]
4. Savini, A.; Savini, G.G. A Short History of 3D Printing, a Technological Revolution Just Started. In Proceedings of the 2015 ICOHTEC/IEEE International History of High-Technologies and their Socio-Cultural Contexts Conference (HISTELCON), Tel-Aviv, Israel, 18–19 August 2015; pp. 1–8.
5. Yakout, M.; Elbestawi, M.A.; Veldhuis, S.C. A Review of Metal Additive Manufacturing Technologies. *Solid State Phenom.* **2018**, *278*, 1–14. [CrossRef]
6. Fang, Z.-C.; Wu, Z.-L.; Huang, C.-G.; Wu, C.-W. Review on Residual Stress in Selective Laser Melting Additive Manufacturing of Alloy Parts. *Opt. Laser Technol.* **2020**, *129*, 106283. [CrossRef]
7. Karayel, E.; Bozkurt, Y. Additive Manufacturing Method and Different Welding Applications. *J. Mater. Res. Technol.* **2020**, *9*, 11424–11438. [CrossRef]
8. Raocelison, R.N.; Verdy, C.; Liao, H. Cold Gas Dynamic Spray Additive Manufacturing Today: Deposit Possibilities, Technological Solutions and Viable Applications. *Mater. Des.* **2017**, *133*, 266–287. [CrossRef]
9. Srikanth, A.; Basha, G.; Venkateshwarlu, B. A Brief Review on Cold Spray Coating Process. *Mater. Today Proc.* **2019**, *22*, 1390–1397. [CrossRef]
10. Vaz, R.F.; Silvello, A.; Sanchez, J.; Albaladejo, V.; Cano, I.G. The Influence of the Powder Characteristics on 316L Stainless Steel Coatings Sprayed by Cold Gas Spray. *Coatings* **2021**, *11*, 168. [CrossRef]
11. Villa, M.; Dosta, S.; Guilemany, J.M. Optimization of 316L Stainless Steel Coatings on Light Alloys Using Cold Gas Spray. *Surf. Coat. Technol.* **2013**, *235*, 220–225. [CrossRef]
12. Yin, S.; Cizek, J.; Yan, X.; Lupoi, R. Annealing Strategies for Enhancing Mechanical Properties of Additively Manufactured 316L Stainless Steel Deposited by Cold Spray. *Surf. Coat. Technol.* **2019**, *370*, 353–361. [CrossRef]

13. Bagherifard, S.; Kondas, J.; Monti, S.; Cizek, J.; Perego, F.; Kovarik, O.; Lukac, F.; Gaertner, F.; Guagliano, M. Tailoring Cold Spray Additive Manufacturing of Steel 316 L for Static and Cyclic Load-Bearing Applications. *Mater. Des.* **2021**, *203*, 109575. [\[CrossRef\]](#)
14. Dikici, B.; Yilmazer, H.; Ozdemir, I.; Isik, M. The Effect of Post-Heat Treatment on Microstructure of 316L Cold-Sprayed Coatings and Their Corrosion Performance. *J. Therm. Spray Technol.* **2016**, *25*, 704–714. [\[CrossRef\]](#)
15. Guerreiro, B.; Vo, P.; Poirier, D.; Legoux, J.-G.; Zhang, X.; Giallonardo, J.D. Factors Affecting the Ductility of Cold-Sprayed Copper Coatings. *J. Therm. Spray Technol.* **2020**, *29*, 630–641. [\[CrossRef\]](#)
16. Wu, H.; Huang, C.; Xie, X.; Liu, S.; Wu, T.; Niendorf, T.; Xie, Y.; Deng, C.; Liu, M.; Liao, H.; et al. Influence of Spray Trajectories on Characteristics of Cold-Sprayed Copper Deposits. *Surf. Coat. Technol.* **2021**, *405*, 126703. [\[CrossRef\]](#)
17. Yin, S.; Jenkins, R.; Yan, X.; Lupoi, R. Microstructure and Mechanical Anisotropy of Additively Manufactured Cold Spray Copper Deposits. *Mater. Sci. Eng. A* **2018**, *734*, 67–76. [\[CrossRef\]](#)
18. Vilardell, A.M.; Cinca, N.; Barriuso, E.; Frigola, J.; Dosta, S.; Cano, I.G.; Guilemany, J.M. X-Ray Microtomographic Characterization of Highly Rough Titanium Cold Gas Sprayed Coating for Identification of Effective Surfaces for Osseointegration. *Microscopy* **2019**, *68*, 413–416. [\[CrossRef\]](#)
19. Vargas-Uscategui, A.; King, P.C.; Yang, S.; Chu, C.; Li, J. Toolpath Planning for Cold Spray Additively Manufactured Titanium Walls and Corners: Effect on Geometry and Porosity. *J. Mater. Process. Technol.* **2021**, *298*, 117272. [\[CrossRef\]](#)
20. Lek, J.Y.; Bhowmik, A.; Tan, A.W.-Y.; Sun, W.; Song, X.; Zhai, W.; Buenconsejo, P.J.; Li, F.; Liu, E.; Lam, Y.M.; et al. Understanding the Microstructural Evolution of Cold Sprayed Ti-6Al-4V Coatings on Ti-6Al-4V Substrates. *Appl. Surf. Sci.* **2018**, *459*, 492–504. [\[CrossRef\]](#)
21. Suhonen, T.; Varis, T.; Dosta, S.; Torrell, M.; Guilemany, J.M. Residual Stress Development in Cold Sprayed Al, Cu and Ti Coatings. *Acta Mater.* **2013**, *61*, 6329–6337. [\[CrossRef\]](#)
22. Bobzin, K.; Wietheger, W.; Knoch, M.A.; Schacht, A.; Reisinger, U.; Sharma, R.; Oster, L. Comparison of Residual Stress Measurements Conducted by X-ray Stress Analysis and Incremental Hole Drilling Method. *J. Therm. Spray Technol.* **2020**, *29*, 1218–1228. [\[CrossRef\]](#)
23. Rech, S.; Trentin, A.; Vezzù, S.; Vedelago, E.; Legoux, J.G.; Irissou, E. Different Cold Spray Deposition Strategies: Single- and Multi-Layers to Repair Aluminium Alloy Components. *J. Therm. Spray Technol.* **2014**, *23*, 1237–1250. [\[CrossRef\]](#)
24. Fan, N.; Cizek, J.; Huang, C.; Xie, X.; Chlup, Z.; Jenkins, R.; Lupoi, R.; Yin, S. A New Strategy for Strengthening Additively Manufactured Cold Spray Deposits through in-Process Densification. *Addit. Manuf.* **2020**, *36*, 101626. [\[CrossRef\]](#)
25. Silvello, A.; Cavaliere, P.; Rizzo, A.; Valerini, D.; Dosta Parras, S.; Garcia Cano, I. Fatigue Bending Behavior of Cold-Sprayed Nickel-Based Superalloy Coatings. *J. Therm. Spray Technol.* **2019**, *28*, 930–938. [\[CrossRef\]](#)
26. Vaßen, R.; Fiebig, J.; Kalfhaus, T.; Gibmeier, J.; Kostka, A.; Schrüfer, S. Correlation of Microstructure and Properties of Cold Gas Sprayed INCONEL 718 Coatings. *J. Therm. Spray Technol.* **2020**, *29*, 1455–1465. [\[CrossRef\]](#)
27. Yan, X.; Huang, C.; Chen, C.; Bolot, R.; Dembinski, L.; Huang, R.; Ma, W.; Liao, H.; Liu, M. Additive Manufacturing of WC Reinforced Maraging Steel 300 Composites by Cold Spraying and Selective Laser Melting. *Surf. Coat. Technol.* **2019**, *371*, 161–171. [\[CrossRef\]](#)
28. Chen, C.; Yan, X.; Xie, Y.; Huang, R.; Kuang, M.; Ma, W.; Zhao, R.; Wang, J.; Liu, M.; Ren, Z.; et al. Microstructure Evolution and Mechanical Properties of Maraging Steel 300 Fabricated by Cold Spraying. *Mater. Sci. Eng. A* **2019**, *743*, 482–493. [\[CrossRef\]](#)
29. Vaz, R.F.; Silvello, A.; Albaladejo, V.; Sanchez, J.; Cano, I.G. Improving the Wear and Corrosion Resistance of Maraging Part Obtained by Cold Gas Spray Additive Manufacturing. *Metals* **2021**, *11*, 1092. [\[CrossRef\]](#)
30. Yin, S.; Cavaliere, P.; Aldwell, B.; Jenkins, R.; Liao, H.; Li, W.; Lupoi, R. Cold Spray Additive Manufacturing and Repair: Fundamentals and Applications. *Addit. Manuf.* **2018**, *21*, 628–650. [\[CrossRef\]](#)
31. Prashar, G.; Vasudev, H. A Comprehensive Review on Sustainable Cold Spray Additive Manufacturing: State of the Art, Challenges and Future Challenges. *J. Clean. Prod.* **2021**, *310*, 127606. [\[CrossRef\]](#)
32. Wu, H.; Xie, X.; Liu, M.; Verdy, C.; Zhang, Y.; Liao, H.; Deng, S. Stable Layer-Building Strategy to Enhance Cold-Spray-Based Additive Manufacturing. *Addit. Manuf.* **2020**, *35*, 101356. [\[CrossRef\]](#)
33. Pattison, J.; Celotto, S.; Morgan, R.; Bray, M.; O'Neill, W. Cold Gas Dynamic Manufacturing: A Non-Thermal Approach to Freeform Fabrication. *Int. J. Mach. Tools Manuf.* **2007**, *47*, 627–634. [\[CrossRef\]](#)
34. Nardi, A.T.; El-Wardany, T.L.; Viens, D.V.; Lynch, M.E.; Hsu, A.; Klecka, M.A.; Gu, W. Additive Topology Optimized Manufacturing for Multi-Functional Components. US20140277669A1, 18 September 2014.
35. Prasad, K.; Khalik, M.A.; Hutasoit, N.; Rahman Rashid, R.A.; Rashid, R.; Duguid, A.; Palanisamy, S. Printability of Low-Cost Pre-Heat-Treated Ball Milled Al7075 Powders Using Compressed Air Assisted Cold Spray Additive Manufacturing. *Addit. Manuf. Lett.* **2022**, *3*, 100046. [\[CrossRef\]](#)
36. Silvello, A.; Cavaliere, P.D.; Albaladejo, V.; Martos, A.; Dosta, S.; Cano, I.G. Powder Properties and Processing Conditions Affecting Cold Spray Deposition. *Coatings* **2020**, *10*, 91. [\[CrossRef\]](#)
37. Gilmore, D.L.; Dykhuizen, R.C.; Neiser, R.A.; Roemer, T.J.; Smith, M.F. Particle Velocity and Deposition Efficiency in the Cold Spray Process. *J. Therm. Spray Technol.* **1999**, *8*, 576–582. [\[CrossRef\]](#)
38. Li, C.-J.; Li, W.-Y.; Wang, Y.-Y. Effect of Spray Angle on Deposition Characteristics in Cold Spraying. In *Thermal Spray 2003: Advancing the Science & Applying the Technology*; Moreau, C., Marple, B.R., Eds.; ASM International: Orlando, FL, USA, 2003; pp. 91–96.

39. Wu, H.; Xie, X.; Liu, M.; Chen, C.; Liao, H.; Zhang, Y.; Deng, S. A New Approach to Simulate Coating Thickness in Cold Spray. *Surf. Coat. Technol.* **2020**, *382*, 1–14. [[CrossRef](#)]
40. Wu, H.; Raelison, R.N.; Zhang, Y.; Deng, S.; Liao, H. Cold Spraying of 3D Parts—Challenges. In *Thermal Spray Coatings*; Thakur, L., Vasudev, H., Eds.; CRC Press: Boca Raton, FL, USA, 2021; pp. 37–58.
41. Matts, O.; Hammoud, H.; Sova, A.; Bensaid, Z.; Kermouche, G.; Klöcker, H.; Bosch, C.; Texier-Mandoki, N. Influence of Cold Spray Nozzle Displacement Strategy on Microstructure and Mechanical Properties of Cu/SiC Composites Coating. *Key Eng. Mater.* **2019**, *813*, 110–115. [[CrossRef](#)]
42. Bae, G.; Kumar, S.; Yoon, S.; Kang, K.; Na, H.; Kim, H.; Lee, C. Bonding Features and Associated Mechanisms in Kinetic Sprayed Titanium Coatings. *Acta Mater.* **2009**, *57*, 5654–5666. [[CrossRef](#)]
43. Ichikawa, Y.; Tokoro, R.; Tanno, M.; Ogawa, K. Elucidation of Cold-Spray Deposition Mechanism by Auger Electron Spectroscopic Evaluation of Bonding Interface Oxide Film. *Acta Mater.* **2019**, *164*, 39–49. [[CrossRef](#)]
44. Sun, W.; Tan, A.W.Y.; Marinescu, I.; Toh, W.Q.; Liu, E. Adhesion, Tribological and Corrosion Properties of Cold-Sprayed CoCrMo and Ti6Al4V Coatings on 6061-T651 Al Alloy. *Surf. Coat. Technol.* **2017**, *326*, 291–298. [[CrossRef](#)]
45. Faizan-Ur-Rab, M.; Zahiri, S.H.; Masood, S.H.; Phan, T.D.; Jahedi, M.; Nagarajah, R. Application of a Holistic 3D Model to Estimate State of Cold Spray Titanium Particles. *Mater. Des.* **2016**, *89*, 1227–1241. [[CrossRef](#)]
46. Zahiri, S.H.; Yang, W.; Jahedi, M. Characterization of Cold Spray Titanium Supersonic Jet. *J. Therm. Spray Technol.* **2009**, *18*, 110–117. [[CrossRef](#)]
47. Champagne, V.K.; Helfritch, D.J.; Dinavahi, S.P.G.; Leyman, P.F. Theoretical and Experimental Particle Velocity in Cold Spray. *J. Therm. Spray Technol.* **2011**, *20*, 425–431. [[CrossRef](#)]
48. Kotoban, D.; Grigoriev, S.; Okunkova, A.; Sova, A. Influence of a Shape of Single Track on Deposition Efficiency of 316L Stainless Steel Powder in Cold Spray. *Surf. Coat. Technol.* **2017**, *309*, 951–958. [[CrossRef](#)]
49. Rokni, M.R.; Nutt, S.R.; Widener, C.A.; Champagne, V.K.; Hrabe, R.H. Review of Relationship Between Particle Deformation, Coating Microstructure, and Properties in High-Pressure Cold Spray. *J. Therm. Spray Technol.* **2017**, *26*, 1308–1355. [[CrossRef](#)]
50. Lynch, M.E.; Gu, W.; El-Wardany, T.; Hsu, A.; Viens, D.; Nardi, A.; Klecka, M. Design and Topology/Shape Structural Optimisation for Additively Manufactured Cold Sprayed Components. *Virtual Phys. Prototyp.* **2013**, *8*, 213–231. [[CrossRef](#)]
51. Tavares, S.S.M.; Rodrigues, C.R.; Pardal, J.M.; da Silva Barbosa, E.; de Abreu, H.F.G. Effects of Post Weld Heat Treatments on the Microstructure and Mechanical Properties of Dissimilar Weld of Supermartensitic Stainless Steel. *Mater. Res.* **2014**, *17*, 1336–1343. [[CrossRef](#)]
52. Yang, K.; Li, W.; Yang, X.; Xu, Y. Anisotropic Response of Cold Sprayed Copper Deposits. *Surf. Coat. Technol.* **2018**, *335*, 219–227. [[CrossRef](#)]
53. Eason, P.D.; Fewkes, J.A.; Kennett, S.C.; Eden, T.J.; Tello, K.; Kaufman, M.J.; Tiryakioğlu, M. On the Characterization of Bulk Copper Produced by Cold Gas Dynamic Spray Processing in as Fabricated and Annealed Conditions. *Mater. Sci. Eng. A* **2011**, *528*, 8174–8178. [[CrossRef](#)]

4.2.2.1. CSAM Traditional and Metal Knitting Strategies for Al Parts

The CSAM-ed Al bulks were evaluated visually and by NT to check the material's porosity distribution. For both samples, the sidewall angles are very close to the normal with the substrate plane. However, the surface aspects differ, as seen in Figure 30, with a smoother surface for the CSAM-ed Al traditional strategy-made sample and a rougher and irregular shape for the other one. The banded parallel waves in both samples result from the principal deposition line path.

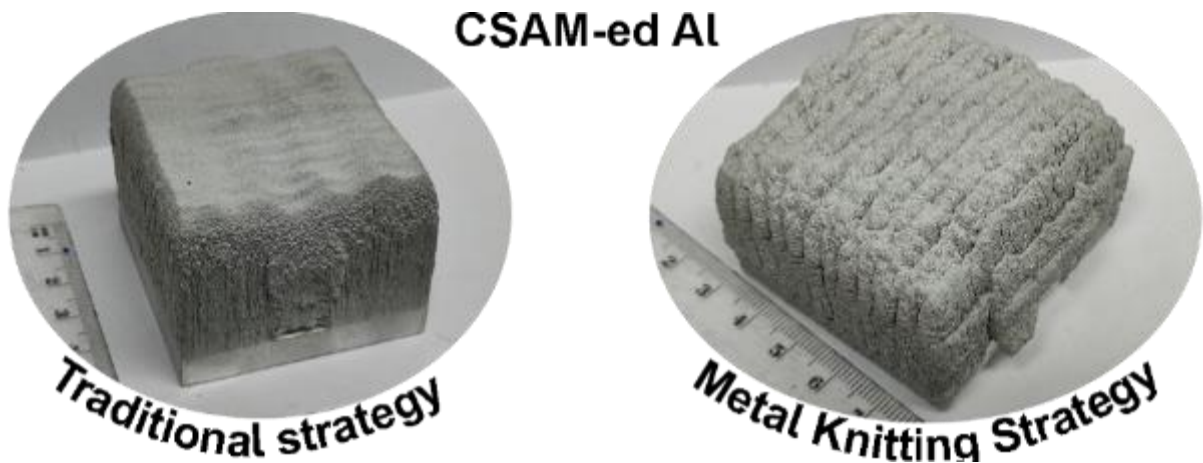


Figure 30: CSAM traditional and Metal Knitting Al parts. Unit mm.

The velocity of particle is higher for the CSAM traditional strategy, as presented in Article 5. By this higher energy at the impact, the CSAM-ed Al particles deform more using this traditional strategy, resulting in a lower porosity than the Metal Knitting sprayed ones. It is presented in the NT results, Figure 31 and Figure 32, where the darker areas represent the dense material and the lighter areas indicate the lower density and, consequently, the concentrate porosity for the CSAM traditional and Metal Knitting Al bulks, respectively.

For the first one, the porosity is close to zero, while for the second one, the porosity is higher than 6%. Besides the porosity value, the porosity distribution is noticed, which surrounds each Metal Knitting layer. It happened because the DE and deposition rate is too high for Al, reaching 10 mm each pass, creating shaded areas for the next CS powder-laden jet.

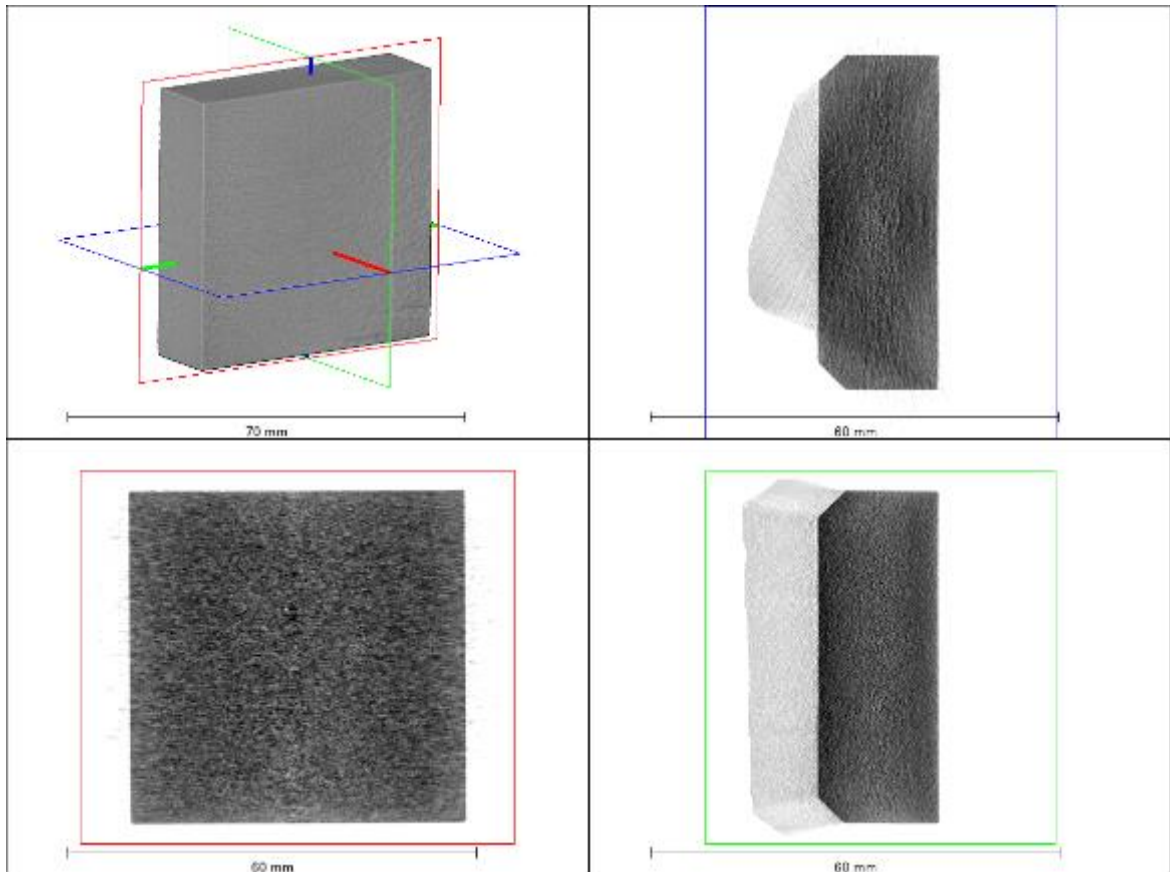


Figure 31: NT images of CSAM traditional AI part.

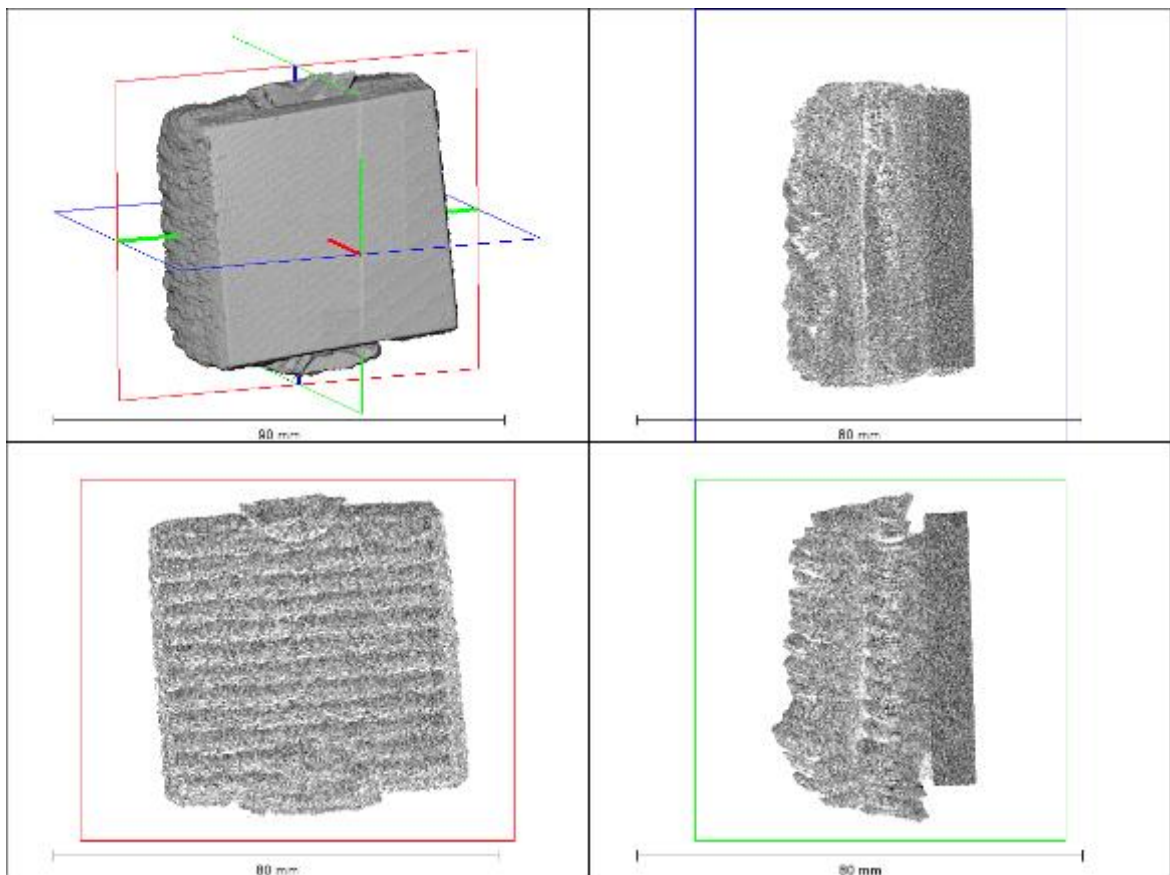


Figure 32: NT images of CSAM Metal Knitting AI part.

Some alternatives to using the CSAM Metal Knitting strategy for Al are reducing this deposition rate, which is possible by accelerating even more the robot arm, reducing the powder feeding, or both. However, the powder feeder of PCS100 CS gun cannot guarantee a constant powder flow employing lower powder feeding values than the actual set, making this solution unfeasible for now. The other possibility is limited by the robot arm inertia, which makes it impractical for the complex movements described for the Metal Knitting strategy. Even though the CSAM Al Metal Knitting presents a lower quality, this strategy seems unnecessary to obtain a sidewall normal to the substrate plane since, employing the traditional strategy, no tapering effect is observed, and a fully dense material is produced.

4.3. CSAM-ed Parts

This section presents the characterization of some CSAM-ed parts and CS-ed coatings, and the materials' properties. The first approach was considering CS for coatings, characterizing these coatings, and measuring their mechanical properties. Evaluating the CS-ed coating properties is a valid starting point since the microstructure does not vary much from CS-ed coating condition to large CSAM-ed parts. Optimizing and validating CS parameters for coatings helps to prevent lengthy CSAM depositions with inadequate conditions. To move from CS-ed coating condition to CSAM-ed bulk production, evaluating residual stresses is essential, mainly regarding their origin, values, compressive or tensile, directions, and distribution. Thus, studying this behavior of the CS-ed coatings considered above is an intermediate step to evaluating the parts/bulks produced by CSAM.

In the following sections, specific characterizations are presented, evaluating different materials, strategies of deposition and post-treatments and characterization techniques.

4.3.1. Characterization of CS-ed Samples

Characterizing CS-ed 316L, Cu, and Ti coatings and measuring their mechanical properties were previously shown in Article 2. The effect of CS-ed coating thickness on the material properties is presented in the following Article 4, which also shows results and discussions of nano-characterizations of CS-ed Cu and Ti coatings, revealing its relationship with the adhesion and performance behavior with different coating thicknesses.

**ARTICLE 4 “FRETTING WEAR AND SCRATCH RESISTANCE OF COLD-
SPRAYED PURE CU AND TI”**

R.F. Váz, A. Silvello, P.D. Cavalière, S. Dosta, I.G. Cano, L. Capodieci, A. Rizzo,
D. Valerini



[10.1007/s13632-021-00758-2](https://doi.org/10.1007/s13632-021-00758-2)

This work analyses the fretting and wear behavior of CS-ed pure Cu and pure titanium coatings. The low porosity and high strength materials led to high resistance to wear damage through the optimal energy dissipation upon fretting. Due to the sprayed particles' deformation mode, the CS-ed materials show non-uniform hardening along the deposition distance, influencing the materials' properties and the response to the wear damage. It was demonstrated by the scratch tests performed on coatings with different thicknesses. CS-ed thicker material revealed the best wear resistance due to the deformation hardening. The harder coatings also revealed a brittle fracture at the experienced highest loads.

Understanding this behavior in coatings is important for CSAM because the superficial condition does not change significantly from a thick CS-ed material to a large CSAM-ed part. In addition, knowing the superficial needs and performance of CS-ed materials supports the use of superficial post-treatments to improve their wear or corrosion performances.



Fretting Wear and Scratch Resistance of Cold-Sprayed Pure Cu and Ti

Rodolpho F. Váz¹ · Alessio Silvello¹ · Pasquale D. Cavalière² · Sergi Dosta¹ · Irene G. Cano¹ · Laura Capodiecì³ · Antonella Rizzo³ · Daniele Valerini³

Received: 18 May 2021 / Revised: 30 June 2021 / Accepted: 2 July 2021
© The Author(s) 2021, corrected publication 2021

Abstract

The paper analyses the fretting and wear behavior of pure copper and pure titanium coatings realized through cold spray. The coatings were designed and produced by employing processing conditions leading to minimum porosity and high hardness; these conditions were 700 °C and 40 bar for Ti powders and 400 °C and 30 bar for Cu ones. The low porosity and high strength materials led to high resistance to wear damaging through the optimal energy dissipation upon fretting. Due to the sprayed particles deformation mode, the sprayed materials show non-uniform hardening along the deposition distance. As a matter of fact, hardness varied in the range 3.7–4.2 GPa for Ti coatings and 1.5–2 GPa for the Cu ones depending on the distance from the substrate and on the coatings thickness. This influenced the materials properties and the response to the wear damaging. This was demonstrated by the scratch tests performed on coatings with different thicknesses. Those coatings sprayed in major thickness revealed the best wear resistance due to the deformation hardening. The harder coatings also revealed brittle fracture at the experienced highest loads.

Keywords Cold spray · Mechanical properties · Hardening · Wear damage · Fretting damage

Introduction

Cold spray is recognized as an optimal additive manufacturing (AM) technology capable of producing sound bulk components [1–4] with exceptional performances experienced by copper-, nickel- and titanium-based materials [5–9]. During cold spray process, a high pressurized gas is employed to accelerate metallic particles at temperatures well below their melting points. The sprayed particles severely deform upon impacting on hard substrates leading to compact deposits. This low-temperature thermal spray technology avoids undesirable oxidation processes or phase modifications in the sprayed materials leading to the obtaining of components characterized by good mechanical properties [10].

The sprayed particles exhibit severe plastic deformation upon impacting; this induces many microstructural modifications that are responsible for the bonding to the substrate and among the different particles [11]. The activated microstructural features are dependent on the sprayed particles properties, the substrate surface and mechanical properties and the employed pressure and temperature of the spray gases. As these properties are varied, different coatings behaviors are expected [12]. In particular, the coatings properties are very sensitive to the selected spray parameters [13, 14]. Many scientific evidences underline that the particle–particle cohesion is due to the achievement of the adiabatic shear instability. This phenomenon leads to local temperature increase supporting the particle deformation that behaves as a viscous material. This allows for the oxides rupture with consequent optimal adhesion and particles interlocking [15, 16]. Other scientific evidences underline that peripheral jets form as a consequence of strong pressure waves due to impact leading to the expansion of the particle edge [17]. By considering the sprayed pure metals behavior, the processing conditions variation largely affects the deformation mechanisms and the consequent mechanical and microstructural properties [18–20]. In general, processing conditions influence the severe plastic deformation levels; this governs the

✉ Pasquale D. Cavalière
pasquale.cavaliere@unisalento.it

¹ Thermal Spray Center CPT, Universitat de Barcelona, Barcelona, Spain

² Department of Innovation Engineering, University of Salento, Lecce, Italy

³ ENEA - Italian National Agency for New Technologies, Energy and Sustainable Economic Development, Brindisi, Italy

metallurgical bonding and is revealed by the flattening ratio of the particles after impact. The measurement of the flattening ratio allows for the determination of the deformation behavior of the material at different distances for the surface toward the substrate [21, 22].

Titanium and its alloys show well-known microstructural and mechanical properties [23] allowing them to be applied in many civil and industrial applications from aerospace [24, 25] to biomedical [26] to protective components [27]. Copper and its alloys are mainly employed in those fields requiring materials with high electrical and thermal properties [28–31].

Ti coatings have been produced in order to increase the resistance to fretting and wear of aluminum and aluminum alloys [32]. Fretting wear evolves through various phenomena due to the continuous contact between two surfaces; the developed microstructural mechanisms lead to fatigue cracking and delamination of the superficial layers. Once continue sliding acts, microcracks nucleate and continue to grow up to fatigue damaging and macroscopic fracture [33]. In general, the fretting behavior of materials involves various microstructural features that continuously interact and overlap during continuous loading [34]. The fretting wear and scratch behavior of cold spray coatings is not so presented in literature [35]. It is well known that material porosity and hardness/elastic modulus are the main factors affecting the wear behavior [36].

In the classical approach, only hardness is considered as the principal aspect governing the wear response of surfaces. As the material hardens, also the elastic modulus starts to play a fundamental role. So, not the hardness and elastic modulus must be taken into consideration to completely characterize such fundamental material behavior. In this direction, the hardness to elastic modulus ratio provides many information about the surface mechanisms acting during sliding. Nanoindentation is a well-established technique developed to precisely measure the local hardness and elastic moduli of bulk materials and coatings [37]. Nano-probe techniques allow for the continuous characterization of mechanical properties as well as the surface ones under contact loading. Anyway, the relationships between local mechanical properties and the wear response are not conclusive. This is complicated in those conditions where complex triaxial stresses act on small volumes [38].

Very few experimental evidences are presented on the scratch response of cold spray deposits [39, 40]. Here, nanoindentation and scratch are employed to continuously characterize the coatings mechanical properties along the deposition path. The analyses of scratch tracks allowed to identify the surface damage consequent to sliding at different load levels. The results are very useful for cold spray design in order to optimize the coatings microstructure, mechanical properties and dimensions.

Experimental Procedure

Materials

Pure copper powders with particle distribution + 18–41 μm and mean dimensions of $27 \pm 1.5 \mu\text{m}$ were provided by Safina (Ploiesti, Romania); pure titanium powders with particle distribution + 15–44 μm and mean dimensions of $30 \pm 2 \mu\text{m}$ were provided by AP&C (Boisbriand, QC, Canada). Granulometry was measured through laser scattering by employing Beckman Coulter LS 13 320 (Brea, CA, USA). Phase analysis was evaluated through XRD Malvern PANalytical X'Pert PRO MPD θ/θ Bragg–Brentano powder diffractometer (Malvern, United Kingdom), with font of Cu $K\alpha$ ($\lambda = 1.5418 \text{ \AA}$) and work power 45 kV–40 mA was used. Scanning electron microscopy (SEM), Thermo Fisher Phenom Pro Desktop SEM (Eindhoven, Netherlands), was employed for microstructural characterization.

The particle dimensions distributions are shown in Fig. 1. The particles are spherical shaped as shown in Fig. 2. The carbon steel substrate was alumina sandblasted before spraying.

The X-ray spectra of the employed particles are plotted in Fig. 3.

Coatings Deposition

The coatings were produced with a CGT Kinetics 4000 (Haun, Germany) with a SiC nozzle. It has a rectangular cross section measuring $2 \times 4 \text{ mm}$ throat and $2 \times 10 \text{ mm}$ exit at CPT facilities (Barcelona, Spain). The employed substrate was a C20 carbon steel. The selected cold spray parameters are shown in

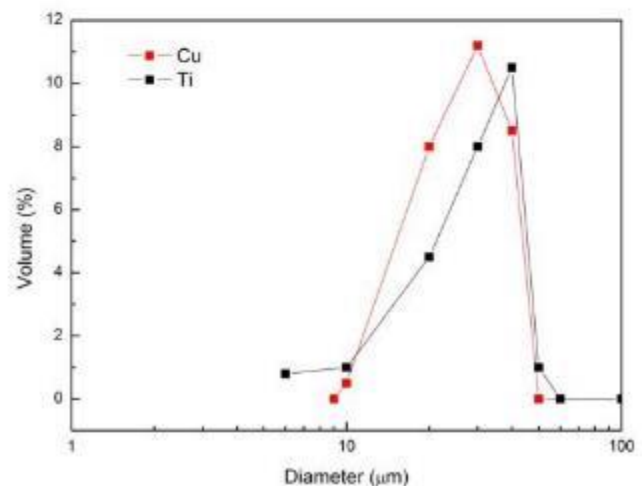


Fig. 1 Particle diameter distribution of the employed powders

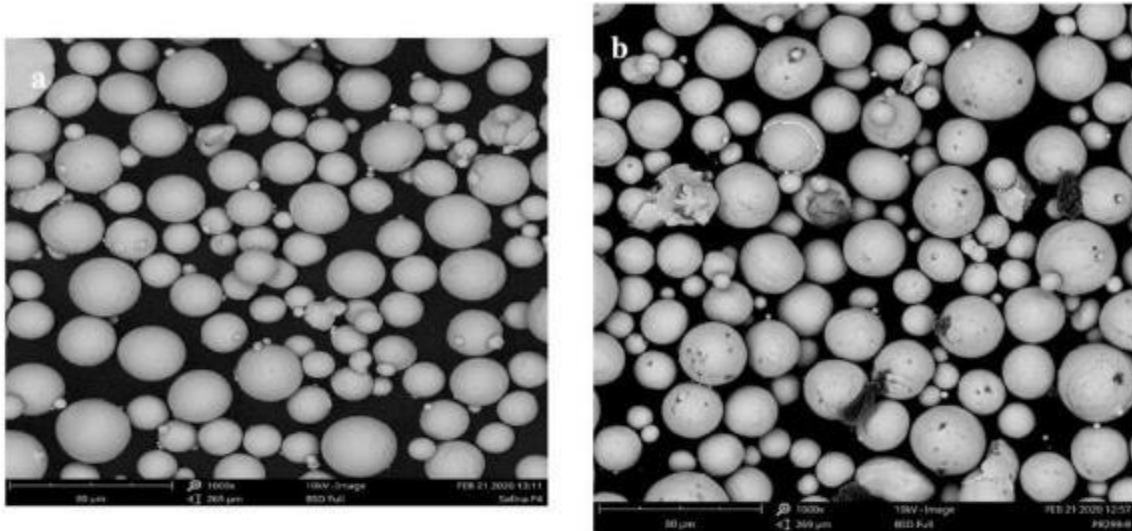


Fig. 2 Powders aspect (a) Cu and (b) Ti

Fig. 3 X-ray analyses results of the studied particles

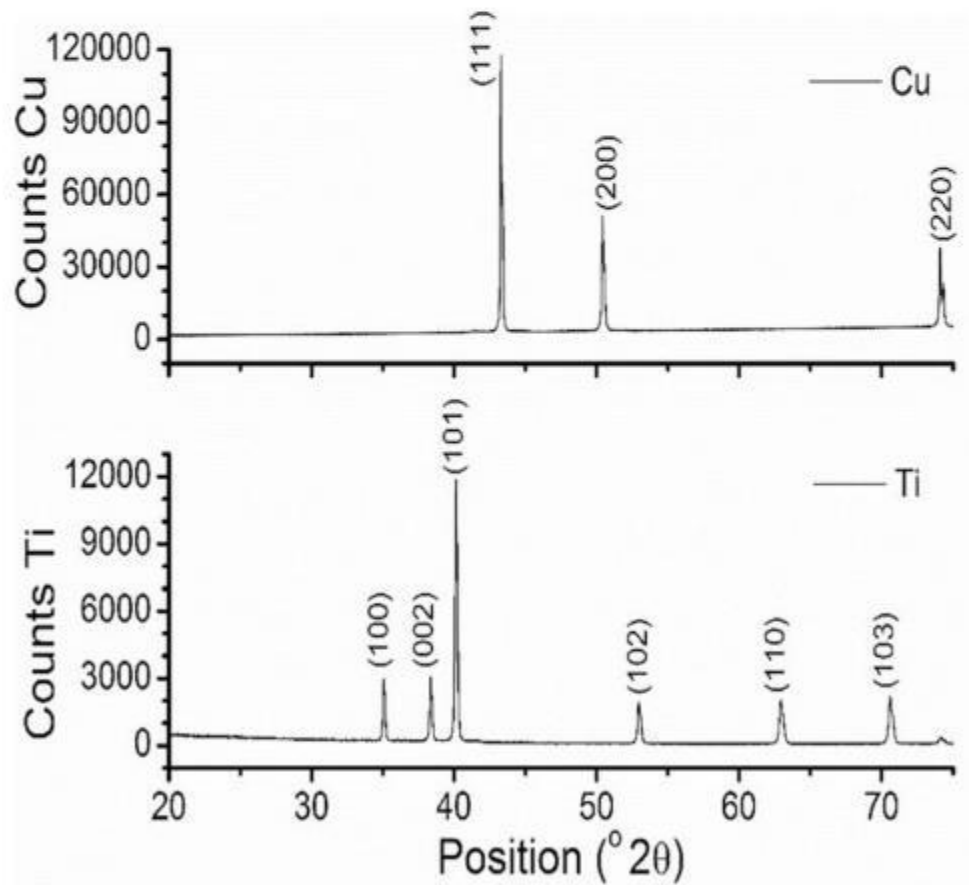


Table 1 Cold spray parameters

Material	N ₂ temperature, °C	N ₂ pressure, bar	Standoff distance, mm	Powder feed, rpm	Robot speed, m s ⁻¹	Step, mm
Ti	700	40	40	3	0.50	1
Cu	400	30	40	2	0.50	1

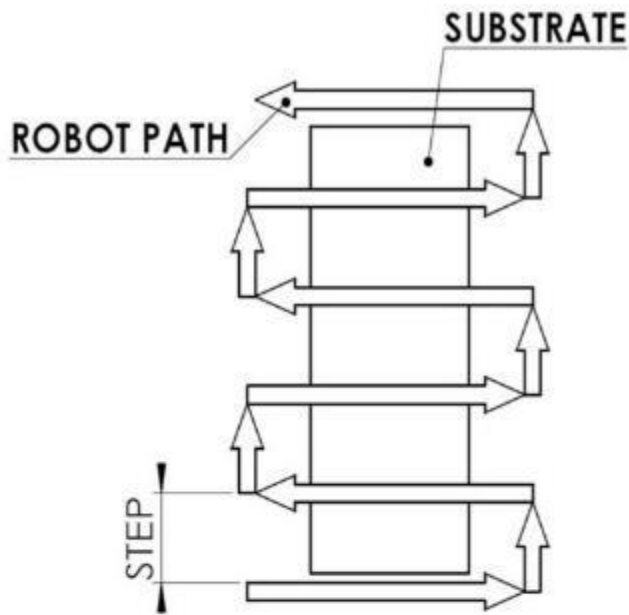


Fig. 4 Robot path employed for cold spray deposition

Table 1. The deposition procedure is shown in Fig. 4. The Cu coatings measured 0.1 and 1 mm in thicknesses, after 1 and 10 passes, respectively, Ti coatings measured 0.2 and 1 mm thicknesses, after 1 and 5 passes, respectively.

Coatings Characterizations

Metallographic preparation was performed according to the ASTM E192. Samples were grinded and polished. Leica DMI5000M (Wetzlar, Germany) microscope was employed for optical microscopy observations. The coatings thickness was measured by employing the Leica picture analyzer. The porosity levels and distribution were calculated by using the Image J processing software.

The coating mechanical properties were evaluated by employing an Anton Paar nanoindentation equipment model TTX-NHT2 (Ostfildern, Germany), with a Berkovich diamond indenter. The tests were developed in load control mode, the loading and unloading rates were 20 mN/min, and the fixed dwell time was 5 s. The coatings mechanical properties were obtained through the Oliver and Pharr methods from the load–depth indentations curves.

ASTM C633 standard was employed for adhesion properties characterization of the coatings. Steel cylinders' top surfaces were sprayed with Cu and Ti powders in the previous described conditions. Then, they were glued to the respective counter-bodies of the same size. The employed glue was a FM-1000-FOOT elastometric wafer (Indestructible Paint Inc.). The adhesive strength of the glue was measured resulting 70 MPa. Tensile tests were then performed on these

cylinders in order to measure the adhesive strength. Seven tests per condition were performed.

Scratch tests were performed by using an Anton Paar Revetest instrument (Ostfildern, Germany) with a Rockwell-C diamond indenter. The normal load was linearly varied from 1 to 200 N. The total scratch length was 10 mm. The scratching speed was 10 mm/min. The fretting wear behavior was analyzed by employing a Nanovea Tribometer T500 (Irvine, CA, USA).

Friction is measured thanks to a load cell mounted on the arm. An image processing system mounted on an optical microscope allows to analyze the traces of wear. A profilometer is employed for measuring the tracks traces. From the profilometer analyses, the wear volume loss is then calculated. The test was performed in dry mode by using a tungsten carbide pin.

Results and Discussions

The morphologies of the coatings cross section obtained by optical microscopy are shown in Fig. 5. The porosity of the Cu coatings was $0.15 \pm 0.05\%$ and $0.25 \pm 0.07\%$, for 0.2 mm and 1.0 mm, respectively, while the porosity of the Ti coatings was $1.72 \pm 0.10\%$ and $1.81 \pm 0.08\%$, for 0.1 mm and 1.0 mm, respectively. The porosity evaluation is fundamental because it strongly influences both the coating adhesion and the overall mechanical behavior.

The porosity of Cu coatings was lower than the values presented by Yin et al. [7] and Huang et al. [28], who obtained the best value of $1.67 \pm 0.21\%$ and $0.8 \pm 0.4\%$, even with higher temperature, 650 and 800 °C, respectively, than the used in this work. The porosity of Ti coatings reached very low levels [25, 41], $1.8 \pm 0.08\%$ and 1.0%, respectively. As the impact velocity increases, the particles flatten more severely; this is favored by increases in gas temperature and pressure. By tuning an ideal impact velocity, a very high particles flattening is obtained and a reduction of the deposit porosity can be recorded. This is accompanied with the particle–particle voids filling as the severe plastic deformation increases [42]. Metallurgical bonding is favored by the increases in impact energy as a consequence of the increases in severe plastic deformation [18]. The deformation level is evaluated through the single particle splatting that leads to the transformation from the spherical shape to the pancake-like one. With low impact energy, particles retain their spherical shape and the particle–particle voids are not filled sufficiently. Now, the main factors influencing the energy at impact are the particles velocity and the impact temperature; the particles energy upon impact is intrinsically related to the particle velocity at the same temperature; as a

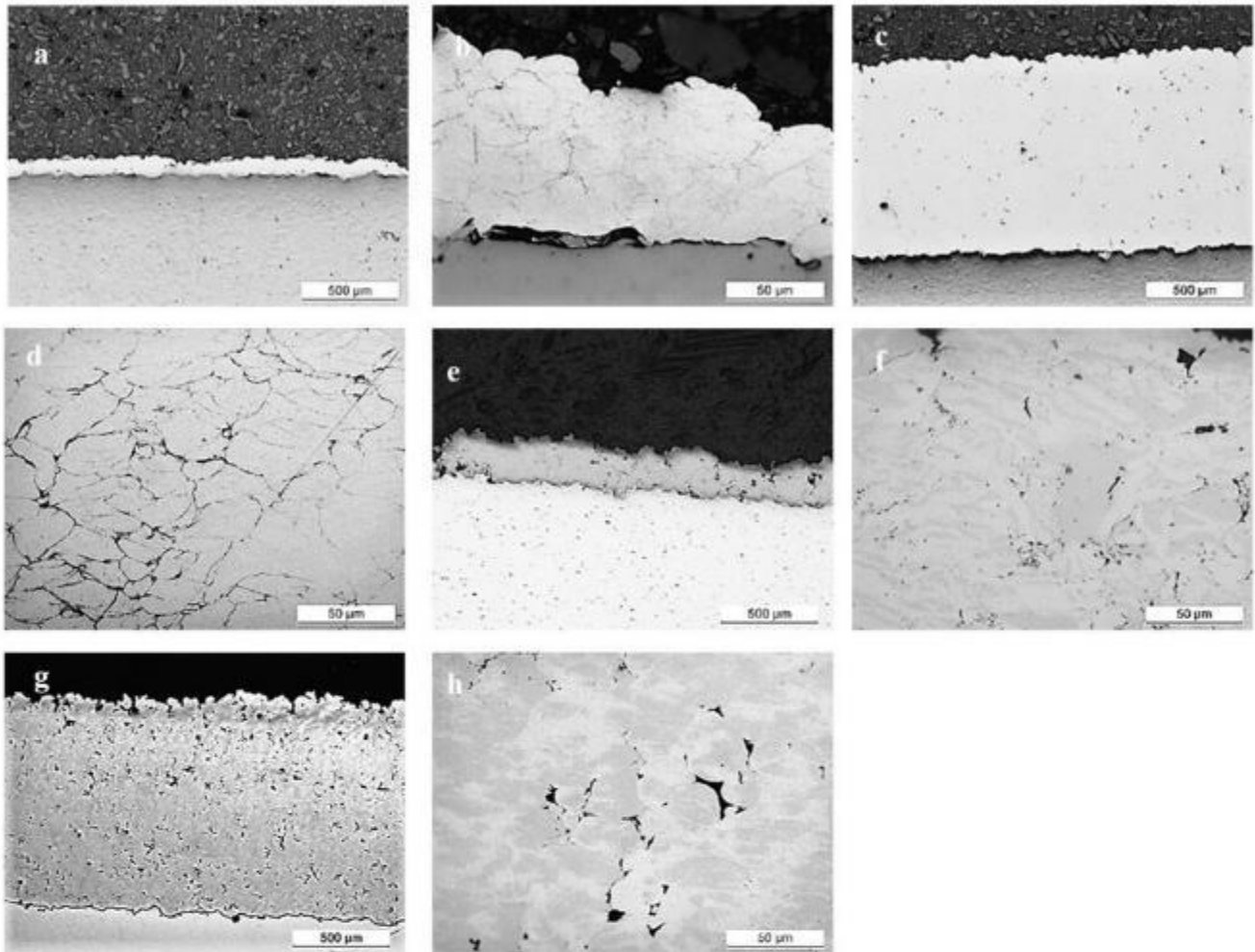


Fig. 5 Images of coatings. (a, b) Cu 0.1 mm, (c, d) Cu 1.0 mm, (e, f) Ti 0.2 mm, and (g, h) Ti 1.0 mm

consequence, porosity shows a dependence on the temperature at impact with an exponential behavior [43].

Figure 5d shows how particles strongly deform by impacting on the substrate; their shape becomes elliptical. This is very different from the Ti powders, Fig. 5h, where the particles deformation is less pronounced. The microhardness of the coatings was 100 ± 11 HV_{0.2}, 123 ± 8 HV_{0.2}, for Cu 0.1 mm and 1.0 mm, respectively, and 224 ± 9 HV_{0.2}, 209 ± 23 HV_{0.2}, for Ti 0.2 mm and 1.0 mm, respectively.

As largely described in the introduction, it is believed that deep analyses of surface response to complex loading require the precise probing of both hardness and elastic modulus in all the coatings volume [44]. Initially, nanoindentations were performed on the polished surface of the sprayed copper and titanium. The results for all the sprayed thicknesses are shown in Fig. 6.

In the first stage of indentation, the deformation is pure elastic for very low loads levels. By increasing the indentation force, the curve does not show the classical Hertzian

trend. This is due to the fact that shear deformation accumulates in the tip region with consequent plastic deformation behavior. This is due to the dislocations accumulation in the strained region; this accumulation is governed by dislocation pile-up that increases as the plastic strain continues. The indentations track on the Cu coatings surfaces is illustrated in Fig. 7a and b. The typical copper ductility is revealed by the intense plastically deformed region around the track. This behavior appears very limited for the titanium coatings, this was due to the higher stiffness of this material if compared with the copper one, and this can be clearly viewed from the indentations tracks in Fig. 7c and d.

For all the sprayed coatings, hardness decreases from the substrate toward the surface (Fig. 8).

This behavior is attributed to the continuous deformation experienced by the coating as a consequence of the progression of impact; in fact, the material continues to develop hardening as a consequence of particles impacting on the previously sprayed material up to the end of the coating

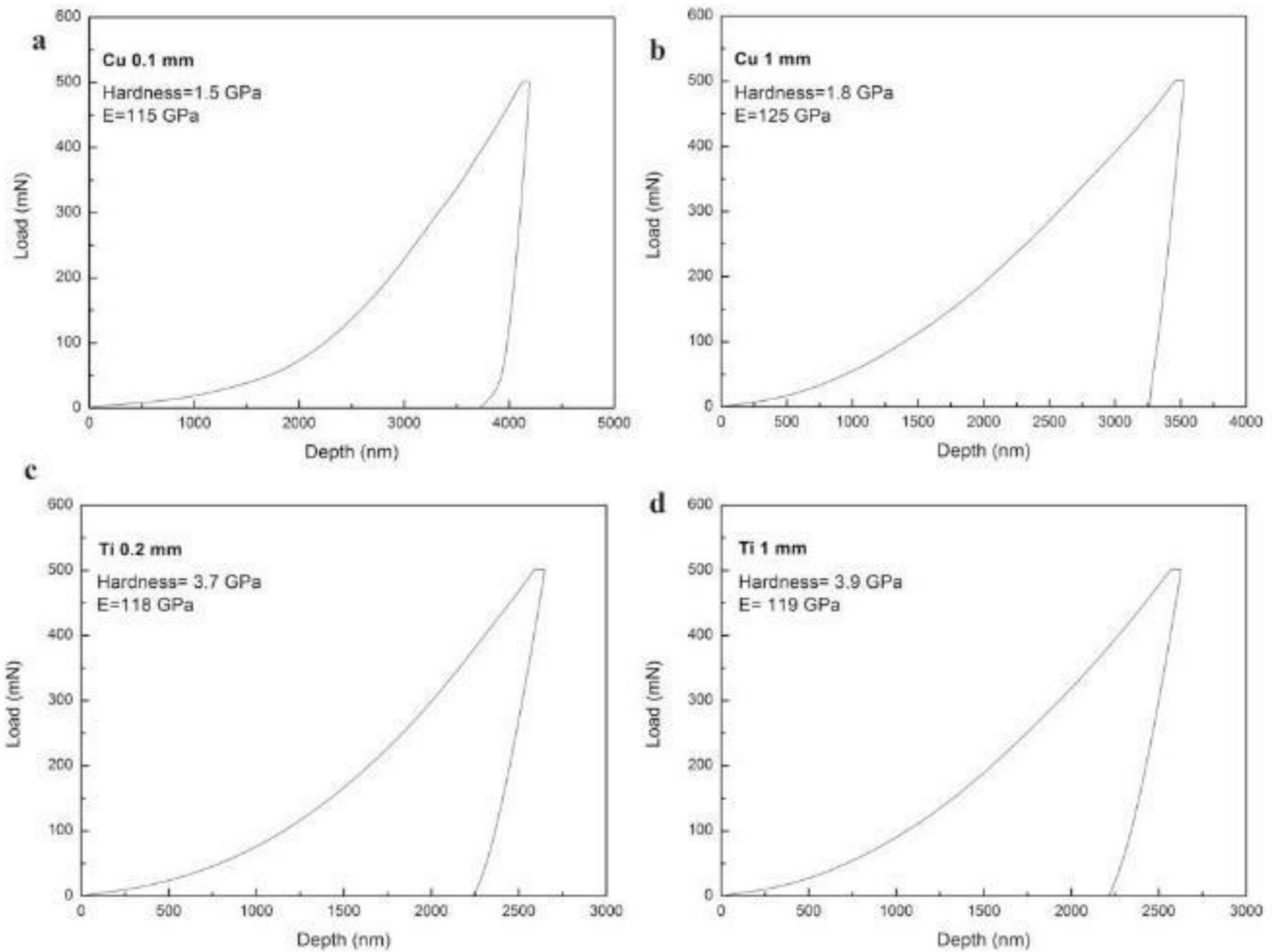


Fig. 6 Nanoindentation curves. (a) Cu 0.1 mm, (b) Cu 1.0 mm, (c) Ti 0.2 mm, and (d) Ti 1.0 mm coatings

deposition. The first deposited particles adhere to the substrate in the first stages of the cold spray process. The further sprayed particles splat by deforming on the previously sprayed material by contributing to the global severe plastic deformation of the coating. In addition, voids are filled as the process continues to evolve. This void filling as well as the continuous plastic deformation contributes to the hardness increase. Obviously this increase is more pronounced as the material is closer to the substrate.

The samples aspect after adhesion tests is shown in Fig. 9.

The measured adhesion strength was 48 ± 4 MPa for copper coatings and 61 ± 5 MPa for titanium coatings. The aspect of the coating materials after tests revealed decohesion among the particles with local plasticity behavior around each particle. This local plastic deformation resulted more pronounced in the case of copper coatings with respect to the titanium ones (Fig. 10).

It can be stated that the failure mode was mainly cohesive. This behavior is related to the energy that is dissipated along with the propagation of cracks' delamination. This is related

to the interface energy at the coating–substrate interface and then to the adhesion strength. The coatings' adhesion strength of the coating is very high if compared to the data belonging to other thermal spray coatings [22].

The coatings mechanical properties as well as the coatings–substrate adhesion were further studied by employing surface scratches at continuously increasing vertical loads. The vertical loads–scratch depths curves are plotted in Fig. 11 for all the sprayed coatings.

For the Cu coating with 0.1 mm in thickness, the linear behavior is altered around the scratch depth of $100 \mu\text{m}$ because of the indent reaching the substrate. The scratched coatings behavior is revealed by the scratch tracks after loading. These are shown in 10, for Cu and Ti coatings.

The deep observation of the load–depth behavior allows to identify the various critical loads (CL). Coatings are progressively damaged upon scratch and consequently some specific mechanisms can be individuated as the vertical load increases. The mechanisms are cracking, fractures and final decohesion. The observation of these features permits to

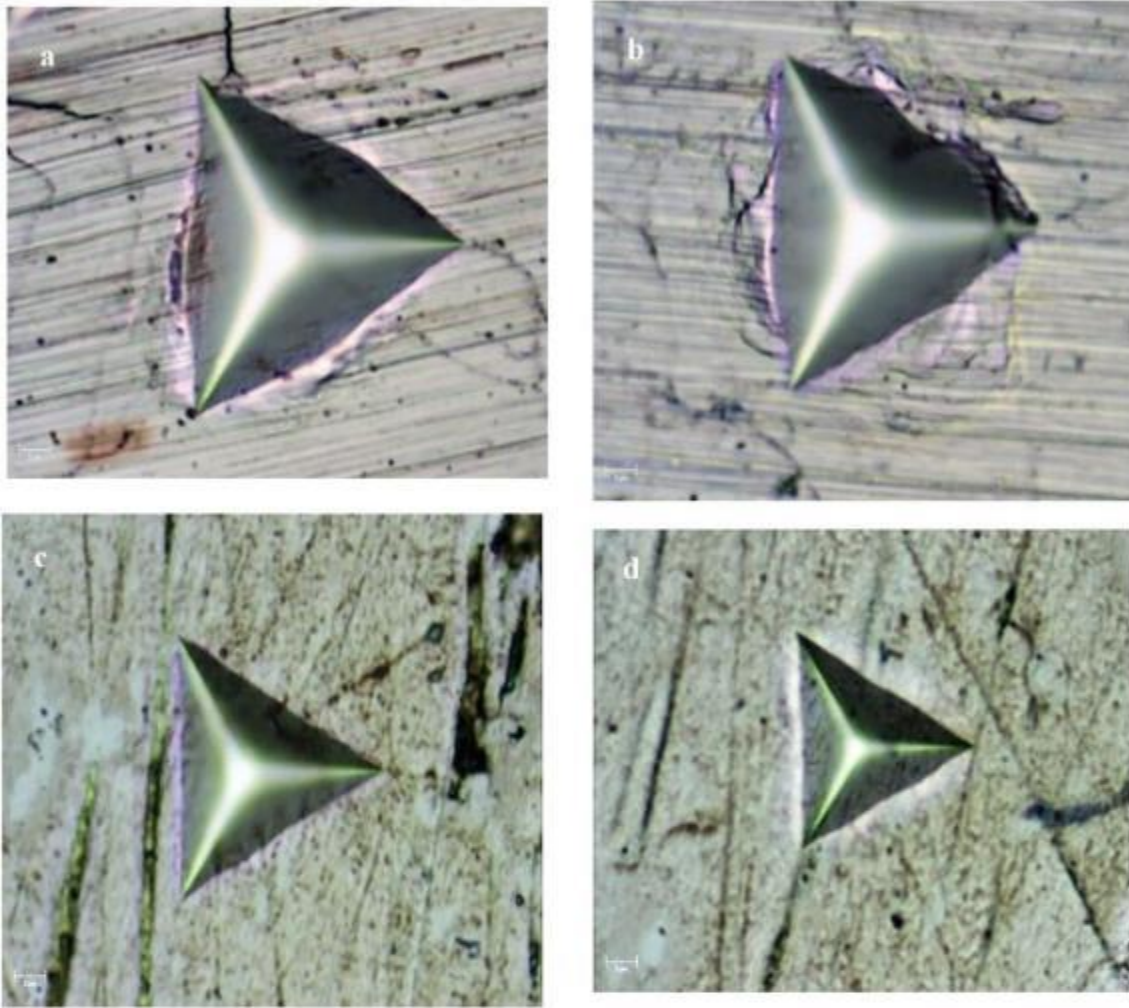


Fig. 7 Indentations aspect: (a) Cu 0.1 mm, (b) Cu 1.0 mm, (c) Ti 0.2 mm, and (d) Ti 1.0 mm coatings

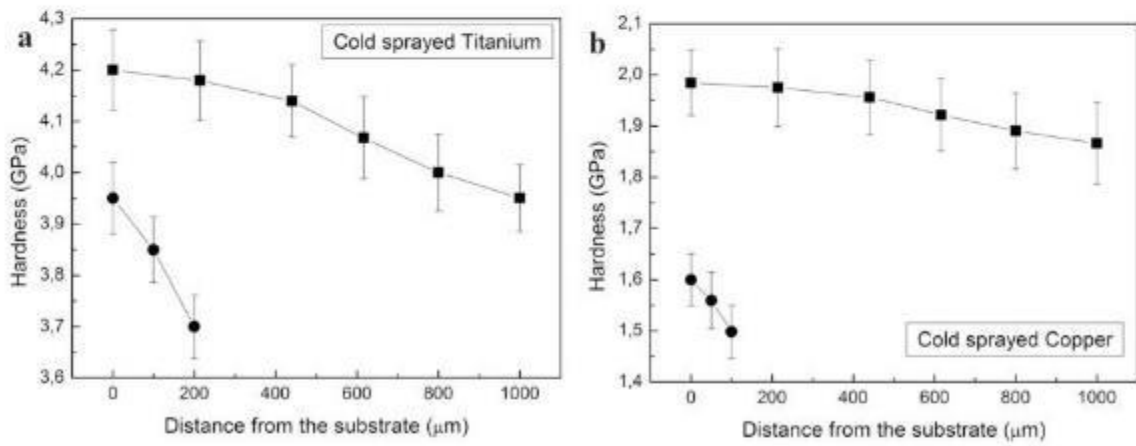


Fig. 8 Hardness variation as a function of the distance from the substrate for all the cold-sprayed coatings

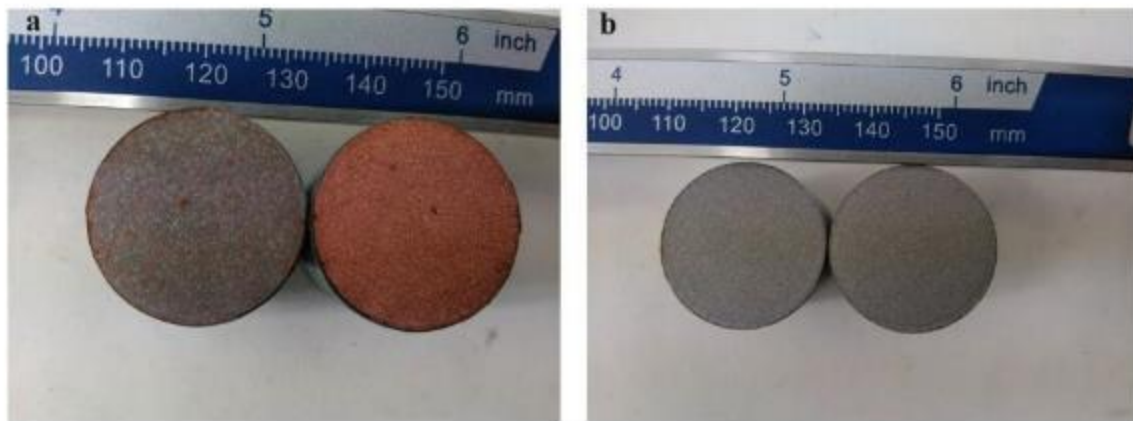


Fig. 9 Coated cylinders after tensile tests performed for adhesion measurement

identify the critical loads that produce such damaging. As the vertical load increases, stress in the coating increases by inducing specific mechanisms in the track. For the case of the studied coatings, the different damage mechanisms were identified through scanning electron microscopy observations of the tracks after scratching. As expected, the coatings show a different scratch behavior depending on the material composition and on the coating thickness. First of all, from the load–depth curves it appears how the copper coatings show a very regular curve while the titanium coatings show continuous variation revealing many microstructural modifications related to the material behavior during scratches. The most regular scratch behavior is shown by the copper coating with 1 mm thickness where the scratch does not show to produce damage in the unscratched material or fractures on the scratch surface. The scratch evolves through the formation of many peripheral copper flakes. Obviously, the flakes volume increases as the maximum load increases (Fig. 12b). By observing the titanium cold-sprayed coating with the same thickness (1 mm), they were observed many microstructural features inside the track and in the peripheral material. The occurrence of the critical loads means that the deformation mode is varying as the scratch continues at increased vertical loads. By setting a linearly increasing vertical load during scratch, a continuous series of damaging mechanisms is observed in the track. The damage mechanisms usually lead to the coating delamination [45]. The first critical load is normally associated with the initial damage mechanisms developing as a consequence of scratching. In the present case, it was individuated as the appearance of the first cracks on the scratch tracks where the compression forces of the indent are predominant with respect to the tangential forces (Fig. 13).

By comparing the cracks presence with the load–depth curve, it is possible to affirm that this first critical load is 48N at 46 μm penetration depth. The cracks intensity is enhanced

as the vertical load is linearly increased. As the vertical load increases, higher compressive state is induced on the surface with consequent damage loading of the scratched material. The second critical load was attributed to the appearance of tongue-shaped cracks (Fig. 14).

These are due to a more complex multiaxial stress field induced in the material as the scratch proceeds. The second critical load was recorded at 100N at 90 μm penetration depth. The last critical load is characteristic of cold-sprayed coatings; in this case the damage is transferred to the material surrounding the scratch with the increase in compressive stresses leading to particles decohesion (Fig. 15a) that becomes very remarkable at the vertical maximum load (Fig. 15b).

This behavior starts at the load of 127N. By comparing these features to the scratch behavior observed in the cold-sprayed titanium with a coating thickness of 0.2 mm, the first cracks appear at a load of 50 N, comparable with the observations of the coating with 1 mm thickness (Fig. 16a). The pronounced tongue-shaped cracks appear at 85 N (Fig. 16b), while the pronounced damage in the material surrounding the scratch with particles decohesion is observed at a vertical load of 135 N (Fig. 16c). The scratch track at the maximum vertical force is shown in Fig. 16d.

Now, also if the mechanical and microstructural behaviors of the two coatings appear very similar, it is believed that the coating thickness influences the scratch behavior. This is very pronounced in a very ductile material as copper. As a matter of fact, the scratch aspect of the coating with 0.1 mm thickness shows a very different behavior if compared to the coating with 1mm thickness. In fact, in this case, small tongue cracks appear on the crack surface at a load of 80 N (Fig. 17a); the dimension of these cracks increases up to the maximum vertical load (Fig. 17b) revealing a larger sensibility to the increase in compressive stresses in cold-sprayed coatings with small thicknesses.

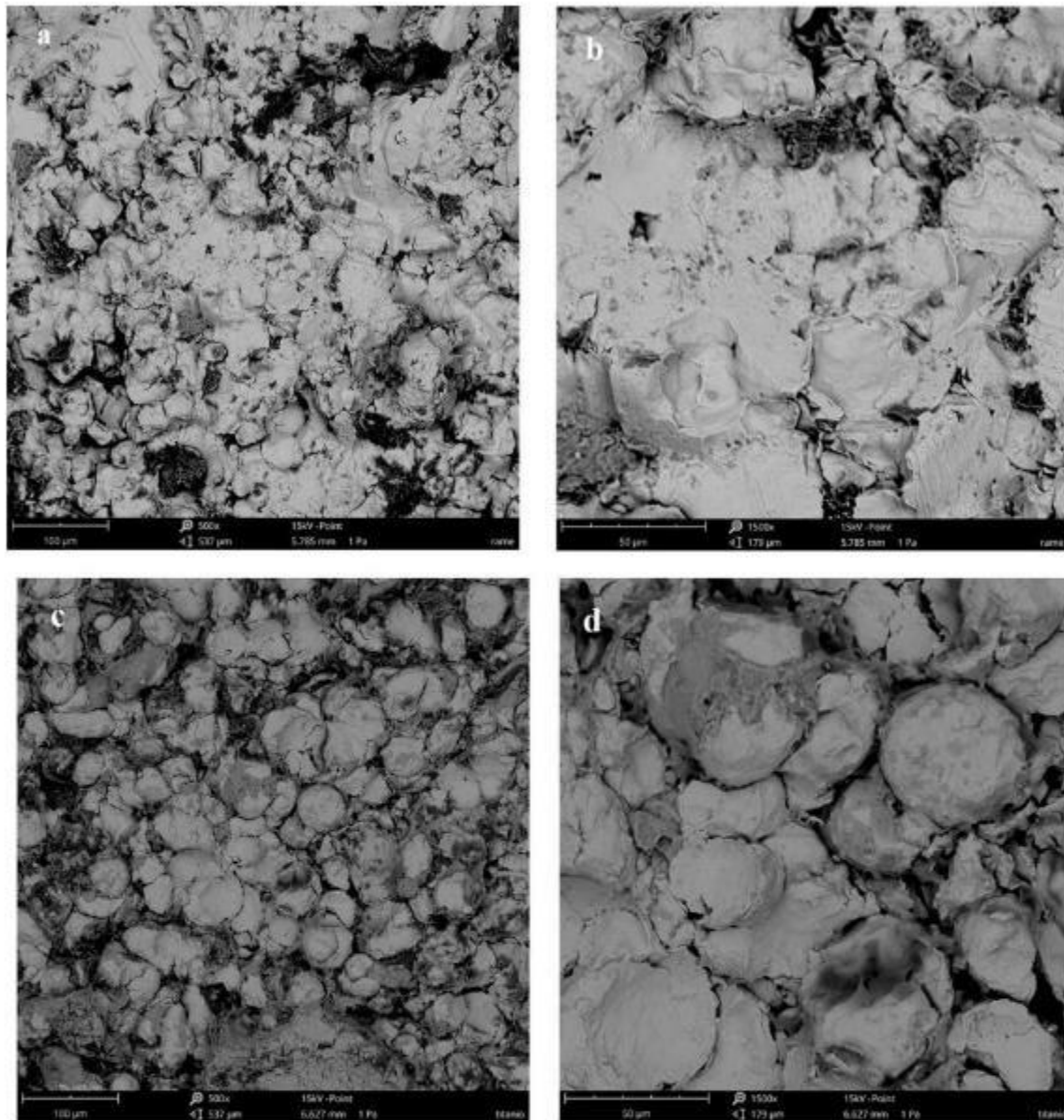


Fig. 10 Surface aspect of copper (a, b) and titanium (c, d) after tensile adhesion tests

The employed vertical loads were set to 50, 100 and 150 N. The wear traces for Cu and Ti at 150 N for all the thicknesses are shown in Fig. 18.

Figure 19 shows the wear aspect and profiles. They were employed to calculate the wear damaging in terms of weight loss.

As expected, the material volume loss increases as increasing the fretting load. The weight loss is more pronounced for the thicker coatings at the same maximum load level. This was due to the increased hardening of the sprayed particles observed as the coatings thickness increases. This was shown by the lower slope of the load-weight loss curves by increasing the maximum load from 50 N to 100 and 150

N. As the maximum wear force increases, the material under wear is progressively more hard as a function of the distance from the substrate. The harder material is more resistant to the wear damaging (Fig. 20).

Due to the relative movement of the contact interfaces, direction and magnitude of the force are constantly changing. This leads to the variation of the contact mechanisms and consequently to the wear behavior. The friction coefficient is the ratio between the tangential contact force during the pin slip and the normal load applied to the contact surface. Cold-sprayed coatings experience low friction at ambient temperature. The friction coefficient decreases as the maximum load increases; this confirms the described

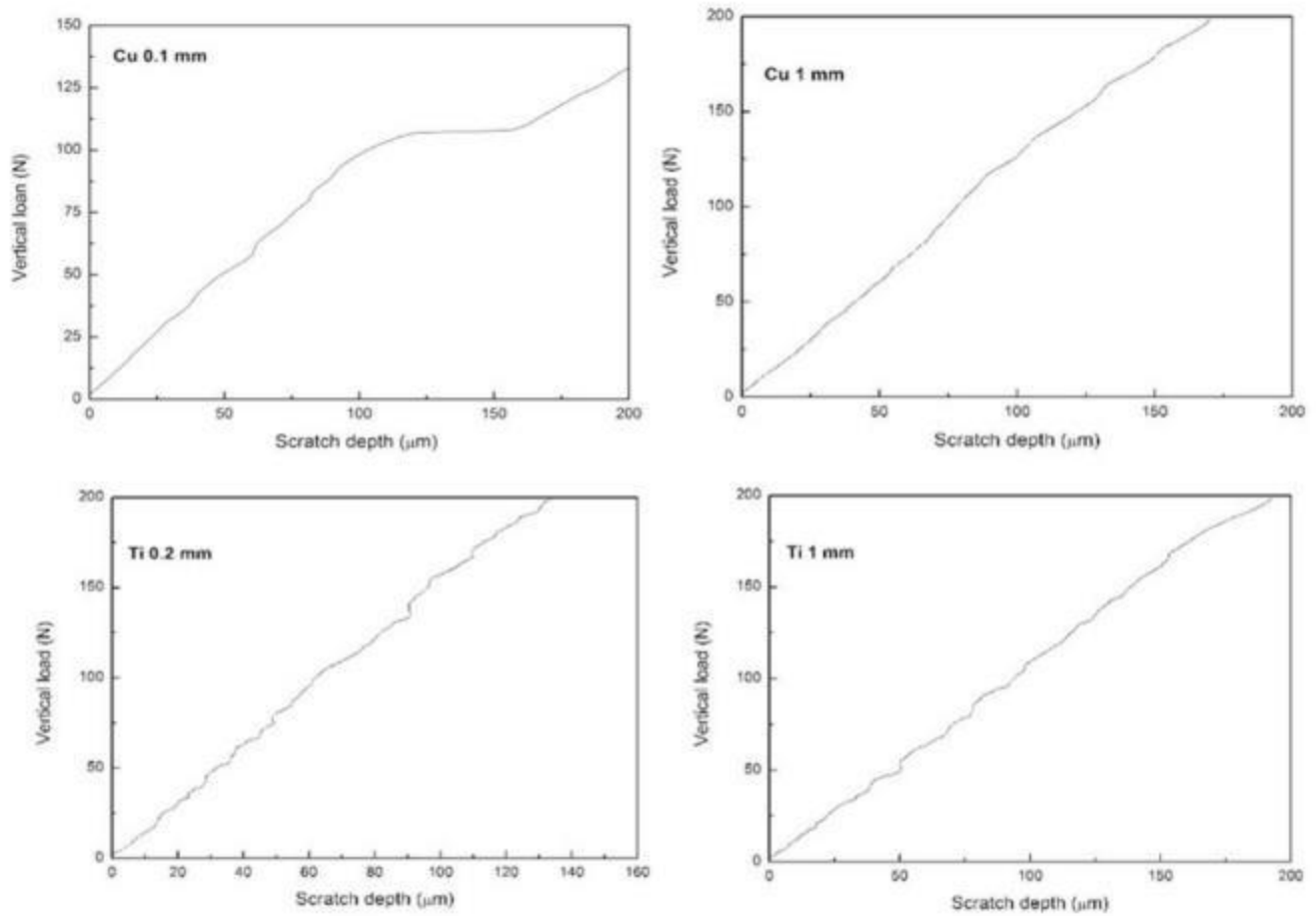


Fig. 11 Vertical load versus scratch depth. (a) Cu 0.1 mm, (b) Cu 1.0 mm, (c) Ti 0.2 mm, and (d) Ti 1.0 mm coatings

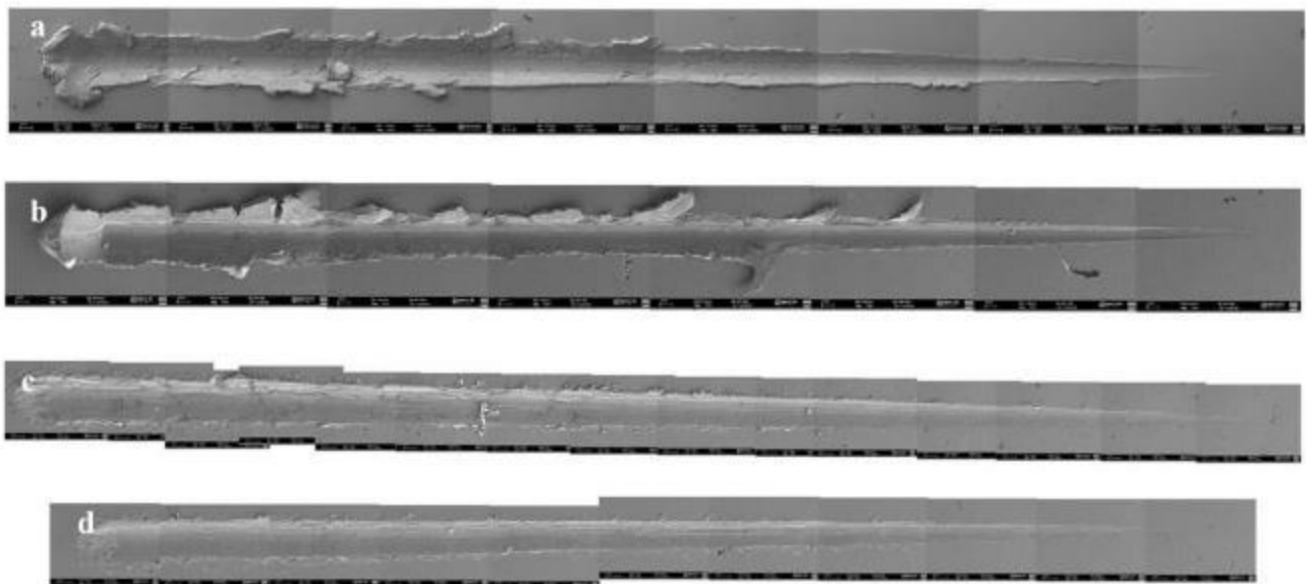


Fig. 12 Scratch tracks. (a) Cu 0.1 mm, (b) Cu 1.0 mm, (c) Ti 0.2 mm, and (d) Ti 1.0 mm coatings

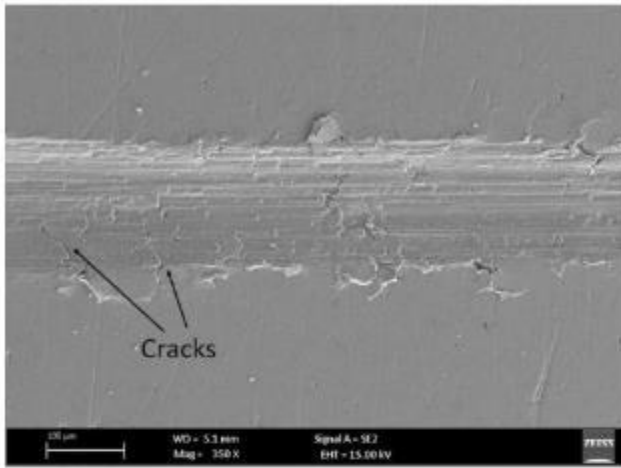


Fig. 13 First cracks appearance in the scratch track of the cold-sprayed Ti with 1 mm thickness

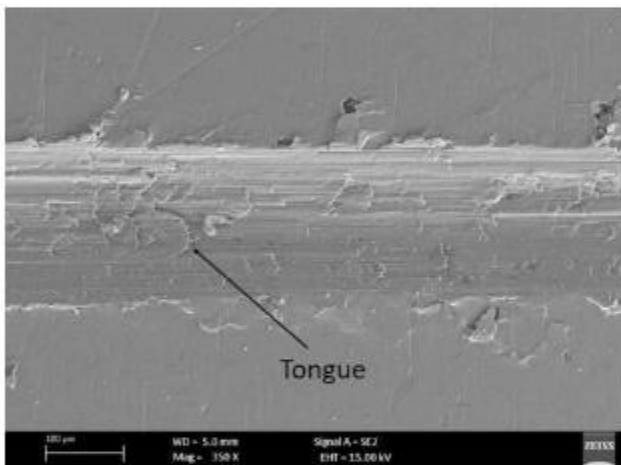
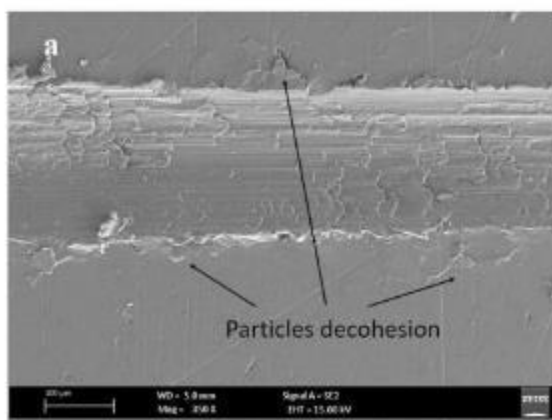


Fig. 14 Tongue shaped cracks in the scratch track of the cold-sprayed Ti with 1 mm thickness



mechanisms due to the increase in hardness as approaching the substrate. The fretting wear of the studied coatings is plotted in Fig. 21 for the different applied maximum loads.

The effect of material hardness on the fretting wear damaging is still under debate. Recent evidences of fretting behavior of heavily hardened steels show that hardness differences reduce damaging while increased weight loss is recorded as the hardness decreases [46, 47]. Various results show the hardness behavior effect on fretting wear damaging [48]. Here, the materials hardening produced higher resistance against wearing. The hardened volume leads to friction reduction and to reduced damaging in the inner material. As the fretting material is harder, it is able to dissipate more energy being capable of resulting more stiff to wear damaging. So, the principal conclusion is that the hardness variation of cold-sprayed materials governs the weight loss and the frictional behavior of the coatings. This behavior reveals a direct relationship between the nanoindentation evolution and the fretting wear damaging.

Conclusions

The wear and fretting behavior of Ti and Cu cold-sprayed coatings with different thickness was described in the present paper. Low porosity was revealed for all the coatings; this was attributed to the optimal processing parameters selected for spraying. Nanoindentation hardness was higher for the thicker coatings because of the increases particles deformation as the particles continue to splat on the substrate and on the previously deposited particles. The coatings behavior was very different for the two materials during scratch and also for different thicknesses. The most regular scratch behavior is shown by the copper coating with 1 mm thickness where the scratch does not show to produce damage in the unscratched material or fractures on the scratch

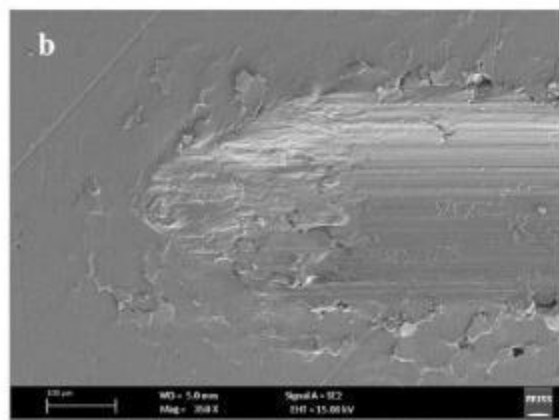


Fig. 15 Macrodamage leading to particles decohesion in the cold-sprayed Ti with 1 mm thickness

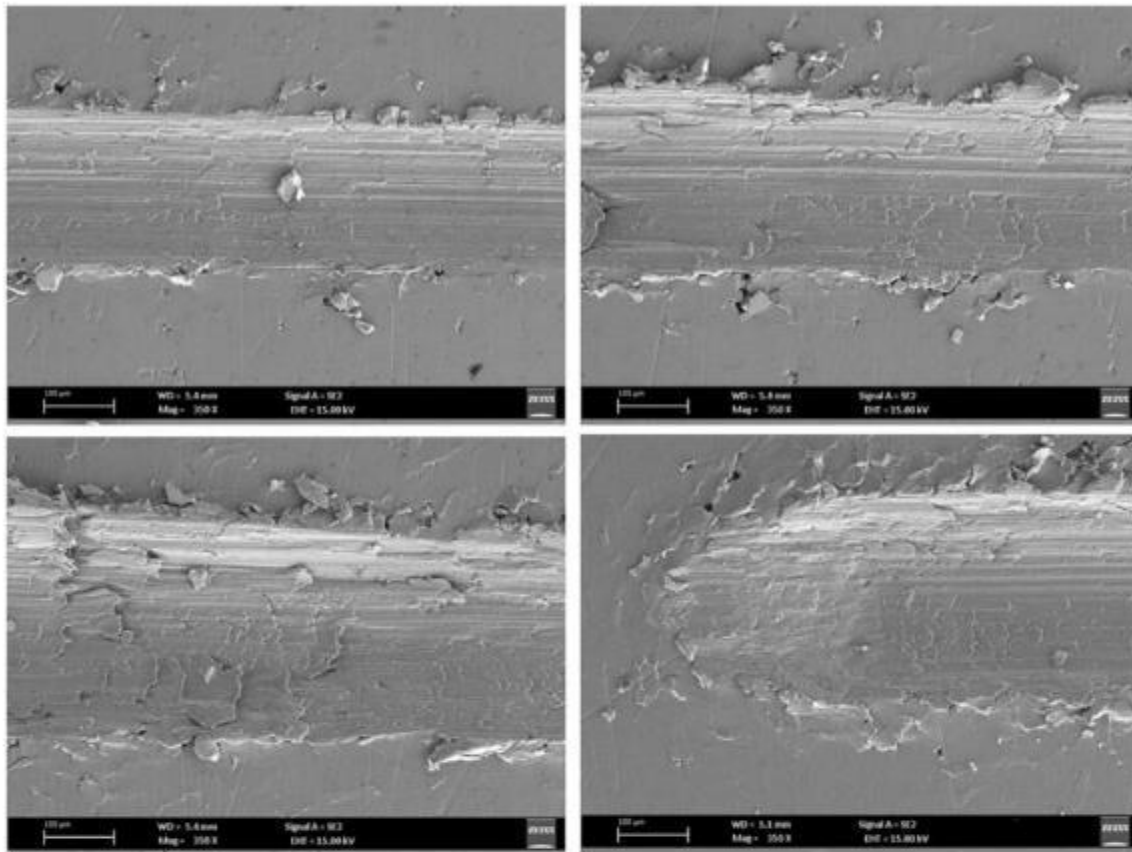


Fig. 16 Damage in the cold-sprayed Ti coating with 0.2 mm thickness

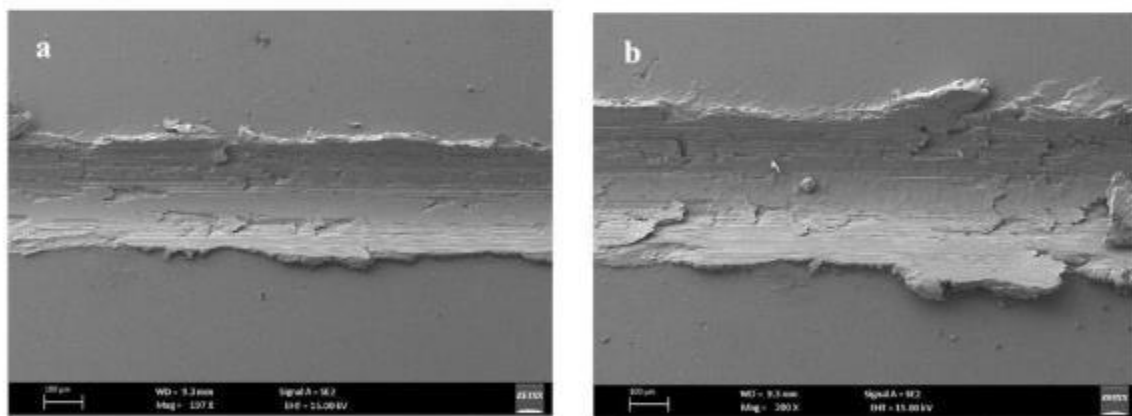


Fig. 17 Damage in the cold-sprayed Cu coating with 0.1 mm thickness

surface. Many damage features are revealed by titanium cold-sprayed coatings with micro-fractures and particles decohesion appearing as the vertical scratch load increases. Also the thickness influences this behavior; this was revealed by the Cu coatings 0.1 mm thick where different fractures appear in the scratch track revealing a completely different behavior with respect to the 1-mm-thick coating. The

fretting results showed that the volume reduction increases for lower coatings thickness. This aspect was due to the enhanced particles severe plastic deformation observed as the coatings thickness is increased. As the maximum force increases, in fact, the fretting material is linearly harder by moving from the surface toward the substrate. This hardening induces higher resistance to wear damaging.

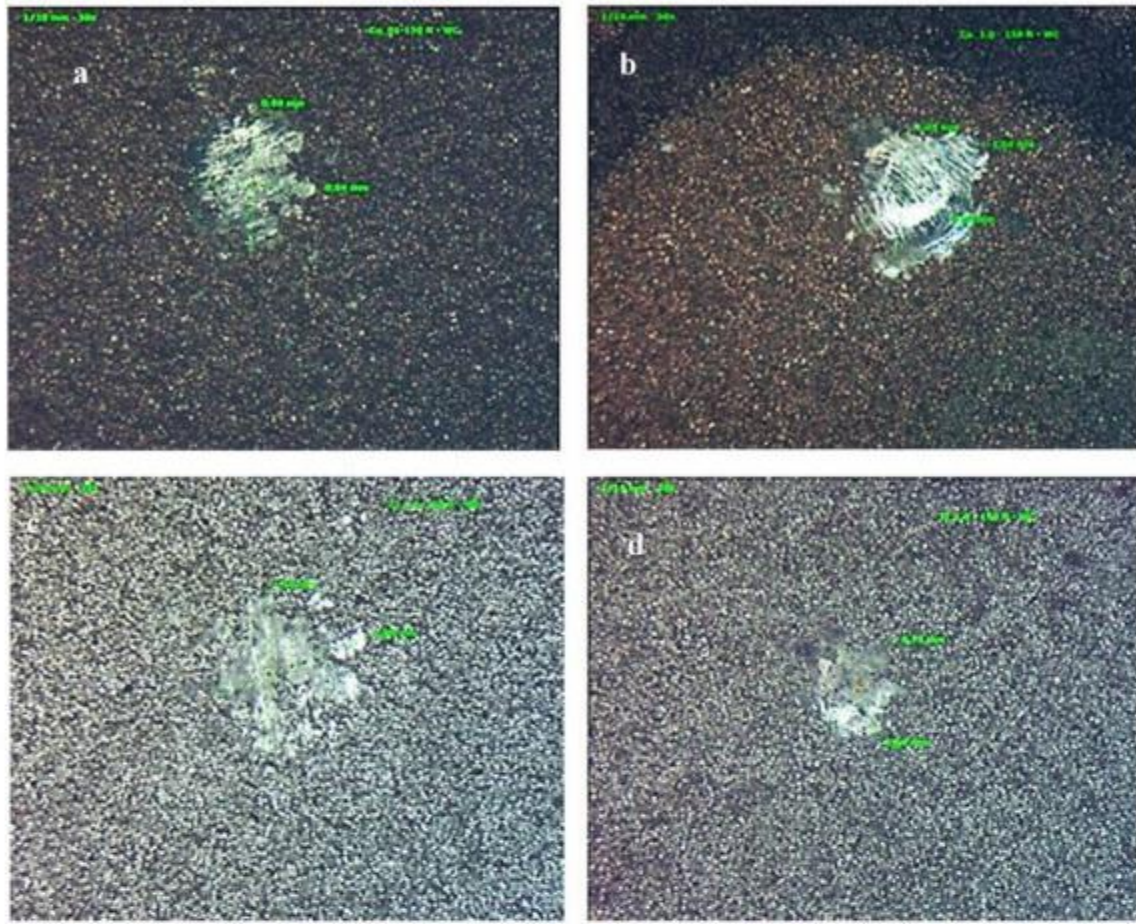


Fig. 18 Wear traces by fretting at a maximum load of 150 N. (a, b) Cu and (c, d) Ti coatings

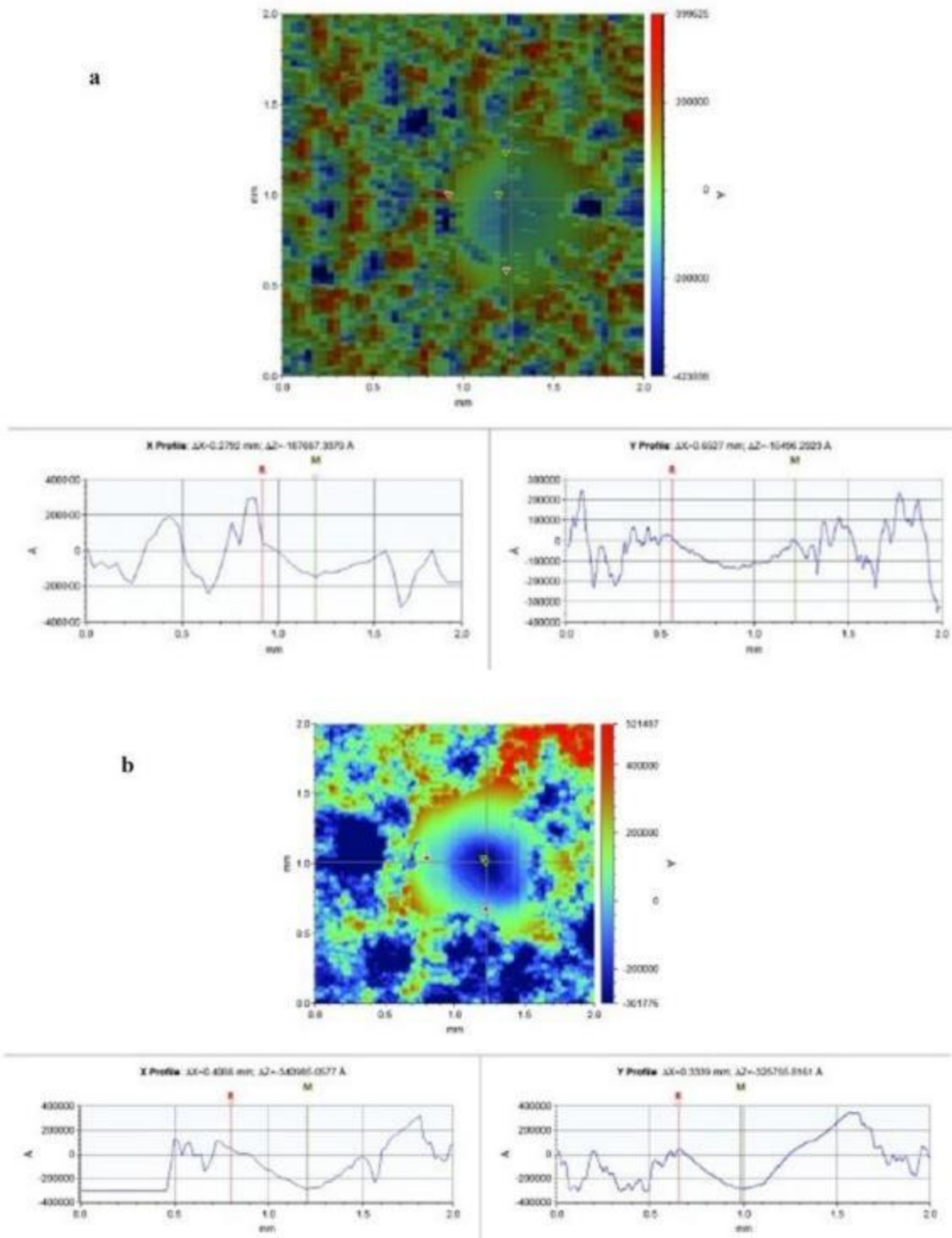


Fig. 19 Wear traces for the studied coatings after wear at a maximum load of 150 N

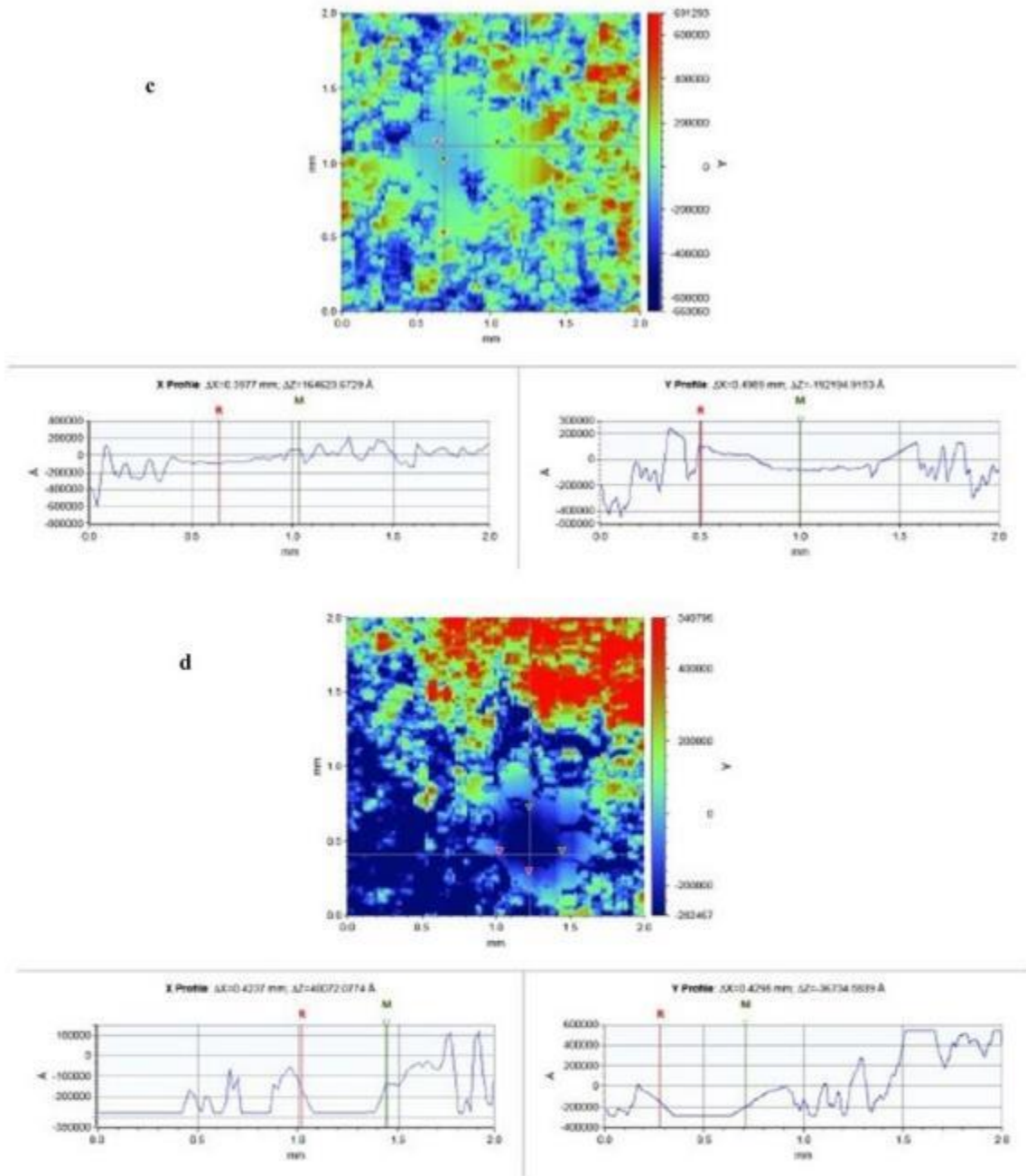


Fig. 19 (continued)

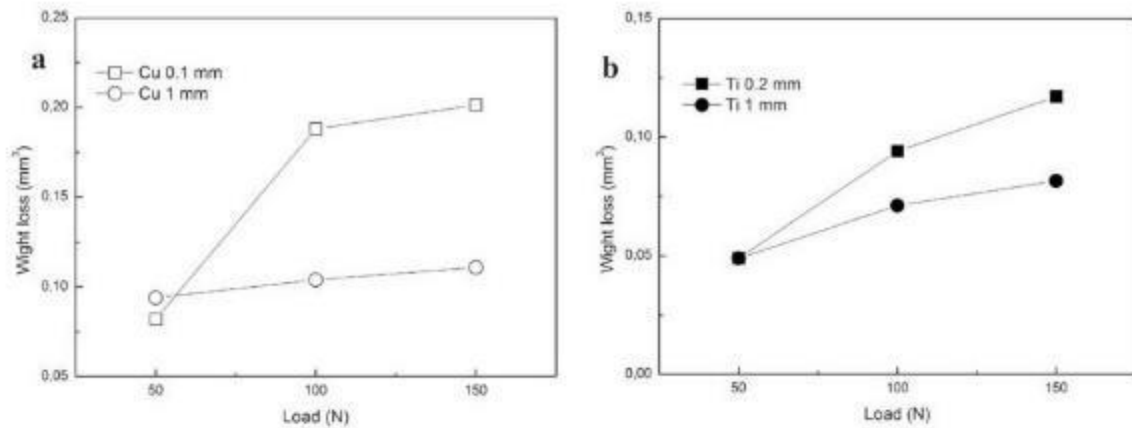


Fig. 20 Weight loss after wear testing. (a) Cu and (b) Ti coatings

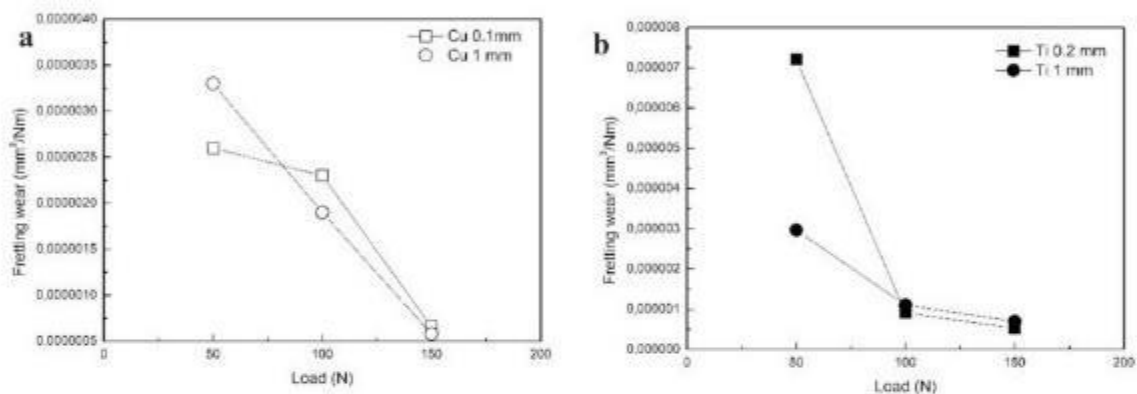


Fig. 21 Fretting wear experienced by all the coatings at different loads

Funding Open access funding provided by Università del Salento within the CRUI-CARE Agreement.

Open Access This article is licensed under a Creative Commons Attribution 4.0 International License, which permits use, sharing, adaptation, distribution and reproduction in any medium or format, as long as you give appropriate credit to the original author(s) and the source, provide a link to the Creative Commons licence, and indicate if changes were made. The images or other third party material in this article are included in the article's Creative Commons licence, unless indicated otherwise in a credit line to the material. If material is not included in the article's Creative Commons licence and your intended use is not permitted by statutory regulation or exceeds the permitted use, you will need to obtain permission directly from the copyright holder. To view a copy of this licence, visit <http://creativecommons.org/licenses/by/4.0/>.

References

1. S. Bagherifard, S. Monti, M.V. Zuccoli, M. Riccio, J. Kondás, M. Guagliano, Cold spray deposition for additive manufacturing of freeform structural components compared to selective laser melting. *Mater. Sci. Eng. A.* **721**, 339–350 (2018). <https://doi.org/10.1016/j.msea.2018.02.094>
2. M.E. Lynch, W. Gu, T. El-Wardany, A. Hsu, D. Viens, A. Nardi, M. Klecka, Design and topology/shape structural optimisation for additively manufactured cold sprayed components. *Virtual Phys. Prototyp.* **8**, 213–231 (2013). <https://doi.org/10.1080/17452759.2013.837629>
3. X. Wang, F. Feng, M.A. Klecka, M.D. Mordasky, J.K. Garofano, T. El-Wardany, A. Nardi, V.K. Champagne, Characterization and modeling of the bonding process in cold spray additive manufacturing. *Addit. Manuf.* **8**, 149–162 (2015). <https://doi.org/10.1016/j.addma.2015.03.006>
4. S. Yin, P. Cavaliere, B. Aldwell, R. Jenkins, H. Liao, W. Li, R. Lupoi, Cold spray additive manufacturing and repair: fundamentals and applications. *Addit. Manuf.* **21**, 628–650 (2018). <https://doi.org/10.1016/j.addma.2018.04.017>
5. A. Sova, S. Grigoriev, A. Okunkova, I. Smurov, Potential of cold gas dynamic spray as additive manufacturing technology. *Int. J. Adv. Manuf. Technol.* **69**, 2269–2278 (2013). <https://doi.org/10.1007/s00170-013-5166-8>
6. C. Chen, Y. Xie, X. Yan, S. Yin, H. Fukunuma, R. Huang, R. Zhao, J. Wang, Z. Ren, M. Liu, H. Liao, Effect of hot isostatic pressing (HIP) on microstructure and mechanical properties of Ti6Al4V alloy fabricated by cold spray additive manufacturing. *Addit. Manuf.* **27**, 595–605 (2019). <https://doi.org/10.1016/j.addma.2019.03.028>

7. S. Yin, R. Jenkins, X. Yan, R. Lupoi, Microstructure and mechanical anisotropy of additively manufactured cold spray copper deposits. *Mater. Sci. Eng. A*. **734**, 67–76 (2018). <https://doi.org/10.1016/j.msea.2018.07.096>
8. W. Li, K. Yang, S. Yin, X. Yang, Y. Xu, R. Lupoi, Solid-state additive manufacturing and repairing by cold spraying: a review. *J. Mater. Sci. Technol.* **34**, 440–457 (2018). <https://doi.org/10.1016/j.jmst.2017.09.015>
9. S.H. Zahiri, W. Yang, M. Jahedi, Characterization of cold spray titanium supersonic jet. *J. Therm. Spray Technol.* **18**, 110–117 (2009). <https://doi.org/10.1007/s11666-008-9278-x>
10. P. Cavaliere, *Cold-Spray Coatings: Recent Trends and Future Perspectives* (Springer, New York, 2018) <https://doi.org/10.1007/978-3-319-67183-3>
11. H. Assadi, F. Gärtner, T. Stoltenho, H. Kreye, Bonding mechanism in cold gas spraying. *Acta Mater.* **51**, 4379–4394 (2003). [https://doi.org/10.1016/S1359-6454\(03\)00274-X](https://doi.org/10.1016/S1359-6454(03)00274-X)
12. M.R. Rokni, S.R. Nutt, C.A. Widener, V.K. Champagne, R.H. Hrabec, Review of relationship between particle deformation, coating microstructure, and properties in high-pressure cold spray. *J. Therm. Spray Technol.* **26**, 1308–1355 (2017). <https://doi.org/10.1007/s11666-017-0575-0>
13. A. Silvello, P.D. Cavaliere, V. Albaladejo, A. Martos, S. Dosta, I.G. Cano, Powder properties and processing conditions affecting cold spray deposition. *Coatings*. **10**(2), 91 (2020). <https://doi.org/10.3390/coatings10020091>
14. P. Cavaliere, A. Silvello, Processing conditions affecting residual stresses and fatigue properties of cold spray deposits. *Int. J. Adv. Manuf. Technol.* **81**(9–12), 1857–1862 (2015). <https://doi.org/10.1007/s00170-015-7365-y>
15. Y. Xie, M.-P. Planche, R. Raoulison, H. Liao, X. Suo, P.J. Hervé, Effect of substrate preheating on adhesive strength of SS316L cold spray coatings. *J. Therm. Spray Technol.* **25**, 123–130 (2016). <https://doi.org/10.1007/s11666-015-0312-5>
16. K. Kim, M. Watanabe, S. Kuroda, Bonding mechanisms of thermally softened metallic powder particles and substrates impacted at high velocity. *Surf. Coat. Technol.* **204**, 2175–2180 (2010). <https://doi.org/10.1016/j.surfcoat.2009.12.001>
17. M. Hassani-Gangaraj, D. Veyssset, V.K. Champagne, K.A. Nelson, C.A. Schuh, Adiabatic shear instability is not necessary for adhesion in cold spray. *Acta Mater.* **158**, 430–439 (2018). <https://doi.org/10.1016/j.actamat.2018.07.065>
18. P. Cavaliere, A. Silvello, Finite element analyses of pure Ni cold spray particles impact related to coating crack behaviour. *Surf. Eng.* **34**(5), 361–368 (2018). <https://doi.org/10.1080/02670844.2017.1287555>
19. P. Cavaliere, A. Perrone, A. Silvello, Pure cobalt cold spray nanostructured coatings. *J. Therm. Spray Technol.* **25**(6), 1168–1176 (2016). <https://doi.org/10.1007/s11666-016-0434-4>
20. P. Cavaliere, A. Perrone, A. Silvello, Crystallization evolution of cold sprayed pure Ni coatings. *J. Therm. Spray Technol.* **25**(6), 1158–1167 (2016). <https://doi.org/10.1007/s11666-016-0430-8>
21. S. Yin, X. Wang, X. Suo, H. Liao, Z. Guo, W. Li, C. Coddet, Deposition behavior of thermally softened copper particles in cold spraying. *Acta Mater.* **61**, 5105–5118 (2013). <https://doi.org/10.1016/j.actamat.2013.04.041>
22. P. Cavaliere, A. Silvello, N. Cinca, H. Canales, S. Dosta, I. Garcia Cano, J.M. Guilemany, Microstructural and fatigue behavior of Cold Sprayed Ni-based superalloys coatings. *Surf. Coat. Technol.* **324**, 390–402 (2017). <https://doi.org/10.1016/j.surfcoat.2017.06.006>
23. N. Cinca, C.R.C. Lima, J.M. Guilemany, An overview of intermetallics research and application: status of thermal spray coatings. *J. Mater. Res. Technol.* **2**, 75–86 (2013). <https://doi.org/10.1016/j.jmrt.2013.03.013>
24. R.R. Boyer, An overview on the use of titanium in the aerospace industry. *Mater. Sci. Eng. A*. **213**, 103–114 (1996). [https://doi.org/10.1016/0921-5093\(96\)10233-1](https://doi.org/10.1016/0921-5093(96)10233-1)
25. J. Ajaja, D. Goldbaum, R.R. Chromik, Characterization of Ti cold spray coatings by indentation methods. *Acta Astronaut.* **69**, 923–928 (2011). <https://doi.org/10.1016/j.actastro.2011.06.012>
26. M. Geetha, A.K. Singh, R. Asokamani, A.K. Gogia, Ti based biomaterials, the ultimate choice for orthopaedic implants—a review. *Prog. Mater. Sci.* **54**, 397–425 (2009). <https://doi.org/10.1016/j.pmatsci.2008.06.004>
27. S.M. Hassani-Gangaraj, A. Moridi, M. Guagliano, Critical review of corrosion protection by cold spray coatings. *Surf. Eng.* **31**, 803–815 (2015). <https://doi.org/10.1179/1743294415Y.0000000018>
28. J. Huang, X. Yan, C. Chang, Y. Xie, W. Ma, R. Huang, R. Zhao, S. Li, M. Liu, H. Liao, Pure copper components fabricated by cold spray (CS) and selective laser melting (SLM) technology. *Surf. Coat. Technol.* **395**, 125936 (2020). <https://doi.org/10.1016/j.surfcoat.2020.125936>
29. C. Silbernagel, L. Gargalis, I. Ashcroft, R. Hague, M. Galea, P. Dickens, Electrical resistivity of pure copper processed by medium-powered laser powder bed fusion additive manufacturing for use in electromagnetic applications. *Addit. Manuf.* **29**, 100831 (2019). <https://doi.org/10.1016/j.addma.2019.100831>
30. E. Napieralska-Juszczak, K. Komezka, F. Morganti, J.K. Sykulski, G. Vega, Y. Zeroukhi, Measurement of contact resistance for copper and aluminium conductors. *Int. J. Appl. Electromagn. Mech.* **53**, 617–629 (2017). <https://doi.org/10.3233/JAE-160025>
31. S. Shah, K.K. Kumar, Experimental study & heat transfer analysis on copper spiral heat exchanger using water based SiO₂ nanofluid as coolant. *World J. Nano Sci. Eng.* **8**, 57–68 (2018). <https://doi.org/10.4236/wjnse.2018.84004>
32. Astarita, A., Rubino, F., Carlone, P., Ruggiero, A., Leone, C., Genna, S., Merola, M., Squillace, A.: On the improvement of AA2024 wear properties through the deposition of a cold-sprayed titanium coating. *Metals (Basel)* **6** (2016). <https://doi.org/10.3390/met6080185>
33. Z. Jia, Y. Wang, J. Ji, X. Sun, Fretting wear properties of thermally deformed Inconel 625 alloy. *Trans. Ind. Inst. Met.* (2020). <https://doi.org/10.1007/s12666-020-02085-6>
34. S.R. Soria, A. Tolley, A. Yawny, Characterization of damage and tribo-particles resulting from fretting of Incoloy 800 steam generator tubes against different materials. *Wear*. **390–391**, 198–208 (2017). <https://doi.org/10.1016/j.wear.2017.07.022>
35. P. Sirvent, M.A. Garrido, S. Lozano-Perez, P. Poza, Oscillating and unidirectional sliding wear behaviour of cold sprayed Ti–6Al–4V coating on Ti–6Al–4V substrate. *Surf. Coat. Technol.* **382**, 125152 (2020). <https://doi.org/10.1016/j.surfcoat.2019.125152>
36. N.W. Khun, A.W.Y. Tan, E. Liu, Mechanical and tribological properties of coldsprayed Ti coatings on Ti–6Al–4V substrates. *J. Therm. Spray Technol.* **25**, 715–724 (2016). <https://doi.org/10.1007/s11666-016-0396-6>
37. P. Cavaliere, Mechanical properties of nanocrystalline metals and alloys studied via multi-step nanoindentation and finite element calculations. *Mater. Sci. Eng. A*. **512**, 1–9 (2009). <https://doi.org/10.1016/j.msea.2009.03.008>
38. Y. Chen, S.R. Bakshi, A. Agarwal, Correlation between nanoindentation and nanoscratch properties of carbon nanotube reinforced aluminum composite coatings. *Surf. Coat. Technol.* **204**, 2709–2715 (2010). <https://doi.org/10.1016/j.surfcoat.2010.02.024>
39. J.-D. Kwon, D.-K. Park, S.-W. Woo, D.-H. Yoon, I. Chung, A study on fretting fatigue life for the Inconel alloy 600 at high temperature. *Nuclear Eng. Des.* **240**, 2521–2527 (2010). <https://doi.org/10.1016/j.nucengdes.2010.05.013>

40. P.D. Cavaliere, A. Rizzo, D. Valerini, L. Capodieci, Wear and fretting behavior of cold sprayed IN625 superalloy. *Metals*, **49**, 1–13 (2021). <https://doi.org/10.3390/met11010049>
41. T. Hussain, Cold spraying of titanium: a review of bonding mechanisms, microstructure and properties. *Key Eng. Mater.* **533**, 53–90 (2012). <https://doi.org/10.4028/www.scientific.net/kem.533.53>
42. A. Silvello, P. Cavaliere, A. Rizzo, D. Valerini, S. Dosta, I. Garcia Cano, Fatigue bending behavior of cold-sprayed nickel-based superalloy coatings. *J. Therm. Spray Technol.* **28**(5), 930–938 (2019). <https://doi.org/10.1007/s11666-019-00865-1>
43. P.D. Eason, J.A. Fewkes, S.C. Kennett, T.J. Eden, K. Tello, M.J. Kaufman, M. Tiryakioglu, On the characterization of bulk copper produced by cold gas dynamic spray processing in as fabricated and annealed conditions. *Mater. Sci. Eng. A*. **528**, 8174–8178 (2011). <https://doi.org/10.1016/j.msea.2011.07.012>
44. A. Leyland, A. Matthews, On the significance of the H/E ratio in wear control: a nanocomposite coating approach to optimized tribological behavior. *Wear*. **246**, 1–11 (2000). [https://doi.org/10.1016/S0043-1648\(00\)00488-9](https://doi.org/10.1016/S0043-1648(00)00488-9)
45. R. Valentini, P. Cavaliere, D. Valerini, Nanoindentation and scratch behaviour of Ni–P electroless coatings. *Tribol. Mater. Surf. Interfaces*. **14**(1), 22–32 (2020). <https://doi.org/10.1080/17515831.2019.1665787>
46. K.G. Budinski, Effect of hardness differential on metal-to-metal fretting damage. *Wear*. **301**, 501–507 (2013). <https://doi.org/10.1016/j.wear.2013.01.003>
47. J. Li, Y. Lu, H. Zhang, L. Xin, Effect of grain size and hardness on fretting wear behavior of Inconel 600 alloys. *Tribol. Int.* **81**, 215–222 (2015). <https://doi.org/10.1016/j.triboint.2014.08.005>
48. L. Xin, B.B. Yang, Z.H. Wang, J. Li, Y.H. Lu, T. Shoji, Microstructural evolution of subsurface on Inconel 690TT alloy subjected to fretting wear at elevated temperature. *Mater. Des.* **104**, 152–161 (2016). <https://doi.org/10.1016/j.matdes.2016.05.030>

Publisher's Note Springer Nature remains neutral with regard to jurisdictional claims in published maps and institutional affiliations.

4.3.2. Residual Stress Evaluation

CS-ed Cu, Ti, and 316L had their residual stress measured by XRD, which is presented in the literature as an adequate technique for coatings but unable to measure larger volumes of material because of the XRD low energy to penetrate them [61]. Thus, ND has been successfully applied for deeper penetration, as described in Article 5. Other post-treatments, SPS and HIP, were evaluated to improve the CSAM-ed material properties.

4.3.2.1. Residual Stress on CS-ed Samples

CS-ed Cu, Ti, and 316L with different coating thicknesses were sprayed using the CS Kinetiks equipment on $200 \times 20 \times 3 \text{ mm}^3$ steel substrate, resulting in the samples presented in Figure 33. As the CS deposition result, 1- and multi-layer coatings had 100/1080, 200/1070, and 335/910 μm thickness for Cu, Ti, and 316L, respectively. During the CS deposition, the samples bent positively, as presented in Figure 34, which is macro evidence of the micro-mechanisms that result in compressive residual stress. The substrate deformation was not higher for a much more material deposited (CSAM-ed 316L), signing that the first CS-ed layers governed the final top shape geometry and more or less represented the final residual stress distribution in the CSAM-ed material.



Figure 33: CS-ed Cu, Ti, and 316L samples for XRD.

This bending deformation or curvature is used for another stress measurement, named in situ coating properties, that correlates this sample deformation during the

spraying time and after it, the cooling time, to the stress by a model presented by Tsui and Clyne [61]. This method is helpful for thermal spraying processes, including thin CS-ed layers, but not for CSAM-ed bulks because of its coating thickness limitation. The model that considers the material properties, coating characteristics, and bending curvature to calculate the stress is presented in (8), where σ_c is the average stress in the coating, E'_c is the in-plane modulus of the coating, E'_s is the in-plane modulus of the substrate, t_s is thickness substrate, and dR is the change in radius caused by deposition of layer thickness dt_c . It calculates deposition and residual stress after the material cools down to room temperature.

$$\sigma_c = \frac{E'_s \cdot t_s \cdot (t_s + \beta^{1.25} \cdot dt_c)}{6 \cdot dR \cdot dt_c}; \beta = \frac{E'_c}{E'_s} \quad (8)$$

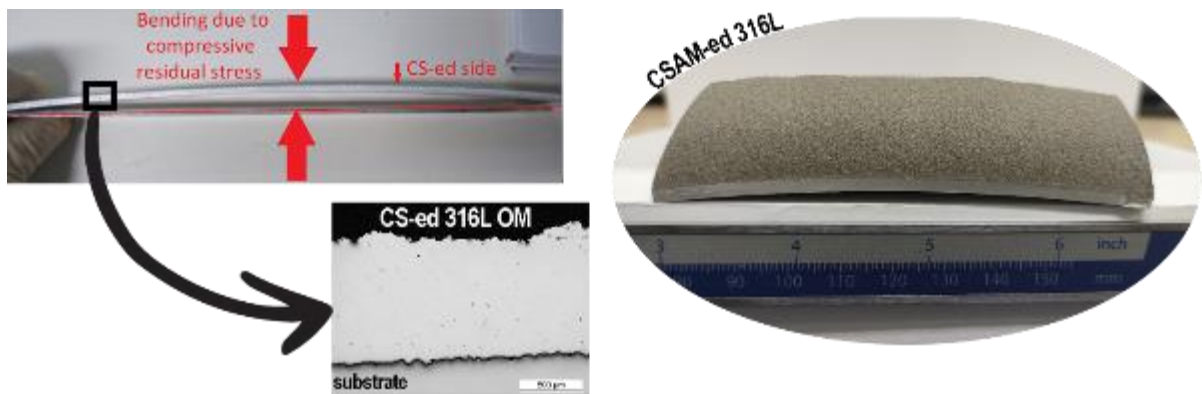


Figure 34: CS-ed and CSAM-ed 316L bent samples due to the compressive residual stress.

The thermal sprayed coatings residual stresses are the result of three distinct mechanisms basically: (a) quenching stresses, (b) peening stresses, and (c) thermal mismatch stresses. Quenching stresses are tensile and arrive from a rapid shrinkage and contraction of the splats during the formation stage of the coating. Peening stresses are compressive and originate from the impacts of the sprayed particles on the substrate or the previously deposited material. Finally, thermal mismatch stresses are generated in the post-deposition cooling stage due to material mismatch between the coating and the substrate, which have different coefficients of thermal expansion (CTE) [62–64].

Figure 35 presents the residual stress measured by XRD for CS-ed Cu, Ti, and 316L in the X- and Y-direction on the XY-plane reference indicated in Figure 33. These stress nomenclatures are also presented in the literature as σ_x and σ_y , where σ indicates a normal stress, not a shear stress, which is represented by τ . It is noticed

that all the values are in the compressive stress field, which indicates that the peening effect stands out over the quenching and the thermal mismatch ones for CS. It is noticed that the bending of the substrate during the CS deposition, Figure 34, acts as a stress relieving mechanism, which reduces the residual stress compressive magnitude that tends to be much higher for a more rigid substrate.

Figure 35 shows that the values in X- and Y-direction were very close, which is a sign of planar isotropy for the sample geometry studied. Another interpretation can be assumed from the effect of coating thickness on the residual stress, considering that low changes can be seen, neither a trend, because for Cu and 316L, a slight increase in residual stress is observed from 1- to multi-layer. However, CS-ed Ti coating had the opposite trend behavior.

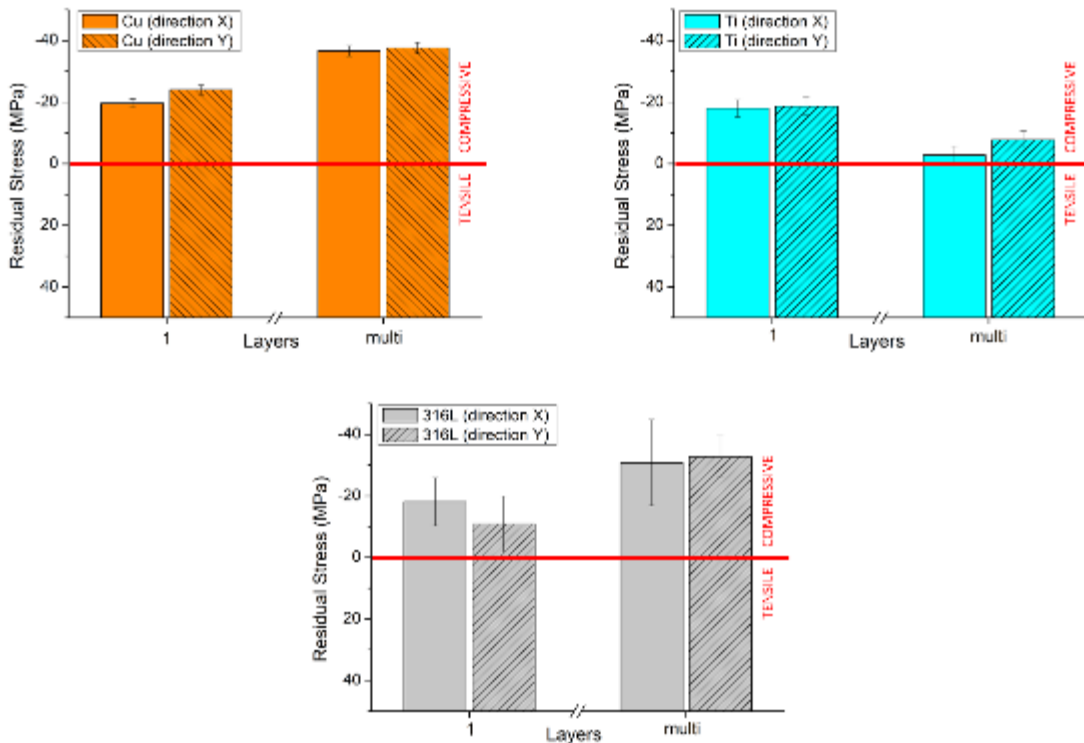


Figure 35: CS-ed Cu, Ti, and 316L residual stress results measured by XRD.

However, compressive stress in the CS-ed coating on a rigid substrate can reach magnitudes high enough to overcome its adhesion or bonding strength to the substrate, resulting in decohesion or debonding. It is a catastrophic result for any coating. It happened for CS Inconel 625 on Inconel 625 substrate, as presented in Figure 36. Increasing the bonding strength and relieving the excessive residual stress

in CSAM-ed repairs is a challenge for scholars, who have employed different techniques to spray low plasticity materials, such as Inconel alloys.

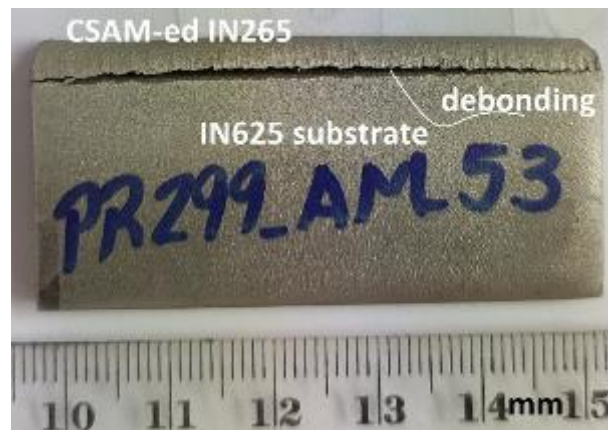


Figure 36: Residual stress overcoming the bonding strength for CS-ed Inconel 625 on Inconel 625 substrate.

4.3.2.2. Residual Stresses on CSAM-ed Samples

For the CSAM-ed materials mechanical properties evaluation, 316L results are presented in Article 5. A significant content about the residual stresses is described there. ND has been successfully applied for deeper penetration, and the effect of different post-treatments, SPS and HIP, were evaluated to improve the CSAM-ed material properties.



**ARTICLE 5 “THE EFFECT OF ANNEALING AND DEPOSITION STRATEGY ON
316L PROPERTIES PRODUCED BY COLD SPRAY ADDITIVE
MANUFACTURING”**

R.F. Váz, V. Luzin, F. Salvemini, V. Albaladejo, J. Sanchez, I.G. Cano



Submitted

This work presents the effect of heat treatment on the properties of CSAM 316L produced by traditional and Metal Knitting strategies. The CSAM traditional strategy resulted in better mechanical properties, while the CSAM Metal Knitting promoted a higher geometric accuracy. Furthermore, after annealing, both materials improved their particle cohesion, decreased their hardness, and changed the residual stress. This last property was measured by neutron diffractometry and became more homogeneous after the post-treatment.

The Effect of Annealing and Deposition Strategy on 316L Properties Produced by Cold Spray Additive Manufacturing

Rodolpho F. Vaz¹, Vladimir Luzin², Filomena Salvemini², Vicente Albaladejo¹, Javier Sanchez¹, Irene Garcia Cano¹

¹*Thermal Spray Centre (CPT). University of Barcelona. Dpt. CMiQF. c/ Marti i Franques 1 08028 Barcelona, Spain.*

²*Australian Nuclear Science and Technology Organisation. Lucas Heights, NSW 2232, Australia*

Abstract: This study investigates the effect of annealing on the characteristics and properties of Cold Spray Additive Manufactured 316L stainless steel, employing traditional and Metal Knitting strategies. 316L feedstock powder characteristics, parts' geometries, material's microstructures, porosity, microhardness, mechanical anisotropy, and residual stress by neutron diffraction were performed in two conditions, as-sprayed and annealed. The heat treatment significantly improved the Ultimate Tensile Stress and the quality of the parts, in general. The CSAM traditional strategy resulted in higher mechanical resistance; however, the Metal Knitting presented a better part geometry control. After heat treatment, both materials had the same microhardness and planar isotropy. A discussion about the mechanisms, microstructural, and residual stress evolution is presented.

Keyword: Cold Spray; 316L; Additive Manufacturing; Isotropy; Mechanical Properties; Microstructure; Residual Stress.

1. Introduction

Cold Spray (CS) is a thermal spray process based on solid-state deposition, accelerating particles to high velocities, up to $1200 \text{ m}\cdot\text{s}^{-1}$, that impact onto a surface, also called substrate [1,2]. Besides a coating technique, CS has been studied in the last years as an Additive Manufacturing (AM) method, employing Ti, Al, steel, and Cu alloys, among others. Comparing CSAM to Selective Laser Melting (SLM) or Direct Laser Deposition (DLD), it produces thicker and denser layers each pass, with theoretically unlimited height and deposition rates in the order of kilograms per hour [3]. CSAM also has the advantage of maintaining the chemical and phase composition of the feedstock material on the deposit [4], which does not occur for Wire Arc Additive Manufacturing (WAAM), SLM, or DLD, for example. The mechanism of CSAM material consolidation is the severe plastic deformation of the sprayed particles upon their impact below the material melting point [5–8]. The literature explains the adhesion and cohesion mechanisms: Adiabatic Shear Instability (ASI), localized melting, diffusion, and mechanical interlocking, which are related to the particles' conditions and high kinetic energy

instead of high temperature seen in other AM processes. In addition, it prevents the recrystallization phenomenon and improves the CS sprayed material's properties by cold-working [9–13].

It is essential to study the CSAM mechanical properties, microstructure, homogeneity, and mechanical isotropy because they influence the CSAM part performance. At the impact, the CS-ed particles deform, and spherical feedstock powders become lens-like particles or splats. Big particles have an internal gradient of grain deformation, with more deformed grains at the particles' surface but retaining undeformed grains in their centre [5,14]. This deformation can be measured by the Flattening Ratio (FR); however, it cannot be interpreted from an irregular shape feedstock powder, as the water atomized ones [15]. As for CSAM, the oriented grain deformation is responsible for anisotropic response in other fabrication processes, such as cold rolling [16], extrusion [17], or friction stir welding [18]. For CSAM isotropy, Cu presented higher Ultimate Tensile Strength (UTS) and elongation (ϵ) in a direction parallel to the gun path direction, X-direction in Figure 1, than in the transversal one, Y-direction in Figure 1 [19–21]. On the other hand, compression loading did not promote anisotropy on CSAM Cu bulk [22]. There is a lack in the literature for the evaluation of isotropy regarding the Z-direction presented in Figure 1, which is a contribution of this work, filling this lack for the CSAM-ed 316L stainless steel since just a few authors considered this direction, which is fundamental for large CSAM parts.

1.1. CSAM Deposition Strategy

It is known that the CSAM deposition strategy influences the material isotropy besides the CSAM part geometry [23,24]. The traditional strategy presented in the literature [19–21,25], Figure 1, limits the CSAM parts' geometries, making high-height thin walls or vertical sidewall parts unfeasible, requiring additional layers with an inclined gun for rectifying the sidewall inclination [26,27]. Yin et al. [25] improved CSAM Cu planar isotropy by alternating the spraying path for the traditional strategy, alternating layers on the X- and Y-directions, Figure 1; however, they neglected its effect on the Z-direction. For these requirements, the Metal Knitting CSAM strategy has been developed, and it was presented in detail by Vaz et al. [28,29], who clarified the understanding of Metal Knitting. The Metal Knitting strategy impresses a circular-like movement on the substrate plane, keeping the CS powder-laden jet not perpendicular to this substrate and describing the final path as a virtual frustum of a cone, as presented schematically in Figure 1. This strategy produced thin vertical sidewalls parts and large bulks of Ti, Cu, 316L, Ti6Al4V, and Al.

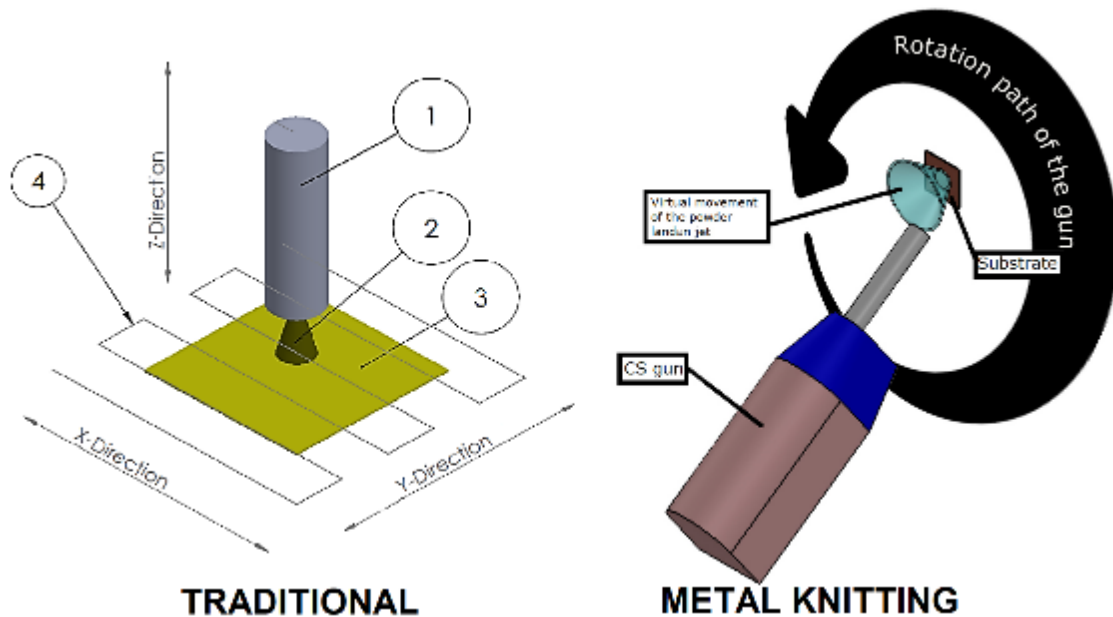


Figure 1: CSAM strategies. (1) CS gun nozzle, (2) powder-laden jet, (3) substrate, (4) robot path.

Heat treatments (HT), in special annealing, have been studied as post-treatments for CSAM to improve the materials' mechanical properties, as presented in the literature for Al, Cu, and 316L stainless steel. The latter had increased mechanical strength and ductility due to the interparticular atomic diffusion and recrystallization phenomena. However, the CS cold work hardening had this effect dwindled or entirely removed by the material recuperation at high temperatures [5,24,25,30–33]. Therefore, this work presents a study considering CSAM-ed 316L produced by the traditional and Metal Knitting strategies before and after an annealing post-treatment.

1.2. CSAM Porosity

CS is a process in which the porosity obtained in the material is controlled, depending on the material application and the component design, e.g., porous implants for the medical sector or dense parts for the aerospace industry. The literature reports that CS-ed Ti can range from a porosity of 40 vol.% [34] to a density very close to 100 vol.% [35]. Porosity is an important material characteristic. The pores morphology, size, and distribution in the CS-ed material, especially when using unconventional CSAM robot strategies, is one of the key indicators of the quality of the material and of the capacity of the new deposition strategy to obtain the desired properties and consequently CSAM-ed performance [27].

At the time of writing, porosity has been characterised by means of different techniques. Image evaluation has been the most straightforward and most commonly used approach by scholars, following the ASTM E2109-01 [36] standard; other methods available are gas or He

pycnometry [37,38], X-ray microtomography [39,40], laser-ultrasonic inspection [41], water absorption or Archimedes method [27,42], and electrochemical impedance spectroscopy [43]. An alternative analytical method is neutron imaging which exploits the interaction between matter and neutron radiation to obtain a spatially resolved map of a specimen or phenomenon. Since, contrarily to X-ray, the neutron attenuation of an isotope is independent of its atomic number, neutron radiation features a higher penetration power for most of the dense materials. In neutron radiography, a two-dimensional map of the attenuation of the probing neutron beam caused by the composition and density of the sample material is measured. The resulting map is a shadow image of the sample yielding information about its inner structure and composition. Neutron Tomography (NT) is the three-dimensional transposition of a radiographic analysis. A typical tomographic scan consists of multiple projections (or radiographs) collected by spinning the sample around its vertical axis with a known angular increment over a range of (at least) 180°. These projections are computed to create a stack of slices that can be recomposed to create a three-dimensional virtual model [44].

In the last decade, the increased application of NT, in particular, as a non-destructive testing tool can be related to the improved spatial resolution and the rapid progress in the digital image recording handling and treatment of the imaging data by sophisticated software [45]. Chankow [46] has shown how appropriate image treatment enables defect identification and quantification, including cracks, flaws, and pores, which is an attractive capability, especially for CSAM characterisation.

Nowadays, NT is broadly applied to various fields, such as fuel cells, hydrogen storage, batteries, engine components, plants, historical and archaeological objects, and geological materials, among others [45,47]. More specifically to AM, Watkins et al. [48] characterized an Inconel 718 turbine blade AM-ed by Direct Laser Metal Sintering (DLMS), revealing internal cooling channels and the high material density; Turner et al. [49] presented a 3D model for the porosity distribution in a Mar-M 247 large bulk produced by Selective Laser Melting (SLM); Brooks et al. [50] showed a skeletonization of the pore structure in Ti6Al4V produced by Electron Beam Melting (EBM); and Grazzi et al. [51] characterized an SLM-ed Maraging nozzle, presenting the higher porosity concentrated in the thicker region of the component. However, the evaluation of CSAM porosity still needs to be improved in the current literature, and NT applied to CSAM can bridge the existing gap. This work aims to provide scholars with a benchmark study on evaluating the three-dimensional distribution and size of porosity produced by different strategies and the annealing effect on the bulk of CSAM-ed 316L samples.

1.3. CSAM Residual Stress

AM processes produce stress during the material consolidation, cooling time, or even by post-treatments, and the result of these stresses is known as residual stress. It can be tensile, neutral, or compressive, creating distortions or cracks in AM-ed components. For example, Cottam et al. [52] presented residual stress between 300 and –300 MPa for DLD-ed H13 steel; Luzin et al. [53] evaluated WAAM-ed Ti6Al4V, resulting in residual stress between 450 and –200 MPa; Bobzin et al. [54] obtained values on the CSAM-ed AlCu6Mn surface between –70 and –120 MPa; while Wu et al. [55] deposited 316L by SLM, resulting in residual stress between 500 and –300 MPa. The material consolidation, i.e., melting, sintering, or solid-state deposition, develops different microstructural characteristics and residual stress evolution.

Tsui and Clyne [56] presented a model for thermal spraying coatings, dividing the material stressing into three stages: intrinsic or quenching stress by the impact and deformation of the sprayed hot particles; mismatch in thermal contraction during cooling due to the materials coefficient of thermal expansion (CTE) discrepancies; and the final value or residual stress that remain in the consolidated material after all the deposition and post-deposition stressing mechanisms. For CS, Luzin et al. [57–59] concluded that the residual stress is highly correlated with the deformation properties of the material, suggesting that the kinetic effects have more importance than the thermal effects. However, a high mismatch between the CTE of the materials, such as Ti and Cu, can result in tensile residual stress instead of the typical compressive residual stress presented in the literature for CS-ed materials [60,61].

Some techniques have been employed to measure the residual stress in CS-ed materials, as listed by Luzin et al. [62]: In-Situ Curvature, X-ray diffraction, Incremental Hole Drilling (IHD), crack compliance, Synchrotron diffraction, and Neutron Diffraction (ND). This last one is presented in the literature as capable of overcoming some limitations of the other techniques. The non-destructive ND technique considers the plastic deformation of the substrate, penetrates the metallic material in order of centimetres, and has high accuracy. However, only a few ND equipment are available worldwide [45], and this technique demands high technical expertise to develop the testing and analyse the results. For ND, a monochromatic beam of neutrons with a chosen wavelength reaches the material, interacting with their atoms' nuclei, reflecting and diffracting. A position-sensitive detector reads the beam diffracted. Microstructural characteristics of the material require changes in the process parameters, and sometimes the evaluation can delay for hours or days [61]. In the present work, ND was employed to measure the residual stress of CSAM-ed 316L.

2. Materials and Methods

The depositions, characterizations, and performance testing were done at the Thermal Spray Centre (CPT), University of Barcelona (Barcelona, Spain), following the sequence of characterisation of feedstock powder, CSAM depositions, annealing, and CSAM-ed material characterization. The ND and NT experiments were performed at the Australian Nuclear Science and Technology Organisation (ANSTO) (Lucas Heights, Australia).

2.1. CSAM Deposition

A PCS 100 equipment (Plasma Giken, Saitama, Japan) fitted with a long glass nozzle was used for the part production, using as working gas N_2 at a pressure of 6 MPa and temperature of 1000 °C, standoff distance of 25 mm, and powder feeding of $0.43 \text{ g}\cdot\text{s}^{-1}$. At this standoff distance, the velocity and size of sprayed particles were measured by HiWatch equipment (Oseir, Tampere, Finland), collecting 150 values to plot results as histogram distributions. The substrate was a 3 mm thick Al plate previously sand-blasted with new alumina to clean and prepare the substrate for thermal spraying [63]. The feedstock powder was water atomized 316L stainless steel (Daye, Shijiazhuang, China), selected among others after a previous study evaluating its good performance over gas atomized ones [15]. The powder size distribution was measured by Laser Scattering (LS) in LS13320 equipment (Beckman Coulter, Brea, CA, USA) in accordance with the ASTM B822-02 [64] standard, in dry via mode. After etching in aqua regia solution (30 mL HCl, 10 mL HNO_3 , and 20 mL H_2O), its shape and cross-section images were obtained by Scanning Electron Microscopy (SEM) in a Pro Desktop SEM equipment (Thermo Fisher Phenom, Eindhoven, the Netherlands). The powder nominal composition was analysed by Inductively Couple Plasma (ICP) using an ICP-OES 3200 RL equipment (Perkin Elmer Optima, Waltham, MA, USA). The powder's apparent density and flowability were measured in accordance with the ASTM B212-99 [65] and ASTM B213-03 [66] standards, respectively.

CSAM traditional strategy was performed moving the gun following the path indicated in Figure 1, keeping the powder-laden jet perpendicular to the substrate surface plane. A layer was completed after the gun scan entirely the substrate area with a velocity of $0.5 \text{ m}\cdot\text{s}^{-1}$. CSAM Metal Knitting strategy used a radius of 3 mm, a cone angle of 35 degrees with the virtual cone axis, and a robot linear speed of $0.2 \text{ m}\cdot\text{s}^{-1}$. The description of each Metal Knitting variable is presented by Vaz et al. [28]. The directions indicated in Figure 1 were used to name the samples to characterize and evaluate the material's properties. For the interpretations of the results, the X- and Y-direction form the XY-plane, and the X- and Z-direction form the XZ-plane.

2.2. Heat Treatment

CSAM-ed 316L stainless steel samples were machined by wire Electrical Discharge Machining (EDM) to eliminate the Al substrate and submitted to an HT of annealing, 1 h at 1000 °C in air in a furnace CRN 4-18 (Hobersal, Caldes de Montbui, Spain). These parameters were selected based on their effect on promoting interparticular bonding and ductility for 316L stainless steel [31,67–69].

2.3. Characterization and Mechanical Properties Testing

The metallographic preparation of the samples' cross-section followed the ASTM E1920-03 [70] and ASTM E3-01 [71] standards. A DMI5000M (Leica, Wetzlar, Germany) microscope was used for the Optical Microscopy (OM) to obtain images to evaluate the materials' microstructures and porosity, which was analysed with the software ImageJ on five OM images at 200× magnification for each sample, according to ASTM E2109-01 [36] standard.

Microhardness was measured utilizing an HMV (Shimadzu, Tokyo, Japan) equipment, following the ASTM E384-99 [72] standard, applying a load of 0.3 kgf ($HV_{0.3}$), resulting in average values of 10 indentations in Vickers scale for each sample. It was measured on the XY- and XZ-plane at different distances in the Z-direction from the substrate interface.

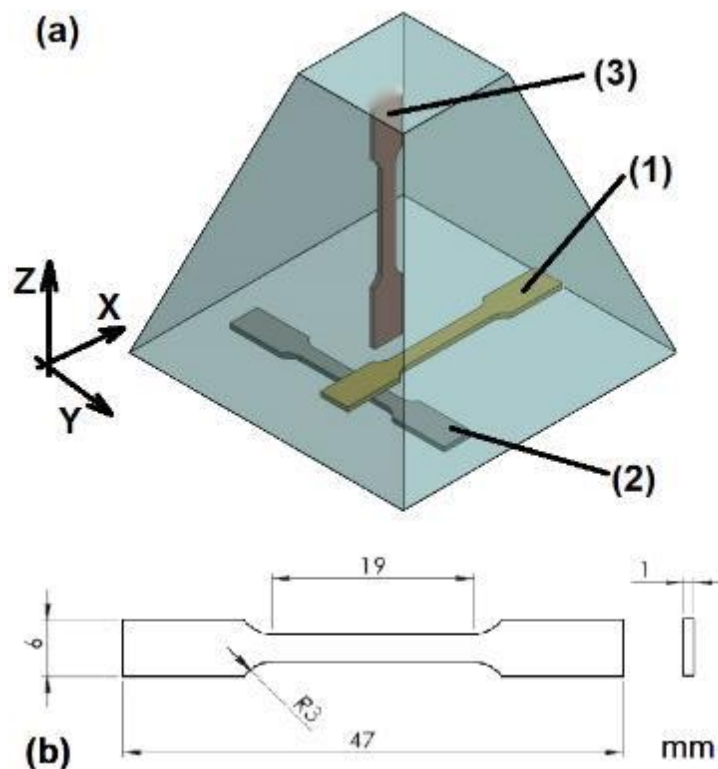


Figure 2: (a) Scheme for tensile samples machining, (1) X-direction on the XY-plane, (2) Y-direction on the XY-plane, and (3) Z-direction on the XZ-plane. (b) Tensile testing sample.

Three samples in each direction were fabricated by wire EDM process for tensile testing, following the drawing in Figure 2, which guarantees a plane-strain tension condition. The surfaces were polished to a maximum roughness of Ra 0.8 μm . A Zmart.Pro equipment with an Xforce P 10 kN load cell (ZwickRoell, Ulm, Germany) was used for the tensile testing, with a load application velocity of 1.0 $\text{mm}\cdot\text{min}^{-1}$. The fractography was performed using SEM images of the fracture surfaces.

2.4. Neutron Tomography

The NT measurement was performed on the imaging beamline Dingo at ANSTO [73]. The instrument was configured in high-resolution acquisition mode, corresponding to an L/D ratio of 1000 (where L is the distance between the beam collimator to the image plane, and D the diameter of the collimator). The CMOS ASI2600MM Pro (ZWO Cameras) (6248 \times 4176) was coupled with a 50 mm lens to yield images with a pixel size of 36 μm over a 224 \times 150 mm^2 field of view. The detector system had a 50 μm thick $^6\text{LiF/ZnS}$ scintillation screen. Projections were acquired with an equiangular step of 0.19 $^\circ$ over 360 $^\circ$ and an exposure time of 70 s each. Flat field normalization with dose correction, dark current subtraction, ring artifacts suppression in frequency, and real space domains were applied to each dataset. The NT stacks were computed using the NeuTomPy toolbox [74]. The Avizo 2020.3.1 software (ThermoFisher Scientific) was employed for data visualisation and evaluation.

2.5. Residual Stress Measurement

ND residual stress measurements have been carried out using the stress diffractometer KOWARI at the ANSTO OPAL research reactor [75]. Stress investigations were performed in conditions optimized for $\gamma\text{-Fe}$ (311) reflection at the wavelength of 1.55 \AA when the scattering angle was close to the optimal 90 $^\circ$ -geometry with the take-off angle of 69 $^\circ$ using Si (400) monochromator.

A cube-like gauge volume with dimensions 5 \times 5 \times 5 mm^3 was provided by means of the focusing collimator. With this gauge volume, 2D scans across a central transverse cross-section of the deposits in the XZ plane. The 2D mesh was chosen congruent to the size of the gauge volume with 4 mm steps in the two dimensions. The mesh was adapted for the real shape of the deposit; thus, the number of measurement points varied from 55 to 67 points. All measurement points were taken in such a way that the gauge volume was always fully submerged in the material. As a result, strain accuracy of 70 μstrain was achieved while the measurement time was varying

greatly depending on the exact neutron beam flightpath in the sample with a particular orientation.

Measurements of three principal sample directions were taken to reconstruct three orthogonal stress components, provided that the proper d_0 is known. Upon completion of the d-spacing measurements, it turned out that the constant- d_0 -value assumption was invalid and not applicable. Instead, the assumption of the near-to-zero stress component in the smallest sample dimension was made, which coincides with the build-up direction. The practical assumption was confirmed in the case of CS in several cases of 3D deposits [59,76,77], ensuring the approach's applicability. Although an alternative solution to the d_0 problem exists through the experimental approach with measurements of small stress-free coupons extracted from the samples, this approach would be destructive and require more neutron beamtime, which was unavailable.

After the calculations of the two remaining stress components, $\sigma_{\text{Transversal}}$ (in-plane, parallel to the measured cross section) and $\sigma_{\text{Longitudinal}}$ (in-plane, normal to the measured cross section), based on the above approach, they were checked to ensure the fulfillment of the available force balance (for $\sigma_{\text{Longitudinal}}$) and stress boundary conditions (for $\sigma_{\text{Transversal}}$). As a result, they both were compliant with the conditions within experimental uncertainties. The achieved experimental uncertainties were ~ 10 MPa, which resulted from the strain accuracy of $50 \mu\text{strains}$ (5×10^{-5}).

For stress calculations from the measured strain, the (hkl) dependent isotropic elastic diffraction constants were used and evaluated in accordance with corresponding single crystal elastic constants using ISODEC software [78].

3. Results and Discussion

3.1. Powder Characterization

The 316L feedstock powder presented a particle size distribution indicated in Figure 3, $-60+15 \mu\text{m}$ (d_{90} and d_{10}), and mean $31 \mu\text{m}$, with an irregular shape, Figure 4 (a), and a dendritic microstructure, Figure 4 (b), which are typical characteristics of water atomized powders [15]. This irregular shape makes an evaluation of the FR impossible, which could help to interpret the material plasticity at the impact. FR also could be evidence to analyse the CSAM microstructural isotropy. The chemical composition, Table 1, indicates that the material followed the ASTM A240/A240M [79] standard for the 316L stainless steel, as desired.

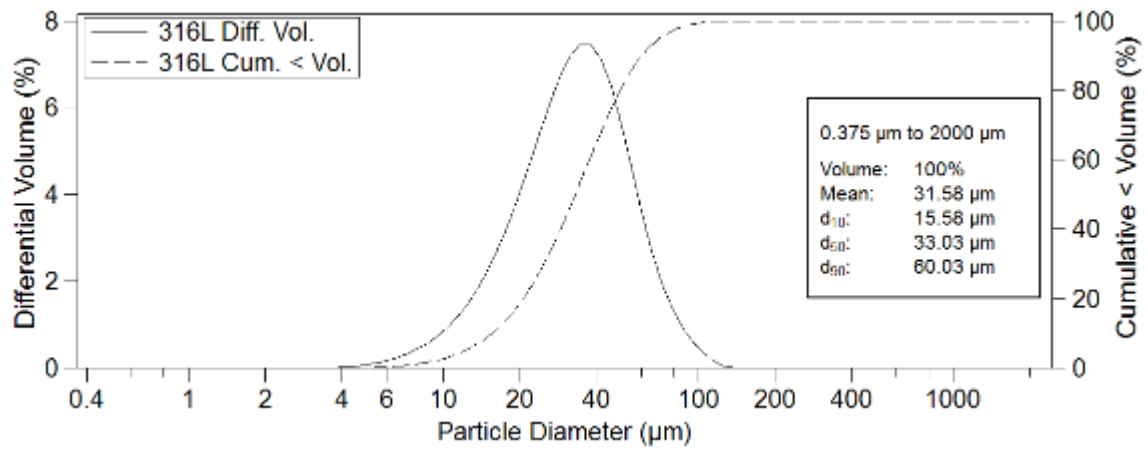


Figure 3: 316L feedstock powder size distribution.

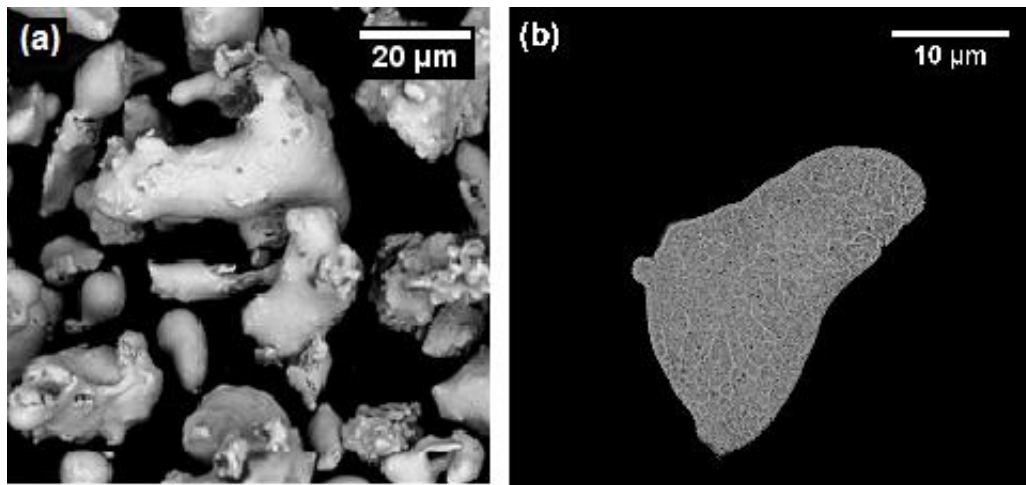


Figure 4: SEM of 316L feedstock powder. (a) Three dimension and (b) etched cross-section.

Table 1: Chemical composition of 316L feedstock powders. wt.%.

	Cr	Ni	Mo	Mn	Fe
316L powder	16.0	12.3	2.6	0.5	Bal.
316L reference [79]	16.0–18.0	10.0–14.0	2.0–3.0	2.0	Bal.

3.2. CSAM part

The substrate geometry is an important factor for the CSAM-ed part geometry, mainly for using the traditional strategy. For example, Vaz et al. [28] and Lynch et al. [80] studied the influence of spraying on edges and flat surfaces for some materials. For 316L, the result was 30 and 70 degrees, respectively. It is a consequence of a deposition efficiency gradient from the CS powder-laden jet center and its periphery due to a lower velocity of particles far from its central region [81]. These results supported the decision to produce the CSAM traditional strategy part on a 50 mm square plate, looking for the minimum sidewall inclination to build the part, saving raw powder. As a result, CSAM traditional strategy produced 221 μm thick layers, requiring

226 layers for a 50 mm height sample and 65 degrees inclined sidewalls. While CSAM Metal Knitting resulted in 3600 μm thick layers, requiring 16 layers for a 58 mm height sample, Figure 5. For ND and NT samples, 30 mm height samples were produced, requiring fewer CSAM-ed layers.

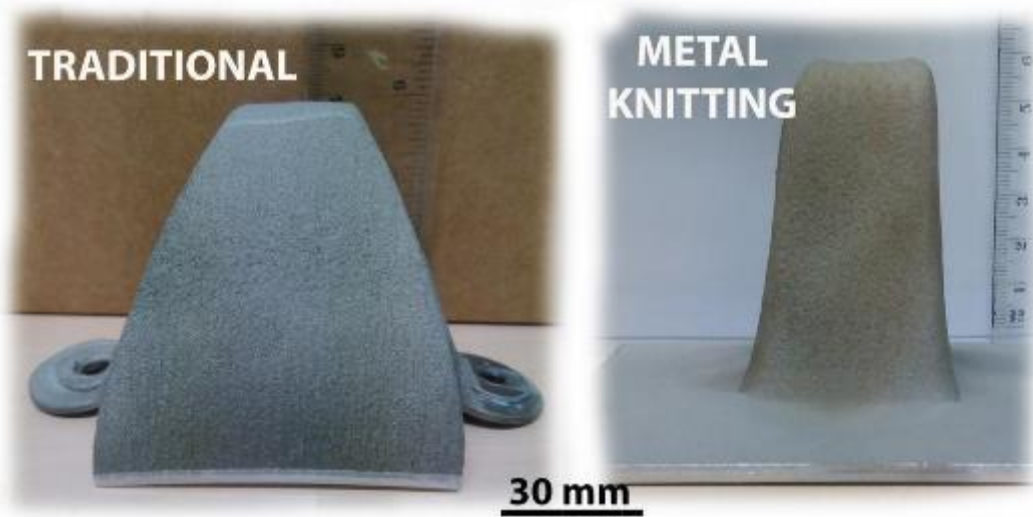


Figure 5: CSAM traditional and Metal Knitting 316L samples as-sprayed for tensile testing.

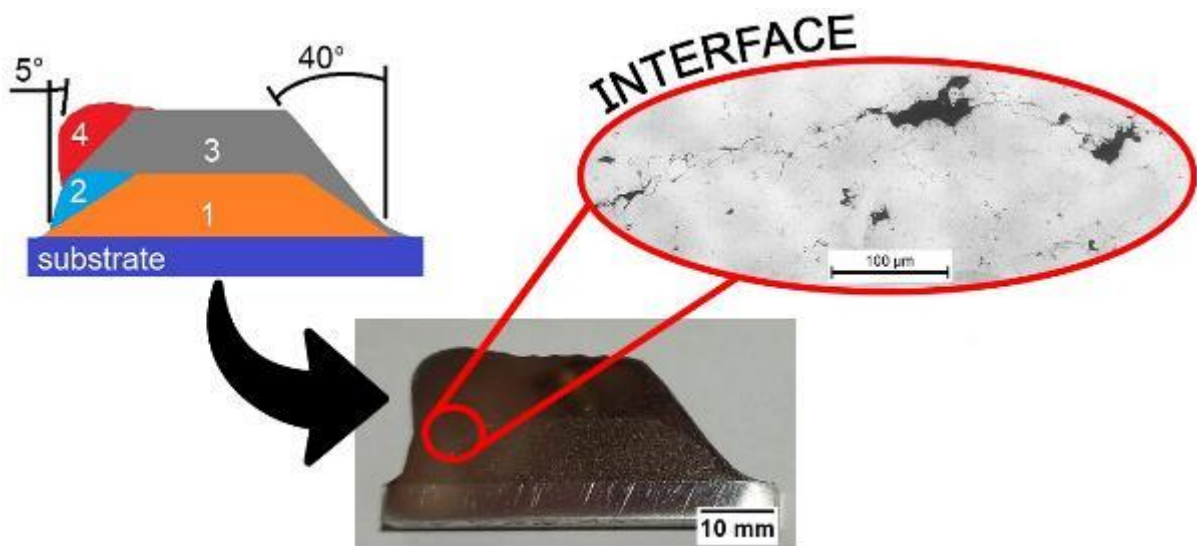


Figure 6: The CSAM traditional 316L applying correction sidewall angles layers. (1) first, (2) second, (3) third, and (4) forth steps of spraying layers.

For the CSAM Metal Knitting 316L sample, the substrate selected was a flat surface, based on the experiments conducted by Vaz et al. [28], indicating that the substrate geometry had not changed the final part sidewall angle for this CSAM strategy. Besides that, spraying on a larger plate made it easier to handle the sample and hold it onto the robot arm. The CSAM Metal Knitting 316L sample is presented in Figure 5 with a sidewall angle of 82 degrees with the

substrate plane. This inclination control provided by the Metal Knitting strategy has microstructural advantages over the sidewall angle correction by spraying additional layers with the inclined gun on the inclined faces, which was proposed by Nardi et al. [26]. This last strategy's effectiveness for 316L is presented in Figure 6 and resulted in a reduction of the sidewall angle from 40 to 5 degrees, applying 25 layers each step.

However, OM images of the bonding interface showed partial adhesion, with pores and separation along the previous sidewall and the correction layer interface. It indicates an aligned lower cohesion of particles in this area, a preferential path for cracks or decohesion of particles under CSAM-ed part operation loading. Wu et al. [82] experienced these inter-layer defects and cracks in CSAM-ed Cu samples with an inter-layers longer time interval, suggesting that the temperature gradient between the CSAM steps of layers, Figure 6, acts reducing the particle anchoring and embedding effects. It is not a theme of oxidation because Wu et al. [82] showed an even worse inter-layer condition for CSAM Cu and Al by machining process between layers, which should eliminate a possible deleterious oxide layer. Sinclair-Adamson et al. [76] presented microstructural heterogeneity employing the inclination correction strategy for CSAM-ed Cu, which became apparent in OM images showing bands or packs of layers from the different spraying directions.

3.3. Influence of CSAM Strategy on the Velocity of Impact of Particles

The deposition efficiency and the CSAM-ed material consolidation result from the particles' kinetic energy converted into plastic deformation at their impact onto the substrate. The deposition window for 316L is between $500 \text{ m}\cdot\text{s}^{-1}$ (V_{critical} or V_{cr}) and $675 \text{ m}\cdot\text{s}^{-1}$ [83] because particles under the V_{cr} do not adhere to the substrate, and particles with an excessive velocity erode the substrate. The velocity values for CS-ed 316L particles at 25 mm from the nozzle exit are indicated in Figure 7, a histogram that relates the frequency of measuring each value range. It is possible to see a few particles under $500 \text{ m}\cdot\text{s}^{-1}$, less than 20 particles, while more than 85 particles were between 600 and $800 \text{ m}\cdot\text{s}^{-1}$, resulting in a mean value of $624 \text{ m}\cdot\text{s}^{-1}$. During the spraying time, all the particles were exposed to the same accelerating gas flow; however, the small ones had insufficient mass to maintain a straight path, spreading the powder-laden jet. In addition, they neither maintained a high velocity, reducing it progressively from the nozzle exit to the substrate.

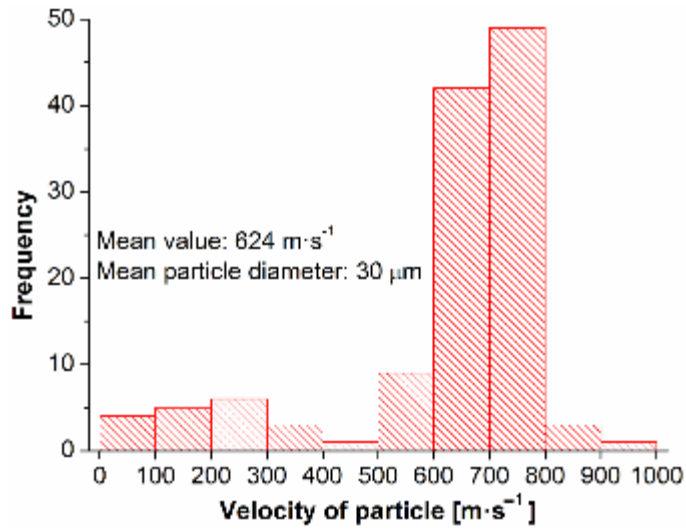


Figure 7: Histogram of velocity of CS-ed 316L particles at the standoff distance.

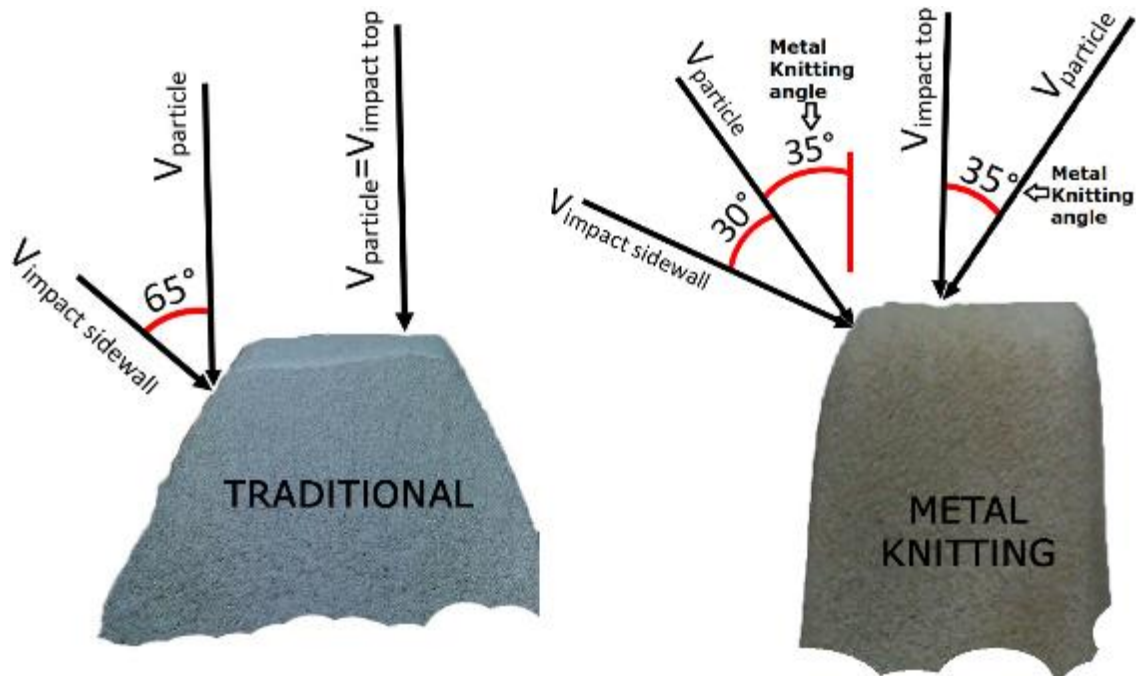


Figure 8: Scheme for V_{impact} of particles for different parts' surfaces, using the CSAM traditional and Metal Knitting strategies.

The velocity of particles' mean value can be used to illustrate the effect of angle of impact of particles on their kinetic energy, which is perpendicular to the impact surface and is converted into plastic deformation and consequently in adherence to the substrate. For example, at 90 degrees, the velocity of impact is the velocity of a CS powder-laden jet, $624 \text{ m}\cdot\text{s}^{-1}$, $V_{\text{impact top}}$ for CSAM traditional strategy, Figure 8. However, for its 25 degrees inclined sidewall, the vector velocity responsible for the particle deformation, $V_{\text{impact sidewall}}$, is only $263 \text{ m}\cdot\text{s}^{-1}$ ($624 \cdot \sin 25$). This velocity is below the 316L V_{critical} of $500 \text{ m}\cdot\text{s}^{-1}$ [83], making the material

consolidation unfeasible on this CSAM part sidewalls. Nevertheless, employing the novel CSAM Metal Knitting strategy with a knitting angle of 35 degrees, the V_{impact} varies between $511 \text{ m}\cdot\text{s}^{-1}$ ($624\cdot\cos 30$) and $540 \text{ m}\cdot\text{s}^{-1}$ ($624\cdot\cos 35$), $V_{\text{impact sidewall}}$ and $V_{\text{impact top}}$, respectively. These values are in the deposition window for 316L but very close to the V_{critical} , $500 \text{ m}\cdot\text{s}^{-1}$, which is the minimum value for promoting adherence and CSAM material consolidation, resulting in a predictable lower particle deformation, but a feasible material anchoring.

3.4. Material Characterization

CSAM traditional and Metal Knitting 316L produced similar material microstructures. Figure 9 shows OM images of the samples' cross-section on the XY-, YZ-, and XZ-plane. It may be observed that all the CSAM samples showed a dense and typical CS as-sprayed microstructure owing to the high CS-ed particle velocity, which results in deformed particles forming the lamellae/splats structure and some pores. As the feedstock powder used was water atomized with an irregular shape, Figure 4, it is impossible to identify an inhomogeneity in particle deformation on the X- or Y-direction and Z-direction (planes parallel and perpendicular to the substrate surface). However, other authors observed this difference, presenting disc-like splats on the XY-plane but a lens-like shape on the XZ-plane [19,20,22,84].

Furthermore, the etching revealed the material with a dendritic microstructure, interparticular limits, and grain boundaries, Figure 10. Also, it showed severe grain deformation and refining in the particles' periphery, while a lower deformation was seen in the centre of the largest particles. SEM images with higher magnification of the interfaces between particles are presented in Figure 11, where arrows indicate some points of micro-welding between the particles, besides their plastic deformation and the intimacy typical of the ASI bonding mechanism [9–13,85].

After the annealing at $1000 \text{ }^{\circ}\text{C}$ for 1 h, the interparticular region disappeared, revealing a uniformity in grain size and distribution and annealing twins throughout the structure, as seen in Figure 10. The CS-ed particles are severely cold-worked, which acts as the driving force for recrystallization. This energy for recrystallization arises from the lattice strains and the crystalline imperfections and dislocations generated in the material during the CS deposition process [86]. Besides the deformation at the impact, the consolidated CSAM-ed material is exposed to more cold work. Consequently, it stores even more energy by the impact of the sequent sprayed particles, known as shot peening effect [60,87]. The material characteristics changing by annealing resulted from the diffusion mechanisms by the HT temperature above the 316L recrystallization level for enough time to promote atomic movement in the crystalline

structure. Therefore, HT for a short time, 1 h, avoided some undesired phenomena decurrent of the annealing at high temperatures and/or a long time, like precipitation of intermetallic $M_{23}C_6$, growing of phase sigma, chi, or Laves, or even Cr depletion and sensitization [88–90]. Therefore, using a short time is feasible for CSAM-ed 316L due to the stored energy in the cold deformed particles. In addition, the atomic diffusion improved the cohesion of particles in the regions of the particles that were intimately close by the ASI bonding mechanism, promoting a micro-welding between the particles, as seen in Figure 11.

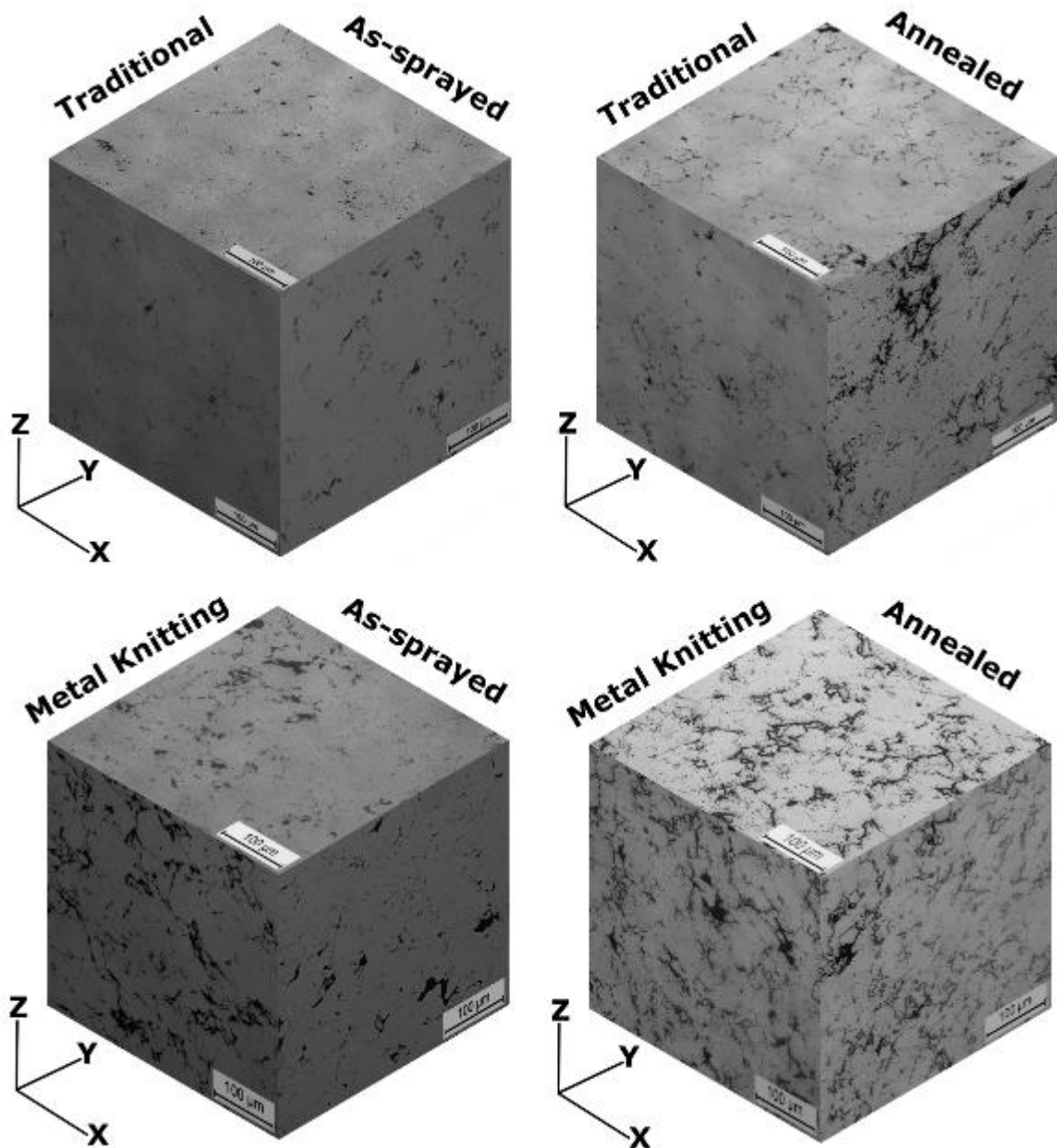


Figure 9: CSAM traditional and Metal Knitting 316L OM cross-section images before and after HT.

By a visual inspection and image analysis, following the ASTM E2109-01 [36] standard, no densification was observed as an effect of the annealing process. For the CSAM traditional

strategy, the porosity of as-sprayed material was $4.1\pm 1.5\%$, and $4.3\pm 0.5\%$, as HT-ed; and for the CSAM Metal Knitting strategy, $7.5\pm 4.6\%$ as-sprayed and $7.7\pm 3.3\%$ as HT-ed. It is worth indicating that these porosity values were calculated as a mean value of five OM images for each sample. For this reason, the OM images shown in Figure 9 and Figure 10 do not necessarily represent this mean value, even though they presented very low porosity. The distribution of pores in the material changed, and the annealing process moved the tiny pores in the 316L microstructure. These pores were previously distributed very thinly and evenly throughout the interparticular areas, but after annealing, they were converted into coarse pores surrounding the particles, as seen in the SEM image presented in Figure 11.

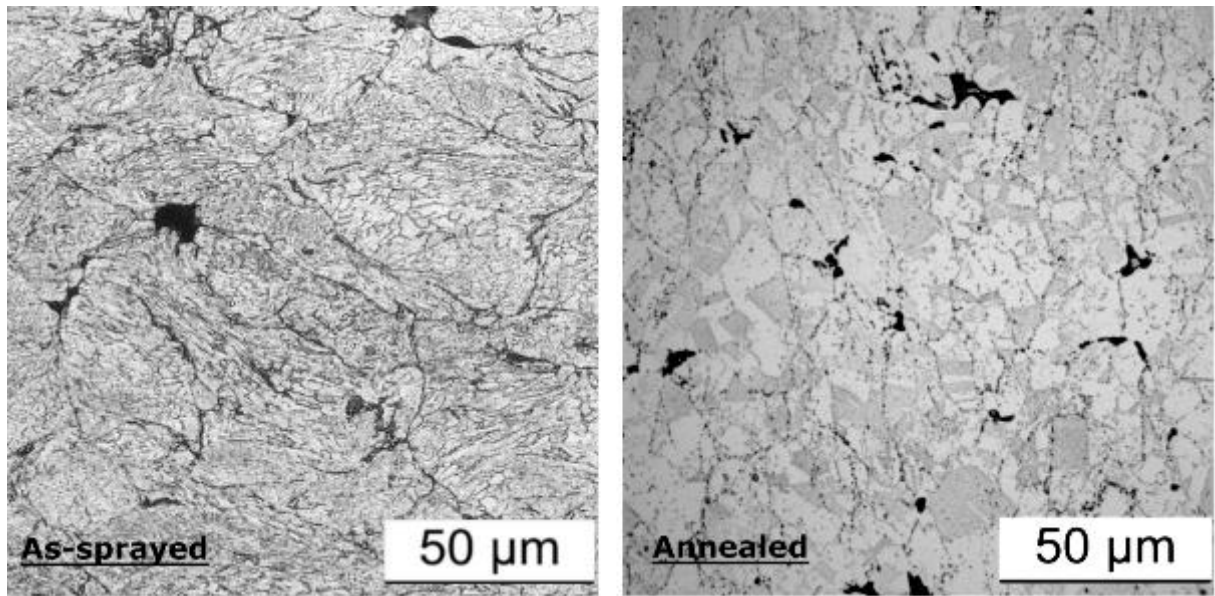


Figure 10: CSAM-ed 316L OM etched cross-section image before and after HT.

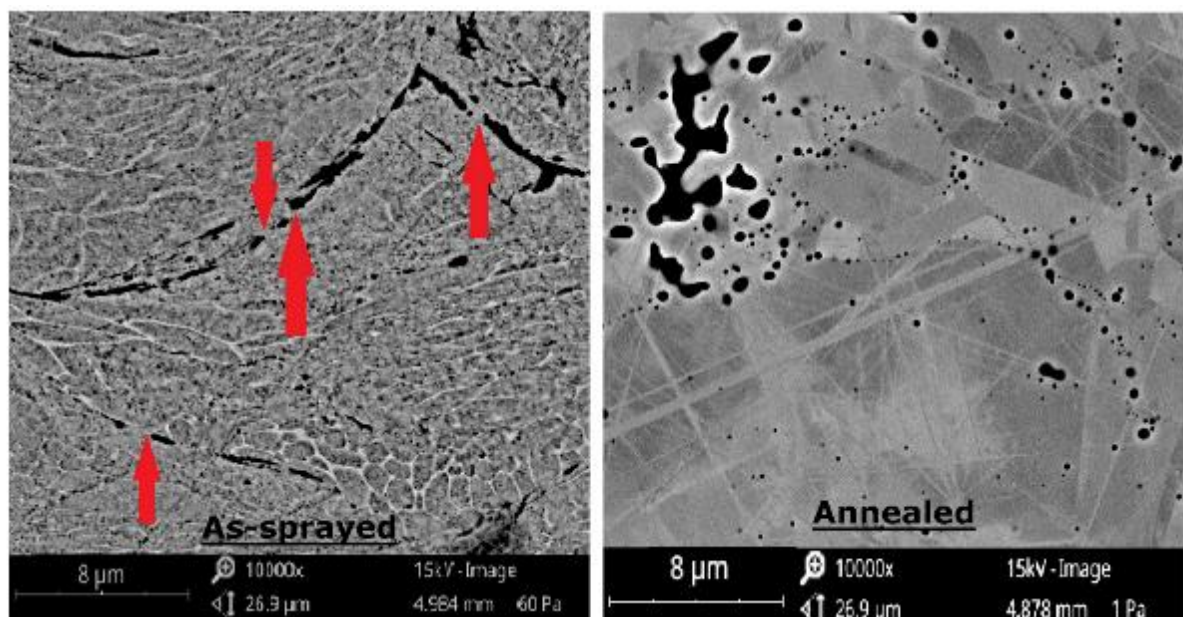


Figure 11: SEM image of the interparticular region before and after HT.

3.5. Neutron Tomography

NT was applied to characterise microstructural features across the samples' volumes. Preliminary observations based on the OM and the SEM analyses on CSAM-ed 316L did not show relevant macroscopic compositional and structural variations, e.g., a heat-affected zone commonly seen in welded materials, or a millimetre scale defect, like a crack, or a decohesion between the CS-ed layers or a large pore. Since the portion of the sample investigated via OM and SEM is generally limited, NT helped to elucidate if the microscopy observations are relevant for the whole sample volume. In fact, differences in grey tone shown in NT images depend on variations in the material density or attenuation power of the metal grains. Grazzi et al. [51] affirmed that the material microstructural features and cavities, with dimensions down to a few hundred microns, can be observed by NT, accrediting the technique for evaluating coarse pores distributed in CSAM-ed material. However, fine porosity in order of micrometre is below the resolution limit of the conventional NT method.

A commonality observed in all investigated samples is the absence of coarse porosity, Figure 12. Since small pores were observed in MO and SEM analyses, assuming homogeneous material composition, visible variation in neutron attenuation (or grey tone) in the NT data can be related to the concurring effect of variation in particles cohesion and the presence of porosity below the detection limit ($<50 \mu\text{m}$).

In the as-sprayed CSAM traditional 316L sample, Figure 12, it is possible to see four horizontal bands on the YZ- and XZ-planes. The two dark bands are probably related to higher cohesion of particles and lower porosities, while the bright bands can be explained as portions with lower cohesion and higher porosities. In fact, these bands coincide with three moments when the CS deposition stopped for refilling the powder feeder reservoir. However, it did not occur for CSAM Metal Knitting deposition because these pauses were unnecessary due to the thicker layer produced during manufacture. This remarks that pauses in the spraying process have been a problem for the CSAM-ed material homogeneity, which makes interfaces weak areas, as further discussed in the fractography section, Figure 16. Furthermore, Figure 12 indicates that the annealing eliminated this horizontal transition, generating a homogeneous microstructure. Comparing the microstructures of those areas, based on MO and SEM, the porosity values did not change much between them, but the size of voids was coarser in the darker areas than in the brighter ones.

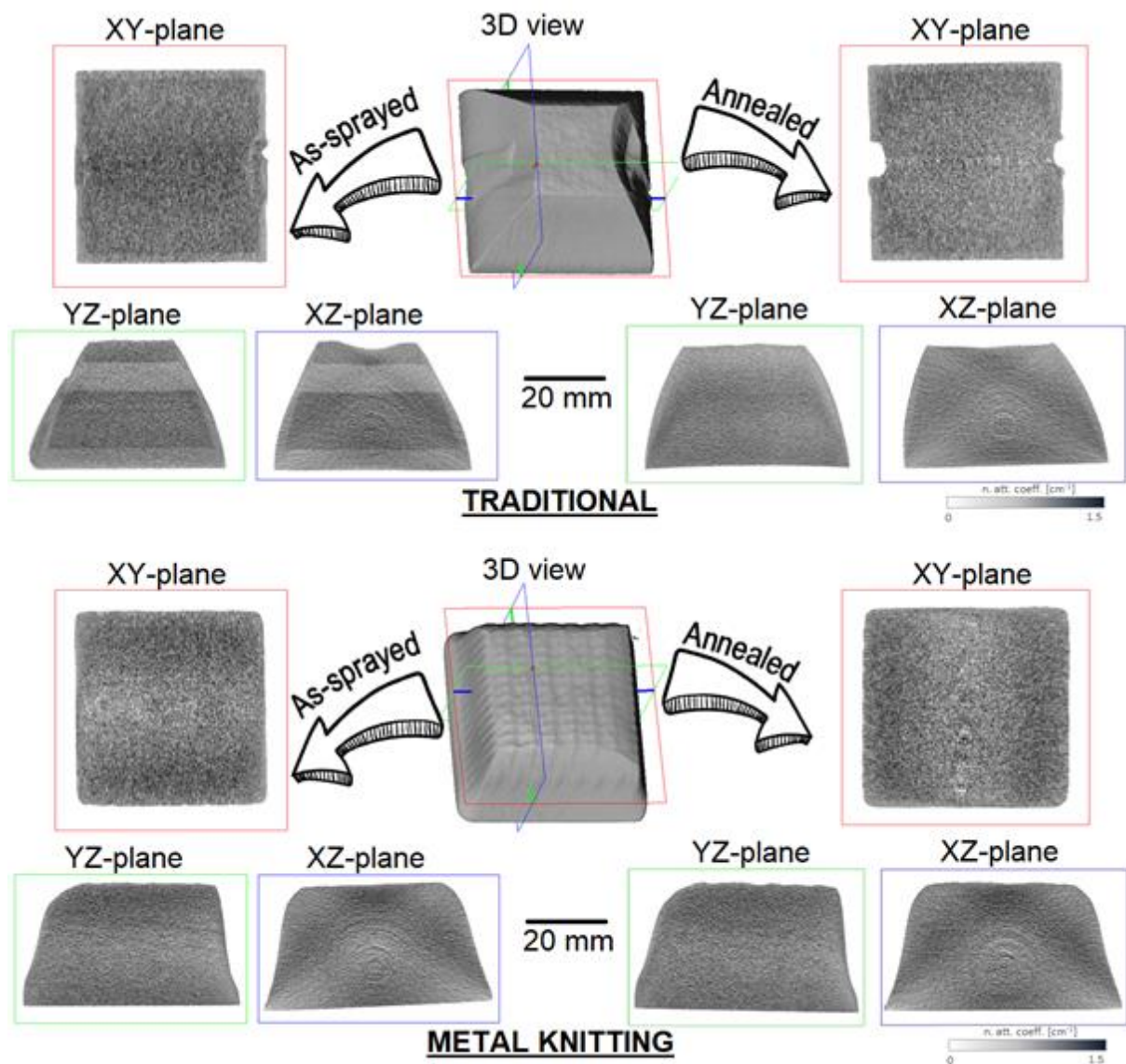


Figure 12: Orthogonal cross sections through the NT reconstructed volume of CSAM traditional (top) and Metal Knitting (bottom) 316L samples are shown. At the centre, the reconstructed three-dimensional models indicate the position of the cross-sections. On the left and the right side of each model, the images refer to the sample before and after HT, respectively.

Figure 12 presents orthogonal cross-sections through the computed NT model of CSAM traditional and Metal Knitting samples in as-sprayed and HT-ed conditions. Based on the NT data, it can be observed that CSAM Metal Knitting samples as-sprayed and HT-ed present similar attenuation and homogeneous structures. However, OM images presented in Figure 9, Figure 10, and Figure 11 showed larger pores in as-sprayed condition but smaller and well-distributed voids in the annealed samples. A slightly brighter grey can be observed for CSAM traditional 316L HT-ed sample, suggesting a more uniformly distributed and finer porosity.

3.6. Microhardness Evolution

Figure 13 presents the microhardness measures at different distances from the substrate interface, before and after annealing for the CSAM traditional and Metal Knitting strategies, comparing the direction of measurement, perpendicular and parallel to the spraying jet axis, XY- and XZ-plane, respectively. For both strategies, the microhardness did not present a variation trend with the distance to the substrate. However, the microhardness on the XY-plane showed a slightly higher mean value than on the XZ-plane, in general. For the CSAM traditional strategy 316L as-sprayed, the values measured were 347 ± 28 HV_{0.3} on the XY-plane and 377 ± 22 HV_{0.3} on the XZ-plane; while for the CSAM Metal Knitting 316L, they were 246 ± 33 HV_{0.3}, and 216 ± 46 HV_{0.3}, respectively. CSAM traditional as-sprayed produced even higher values than laser-made AM 316L parts, but the same value after annealing is seen for both CSAM and SLM processes [91,92].

The lower microhardness for the CSAM Metal Knitting 316L samples as-sprayed is evidence of their lower cold working, corroborating the higher porosity discussed previously. Furthermore, it is related to a lower velocity of particles at the impact since the lower the velocity, the lower the kinetic energy converted into plastic deformation. For a flat surface, i.e., the first CSAM layer, this reduction of the velocity of particles, and consequently their kinetic energy, is due to the decomposition of the vector velocity by the cosine of the Metal Knitting angle selected, 35 degrees, resulting in a reduction of 27% in velocity. However, from the second layer onwards, the previously consolidated CSAM-ed material is no longer a flat surface. This is because the Metal Knitting angle became favorable to adhere the CS-ed particles to this curved surface, even though with a decomposed vector velocity.

The annealing post-process reduced the material hardness due to the recrystallization and recuperation phenomena [30,86,93]. In addition, this post-treatment reduced or eliminated the effect of deformation-induced dislocation density, which is typical for the CS-ed particles during their deposition [20,69,93], resulting in a final microhardness between 200 and 250 HV_{0.3} for both CSAM deposition strategies, Figure 13, pretty close to the results presented in the literature for 316L [31,67–69].

Figure 13 presents indentation marks on samples before and after HT. Those characteristics were seen for all indentations performed on the XY- and XZ-plane. Diamond-like marks with no cracks or micro-cracks on or near their corners were obtained for the CSAM traditional strategy samples, indicating the excellent toughness of the CSAM-ed 316L part. Nevertheless, some delamination or interparticular cracks were observed for some indentations on CSAM

Metal Knitting samples. These values were not considered as microhardness results, but the material's behavior under loading was considered for evidencing the lower cohesion of particles for the CSAM Metal Knitting material. In addition, in as-sprayed samples, marks with a bit of deviation from the perfect diamond-like shape and deformation pile-up in the indentation vicinity were not evidenced in the marks observed on annealed samples. It is related to the annealed material's higher plasticity and ductility [94–96]. The indentation in the as-sprayed sample also showed a decohesion between particles by the microhardness loading, 0.3 kgf for 15 s, which was not observed in annealed samples, bolstering the improvement of cohesion by the HT.

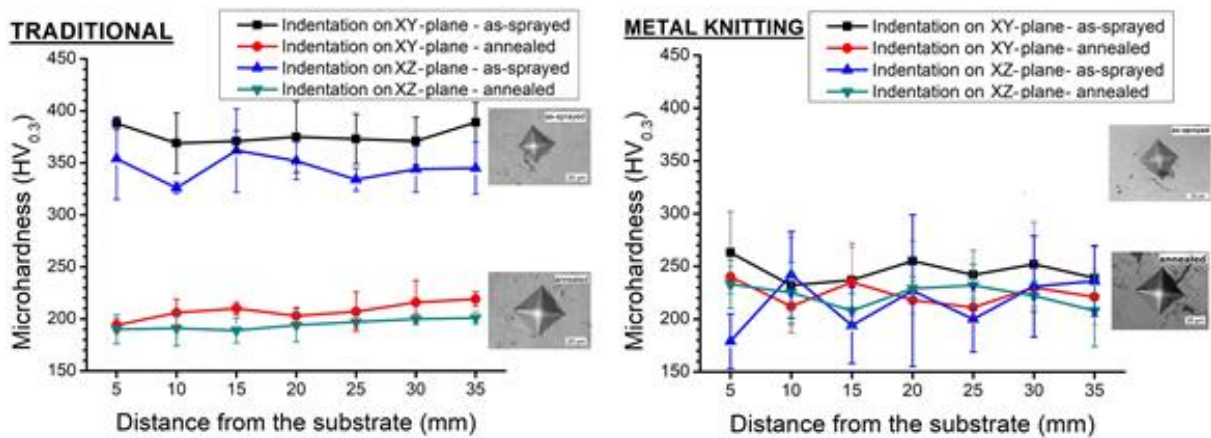


Figure 13: CSAM traditional and Metal Knitting 316L samples microhardness profile results before and after HT.

3.7. Tensile Properties

Figure 14 shows the UTS values measured for the CSAM traditional and Metal Knitting strategies 316L samples before and after heat treatment. In the as-sprayed condition, the CSAM traditional strategy resulted in higher UTS than the CSAM Metal Knitting strategy in all evaluated directions. The lower mechanical resistance seen for the CSAM Metal Knitting samples corroborates their higher porosity and lower microhardness measurements previously presented. It is attributed to a lower cold working and particle plastic deformation due to a lower particle kinetic energy resulting from the vector velocity decomposition by the impacting angle of the particles, Figure 8. The CSAM Metal Knitting keeps the spraying angle in constant movement, helping to improve the deposition efficiency on the CSAM-ed part sidewalls, controlling its geometry, but not employing the highest velocity possible, which is at 90 degrees between the substrate and the powder-laden jet axis. This condition of normal angle occurred for the CSAM traditional strategy at the centre of the sample, where the tensile specimens were machined.

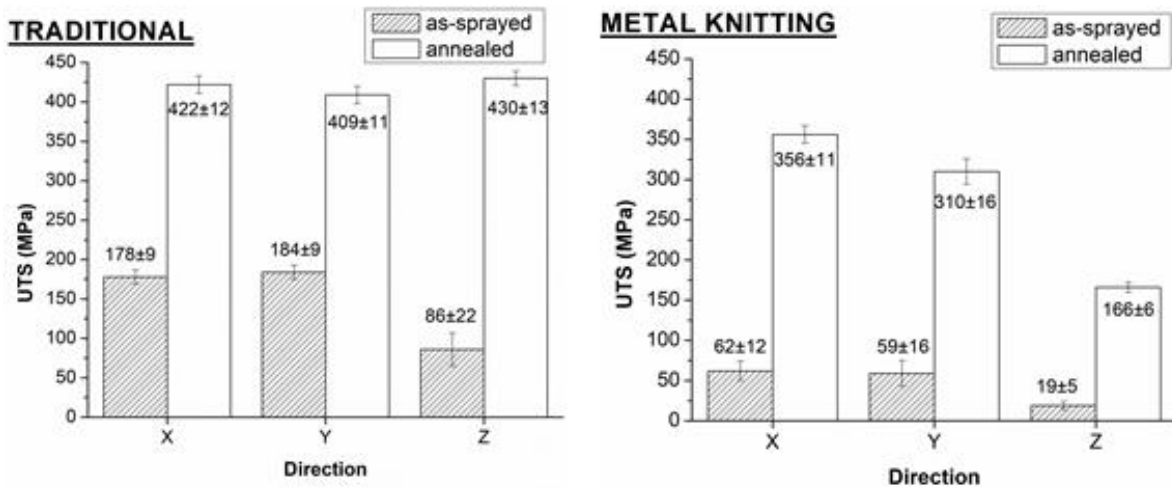


Figure 14: CSAM traditional and Metal Knitting 316L samples tensile testing results before and after HT.

It is a clear isotropy on the X- and Y-direction for the CSAM 316L traditional and Metal Knitting strategies samples, indicating homogeneity of particles deformation for these axes, which other authors did not observe. To evaluate the planar isotropy qualitatively, an index UTS_y/UTS_x was plotted, Figure 15, presenting representative results obtained by other authors and different AM strategies, processes, and materials. This work resulted in higher planar isotropy for the as-sprayed condition than CSAM Cu or cold-worked 316L and close results to the CSAM and SLM 316L samples [91,97,98]. It is important to notice that SLM consists of a fusion of the fed powder, resulting in a dendritic microstructure without an interparticular region. Hence, an AM part is produced based on the powder's metallurgical joining.

In contrast, CSAM is wholly based on particle deformation, dependent on the spraying strategy, as seen for Cu and Al samples [19,20,25,91,92,99]. Regarding the index UTS_z/UTS_x , there needs to be more in the literature because too few works evaluated the mechanical properties of the Z-direction. The authors who studied it are indicated in Figure 15. The CSAM 316L resulted in a severe Z/X anisotropy, mainly because of the inhomogeneity of particle deformation in the cited directions, affecting the cohesion of particles mechanisms and making it weaker in the Z-direction than in the X-direction. Furthermore, the contact area between the particles is smaller on the XZ-plane because the particles deform in the jet direction, generating lens-like splats and flattening on the XY-plane, promoting a better mechanical anchoring or interlocking on this plane. It does not occur for processes usually applied to produce high-height AM parts, such as SLM or WAAM [91,98,100–103]. For the CSAM traditional strategy as-sprayed, UTS_z/UTS_x was 0.48, while for the Metal Knitting, it was 0.31, which one more time confirms a higher cohesion of particles in the CSAM traditional-made samples.

The annealing process improved the UTS for all the samples, CSAM strategies, and directions, as seen in Figure 14. A highlight for the UTS_z , which had increased its value by five and almost nine times, for the CSAM traditional and Metal Knitting strategies, respectively. The annealed samples presented higher isotropy than the as-sprayed samples, as presented in Figure 15. For the planar isotropy or index UTS_y/UTS_x , the CSAM traditional and Metal Knitting made parts were close to 1.0, the perfect isotropy.

However, regarding the index UTS_z/UTS_x , the Metal Knitting samples had this index improved from 0.31 to 0.48, while the CSAM traditional sprayed samples changed it from 0.48 to 1.02, reaching the isotropy with the X- and Y-direction. The mechanism to improve the CSAM 316L cohesion of particles and the mechanical properties is dependent on the intimate contact between the particles because it makes feasible the atomic diffusion and metallurgic bonding or union of them.

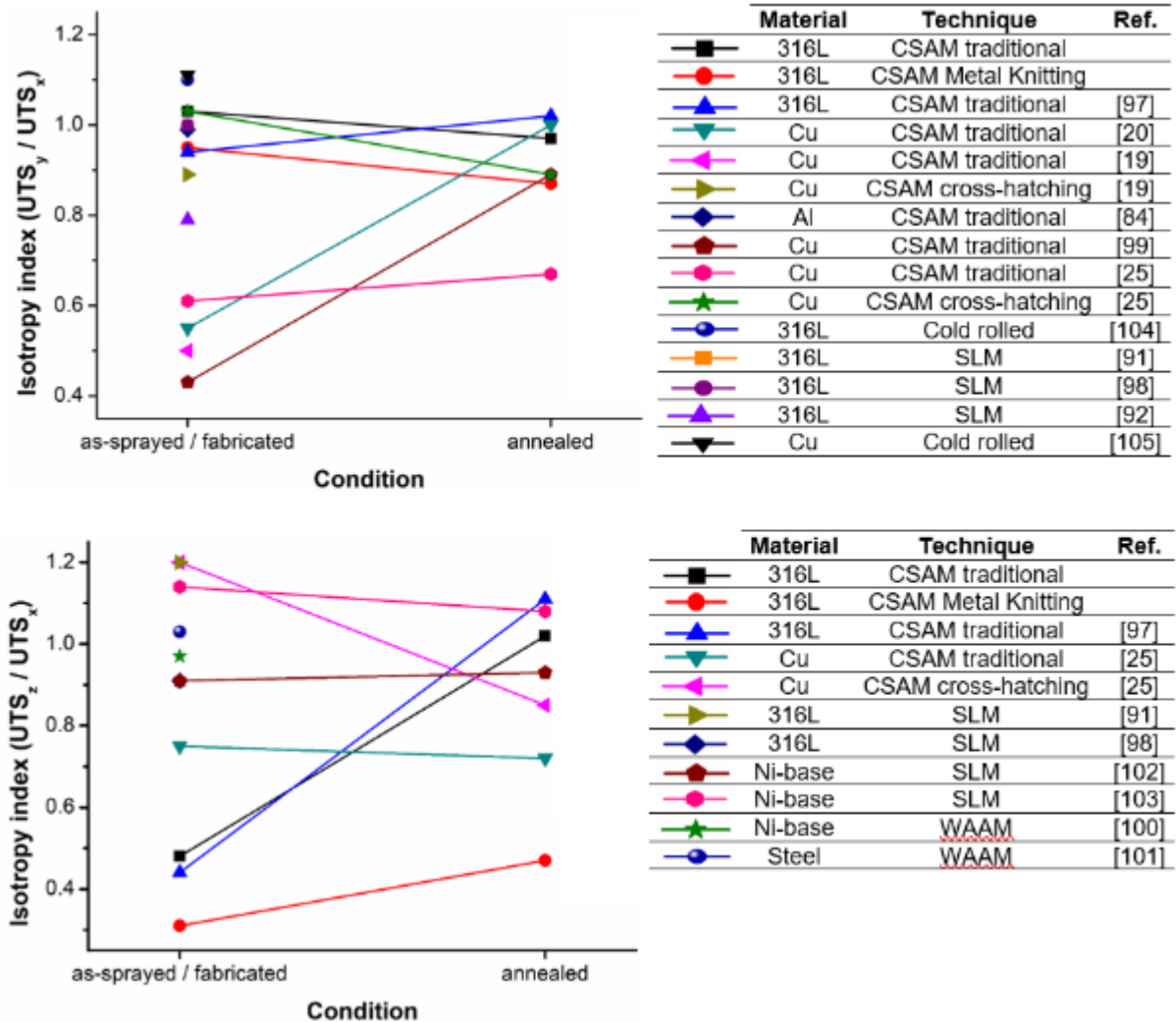


Figure 15: Effect of AM technique, AM strategy, and HT on material isotropy.

The mechanism to improve the CSAM 316L cohesion of particles and the mechanical properties depends on the intimate contact between the particles because it makes their atomic diffusion and metallurgic bonding or union feasible. However, this HT effect is harder for the CSAM Metal Knitting samples under treatment, starting from lower deformed particles with less material intimacy than the CSAM traditional ones.

3.8. Fractography

Figure 16 presents a CSAM traditional 316L tensile testing sample EDM machined on the Z-direction in as-machined condition before and as-polished after the testing. The samples were designed to guarantee the plane strain, and the literature shows that for a ductile bulk material, the fracture mechanism is the plastic deformation by shear stress in the material under external axial loading, resulting in a fracture angled 45 degrees with the sample symmetry axis [106]. However, all the CSAM-ed 316L as-sprayed had the fracture perpendicular to this symmetry axis, as seen in Figure 16, characterizing it as a brittle fracture. Furthermore, it evidences and confirms the weak interface region observed in YZ- and XZ-planes NT images of the CSAM traditional 316L sample presented in Figure 12, because the position of fractures of the Z-direction tensile samples coincides with one of those transition interfaces.

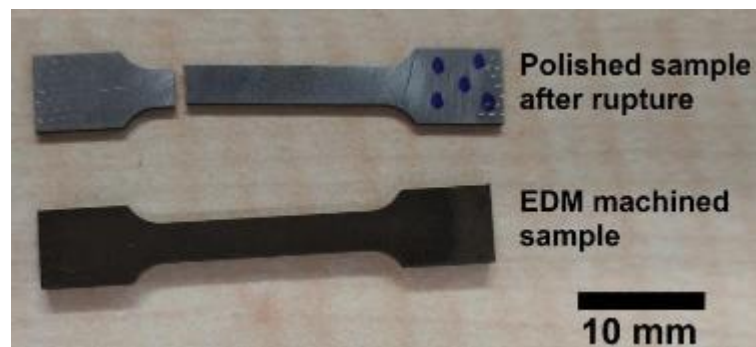


Figure 16: Z-direction tensile testing samples.

For both CSAM strategies studied, the fracture morphology was observed by SEM to investigate the characteristics and properties of fracture, and Figure 17 shows representative images of the fractures' surfaces. Before the heat treatment, the fractures occurred by cleavage-like or decohesion, which means detaching particles from their neighbors, also known as interparticular or trans-particle fracture. It confirms that the interface between them was the preferential crack growing path and that this interparticular area was the weakest region of the material. The same behavior is reported in the literature for monotonic and cyclic testing for CSAM Al 7075 [107], Al 6061 [84], FeCoCrNiMn [108], Ti [109], and Cu [19,20,22,109], suggesting how important is improving the cohesion of particles for any use.

The fracture surfaces of the annealed samples revealed many dimples, indicating the emergence of the ductile mechanism of fracture, which is a consequence of a higher cohesion of particles that results from the micro welding phenomena by the atomic diffusion mechanism in the interparticular region. This improvement is numerically confirmed by the UTS results presented in Figure 14. This fracture behaviour is a characteristic of more ductile CS as-sprayed materials, such as pure Al and Ni [109]. Besides the dimples, for the CSAM Metal Knitting samples, large interconnected defects or pores were observed, which represent regions of weaker bonding and serve as a potential cause for a lower UTS and cohesion seen for these samples, even after the heat treatment, which did not reduce the porosity.

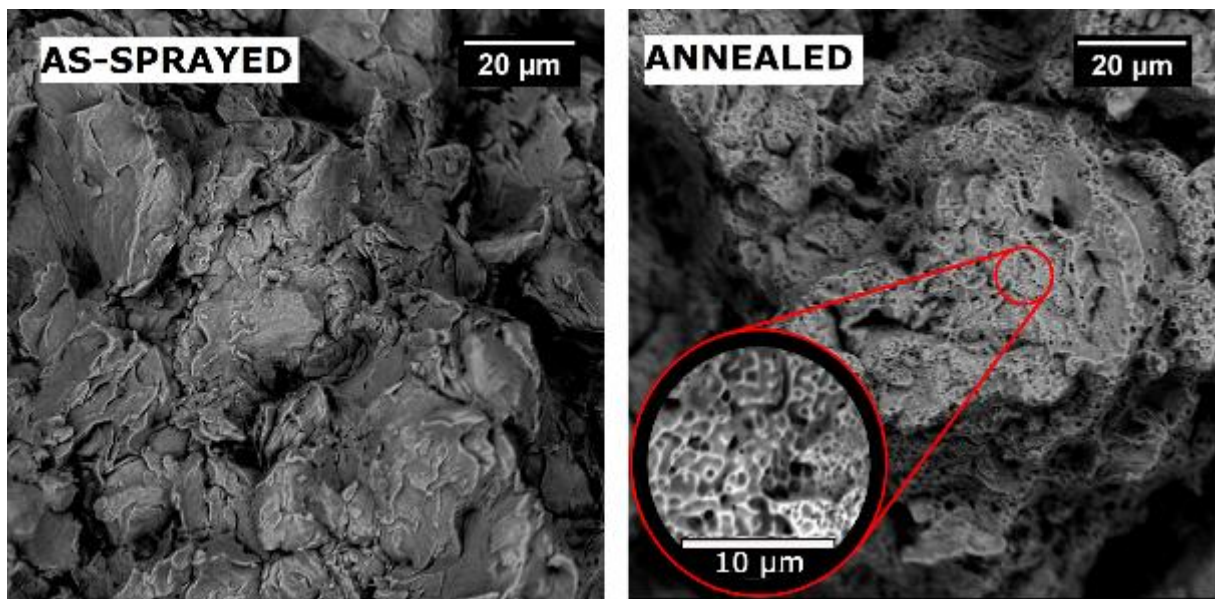


Figure 17: SEM images of fracture surface of tensile tested samples before and after HT.

3.9. Residual Stress

It is possible to consider two sources of residual stress in the CSAM deposits. One source is due to the interaction between the deposit and the substrate, while the second one is due to the deposition process that results in the specific stress distribution in the deposit itself when the substrate is separated. This approach of decomposition of the overall stress was used previously [60,76].

Considering the contribution due to the substrate-deposit interaction, the corresponding stress can be significant or even dominant when the CTE mismatch of the substrate and deposit material is great enough. Luzin et al. [59] presented such case for a relatively thick Ti deposit on steel and Al substrate by CSAM, with the CTE mismatch stress being ten times higher than the deposition stress. The second way of the substrate-deposit interaction arises from the fact that the substrate plays the role of constraint when layers are deposited on it and, therefore,

takes part in the overall stress distribution. Suppose the layer is deposited on the substrate with a typical CS compressive stress. As a result, the substrate acquires some tensile stress and gets a concave bending to equilibrate the overall forces and moments. In the case studied in this work, CSAM traditional and Metal Knitting 316L, the 3 mm thick Al substrate bent a little with inward (concave) curvature during the CS deposition of the first layers, relieving the dominance of the peening effects over the CTE related effects. Similar evidence of compressive residual stress imposed by the peening effect and bonding between the particles was also presented by Nault et al. [4].

When the Al substrates were machined by EDM (with the intent to minimize the impact of the machining process on the CSAM-ed material residual stress), so that Al substrate does not contribute to the final residual stress distribution, the remaining stress field is only due to the deposition process relieving the CSAM-ed compressive residual stress and peening nature. The experimental stress maps of the two stress components, $\sigma_{\text{Transversal}}$ and $\sigma_{\text{Longitudinal}}$ in the CSAM-ed 316L, are shown in Figure 18. The maps interpretation must consider the experimental uncertainties of ~ 10 MPa, while the stress values are in the range of ± 100 MPa. Through stress component $\sigma_{\text{Longitudinal}}$, which is integrally balanced to zero in the whole XZ cross-section (Figure 18), it is noticed that the CSAM-ed 316L samples in the as-sprayed condition have their surfaces characterized mainly by a compressive stress condition, except on a region on the top area of the CSAM Metal Knitting as-sprayed sample. Since the deposition stress is the overall result of the composition of the competing quenching and peening mechanisms, e.g., Luzin et al. [59], it is possible that in some locations where the peening effect is reduced (or quenching effect is increased, the overall deposition stress can have sign changed. In corroboration, Boruah et al. [61] explain that the tensile areas result from the quenching mechanism due to the high energy applied for harder CS-ed particles, like Ti6Al4V or 316L, requiring high gas temperature and pressure, 1000 °C and 6 MPa. In these zones, the quenching mechanism prevailed over the peening one because of the lower velocity of impact of the particles seen for the CSAM Metal Knitting strategy.

Although the term “surface residual stress” is conceptually incorrect because stress is a bulk quantity and cannot be interpreted in an exposed surface but in a volume of material, which in this work was $5 \times 5 \times 5 \text{ mm}^3$, it has been employed and understood by scholars, and also used in this discussion conditionally as a stress in an infinitesimally thin layer of material at the surface. This surface condition is attractive for improving the material performance, reducing the stress concentration and crack nucleation under external loads, as presented by Bagherifard and Gugliano [110], studying CSAM-ed materials and CS-ed coatings in fatigue testing. Fatigue

cracks always nucleate in the areas with concentrated tension, such as surface defects, part geometry, or even excessive roughness, which have their effect amplified by superficial tensile residual stress. The changing material surface stress state has been the focus of several studies, as mentioned by Maleki et al. [111], highlighting the mechanical treatments, like blasting and different peening processes, which improve the surface compressive residual stress.

It is important to notice that the CSAM traditional and Metal Knitting 316L had a surface stress state with a moderate compressive residual stress, favorable for a good performance in the as-sprayed condition, similar to the DLD-ed H13 steel that reached peaks of -300 MPa on its sidewalls [52], or WAAM-ed Ti6Al4V with -200 MPa [53]. In terms of residual stress state, CSAM-ed 316L demonstrated better results than the SLM-ed one, as presented by Wu et al. [55] and Yaghi et al. [112], with compressive residual stress in its centre, and tensile residual stress near to the surface, reaching values close to 500 MPa.

For the CSAM traditional 316L as-sprayed sample, the condition of the particles at the impact favored its higher compressive residual stress by the peening effect, not simply because of the V_{impact} of the particles, $624 \text{ m}\cdot\text{s}^{-1}$ over 511 to $540 \text{ m}\cdot\text{s}^{-1}$ of the CSAM Metal Knitting ones. Besides that, another factor that corroborates a higher compressive residual stress in CSAM traditional 316L samples was the layer thickness, 221 and $3600 \mu\text{m}$, for the CSAM traditional and Metal Knitting, respectively. The peening effect, responsible for the compressive residual stress, has its effect limited to a few dozens of microns, and thinner layers are more affected by it, as presented by Singh et al. [113], obtaining a reduction in compressive stress from -1291 to -134 MPa, by increasing the CS-ed IN718 layer thickness from 216 to $1173 \mu\text{m}$. With this understanding, a possibility to improve the compressive residual stress in CSAM Metal Knitting 316L samples is to reduce the feedstock powder feeding or increase the robot speed to decrease the layer thickness obtained.

The alternative HT post-processing resulted in a homogenization of residual stress in the CSAM-ed 316L for both deposition strategies, traditional and Metal Knitting, as interpreted from the mappings presented in Figure 18. These mappings of HT-ed samples showed a low magnitude tensile residual stress in the centre of the sample and a low compressive stress on their surfaces. Although these features might resemble the peening effect in the as-sprayed samples, the nature of these distributions is different. The cooling after annealing (with no control cooling rate) resulted in the tensile residual stress in the core part of the sample. In contrast, the outer parts of the deposits gain the compressive stress, typical features of the

quenching residual stress distribution. Therefore, this internal tensile stress cannot be considered a more significant risk factor.

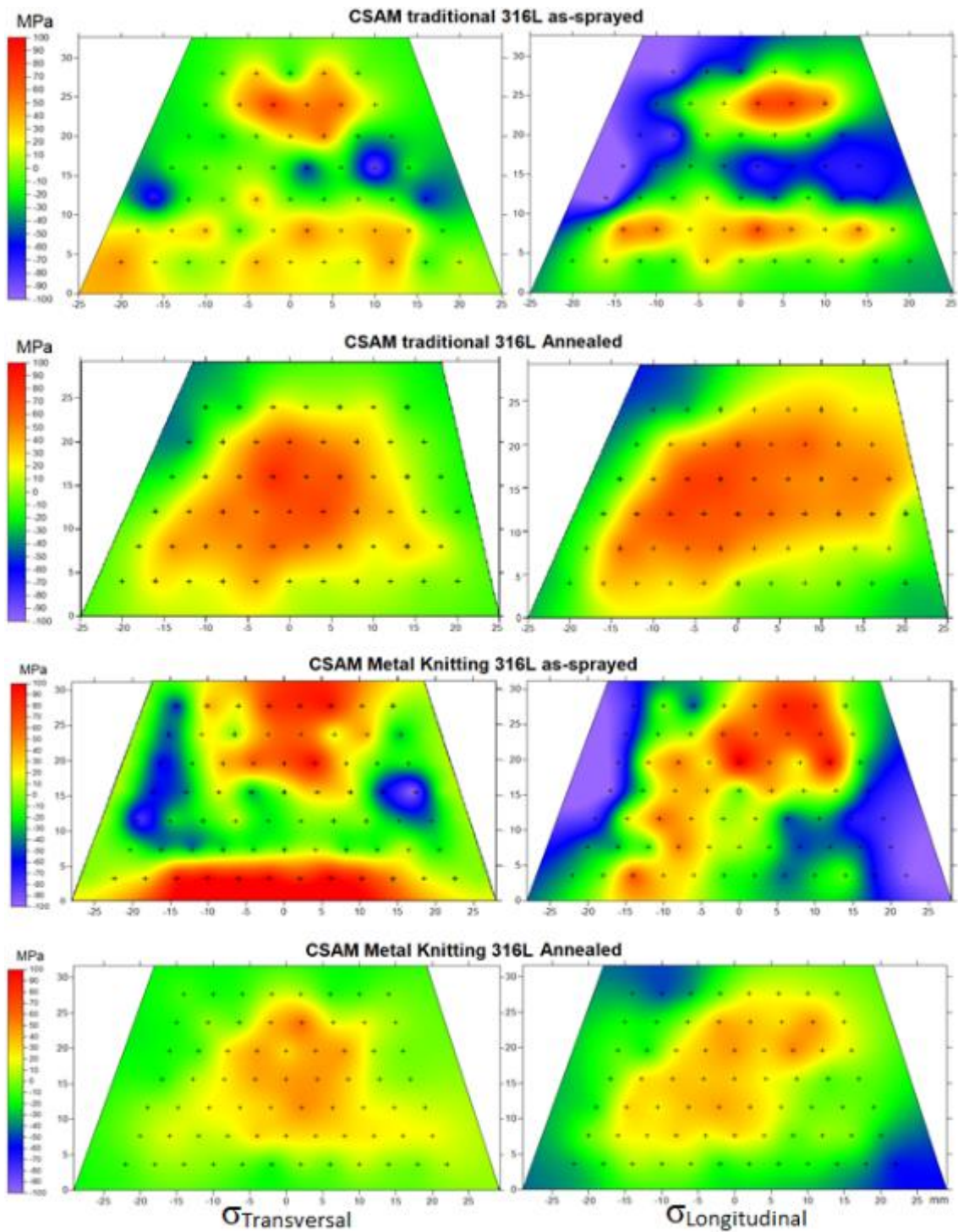


Figure 18: Residual stress distribution in the XZ-plane cross-section for CSAM traditional and Metal Knitting 316L samples before and after HT. Two stress components are presented: $\sigma_{\text{Transversal}}$ (left column) and $\sigma_{\text{Longitudinal}}$ (right column), while σ_{Normal} is considered to be approximately zero.

4. Conclusions

This study analysed the influence of different CSAM 316L deposition strategies, traditional and Metal Knitting, and the use of HT post-treatment on the CSAM-ed part characteristics and properties. As a result, the following conclusions could be drawn:

The CSAM Metal Knitting strategy has better control of the 316L part geometry made than the CSAM traditional strategy, i.e., its sidewall inclination grows vertically or at least under control, while the CSAM traditional strategy demands correction layers that produce a lower inter-layer adhesion;

The CSAM Metal Knitting promotes a lower V_{impact} of particles than the CSAM traditional strategy, resulting for 316L a lower microhardness, lower UTS, and higher porosity using that strategy due to the lower kinetic energy of the particles and consequent lower particle deformation;

The tensile testing mechanism of fracture is decohesion of particles or interparticular for the CSAM-ed 316L in as-sprayed condition. However, the annealing improves the cohesion of particles by atomic diffusion and micro welding, changing the mechanism of fracture to predominantly ductile;

CSAM Metal Knitting and traditional strategies produce planar isotropy in XY-plane; however, anisotropy is evident when contrasting the Z- with X- or Y-direction due to a lower cohesion of particles in the XZ-plane. It occurs because there are smaller contact areas between the particles and less bonding by the ASI mechanism;

Both strategies produced the centre of the sample being in tensile residual stress, balanced with a compressive one on the near-surfaces regions. The magnitude of the residual stress is low, under 100 MPa absolute value. The higher velocity of particles promoted by the CSAM traditional strategy resulted in higher compressive residual stress values than CSAM Metal Knitting due to the higher deformation of particles and peening effect;

The HT relieves the initial residual stress from the deposition process, homogenising it in the material. Although the annealing parameters, 1000 °C for 1 h, promote the microstructural changes in CSAM-ed 316L and improve the mechanical properties, the cooling rate in the furnace promotes a quenching effect in the CSAM-ed 316L particular structure, resulting in a moderate final tensile residual stress in the centre of the material, <100 and <50 MPa for CSAM

traditional and Metal Knitting strategies, respectively. Still, the low compressive residual stress prevails in the materials' HT-ed surface.

5. Acknowledgments

Grant PID2020-115508RB-C21 funded by MCIN/AEI/10.13039/501100011033 and, as appropriate, by “ERDF A way of making Europe”, by the “European Union” or by the “European Union NextGenerationEU/PRTR”. Government of Catalonia, SGR 2021SGR00712. R.F. Vaz has a Ph.D. grant from AGAUR, Government of Catalonia, 2020 FISDU 00305. Research Project P13534 approved at the Australian Centre for Neutron Scattering (ACNS) & National Deuteration Facility (NDF) 2022-1 round.

References

- [1] H. Wu, C. Huang, X. Xie, S. Liu, T. Wu, T. Niendorf, Y. Xie, C. Deng, M. Liu, H. Liao, S. Deng, Influence of Spray Trajectories on Characteristics of Cold-Sprayed Copper Deposits, *Surf. Coatings Technol.* 405 (2021) 126703. doi.org/10.1016/j.surfcoat.2020.126703.
- [2] B. Al-Mangour, Fundamentals of Cold Spray Processing: Evolution and Future Perspectives, in: P. Cavaliere (Ed.), *Cold-Spray Coatings Recent Trends Futur. Perspect.*, Elsevier, Cham, Switzerland, 2018: pp. 3–24.
- [3] S. Bagherifard, S. Monti, M.V. Zuccoli, M. Riccio, J. Kondás, M. Guagliano, Cold Spray Deposition for Additive Manufacturing of Freeform Structural Components Compared to Selective Laser Melting, *Mater. Sci. Eng. A.* 721 (2018) 339–350. doi.org/10.1016/j.msea.2018.02.094.
- [4] I.M. Nault, G.D. Ferguson, V. Champagne, A. Nardi, Design of Residual-Stress-Compensating Molds for Cold Spray Additive Manufacturing Applications, *J. Therm. Spray Technol.* 29 (2020) 1466–1476. doi.org/10.1007/s11666-020-00984-0.
- [5] M.R. Rokni, S.R. Nutt, C.A. Widener, V.K. Champagne, R.H. Hrabe, Review of Relationship Between Particle Deformation, Coating Microstructure, and Properties in High-Pressure Cold Spray, *J. Therm. Spray Technol.* 26 (2017) 1308–1355. doi.org/10.1007/s11666-017-0575-0.
- [6] H. Assadi, F. Gärtner, T. Stoltenhoff, H. Kreye, Bonding mechanism in cold gas spraying, *Acta Mater.* 51 (2003) 4379–4394. doi.org/10.1016/S1359-6454(03)00274-X.
- [7] X. Wang, F. Feng, M.A. Klecka, M.D. Mordasky, J.K. Garofano, T. El-Wardany, A. Nardi, V.K. Champagne, Characterization and Modeling of the Bonding Process in Cold Spray Additive Manufacturing, *Addit. Manuf.* 8 (2015) 149–162. doi.org/10.1016/j.addma.2015.03.006.
- [8] S. Yin, J. Cizek, J. Cupera, M. Hassani, X. Luo, R. Jenkins, Y. Xie, W. Li, R. Lupoi, Formation Conditions of Vortex-like Intermixing Interfaces in Cold Spray, *Mater. Des.* 200 (2021) 1–10. doi.org/10.1016/j.matdes.2020.109444.
- [9] M. Hassani-Gangaraj, D. Veysset, V.K. Champagne Jr, K.A. Nelson, Adiabatic Shear Instability is not Necessary for Adhesion in Cold Spray, *Acta Mater.* 158 (2018) 430–439. doi.org/10.1016/j.actamat.2018.07.065.
- [10] G. Bae, S. Kumar, S. Yoon, K. Kang, H. Na, H. Kim, C. Lee, Bonding Features and Associated Mechanisms in Kinetic Sprayed Titanium Coatings, *Acta Mater.* 57 (2009) 5654–5666. doi.org/10.1016/j.actamat.2009.07.061.
- [11] T. Hussain, Cold Spraying of Titanium: A Review of Bonding Mechanisms, Microstructure and Properties, *Key Eng. Mater.* 533 (2012) 53–90. doi.org/10.4028/www.scientific.net/kem.533.53.
- [12] Y. Ichikawa, R. Tokoro, M. Tanno, K. Ogawa, Elucidation of Cold-Spray Deposition Mechanism by Auger Electron Spectroscopic Evaluation of Bonding Interface Oxide Film, *Acta Mater.* 164 (2019) 39–49. doi.org/10.1016/j.actamat.2018.09.041.
- [13] H. Assadi, F. Gärtner, T. Klassen, H. Kreye, Comment on ‘Adiabatic Shear Instability is not Necessary for Adhesion in Cold Spray,’ *Scr. Mater.* 162 (2019) 512–514. doi.org/10.1016/j.scriptamat.2018.10.036.
- [14] K. Kim, M. Watanabe, J. Kawakita, S. Kuroda, Grain Refinement in a Single Titanium Powder Particle Impacted at High Velocity, *Scr. Mater.* 59 (2008) 768–771. doi.org/10.1016/j.scriptamat.2008.06.020.
- [15] R.F. Vaz, A. Silvello, J. Sanchez, V. Albaladejo, I.G.G. Cano, The Influence of the Powder Characteristics on 316L Stainless Steel Coatings Sprayed by Cold Gas Spray, *Coatings.* 11 (2021) 168. doi.org/10.3390/coatings11020168.

- [16] M. Park, M.S. Kang, G.-W. Park, H.C. Kim, H.-S. Moon, B. Kim, J.B. Jeon, H. Kim, H.-S. Park, S.-H. Kwon, B.J. Kim, Effects of Annealing Treatment on the Anisotropy Behavior of Cold-Rolled High-Manganese Austenite Stainless Steels, *Met. Mater. Int.* 27 (2021) 3839–3855. doi.org/10.1007/s12540-020-00785-8.
- [17] C.M. Park, J. Jung, B.C. Yu, Y.H. Park, Anisotropy of the Wear and Mechanical Properties of Extruded Aluminum Alloy Rods (AA2024-T4), *Met. Mater. Int.* 25 (2019) 71–82. doi.org/10.1007/s12540-018-0164-x.
- [18] Z.H. Zhang, W.Y. Li, Y. Feng, J.L. Li, Y.J. Chao, Global Anisotropic Response of Friction Stir Welded 2024 Aluminum Sheets, *Acta Mater.* 92 (2015) 117–125. doi.org/10.1016/j.actamat.2015.03.054.
- [19] K. Yang, W. Li, X. Yang, Y. Xu, Anisotropic Response of Cold Sprayed Copper Deposits, *Surf. Coatings Technol.* 335 (2018) 219–227. doi.org/10.1016/j.surfcoat.2017.12.043.
- [20] K. Yang, W. Li, X. Guo, X. Yang, Y. Xu, Characterizations and Anisotropy of Cold-Spraying Additive-Manufactured Copper Bulk, *J. Mater. Sci. Technol.* 34 (2018) 1570–1579. doi.org/10.1016/j.jmst.2018.01.002.
- [21] H. Seiner, J. Cizek, P. Sedlák, R. Huang, J. Cupera, I. Dlouhy, M. Landa, Elastic Moduli and Elastic Anisotropy of Cold Sprayed Metallic Coatings, *Surf. Coatings Technol.* 291 (2016) 342–347. doi.org/10.1016/j.surfcoat.2016.02.057.
- [22] M.-S. Baek, H.-J. Kim, K.-A. Lee, Anisotropy of Compressive Deformation Behavior in Cold Sprayed Cu Bulk Material, *J. Nanosci. Nanotechnol.* 19 (2019) 3935–3942. doi.org/10.1166/jnn.2019.16147.
- [23] J. Pattison, S. Celotto, R. Morgan, M. Bray, W. O’Neill., Cold gas dynamic manufacturing: A non-thermal approach to freeform fabrication, *Int. J. Mach. Tools Manuf.* 47 (2007) 627–634. doi.org/10.1016/j.ijmachtools.2006.05.001.
- [24] R.F. Vaz, A. Garfias, V. Albaladejo, J. Sanchez, I.G. Cano, A Review of Advances in Cold Spray Additive Manufacturing, *Coatings.* 13 (2023) 267. doi.org/10.3390/coatings13020267.
- [25] S. Yin, R. Jenkins, X. Yan, R. Lupoi, Microstructure and Mechanical Anisotropy of Additively Manufactured Cold Spray Copper Deposits, *Mater. Sci. Eng. A.* 734 (2018) 67–76. doi.org/10.1016/j.msea.2018.07.096.
- [26] A.T. Nardi, T.I. El-Wardany, D. V Viens, M.E. Lynch, A. Hsu, M.A. Klecka, W. Gu, Additive topology optimized manufacturing for multi-functional components, US 2014/0277669 A1, 2014.
- [27] A. Vargas-Uscategui, P.C. King, S. Yang, C. Chu, J. Li, Toolpath Planning for Cold Spray Additively Manufactured Titanium Walls and Corners: Effect on Geometry and Porosity, *J. Mater. Process. Technol.* 298 (2021) 117272. doi.org/10.1016/j.jmatprotec.2021.117272.
- [28] R.F. Vaz, V. Albaladejo-Fuentes, J. Sanchez, U. Ocaña, Z.G. Corral, H. Canales, I.G. Cano, Metal Knitting: A New Strategy for Cold Gas Spray, *Materials.* 15 (2022) 1–17. doi.org/10.3390/ma15196785.
- [29] R.F. Vaz, H. Canales, J. Sanchez, U. Ocaña, V. Albaladejo, I. Garcia Cano, Metal Knitting: A Method to Control Morphology and Properties in Cold Spray Additive Manufacturing, in: *Therm. Spray 2022 Proc. from Int. Therm. Spray Conf., 2022*: pp. 614–621. doi.org/10.31399/asm.cp.itsc2022p0614.
- [30] R. Huang, M. Sone, W. Ma, H. Fukanuma, The effects of heat treatment on the mechanical properties of cold-sprayed coatings, *Surf. Coatings Technol.* 261 (2015) 278–288. doi.org/10.1016/j.surfcoat.2014.11.017.
- [31] B. Al-Mangour, P. Vo, R. Mongrain, E. Irissou, S. Yue, Effect of Heat Treatment on the Microstructure and Mechanical Properties of Stainless Steel 316L Coatings Produced by Cold Spray for Biomedical Applications, *J. Therm. Spray Technol.* 23 (2014) 641–652. doi.org/10.1007/s11666-013-0053-2.
- [32] X. Qiu, J. Wang, N. ul H. Tariq, L. Gyansah, J. Zhang, T. Xiong, Effect of Heat Treatment on Microstructure and Mechanical Properties of A380 Aluminum Alloy Deposited by Cold Spray, *J. Therm. Spray Technol.* 26 (2017) 1898–1907. doi.org/10.1007/s11666-017-0640-8.
- [33] P.D. Eason, J.A. Fewkes, S.C. Kennett, T.J. Eden, K. Tello, M.J. Kaufman, M. Tiryakioğlu, On the Characterization of Bulk Copper Produced by Cold Gas Dynamic Spray Processing in as Fabricated and Annealed Conditions, *Mater. Sci. Eng. A.* 528 (2011) 8174–8178. doi.org/10.1016/j.msea.2011.07.012.
- [34] K. Wathanyu, K. Tuchinda, S. Daopiset, S. Sirivisoot, J. Kondas, C. Bauer, Study of the Properties of Titanium Porous Coating with Different Porosity Gradients on 316L Stainless Steel by a Cold Spray Process, *J. Therm. Spray Technol.* 31 (2022) 545–558. doi.org/10.1007/s11666-021-01316-6.
- [35] R.F. Váz, A. Silvello, P.D. Cavalière, S. Dosta, I.G. Cano, L. Capodici, A. Rizzo, D. Valerini, Fretting Wear and Scratch Resistance of Cold-Sprayed Pure Cu and Ti, *Metallogr. Microstruct. Anal.* 10 (2021) 496–513. doi.org/10.1007/s13632-021-00758-2.
- [36] ASTM, E2109-01 - Standard test methods for determining area percentage porosity in thermal sprayed coatings, ASTM International, West Conshohocken, PA, USA, 2021. doi.org/10.1520/E2109-01R21.
- [37] A.A. Baker, R. Thuss, N. Woollett, A. Maich, E. Stavrou, S.K. McCall, H.B. Radousky, Cold Spray Deposition of Thermoelectric Materials, *JOM.* 72 (2020) 2853–2859. doi.org/10.1007/s11837-020-04151-2.
- [38] T. Van Steenkiste, J.R. Smith, Evaluation of Coatings Produced via Kinetic and Cold Spray Processes, *J. Therm. Spray Technol.* 13 (2004) 274–282. doi.org/10.1361/10599630419427.

- [39] Y. Wang, J. Adrien, B. Normand, Porosity Characterization of Cold Sprayed Stainless Steel Coating Using Three-Dimensional X-ray Microtomography, *Coatings*. 8 (2018) 326. doi.org/10.3390/coatings8090326.
- [40] S.H. Zahiri, S.C. Mayo, M. Jahedi, Characterization of Cold Spray Titanium Deposits by X-Ray Microscopy and Microtomography, *Microsc. Microanal.* 14 (2008) 260–266. doi.org/10.1017/S1431927608080355.
- [41] D. Lévesque, C. Bescond, C. Cojocar, Laser-ultrasonic inspection of cold spray additive manufacturing components, *AIP Conf. Proc.* 2102 (2019) 020026. doi.org/10.1063/1.5099730.
- [42] Y.-J. Li, X.-T. Luo, C.-J. Li, Dependency of Deposition Behavior, Microstructure and Properties of Cold Sprayed Cu on Morphology and Porosity of the Powder, *Surf. Coatings Technol.* 328 (2017) 304–312. doi.org/10.1016/j.surfcoat.2017.08.070.
- [43] Q.J. Zhu, K. Wang, X.H. Wang, B.R. Hou, Electrochemical Impedance Spectroscopy Analysis of Cold Sprayed and Arc Sprayed Aluminium Coatings Serviced in Marine Environment, *Surf. Eng.* 28 (2012) 300–305. doi.org/10.1179/1743294411Y.0000000036.
- [44] I.S. Anderson, R.L. McGreevy, H.Z. Bilheux, *Neutron Imaging and Applications: A Reference for the Imaging Community*, Springer, New York, 2009.
- [45] M. Strobl, I. Manke, N. Kardjilov, A. Hilger, M. Dawson, J. Banhart, Advances in Neutron Radiography and Tomography, *J. Phys. D. Appl. Phys.* 42 (2009) 243001. doi.org/10.1088/0022-3727/42/24/243001.
- [46] N. Chankow, Neutron Radiography, in: M. Omar (Ed.), *Nondestruct. Test. Methods New Appl.*, IntechOpen, Rijeka, 2012: pp. 73–100.
- [47] K.M. Podurets, S.E. Kichanov, V.P. Glazkov, E.S. Kovalenko, M.M. Murashev, D.P. Kozlenko, E. V. Lukin, E.B. Yatsishina, Modern Methods of Neutron Radiography and Tomography in Studies of the Internal Structure of Objects, *Crystallogr. Reports.* 66 (2021) 254–266. doi.org/10.1134/S1063774521020115.
- [48] T. Watkins, H. Bilheux, K. An, A. Payzant, R. Dehoff, C. Duty, W. Peter, C. Brice, Neutron Characterization for Additive Manufacturing, *Adv. Mater. Process.* (2013) 23–27.
- [49] R.P. Turner, C. Panwisawas, Y. Lu, I. Dhiman, H.C. Basoalto, J.W. Brooks, Neutron Tomography Methods Applied to a Nickel-based Superalloy Additive Manufacture Build, *Mater. Lett.* 230 (2018) 109–112. doi.org/10.1016/j.matlet.2018.07.112.
- [50] A.J. Brooks, J. Ge, M.M. Kirka, R.R. Dehoff, H.Z. Bilheux, N. Kardjilov, I. Manke, L.G. Butler, Porosity Detection in Electron Beam-Melted Ti-6Al-4V Using High-Resolution Neutron Imaging and Grating-Based Interferometry, *Prog. Addit. Manuf.* 2 (2017) 125–132. doi.org/10.1007/s40964-017-0025-z.
- [51] F. Grazi, C. Cialdai, M. Manetti, M. Massi, M.P. Morigi, M. Bettuzzi, R. Brancaccio, F. Albertin, T. Shinohara, T. Kai, A. Fedrigo, A. Di Giovanni, F. Arneodo, R. Torres, O. Al-Ketan, J. Elhashemi, F. Taccetti, L. Giuntini, A Multi-Technique Tomography-Based Approach for Non-Invasive Characterization of Additive Manufacturing Components in View of Vacuum/UHV Applications: Preliminary Results, *Rend. Lincei. Sci. Fis. e Nat.* 32 (2021) 463–477. doi.org/10.1007/s12210-021-00994-2.
- [52] R. Cottam, J. Wang, V. Luzin, Characterization of Microstructure and Residual Stress in a 3D H13 Tool Steel Component Produced by Additive Manufacturing, *J. Mater. Res.* 29 (2014) 1978–1986. doi.org/10.1557/jmr.2014.190.
- [53] V. Luzin, N. Hoyer, Stress in Thin Wall Structures Made by Layer Additive Manufacturing, in: *Residual Stress*. 2016, 2017: pp. 497–502. doi.org/10.21741/9781945291173-84.
- [54] K. Bobzin, W. Wietheger, M.A. Knoch, A. Schacht, U. Reisinger, R. Sharma, L. Oster, Comparison of Residual Stress Measurements Conducted by X-ray Stress Analysis and Incremental Hole Drilling Method, *J. Therm. Spray Technol.* 29 (2020) 1218–1228. doi.org/10.1007/s11666-020-01056-z.
- [55] A.S. Wu, D.W. Brown, M. Kumar, G.F. Gallegos, W.E. King, An Experimental Investigation into Additive Manufacturing-Induced Residual Stresses in 316L Stainless Steel, *Metall. Mater. Trans. A.* 45 (2014) 6260–6270. doi.org/10.1007/s11661-014-2549-x.
- [56] Y.C. Tsui, T.W. Clyne, An Analytical Model for Predicting Residual Stresses in Progressively Deposited Coatings Part 1: Planar Geometry, *Thin Solid Films.* 306 (1997) 23–33. doi.org/10.1016/S0040-6090(97)00199-5.
- [57] V. Luzin, K. Spencer, M.X. Zhang, Residual stress and thermo-mechanical properties of cold spray metal coatings, *Acta Mater.* 59 (2011) 1259–1270. doi.org/10.1016/j.actamat.2010.10.058.
- [58] V. Luzin, K. Spencer, M.X. Zhang, N. Matthews, Residual Stress in Coatings Produced by Cold Spray, *Mater. Sci. Forum.* 772 (2013) 155–159. doi.org/10.4028/www.scientific.net/MSF.772.155.
- [59] V. Luzin, O. Kirstein, S.H. Zahiri, D. Fraser, Residual Stress Buildup in Ti Components Produced by Cold Spray Additive Manufacturing (CSAM), *J. Therm. Spray Technol.* 29 (2020) 1498–1507. doi.org/10.1007/s11666-020-01048-z.
- [60] V. Luzin, K. Spencer, M. Zhang, N. Matthews, J. Davis, M. Saleh, Residual Stresses in Cold Spray Coatings, in: P.D. Cavaliere (Ed.), *Cold-Spray Coatings*, Springer, 2018: pp. 451–480. doi.org/10.1007/978-3-319-67183-3_16.

- [61] D. Boruah, B. Ahmad, T.L. Lee, S. Kabra, A.K. Syed, P. McNutt, M. Doré, X. Zhang, Evaluation of Residual Stresses Induced by Cold Spraying of Ti-6Al-4V on Ti-6Al-4V Substrates, *Surf. Coatings Technol.* 374 (2019) 591–602. doi.org/10.1016/j.surfcoat.2019.06.028.
- [62] V. Luzin, S. Kuroda, S. Yin, A.S.M. Ang, Advanced Residual Stress Analysis in Thermal Spray and Cold Spray Processes, *J. Therm. Spray Technol.* 29 (2020) 1211–1217. doi.org/10.1007/s11666-020-01083-w.
- [63] R.F. Vaz, A.G.M. Pukasiewicz, G.B. Sucharski, I.B.A.F. Siqueira, S.M.Z. Odake, R.S.C. Paredes, The Reuse of Alumina for Grit Blasting Preparation of Steel Surface for Thermal Spraying, *Int. J. Abras. Technol.* 10 (2021) 235. doi.org/10.1504/IJAT.2021.120261.
- [64] ASTM, B822-02 - Standard Test Method for Particle Size Distribution of Metal Powders and Related Compounds by Laser Scattering, ASTM International, West Conshohocken, PA, USA, 2002. doi.org/10.1520/B0822-20.
- [65] ASTM, B212-21 - Standard Test Method for Apparent Density of Powders Using the Hall Flowmeter Funnel, ASTM International, West Conshohocken, PA, USA, 2021. doi.org/10.1520/B0212-21.
- [66] ASTM, B213-20 - Standard Test Method for Flow Rate of Metal Powders, ASTM International, West Conshohocken, PA, USA, 2020. doi.org/10.1520/B0213-20.
- [67] B. Dikici, H. Yilmazer, I. Ozdemir, M. Isik, The Effect of Post-Heat Treatment on Microstructure of 316L Cold-Sprayed Coatings and Their Corrosion Performance, *J. Therm. Spray Technol.* 25 (2016) 704–714. doi.org/10.1007/s11666-016-0402-z.
- [68] S. Bagherifard, J. Kondas, S. Monti, J. Cizek, F. Perego, O. Kovarik, F. Lukac, F. Gaertner, M. Guagliano, Tailoring cold spray additive manufacturing of steel 316 L for static and cyclic load-bearing applications, *Mater. Des.* 203 (2021) 109575. doi.org/10.1016/j.matdes.2021.109575.
- [69] S. Yin, J. Cizek, X. Yan, R. Lupoi, Annealing Strategies for Enhancing Mechanical Properties of Additively Manufactured 316L Stainless Steel Deposited by Cold Spray, *Surf. Coatings Technol.* 370 (2019) 353–361. doi.org/10.1016/j.surfcoat.2019.04.012.
- [70] ASTM, E1920-03 - Standard guide for metallographic preparation of thermal sprayed coatings, ASTM International, West Conshohocken, PA, USA, 2021. doi.org/10.1520/E1920-03R21.
- [71] ASTM, E3-11 - Standard Guide for Preparation of Metallographic Specimens, ASTM International, West Conshohocken, PA, USA, 2017. doi.org/10.1520/E0003-11R17.
- [72] ASTM, E384-22 - Standard Test for Microindentation Hardness of Materials, ASTM International, West Conshohocken, PA, USA, 2022. doi.org/10.1520/E0384-22.
- [73] U. Garbe, T. Randall, C. Hughes, G. Davidson, S. Pangelis, S.J. Kennedy, A New Neutron Radiography / Tomography / Imaging Station DINGO at OPAL, *Phys. Procedia.* 69 (2015) 27–32. doi.org/10.1016/j.phpro.2015.07.003.
- [74] D. Micieli, T. Minniti, G. Gorini, NeuTomPy toolbox, a Python package for tomographic data processing and reconstruction, *SoftwareX.* 9 (2019) 260–264. doi.org/10.1016/j.softx.2019.01.005.
- [75] O. Kirstein, V. Luzin, U. Garbe, The Strain-Scanning Diffractometer Kowari, *Neutron News.* 20 (2009) 34–36. doi.org/10.1080/10448630903241175.
- [76] R. Sinclair-Adamson, V. Luzin, A. Duguid, K. Kannoorpatti, R. Murray, Residual Stress Distributions in Cold-Sprayed Copper 3D-Printed Parts, *J. Therm. Spray Technol.* 29 (2020) 1525–1537. doi.org/10.1007/s11666-020-01040-7.
- [77] A. Vargas-Uscategui, P.C. King, M.J. Styles, M. Saleh, V. Luzin, K. Thorogood, Residual Stresses in Cold Spray Additively Manufactured Hollow Titanium Cylinders, *J. Therm. Spray Technol.* 29 (2020) 1508–1524. doi.org/10.1007/s11666-020-01028-3.
- [78] T. Gnäupel-Herold, ISODEC: software for calculating diffraction elastic constants, *J. Appl. Crystallogr.* 45 (2012) 573–574. doi.org/10.1107/S0021889812014252.
- [79] ASTM, A240/A240M-22a - Standard Specification for Chromium and Chromium-Nickel Stainless Steel Plate, Sheet, and Strip for Pressure Vessels and for General Applications, ASTM International, West Conshohocken, PA, USA, 2022. doi.org/10.1520/A0240_A0240M-22A.
- [80] M.E. Lynch, W. Gu, T. El-Wardany, A. Hsu, D. Viens, A. Nardi, M. Klecka, Design and topology/shape structural optimisation for additively manufactured cold sprayed components, *Virtual Phys. Prototyp.* 8 (2013) 213–231. doi.org/10.1080/17452759.2013.837629.
- [81] D. Kotoban, S. Grigoriev, A. Okunkova, A. Sova, Influence of a Shape of Single Track on Deposition Efficiency of 316L Stainless Steel Powder in Cold Spray, *Surf. Coatings Technol.* 309 (2017) 951–958. doi.org/10.1016/j.surfcoat.2016.10.052.
- [82] H. Wu, X. Xie, S. Liu, S. Xie, R. Huang, C. Verdy, M. Liu, H. Liao, S. Deng, Y. Xie, Bonding Behavior of Bi-Metal-Deposits Produced by Hybrid Cold Spray Additive Manufacturing, *J. Mater. Process. Technol.* 299 (2022) 117375. doi.org/10.1016/j.jmatprotec.2021.117375.
- [83] F. Gärtner, T. Stoltenhoff, T. Schmidt, H. Kreye, The Cold Spray Process and its Potential for Industrial Applications, *J. Therm. Spray Technol.* 15 (2006) 223–232. doi.org/10.1361/105996306X108110.
- [84] S.E. Julien, A. Nourian-Avval, W. Liang, T. Schwartz, O.C. Ozdemir, S. Müftü, Bulk Fracture Anisotropy in Cold-Sprayed Al 6061 Deposits, *Eng. Fract. Mech.* 263 (2022) 1–17. doi.org/10.1016/j.engfracmech.2022.108301.

- [85] K.H. Ko, J.O. Choi, H. Lee, Intermixing and Interfacial Morphology of Cold-Sprayed Al Coatings on Steel, *Mater. Lett.* 136 (2014) 45–47. doi.org/10.1016/j.matlet.2014.07.142.
- [86] F.J. Humphreys, G.S. Rohrer, A. Rollett, *Recrystallization and Related Annealing Phenomena*, 3rd ed., Elsevier, Amsterdam, 2017.
- [87] Y. Xie, C. Chen, M.P. Planche, S. Deng, R. Huang, Z. Ren, H. Liao, Strengthened Peening Effect on Metallurgical Bonding Formation in Cold Spray Additive Manufacturing, *J. Therm. Spray Technol.* 28 (2019) 769–779. doi.org/10.1007/s11666-019-00854-4.
- [88] F.P. de Moraes, S.F. Alves, R.L. Plaut, A.F. Padilha, Degradation of Microstructure and Properties of an AISI 316L Steel Pipe After More Than 100,000 hours Usage at 640°C in a Petrochemical Industry, *Procedia Struct. Integr.* 17 (2019) 131–137. doi.org/10.1016/j.prostr.2019.08.018.
- [89] K. Bártoová, M. Dománková, J. Bárta, P. Pastier, Influence of 40% Cold Working and Annealing on Precipitation in AISI 316L Austenitic Stainless Steel, *Materials*. 15 (2022) 6484. doi.org/10.3390/ma15186484.
- [90] X. Tang, Sigma Phase Characterization in AISI 316 Stainless Steel, *Microsc. Microanal.* 11 (2005) 78–79. doi.org/10.1017/S143192760550374X.
- [91] A.A. Deev, P.A. Kuznetsov, S.N. Petrov, Anisotropy of Mechanical Properties and its Correlation with the Structure of the Stainless Steel 316L Produced by the SLM Method, *Phys. Procedia*. 83 (2016) 789–796. doi.org/10.1016/j.phpro.2016.08.081.
- [92] L. Hitzler, J. Hirsch, B. Heine, M. Merkel, W. Hall, A. Öchsner, On the Anisotropic Mechanical Properties of Selective Laser-Melted Stainless Steel, *Materials*. 10 (2017) 1136. doi.org/10.3390/ma10101136.
- [93] W. Sun, A.W.-Y. Tan, K. Wu, S. Yin, X. Yang, I. Marinescu, E. Liu, Post-Process Treatments on Supersonic Cold Sprayed Coatings: A Review, *Coatings*. 10 (2020) 123. doi.org/10.3390/coatings10020123.
- [94] N. Fan, J. Cizek, C. Huang, X. Xie, Z. Chlup, R. Jenkins, R. Lupoi, S. Yin, A New Strategy for Strengthening Additively Manufactured Cold Spray Deposits Through in-Process Densification, *Addit. Manuf.* 36 (2020) 1–11. doi.org/10.1016/j.addma.2020.101626.
- [95] L.L. Silveira, G.B. Sucharski, A.G.M. Pukasiewicz, R.S.C. Paredes, Influence of Particle Size Distribution on the Morphology and Cavitation Resistance of High-Velocity Oxygen Fuel Coatings, *J. Therm. Spray Technol.* 27 (2018) 695–709. doi.org/10.1007/s11666-018-0708-0.
- [96] D. Goldbaum, J. Ajaja, R.R. Chromik, W. Wong, S. Yue, E. Irissou, J.-G. Legoux, Mechanical Behavior of Ti Cold Spray Coatings Determined by a Multi-scale Indentation Method, *Mater. Sci. Eng. A*. 530 (2011) 253–265. doi.org/10.1016/j.msea.2011.09.083.
- [97] Y. Yamazaki, H. Fukanuma, N. Ohno, Anisotropic mechanical properties of the free-standing cold sprayed SUS316 coating and effect of the post-spray heat treatment on it, *J. Japan Therm. Spray Soc.* 53 (2016) 91–95. doi.org/10.11330/jtss.53.91.
- [98] A. Charmi, R. Falkenberg, L. Ávila, G. Mohr, K. Sommer, A. Ulbricht, M. Sprengel, R. Saliwan Neumann, B. Skrotzki, A. Evans, Mechanical anisotropy of additively manufactured stainless steel 316L: An experimental and numerical study, *Mater. Sci. Eng. A*. 799 (2021) 140154. doi.org/10.1016/j.msea.2020.140154.
- [99] K. Yang, W. Li, X. Yang, Y. Xu, A. Vairis, Effect of heat treatment on the inherent anisotropy of cold sprayed copper deposits, *Surf. Coatings Technol.* 350 (2018) 519–530. doi.org/10.1016/j.surfcoat.2018.07.046.
- [100] T. Hassel, T. Carstensen, Properties and Anisotropy Behaviour of a Nickel Base Alloy Material Produced by Robot-based Wire and Arc Additive Manufacturing, *Weld. World*. 64 (2020) 1921–1931. doi.org/10.1007/s40194-020-00971-7.
- [101] L. Sun, F. Jiang, R. Huang, D. Yuan, C. Guo, J. Wang, Anisotropic Mechanical Properties and Deformation Behavior of Low-carbon High-strength Steel Component Fabricated by Wire and Arc Additive Manufacturing, *Mater. Sci. Eng. A*. 787 (2020) 139514. doi.org/10.1016/j.msea.2020.139514.
- [102] D. Deng, R.L. Peng, H. Brodin, J. Moverare, Microstructure and mechanical properties of Inconel 718 produced by selective laser melting: Sample orientation dependence and effects of post heat treatments, *Mater. Sci. Eng. A*. 713 (2018) 294–306. doi.org/10.1016/j.msea.2017.12.043.
- [103] D. Tomus, Y. Tian, P.A. Rometsch, M. Heilmaier, X. Wu, Influence of post heat treatments on anisotropy of mechanical behaviour and microstructure of Hastelloy-X parts produced by selective laser melting, *Mater. Sci. Eng. A*. 667 (2016) 42–53. doi.org/10.1016/j.msea.2016.04.086.
- [104] Z. You, H. Fu, S. Qu, W. Bao, L. Lu, Revisiting Anisotropy in the Tensile and Fracture Behavior of Cold-rolled 316L Stainless Steel with Heterogeneous Nano-lamellar Structures, *Nano Mater. Sci.* 2 (2020) 72–79. doi.org/10.1016/j.nanoms.2020.03.001.
- [105] A.A. Bryukhanov, A.F. Voitenko, V. V. Usov, A.A. Chernyi, Anisotropy of the Elastic and Strength Properties of Cold-rolled Copper Sheets, *Strength Mater.* 11 (1979) 914–917. doi.org/10.1007/BF00770396.
- [106] H. Li, M.W. Fu, J. Lu, H. Yang, Ductile fracture: Experiments and computations, *Int. J. Plast.* 27 (2011) 147–180. doi.org/10.1016/j.ijplas.2010.04.001.

- [107] Y. Ren, N. ul H. Tariq, H. Liu, L. Zhao, X. Cui, Y. Shen, J. Wang, T. Xiong, Study of Microstructural and Mechanical Anisotropy of 7075 Al Deposits Fabricated by Cold Spray Additive Manufacturing, *Mater. Des.* 212 (2021) 110271. doi.org/10.1016/j.matdes.2021.110271.
- [108] P. Cavaliere, A. Perrone, A. Silvello, A. Laska, G. Blasi, I.G. Cano, Fatigue Bending of V-Notched Cold-Sprayed FeCoCrNiMn Coatings, *Metals*. 12 (2022) 780. doi.org/10.3390/met12050780.
- [109] O. Kovarik, J. Siegl, J. Cizek, T. Chraska, J. Kondas, Fracture Toughness of Cold Sprayed Pure Metals, *J. Therm. Spray Technol.* 29 (2020) 147–157. doi.org/10.1007/s11666-019-00956-z.
- [110] S. Bagherifard, M. Guagliano, Fatigue performance of cold spray deposits: Coating, repair and additive manufacturing cases, *Int. J. Fatigue*. 139 (2020) 105744. https://doi.org/10.1016/j.ijfatigue.2020.105744.
- [111] E. Maleki, S. Bagherifard, M. Bandini, M. Guagliano, Surface Post-Treatments for Metal Additive Manufacturing: Progress, Challenges, and Opportunities, *Addit. Manuf.* 37 (2021) 101619. doi.org/10.1016/j.addma.2020.101619.
- [112] A. Yaghi, S. Ayvar-Soberanis, S. Moturu, R. Bilkhu, S. Afazov, Design Against Distortion for Additive Manufacturing, *Addit. Manuf.* 27 (2019) 224–235. doi.org/10.1016/j.addma.2019.03.010.
- [113] R. Singh, S. Schrufer, S. Wilson, J. Gibmeier, R. Vassen, Influence of coating thickness on residual stress and adhesion-strength of cold-sprayed Inconel 718 coatings, *Surf. Coatings Technol.* 350 (2018) 64–73. doi.org/10.1016/j.surfcoat.2018.06.080.

4.3.3. CSAM-ed Parts Obtained

By employing CSAM traditional and Metal Knitting strategies, several parts were produced to understand the effects of the strategy parameters on the part characteristics and properties, as to make samples with these optimized parameters. The results are presented in Figures 11 to 14 of Article 3, and Figure 5 of Article 5, some with simple shapes, others controlling the vertical sidewalls, and finally, more complex, e.g., curved walls or varying thickness with the part height. Figure 37 presents examples of the geometries obtained, detailing the CSAM strategy and materials employed. Chapter 8, “Appendix”, contains a Section, “CSAM-ed Parts”, with a more representative Table listing the CSAM-ed parts produced by CSAM traditional and Metal Knitting strategies, their parameters, materials, and visual aspects; however, neither mechanical properties nor materials performances are shown or discussed in this Section, which is focused on the geometric aspects exclusively.

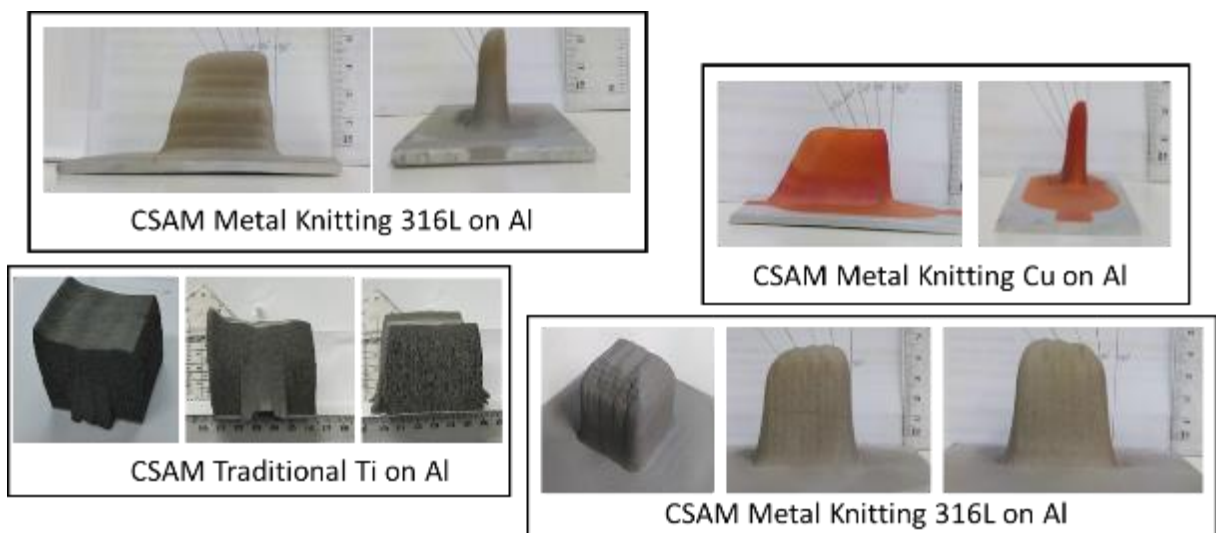


Figure 37: Examples of CSAM-ed geometries obtained.

The CSAM geometries versatility has been improved by developing new deposition strategies, as variations of the traditional one, as presented in the literature, spraying with inclined gun to correct sidewall inclination [43,65], e.g., the scheme presented in Figure 6 of Article 5. This strategy is presented by Vargas-Usgategui et al. [43] as an effective alternative to make relative thin walls, in the order of millimeters. A limitation faced by Vargas-Usgategui et al. [43], as by employing CSAM Metal Knitting, is that each sprayed powder, results in a deposit with distinct geometrical characteristics, especially layer thickness, and sidewall angle generated. For example,

CSAM traditional 316L always produces a pyramid-like shape but CSAM traditional Ti sprayed on substrate's borders produces vertical sidewalls; however, CSAM traditional Ti sprayed on a flat surface builds a pyramid-like shape, as observed in the Chapter 8, "Appendix", Section 8.4 "CSAM-ed Parts, Strategy, Parameters, Geometric Aspects, and Images". It inputs difficulties to the implementation of CSAM industrially, because each application demands a series of testing and parameters optimization.

The possibility of copying the substrate shape and keeping building material with the same width and length, as seen in Figure 12 of Article 3, is a good advantage for CSAM Metal Knitting to make AM hybrid systems, i.e., make a part with more complex regions by laser processing, and other less complex volumes by CSAM, which is much faster than laser, e.g., laser deposits typically less than 50 μm per layer and CSAM Metal Knitting reaches 7000 μm per layer. Still in hybrid systems, another promising application is Wire Arc Additive Manufacturing (WAAM), presented in the literature as a process that deposits large volumes of material by arc welding [66], complemented by depositing materials with poor weldability using CSAM.

Another use is employing CSAM Metal Knitting for repairing damaged components, especially those made with complex alloys or materials with poor weldability. It reduces the post-machining services by selecting the adequate Metal Knitting parameters, and a post-treatment can be done to improve the CSAM-ed material properties and bonding strength, as presented by Garfias et al. [67], obtaining an increase in adhesion of CSAM Metal Knitting Ti6Al4V on Ti6Al4V substrate from 15 to 160 MPa, as-sprayed and HT-ed, respectively.

4.3.4. Post-treatments

The CSAM-ed materials have presented their mechanical properties reduced compared with other AM processing techniques because of the weak bonding between the particles. This interparticular region is inherent to the CS-ed material consolidation, as presented in the literature [68–70]. Improving this cohesion of particles has been the focus of post-treatments, such as HT, SPS, HIP, among others, as listed in Article 1. As follows, the post-treatments studied in this thesis improved the microstructural characteristics of CSAM-ed 316L, Ti alloys, and Al.

4.3.4.1. Heat Treatments

4.3.4.1.1. Heat Treatment of CSAM-ed 316L

CSAM-ed 316L traditional and Metal Knitting samples were characterized by EBSD, complementing the results and discussions presented in Article 5. For this technique, the term indexing refers to the process of determining the crystallographic orientation of a material based on the diffraction patterns obtained from an electron beam interacting with the material's surface. Indexing involves comparing the collected diffraction patterns with a known crystal structure and orientation database. Suppose the collected data does not fit the information from the database, such as crystal symmetries, lattice parameters, and orientation relationships. In that case, the software considers this pattern a non-indexed area; however, some EBSD post-processing methodologies have been developed to improve the maps' quality and indexing rate [71]. As results of the EBSD technique, it is noticed the materials' grain size, grain shape, phase identification and distribution, recrystallization, deformation, orientation relationships, twinning, etc.

Figure 38 presents the water atomized 316L powder cross-section EBSD map. The large black areas were bakelite where the powder particles were mounted; however, small non-indexed areas can be seen in the powder particles. It was not evidence of amorphous zones or strained areas in the particles, just that a few points were unclear for the software interpretation and comparison with its database. Many black areas were previously processed to increase the visual map aspects and resolution. The powder starting condition is important for comparison with the CSAM as-sprayed and HT-ed conditions, 1000 °C for 1 h in air. It is noticed that each particle is composed of many grains, and larger particles have large grains, as smaller particles have small grains.

Figure 39 and Figure 40 present EBSD maps for CSAM-ed 316L traditional and Metal Knitting strategies made, respectively. The black areas in these maps refer to non-indexed areas. Besides the material porosity and consequent absence of material backscattering the electrons, these black areas can be attributed to a pattern outfit to the software database. Low indexing can represent an inadequate sample preparation, with a damaged or deformed surface, which affects the EBSD results since the diffraction pattern displays information from a depth lower than 50 nm. In addition, grain and phase boundaries typically present low indexing. Although low indexing can

come from the material characteristics also, because of processing that severely deforms plastically the material generating a high density of dislocations, which alters locally the diffraction pattern to a database outranges values, non-indexed. [72,73].

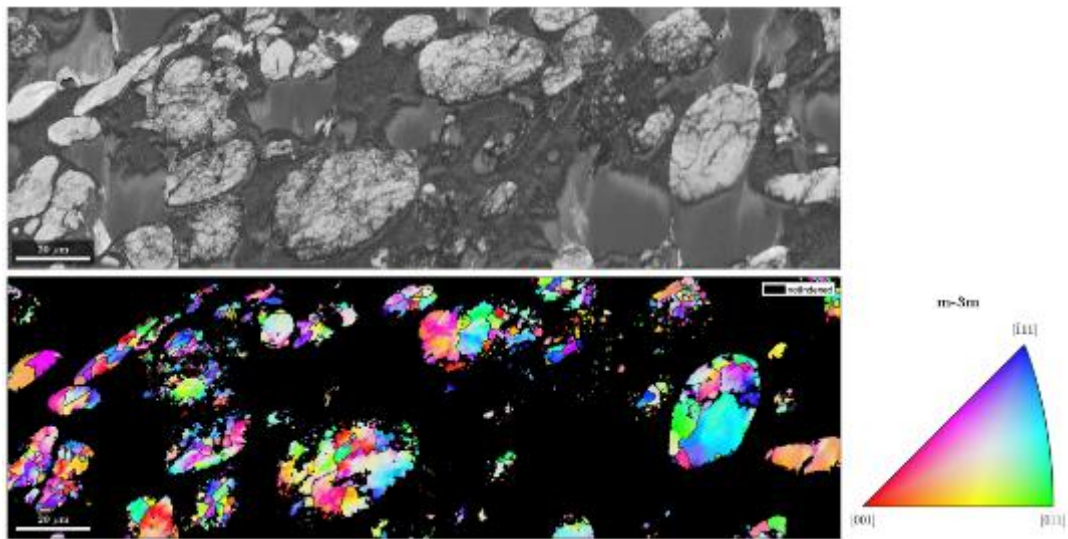


Figure 38: EBSD map of CSAM 316L feedstock powder.

CSAM-ED 316L TRADITIONAL STRATEGY

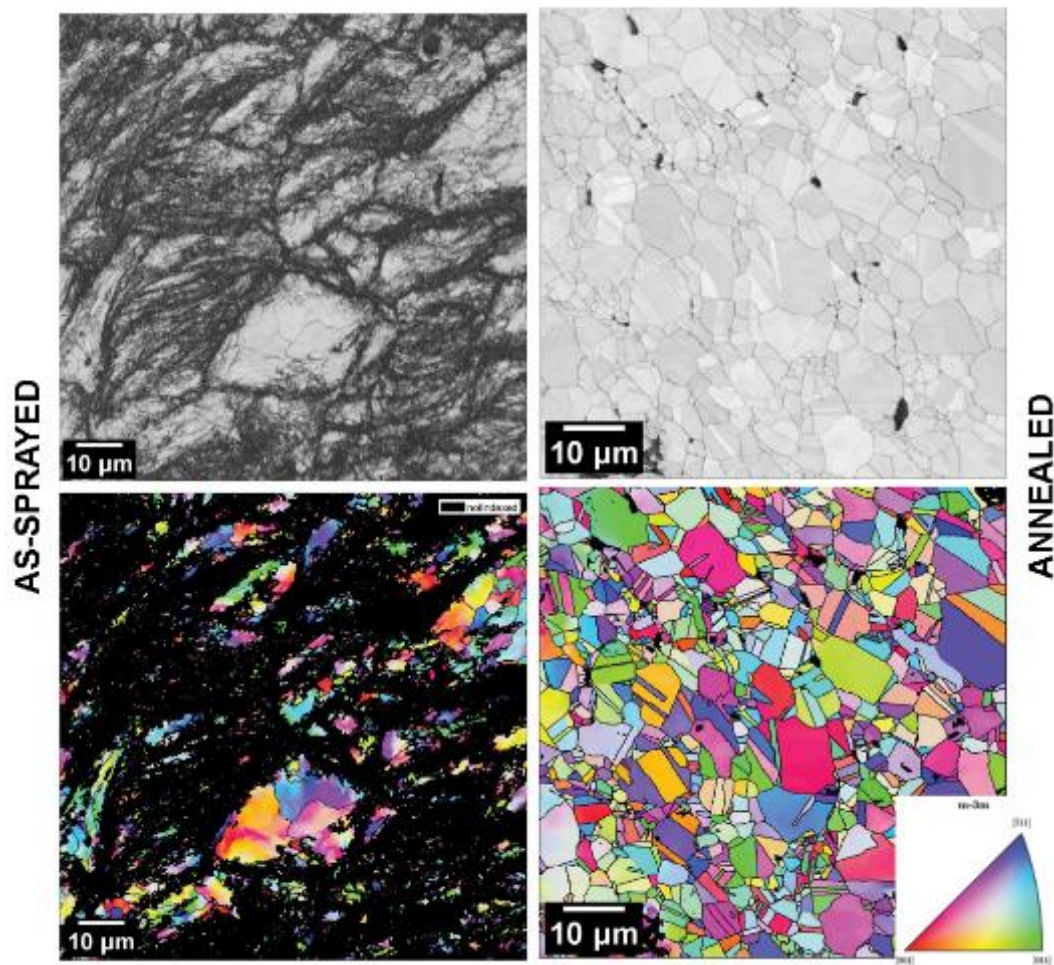


Figure 39: EBSD maps of CSAM-ed 316L traditional strategy as-sprayed and HT-ed.

CSAM-ED 316L KNITTING STRATEGY

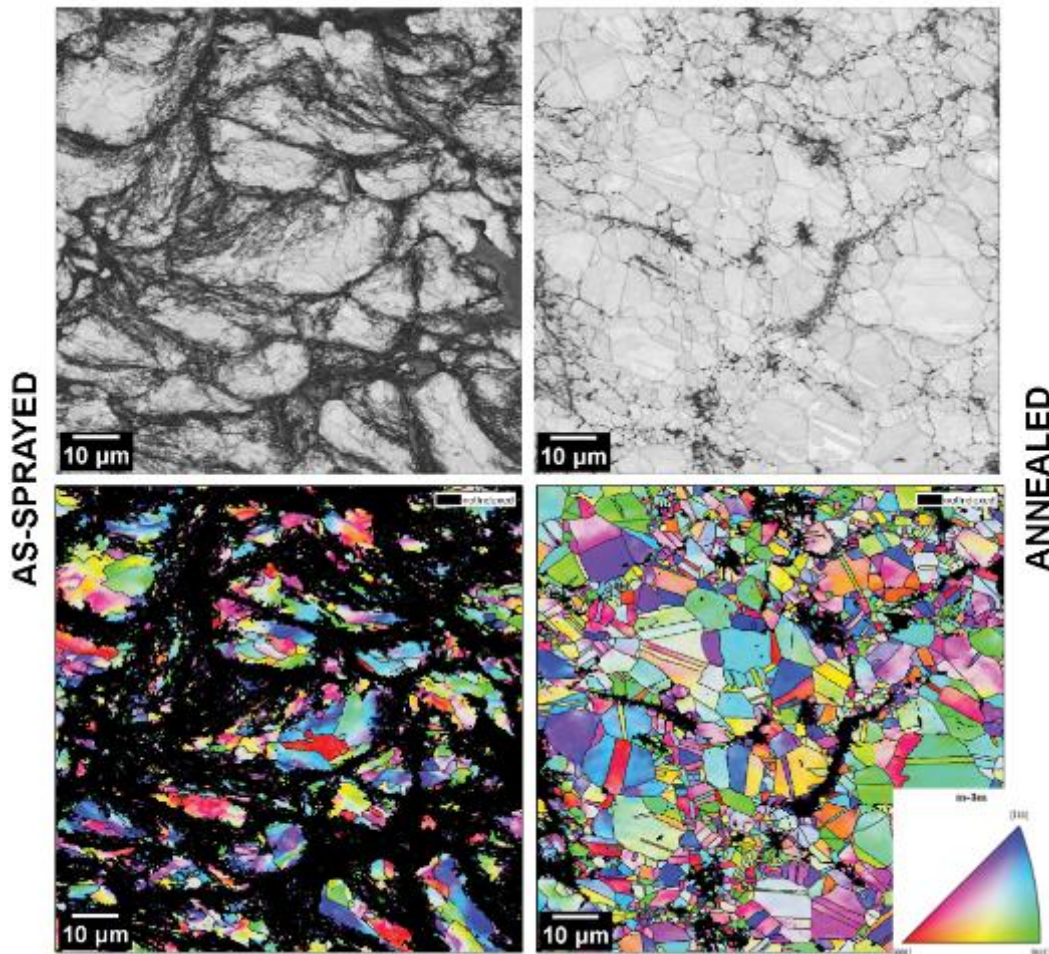


Figure 40: EBSD maps of CSAM-ed 316L Metal Knitting strategy as-sprayed and HT-ed.

EBSD maps reaffirmed the microstructure evolution due to the HT of CSAM-ed 316L. For the traditional and Metal Knitting strategies, the as-sprayed condition presented severely deformed grains in the surface of the particles, which is altered by the recrystallization and diffusion phenomena during the annealing post-processing, resulting in equiaxed grains microstructure with small grains in the previous interparticular region. It evidences a material recovery and recrystallization but not a grain coarsening. The coarsening and grain growth should occur for a longer HT; however, keeping small grains is favorable to improve the material mechanical properties, mainly because the grain boundaries act as barriers for the dislocation movements, improving the material strength and hardness.

From the Inverse Pole Figure (IPF), which are the color images in Figure 39 and Figure 40, and their respective Euler angles with the reference axis perpendicular to the image plane, it is not noticed a microstructure texture for as-sprayed nor directional recrystallization for HT-ed material. Another interpretation for EBSD was possible by

Grain Orientation Spread (GOS) and Kernel Average Misorientation (KAM) maps, which showed a lower misorientation index in the grains for the HT-ed CSAM 316L traditional sample, indicating a higher effect of recrystallization in this material than in CSAM-ed 316L Metal Knitting, which presented large areas with remaining deformed grains after the annealing post-treatment.

It can be attributed to the higher deformation and strained particles by the higher V_{impact} of the CSAM traditional strategy, storing energy in a deformed microstructure and pushing the recrystallization phenomena, as presented by Padilha, Plaut, and Rios [74], who presented this storing by strain-induced martensite transformation or a cellular dislocation distribution without phase transformation, depending on the material Stacking Fault Energy (SFE) value. Low SFE promotes strain-induced martensitic transformation [75].

4.3.4.1.2. Heat Treatment of CSAM-ed Ti Alloys

Besides the 316L, mechanical properties and HT effects were evaluated for CSAM traditional and Metal Knitting made Ti and Ti6Al4V. The HT was performed in a furnace under 1000 °C for 4 h in Ar atmosphere and characterized by SEM images, microhardness, and tensile testing. The typical microstructure of the pure Ti (Ti grade 2) and Ti6Al4V (Ti grade 5) are presented in Figure 41 and Figure 42, respectively.

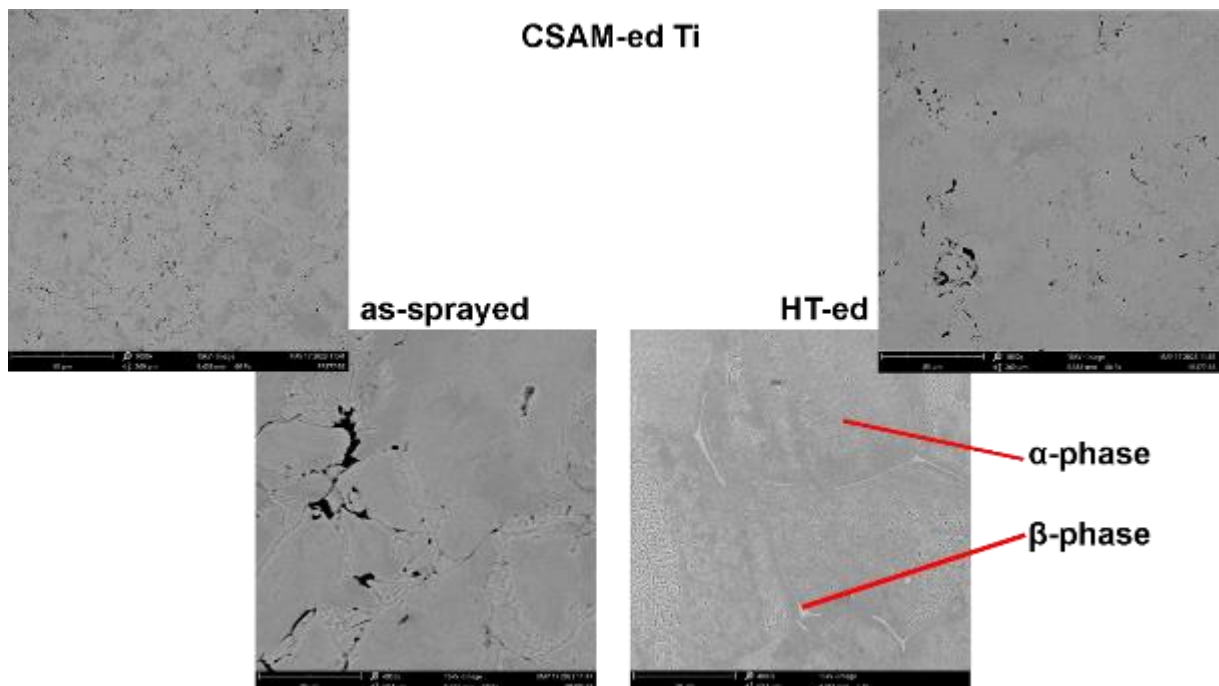


Figure 41: SEM of CSAM-ed Ti as-sprayed and HT-ed.

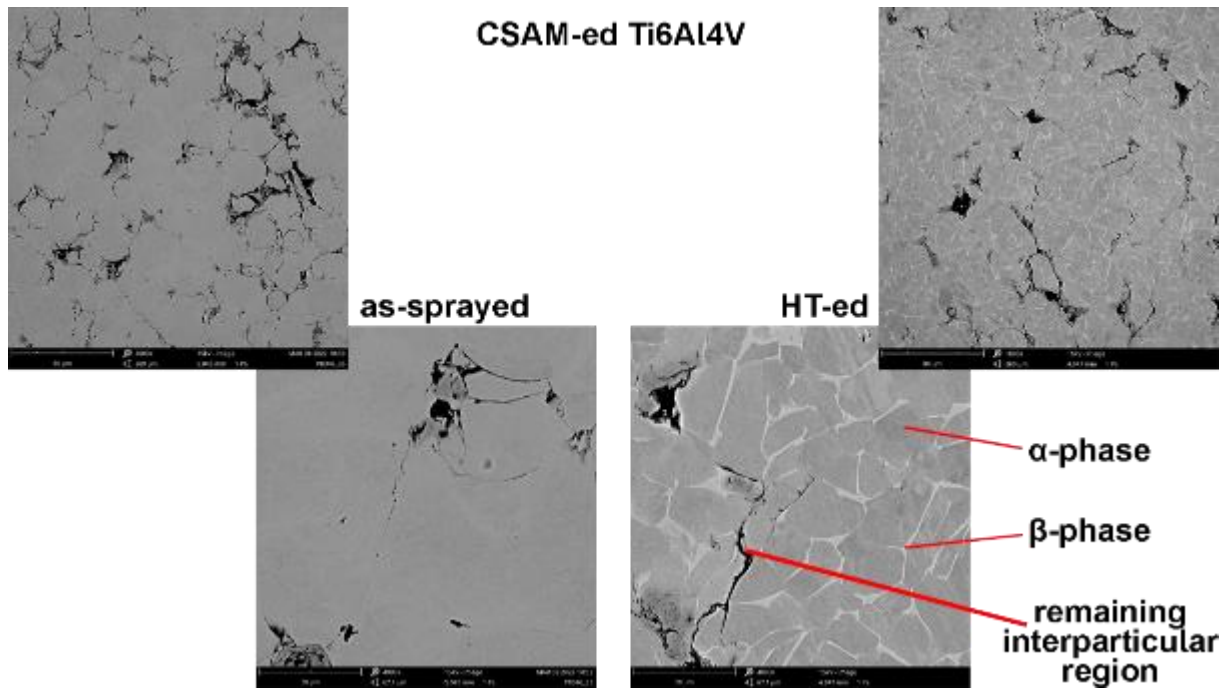


Figure 42: SEM of CSAM-ed Ti6Al4V as-sprayed and HT-ed.

The HCP α phase regions are dark gray, and the BCC β phase regions are light gray, with this last one formed in the α grains boundaries as an HT effect. For Ti6Al4V, a lower deformation of particles results from its lower plasticity or ductility than the pure Ti, as presented by Purcek et al. [76]. Chen et al. [77] explain this lower ductility due to the limited slipping planes in HCP α crystal structure, which is not a problem for FCC and BCC materials, i.e., Cu, Al, or austenitic steels.

The low plasticity resulted in a higher porosity in the interparticular region of Ti6Al4V, $18\pm 1\%$ as-sprayed and $8.5\pm 1\%$ as HT-ed, than for pure Ti, $<1\%$ for both conditions. It is also attributed to the Ti6Al4V higher hardness and lower dislocation mobility due to Al and V substitutional alloying elements in the Ti matrix. This porosity is a mean value of ten images, and Figure 41 and Figure 42 do not represent these measurements, but they are representative for the microstructural evolution due to the HT. Improving the Ti6Al4V deformation during the CS deposition has been the focus of much research, employing He as working gas to increase the V_{particle} [77], applying in-situ shot peening to deform the bonded particles [78], or other processing optimizations. The processing and post-processing densifying procedures are reported in Article 1.

For CSAM-ed Ti, HT increased the material hardness from 207 ± 12 to 324 ± 21 HV_{0.3}, as-sprayed and HT-ed, respectively. However, for Ti6Al4V, HT did not

alter its hardness drastically, increasing it from 319 ± 19 to 355 ± 16 $HV_{0.3}$, which is consonant with other results presented in the literature [77,79,80], where the hardness decreasing by the phase changing is also presented. Furthermore, during the CSAM deposition, the HCP α' - or orthorhombic α'' -martensite can be formed due to the severe localized plastic deformation [81], contributing to improving the material hardness; however, the HT post-processing eliminates this phase because the HT temperature stabilizes β phase, which is converted in α during the low cooling rate, resulting in an $\alpha+\beta$ microstructure, as seen in Figure 42.

HT improved the cohesion of particles, increasing the material strength, as presented in Figure 43, for CSAM-ed Ti and Ti6Al4V in three directions, following the scheme of Figure 12. The highlights were CSAM-ed Ti in the X-direction, which had improved by 370% the UTS, and CSAM-ed Ti6Al4V in the Z-direction with 224% higher UTS for the HT-ed condition. In general, besides the UTS values, the material isotropy was incremented by HT post-processing, as interpreted from the UTS_y/UTS_x and UTS_z/UTS_x indexes presented in Table 6, which complements the Figure 15 of Article 5. The index 1.0 means a perfect isotropy, and the worst values were seen in UTS_z/UTS_x for CSAM-ed Ti HT-ed and CSAM-ed Ti6Al4V as-sprayed. Notably, the isotropy between the X- and Y-direction is higher than between the Z- and X-direction because of the CS powder-laden jet direction, which is in the Z-direction, favoring the deformation and higher bonding strength in the XY-plane; consequently, the cohesion of particles in X- and Y-direction.

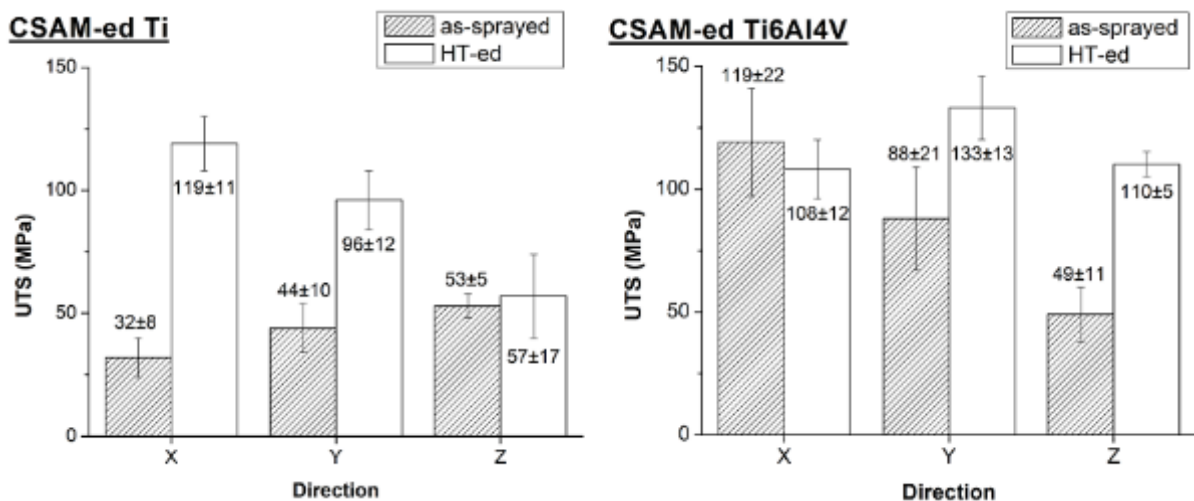


Figure 43: HT effects on UTS of CSAM-ed Ti and Ti6Al4V.

Table 6: Effect of HT on the isotropy index of CSAM-ed Ti and Ti6Al4V.

Material	Condition	UTS _y /UTS _x index	UTS _z /UTS _x index
Ti	as-sprayed	1.4	1.6
Ti	HT-ed	0.8	0.5
Ti6Al4V	as-sprayed	0.7	0.4
Ti6Al4V	HT-ed	1.2	1.0

4.3.4.1.3. Heat Treatment of CSAM-ed Al

HT, 450 °C for 4 h in Ar atmosphere, was applied on CSAM-ed Metal Knitting Al samples, made as straight, thin, and high walls, employing one single line for each deposited layer. Metal Knitting parameters were varied to understand their individual effects on the CSAM-ed Al part geometry and properties. The Metal Knitting radius was 1 or 2 mm, the angle was 20 or 30 degrees, and the step was 1 or 2.5 mm. This resulted in different layer thicknesses, demanding more layers for the thinner ones to obtain the planned 30 mm height samples, as presented in Figure 44.

Figure 44 also presents the cross-sections of the samples, and by interpreting these images, it is noticed that 1 mm change in radius was not enough to promote any substantial shape change; however, employing an angle of 30 instead of 20 degrees, a thicker wall was produced, 10 and 6 mm, respectively. The step distance, the distance between the circles described by each Metal Knitting movement, altered the layer thickness drastically, and steps of 1 mm resulted in 8±2 mm-thick layers, while steps of 2.5 mm produced 4±1 mm-thick layers.

Figure 44 presents OM images of CSAM Metal Knitting Al samples before and after HT, revealing a higher porosity in the as-sprayed condition. The white arrows indicate some examples of particle boundaries or interparticular regions, which was the weakest region of the material. Evaluating the effect of the CSAM Metal Knitting parameters on the CSAM-ed Al microstructural characteristics, the highest porosity was seen by using a higher Metal Knitting angle, 30 degrees, 18±3%. Liu et al. [82] present CS-ed traditional Al with higher than 15% of porosity, which was reduced drastically by these authors employing an in-situ micro-forging CS processing, which consisted of spraying big stainless steel powder (−291+118 μm) mixed with Al powder. Their objective was that these big stainless steel particles deform plastically the CS-ed Al but not bond to the coating, which was achieved after optimization of the process.

It should be a strategy to improve the CSAM Metal Knitting properties by densification for any sprayed material.

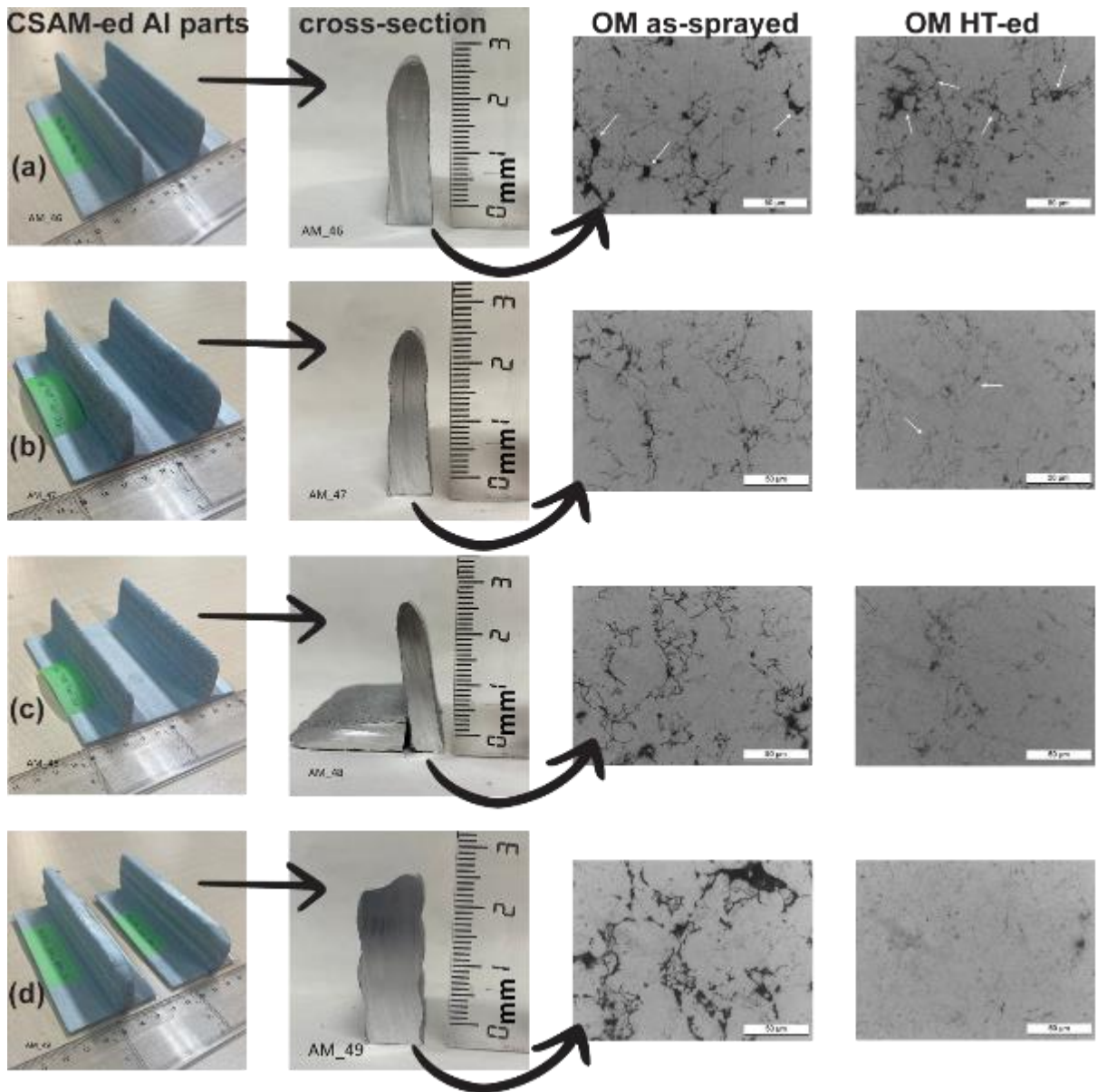


Figure 44: CSAM Metal Knitting Al. Metal Knitting parameters:
 (a) radius 2 mm / angle 20 degrees / pass 1 mm / 4 layers;
 (b) radius 1 mm / angle 20 degrees / pass 1 mm / 3 layers;
 (c) radius 2 mm / angle 20 degrees / pass 2.5 mm / 7 layers;
 (d) radius 2 mm / angle 30 degrees / pass 1 mm / 3 layers.

For the other CSAM-ed Al samples, the porosity was below 10% in the as-sprayed condition, as seen in Figure 45. The HT improved the material density for all samples, with a mean value below 7% for all HT-ed materials. Almost no influence was observed by HT post-processing for the material hardness, as seen in Figure 45. The cohesion of particles was improved by HT, which can be interpreted from the material strength, Ultimate Tensile Stress (UTS), presented in Figure 45. CSAM-ed Metal

Knitting AI in the as-sprayed condition reached the highest value for the Parameter (c) made samples, which had the thinnest layers, between 4 and 5 mm, demanding 7 layers to achieve the designed 30 mm height sample. The literature presents that thin layers promote a higher cohesion of particles and improve the compressive residual stress by a more substantial effect of the peening and densifying mechanisms [83,84].

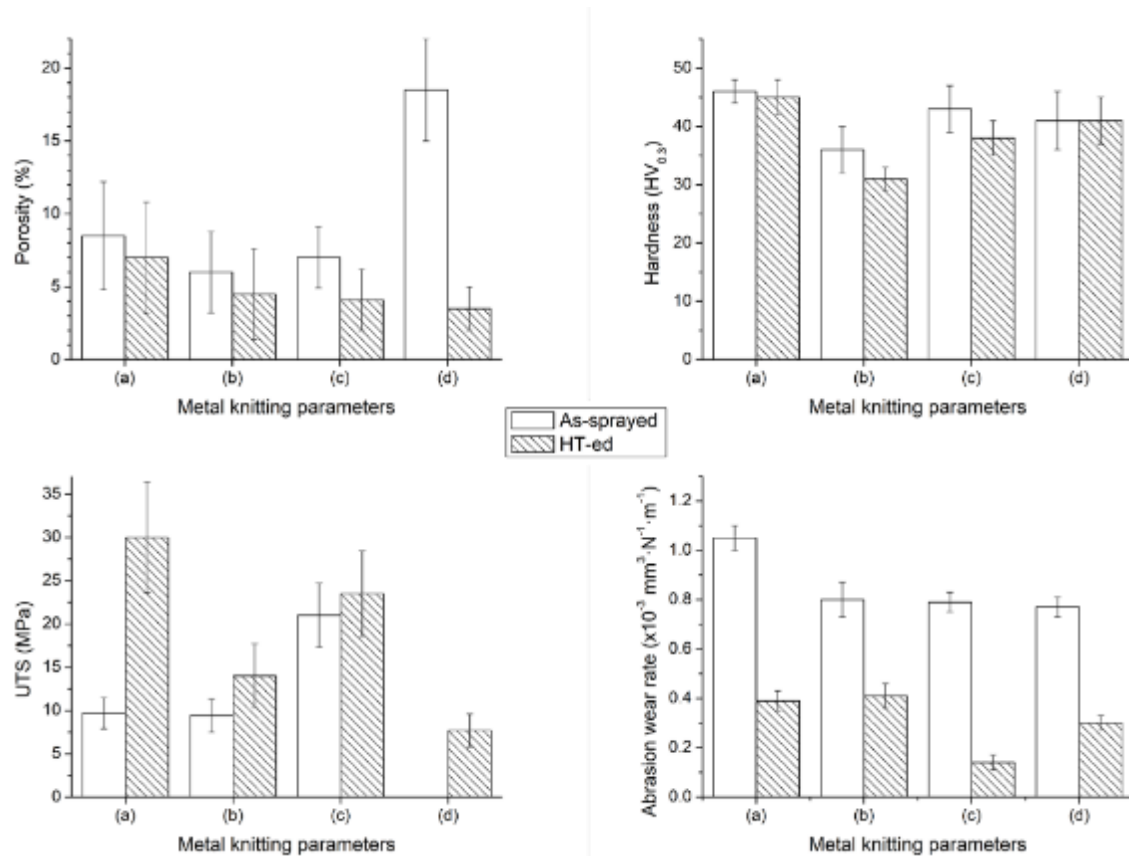


Figure 45: Effect of HT on the CSAM-ed Metal Knitting AI properties. Metal Knitting parameters: (a) radius 2 mm / angle 20 degrees / pass 1 mm / 4 layers; (b) radius 1 mm / angle 20 degrees / pass 1 mm / 3 layers; (c) radius 2 mm / angle 20 degrees / pass 2.5 mm / 7 layers; (d) radius 2 mm / angle 30 degrees / pass 1 mm / 3 layers.

Using an angle of 30 degrees, Parameter (d) resulted in lower particle deformation and cohesion, which impacted the tensile testing. These samples broke or fractured prematurely during the machining or the early testing stages. Figure 45 does not present any value for Parameter (d) as-sprayed since no results were collected. However, HT improved its cohesion of particles and the material strength, resulting in a UTS of 7.7 ± 1.9 MPa. The highest UTS was obtained for Parameter (a) HT-ed, 30.1 ± 6.4 MPa, followed by Parameter (c) HT-ed, 23.5 ± 4.9 MPa.

The fracture mechanism observed on the tensile testing samples changed from the as-sprayed to the HT-ed conditions. For this last one, the rupture occurred partially

by decohesion of the particles with the cracks following the interparticular regions and partially by ductile mechanism, with dimples formed by the plastic deformation of the metallurgically joined regions of the particles, observed in Figure 46. Only the decohesion mechanism was observed in the as-sprayed condition samples, resulting in lower UTS values, as seen in Figure 45.

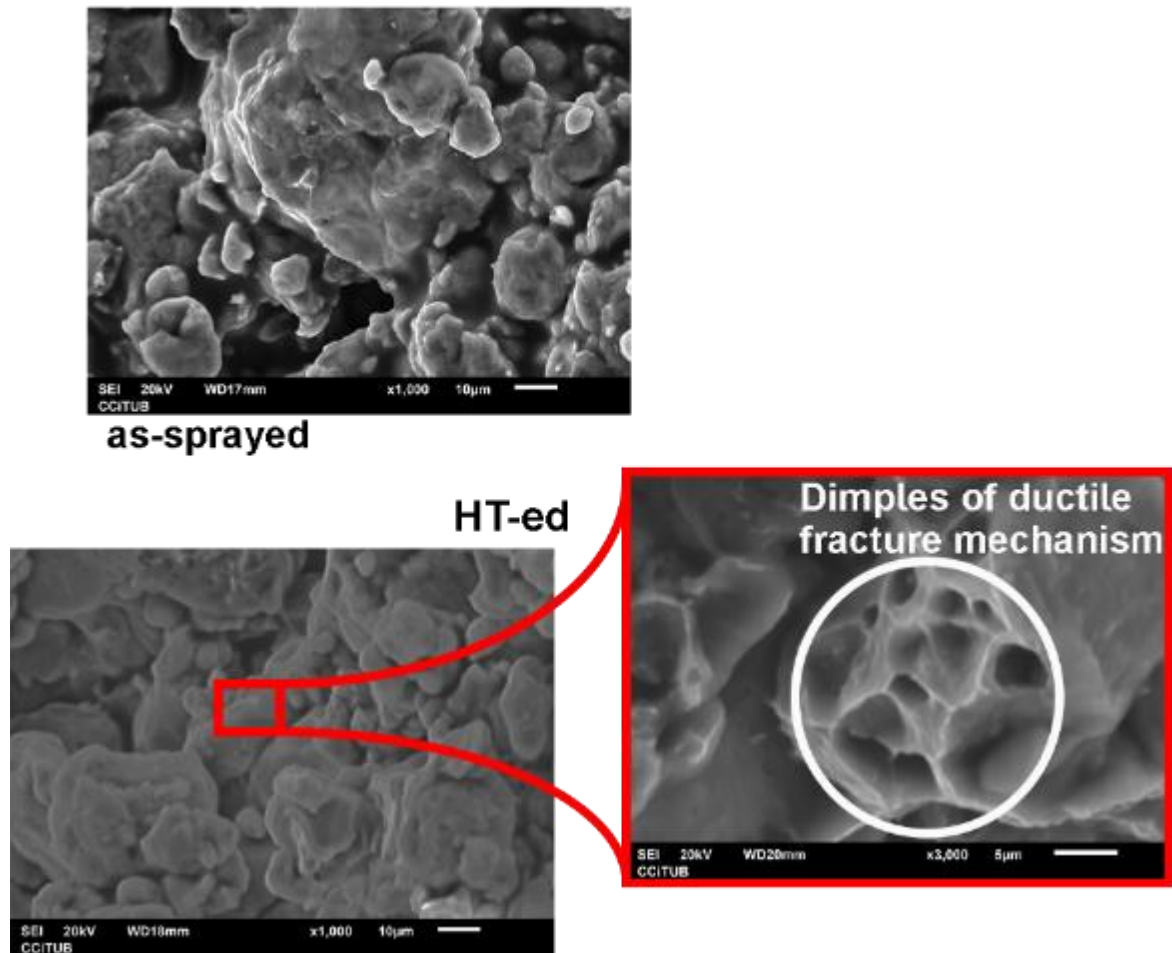


Figure 46: SEM images of the CSAM-ed Metal Knitting Al tensile testing fracture surface.

The abrasion wear following the ASTM G65-16 standard [29] was evaluated for CSAM Metal Knitting Al as-sprayed and HT-ed with the intent to correlate the wear resistance with the cohesion of particles improving. Figure 45 presents the wear rate results. HT affected the abrasion wear resistance, reducing the wear rate for all the CSAM-ed parameters, highlighting the lowest value for the Parameter (c), $1.4 \pm 0.3 \times 10^{-4} \text{ mm}^3 \cdot \text{N}^{-1} \cdot \text{m}^{-1}$. The CSAM-ed Al is not a good solution for wear-resistant applications; however, the improvement in this property presented the influence of the cohesion of particles on the material performance, corroborating with the UTS results. The surface condition should be modified to improve the material wear resistance, as detailed in Article 6, employing HVOF WC hard coatings on CSAM-ed material.

4.3.4.2. Hot Isostatic Pressing

HIP involves subjecting a solid material to high temperature and pressure in an inert gas environment to achieve consolidation, bonding, and improved material properties. While CSAM can provide good adhesion and high density, residual porosity and insufficient particle bonding may remain. HIP has been used as a post-treatment step to address these issues and enhance the quality of the CSAM-ed material [77,85]. HIP results in densification, enhanced bonding, homogenization of microstructure, and stress relief.

HIP post-processing can be developed by two methodologies, pressing within deformable capsules and capsule-free HIP, considering this last one adequate to densify parts with internal closed well-isolated pores [85,86]. For the CSAM-ed Ti6Al4V, this last one was chosen because a previous evaluation of the material microstructure presented isolated porosity and was not open to the surface or connected voids.

For CSAM traditional and Metal Knitting Ti6Al4V samples, HIP minimized the surface and subsurface defects, especially shrinking porosity and improving the cohesion of particles, as seen in Figure 48. Increasing the CSAM-ed material fatigue resistance is of great value because this degradation mechanism is severely affected by defects on the material surface or its surface characteristics. However, Kahlin [87] presented that this material evolution by HIP can be less effective if a rough surface is maintained because excessive roughness acts as stress concentration, drastically reducing the material fatigue life. The intimate interparticular regions were eliminated for both strategies, resulting in a metallurgic union between the particles by atomic diffusion.

For CSAM traditional and Metal Knitting Ti6Al4V, the porosity was not altered from the as-sprayed to HIP-ed conditions, $11\pm 1\%$ to $12\pm 1\%$, and $22\pm 1\%$ to $21\pm 1\%$, for traditional and Metal Knitting made, respectively. This unchanging porosity can result from a gas transport between pores by the interparticular region since the HIP capsule-free method was used for the experiments. Bocanegra-Bernal [86] explains that HIP within deformable capsules, encapsulated, can be applied to prevent this phenomenon, with the gas inside the capsule removed by a vacuum pump before placing the capsule inside the HIP vessel. On the other hand, Chen et al. [77]

presented a low porosity reduction for CSAM-ed Ti6Al4V by using N₂ as working gas, but a fully dense material was obtained by HIP the samples made with He as working gas. It can be attributed to the higher cohesion of particles in as-sprayed condition obtained by the higher $V_{particle}$ reached by using He. The higher bonding prevents the HIP gas flow in the material interparticular region.

The HIP-ed material presented a dark grey color, Figure 47 and Figure 48, which can be attributed to oxidizing at high temperatures. It could result from O impurities in the HIP vessel Ar atmosphere, and its deleterious effect is even more evident for CSAM Metal Knitting, Figure 48, with this oxidizing concentrated in the interlayer region, where the porosity is high. It confirms that HIP could not reduce the porosity for the studied samples or, even worse, retain the O-rich gas in the material, promoting its internal oxidizing. For CSAM traditional Ti6Al4V, the deposition layers' marks became apparent, and some large cracks grew in the interlayer regions, Figure 47.

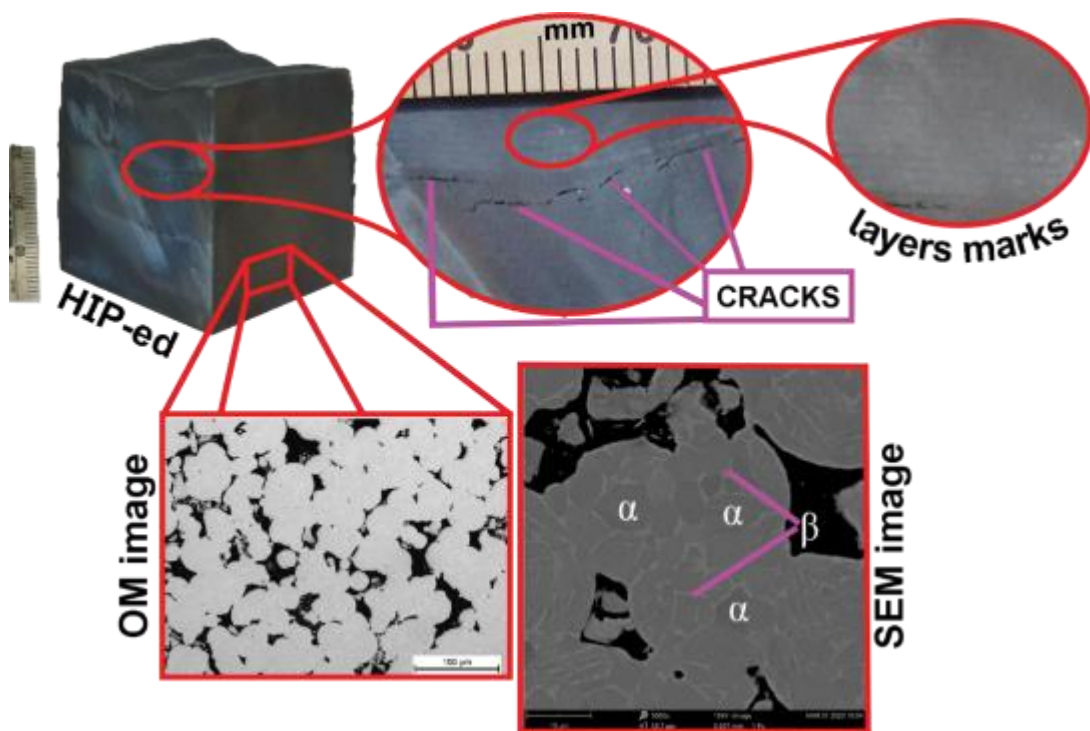


Figure 47: HIP effects on CSAM traditional Ti6Al4V.

These cracks should already exist internally to the material since they were not surface open at the as-sprayed condition, and the external loading imposed by HIP propagated them until the material surface. However, the opposite was expected by applying the isostatic pressing to the material, shrinking porosity and the small cracks. The crack growth direction is expected because the interparticular and especially

interlayer are the weakest regions of the CSAM-ed material due to the lower bonding strength, as discussed in Article 5.

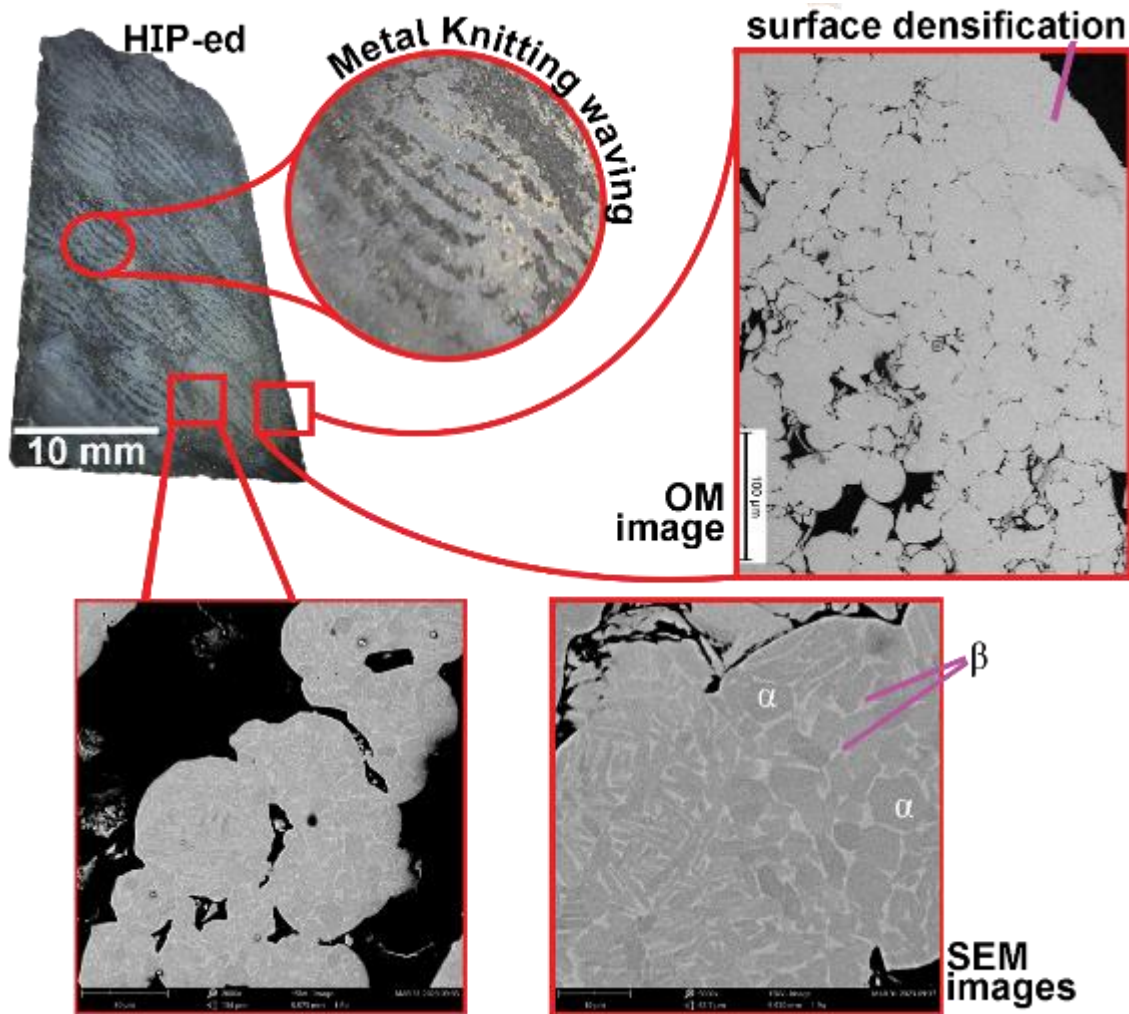


Figure 48: HIP effects on CSAM Metal Knitting Ti6Al4V.

Both CSAM traditional and Metal Knitting Ti6Al4V samples had their hardness slightly reduced by HIP, from 363 ± 22 to 358 ± 10 HV_{0.3} and from 367 ± 25 to 343 ± 27 HV_{0.3}, respectively. It results from the phase transformation and growth of the β phase by atomic diffusion and by dwindling the cold-work effect in the particles' periphery by their plastic deformation during the CS deposition. The β phase became well distributed in the α grains boundaries, as presented in Figure 47 and Figure 48. This phase distribution changes by HIP explains the hardness reduction by the alloy elements diffusion during the high temperature, i.e., β phase concentrates V by its higher solubility in this phase [85], but with a deleterious effect of reducing this element as a solid solution in α phase, impacting negatively in the material hardness. Besides that, any residual hard α' - and α'' -martensite phase regions were transformed to $\alpha + \beta$ phase structure, contributing to the hardness decreasing.

4.3.4.3. Spark Plasma Sintering

Spark Plasma Sintering (SPS) is a technique that consolidates and densifies materials, particularly ceramics, metals, and composites, into solid components with enhanced properties. It involves the application of a high electrical current and pressure to the material, enabling rapid sintering at relatively low temperatures compared to conventional sintering methods. The SPS principles are heating the material by the Joule effect, employing pulsed current, and submitting the material to a high uniaxial pressure [88]. Figure 49 presents an SPS scheme and the sintering mechanisms, heating by plasma discharge between the adjacent particles, and Joule effects after a metallurgic union.

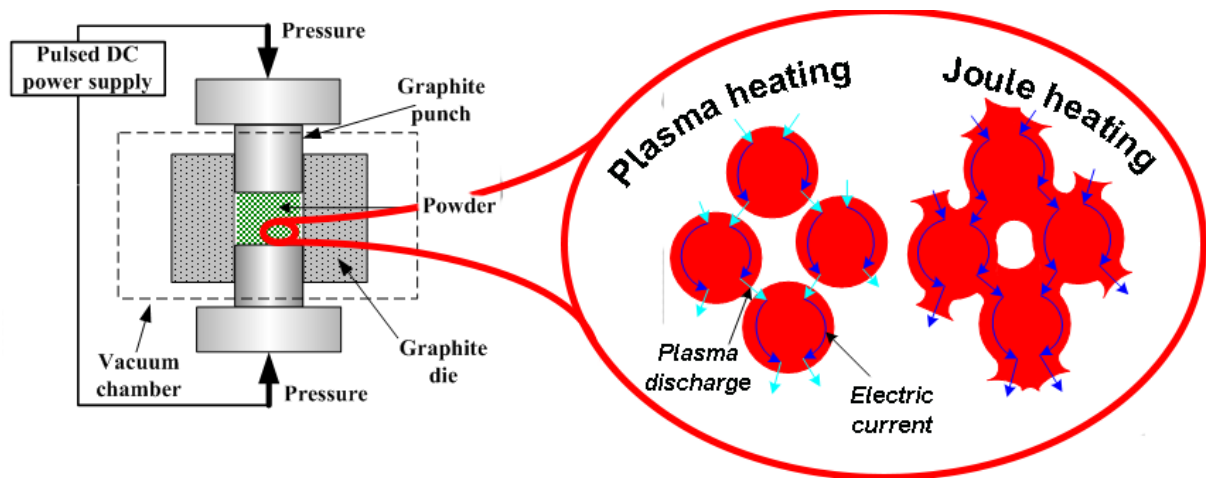


Figure 49: SPS scheme and sintering mechanisms.

Adapted from http://www.substech.com/dokuwiki/doku.php?id=spark_plasma_sintering&s=sps.

Typically, CSAM-ed Ti6Al4V has low deformed particles, and the SPS post-processing was applied to densify the consolidated material. Using the CSAM traditional strategy resulted in lower porosity in as-sprayed condition than the CSAM Metal Knitting strategy, 12 ± 1 and $22\pm 1\%$, respectively. The higher porosity of this last strategy was previously discussed in Article 5, correlating the porosity with the V_{impact} . CSAM traditional and Metal Knitting Ti6Al4V were SPS-ed, resulting in a drastic geometry change, as seen in Figure 50, which results from the pressure of 40 MPa imposed on the material under high temperatures and a short time, 10 min. The selected temperatures were 650 and 800 °C, which are below the β phase transformation, close to 950 °C, keeping the Ti alloy in the α field and preventing a rapid grain growth above the α - β transition [89]. This effect of rapid grain growth was

reported by Weston et al. [88], applying SPS above 950 °C, who obtained a fully dense gas atomized Ti6Al4V using SPS at 1200 °C and 35 MPa for 30 min.

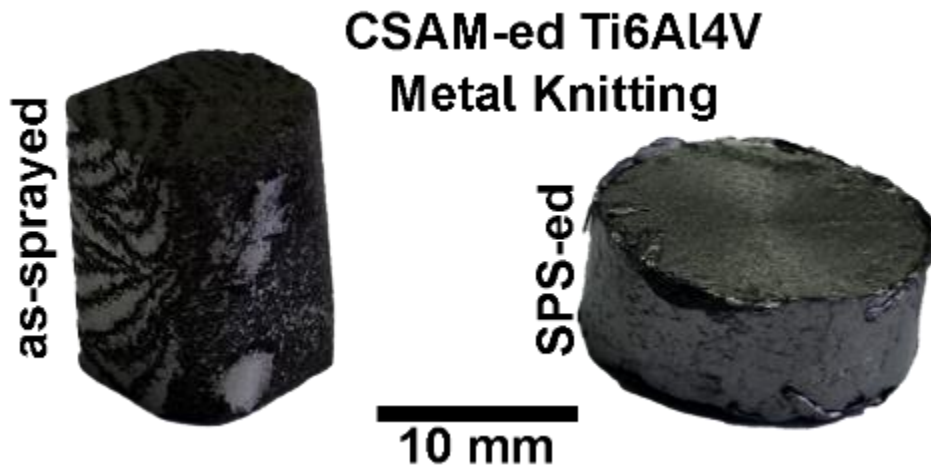


Figure 50: CSAM Metal Knitting Ti6Al4V sample. Before and after SPS.

This severe volume reduction is a limitation in using SPS for CSAM-ed parts because one of the most attractive characteristics of this process is to make near-net-shape parts, requiring minimum machining post-processing. However, for applications that require a very dense material, an exceeding CSAM-ed volume can be achieved for the SPS-ed near-net-shape geometry. Another limitation in this post-processing is that the final shape has to be symmetrical, e.g., cylindrical, for this experiment, because the punches move axially during the pressing, differently to HIP, where the pressing is not mechanical but by a high-pressure gas surrounding the material.

For CSAM Metal Knitting Ti6Al4V SPS-ed at 650 °C, the intimate interparticular region had a metallurgical bonding by the Joule heating effect, promoting the atomic diffusion even for a short heating time, 10 min. However, the particles had not enough plasticity to suppress the large porous, which occurred by employing a higher SPS temperature, 800 °C, densifying the material with some remaining isolated voids, as seen in Figure 52. Besides the densification, the β phase content increased by this higher temperature, growing by diffusion in the α grain boundaries. The SPS improved the material density for both strategies, and the higher SPS temperature clearly reduced the porosity, as presented in Table 7.

Table 7: Effect of SPS on the CSAM-ed Ti6Al4V hardness and porosity.

Processing	Condition	Hardness [HV _{0.3}]	Porosity [%]
CSAM traditional Ti6Al4V	As-sprayed	319±19	12±1
	SPS-ed 650 °C, 40 MPa, 10 min	346±18	<1
	SPS-ed 800 °C, 40 MPa, 10 min	378±8	<1
CSAM Metal Knitting Ti6Al4V	As-sprayed	367±25	22±1
	SPS-ed 650 °C, 40 MPa, 10 min	360±21	19±1
	SPS-ed 800 °C, 40 MPa, 10 min	388±26	2±1

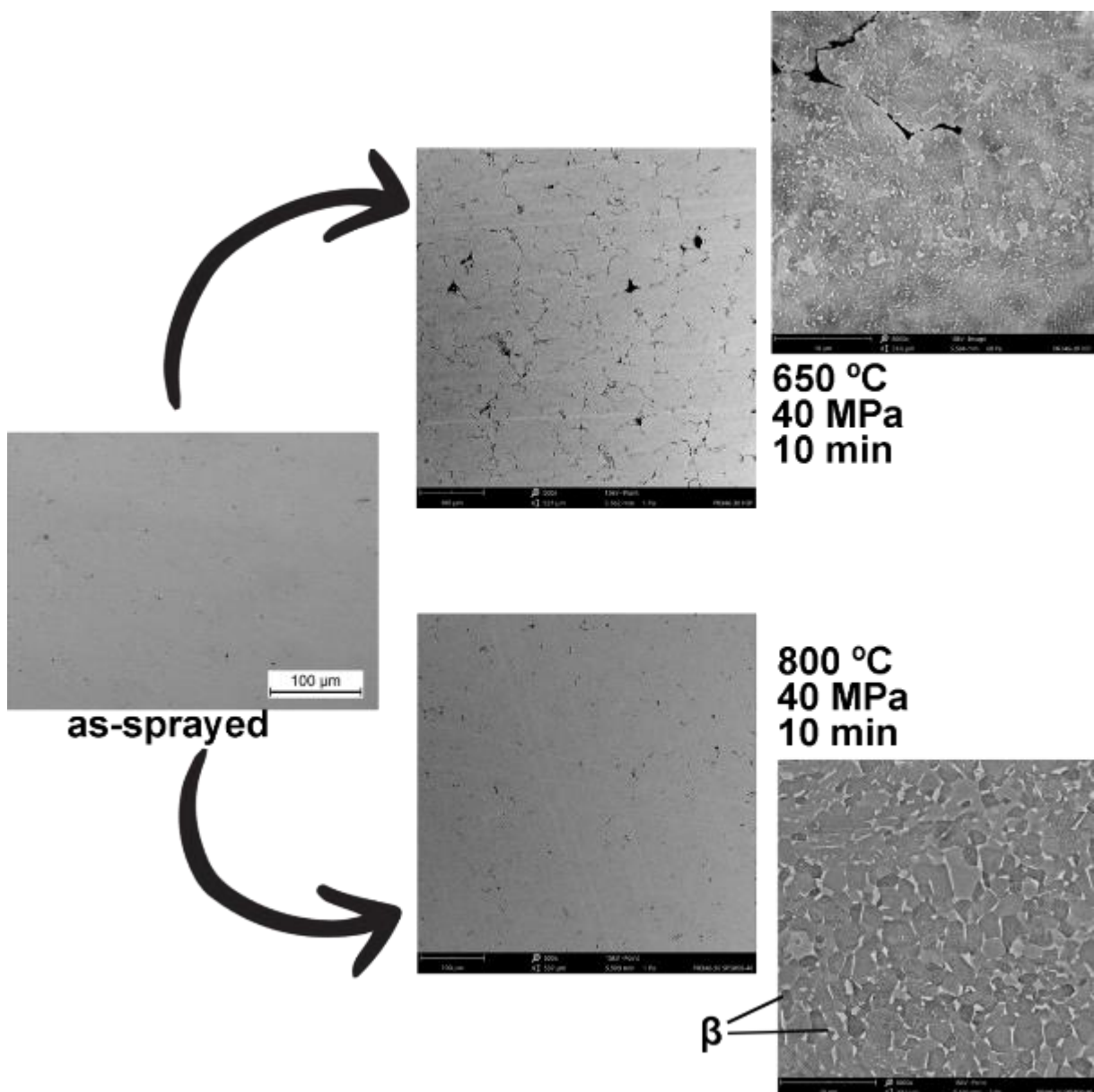


Figure 51: Effect of SPS on the microstructure evolution of CSAM traditional Ti6Al4V sample.

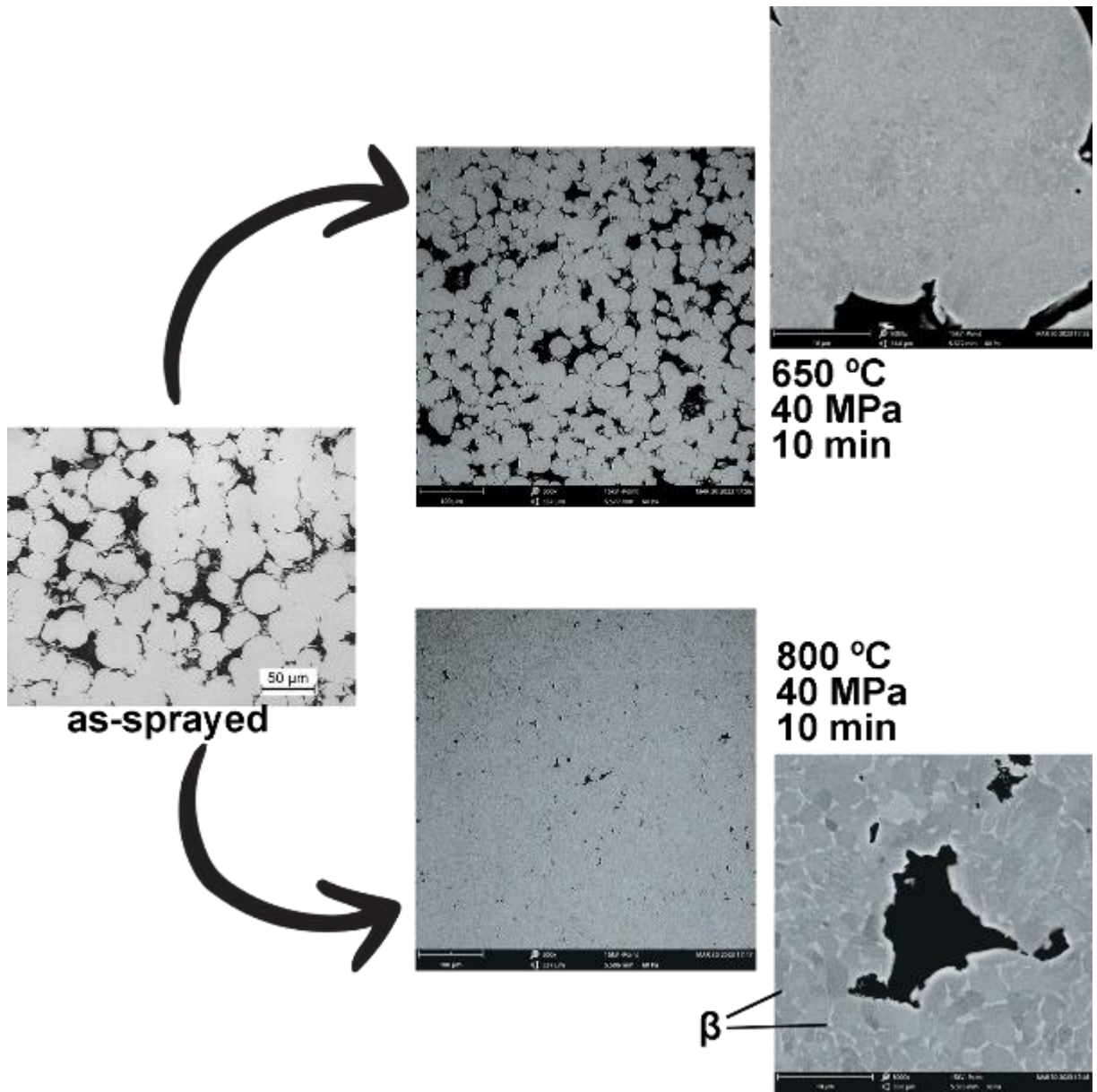


Figure 52: Effect of SPS on the microstructure evolution of CSAM Metal Knitting Ti6Al4V sample.

4.4. Hybrid Thermal Spray System for AM

4.4.1. HVOF Feedstock Powders Characterization

HVOF deposition was used as a post-processing for CSAM-ed Maraging, as presented in Article 6; however, this paper did not show in detail the feedstock powder characterization, which is presented below. For HVOF depositions, WC-10Co4Cr and WC-12Co were selected due to their high industrial usage as wear-resistant coatings. WC-10Co4Cr has been presented in the literature as an alternative to the second one with the benefit of preventing decarburization while improving the matrix binding. Considering that during the thermal spraying processes of hard metals, the WC suffers decarburization and oxidation, reacting inconveniently to form di-tungsten carbide (W_2C), metallic tungsten (W), and oxy carbides [90–92]. The powders' shapes are near-spherical, typical of agglomerated sintered powders, with the WC hard particles embedded in the Co or Co-Cr binder and without apparent aggregation between the powders, presented in Figure 53.

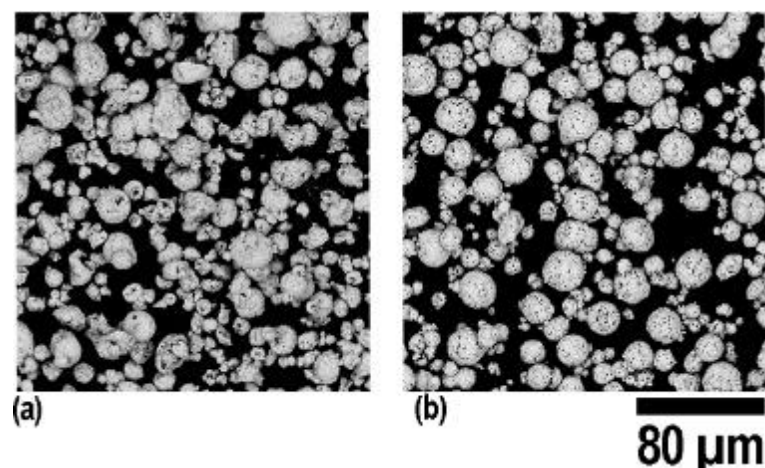


Figure 53: SEM images HVOF feedstock powders of free surface. (a) WC-10Co4Cr, (b) WC-12Co.

Both WC- powders showed a homogeneous distribution, as expected for commercial feedstock materials, which has been optimized for a long time by scholars and manufacturers for the best sprayability and performance. It is in consonant with the results presented in the literature [90–94]. Notwithstanding some works showing that the carbide size matters for the HVOF-ed coating instead of the particle size [95,96], the particle size and spraying parameters enormously impact the coating characteristics and quality. Bigger and heavier particles need more energy to reach high kinetic energy, but small particles are more exposed to overheating or decarburization. Comparing WC-12Co and WC-10Co4Cr, no relevant differences were

observed between the two WC powders evaluated, as seen in Figure 54, which are in the ideal range for HVOF spraying.

Table 8 shows the WC powders' apparent densities and free-flowing flowability, this last one is less important for HVOF feeding, since the gun receives the powder dragged by a feeding gas, N₂ in this work, and a bad free-flowing characteristic of the powder is compensated by this pressurized feeding system. The WC apparent densities presented in Table 8 are in the range presented by the literature [97,98]. This feedstock powder property is important to understand and preview the porosity in the coating microstructure, mainly in processes that apply low kinetic energy, e.g., filling a powder bed for SLS or SLM AM process. However, HVOF produces typically dense coatings by deforming the partially melted particles impacting the substrate with high velocity [99].

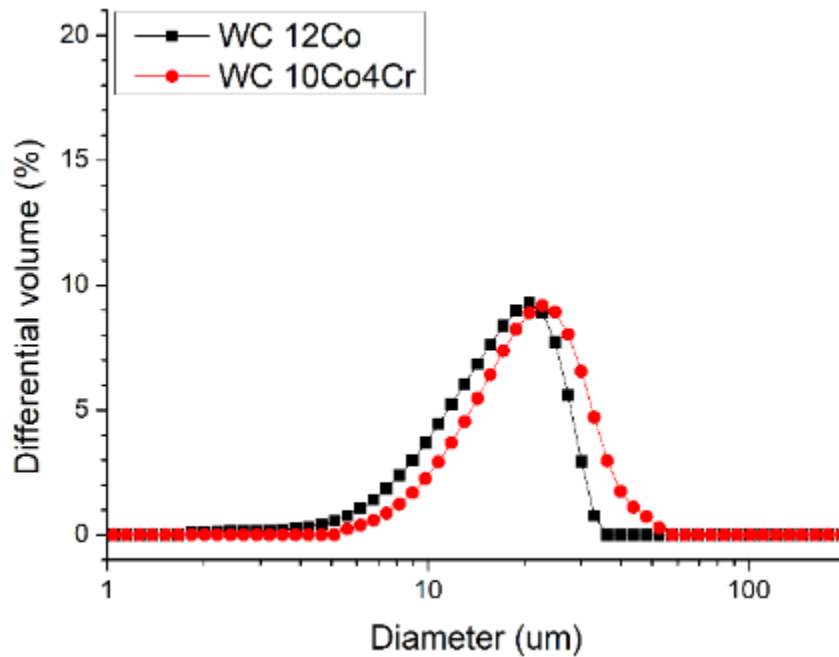


Figure 54: HVOF feedstock powders' particle size distribution.

Table 8: HVOF feedstock powders' characteristics.

Material	Particle Size Distribution [µm]		Shape	Apparent Density [g·cm ⁻³]	Flow Rate [g·s ⁻¹]
	d ₁₀	d ₉₀			
WC-10Co4Cr	11	34	Spherical	1.76 ± 0.02	3.91 ± 0.23
WC-12Co	9	27	Spherical	2.18 ± 0.01	¹

¹ did not flow.

The XRD patterns of WC- feedstock powders were almost identical, consisting of WC and minor Co phases, as presented in Figure 55. Although the literature has reported the generation of other phases during powder preparation, W_2C , Co_3W_3C , and Co_6W_6C , because of the oxidation and dissolution of WC in the Co binder [92,93,100], it was not observed in the characterized WC- feedstock powders. It qualifies the WC-12Co and WC-10Co4Cr for good performance as HVOF wear-resistant coatings, emphasizing that selecting HVOF parameters can drastically affect this initial condition, decarburizing during the deposition process.

HVOF WC coatings have been widely used in industry; however, inadequate HVOF parameters or powder selection can result in material degradation during the deposition and, consequently, a coating with lower properties than expected, such as hardness and wear resistance. The parameters presented in Article 6 are optimized by the CPT's group, which has worked with hard coatings for several years.

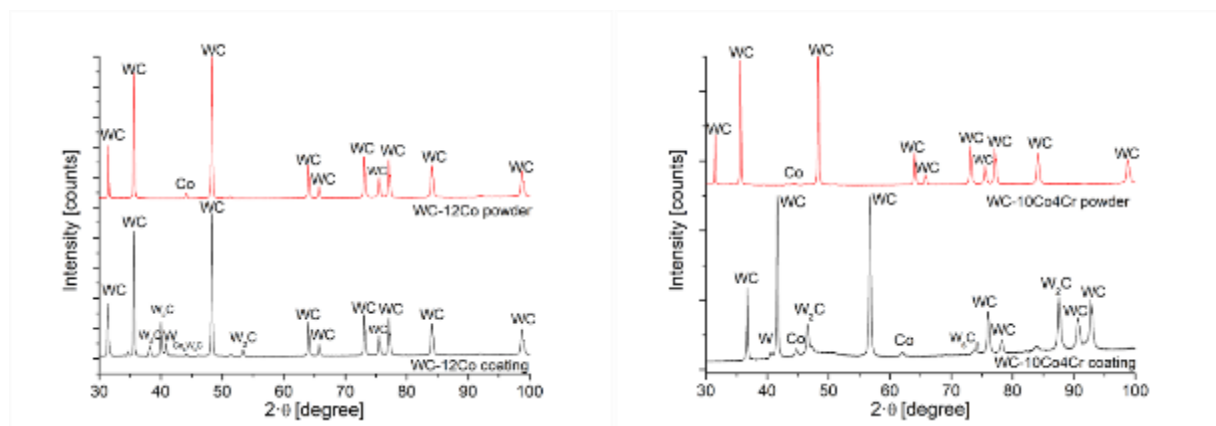


Figure 55: XRD patterns of the HVOF WC-12Co and WC-10Co4Cr coatings and feedstock powders.

Decarburizing refers to removing or reducing C from the WC particles during the coating process by forming low-resistant carbides or oxidizing, W_2C metallic W or oxycarbides due to the high temperatures to which the particles are exposed during the deposition. The literature presents that changing the binder from pure Co to Co-Cr helps to mitigate this decarburizing [101]. Another strategy is using high-velocity processes with lower flame temperature, as presented by Grafias et al. [90], i.e., High-Velocity Air-Fuel (HVOF). In this hot environment, the mechanism of decarburizing starts melting the metallic binder, Co or Co-Cr, which have a much lower melting point than WC. Afterward, the WC grains dissolve in the molten metal, and C is released by its reaction with the O from the environment. After the impact with the substrate, the

particles are rapidly quenched, and the dissolved supersaturated WC grains result in W_2C , W_6C_2 , and Co-containing phases [90,102].

XRD was used to identify the phase composition of the WC coatings, which were compared with their respective powder's XRD diffractograms. Figure 55 presents this comparison between powder and as-sprayed WC-12Co and WC-10Co4Cr coatings. The presence of W_2C and W metallic in as-sprayed condition was not evidenced in powder condition before the HVOF deposition. This decarburizing did not affect the performance of the coatings, which can be interpreted from the coatings' microstructural characterization, corrosion, and wear testing results presented in Article 6. The objective of using HVOF WC- coatings was to improve the wear and corrosion resistance of a CSAM-ed Maraging, a thermal spraying hybrid system, which was successfully achieved.



**ARTICLE 6 “IMPROVING THE WEAR AND CORROSION RESISTANCE OF
MARAGING PART OBTAINED BY COLD GAS SPRAY ADDITIVE
MANUFACTURING”**

R.F. Váz, A. Silvello, V. Albaladejo, J. Sanchez, I.G. Cano



[10.3390/met11071092](https://doi.org/10.3390/met11071092)

This work presents the use of CSAM to produce Maraging parts, representing a gain for the industry by saving machining time and preventing raw material waste. Maraging is a class of hard materials, and deposit successfully it is a challenge for scholar that study CS. This paper shows that an adequate selection of parameters and spraying conditions makes possible the use of CSAM to make Maraging parts.

Another contribution is depositing WC hard coatings by HVOF on CSAM-ed Maraging, improving its wear resistance and corrosion behavior even more. This work presents the feasibility of applying post-treatments on CSAM-ed material, in this case, another thermal spraying process to obtain a fast 3D printed part with good wear resistance.

Improving the Wear and Corrosion Resistance of Maraging Part Obtained by Cold Gas Spray Additive Manufacturing

Rodolpho F. Vaz, Alessio Silvello *, Vicente Albaladejo, Javier Sanchez and Irene García Cano

Thermal Spray Center CPT, University of Barcelona. Martí i Franqués 1, 7a Planta, 08028 Barcelona, Spain; rvaz@cptub.eu (R.F.V.); valbaladejo@cptub.eu (V.A.); jsanchez@cptub.eu (J.S.); igcano@cptub.eu (I.G.C.)

* Correspondence: asilvello@cptub.eu

Abstract: The use of the cold gas spray (CGS) process as a metal additive manufacturing (MAM) technique for metallic part production has been deeply studied recently, mainly due to its advantages over other MAM techniques. CGS MAM is a high-productivity technique with a very low level of particle oxidation, microstructural changes, phase transformations, or deleterious residual thermal stresses in the part. The use of CGS MAM to produce maraging parts represents a gain for the industry by saving machining time and preventing raw material waste. Its wear resistance and corrosion behavior were evaluated in this work and were compared with cermet coatings deposited by high-velocity oxy-fuel (HVOF) on the CGS MAM maraging. This work presents the innovative and effective combination of different thermal spraying processes and materials to obtain MAM maraging parts with higher wear resistance, evaluating abrasion, sliding, and water erosion wear types.

Keywords: cold gas spray; metal additive manufacturing; maraging; wear; corrosion

Citation: Vaz, R.F.; Silvello, A.; Albaladejo, V.; Sanchez, J.; Cano, I.G. Improving the Wear and Corrosion Resistance of Maraging Part Obtained by Cold Gas Spray Additive Manufacturing. *Metals* **2021**, *11*, 1092. <https://doi.org/10.3390/met11071092>

Academic Editor: Eric Hug

Received: 27 May 2021

Accepted: 6 July 2021

Published: 8 July 2021

Publisher's Note: MDPI stays neutral with regard to jurisdictional claims in published maps and institutional affiliations.



Copyright: © 2021 by the authors. Licensee MDPI, Basel, Switzerland. This article is an open access article distributed under the terms and conditions of the Creative Commons Attribution (CC BY) license (<http://creativecommons.org/licenses/by/4.0/>).

1. Introduction

Metal additive manufacturing (MAM) as a category encompasses a series of processes to produce components layer-by-layer as an alternative to the conventional methods, such as machining, rolling, or stamping, or formative methods such as injection molding. MAM's main advantages are the possibility of producing parts with complex geometries and added functionalities, avoiding material waste, and the savings coming from a distributed production and less stock required, among others. The MAM technology has drawn much attention and has been the focus of many publications regarding the different techniques, such as powder bed fusion (PBF), binder jetting, metal material extrusion, and direct energy deposition processes (e.g., laser, electron beam, and welding processes) [1–5]. An alternative for MAM freeform part production is the cold gas spray (CGS) thermal spray process, which operates by accelerating powder particles by a supersonic gas jet, under the material melting point, preventing severe oxidation, microstructural changes, phase transformations, and thermal stresses typical in high-temperature fabrication processes [6–8]. CGS also produces parts with very high density, due to the very high velocity and consequently kinetic energy imposed on the particles, deforming them at the impact and consolidating the MAM part. A high productivity is also an advantage of CGS over other MAM technologies [8–11]. The particles' energy at the impact on the substrate can break the thin oxide film on the substrate surface, promoting the intimate contact with the fresh metal surface, which can lead to a strong metallurgical bonding, the adiabatic shear instability (ASI) [12–14].

Regarding the materials applied by CGS MAM, the literature reports the production of Cu alloys, Al alloys, Ti alloys, Ni alloys, and steel parts [6,7,9–11,15,16]. Recently, researchers have devoted efforts to CGS maraging, which is a material with a good combination between high strength, toughness, and ductility, working well in a harsh

environment [17,18]. Maraging steels' have been heat treated to create a martensitic microstructure responsible for their properties. This microstructure stabilizes Ni-rich intermetallic compounds, including Ni₃Ti, Ni₃Al, NiAl, and NiMn [19]. The maraging steel is applied in different sectors, such as automotive, military, medical, and aeronautics, and a special application is the fabrication of molds for plastic injection [18,20]. Traditionally, maraging is produced by melting [18] and machining to obtain a part; however, for MAM parts, the PBF (Powders Bed Fusion) processes are the most common processes used [21–24]. As an innovative technique, the CGS MAM has been studied to produce maraging parts, and it has been the focus of recent publications reporting the microstructure and properties of as-sprayed and solution-aged samples [19]. Other work presented the addition of WC in maraging feedstock powder to obtain high-performance metal matrix composites (MMCs) by CGS [20]. The maraging obtained by melting processes presented high hardness and good wear resistance, with 650 HV, coefficient of friction (CoF) under 0.1 in pin-on-disk testing, and wear rate under $5.0 \times 10^{-4} \text{ mm}^3 \cdot \text{m}^{-1}$ [25]. However, there is no information available in the literature about the wear and corrosion behavior of CGS MAM maraging, and this work evaluates this material under different types of wear.

The demand for improvement of wear and/or corrosion resistance in CGS MAM maraging parts motivated the study of the deposition of wear resistant coatings on maraging. The use of cermet coatings is a widely accepted choice to improve the wear resistance of metallic parts [26–31]. The literature reports, in general, an excellent wear performance of cermets thermally sprayed by high-velocity oxy-fuel (HVOF), due to their high hardness, around 1000 HV [27], which results in a low volume loss rate in abrasion test, below $2.0 \times 10^{-5} \text{ mm}^3 \cdot \text{N} \cdot \text{m}^{-1}$ [28]. Nevertheless, the deposition of cermets by HVOF on CGS MAM maraging has not been explored and is not present in the literature yet. This work contributes to understanding the viability of this procedure, which is useful to design new MAM maraging components.

This work aimed to evaluate the performance of CGS MAM maraging under different wear conditions and compare it with the performance of cermets HVOF sprayed on this maraging. To meet this objective, the authors evaluated the materials' microstructure; measured their hardness; and performed abrasion, sliding, jet erosion, and corrosion testing.

2. Materials and Methods

2.1. Materials

The substrate chosen was low carbon steel in the shape of plates (S235JR type, $50 \times 20 \times 5 \text{ mm}$) previously grit-blasted to a minimum roughness $R_a 6 \mu\text{m}$ and $R_y 40 \mu\text{m}$, coated sequentially with the materials Dycomet 1008 (Akkum, Netherlands), maraging (Rovalma, Barcelona, Spain), and WC-12Co (Oerlikon WOKA 3110, Westbury, NY, USA) or WC-10Co4Cr (Fujimi, Kiyosu, Japan). To characterize the feedstock powders, the particle size distribution was obtained by laser scattering (LS) technique in an LS 13 320 (Beckman Coulter, Brea, CA, USA) equipment, following the ASTM B822-02 [32] standard. The images of the powders were obtained by scanning electron microscopy using a Pro Desktop scanning electron microscope (SEM) (Thermo Fisher Phenom, Eindhoven, Netherlands) with back-scattered electron (BSE) mode and accelerating voltage 15 kV. This equipment was also used to measure the powders' chemical composition by energy-dispersive X-ray spectroscopy (EDS) on their polished cross-sections.

2.2. Thermal Spray Deposition

For the maraging and Dycomet 1008 powders, the CGS equipment used was a PCS 100 (Plasma Giken, Saitama, Japan), using N₂ as working gas, while for deposition of carbide powders, the HVOF equipment DJH2600 (Sulzer Metco, Westbury, NY, USA) was

used. The spraying parameters for maraging and Dycomet 1008 were the same, as well as for both WC powders, as presented in Table 1. The deposition efficiency of the material with the focus in MAM, the maraging, was measured following the ISO 17836:2004(E) [33] standard, using its recommendations for plate sample, but in a smaller sample than that indicated in this standard.

Table 1. Spraying parameters. CGS: cold gas spray. HVOF: high-velocity oxy-fuel.

Parameter	CGS	HVOF
N ₂ Pressure (MPa)	7.0	/
N ₂ Temperature (°C)	975	/
H ₂ Pressure (MPa)	/	1.0
O ₂ Temperature (MPa)	/	1.2
Standoff Distance (mm)	25	225
Powder Feeding (g·s ⁻¹)	0.43	0.50
Robot Speed (m·s ⁻¹)	0.5	0.5
Layers	4	10

2.3. Coating Characterization

The metallographic preparation of the coating cross-sections was carried out following the ASTM E1920-03 [34] and ASTM E3-01 [35] standards. The maraging was etched by aqua regia solution for 3 min to reveal its microstructure. A DMI5000M (Leica, Wetzlar, Germany) microscope was used for the optical microscopy (OM) and coating thickness measurement, following the ASTM B487-85 [36] standard, as an average of ten thickness values. The SEM images were obtained in a Pro Desktop SEM (Thermo Fisher Phenom, Eindhoven, Netherlands), which was also used for the energy-dispersive X-ray (EDS) analysis. The coatings' porosity was analyzed with the software ImageJ version 1.50i using 10 OM images at 200× magnification, according to ASTM E2109-01 [37] standard.

Microhardness of coatings was measured by means of an HMV (Shimadzu, Tokyo, Japan), following the ASTM E384-99 [38] standard, applying a load of 300 gf (HV_{0.3}) for 15 s. The result is an average value of ten measures. The adherence of the maraging coating on the carbon steel substrate and on the Dycomet 1008 layer was assessed using the ASTM C633-13 [39] standard.

2.4. Wear Testing

The coatings were tested in abrasive conditions by means of the rubber wheel testing method, ASTM G65-00 [40] standard, which was performed with the OL-2000 (CM4, Cervello, Spain) equipment at a velocity of 139 rpm, a load of 125 N, a 226 mm diameter rubber wheel, and Ottawa silica sand as the abrasive agent (Sibelco, Barcelona, Spain). The mass of the sample was measured on an AE100 scale (Mettler, Columbus, OH, USA) at specific testing elapsed times, and the results of mass loss were converted into volume loss, considering the density of each material, which was obtained after their type evaluation, considering the known bulk material density less the measured porosity.

For the analysis of the sliding wear resistance of the coatings, ball-on-disk tests were carried out, following the ASTM G99-04 [41] standard. For this test, the sample testing surfaces were previously prepared by grinding and polishing to the maximum roughness R_a 0.8 µm. The tests were performed at room temperature (27 ± 2 °C) and maximum 20% moisture in dry conditions, using a WC-Co ball (diameter 11 mm), with a sliding rate of 0.13 m·s⁻¹ for a total sliding distance of 995 m. During the test, the CoF between the surfaces was recorded and plotted for the load of 15 N with the acquisition rate of 1 value per lap, with a total of 22,737 CoF values. The wear volume loss of the ball-on-disk samples was calculated by Equation (1), as recommended by the ASTM G99-04 [41] standard, where R is the wear track radius, d is the wear track width, and r is the ball

radius. The friction wear rate is calculated by dividing the disk volume loss by the load, times the sliding distance.

$$\text{Disk Volume Loss} = 2\pi R \left[r^2 \sin^{-1} \left(\frac{d}{2r} \right) - \left(\frac{d}{4} \right) (4r^2 - d^2)^{1/2} \right] \quad (1)$$

In addition, the jet erosion tests, ASTM G73-10 [42], were carried out. In jet erosion, a sample is abraded by repeated impacts of water jets until the degradation/destruction of the coating. The unique jet erosion apparatus (Figure 1a) (CM4, Cervello, Spain) in CPT (Centro de Proyección Térmica) facilities consists of two water jets and a central rotating arm (Figure 1b), which can reach high rotation speed. At the end of the arm, a sample holder keeps the sample parallel to the water jets. The water jet diameter is 4 mm and the process parameters are the water pressure (from 0.01 to 0.2 MPa), rotation speed (from 14 up to 100 m·s⁻¹), and test time. The experiments were carried out at 53 m·s⁻¹, with the pressure of water at 0.1 MPa, controlling the sample every 30 or 60 min to measure the weight loss and the aspects of the damaged area. The test was repeated three times for each sample and the erosion rate was measured, following the ASTM G73-10 [42] standard, plotting the mass loss slopes.

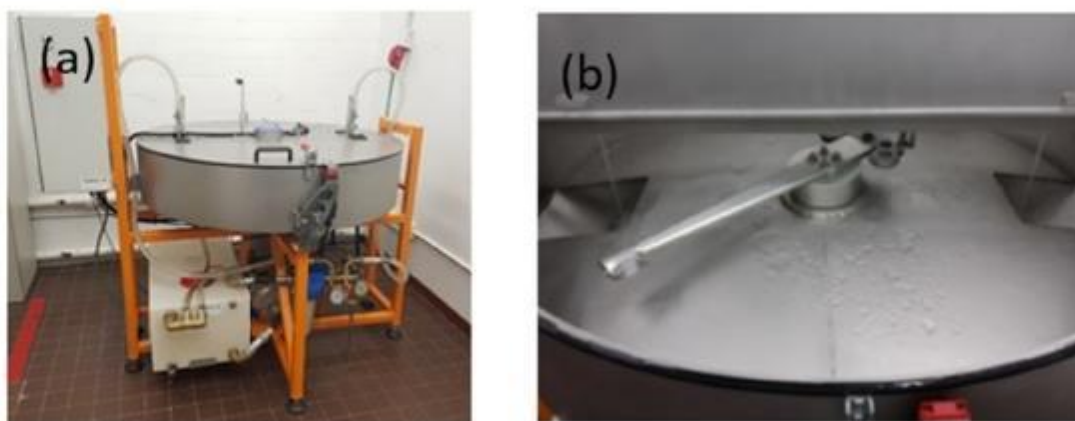


Figure 1. (a) Jet erosion equipment; (b) Detail of the rotating arm, where the sample is fixed.

To benchmark the wear behavior of CGS and HVOF coatings, the behavior of 316L and carbon steel bulk materials was also evaluated carrying out rubber wheel, ball-on-disk, and jet erosion tests.

2.5. Corrosion Testing

Potentiodynamic polarization measurements were carried out, following the ASTM G59-97 [43] and ASTM G102-89 [44] standards, to determine the corrosion resistance of the coatings in 3.5 wt.% NaCl water solution. Two different areas of each sample were used for corrosion tests as working electrode, with an exposed area of 1.0 cm², which were previously polished up to the maximum roughness R_a 0.3 μm. A saturated calomel (3.0 M KCl) was the reference electrode and platinum was the counter electrode in the tests. A scan rate of 0.05 mV·s⁻¹ and a potential range of ±25 mV with respect to E_{ocp} were used to acquire the polarization resistance (R_p), and a potential range from −250 to 1050 mV with respect to E_{ocp} was used to acquire the polarization curves with a VSP (Biologic Science Instruments, Seyssinet-Pariset, France). The corrosion potential (E_{corr}) and corrosion current (I_{corr}) were calculated with the software EC-Lab V10.44. E_{corr} was obtained from a Tafel fit extrapolation, while I_{corr} was calculated according to the Stern–Geary equation (Equation (2)), where β_a and β_c are the anodic and cathodic currents, respectively, and R_p is the polarization resistance.

$$I_{\text{corr}} = \frac{(\beta_a \cdot \beta_c)}{2.303 \cdot (\beta_a + \beta_c) \cdot R_p} \quad (2)$$

To benchmark the corrosion behavior of CGS and HVOF coatings, the behavior of 316L and carbon steel bulk materials was also evaluated.

3. Results and Discussion

The results are presented comparing the characteristics and performance in testing of the different coatings and reference bulks, with pertinent discussions about these results.

3.1. Characterization of Powders

The micrographs of feedstock powders are presented in Figure 2, indicating a higher spheroidicity for the Dycomet 1008 powder than for the maraging one and an identical shape for the carbides. The Dycomet 1008 and maraging chemical compositions are presented in Table 2, and their particle size distributions are shown in Figure 3, from where it can be seen that the maraging particles are slightly larger than the Dycomet 1008 particles and that the distribution curves for the carbides WC-12Co and WC-10Co4Cr are very similar.

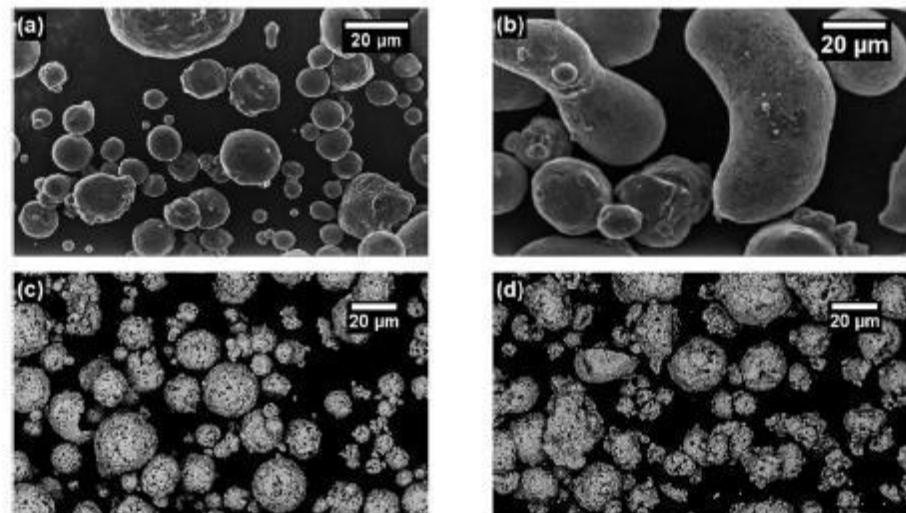


Figure 2. SEM (scanning electron microscope) images of feedstock powders. (a) Maraging, (b) Dycomet 1008, (c) WC-12Co, (d) WC-10Co4Cr.

Table 2. CGS feedstock material chemical compositions.

Powder	Nominal Composition (wt.%)							
	Cr	Ni	Mo	Mn	Co	Ti	Al	Fe
Dycomet 1008	17.8	4.9	14.7	2.7	-	-	-	Bal.
Maraging	7.5	11.4	3.3	1.6	3.9	1.8	1.1	Bal.

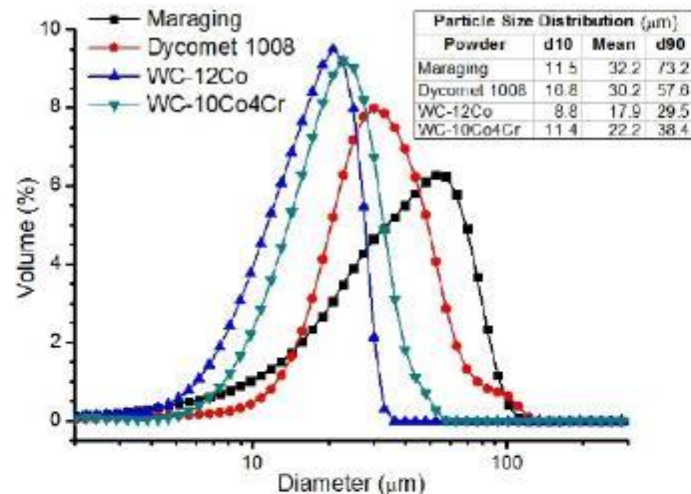


Figure 3. Feedstock powder particle size distributions.

3.2. Characterization of Coatings

The images of coatings' cross-sections are presented in Figure 4, where it is possible to observe that the particles deformed due to their impact at high velocity in CGS MAM maraging, resulting in a dense material, which was revealed by the etching (Figure 4a). The periphery of the maraging particles had severe grain deformation, while the center of the particles remained with an equiaxial microstructure, which is typical for CGS sprayed layers [16]. The porosity was calculated as a mean of 10 image analyses, and Figure 4 does not represent this average porosity value, which is indicated in Table 3. The average value of hardness of as-sprayed maraging was 378 HV_{0.3}, and a gradient of hardness value was not observed from the material closer to the substrate to the region closer to the WC coating. The maraging deposition efficiency was 75%. The interface between the CGS sprayed maraging and the HVOF cermet is presented in Figure 4b, from where it is possible to interpret a good adhesion, without porosity or cracks on this interface.

The carbide coating micrographs are presented in Figure 4c,d for WC-12Co and WC-10Co4, respectively. Both coatings had porosity under 1% and hardness above 1200 HV_{0.3}, as shown in Table 3, which is consonant with values published by other authors [45,46]. The morphology is composed of particles of WC, which is the lighter phase uniformly distributed in Figure 4c,d, and the metal matrix or binder, the darker phase in Figure 4c,d. The carbides presented were well adhered to the maraging, with no cracks or delamination, and visual uniformity of thickness, which was confirmed by the narrow range of thickness standard deviation values in Table 3, ± 5 μm for WC-12Co and ± 23 μm for WC-10Co4Cr coatings, which is under 10% of thickness variation. CGS MAM maraging had this level of thickness variation also.

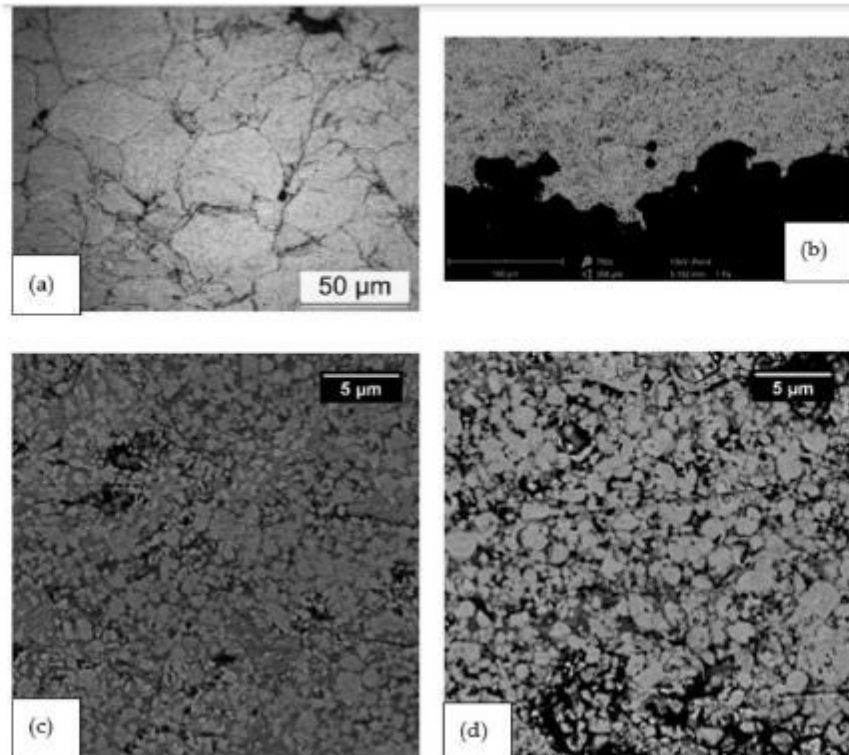


Figure 4. (a) OM (optical microscopy) image of CGS MAM maraging after etching. SEM images of (b) interface maraging (darker area) and cermet (lighter area); (c) WC-12Co, magnification 7500 \times ; (d) WC-10Co4Cr.

The effectiveness of applying the Dycomet 1008 layer to improve the CGS MAM maraging adherence on the C-steel substrate was proven by the large thickness of maraging obtained, above 800 μm . A poor adherence makes it not possible to grow this amount of material on the substrate without delaminating or cracking in the interface coating/substrate, as tested previously by the authors. The adhesion testing with a couple of Dycomet 1008 plus maraging resulted in a value of 52 ± 6 MPa. Figure 5 clearly indicates that this Dycomet 1008 layer promotes the good adherence of the maraging, even showing clear bonding mechanisms of CGS adhesion, such as the severe plastic deformation of the C-steel substrate, which is related to the adiabatic shear instability (ASI), the jetting, and consequent interlocking [13,47,48].

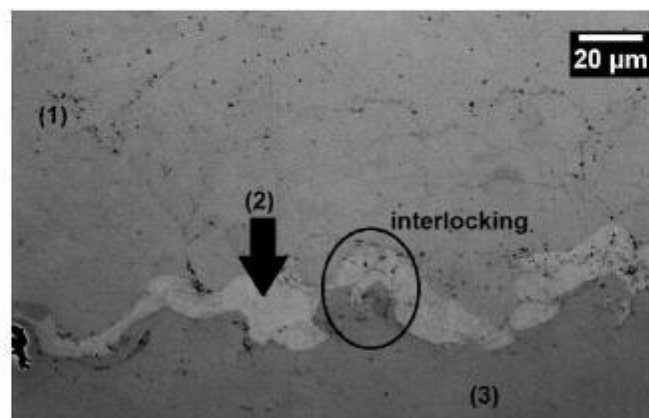


Figure 5. OM image of the Dycomet 1008 layer. (1) Maraging, (2) Dycomet 1008, (3) C-steel substrate.

The same HVOF process parameters were applied to spray both carbide powders, which have almost identical particle size distribution, as seen in Figure 4, and very close thickness values were obtained, as presented in Table 3. This indicates that the WC-12Co and WC-10Co4Cr had very similar deposition efficiency values, and no influence of the matrix composition was observed on the deposition efficiency.

Table 3. Material characteristics and properties.

Material	Thickness (μm)	Hardness ($\text{HV}_{0.05}$)	Porosity (%)
Maraging	874 ± 71	378 ± 63	<1.0
WC-12Co	242 ± 5	1249 ± 72	<1.0
WC-10Co4Cr	234 ± 23	1345 ± 133	<1.0
316L bulk	-	350 ± 13	-
C-steel bulk	-	241 ± 9	-

3.3. Wear Performance

The friction wear testing was performed on ball-on-disk testing and the CoF evolution between a WC-Co ball counterpart and the tested materials was plotted (Figure 6). The mean CoF values after the wear regimen stabilized are indicated in Table 4. The value indicated for the reference material 316L bulk, 0.67, is close to the value presented in the literature, 0.7 [16,49]. The CGS MAM maraging presented the highest CoF, 0.86, while the WC-10Co4Cr had the lowest, 0.14, among the evaluated materials.

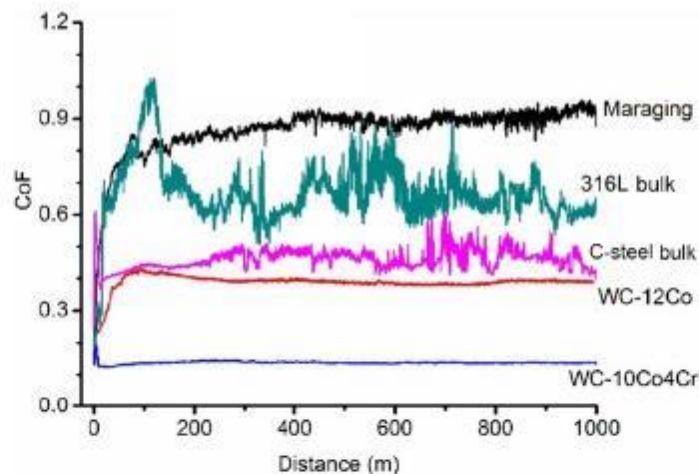


Figure 6. CoF (coefficient of friction) results from ball-on-disk testing.

CGS MAM maraging, 316L bulk, and C-steel bulk presented on the wear track both the abrasive and the adhesive wear mechanisms. The abrasive mechanism is evidenced by furrows in the direction of ball moving, indicated by arrows in Figure 7b. The adhesive wear mechanism results from the adhesion of some debris on the wear track, after severe deformation and oxidation, as revealed by EDS analysis. The darker areas in Figure 7b indicate this attached debris. This combination of mechanisms made the CoF values oscillate, as observed in the CoF curves for the CGS MAM maraging, 316L bulk, and C-steel bulk.

The WC-Co HVOF coatings under the ball-on-disk testing presented a very thin and shallow wear track, as indicated by arrows as the darker area in Figure 7a, which did not present oxidation, as revealed by EDS analysis. The WC-Co coatings resulted in a very low friction wear rate, highlighting the WC-12Co with $0.013 \times 10^{-5} \text{ mm}^3 \cdot \text{N}^{-1} \cdot \text{m}^{-1}$, around 177 times lower than CGS MAM maraging and 1300 times lower than 316L bulk. This

better performance in the friction testing indicates that both WC coatings can serve as friction wear protectors for CGS MAM maraging, as well as for 316L and C-steel bulk. In general, friction and wear of carbides are believed to result from three mechanisms, adhesion, plowing or abrasion, and asperity deformation [50]. In the present study, the wear track of both WC-Co coatings presented few marks of plowing and surface deformation, without any adhesion, which resulted in a very flat CoF curve for both cermets, as seen in Figure 6.

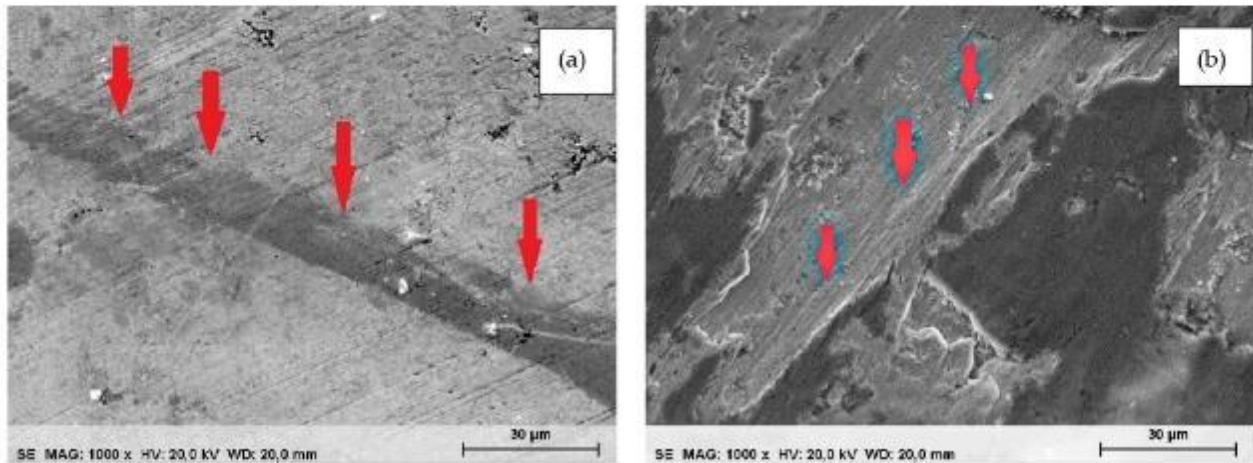


Figure 7. SEM images of worn tracks from ball-on-disk testing. (a) WC-12Co, with arrows indicating the wear track. (b) 316L bulk, with the arrows indicating furrows in the direction of ball moving.

The abrasion rates from the rubber wheel testing (Table 4) indicated that WC-Co coatings were dozens of times more resistant than the maraging, C-steel bulk, and 316L bulk. The most relevant of these was the WC-12Co, with an abrasion rate of $0.76 \times 10^{-5} \text{ mm}^3 \cdot \text{N}^{-1} \cdot \text{m}^{-1}$, which is even lower than that reported in the literature, close to $1.0 \times 10^{-5} \text{ mm}^3 \cdot \text{N}^{-1} \cdot \text{m}^{-1}$ [28,51,52]. This behavior is also presented graphically in Figure 8 with the cermet curves appearing much flatter than those the other tested materials. The higher hardness of cermet coatings in comparison to the other tested materials (Table 3) is an explanation for their better abrasion resistance, as reported by Gee, Gant, and Roebuck [52] and Gant, Gee, and May [51], who presented an exponential relation between the volume loss and the material hardness in rubber wheel low-stress abrasion testing.

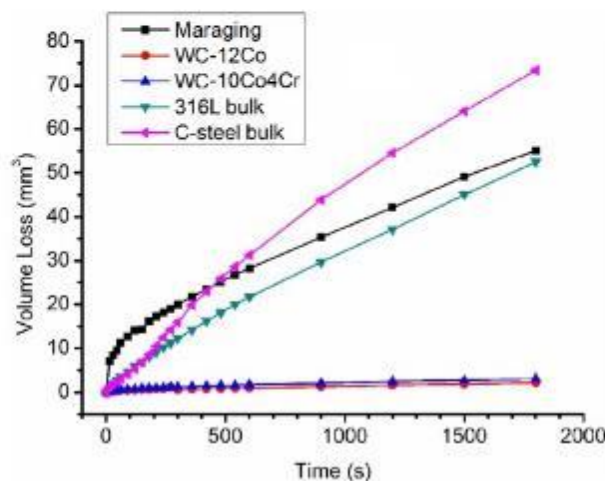


Figure 8. Accumulated volume loss from abrasion testing.

Evaluating the HVOF cermet coatings' morphology in Figure 4, the WC-10Co4Cr presents larger WC particles than the WC-12Co, which is reflected in the abrasion rate, as explained by Gokul Lakshmi, Reddy, and Roy [53], who revealed that the abrasion resistance for low-stress testing increases with the amount of large hard particles. This is related to the incapacity of the erodents to penetrate the coating as they are fragmented and smashed by the coating's hard carbides. Merrick and Miller [54] indicated that only abrasives that penetrate the coating with a depth larger than the size of the WC particles are capable of abrading the composite materials.

Table 4. Wear testing results.

Material	Abrasion Rate ($\text{mm}^3\cdot\text{N}^{-1}\cdot\text{m}^{-1}$)	CoF (N N^{-1})	Friction Wear Rate ($\text{mm}^3\cdot\text{N}^{-1}\cdot\text{m}^{-1}$)	Jet Erosion Rate ($\text{mg}\cdot\text{min}^{-1}$)
Maraging	21.61×10^{-5}	0.86 ± 0.08	2.302×10^{-5}	1654.67 ± 115.64
WC-12Co	0.76×10^{-5}	0.38 ± 0.03	0.013×10^{-5}	15.66 ± 1.69
WC-10Co4Cr	1.29×10^{-5}	0.14 ± 0.01	0.032×10^{-5}	137.33 ± 3.46
316L bulk	16.73×10^{-5}	0.67 ± 0.11	17.051×10^{-5}	2.55 ± 0.00
C-steel bulk	23.94×10^{-5}	0.46 ± 0.03	2.841×10^{-5}	69.88 ± 3.22

Regarding another wear mechanism, the erosion by water impact is relevant for structures exposed to water droplets at high velocities, such as wind turbine blades, steam turbines, gas turbine components, or airplane fuselages [30,31,55]. The jet erosion testing was performed, and the evolution of mass loss versus testing elapsed time is plotted in Figure 9, while the wear rate is presented in Table 4. The CGS MAM maraging had the highest erosion rate, more than 10 times that of the WC-10Co4Cr and 100 times that of the WC-12Co. The bulk reference materials had a lower erosion rate than the thermally sprayed materials, and among the bulks, 316L stainless steel had the smallest value, $2.55 \text{ mg}\cdot\text{min}^{-1}$. According to ASTM G73 [42], the testing ends at the rupture of the coating, which is clearly seen in the cermet curves, at 120 min for WC-10Co4Cr and 420 min for WC-12Co, since from these points their erosion rate curves follow the CGS MAM maraging slope.

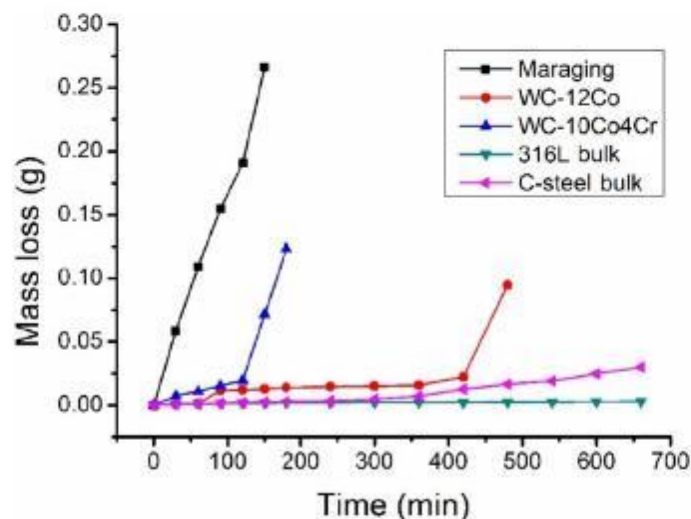


Figure 9. Accumulated mass loss from jet erosion testing.

The erosion mechanism presented in the literature for the water jet erosion is the same as that observed for the cavitation erosion [31]. The erosion slopes typically present three stages: the incubation, when the material absorbs energy and is not eroded; the second stage, characterized by the beginning of mass loss and the increment in the mass

loss rate up to the maximum value; and the third stage, which is characterized as a regime of steady-state mass loss rate [56]. The thermally sprayed materials, maraging and cermets, did not have the incubation period; however, the C-steel bulk stayed in the incubation period for 240 min and the 316L bulk did not evolve to the second stage after 660 min, as interpreted visually from their slopes. Other authors reported this inexistence of incubation for thermally sprayed coatings under water erosion, such as HVOF and arc sprayed FeMnCrSi alloys [56], HVOF sprayed cermets and Ti alloys [31], and HVOF-kerosene fuel sprayed cermets [27].

3.4. Corrosion Behavior

For the evaluation of the performance of the materials in a corrosive media, 3.5 wt.% NaCl water solution, and to understand the effectiveness of applying WC coatings on CGS MAM maraging, as corrosion protection, potentiodynamic experiments were conducted with the as-sprayed maraging and WC-coated samples and the reference C-steel and 316L bulks. The polarization curves obtained in these experiments are shown in Figure 10. The potential of corrosion, E_{corr} , and the corrosion current, I_{corr} , values characteristic for each material were calculated by Equation (2) and are presented in Table 5, as is the polarization resistance, R_p . A significant difference in these parameters can be observed between the sprayed materials and the bulks, with the 316L bulk as the noblest material, -179.80 mV, and the worst behavior for C-steel bulk, -753.97 mV. These results are consonant with those presented in the literature, -239 mV [16] and -260 mV [57] for 316L bulk and -726 mV [46] and -719 mV [58] for C-steel.

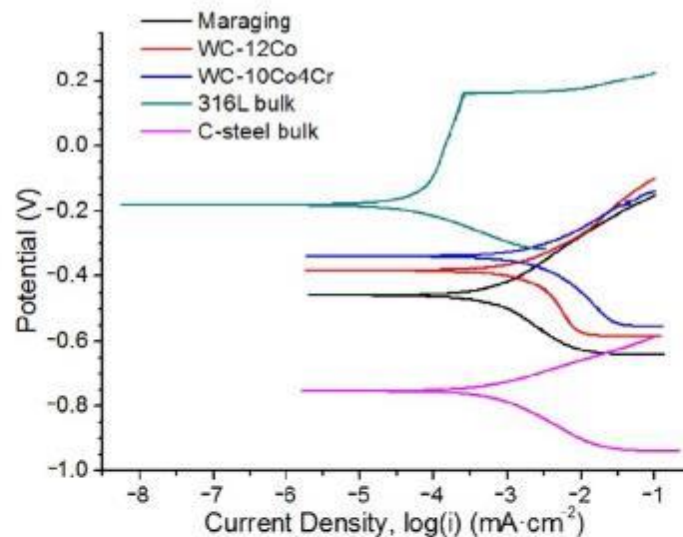


Figure 10. Tafel slopes from potentiodynamic experiments.

Regarding the sprayed materials, their results were lower than the 316L bulk stainless steel ones and higher than the C-steel bulk ones. All of the coatings had low porosity, which is mandatory for good corrosion protection of the substrate. Both WC HVOF coatings had higher E_{corr} values than the CGS MAM maraging in 3.5% NaCl water solution, showing that these coatings could extend the service life of CGS MAM maraging parts when operating in this medium. The close, but different, values seen for the WC-12Co and WC-10Co4Cr are related to the binder material amount and composition, as reported by Bulnes et al. [46], who presented the metal matrix -10Co4Cr as nobler than the -12Co one for the studied hard coatings. Despite this, when the potential was shifted from the cathodic to the anodic region, the cermets had different behaviors, with the WC-

12Co presenting lower I_{corr} than WC-10Co4Cr, which indicates slower corrosion for the WC-12Co under these polarization conditions.

Table 5. Results of potentiodynamic experiments.

Material	Current density I_{corr} ($\mu\text{A}\cdot\text{cm}^{-2}$)	Potential of Corrosion E_{corr} (mV)	Polarization Resistance R_p (k Ω)
Maraging	0.41	−457.19	39.08
WC-12Co	1.47	−381.50	16.34
WC-10Co4Cr	1.79	−339.48	10.25
316L bulk	0.07	−179.80	58.00
C-steel bulk	0.53	−753.97	8.08

4. Conclusions

Considering the microstructures characterized, the mechanical properties measured, and the wear and corrosion testing results for CGS MAM maraging and the HVOF cermet coatings, it is possible to conclude the following:

The production of a dense maraging part by CGS MAM on a C-steel substrate benefits from the previously deposited layer of CGS Dycomet, which improves the adhesion of the maraging sprayed by CGS.

The deposition of cermets, WC-12Co and WC-10Co4Cr, by HVOF on CGS MAM maraging results in well-adhered hard coatings, which improve the component's wear resistance. The sliding wear and water erosion rates are reduced more than 100 times, while the abrasion wear rate is reduced almost 30 times. The potential of corrosion is also reduced, although the 316L bulk is still the noblest material among the evaluated samples and the C-steel bulk has the highest E_{corr} .

Author Contributions: Conceptualization, R.F.V., A.S., and J.S.; funding acquisition, J.S. and I.G.C.; investigation, R.F.V. and A.S.; methodology, R.F.V., A.S., and J.S.; project administration, I.G.C.; writing—original draft preparation, R.F.V., A.S., J.S., and V.A.; writing—review and editing, R.F.V., A.S., and J.S.; supervision, I.G.C. All authors have read and agreed to the published version of the manuscript.

Funding: The authors wish to thank COMRDI16-1-0007-5 “RIS3CAT 3D TOOLING”.

Institutional Review Board Statement: Not applicable.

Informed Consent Statement: Not applicable.

Data Availability Statement: The data presented in this study are available on request from the corresponding author.

Conflicts of Interest: The authors declare no conflict of interest. The funders had no role in the design of the study; in the collection, analyses, or interpretation of data; in the writing of the manuscript; or in the decision to publish the results.

References

- Frazier, W.E. Metal additive manufacturing: A review. *J. Mater. Eng. Perform.* **2014**, *23*, 1917–1928, doi:10.1007/s11665-014-0958-z.
- Herzog, D.; Seyda, V.; Wycisk, E.; Emmelmaru, C. Additive manufacturing of metals. *Acta Mater.* **2016**, *117*, 371–392, doi:10.1016/j.actamat.2016.07.019.
- Ahmed, G.M.S.; Badruddin, I.A.; Tirth, V.; Algahtani, A.; Ali, M.A. Wear resistance of maraging steel developed by direct metal laser sintering. *Mater. Express* **2020**, *10*, 1079–1090, doi:10.1166/mex.2020.1715.
- Pan, Z.; Ding, D.; Wu, B.; Cuiuri, D.; Li, H.; Norrish, J. Arc welding processes for additive manufacturing: A review. In *Transactions on Intelligent Welding Manufacturing*; Chen, S., Zang, Y., Feng, Z., Eds.; Springer: Singapore, 2018; pp. 3–24. ISBN 9789811053559.
- Karayel, E.; Bozkurt, Y. Additive manufacturing method and different welding applications. *J. Mater. Res. Technol.* **2020**, *9*, 11424–11438, doi:10.1016/j.jmrt.2020.08.039.
- Li, W.; Yang, K.; Yin, S.; Yang, X.; Xu, Y.; Lupoi, R. Solid-state additive manufacturing and repairing by cold spraying: A review. *J. Mater. Sci. Technol.* **2018**, *34*, 440–457, doi:10.1016/j.jmst.2017.09.015.

7. Assadi, H.; Kreye, H.; Gärtner, F.; Klassen, T. Cold spraying—A materials perspective. *Acta Mater.* **2016**, *116*, 382–407, doi:10.1016/j.actamat.2016.06.034.
8. Oyinbo, S.T.; Jen, T. C. A comparative review on cold gas dynamic spraying processes and technologies. *Manuf. Rev.* **2019**, *6*, 1–20, doi:10.1051/mfreview/2019023.
9. Yin, S.; Cavaliere, P.; Aldwell, B.; Jenkins, R.; Liao, H.; Li, W. Cold spray additive manufacturing and repair: Fundamentals and applications. *Addit. Manuf.* **2018**, *21*, 628–650, doi:10.1016/j.addma.2018.04.017.
10. Bagherifard, S.; Monti, S.; Zuccoli, M.V.; Riccio, M.; Kondás, J.; Guagliano, M. Cold spray deposition for additive manufacturing of freeform structural components compared to selective laser melting. *Mater. Sci. Eng. A* **2018**, *721*, 339–350, doi:10.1016/j.msea.2018.02.094.
11. Raelison, R.N.; Verdy, C.; Liao, H. Cold gas dynamic spray additive manufacturing today: Deposit possibilities, technological solutions and viable applications. *Mater. Des.* **2017**, *133*, 266–287, doi:10.1016/j.matdes.2017.07.067.
12. Yan, X.; Huang, C.; Chen, C.; Bolot, R.; Dembinski, L.; Huang, R.; Ma, W.; Liao, H.; Liu, M. Additive manufacturing of WC reinforced maraging steel 300 composites by cold spraying and selective laser melting. *Surf. Coat. Technol.* **2019**, *371*, 161–171, doi:10.1016/j.surfcoat.2018.03.072.
13. Bae, G.; Kumar, S.; Yoon, S.; Kang, K.; Na, H.; Kim, H.; Lee, C. Bonding features and associated mechanisms in kinetic sprayed titanium coatings. *Acta Mater.* **2009**, *57*, 5654–5666, doi:10.1016/j.actamat.2009.07.061.
14. Yin, S.; Cizek, J.; Cupera, J.; Hassani, M.; Luo, X.; Jenkins, R.; Xie, Y.; Li, W.; Lupoi, R. Formation conditions of vortex-like intermixing interfaces in cold spray. *Mater. Des.* **2021**, *200*, 1–10, doi:10.1016/j.matdes.2020.109444.
15. Cormier, Y.; Dupuis, P.; Jodoin, B.; Corbeil, A. Pyramidal fin arrays performance using streamwise anisotropic materials by cold spray additive manufacturing. *J. Therm. Spray Technol.* **2016**, *25*, 170–182, doi:10.1007/s11666-015-0267-6.
16. Vaz, R.F.; Silvello, A.; Sanchez, J.; Albaladejo, V.; Cano, I.G. The influence of the powder characteristics on 316L stainless steel coatings sprayed by cold gas spray. *Coatings* **2021**, *11*, 1–18, doi:10.3390/coatings11020168.
17. Jiao, Z.B.; Luan, J.H.; Miller, M.K.; Chung, Y.W.; Liu, C.T. Co-precipitation of nanoscale particles in steels with ultra-high strength for a new era. *Mater. Today* **2017**, *20*, 142–154, doi:10.1016/j.mattod.2016.07.002.
18. Würzinger, P.; Rabitsch, R.; Meyer, W. Production of maraging steel grades and the influence of specified and nonspecified elements for special applications. *J. Mater. Sci.* **2004**, *39*, 7295–7302, doi:10.1023/B:JMSC.0000048744.03279.ec.
19. Chen, C.; Yan, X.; Xie, Y.; Huang, R.; Kuang, M.; Ma, W.; Zhao, R.; Wang, J.; Liu, M.; Ren, Z.; et al. Microstructure evolution and mechanical properties of maraging steel 300 fabricated by cold spraying. *Mater. Sci. Eng. A* **2019**, *743*, 482–493, doi:10.1016/j.msea.2018.11.116.
20. Chen, C.; Xie, Y.; Yan, X.; Huang, R.; Kuang, M.; Ma, W.; Zhao, R.; Wang, J.; Liu, M.; Ren, Z.; et al. Cold sprayed WC reinforced maraging steel 300 composites: Microstructure characterization and mechanical properties. *J. Alloy. Compl.* **2019**, *785*, 499–511, doi:10.1016/j.jallcom.2019.01.135.
21. Turk, C.; Zunko, H.; Aumayr, C.; Leitner, H.; Kapp, M. Advances in Maraging steels for additive manufacturing. *B. Huettenmaenn. Monatsh.* **2019**, *164*, 112–116, doi:10.1007/s00501-019-0835-z.
22. Jäggle, E.A.; Sheng, Z.; Kümsteiner, P.; Ocylok, S.; Weisheit, A.; Raabe, D. Comparison of maraging steel micro- and nanostructure produced conventionally and by laser additive manufacturing. *Materials* **2017**, *10*, 8, doi:10.3390/ma10010008.
23. Takata, N.; Nishida, R.; Suzuki, A.; Kobashi, M.; Kato, M. Crystallographic features of microstructure in Maraging steel fabricated by selective laser melting. *Metals* **2018**, *8*, 1–10, doi:10.3390/met8060440.
24. Ansell, T.Y.; Ricks, J.P.; Park, C.; Tipper, C.S.; Luhrs, C.C. Mechanical properties of 3D-printed maraging steel induced by environmental exposure. *Metals* **2020**, *10*, 218, doi:10.3390/met10020218.
25. Sun, K.; Peng, W.; Wei, B.; Yang, L.; Fang, L. Friction and wear characteristics of 18Ni(300) maraging steel under high-speed dry sliding conditions. *Materials* **2020**, *13*, 1485, doi:10.3390/ma13071485.
26. Wang, H.; Qiu, Q.; Gee, M.; Hou, C.; Liu, X.; Song, X. Wear resistance enhancement of HVOF-sprayed WC-Co coating by complete densification of starting powder. *Mater. Des.* **2020**, *191*, 1–13, doi:10.1016/j.matdes.2020.108586.
27. Lamana, M.S.; Pukasiewicz, A.G.M.; Sampath, S. Influence of cobalt content and HVOF deposition process on the cavitation erosion resistance of WC-Co coatings. *Wear* **2018**, *398–399*, 209–219, doi:10.1016/j.wear.2017.12.009.
28. Magnani, M.; Suegama, P.H.; Espallargas, N.; Dosta, S.; Fugivara, C.S.; Guilemany, J.M.; Benedetti, A. V Influence of HVOF parameters on the corrosion and wear resistance of WC-Co coatings sprayed on AA7050 T7. *Surf. Coatings Technol.* **2008**, *202*, 4746–4757, doi:10.1016/j.surfcoat.2008.04.055.
29. Pulsford, J.; Venturi, F.; Kamnis, S.; Hussain, T. Sliding wear behaviour of WC-Co reinforced NiCrFeSiB HVOAF thermal spray coatings against WC-Co and Al₂O₃ counterbodies. *Surf. Coatings Technol.* **2020**, *386*, 1–11, doi:10.1016/j.surfcoat.2020.125468.
30. Mahdipoor, M.S.; Tarasi, F.; Moreau, C.; Dolatabadi, A.; Medraj, M. HVOF sprayed coatings of nano-agglomerated tungsten-carbide/cobalt powders for water droplet erosion application. *Wear* **2015**, *330–331*, 338–347, doi:10.1016/j.wear.2015.02.034.
31. Shipway, P.H.; Gupta, K. The potential of WC-Co hardmetals and HVOF sprayed coatings to combat water-droplet erosion. *Wear* **2011**, *271*, 1418–1425, doi:10.1016/j.wear.2010.12.058.
32. ASTM. B822-02—Standard Test Method for Particle Size Distribution of Metal Powders and Related Compounds by Laser Scattering; ASTM International: West Conshohocken, PA, USA, 2002.
33. ISO. 17836:2004—Thermal Spraying—Determination of Deposition Efficiency for Thermal Spraying; ISO: Geneva, Switzerland, 2004.
34. ASTM. E1920-03—Standard Guide for Metallographic Preparation of Thermal Sprayed Coatings; ASTM International: West Conshohocken, PA, USA, 2003.

35. ASTM. E3-01—Standard Guide for Preparation of Metallographic Specimens; ASTM International: West Conshohocken, PA, USA, 2001.
36. ASTM. B487-85—Standard Test. Method for Measurement of Metal and Oxide Coating Thickness by Microscopical Examination of a Cross Section; ASTM International: West Conshohocken, PA, USA, 2002.
37. ASTM. E2109-01—Standard Test. Methods for Determining Area Percentage Porosity in Thermal Sprayed Coatings; ASTM International: West Conshohocken, PA, USA, 2002.
38. ASTM. E384-99—Standard Test. Method for Microindentation Hardness of Materials; ASTM International: West Conshohocken, PA, USA, 2000.
39. ASTM. C633-13—Standard Test. Method for Adhesion or Cohesion Strength of Thermal Spray Coatings; ASTM International: West Conshohocken, PA, USA, 2017.
40. ASTM. G65-00—Standard Test. Method for Measuring Abrasion Using the Dry Sand Rubber Wheel Apparatus; ASTM International: West Conshohocken, PA, USA, 2000.
41. ASTM. G99-04—Standard Test. Method for Wear Testing with A Pin-on-Disk Apparatus; ASTM International: West Conshohocken, PA, USA, 2004.
42. ASTM. G73-10—Standard Test. Method for Liquid Impingement Erosion Using Rotating Apparatus; ASTM International: West Conshohocken, PA, USA, 2010.
43. ASTM. G59-97—Standard Test. Method for Conducting Potentiodynamic Polarization Resistance Measurements; ASTM International: West Conshohocken, PA, USA, 1997.
44. ASTM. G102-89—Standard Practice for Calculation of Corrosion Rates and Related Information from Electrochemical Measurements; ASTM International: West Conshohocken, PA, USA, 1999.
45. Ahmed, R.; Vourlias, G.; Algoburi, A.; Vogiatzis, C.; Chaliampalias, D.; Skolianos, S.; Berger, L.-M.; Paul, S.; Faisal, N.H.; Toma, F.-L.; et al. Comparative study of corrosion performance of HVOF-sprayed coatings produced using conventional and suspension WC-Co feedstock. *J. Therm. Spray Technol.* **2018**, *27*, 1579–1593, doi:10.1007/s11666-018-0775-2.
46. Bulnes, A.G.; Fuentes, V.A.; Cano, I.G.; Dosta, S. Understanding the influence of high velocity thermal spray techniques on the properties of different anti-wear WC-based coatings. *Coatings* **2020**, *10*, 1157, doi:10.3390/coatings10121157.
47. Grujicic, M.; Zhao, C.L.; DeRosset, W.S.; Helfritsch, D. Adiabatic shear instability based mechanism for particles/substrate bonding in the cold-gas dynamic-spray process. *Mater. Des.* **2004**, *25*, 681–688, doi:10.1016/j.matdes.2004.03.008.
48. Ko, K.H.; Choi, J.O.; Lee, H. Intermixing and interfacial morphology of cold-sprayed Al coatings on steel. *Mater. Lett.* **2014**, *136*, 45–47, doi:10.1016/j.matlet.2014.07.142.
49. Qin, W.; Kang, J.; Li, J.; Yue, W.; Liu, Y.; She, D.; Mao, Q.; Li, Y. Tribological behavior of the 316L stainless steel with heterogeneous lamella structure. *Materials* **2018**, *11*, 1839, doi:10.3390/ma11101839.
50. Jianxin, D.; Hui, Z.; Ze, W.; Yunsong, L.; Jun, Z. Friction and wear behaviors of WC/Co cemented carbide tool materials with different WC grain sizes at temperatures up to 600 °C. *Int. J. Refract. Met. Hard Mater.* **2012**, *31*, 196–204, doi:10.1016/j.ijrmhm.2011.11.003.
51. Gant, A.J.; Gee, M.G.; May, A.T. The evaluation of tribo-corrosion synergy for WC-Co hardmetals in low stress abrasion. *Wear* **2004**, *256*, 500–516, doi:10.1016/j.wear.2003.04.001.
52. Gee, M.G.; Gant, A.; Roebuck, B. Wear mechanisms in abrasion and erosion of WC/Co and related hardmetals. *Wear* **2007**, *263*, 137–148, doi:10.1016/j.wear.2006.12.046.
53. Gokul Lakshmi, S.; Reddy, G.M.; Roy, M. A Comparison of Wear Due to Abrasion of WC-Ni Coatings on Aluminium Alloy Sprayed by HVOF and Detonation Gun. *Trans. Indian Inst. Met.* **2018**, *71*, 1389–1399, doi:10.1007/s12666-018-1280-5.
54. Merrick, S.J.; Miller, R.F. The role of carbides in iron base hardsurfacing deposits. In *Proceedings of the Advances in Thermal Spraying*; Pergamon Press: Montreal, QC, Canada, 1986; pp. 633–642.
55. Ibrahim, M.E.; Medraj, M. Water droplet erosion of wind turbine blades: Mechanics, testing, modeling and future perspectives. *Materials* **2020**, *13*, 157, doi:10.3390/ma13010157.
56. Vaz, R.F.; Sucharski, G.B.; Chicoski, A.; Siqueira, I.B.A.F.; Tristante, R.; Pukasiewicz, A.G.M. Comparison of FeMnCrSi cavitation resistance coatings deposited by Twin-Wire Electric Arc and High-Velocity Oxy-Fuel processes. *J. Therm. Spray Technol.* **2021**, *30*, 754–771, doi:10.1007/s11666-020-01145-z.
57. Bellie, V.; Suresh, J.; Ragunath, L. HVOF sprayed mullite coatings for use in extreme environments. *J. Therm. Spray Eng.* **2020**, *2*, 43–49, doi:10.1016/j.jtse.2020.1474/2-1.2.
58. Othman, N.K.; Yahya, S.; Awizar, D.A. Anticorrosive properties of nano silicate from paddy husk in salt medium. *Sains Malays.* **2016**, *45*, 1253–1258.

Chapter 5

OVERALL DISCUSSIONS

5. OVERALL DISCUSSIONS

This section summarizes the discussions from Chapter 4, “Results and Discussions”, of this thesis. The main objective, “develop spraying strategies or methodologies to obtain better CSAM-ed parts quality”, was achieved by the feasibility of making more complex geometry parts and better mechanical properties. Each article approached different CSAM-ed materials, characterization, and performance testing. This section, however, also sheds a more comprehensive and general light on the subjects previously discussed:

AM is competing in the industry with some more mature manufacturing techniques, such as casting, machining, and forging, among many others. For some applications, AM can substitute the older techniques, but AM still has some limitations to overcome. One of the challenges for AM is the production time. For this, CSAM has advantages over other AM processes, because it achieves high deposition rates, in magnitude of $\text{kg}\cdot\text{h}^{-1}$. An example of this production was presented in Article 5 for $50\times 50\times 50\text{ mm}^3$ 316L bulks made in just a few minutes. Using new and optimized CSAM deposition strategies has decreased the production time by optimizing the robot path, DE, and spraying time. It makes the CSAM a feasible AM technique for large parts with non-complex shapes or geometries.

5.1. Influence of Feedstock Powders on CSAM-ed part Properties

The feedstock powders represent a high cost for AM processes, especially those with low DE. Some powders for CS have very high DE, close to 100%, e.g., Ti, 316L, and Cu; however, others do not, like Inconel 718 or hard alloys. Recycling feedstock materials for AM has been researched, as presented by Hegab et al. [103]. The studies have been focused on the sustainability proposed by the AM techniques, and technically, for metal AM, the scholars have shown how the unconsolidated or rebounded powder can be redeposited by the same AM technique or other. More advances in powder recycling are found for powder-bed AM processes, i.e., laser [104,105], presenting a lack in the literature for CSAM. For CSAM, recycling powder is a challenge for the service conditions, e.g., the most adequate method to collect the unconsolidated powder. Besides that, harder and brittle particles can break at the impact, reducing the particle size distribution for the next use, requiring higher V_{impact} and more energetic CS parameters. This inverse relation between the particle size and

V_{cr} was presented in the literature [39,51]. An alternative to improve the V_{impact} is using He as working gas instead of N_2 , which makes the CSAM deposition much more expensive.

Furthermore, the CS-ed powder that did not bond can be deformed during the impact on the substrate, reducing its plasticity for subsequent use. It is well known that the CS bonding mechanisms depend on the material plasticity [106–108]. Considering these points, more research is required to advance the use of recycled powder for CSAM use, maybe limiting how many times a powder can be re-sprayed or which powders can be recycled.

The use of irregular particles for CSAM, instead of the spherical gas atomized ones, was validated for 316L in Article 2, resulting that a less costly water atomized and a high-cost gas atomized powder are capable of reaching the same or very similar CS-ed coating performance, considering wear resistance and corrosion behavior. The velocity of CS spraying of 316L and pure Ti irregular and spherical particles was also compared, resulting in similar values. The literature presents that the particles' bonding and cohesion strength strongly depend on their in-flight velocity [52,109]. The similarity of in-flight conditions for irregular and spherical particles justifies their microstructural similarity, supporting the use of less costly feedstock powders. It places CSAM as an economically attractive AM process.

5.2. Improvement of Geometric Accuracy

Geometric accuracy is another limitation for CSAM industrial maturity increase. Scholars have employed time and effort to improve the CSAM capacity for making more complex geometries. For example, the literature presents that by varying the spraying angle, it is possible to grow vertical sidewalls CSAM-ed parts or thin and high walls [43,59,65,110]. An alternative successfully studied in this work is the constant deposition angle correction, developing a cone-like path described by the CS jet, named Metal Knitting, and presented in detail in Article 3.

However, both strategies, the first one with single or multiple layers at different spraying angles and the second one, Metal Knitting, with a cone-like CS gun movement, resulted in regions with low cohesion of particles or aligned porosity. It can be a problem and limitation for the industrial application of CSAM. For example, these strategies work correctly to make prototypes, models, or any part for which the

geometry is the most important, leaving the mechanical properties in second place. Nevertheless, for structural components, improving the CSAM-ed material mechanical properties is imperative, and some processing or post-treatment strategies have been presented to do it, such as HT [111], in-situ micro-forging [112,113], or hybrid systems deposition, e.g., laser-assisted CSAM [114]. Some strategies were tested and evaluated in this thesis.

CSAM Metal Knitting presented limitations to making good parts with a thick layer thickness, e.g., pure Al. A thick layer creates shaded areas for the next Metal Knitting movement, increasing the material porosity and reducing the material properties, especially the strength and cohesion of particles. However, it is important to notice that for Al bulks, the innovative CSAM Metal Knitting strategy is not needed since the traditional one produces vertical sidewalls. For thin walls, where a single-line Metal Knitting path is required, this shading effect is not seen, and the material density achieved is as good as the CSAM traditional part made.

5.3. CSAM-ed Parts Mechanical Properties

The CSAM-ed material characteristics have been controlled by process optimization. Achieving the minimum porosity is usually the objective, but a controlled one is more important for some applications, e.g., aircraft Al parts [115] or Ti implants [116]. High CSAM-ed materials' density has been achieved by improving the CS-ed particle velocity, keeping it inside the window of deposition presented in the literature as limits of minimum and maximum values [52,109]. Using the CSAM Metal Knitting strategy resulted in higher porosity than the CSAM traditional one due to the lower velocity and shaded areas during the cone-like path described by the gun during the first strategy. A thinner layer can reduce this shaded area and, consequently, improve the mechanical properties by a more effective peening effect during the deposition, as presented by Moridi et al. [83] and Tan et al. [84].

Reducing the CSAM-ed layer thickness requires a lower powder feeding rate or an increased robot velocity. The first option results in an unstable powder flow for the equipment used in this thesis, which was limited to 1 rpm for PCS100 CS gun, close to $0.5 \text{ g}\cdot\text{s}^{-1}$ for 316L powder. An instable powder feeding reduces the deposition quality creating high porosity regions and rough and waved part surface. The second option, increasing the robot velocity, is limited by the robot's top acceleration, which was

reached with $V_{\text{tangential}}$ of $500 \text{ m}\cdot\text{s}^{-1}$. Employing a newer powder feeder or a more robust robot should be attractive to improve the CSAM Metal Knitting material quality.

The material microstructural characteristics, such as strength or fatigue life, severely influence the loading performance. The literature presents how the CSAM-ed materials have lower performance than the wrought reference materials, which is a consequence of the bonding and cohesion mechanisms, especially the adiabatic shear instability (ASI) that does not promote a metallurgic union between the particles [117,118]. This bonding weakness was evaluated and presented in Article 5. Post-processing, in particular HT, promoted an atomic diffusion in the CS-ed material, improving the strength and the material isotropy by changing the particle bonding primary mechanism from ASI to a metallurgic one, which also changes the fracture mode from decohesion of particles in the interparticular region to a ductile one.

For Ti alloys, the same trend was obtained, improving the material isotropy, changing the fracture mode, and increasing the cohesion of particles, but not significantly altering the material density, i.e., keeping the same porosity in as-sprayed and post-treated material. It occurs because the high temperature is enough to promote the metallurgic union of the particles that already were intimately close to each other and not approaching the distant particle surfaces, i.e., the atomic diffusion does not eliminate the porosity, but it occurs with the interparticular region. This porosity reduction was observed by SPS post-treatment, deforming the CSAM-ed material plastically, reducing the porosity from 38 to an impressive 2.7% for CSAM Metal Knitting Ti6Al4V. Using the traditional strategy, SPS reached $<1\%$, starting from 12% in as-sprayed condition. However, SPS altered the CSAM-ed part geometry, limiting SPS when using CSAM for complex and near-net-shape geometries. Special graphite dies, and punches can be designed for symmetrical shapes, enabling SPS for CSAM-ed special dense parts, resulting in high mechanical properties. Another positive point for using SPS is achieving dense materials with irregular and less costly feedstock powders, which, even resulting in high porosity in as-sprayed condition, can reach high cohesion of particles and density by selecting optimized SPS parameters [88].

HIP is another post-treatment presented in the literature for sintering processing and making high-performance materials [119]. HIP improved the density of CSAM-ed Ti6Al4V samples in their surface and subsurface regions. However, much porous remained internally, unchanging the initial as-sprayed density, especially for the CSAM

Metal Knitting made ones. HIP slightly reduced the material hardness and improved the cohesion of particles by metallurgic bonding due to atomic diffusion in the most intimate material interparticular regions. Employing capsule-free HIP for CSAM-ed Ti6Al4V with apparent unopened porosity did not promote material densification, indicating that the encapsulated HIP methodology is imperative for CSAM-ed materials.

5.4. Thermal Spraying Hybrid System

The wear and corrosion performances are dependent on the surface characteristics and properties. For CSAM-ed parts, it is not different and, alternative strategies can be applied to improve the material's surface properties. Induction HT, nitriding, boriding, painting, etc. For this thesis, the core is the thermal spraying process, and Article 6 presents how successful can be an HVOF deposition on CSAM-ed material.

For this thesis, CSAM-ed Maraging was coated by HVOF WC, which improved the part's surface properties, especially the wear resistance. The literature had a lack regarding this hybrid system, which is partially filled by this academic contribution. It was presumable that a carbide coating would improve these properties; however, the adherence mechanisms of a HVOF-ed coating on a CSAM-ed hard material was unknown.

An important and exciting use of this hybrid strategy, mixing CSAM and HVOF, is depositing the wear-resistant coating on specific regions of the CSAM-ed part, e.g., HVOF WC on CSAM-repaired hydraulic turbine blades, with the WC or other cavitation-resistant coating applied precisely where the cavitation phenomenon occurs. Another possibility is to use HVOF coatings internally on CSAM Metal Knitting piping.

5.5. Final Considerations

Considering the results and discussions presented in this thesis for CSAM, the decision flowchart shown in Figure 56 can achieve a final summary. It is considered that at the starting point, the user had previously designed the final part's geometry and properties required. Besides that, it is considered that the user elected CSAM based on the advantages this process has over other AM techniques or on the limitations that other AM techniques present and CSAM does not, e.g., material

oxidation during the deposition. The flowchart scheme endpoint may not be the final part ready to use, as it may require a final machining or adjusting for assembling or final fitting, depending on the real part application.

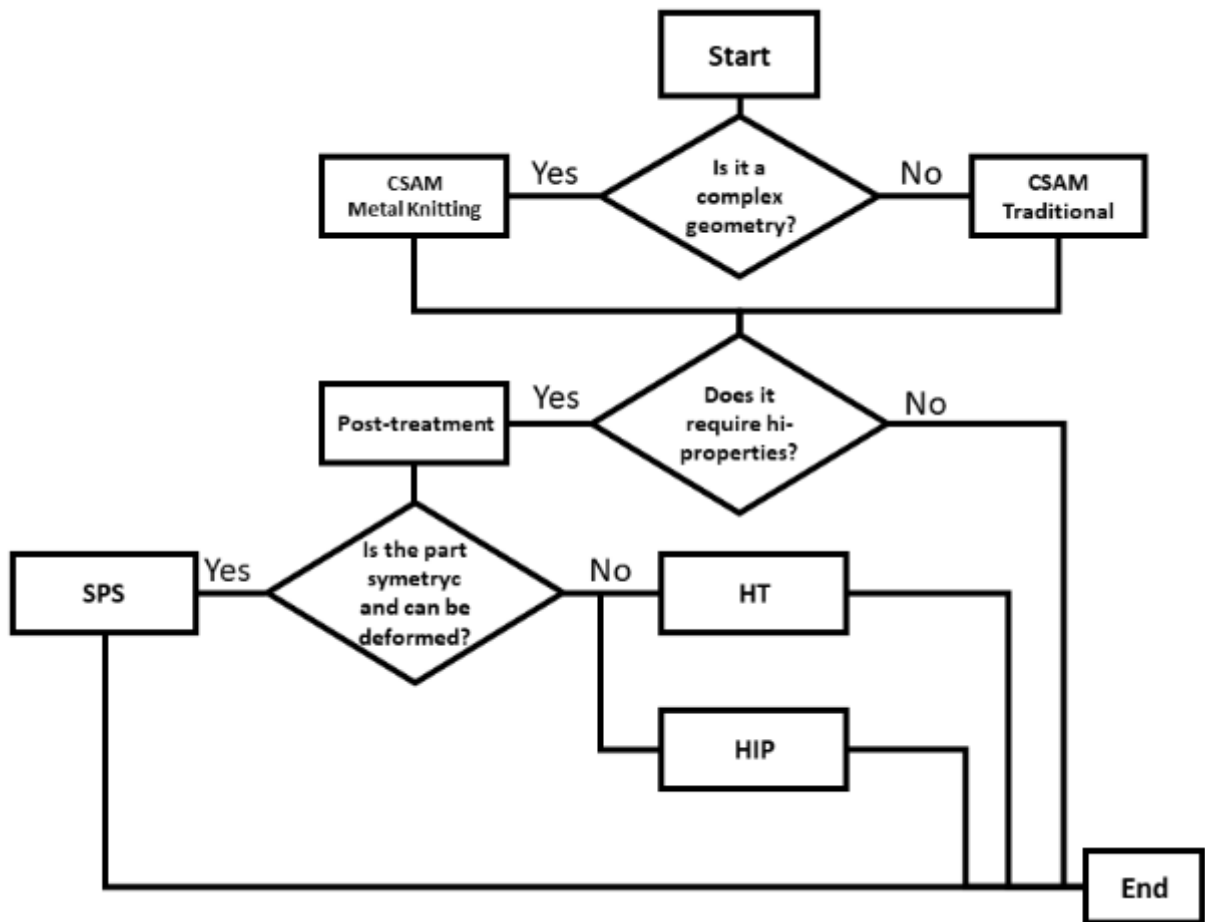


Figure 56: CSAM deposition decision flowchart

Chapter 6

CONCLUSIONS

6. CONCLUSIONS

In the different sections of this thesis, each article presented specific conclusions and remarks, which finally lead to the general conclusions listed below:

CSAM is a valid technique to produce parts with many metallic materials, highlighting Al, Cu, Ti, Ti6Al4V, 316L, Maraging, and Inconel 625. Each material needs optimized parameters, which are different for each CS equipment, to obtain V_{particle} in the window of deposition range. Different particle size distributions and shapes are available in the market with the same chemical composition. For CS spraying, they have to be appropriately selected, with consequences on the bonding, DE, material quality, and CSAM processing costs.

It is possible to reduce the CSAM costs by employing less expensive feedstock powders, which is attributed to similar microstructures obtained by irregular and spherical powders because the optimization of CS parameters imposes on the particles enough velocity to promote excellent bonding and particle deformation, as evidenced by similar adhesion, abrasion and friction wear resistance, and corrosion behavior. For a study conducted specifically for CS 316L, it can be concluded that there is no particular advantage in using the expensive gas atomized 316L powders over the cheaper water atomized ones.

The rotation strategy is useful for simple and symmetric geometries, resulting in good adhesion to the substrate; additionally, making complex geometries by CSAM is possible by employing adequate deposition and robot strategies. The rectifying passes eliminate the pyramid-like shape but demands alternated passes with different and specific spraying angles. However, for a continuous angle rectifying strategy, the CSAM Metal Knitting strategy is an excellent option for ductile materials, such as Cu and 316L, producing parts with good mechanical properties and similar microstructures to the traditional CSAM strategy. For harder materials, e.g., Ti6Al4V, CSAM Metal Knitting inputs lower velocity to the particles, resulting in a material with lower density than the obtained by CSAM traditional.

CSAM Metal Knitting strategy is not necessarily a substitute for the traditional one. Still, it can be a complementary stage to this one, redressing the sidewalls to lower angles. Therefore, a combination of robot strategies could be a solution for

specific applications, e.g., to build a large bulk. The traditional strategy can be applied for its central area, while knitting is used on the edges. This would prevent the sidewalls inclination and promote the best spraying angle deposition on the central location, which is 90 degrees, typical of the traditional strategy. In addition, Metal Knitting can be used for repairing elements, such as thin, worn, or damaged walls, e.g., Ti turbine blades.

Improve the CSAM-ed material mechanical properties is achieved by post-treatments, especially those involving high temperatures. HT, HIP, and SPS improve the cohesion of particles, consequently, the material strength; however, they promote phase changes, recrystallization, and decrease or complete elimination of cold work effects in the material. The HT is simpler and less costly than HIP and SPS ones, resulting in similar or identical final mechanical properties and microstructure, depending on the CS-ed material and post-treatment process parameters.

The interparticular region is the weakest part of the CSAM-ed material in as-sprayed condition, with the tensile testing fracture mechanism being the detachment of the particles following this interparticular path. However, the annealing improves the cohesion of particles by atomic diffusion and micro welding, changing the fracture mechanism to predominantly ductile.

Considering the CSAM-ed material isotropy, CSAM Metal Knitting and traditional strategies produce planar isotropy; nevertheless, anisotropy is evident when contrasting the substrate plane and the building direction, with this one weaker due to a lower cohesion of particles in this direction. HT can reduce this anisotropy, improving the material microstructural homogeneity. The HT also relieves the initial residual stress from the deposition process, homogenising it in the material.

CSAM produces compressive residual stress on the material surface and tensile one in the central volume, primarily due to the peening effect. It is an attractive property for fatigue life; however, the interparticular region weakness prevails over the residual stress state, reducing the fatigue life by the lower CSAM-ed material strength compared to the wrought material. HT post-treatment alters this residual stress distribution, homogenizing it in the material.

The use of CSAM as one of the steps of a part production is effective, and a hybrid process with thermal spraying HVOF produces parts with high wear and

corrosion resistance. The deposition of cermets, WC-12Co and WC-10Co4Cr, by HVOF on CSAM-ed Maraging improves the component's wear resistance. The sliding, abrasion wear, and water erosion rates were reduced drastically due to the hard coating. The hard coating also reduces the potential of corrosion.

Chapter 7

REFERENCES

7. REFERENCES

This section presents the references used in this work. However, each article has its own reference section, and some of the works listed below can be duplicated in the articles' reference section.

1. ISO/ASTM 52900-21 - *Standard Terminology for Additive Manufacturing – General Principles – Terminology*; ISO/ASTM: West Conshohocken, PA, USA, 2015;
2. ASTM E1920-03 - *Standard Guide for Metallographic Preparation of Thermal Sprayed Coatings*; ASTM International: West Conshohocken, PA, USA, 2021;
3. ASTM E3-11 - *Standard Guide for Preparation of Metallographic Specimens*; ASTM International: West Conshohocken, PA, USA, 2017;
4. ASTM B822-02 - *Standard Test Method for Particle Size Distribution of Metal Powders and Related Compounds by Laser Scattering*; ASTM International: West Conshohocken, PA, USA, 2002;
5. ASTM B212-21 - *Standard Test Method for Apparent Density of Powders Using the Hall Flowmeter Funnel*; ASTM International: West Conshohocken, PA, USA, 2021;
6. ASTM B213-20 - *Standard Test Method for Flow Rate of Metal Powders*; ASTM International: West Conshohocken, PA, USA, 2020;
7. ASTM B417-22 - *Standard Test Method for Apparent Density of Non-Free-Flowing Metal Powders Using the Carney Funnel*; ASTM International: West Conshohocken, PA, USA, 2022;
8. ISO 17836:2004 - *Thermal Spraying - Determination of Deposition Efficiency for Thermal Spraying*; ISO: Geneva, 2004;
9. Al-Mangour, B.; Vo, P.; Mongrain, R.; Irissou, E.; Yue, S. Effect of Heat Treatment on the Microstructure and Mechanical Properties of Stainless Steel 316L Coatings Produced by Cold Spray for Biomedical Applications. *J. Therm. Spray Technol.* **2014**, *23*, 641–652, doi:10.1007/s11666-013-0053-2.
10. Dikici, B.; Yilmazer, H.; Ozdemir, I.; Isik, M. The Effect of Post-Heat Treatment on Microstructure of 316L Cold-Sprayed Coatings and Their Corrosion Performance. *J. Therm. Spray Technol.* **2016**, *25*, 704–714, doi:10.1007/s11666-016-0402-z.
11. Bagherifard, S.; Kondas, J.; Monti, S.; Cizek, J.; Perego, F.; Kovarik, O.; Lukac, F.; Gaertner, F.; Guagliano, M. Tailoring Cold Spray Additive Manufacturing of Steel 316 L for Static and Cyclic Load-Bearing Applications. *Mater. Des.* **2021**, *203*, 109575, doi:10.1016/j.matdes.2021.109575.
12. Yin, S.; Cizek, J.; Yan, X.; Lupoi, R. Annealing Strategies for Enhancing Mechanical Properties of Additively Manufactured 316L Stainless Steel Deposited by Cold Spray. *Surf. Coatings Technol.* **2019**, *370*, 353–361, doi:10.1016/j.surfcoat.2019.04.012.
13. Brassart, L.-H.; Besson, J.; Delloro, F.; Haboussa, D.; Delabrouille, F.; Rolland,

- G.; Shen, Y.; Gourgues-Lorenzon, A.-F. Effect of Various Heat Treatments on the Microstructure of 316L Austenitic Stainless Steel Coatings Obtained by Cold Spray. *J. Therm. Spray Technol.* **2022**, *31*, 1725–1746, doi:10.1007/s11666-022-01402-3.
14. Matizamhuka, W.R. Spark Plasma Sintering (SPS) - An Advanced Sintering Technique for Structural Nanocomposite Materials. *J. South. African Inst. Min. Metall.* **2016**, *116*, 1171–1180, doi:10.17159/2411-9717/2016/v116n12a12.
 15. Guillon, O.; Gonzalez-Julian, J.; Dargatz, B.; Kessel, T.; Schierring, G.; Räthel, J.; Herrmann, M. Field-Assisted Sintering Technology/Spark Plasma Sintering: Mechanisms, Materials, and Technology Developments. *Adv. Eng. Mater.* **2014**, *16*, 830–849, doi:10.1002/adem.201300409.
 16. ASTM E2109-01 - *Standard Test Methods for Determining Area Percentage Porosity in Thermal Sprayed Coatings*; ASTM International: West Conshohocken, PA, USA, 2021;
 17. Garbe, U.; Randall, T.; Hughes, C.; Davidson, G.; Pangelis, S.; Kennedy, S.J. A New Neutron Radiography / Tomography / Imaging Station DINGO at OPAL. *Phys. Procedia* **2015**, *69*, 27–32, doi:10.1016/j.phpro.2015.07.003.
 18. Micieli, D.; Minniti, T.; Gorini, G. NeuTomPy Toolbox, a Python Package for Tomographic Data Processing and Reconstruction. *SoftwareX* **2019**, *9*, 260–264, doi:10.1016/j.softx.2019.01.005.
 19. ASTM E384-22 - *Standard Test for Microindentation Hardness of Materials*; ASTM International: West Conshohocken, PA, USA, 2022;
 20. ASTM C633-13 - *Standard Test Method for Adhesion or Cohesion Strength of Thermal Spray Coatings*; ASTM International: West Conshohocken, PA, USA, 2021;
 21. Oliver, W.C.; Pharr, G.M. An Improved Technique for Determining Hardness and Elastic Modulus Using Load and Displacement Sensing Indentation Experiments. *J. Mater. Res.* **1992**, *7*, 1564–1583, doi:10.1557/JMR.1992.1564.
 22. ASTM E8-22 - *Standard Test Methods for Tension Testing of Metallic Materials*; ASTM International: West Conshohocken, PA, USA, 2022;
 23. Luo, Q. A Modified X-Ray Diffraction Method to Measure Residual Normal and Shear Stresses of Machined Surfaces. *Int. J. Adv. Manuf. Technol.* **2022**, *119*, 3595–3606, doi:10.1007/s00170-021-08645-4.
 24. Kirstein, O.; Luzin, V.; Garbe, U. The Strain-Scanning Diffractometer Kowari. *Neutron News* **2009**, *20*, 34–36, doi:10.1080/10448630903241175.
 25. Sinclair-Adamson, R.; Luzin, V.; Duguid, A.; Kannoorpatti, K.; Murray, R. Residual Stress Distributions in Cold-Sprayed Copper 3D-Printed Parts. *J. Therm. Spray Technol.* **2020**, *29*, 1525–1537, doi:10.1007/s11666-020-01040-7.
 26. Luzin, V.; Kirstein, O.; Zahiri, S.H.; Fraser, D. Residual Stress Buildup in Ti Components Produced by Cold Spray Additive Manufacturing (CSAM). *J. Therm. Spray Technol.* **2020**, *29*, 1498–1507, doi:10.1007/s11666-020-01048-z.
 27. Vargas-Uscategui, A.; King, P.C.; Styles, M.J.; Saleh, M.; Luzin, V.; Thorogood,

- K. Residual Stresses in Cold Spray Additively Manufactured Hollow Titanium Cylinders. *J. Therm. Spray Technol.* **2020**, *29*, 1508–1524, doi:10.1007/s11666-020-01028-3.
28. Gnäupel-Herold, T. ISODEC: Software for Calculating Diffraction Elastic Constants. *J. Appl. Crystallogr.* **2012**, *45*, 573–574, doi:10.1107/S0021889812014252.
 29. ASTM G65-16 - *Standard Test Method for Measuring Abrasion Using the Dry Sand Rubber Wheel Apparatus*; ASTM International: West Conshohocken, PA, USA, 2021;
 30. ASTM G99-17 - *Standard Test Method for Wear Testing with a Pin-on-Disk Apparatus*; ASTM International: West Conshohocken, PA, USA, 2017;
 31. ASTM G73-10 - *Standard Test Method for Liquid Impingement Erosion Using Rotating Apparatus*; ASTM International: West Conshohocken, PA, USA, 2021;
 32. ASTM G171-03 - *Scratch Hardness of Materials Using a Diamond Stylus*; ASTM International: West Conshohocken, PA, USA, 2017;
 33. ASTM G59-97 - *Standard Test Method for Conducting Potentiodynamic Polarization Resistance Measurements*; ASTM International: West Conshohocken, PA, USA, 2020;
 34. ASTM G102-23 - *Standard Practice for Calculation of Corrosion Rates and Related Information from Electrochemical Measurements*; ASTM International: West Conshohocken, PA, USA, 2023;
 35. Pukasiewicz, A.G.M.; de Oliveira, W.R.; Váz, R.F.; de Souza, G.B.; Serbena, F.C.; Dosta, S.; Cano, I.G. Influence of the Deposition Parameters on the Tribological Behavior of Cold Gas Sprayed FeMnCrSi Alloy Coatings. *Surf. Coatings Technol.* **2021**, *428*, 127888, doi:10.1016/j.surfcoat.2021.127888.
 36. Ben Ohoud, M.; Obrecht, F.; Gatineua, L.; Levitz, P.; Van Damme, H. Surface Area, Mass Fractal Dimension, and Apparent Density of Powders. *J. Colloid Interface Sci.* **1988**, *124*, 156–161, doi:10.1016/0021-9797(88)90336-0.
 37. Zegzulka, J.; Gelnar, D.; Jezerska, L.; Prokes, R.; Rozbroj, J. Characterization and Flowability Methods for Metal Powders. *Sci. Rep.* **2020**, *10*, 21004, doi:10.1038/s41598-020-77974-3.
 38. Jenike, A. *Storage and Flow of Solids*; 1964; Vol. 53;.
 39. Palodhi, L.; Das, B.; Singh, H. Effect of Particle Size and Morphology on Critical Velocity and Deformation Behavior in Cold Spraying. *J. Mater. Eng. Perform.* **2021**, *30*, 8276–8288, doi:10.1007/s11665-021-05997-6.
 40. Nouri, A.; Sola, A. Metal Particle Shape: A Practical Perspective. *Met. Powder Rep.* **2018**, *73*, 276–282, doi:10.1016/j.mprp.2018.04.001.
 41. Fedina, T.; Sundqvist, J.; Powell, J.; Kaplan, A.F.H. A Comparative Study of Water and Gas Atomized Low Alloy Steel Powders for Additive Manufacturing. *Addit. Manuf.* **2020**, *36*, 101675, doi:10.1016/j.addma.2020.101675.
 42. Boisvert, M.; Christopherson, D.; Beaulieu, P.; L'Espérance, G. Treatment of Ferrous Melts for the Improvement of the Sphericity of Water Atomized Powders. *Mater. Des.* **2017**, *116*, 644–655, doi:10.1016/j.matdes.2016.12.059.

43. Vargas-Uscategui, A.; King, P.C.; Yang, S.; Chu, C.; Li, J. Toolpath Planning for Cold Spray Additively Manufactured Titanium Walls and Corners: Effect on Geometry and Porosity. *J. Mater. Process. Technol.* **2021**, *298*, 117272, doi:10.1016/j.jmatprotec.2021.117272.
44. Lohse, R.; Palzer, U. Drag Model for Coupled CFD-DEM Simulations of Non-Spherical Particles. In *OpenFOAM*; Springer International Publishing: Cham, 2019; pp. 121–131 ISBN 9783319608464.
45. ASTM A240/A240M-22a - Standard Specification for Chromium and Chromium-Nickel Stainless Steel Plate, Sheet, and Strip for Pressure Vessels and for General Applications; ASTM International: West Conshohocken, PA, USA, 2022;
46. Kim, K.; Li, W.; Guo, X. Detection of Oxygen at the Interface and Its Effect on Strain, Stress, and Temperature at the Interface between Cold Sprayed Aluminum and Steel Substrate. *Appl. Surf. Sci.* **2015**, *357*, 1720–1726, doi:10.1016/j.apsusc.2015.10.022.
47. Li, W.-Y.; Li, C.-J.; Liao, H. Significant Influence of Particle Surface Oxidation on Deposition Efficiency, Interface Microstructure and Adhesive Strength of Cold-Sprayed Copper Coatings. *Appl. Surf. Sci.* **2010**, *256*, 4953–4958, doi:10.1016/j.apsusc.2010.03.008.
48. Luo, X.-T.; Ge, Y.; Xie, Y.; Wei, Y.; Huang, R.; Ma, N.; Ramachandran, C.S.; Li, C.-J. Dynamic Evolution of Oxide Scale on the Surfaces of Feed Stock Particles from Cracking and Segmenting to Peel-off While Cold Spraying Copper Powder Having a High Oxygen Content. *J. Mater. Sci. Technol.* **2021**, *67*, 105–115, doi:10.1016/j.jmst.2020.06.019.
49. Fonseca, D.P.M. da; Feitosa, A.L.M.; Carvalho, L.G. de; Plaut, R.L.; Padilha, A.F. A Short Review on Ultra-High-Strength Maraging Steels and Future Perspectives. *Mater. Res.* **2021**, *24*, 1–11, doi:10.1590/1980-5373-mr-2020-0470.
50. Motyka, M.; Kubiak, K.; Sieniawski, J.; Ziaja, W. Phase Transformations and Characterization of $\alpha + \beta$ Titanium Alloys. In *Comprehensive Materials Processing*; Elsevier, 2014; Vol. 2, pp. 7–36.
51. Mauer, G.; Singh, R.; Rauwald, K.-H.; Schrüfer, S.; Wilson, S.; Vaßen, R. Diagnostics of Cold-Sprayed Particle Velocities Approaching Critical Deposition Conditions. *J. Therm. Spray Technol.* **2017**, *26*, 1423–1433, doi:10.1007/s11666-017-0596-8.
52. Schmidt, T.; Gärtner, F.; Assadi, H.; Kreye, H. Development of a Generalized Parameter Window for Cold Spray Deposition. *Acta Mater.* **2006**, *54*, 729–742, doi:10.1016/j.actamat.2005.10.005.
53. Ardeshiri Lordejani, A.; Colzani, D.; Guagliano, M.; Bagherifard, S. An Inclusive Numerical Framework to Assess the Role of Feedstock Features on the Quality of Cold Spray Deposits. *Mater. Des.* **2022**, *224*, 111374, doi:10.1016/j.matdes.2022.111374.
54. Rokni, M.R.; Nutt, S.R.; Widener, C.A.; Champagne, V.K.; Hrabec, R.H. Review of Relationship Between Particle Deformation, Coating Microstructure, and Properties in High-Pressure Cold Spray. *J. Therm. Spray Technol.* **2017**, *26*,

1308–1355, doi:10.1007/s11666-017-0575-0.

55. Assadi, H.; Kreye, H.; Gärtner, F.; Klassen, T. Cold Spraying – A Materials Perspective. *Acta Mater.* **2016**, *116*, 382–407, doi:10.1016/j.actamat.2016.06.034.
56. Brewer, L.N.; Schiel, J.F.; Menon, E.S.K.; Woo, D.J. The Connections between Powder Variability and Coating Microstructures for Cold Spray Deposition of Austenitic Stainless Steel. *Surf. Coatings Technol.* **2018**, *334*, 50–60, doi:10.1016/j.surfcoat.2017.10.082.
57. Wu, H.; Raelison, R.N.; Zhang, Y.; Deng, S.; Liao, H. Cold Spraying of 3D Parts – Challenges. In *Thermal Spray Coatings*; Thakur, L., Vasudev, H., Eds.; CRC Press: Boca Raton, 2021; pp. 37–58.
58. Matts, O.; Hammoud, H.; Sova, A.; Bensaid, Z.; Kermouche, G.; Klöcker, H.; Bosch, C.; Texier-Mandoki, N. Influence of Cold Spray Nozzle Displacement Strategy on Microstructure and Mechanical Properties of Cu/SiC Composites Coating. *Key Eng. Mater.* **2019**, *813*, 110–115, doi:10.4028/www.scientific.net/KEM.813.110.
59. Nardi, A.T.; El-Wardany, T.I.; Viens, D. V.; Lynch, M.E.; Hsu, A.; Klecka, M.A.; Gu, W. Additive Topology Optimized Manufacturing for Multi-Functional Components. *Pat. US 2014/0277669 A1* 2014, 1–33.
60. Wu, H.; Xie, X.; Liu, M.; Verdy, C.; Zhang, Y.; Liao, H.; Deng, S. Stable Layer-Building Strategy to Enhance Cold-Spray-Based Additive Manufacturing. *Addit. Manuf.* **2020**, *35*, 101356, doi:10.1016/j.addma.2020.101356.
61. Tsui, Y.C.; Clyne, T.W. An Analytical Model for Predicting Residual Stresses in Progressively Deposited Coatings Part 1: Planar Geometry. *Thin Solid Films* **1997**, *306*, 23–33, doi:10.1016/S0040-6090(97)00199-5.
62. Clyne, T.W.; Gill, S.C. Residual Stresses in Thermal Spray Coatings and Their Effect on Interfacial Adhesion: A Review of Recent Work. *J. Therm. Spray Technol.* **1996**, *5*, 401–418, doi:10.1007/BF02645271.
63. Luzin, V.; Kuroda, S.; Yin, S.; Ang, A.S.M. Advanced Residual Stress Analysis in Thermal Spray and Cold Spray Processes. *J. Therm. Spray Technol.* **2020**, *29*, 1211–1217, doi:10.1007/s11666-020-01083-w.
64. Vaßen, R.; Fiebig, J.; Kalfhaus, T.; Gibmeier, J.; Kostka, A.; Schrüfer, S. Correlation of Microstructure and Properties of Cold Gas Sprayed INCONEL 718 Coatings. *J. Therm. Spray Technol.* **2020**, *29*, 1455–1465, doi:10.1007/s11666-020-00988-w.
65. Nguyen, X.A.; Vargas-Uscategui, A.; Lohr, H.; Chu, C. A Continuous Toolpath Strategy from Offset Contours for Robotic Additive Manufacturing. *Int. J. Adv. Manuf. Technol.* **2022**, 1–17, doi:10.21203/rs.3.rs-2211954/v1.
66. Pan, Z.; Ding, D.; Wu, B.; Cuiuri, D.; Li, H.; Norrish, J. Arc Welding Processes for Additive Manufacturing: A Review. In *Transactions on Intelligent Welding Manufacturing*; Chen, S., Zang, Y., Feng, Z., Eds.; Springer: Singapore, 2018; pp. 3–24 ISBN 9789811053559.
67. Garfias, A.; Vaz, R.; Albaladejo-Fuentes, V.; Sánchez, J.; Cano, I.G. Geometry and Microstructure Control of Remanufactured Metallic Parts by Cold Spray

- Additive Manufacturing. *Materials (Basel)*. **2023**, *16*, 4735, doi:10.3390/ma16134735.
68. Julien, S.E.; Nourian-Avval, A.; Liang, W.; Schwartz, T.; Ozdemir, O.C.; Müftü, S. Bulk Fracture Anisotropy in Cold-Sprayed Al 6061 Deposits. *Eng. Fract. Mech.* **2022**, *263*, 1–17, doi:10.1016/j.engfracmech.2022.108301.
69. Lek, J.Y.; Bhowmik, A.; Tan, A.W.-Y.; Sun, W.; Song, X.; Zhai, W.; Buenconsejo, P.J.; Li, F.; Liu, E.; Lam, Y.M.; et al. Understanding the Microstructural Evolution of Cold Sprayed Ti-6Al-4V Coatings on Ti-6Al-4V Substrates. *Appl. Surf. Sci.* **2018**, *459*, 492–504, doi:10.1016/j.apsusc.2018.07.175.
70. Hussain, T. Cold Spraying of Titanium: A Review of Bonding Mechanisms, Microstructure and Properties. *Key Eng. Mater.* **2012**, *533*, 53–90, doi:10.4028/www.scientific.net/kem.533.53.
71. Wright, S.I.; Nowell, M.M.; Lindeman, S.P.; Camus, P.P.; De Graef, M.; Jackson, M.A. Introduction and Comparison of New EBSD Post-Processing Methodologies. *Ultramicroscopy* **2015**, *159*, 81–94, doi:10.1016/j.ultramic.2015.08.001.
72. Wilde, G.; Divinski, S. Grain Boundaries and Diffusion Phenomena in Severely Deformed Materials. *Mater. Trans.* **2019**, *60*, 1302–1315, doi:10.2320/matertrans.MF201934.
73. Lin, Y.C.; He, D.G.; Chen, M.S.; Chen, X.M.; Zhao, C.Y.; Ma, X.; Long, Z.L. EBSD Analysis of Evolution of Dynamic Recrystallization Grains and δ Phase in a Nickel-Based Superalloy during Hot Compressive Deformation. *Mater. Des.* **2016**, *97*, 13–24, doi:10.1016/j.matdes.2016.02.052.
74. Padilha, A.F.; Plaut, R.L.; Rios, P.R. Annealing of Cold-Worked Austenitic Stainless Steels. *ISIJ Int.* **2003**, *43*, 135–143, doi:10.2355/isijinternational.43.135.
75. Blinov, V.M.; Bannykh, I.O.; Lukin, E.I.; Bannykh, O.A.; Blinov, E. V.; Chernogorova, O.P.; Samoilova, M.A. Effect of Substitutional Alloying Elements on the Stacking Fault Energy in Austenitic Steels. *Russ. Metall.* **2021**, *2021*, 1325–1332, doi:10.1134/S0036029521100086.
76. Purcek, G.; Yapici, G.G.; Karaman, I.; Maier, H.J. Effect of Commercial Purity Levels on the Mechanical Properties of Ultrafine-Grained Titanium. *Mater. Sci. Eng. A* **2011**, *528*, 2303–2308, doi:10.1016/j.msea.2010.11.021.
77. Chen, C.; Xie, Y.; Yan, X.; Yin, S.; Fukunuma, H.; Huang, R.; Zhao, R.; Wang, J.; Ren, Z.; Liu, M.; et al. Effect of Hot Isostatic Pressing (HIP) on Microstructure and Mechanical Properties of Ti6Al4V Alloy Fabricated by Cold Spray Additive Manufacturing. *Addit. Manuf.* **2019**, *27*, 595–605, doi:10.1016/j.addma.2019.03.028.
78. Luo, X.T.; Wei, Y.K.; Wang, Y.; Li, C.J. Microstructure and Mechanical Property of Ti and Ti6Al4V Prepared by an In-Situ Shot Peening Assisted Cold Spraying. *Mater. Des.* **2015**, *85*, 527–533, doi:10.1016/j.matdes.2015.07.015.
79. Khalik, M.A.; Zahiri, S.H.; Masood, S.H.; Gulizia, S.; Faizan-Ur-Rab, M.; Palanisamy, S. Simultaneous Densification and Improvement of Cold Spray Additively Manufactured Ti-6Al-4 V Properties via Electro-Plastic Treatment. *Int. J. Adv. Manuf. Technol.* **2023**, *126*, 4297–4316, doi:10.1007/s00170-023-11401-

5.

80. Boruah, D.; Zhang, X.; McNutt, P.; Khan, R.; Begg, H. Effect of Post-Deposition Thermal Treatments on Tensile Properties of Cold Sprayed Ti6Al4V. *Metals (Basel)*. **2022**, *12*, 1908, doi:10.3390/met12111908.
81. Motyka, M. Martensite Formation and Decomposition during Traditional and AM Processing of Two-Phase Titanium Alloys—An Overview. *Metals (Basel)*. **2021**, *11*, 481, doi:10.3390/met11030481.
82. Liu, Q.; Wei, Y.; Luo, X.; Chen, C.; Wang, J.; Li, C.-J. Processing Map of the In-Situ Micro-Forging (MF) Assisted Cold Spray for Additive Manufacturing of Fully Dense Metals without MF Particle Inclusion. *Addit. Manuf.* **2023**, 103644, doi:10.1016/j.addma.2023.103644.
83. Moridi, A.; Hassani Gangaraj, S.M.; Vezzu, S.; Guagliano, M. Number of Passes and Thickness Effect on Mechanical Characteristics of Cold Spray Coating. *Procedia Eng.* **2014**, *74*, 449–459, doi:10.1016/j.proeng.2014.06.296.
84. Tan, A.W.-Y.; Sun, W.; Bhowmik, A.; Lek, J.Y.; Marinescu, I.; Li, F.; Khun, N.W.; Dong, Z.; Liu, E. Effect of Coating Thickness on Microstructure, Mechanical Properties and Fracture Behaviour of Cold Sprayed Ti6Al4V Coatings on Ti6Al4V Substrates. *Surf. Coatings Technol.* **2018**, *349*, 303–317, doi:10.1016/j.surfcoat.2018.05.060.
85. Petrovskiy, P.; Travyanov, A.; Cheverikin, V. V; Cheresheva, A.A.; Sova, A.; Smurov, I. Effect of Encapsulated Hot Isostatic Pressing on Properties of Ti6Al4V Deposits Produced by Cold Spray. *Int. J. Adv. Manuf. Technol.* **2020**, *107*, 437–449, doi:10.1007/s00170-020-05080-9.
86. Bocanegra-Bernal, M.H. Hot Isostatic Pressing (HIP) Technology and Its Applications to Metals and Ceramics. *J. Mater. Sci.* **2004**, *39*, 6399–6420, doi:10.1023/B:JMSE.0000044878.11441.90.
87. Kahlin, M. Fatigue Performance of Additive Manufactured Ti6Al4V in Aerospace Applications, Linköping University Electronic Press, 2017.
88. Weston, N.S.; Derguti, F.; Tudball, A.; Jackson, M. Spark Plasma Sintering of Commercial and Development Titanium Alloy Powders. *J. Mater. Sci.* **2015**, *50*, 4860–4878, doi:10.1007/s10853-015-9029-6.
89. Zadra, M.; Casari, F.; Girardini, L.; Molinari, A. Microstructure and Mechanical Properties of Cp-Titanium Produced by Spark Plasma Sintering. *Powder Metall.* **2008**, *51*, 59–65, doi:10.1179/174329008X277000.
90. Garfias Bulnes, A.; Albaladejo Fuentes, V.; Garcia Cano, I.; Dosta, S. Understanding the Influence of High Velocity Thermal Spray Techniques on the Properties of Different Anti-Wear WC-Based Coatings. *Coatings* **2020**, *10*, 1157, doi:10.3390/coatings10121157.
91. Pulsford, J.; Kamnis, S.; Murray, J.; Bai, M.; Hussain, T. Effect of Particle and Carbide Grain Sizes on a HVOAF WC-Co-Cr Coating for the Future Application on Internal Surfaces: Microstructure and Wear. *J. Therm. Spray Technol.* **2018**, *27*, 207–219, doi:10.1007/s11666-017-0669-8.
92. Couto, M.; Dosta, S.; Fernández, J.; Guilemany, J.M. Comparison of the Mechanical and Electrochemical Properties of WC-25Co Coatings Obtained by

- High Velocity Oxy-Fuel and Cold Gas Spraying. *J. Therm. Spray Technol.* **2014**, 23, 1251–1258, doi:10.1007/s11666-014-0123-0.
93. Lamana, M.S.; Pukasiewicz, A.G.M.M.; Sampath, S. Influence of Cobalt Content and HVOF Deposition Process on the Cavitation Erosion Resistance of WC-Co Coatings. *Wear* **2018**, 398–399, 209–219, doi:10.1016/j.wear.2017.12.009.
 94. Marques, A.S.; Dalcin, R.L.; Oliveira, L.F.; da Silva, L.A. V.; dos Santos, G.R.; da Silva Rocha, A. Comparative Analysis of the Friction and Microstructural Properties of WC-10Co-4Cr and Cr₃C₂-25NiCr Coatings Sprayed by High-Velocity Oxy-Fuel (HVOF). *Am. J. Mater. Sci.* **2018**, 8, 51–57, doi:10.5923/j.materials.20180803.02.
 95. Wood, R.J.K. Tribology of Thermal Sprayed WC-Co Coatings. *Int. J. Refract. Met. Hard Mater.* **2010**, 28, 82–94, doi:10.1016/j.ijrmhm.2009.07.011.
 96. Ding, X.; Cheng, X.D.; Shi, J.; Li, C.; Yuan, C.Q.; Ding, Z.X. Influence of WC Size and HVOF Process on Erosion Wear Performance of WC-10Co4Cr Coatings. *Int. J. Adv. Manuf. Technol.* **2018**, 96, 1615–1624, doi:10.1007/s00170-017-0795-y.
 97. Martins, V.; Rodrigues, W.C.; Ferrandini, P.L.; Villarinho, D.J.; Knörnschild, G.H.; Schaeffer, L. Comparative Studies of WC-Co and WC-Co-Ni Composites Obtained by Conventional Powder Metallurgy. *Mater. Res.* **2011**, 14, 274–279, doi:10.1590/S1516-14392011005000037.
 98. Fayyaz, A.; Muhamad, N.; Sulong, A.B.; Yunn, H.S.; Amin, S.Y.M.; Rajabi, J. Effect of Dry and Wet Ball Milling Process on Critical Powder Loading and Mixture Properties of Fine WC-10Co-0.8VC Powder. *J. Teknol.* **2012**, 59, 141–144, doi:10.11113/jt.v59.2580.
 99. Pukasiewicz, A.G.M.; de Boer, H.E.; Sucharski, G.B.; Vaz, R.F.; Procopiak, L.A.J. The Influence of HVOF Spraying Parameters on the Microstructure, Residual Stress and Cavitation Resistance of FeMnCrSi Coatings. *Surf. Coatings Technol.* **2017**, 327, 158–166, doi:10.1016/j.surfcoat.2017.07.073.
 100. Li, C.J.; Ohmori, A.; Harada, Y. Effect of Powder Structure on the Structure of Thermally Sprayed WC-Co Coatings. *J. Mater. Sci.* **1996**, 31, 785–794, doi:10.1007/BF00367900.
 101. Perry, J.M.; Neville, A.; Hodgkiess, T. A Comparison of the Corrosion Behavior of WC-Co-Cr and WC-Co HVOF Thermally Sprayed Coatings by In Situ Atomic Force Microscopy (AFM). *J. Therm. Spray Technol.* **2002**, 11, 536–541, doi:10.1361/105996302770348673.
 102. Magnani, M.; Suegama, P.H.; Espallargas, N.; Dosta, S.; Fugivara, C.S.; Guilemany, J.M.; Benedetti, A. V Influence of HVOF Parameters on the Corrosion and Wear Resistance of WC-Co Coatings Sprayed on AA7050 T7. *Surf. Coatings Technol.* **2008**, 202, 4746–4757, doi:10.1016/j.surfcoat.2008.04.055.
 103. Hegab, H.; Khanna, N.; Monib, N.; Salem, A. Design for Sustainable Additive Manufacturing: A Review. *Sustain. Mater. Technol.* **2023**, 35, e00576, doi:10.1016/j.susmat.2023.e00576.
 104. Soundarapandiyan, G.; Leung, C.L.A.; Johnston, C.; Chen, B.; Khan, R.H.U.; McNutt, P.; Bhatt, A.; Atwood, R.C.; Lee, P.D.; Fitzpatrick, M.E. In Situ

- Monitoring the Effects of Ti6Al4V Powder Oxidation during Laser Powder Bed Fusion Additive Manufacturing. *Int. J. Mach. Tools Manuf.* **2023**, *190*, 104049, doi:10.1016/j.ijmachtools.2023.104049.
105. Dejene, N.D.; Lemu, H.G. Current Status and Challenges of Powder Bed Fusion-Based Metal Additive Manufacturing: Literature Review. *Metals (Basel)*. **2023**, *13*, 424, doi:10.3390/met13020424.
 106. Seraj, R.A.; Abdollah-zadeh, A.; Dosta, S.; Canales, H.; Assadi, H.; Cano, I.G. The Effect of Traverse Speed on Deposition Efficiency of Cold Sprayed Stellite 21. *Surf. Coatings Technol.* **2019**, *366*, 24–34, doi:10.1016/j.surfcoat.2019.03.012.
 107. Assadi, H.; Gärtner, F.; Stoltenhoff, T.; Kreye, H. Bonding Mechanism in Cold Gas Spraying. *Acta Mater.* **2003**, *51*, 4379–4394, doi:10.1016/S1359-6454(03)00274-X.
 108. Singh, S.; Raman, R.K.S.; Berndt, C.C.; Singh, H. Influence of Cold Spray Parameters on Bonding Mechanisms: A Review. *Metals (Basel)*. **2021**, *11*, 2016, doi:10.3390/met11122016.
 109. Canales, H.; Cano, I.G.; Dosta, S. Window of Deposition Description and Prediction of Deposition Efficiency via Machine Learning Techniques in Cold Spraying. *Surf. Coatings Technol.* **2020**, *401*, 1–10, doi:10.1016/j.surfcoat.2020.126143.
 110. Lynch, M.E.; Gu, W.; El-Wardany, T.; Hsu, A.; Viens, D.; Nardi, A.; Klecka, M. Design and Topology/Shape Structural Optimisation for Additively Manufactured Cold Sprayed Components. *Virtual Phys. Prototyp.* **2013**, *8*, 213–231, doi:10.1080/17452759.2013.837629.
 111. Sun, W.; Tan, A.W.-Y.; Wu, K.; Yin, S.; Yang, X.; Marinescu, I.; Liu, E. Post-Process Treatments on Supersonic Cold Sprayed Coatings: A Review. *Coatings* **2020**, *10*, 123, doi:10.3390/coatings10020123.
 112. Luo, X.T.; Yao, M.L.; Ma, N.; Takahashi, M.; Li, C.J. Deposition Behavior, Microstructure and Mechanical Properties of an in-Situ Micro-Forging Assisted Cold Spray Enabled Additively Manufactured Inconel 718 Alloy. *Mater. Des.* **2018**, *155*, 384–395, doi:10.1016/j.matdes.2018.06.024.
 113. Liu, Q.; Wei, Y.-K.; Luo, X.-T.; Chen, C.-Y.; Wang, J.; Li, C.-J. Processing Map of the In-Situ Micro-Forging (MF) Assisted Cold Spray for Additive Manufacturing of Fully Dense Metals without MF Particle Inclusion. *Addit. Manuf.* **2023**, *73*, 103644, doi:10.1016/j.addma.2023.103644.
 114. Barton, D.J.; Bhattiprolu, V.S.; Thompson, G.B.; Brewer, L.N. Laser Assisted Cold Spray of AISI 4340 Steel. *Surf. Coatings Technol.* **2020**, *400*, 126218, doi:10.1016/j.surfcoat.2020.126218.
 115. Hamweendo, A.; Botef, I. Cold Spray Technology for Light Metals and Porous Structures. *Adv. Mater. Res.* **2014**, *1019*, 126–132, doi:10.4028/www.scientific.net/AMR.1019.126.
 116. Sun, J.; Han, Y.; Cui, K. Innovative Fabrication of Porous Titanium Coating on Titanium by Cold Spraying and Vacuum Sintering. *Mater. Lett.* **2008**, *62*, 3623–3625, doi:10.1016/j.matlet.2008.04.011.

117. Grujicic, M.; Zhao, C.L.; DeRosset, W.S.; Helfritch, D. Adiabatic Shear Instability Based Mechanism for Particles/Substrate Bonding in the Cold-Gas Dynamic-Spray Process. *Mater. Des.* **2004**, *25*, 681–688, doi:10.1016/j.matdes.2004.03.008.
118. Hussain, T.; McCartney, D.G.; Shipway, P.H.; Zhang, D. Bonding Mechanisms in Cold Spraying: The Contributions of Metallurgical and Mechanical Components. *J. Therm. Spray Technol.* **2009**, *18*, 364–379, doi:10.1007/s11666-009-9298-1.
119. Atkinson, H. V.; Davies, S. Fundamental Aspects of Hot Isostatic Pressing: An Overview. *Metall. Mater. Trans. A* **2000**, *31*, 2981–3000, doi:10.1007/s11661-000-0078-2.

Chapter 8:

APPENDIX

8. APPENDIX

This section presents works presented in congresses, symposiums, and conferences or submitted to journals, besides projects awarded projects and prizes received during the doctorate period (2019-2023). Some works do not contemplate additive manufacturing, which is this thesis theme; however, those academic documents presented processing by thermal spraying techniques and wear-resistant materials testing, which are themes of interest for the Ph.D. candidate.

Besides contributing as the first author and co-author of papers and congress works, the Ph.D. candidate collaborated with the academic community as articles and manuscripts reviewer. 28 works were reviewed during the doctorate period (2019-2023).

8.1. Works Published

#1	Journal:	Coatings, v.10, n.4, 417, p.1-13
	JCR Impact Factor:	3.4 (2022)
	Rank by Impact Factor:	Q2 in category Materials Science, Coating and Films (2022)
	DOI:	10.3390/coatings10040417
	Title:	Study of particle properties of different steels sprayed by arc spray process
	Authors:	R.F. Vaz, A.G.M. Pukasiewicz, H.D.C. Falls, L.A. Lourençato, R.S.C. Paredes
	Date:	04/2020

#2	Journal:	Ultrasonics-Sonochesmitry, v.69, n.105271, p.1-9
	JCR Impact Factor:	8.4 (2022)
	Rank by Impact Factor:	Q1 in category Acoustics (2022)
	DOI:	10.1016/j.ultsonch.2020.105271
	Title:	Evaluation of cavitation/corrosion synergy of the Cr ₃ C ₂ -25NiCr coating deposited by HVOF process
	Authors:	A.R. Mayer, K. Bertuol, I.B.A.F. Siqueira, A. Chicoski, R.F. Vaz, M.J. de Sousa, A.G.M. Pukasiewicz
	Date:	12/2020

#3	Journal:	Journal of Thermal Spray Technology, v.30, p.754-771
	JCR Impact Factor:	3.1 (2022)
	Rank by Impact Factor:	Q3 in category Materials Science, Coating and Films (2022)
	DOI:	10.1007/s11666-020-01145-z
	Title:	Comparison of FeMnCrSi cavitation resistance coatings deposited by twin-wire electric arc and high-velocity oxy-fuel processes
	Authors:	R.F. Vaz, G.B. Sucharski, A. Chicoski, I.B.A.F. Siqueira, R. Tristante, A.G.M. Pukasiewicz
	Date:	01/2021

#4	Journal:	Coatings, v.11, n.2, 168, p.1-18
	JCR Impact Factor:	3.4 (2022)
	Rank by Impact Factor:	Q2 in category Materials Science, Coating and Films (2022)
	DOI:	10.3390/coatings11020168
	Title:	The influence of the powder characteristics on 316L coatings sprayed by cold gas spray
	Authors:	R.F. Vaz, A. Silvello, J. Sanchez, V. Albaladejo, I.G. Cano
	Date:	01/2021

#5	Journal:	Soldagem e Inspeção, v.26, n.e2540, p.1-13
	JCR Impact Factor:	0.6 (2022)
	Rank by Impact Factor:	Q4 in category Metallurgy and Metallurgical Engineering (2022)
	DOI:	10.1590/0104-9224/SI25.40
	Title:	Welding and thermal spray processes for maintenance of hydraulic turbine runners: case studies
	Authors:	R.F. Vaz, R. Tristante, A.G.M. Pukasiewicz, A.R. Capra, A. Chicoski, C.G. Filippin, R.S.C. Paredes, S.L. Henke
	Date:	04/2021

#6	Journal:	Wear, v.477, n.203797, p.1-11
	JCR Impact Factor:	5.0(2022)
	Rank by Impact Factor:	Q1 in category Engineering, Mechanical (2022)
	DOI:	10.1016/j.wear.2021.203797
	Title:	Artificial neural networks applied to the analysis of performance and wear resistance of binary coatings Cr ₃ C ₂ -37WC-18M and WC-20Cr ₃ C ₂ -7Ni
	Authors:	A. Becker, A.G.M. Pukasiewicz, H.D.C. Fals, A.S. Roca, I.B.A.F. Siqueira, F.R. Caliani, J.R. da Cruz, R.F. Vaz, M.J. de Sousa
	Date:	07/2021

#7	Journal:	Metals, v.11, n.7, 1092, p.1-14
	JCR Impact Factor:	2.9 (2022)
	Rank by Impact Factor:	Q2 in category Metallurgy and Metallurgical Engineering (2022)
	DOI:	10.3390/met11071092
	Title:	Improving the wear and corrosion resistance of Maraging part obtained by cold gas spray additive manufacturing
	Authors:	R.F. Vaz, A. Silvello, V. Albaladejo, J. Sanchez, I.G. Cano
	Date:	07/2021

#8	Journal:	Metallography, Microstructure, and Analysis, v.10, p.496-513
	JCR Impact Factor:	1.6 (2022)
	Rank by Impact Factor:	Q2 in category Metallurgy and Metallurgical Engineering (2022)
	DOI:	10.1007/s13632-021-00758-2
	Title:	Fretting wear and scratching resistance of cold sprayed pure Cu and Ti
	Authors:	R.F. Vaz, A. Silvello, P.D. Cavalieri, S. Dosta, I.G. Cano, L. Capodieci, A. Rizzo, D. Valerini
	Date:	07/2021

#9	Journal:	Surface and Coatings Technology, v.428, n.127888, p.1-15
	JCR Impact Factor:	5.4 (2022)
	Rank by Impact Factor:	Q1 in category Materials Sciences, Coatings and Films (2022)
	DOI:	10.1016/j.surfcoat.2021.127888
	Title:	Influence of the deposition parameters on the tribological behavior of cold gas sprayed FeMnCrSi alloy coatings
	Authors:	A.G.M. Pukasiewicz, R.F. Vaz, G.B. de Souza, F.C. Serbena, S. Dosta, I.G. Cano
	Date:	11/2021

#10	Journal:	International Journal of Abrasive Technology, v.10, n.4, p.235-258
	SJR Impact Factor:	0.3 (2022)
	Rank by Impact Factor:	Q3 in category Engineering – Industrial and Manufacturing Engineering (2022)
	DOI:	10.1504/IJAT.2021.120261
	Title:	The reuse of alumina for grit blasting preparation of steel surface for thermal spraying
	Authors:	R.F. Vaz, A.G.M. Pukasiewicz, G.B. Sucharski, I.B.A.F. Siqueira, S.M.Z. Odake, R.S.C. Paredes
	Date:	01/2021

#11	Journal:	Surface and Coatings Technology, v.438, n.128398, p.1-15
	JCR Impact Factor:	5.4 (2022)
	Rank by Impact Factor:	Q1 in category Materials Sciences, Coatings and Films (2022)
	DOI:	10.1016/j.surfcoat.2022.128398
	Title:	Evaluation of high temperature corrosion resistance of CrN, AlCrN, and TiAlN coatings obtained by PVD on Waspaloy
	Authors:	G. Biava, I.B.A.F. Siqueira, R.F. Vaz, G.B. de Souza, H.C.M. Jambo, A.G.M. Pukasiewicz
	Date:	03/2022

#12	Journal:	Materials, v.15, n.19, 6785, p.1-17
	JCR Impact Factor:	3.4 (2022)
	Rank by Impact Factor:	Q2 in category Metallurgy and Metallurgical Engineering (2022)
	DOI:	10.3390/ma15196785
	Title:	Metal Knitting: a new strategy for cold gas spray additive manufacturing
	Authors:	R.F. Vaz, V. Albaladejo, J. Sanchez, U. Ocaña, Z. García Corral, H. Canales, I.G. Cano
	Date:	09/2022

#13	Journal:	Coatings, v.13, n.2, 267, p.1-46
	JCR Impact Factor:	3.4 (2022)
	Rank by Impact Factor:	Q2 in category Materials Science, Coating and Films (2022)
	DOI:	10.3390/coatings13020267
	Title:	A review of advances in cold spray additive manufacturing
	Authors:	R.F. Vaz, A. Garfias, V. Albaladejo, J. Sanchez, I.G. Cano
	Date:	01/2023

#14	Journal:	Additive Manufacturing
	JCR Impact Factor:	11.0 (2022)
	Rank by Impact Factor:	Q1 in category Engineering, Manufacturing (2022)
	DOI:	
	Title:	The effect of annealing and deposition strategy on 316L properties produced by cold spray additive manufacturing
	Authors:	R.F. Vaz, V. Luzin, F. Salvemini, V. Albaladejo, J. Sanchez, I.G. Cano
	Date:	Submitted

#15	Journal:	Materials
	JCR Impact Factor:	3.4 (2022)
	Rank by Impact Factor:	Q2 in category Metallurgy and Metallurgical Engineering (2022)
	DOI:	10.3390/ma16134735
	Title:	Geometry and microstructure control of remanufactured metallic parts by Cold Spray Additive Manufacturing
	Authors:	A. Garfias, R.F. Vaz, V. Albaladejo, J. Sanchez, I.G. Cano
	Date:	06/2023

#16	Journal:	Surface and Coatings Technology
	JCR Impact Factor:	5.4 (2022)
	Rank by Impact Factor:	Q1 in category Materials Sciences, Coatings and Films (2022)
	DOI:	
	Title:	Cavitation resistance of FeMnCrSi coatings processed by different thermal spray processes
	Authors:	R.F. Vaz, L.L. Silveira, J.R. da Cruz, A.G.M. Pukasiewicz
	Date:	Submitted

8.2. Works Presented in Congresses

Event:	Holistic Innovation in Additive Manufacturing (HI-AM) 2020
Organizer:	Natural Sciences and Engineering Research Council of Canada (NSERC)
Location:	online
Date:	25-26 June 2020
Title:	Influence of thickness of coating on adherence of 316L and Cu coatings deposited by cold gas spraying
Authors:	R.F. Vaz, A. Silvello, J. Sanchez, I.G. Cano, S. Dosta
Presentation:	Poster

Event:	International Thermal Spray Conference (ITSC 2021)
Organizer:	Thermal Spray Society (TSS) of American Society for Metals (ASM)
Location:	online
Date:	24-28 May 2021
Title:	Thermal spraying of FeMnCrSi alloys: an overview
Authors:	R.F. Vaz, A.G.M. Pukasiewicz, I.B.A.F. Siqueira, G.B. Sucharski, R. Tristante
Presentation:	Oral

Event:	International Thermal Spray Conference (ITSC 2021)
Organizer:	Thermal Spray Society (TSS) of American Society for Metals (ASM)
Location:	online
Date:	24-28 May 2021
Title:	Tribological properties of Cold Gas Spraying FeMnCrSi alloy
Authors:	R.F. Vaz, A.G.M. Pukasiewicz, S. Dosta, I.G. Cano
Presentation:	Oral

Event:	International Thermal Spray Conference (ITSC 2021)
Organizer:	Thermal Spray Society (TSS) of American Society for Metals (ASM)
Location:	online
Date:	24-28 May 2021
Title:	Influence of fuel/oxygen ratio on coating properties and cavitation resistance of WC and Cr ₃ C ₂ cermet coatings deposited by HVOF
Authors:	A. Becker, K. Bertuol, A.G.M. Pukasiewicz, I.B.A.F. Siqueira, A. Chicoski, F.R. Caliar, R.F. Vaz, M.J. de Sousa
Presentation:	Oral

Event:	23 rd International Conference on Wear of Materials (WOM 2021)
Organizer:	Elsevier
Location:	Online
Date:	25-26 June 2020
Title:	Artificial neural networks applied to the analysis of performance and wear resistance of binary coatings Cr ₃ C ₂ -37WC-18M and WC-20Cr ₃ C ₂ -7Ni
Authors:	A. Becker, A.G.M. Pukaszewicz, H.D.C. Fals, A.S. Roca, I.B.A.F. Siqueira, F.R. Caliani, J.R. da Cruz, R.F. Vaz, M.J. de Sousa
Presentation:	Oral

Event:	International Thermal Spray Conference (ITSC 2022)
Organizer:	Thermal Spray Society (TSS) of American Society for Metals (ASM)
Location:	Vienna, Austria
Date:	04-06 May 2022
Title:	CGS metallization of polymers for 3D printing
Authors:	R.F. Vaz, A. Garfias, V. Albaladejo, J. Sánchez, I.G. Cano
Presentation:	Poster

Event:	International Thermal Spray Conference (ITSC 2022)
Organizer:	Thermal Spray Society (TSS) of American Society for Metals (ASM)
Location:	Vienna, Austria
Date:	04-06 May 2022
Title:	Metal Knitting: A method to control morphology and properties in cold spray additive manufacturing
Authors:	R.F. Vaz, H. Canales, J. Sanchez, U. Ocaña, V. Albaladejo, I.G. Cano
Presentation:	Oral

Event:	International Thermal Spray Conference (ITSC 2022)
Organizer:	Thermal Spray Society (TSS) of American Society for Metals (ASM)
Location:	Vienna, Austria
Date:	04-06 May 2022
Title:	Influence of the substrate properties on the cold gas spray deposition efficiency
Authors:	V. Albaladejo, R.F. Vaz, A. Garfias, J. Sanchez, I.G. Cano
Presentation:	Poster

Event:	Congreso Nacional de Materiales (CNMAT 2022)
Organizer:	Sociedad Española de Materiales (SOCIEMAT)
Location:	Ciudad Real, Spain
Date:	25-26 June 2022
Title:	Efecto de tratamiento térmico en piezas metálicas hechas por manufactura aditiva por proyección fría
Authors:	R.F. Vaz, V. Albaladejo, J. Sánchez, I.G. Cano
Presentation:	Oral

Event:	Congreso Nacional de Materiales (CNMAT 2022)
Organizer:	Sociedad Española de Materiales (SOCIEMAT)
Location:	Ciudad Real, Spain
Date:	25-26 June 2022
Title:	Preparación de geometrías planas mediante fabricación aditiva con proyección fría
Authors:	A. Garfías, R.F. Vaz, J. Sánchez, V. Albaladejo, I.G. Cano
Presentation:	Poster

Event:	III Congreso Internacional de Ingeniería Mecánica (COIIM)
Organizer:	Universidad Señor de Sipán
Location:	Online
Date:	27-28 October 2022
Title:	La evolución de la manufactura aditiva de metales y el empleo del proceso de proyección fría
Authors:	R.F. Vaz
Presentation:	Conferencia Magistral

Event:	23as Jornadas Técnicas de Soldadura y Tecnologías de Unión
Organizer:	Asociación Española de Soldadura y Tecnologías de Unión (CESOL)
Location:	Irún, Spain
Date:	7-9 March 2023
Title:	Comparación de recubrimientos de FeMnCrSi hechos por proyección fría y plasma de arco transferido
Authors:	R.F. Vaz, J. Sanchez, I.G. Cano, A.G.M. Pukasiewicz
Presentation:	Oral

Event:	23as Jornadas Técnicas de Soldadura y Tecnologías de Unión
Organizer:	Asociación Española de Soldadura y Tecnologías de Unión (CESOL)
Location:	Irún, Spain
Date:	7-9 March 2023
Title:	El efecto de la normalización en las propiedades del 316L obtenido por proyección fría
Authors:	R.F. Vaz, V. Albaladejo, J. Sanchez, I.G. Cano
Presentation:	Oral

Event:	International Thermal Spray Conference (ITSC 2023)
Organizer:	Thermal Spray Society (TSS) of American Society for Metals (ASM)
Location:	Quebec City, QC, Canada
Date:	22-25 May 2023
Title:	Effect of mixing He/N ₂ as cold spray atomizing gas on Ti6Al4V properties
Authors:	R.F. Vaz, N. Shukla, J. Sanchez, V. Gomez, I.G. Cano
Presentation:	Poster

Event:	International Thermal Spray Conference (ITSC 2023)
Organizer:	Thermal Spray Society (TSS) of American Society for Metals (ASM)
Location:	Quebec City, QC, Canada
Date:	22-25 May 2023
Title:	Near-net shape repair of Ti6Al4V thin-walled components by CSAM
Authors:	A. Garfias, R.F. Vaz, V. Albaladejo, Z. Garcia Corral, J. Sanchez, I.G. Cano
Presentation:	Poster

Event:	International Thermal Spray Conference (ITSC 2023)
Organizer:	Thermal Spray Society (TSS) of American Society for Metals (ASM)
Location:	Quebec City, QC, Canada
Date:	22-25 May 2023
Title:	Metal 3D printing of new structured surface BPPs for PEMWEs by Cold Gas Spraying
Authors:	A. Garfias, R.F. Vaz, A. Rocha, V. Albaladejo, R. Ferreira, J. Sanchez, M. Sarret, D. Falcão, I.G. Cano, A.M.F.R. Pinto, T. Andreu
Presentation:	Oral

Event:	CEIPM 2023 – Congreso Español Iberoamericano de Pulvimetalurgia. VIII Congreso Nacional / III Congreso Iberoamericano
Organizer:	Comité Español de Pulvimetalurgia (CEP)
Location:	San Sebastian, Spain
Date:	29-31 May 2023
Title:	Annealing effect on the microstructure of reconstructed metallic parts by the cold spray Metal Knitting method
Authors:	A. Garfias, R.F. Vaz, V. Albaladejo, J. Sánchez, I.G. Cano
Presentation:	Oral

8.3. Awards and Funding Projects

Grant:	FI-SDUR grant for pre-doctoral researchers
Funder:	Catalonia Government (Generalitat de Catalunya)
Title:	Development of strategy to make thick hard coatings by cold spray
Authors:	R.F. Vaz
Date:	20 October 2020
Funding:	68,197.78€

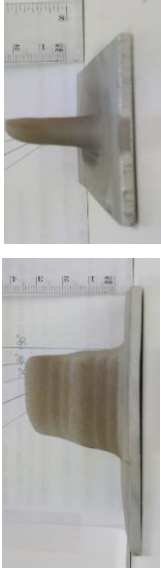

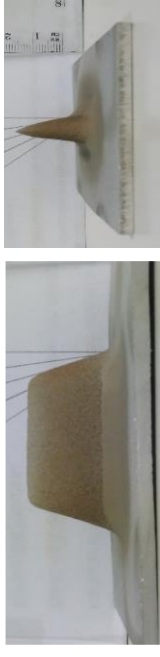


Project:	Calling: ACNS & NDF 2022-1 Proposal: 13534
Funder:	Australian Centre for Neutron Scattering
Title:	Evaluation of residual stress in 316L and Al cold gas spray additive manufacturing parts
Authors:	R.F. Vaz, V. Luzin, I.G. Cano, J. Sanchez
Date:	13 June 2022
Funding:	9 days of Kowari equipment using for neutron diffraction

Project:	Calling: PETRA III 2023/1 Proposal: I-20230101
Funder:	Deutsches Elektronen-Synchrotron DESY
Title:	Residual Stress Evolution by Heat Treatment of Ti alloys parts produced by Cold Spray Additive Manufacturing
Authors:	R.F. Vaz, J.A. Avila, I.G. Cano, J. Sanchez
Date:	03 June 2023
Funding:	48 h in beamline P61


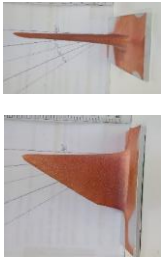
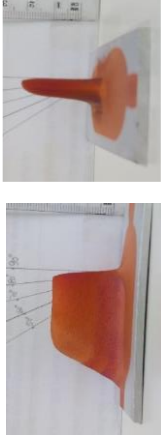


Award:	Editor's choice paper
Journal:	Coatings
Organizer	Multidisciplinary Digital Publishing Institute (MDPI)
Title:	The influence of the powder characteristics on 316L coatings sprayed by cold gas spray
Authors:	R.F. Vaz, A. Silvello, J. Sanchez, V. Albaladejo, I.G. Cano
Date:	20 October 2022
Prize:	A free article publishing in MPDI journals ($\pm 2,050\text{€}$)

Award:	Best presentation of the “Fabricación Aditiva” session
Event:	23as Jornadas Técnicas de Soldadura y Tecnologías de Unión
Organizer	Asociación Española de Soldadura y Tecnologías de Unión (CESOL)
Title:	Comparación de recubrimientos de FeMnCrSi hechos por proyección fría y plasma de arco transferido
Authors:	R.F. Vaz, J. Sanchez, I.G. Cano, A.G.M. Pukasiewicz
Date:	09 March 2023
Prize:	1,000€



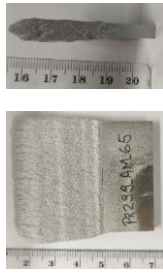
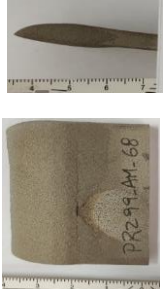

8.4. CSAM-ed Parts, Strategy, Parameters, Geometric Aspects, and Images

Materials	Parameters							Results				Images			
	Strategy	Radius [mm]	Angle [°]	Robot Speed [mm/s]	Step [mm]		Amount of steps	Layers	Thickness [mm]	Sidewall angle [°]					
					Hor.	Vert.				Per layer	Top		Bottom	Sides	
316L on Al	Metal Knitting	2	35	200	1	0	40	1	4	24	6	90	85	85	
316L on Al	Metal Knitting	2	45	200	1	0	40	1	7	30	4.5	90	85	90	
316L on Al	Metal Knitting	2	15	200	1	0	40	1	5	18.2	5	80	80	80	
316L on Al	Metal Knitting	2	35	200	1	3	40	13	1	14	14	90	50	70	
316L on steel	Metal Knitting	2	30	200	1	0	66	1	4	16	4	90	90	90	





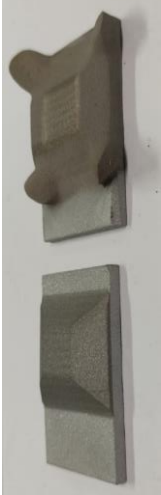
continued

Materials	Parameters						Results				Images				
	Strategy	Radius [mm]	Angle [°]	Robot Speed [mm/s]	Step [mm]		Amount of steps	Layers	Thickness [mm]	Sidewall angle [°]					
					Hor.	Vert.				Hor.		Vert.	Total	Per layer	Top
Ti on Ti	Metal Knitting	2	30	200	1	0	69	1	3	15	5	90	90	100	 <p>after and before post-machining process</p>
Cu on Al	Metal Knitting	2	30	200	1	0	40	1	12	64	6.0	90	50	90	 <p>↓ number of horizontal steps each layer to control the bottom angle</p>
Cu on Al	Metal Knitting	2	30	200	1	0	40	1	4	24	6.0	85	60	90	
316L on Al	Metal Knitting	3	35	200	1.5	1.5	24	24	16	58	3.5	90	80	85	
IN625 on IN625	Metal Knitting	2	30	200	1	0	67	1	1	3	3.0	80	80	80	 <p>Bonding failure in the interface CSAM-ed/substrate</p>


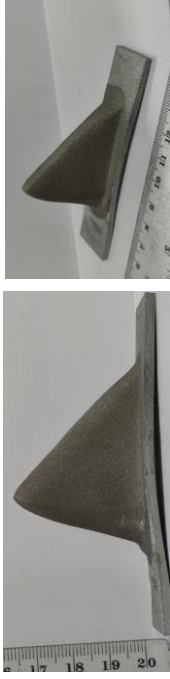



continued

Materials	Parameters						Results				Images				
	Strategy	Radius [mm]	Angle [°]	Robot Speed [mm/s]	Step [mm]		Layers	Thickness [mm]	Sidewall angle [°]						
					Hor.	Vert.			Total	Per layer		Top	Bottom	Sides	
															Hor. Vert.
Cu on Cu	Metal Knitting	2	20	200	1	0	57	1	4	23	6.0	90	90	95	
Ti on Ti	Metal Knitting	2	20	200	1	0	57	1	6	22	3.5	90	90	90	
Al on Al	Metal Knitting	3	30	200	1	0	40	1	6	34	5.5	90	90	90	
316L on steel	Metal Knitting	3	30	200	1	0	40	1	8	20	3.0	90	90	90	
Ti6Al4V on Ti6Al4V	Metal Knitting	2	30	200	1	0	40	1	4	30	7.5	95	95	95	




continued

Materials	Parameters						Results				Images				
	Strategy	Radius [mm]	Angle [°]	Robot Speed [mm/s]	Step [mm]		Amount of steps		Layers	Thickness [mm]		Sidewall angle [°]			
					Hor.	Vert.	Hor.	Vert.				Total	Per layer	Top	Bottom
Ti6Al4V on Al	Traditional			500	1		50		100	50.5	0.5	90	90	90	
Ti6Al4V on Al	Metal Knitting	3	30	200	3	4	13	9	6	50	8.0	85	80	85	
Ti on Al	Traditional			500	1		50		360	47	0.1	90	90	90	
316L on Al	Traditional			250	1		20		18	3	0.2	85	75	90	
316L on Al	Traditional			250	1		20		20	3	0.2				 <p>Before and after CSAM of sidewall angle correction layers, inclined gun, surrounding the inclined sidewalls. Accumulated material on the corners.</p>

continued

Materials	Parameters						Results				Images			
	Strategy	Radius [mm]	Angle [°]	Robot Speed [mm/s]	Step [mm]		Amount of steps	Layers	Thickness [mm]			Sidewall angle [°]		
					Hor.	Vert.			Total	Per layer		Top	Bottom	Sides
316L on Al	Traditional			250	1		100	132	19	0.1	80	80	80	
316L on Al	Metal Knitting	2.5	25	200	1	1.25	1	40	14	2.5	20	45	90	
Al on Al	Traditional			500	0.75		45	110	32	0.3	90	90	90	
Al on Al	Metal Knitting	2	30	200	2	2	30	2	29	14.5	95	95	95	
316L on steel	Traditional			250	1		45	155	33	0.2	75	75	75	

continued

Materials	Parameters							Results				Images			
	Strategy	Radius [mm]	Angle [°]	Robot Speed [mm/s]	Step [mm]		Amount of steps	Layers	Thickness [mm]		Sidewall angle [°]				
					Hor.	Vert.			Total	Per layer	Top		Bottom	Sides	
316L on steel	Metal Knitting	3	30	200	3	3	18	18	16	30	2.0	90	80	85	
IN718 on Al	Metal Knitting	1	25	200	1	0	250	1	10	30	3.0	90	90	90	
316L on Al	Metal Knitting	1	25	200	1	0	250	1	10	15	1.5	85	85	85	
316L on Al	Traditional			500	1		40		30	36	1.2	70	65	70	